

**Impact of Organic Osmolytes and Crowding on  
the Protein-Protein Interaction at High Pressures**  
-  
**A Small-Angle X-ray Scattering Study**

Dissertation  
for obtaining the academic degree  
Doctor rerum naturalium  
(Dr. rer. nat.)  
from the TU Dortmund University

submitted to the Faculty of Physics by

M.Sc. Karin Julius  
from Marienheide

Dortmund 2019

Referee/Supervisor

Prof. Dr. M. Tolan

Prof. Dr. R. Winter

Work presented here has been carried out at the Faculty of Physics,  
Experimental Physics E IA / DELTA, TU Dortmund University.

Financial support by the Cluster of Excellence RESOLV (EXC 1069) funded by the Deutsche Forschungsgemeinschaft is gratefully acknowledged (Deutsche Forschungsgemeinschaft (DFG, German Research Foundation) under Germany's Excellence Strategy, EXC-2033, Projektnummer 390677874.).



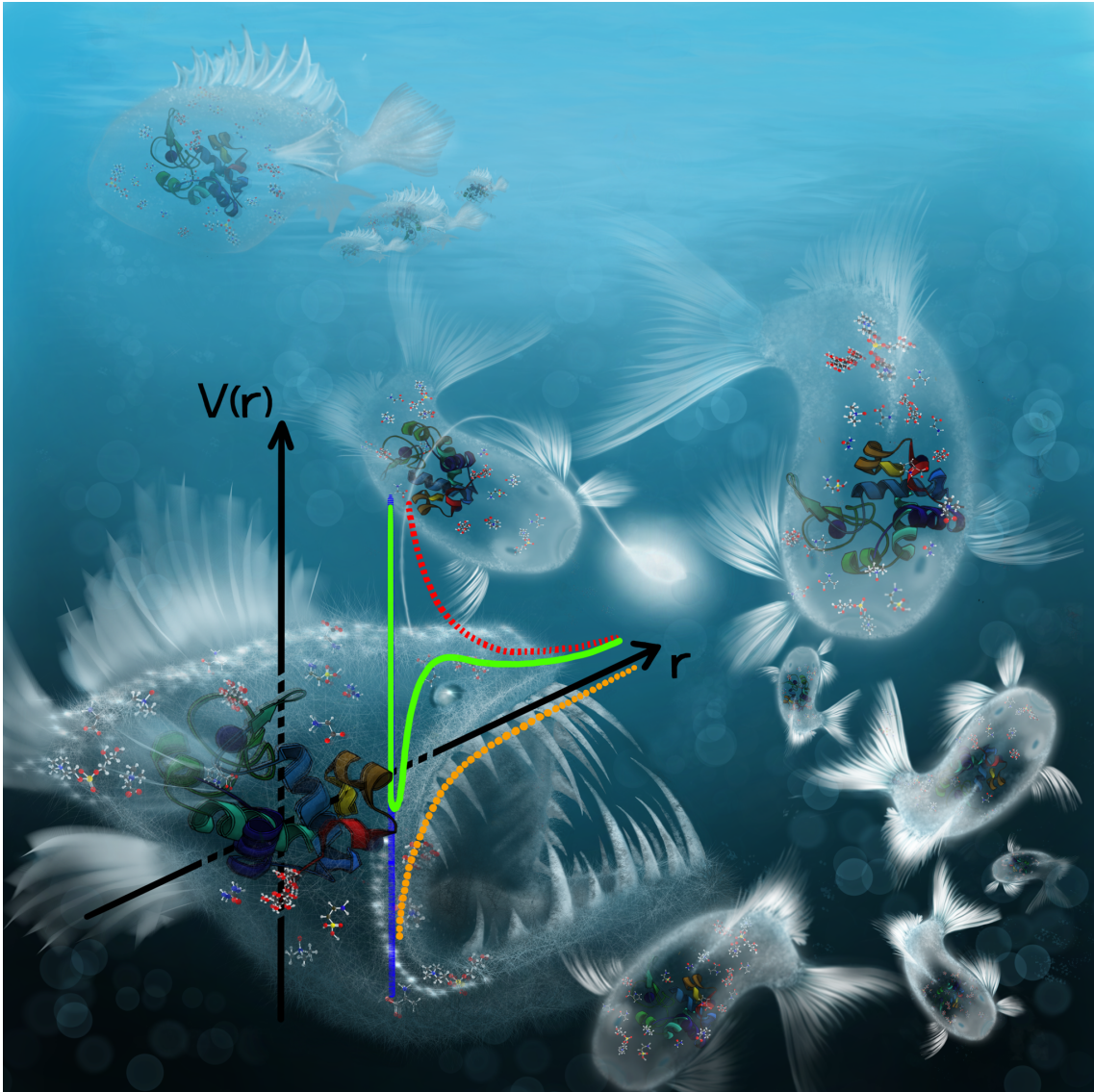


Figure 1: Natural osmolytes such as Trimethylamine N-oxide (TMAO) are not only able to stabilize the folded structure of proteins, they control intermolecular interactions as well and prevent protein from pressure-induced deterioration and aggregation in extreme environments. Reprinted with permission from [Julius et al., 2018b], Copyright © 2018 American Physical Society.

# Contents

<b>1</b>	<b>Motivation</b>	<b>1</b>
<b>2</b>	<b>Theory</b>	<b>6</b>
2.1	The Cellular Milieu . . . . .	6
2.1.1	Molecular Crowding - The Excluded Volume Effect . . . . .	6
2.1.2	Organic Osmolytes - Cellular Adaption to Environmental Stresses . . . . .	12
2.2	Model Systems and Intermolecular Interaction Potentials in Aqueous Biomolecular Systems . . . . .	17
2.2.1	Lifshitz Theory - Van der Waals Interaction between Macroscopic Particles . . . . .	18
2.2.2	Depletion Theory and Osmotic Attraction Potential . . . . .	21
2.2.3	Derjaguin Landau Verwey Overbeek (DLVO) - Theory of Colloidal Stability . . . . .	24
2.3	High Hydrostatic Pressure Effects on Biomolecular Systems . . . . .	28
2.3.1	Temperature- and Pressure-Induced Unfolding and Denaturation . . . . .	28
2.3.2	Pressure Induced Dissociation of Oligomeric Proteins . . . . .	31
2.3.3	Pressure Effects on Protein Intermolecular Interactions . . . . .	33
2.3.4	Pressure Effects on Protein Liquid-Liquid Phase Behavior and Crystallization . . . . .	36
2.4	Small Angle X-ray Scattering (SAXS) . . . . .	43
2.4.1	Xray Scattering from Discrete Particles in Dilute and Concentrated Suspensions . . . . .	44
2.4.2	Dilute solutions . . . . .	48
2.4.3	Dilute polydisperse solutions . . . . .	59
2.4.4	Concentrated solutions . . . . .	60
<b>3</b>	<b>Experimental Setup</b>	<b>66</b>
3.1	Materials and Sample Preparation . . . . .	66
3.2	(High-Pressure) Small Angle X-ray Scattering Experiment . . . . .	69
3.2.1	High-Pressure SAXS Setup . . . . .	70
3.2.2	Beamlines . . . . .	73
3.2.3	Basic Data Treatment and Refinement . . . . .	80
3.3	Liquid-Liquid Phase Separation (LLPS)-Turbidity Measurement . . . . .	81
3.4	Refractometry . . . . .	82
3.5	Dielectric Spectroscopy . . . . .	82
3.6	High-Pressure Isothermal Solvent Compressibility Measurement . . . . .	84
<b>4</b>	<b>Impact of Macromolecular Crowding and Compression on Protein-Protein Interactions and Liquid-Liquid Phase Separation Phenomena</b>	<b>87</b>
4.1	Pressure Dependence of the Protein's Radius of Gyration in the Presence of PEG . . . . .	89
4.2	Influence of Macro- and Nanomolecular Crowders on the Protein-Protein Interaction . . . . .	91
4.2.1	Spatial Distribution of the Protein Molecules . . . . .	98
4.2.2	Depletion Interaction . . . . .	100
4.2.3	van der Waals Interactions . . . . .	104
4.2.4	Protein-Polymer Interactions . . . . .	104
4.2.5	Hydration Effects . . . . .	106
4.2.6	HHP Effects on the Protein-Protein Interaction . . . . .	106
4.3	Liquid-Liquid Phase Separation of Lysozyme . . . . .	108

4.4	Conclusions . . . . .	110
<b>5</b>	<b>Water-Mediated Protein-Protein Interactions at High Pressures are Controlled by a Deep-Sea Osmolyte</b>	<b>112</b>
5.1	Pressure Dependence of the Protein's Radius of Gyration at Various Solution Conditions . . . . .	113
5.2	Effects of Single Cosolvents on the Pressure-Dependent Protein-Protein Interaction Potential . . . . .	115
5.3	Cosolvent Mixtures Mimicking Deep-Sea Conditions . . . . .	123
5.3.1	Counteracting the Effect of TMAO . . . . .	124
5.4	Water-Mediated Changes of the Protein-Protein Interactions . . . . .	126
5.5	Conclusions . . . . .	127
<b>6</b>	<b>The Effect of Osmolytes and Crowding on the Pressure-Induced Dissociation and Inactivation of Dimeric Horse Liver Alcohol Dehydrogenase</b>	<b>129</b>
6.1	Horse Liver Alcohol Dehydrogenase (LADH) . . . . .	130
6.2	Quantitative Estimation of the Monomer-Dimer Ratio in LADH Solutions from the Theoretical SAXS Profiles . . . . .	131
6.3	The Dissociation of LADH under Pressure in Pure Buffer Solution . . . . .	133
6.4	The Effect of Crowders and Organic Osmolytes on the Dissociation of LADH upon Pressurization . . . . .	135
6.5	Conclusions . . . . .	137
<b>7</b>	<b>Macromolecular Crowding of Protein Solutions by the Polysaccharide Ficoll</b>	<b>140</b>
7.1	Macromolecular Crowding Agent: Ficoll PM 70/400 . . . . .	140
7.2	Effect of Concentration and Hydrostatic Pressure on the Conformation of Ficoll PM 70 / PM 400 in Aqueous Solution . . . . .	141
7.2.1	Dilute Regime . . . . .	143
7.2.2	Concentrated Regime . . . . .	145
7.3	Impact of Ficoll PM 70 / 400 on the Pressure-Dependent Protein Pair-Interaction . . . . .	148
7.3.1	Modulation of the Reentrant LLPS-Boundaries at High Pressures by Ficoll PM 70 . . . . .	151
7.4	Conclusions . . . . .	152
<b>8</b>	<b>General Conclusions and Outlook</b>	<b>153</b>
<b>A</b>	<b>Supplementary Information for Chapter 4</b>	<b>159</b>
<b>B</b>	<b>Supplementary Information for Chapter 5</b>	<b>165</b>

# Chapter 1

## Motivation

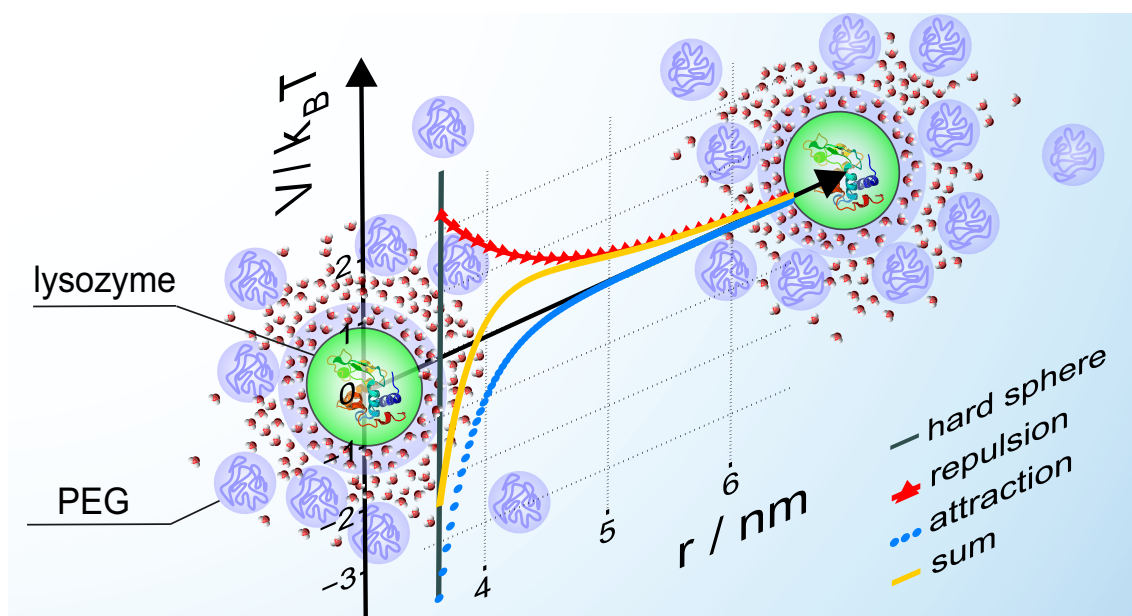


Figure 1.1: Macro- and nanomolecular crowding modulates the intermolecular interactions between biomolecules. Reprinted with permission from [Julius et al., 2019], Copyright © 2018 American Chemical Society.

In most of our biosphere, life is confronted with extreme environmental conditions such as high pressures, high and low temperatures, pH and salinity [Wharton, 2002, Mentré and Hoa, 2001, Gross and Jaenicke, 1994, Abe et al., 1999, Hausmann and Kremer, 1994, Bartlett, 2002]. However, life has found ways to adapt to these conditions. Although high hydrostatic pressures strongly influence both structural properties and cell functionality, life still exists in the deep sea [Meersman et al., 2013, Ellis, 1996, Vanlint et al., 2011], where organisms are exposed to unfavorable conditions such as pressures up to 1.1 kbar [Rivalain et al., 2010, Jannasch and Taylor, 1984]. Therefore, both intrinsic and extrinsic adaptation strategies must exist to ensure the lives of extremophiles. Although of high biological relevance, the mechanisms underlying the adaptation of biomolecular systems to harsh environment conditions and their strategies for pressure resistance are far from being understood [Takahashi and Sugimoto, 2013, Gao et al., 2017a]. The deep sea is also presumed to be the cradle of life on Earth [Daniel et al., 2006], since similar conditions could have prevailed in the depths of the proto-ocean of Hadean Earth. Thus, knowledge about the mechanisms of counteracting these environmental extremes is also relevant for prebiotic chemistry and studies on the origin-of-life [Daniel et al., 2006, Prieur, 1998, Gao et al., 2017b]. In the control and regulation of chemical processes within living cells as well as in the formation

of structures in living bodies, proteins are an indispensable component alongside water [Winter et al., 2007]. Globular proteins and double-stranded nucleic acids in particular are considered to be very stable under pressure. Conversely, quaternary interactions of proteins, which are essential for cell functionality, are highly pressure-sensitive. For instance, oligomeric proteins and multi-protein assemblies are rather fragile and often dissociate into individual subunits already at low pressures [Winter et al., 2007, Mozhaev et al., 1996, Robinson and Sligar, 1995, Meersman et al., 2013], accompanied by a loss of enzymatic activity. The relationship between structure and activity of oligomeric enzymes under high pressure is crucial for understanding the intermolecular interactions and reactivity of proteins in the cells of organisms thriving under harsh environmental conditions. Increased pressure-sensitivity can also be observed for protein self-assemblies such as filamentous components of the cytoskeleton, which are responsible for the mechanical integrity and functional architecture of the cell [Ikkai and Ooi, 1966, Salmon, 1975]. Further, *in vitro* high pressure studies found intermolecular pair-interactions in dense protein solutions being markedly modulated upon pressurization [Möller et al., 2012, Schroer et al., 2016, Schroer et al., 2011a]. It has been shown that changes in the pressure-dependent protein-protein interaction potentials modulate the macroscopic phase behavior of dense protein solutions, e.g. the region of liquid-liquid phase separation (LLPS) in which the homogeneous protein solution separates into two coexisting liquid phases of different protein concentrations [Möller et al., 2014a, Schroer et al., 2016, Cinar et al., 2018]. LLPS phenomena of biomolecules such as proteins are regarded as highly relevant for the spatial-temporal control of biological processes *in cellulo*. Recently, next to lipid vesicles also membrane-less organelles were found to play a major role in compartmentalizing the cell, thereby achieving the necessary physical separation of the cellular compounds and processes. They consist of multicomponent viscous liquid droplets (coacervates), which form via segregation of molecules from protein or protein-nucleic acid mixtures by spontaneous LLPS [Brangwynne et al., 2015]. The propagation by division and subsequent growth of such active self-organized liquid droplets may have served as prebiotic protocells [Zwicker et al., 2017]. Whilst the macromolecular diversity in cytoplasm abounds and the effective concentration of biological macromolecules in cell is high as 80 - 400 mg mL<sup>-1</sup>, the concentration of the individual species are generally too low for phase separation to occur [Luby-Phelps, 1999]. Still, solutions of different macromolecular species tend to phase separate upon mixing above certain concentrations. The requirements for multi phase separation in the liquid phase of the cytoplasm is met by both the diversity of proteins present at high concentrations in the liquid phase *and* macromolecular crowding [Walter and Brooks, 1995, Walter, 1999]. In presence of inert 'background' molecules the volume available for a single molecule is significantly reduced and the local concentration of the solutes can be effectively increased. Thereby, phase separation can take place at concentrations much lower than in absence of uninvolved species (crowding) [Johansson et al., 1999]. In living cells, the high fractional volume occupancy ( $\gtrsim 30\%$ ) of molecular 'background' species like osmolytes, proteins, nucleic acids and other biopolymers [Ellis and Minton, 2003, Zimmerman and Trach, 1991] strongly influences the equilibria and rates of biochemical reactions as well as the conformational stability of biomolecules such as proteins, which changes also their resistance to temperature and pressure [Erlkamp et al., 2014, Erlkamp et al., 2015, Ellis, 2001, Minton, 2005, Ellis, 2007, van den Berg et al., 1999]. In addition to direct intermolecular interactions resulting from electrostatic, van der Waals or hydrophobic forces, attractive forces between the proteins can be induced in the presence of crowders by the entropically driven excluded volume effect. Therefore, shape, size and concentration of such crowding agents modulate protein-protein interactions and thus influence their dynamics, phase behavior and spatial-temporal organization. Information on the molecular interactions and the microscopic structure of ternary protein-cosolute-water systems as well as their implications for the temperature and pressure dependent phase behavior of protein systems are still largely *terra incognita*. Moreover, although the so-called molecular crowding effect on the stability of monomeric proteins is well understood, knowledge of the effect of crowders, particularly the interplay of hydrostatic pressure, osmotic pressure and the reduced free space, on the pressure-dependent stability and activity of oligomeric enzymes is largely lacking.

Cosolvents or osmolytes, like free amino acids, methylamines, sugars and polyols as well as the denaturant urea are accumulated by the cells in relatively high concentrations. These typically small and abundant molecules adjust cell volume and osmotic pressure to harsh extracellular environments, such as high temperature, freezing, anhydrobiosis, or to high hydrostatic pres-



sure as encountered in the deep sea [Hochachka and Somero, 2002, Timasheff, 1993, Timasheff, 2002, Yancey and Siebenaller, 2015]. Osmolytes modulate the inter- and intramolecular interactions like protein folding and unfolding, the interactions with lipid membranes, DNA and associating/dissociating ligands. Aside from the osmoregulation, some of them act as cytoprotective agents by protecting metabolic reactions and/or by counteracting the destabilizing forces on cellular macromolecules [Yancey et al., 1982, Yancey, 2005]. In nature, mixtures of counteracting osmolytes, like stabilizers and perturbants, are often found to be more beneficial to cells and protein function than single ones. Correlating with habitat depth, significant differences in the osmolyte compositions of cellular fluids in marine organisms are reported. Even though of high importance, the underlying mechanisms of the solvent-mediated stabilization of macromolecules and, in particular, the linkage to the intermolecular interactions between proteins in such natural cosolvent mixtures as encountered in the living cell at ambient as well as at elevated pressures are still largely unknown. While first studies of the effect of single organic osmolytes and binary mixtures thereof on structural and dynamical properties of proteins in solution at high hydrostatic pressures show interesting features [Schroer et al., 2011b], data of the effects of more complex mixtures on the pressure-dependent protein-protein interaction potential are lacking. Moreover, the effect of naturally occurring, counteracting (de)stabilizing organic osmolytes on the pressure-dependent stability and activity of oligomeric enzymes is still largely *terra incognita*, though of high biological relevance.

Hence, the aim of this work is to shed light on the biophysical mechanisms underlying the adaption of biomolecular systems to hydrostatic pressure, which occur in organisms under extreme environmental conditions [Takahashi and Sugimoto, 2013, Gao et al., 2017b]. In particular, this thesis will address the specific role of the cellular molecular crowding phenomenon in counteracting pressure sensitivity as well as if and how small organic cosolutes serve as piezolytes for improved pressure resistance. We will answer how both effects modulate the intermolecular interaction potential, conformational stability and phase behavior of model protein systems over a wide temperature and pressure range. In this thesis, the tertiary structure of dissolved oligomeric and monomeric proteins, like shape and size, as well as their spatial arrangement in dense solutions, correlated to the intermolecular forces acting in solution, are studied by small-angle X-ray scattering (SAXS) - a well established, non-invasive method for analyzing structures of systems with random arrangement at the mesoscopic scale (1 nm to 1  $\mu$ m).

Applying SAXS in combination with a liquid state theoretical approach, we studied the intermolecular interaction potentials governing the spatial distribution of proteins in solution and reveal how they are modulated by various crowding environments employing lysozyme as a model protein. In order to mimic aspects of a eukaryotic cell, such as the dynamic cytoskeleton network, and reveal the particular effects of macro vs. nanomolecular crowding on protein intermolecular interactions, the synthetic, biocompatible polymer polyethylene glycol (PEG), the polysaccharide Ficoll PM 70/400 as well as its subunit sucrose are employed as crowding agents over a wide concentration range.

Further, we focus on osmolyte mixtures mimicking cellular fluids encountered in deep-sea organisms, such as shallow- and deep-living crabs, skates and shrimps [Kelly and Yancey, 1999], in order to go one-step further towards a better understanding of 'real' biological intracellular fluids as they appear *in cellulo*, and reveal details and differential effects of their protecting properties.

In order to explore the intermolecular interactions and reactivity of proteins *in cellulo* of organisms thriving at extreme environmental conditions, the correlation between enzyme structure and function is investigated by the effect of pressure-induced dissociation/inactivation of the well-studied dimeric enzyme horse liver alcohol dehydrogenase (LADH) [Brändén et al., 1975, Winter et al., 2007, Trovaslet et al., 2003, Cioni and Strambini, 1996, Dalziel and Dickinson, 1966, Dallet and Legoy, 1996, Klinman, 1981, Eklund and Brändén, 1987, Petterson, 1987, Wang et al., 2000] in the presence of solution additives like crowder and (de)stabilizing organic osmolytes, mimicking conditions as encountered inside the biological cell.

To fundamentally understand the assembly and disassembly of biomolecular condensates as found *in cellulo* [Banani et al., 2017, Long et al., 2005] and their role for cellular function in the presence of internal and external stress factors, such as high osmotic pressure induced by high osmolyte and crowder concentrations, extreme temperatures or high hydrostatic pressure, the

pressure-dependent LLPS behavior of dense ternary protein-crowder-solvent mixtures will also be focus of this work.

Such studies might also be of great interest for biotechnological and biomedical applications as well as for food science and high-pressure enzymology [Masson et al., 2001, Silva et al., 2014, Huang et al., 2017]. In the field of medical research, drug design and disease treatment, the LLPS mechanism may prompt strategies to suppress crystallization and aggregation in the human body, processes that underlie protein-condensation diseases such as sickle cell anemia [San Biagio and Palma, 1991], Alzheimer’s disease [Selkoe, 1994, Koo et al., 1999] and cataract [Thomson et al., 1987, Berland et al., 1992, Pande et al., 2001, Benedek, 1997]. The high-pressure phase behavior of biomolecular systems is of growing biotechnological interest and also for many industrial applications of colloids [Everett, 1988].

Further, the characterization of the pressure-dependent effective protein-protein interactions by the second osmotic virial coefficient depending on different physio-chemical conditions (background ionic strength, nature of crowder, crowder size and concentration), helps to predict  $p$ - $T$  protein phase diagrams for different precipitant sizes and concentrations. Since crystal formation is highly dependent on solvent-mediated intermolecular interactions, a deeper understanding of these interactions could help to predict phase stability and improve the design and control of crystal contacts and specific crystal shapes, as well as the growth of crystals with higher diffraction resolution. [Durbin and Feher, 1996, Tardieu et al., 2001].

## Outline of this thesis

The thesis is organized as follows: First, in chapter 2, the basic concepts of the osmolyte effects in cellular adaption to harsh extracellular environments as well as of the cellular effect of molecular crowding (excluded volume) are introduced. Further, we discuss the impact of high hydrostatic pressure on the thermodynamics and kinetics of biomolecules, intra- and intermolecular interactions in biomolecular systems including liquid-liquid phase separation phenomena and crystallization. The molecular pair-interaction potentials used to model intermolecular interactions in aqueous protein solutions are discussed, followed by a description of the main concepts and methods for the interpretation of small-angle X-ray Scattering (SAXS) data of biological macromolecules in solution. In the following chapter 3, detailed insight into the materials, experimental methods and general data treatment is provided. The results obtained are presented in the subsequent chapters. Chapter 4 contains the results on the impact of macromolecular crowding and compressibility on protein-protein interactions and liquid-liquid phase separation phenomena. Chapter 5 shows how water-mediated protein-protein interactions at high pressures are controlled by the deep-sea osmolyte Trimethylamine N-oxide (TMAO), as well as by more complex osmolyte mixtures as found in cellular fluids of marine organisms. Chapter 6 focuses on the effect of organic osmolytes and crowding on the pressure-induced dissociation and inactivation of dimeric horse liver alcohol dehydrogenase (LADH). Studies presented in chapter 7 describe the influence of hydrostatic pressure and concentration, ranging from the dilute to the semi-dilute regime, on the conformation of the polysaccharides Ficoll PM 70/400 in aqueous solution as well as the effects of the macromolecular crowding agent on the pressure dependent boundaries of the (metastable) liquid-liquid phase separation (LLPS) region of dense lysozyme solutions. Finally, chapter 8 will summarize the results of the different studies performed, provide a general conclusion about the impact of nano- and macromolecular crowding as well as organic osmolytes on the pressure-dependent inter- and intramolecular interactions in different biomolecular systems and close with a short outlook.

This work was carried out as part of a cooperation between the groups of Prof. M. Tolan (Experimental Physics E IA / DELTA, Faculty of Physics, TU Dortmund University) and Prof. R. Winter (Physical Chemistry I - Biophysical Chemistry, Faculty of Chemistry and Chemical Biology, TU Dortmund University) and is partially based on the following original publications:

**Chapter 4:**

Julius, K., Weine, J., Gao, M., Latarius, J., Elbers, M., Paulus, M., Tolan, M., and Winter, R. (2019). Impact of Macromolecular Crowding and Compression on Protein-Protein Interactions and Liquid-Liquid Phase Separation Phenomena, *Macromolecules*, 52(4):1772-1784

**Chapter 5:**

Julius, K., Weine, J., Berghaus, M., König, N., Gao, M., Latarius, J., Paulus, M., Schroer, M.A., Tolan, M., and Winter, R. (2018). Water-Mediated Protein-Protein Interactions at High Pressures are Controlled by a Deep-Sea Osmolyte, *Phys. Rev. Lett.*, 121(3):038101

**Chapter 6:**

Julius, K., Al-Ayoubi, S.R., Paulus, M., Tolan, M., and Winter, R. (2018). The effects of osmolytes and crowding on the pressure-induced dissociation and inactivation of dimeric LADH, *Phys. Chem. Chem. Phys.*, 20(10):7093-7104



# Chapter 2

## Theory

This chapter is organized as follows: First, we discuss how the physical-chemical conditions in the living cell deviate from an ideal diluted solution, focusing on the effects of macromolecular crowding and cosolvents on key cellular functions and processes, and how these affect the intermolecular forces acting in aqueous biomolecular systems (see section 2.1). In the following section 2.2, model pair interaction potentials, suitable for describing the forces, which control the particle distribution, phase diagram as well as the crystallization process, are exemplified. Section 2.3 gives a scientific background of the hydrostatic pressure effect on biomolecular systems, especially its implications on protein folding and intra-/intermolecular interactions. Further, it provides detailed insight in the physics of (pressure-dependent) aqueous liquid-liquid phase separation in protein solution which is also considered as self-organizing force in the cell interior. Finally, section 2.4 focuses on the theoretical background of small angle X-ray scattering, the experimental method of choice in this thesis to investigate the effects of hydrostatic pressure, organic osmolytes and crowding on protein structure and the intermolecular interactions between protein molecules in aqueous solution.

### 2.1 The Cellular Milieu

Biochemical assays employed *in vitro* and in dilute solutions under ideal thermodynamic conditions rarely take into account that the chemistry of life takes place within an extremely packed, heterogeneous and viscous environment [Fulton, 1982]. The living cell is highly occupied by a large amount ( $\sim 80 - 400 \text{ mg mL}^{-1}$ ) of soluble and insoluble macromolecules, including proteins, lipids, ribosomes, biopolymers, nucleic acids and carbohydrates (polysaccharides) [van den Berg et al., 1999, Zimmerman and Trach, 1991, Rivas et al., 2004]. Since no single macromolecular species may be present at high concentration, such media are referred to as 'crowded' rather than 'concentrated' and molecular species not directly participating in a particular reaction nor binding specifically to another species are termed 'background' molecules or crowder [Minton, 1997]. Next to the macromolecules, small organic molecules such as osmolytes and metabolites are highly present *in cellulo* as well.

#### 2.1.1 Molecular Crowding - The Excluded Volume Effect

Biological solutions are complex heterogeneous systems with a restricted amount of free water and with a significant fraction of the intracellular space ( $\sim 10 - 40\%$ ) unavailable to other macromolecular species. The mean intermolecular spacing in such a densely packed system can be much smaller than the molecules dimension [Homouz et al., 2008]. Intracellular macromolecules are typically separated by distances of 1 - 2 nm, only [Ball, 2008]. Due to steric hindrance, two impenetrable molecules cannot occupy the same space at the same time [Ellis and Minton, 2003, Zimmerman and Minton, 1993, Fulton, 1982, Minton, 1997, Ellis, 2001, Minton, 2000]. Steric repulsion is the most fundamental of all intermolecular interactions and is always present regardless of any other repulsive or attractive interactions that might occur. Macromolecular crowding has a strong impact on intermolecular interactions.

## Volume Exclusion Phenomena and its Entropic Consequences

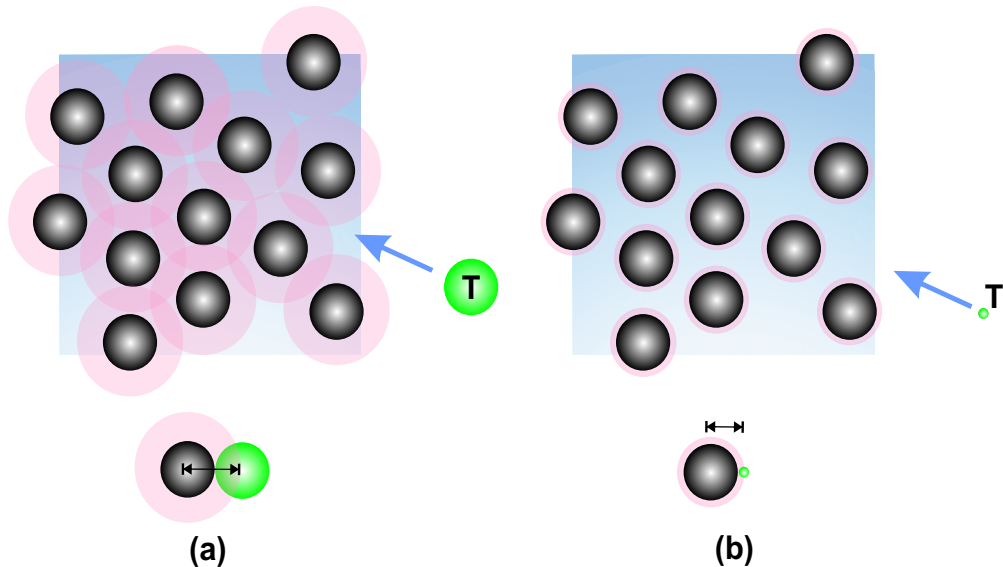


Figure 2.1: The efficiency of the excluded volume effect in dependency of the size ratio between crowder (*black*) and a test molecule T (*green*) added to the system. The volume unavailable to the test molecules center of mass is visualized in *magenta*. Picture modified from [Minton, 2001].

We consider a model system of identical spherical particles. The particle position in the system is completely specified by the position of its center of mass. Since two particles cannot occupy the same space at the same time, each particle excludes the remainder from its neighborhood. The limiting distance of closest approach between two particles is equal to the sum of their radii. Thus, each particle is surrounded by a spherical volume from which the centers of mass of the neighboring particles are 'excluded' [Ralston, 1990]. The presence of crowding agents places steric constraints on any particle added to the system. The number of possible ways to add a further test particle T to the solution is limited with increasing number density and the available space is progressively restricted. Hence, the efficiency of macromolecular crowding depends on the ratio between the occupied volume (i.e. shape, size) of the crowder and the particle as well as the number density of background molecules. This relationship is illustrated in Figure 2.1. When the pre-existing crowding agents (*black spheres*) and the added test particle T (*green sphere*) are of equal size, the volume occupied by the crowder and thereby unavailable to the test molecule is maximal (see Figure 2.1 (a)). In contrast, for crowder much larger than the test particle, the area from which the particles center of mass is excluded (*magenta*) diminishes and the free volume in which its center of mass can be placed (*blue*) increases (see Figure 2.1 (b)). In fact, the effective concentration defined by the available volume per molecule can be much higher than the actual concentration in the crowded solution. [Minton, 2001]. The effective concentration,  $a_i$  of a solute species  $i$  is related to the actual concentration,  $c_i$ , by

$$\gamma_i \equiv \left( \frac{a_i}{c_i} \right) = \left( \frac{V_{\text{tot}}}{V_{a,i}} \right), \quad (2.1)$$

wherein  $V_{\text{tot}}$  denotes the total volume and  $V_{a,i}$  the volume available to the center of mass of the species  $i$  [Lebowitz et al., 1965, Minton, 2001]. As a result, the crowding-induced modulations of equilibria and reaction rates might exhibit a highly non-linear behavior with respect to crowder size and concentration [Ellis, 2001].

Resulting from an increased number density of molecules and an increased steric hindrance (repulsion), the randomness of the particle distribution and the single particle's steric freedom are reduced leading to a decrease in configurational entropy. Thus, by simply excluding volume, crowder increase both the free energy of the solution and the chemical potential of each species of

macromolecules present in the solution, regardless the respective concentration [Minton, 2000]. The effectiveness of the excluded volume effect is dependent upon the relative sizes and shapes of concentrated 'background' crowding species and the dilute macromolecular reactants/products [Rivas et al., 2004, Ralston, 1990, Zhou, 2008].

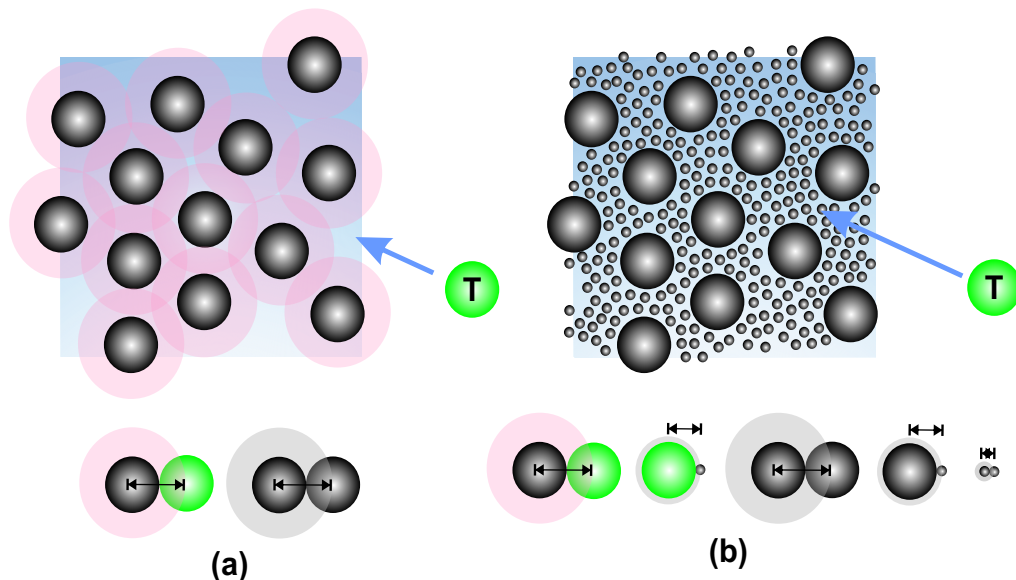


Figure 2.2: Size effects in macromolecular crowding. The volume unavailable to the test molecules (*green*) and the crowders' (*black*) center of masses is visualized in *magenta* and in *light gray*, respectively. Picture modified from [Minton, 2001] and [Sharp, 2015].

In the scenario depicted in Figure 2.2 (a), the test molecule T (*green sphere*, e.g. protein) added to a solution of equally sized crowder molecules (*black spheres*) is constrained to the small regions in between the crowders, since the molecules must avoid energetically costly steric overlaps. However, Figure 2.2 (b) displays a system where the volume between big macromolecular crowding molecules is filled with small crowder molecules. The different sized crowder molecules also cannot overlap due to steric interactions. The avoidance of an overlap with the protein and each other results in a loss of conformational freedom and entropy of all crowder molecules (small and large) which the protein may encounter when entering the system. As a result, changes in the local density distributions occur for the crowder molecules close or in contact with the protein. The net entropy change depends on both the magnitude of local density changes and the number of molecules affected and is independent of the crowder size for a given change in local density. Even though in both Figure 2.2 (a) + (b) the protein's partial molar volume is the same, more molecules are affected in (b) by the presence of the protein. Consequently, for a fixed volume excluded the enhancement of association reactions (i.e. in attractive intermolecular interactions) may be most pronounced for smaller background molecules [Zimmerman and Minton, 1993, Schellman, 2003, Sharp, 2015].

Molecular crowding, driven by the excluded volume effect, stimulates any reaction that amplifies the available volume [Zhou et al., 2004, Minton, 2005, Minton, 2005, Zimmerman and Minton, 1993]. In this sense, crowding modulates the thermodynamics and kinetics of many biological processes and equilibria affecting protein folding and binding by preferentially destabilizing either reactants and products in favor of the state that excludes the least volume [Hatters et al., 2002, Phillip et al., 2009, van den Berg et al., 2000, van den Berg et al., 1999, Cheung et al., 2005, Uversky et al., 2002, Ai et al., 2006, Gao et al., 2016, Du et al., 2006, Batra et al., 2009]. Macromolecular crowding has large effects on conformational dynamics and stability and compaction of disordered proteins [Soranno et al., 2014], since a compact, globular conformation excludes less volume to other macromolecules than an extended, swollen conformation. In the presence of high volume occupancy, the free energy landscape is shifted favoring more compact structures in the native as well as the denatured

state [Stagg et al., 2007, Hong and Gierasch, 2010, Tokuriki et al., 2004, Minton, 2000].

The same mechanism also applies to the structural properties of multimeric proteins in solution as oligomeric or polymeric aggregates occupy less volume than an equal number of their subunits [Zhang et al., 2012a, Dhar et al., 2010, Stagg et al., 2007, Rajapaksha et al., 2015] (see also section 2.2.2). Association reactions are entropically preferred, since a partial overlap of the excluded regions when two particles approach each other effectively increases the available volume in the system [Ralston, 1990, Minton, 2000, Minton, 2001, Ellis, 2001, Minton, 2005].

Further, crowding enhances the enzymatic activity [Dhar et al., 2010, Ellis, 2001, Minton, 2005, Zimmerman and Minton, 1993, Totani et al., 2008, Sasaki et al., 2007], can considerably decrease the diffusional mobility of proteins [Zimmerman and Minton, 1993, Kozer et al., 2007, Ellis and Minton, 2003] and promotes precipitation and crystal growth [Tardieu et al., 2002, Vivarès et al., 2002, Wilf and Minton, 1981, Tanaka and Ataka, 2002].

Crowding can also lead to a stabilization of protein solutions. The steric exclusion of the crowder from the protein surface and the solvophobic effect, i.e. the inability of the crowder to form as many hydrogen bonds in the vicinity of the protein surface as opposed to the bulk, are responsible for the preferential hydration of the protein in presence of crowders like PEG and polyols like glycerol [Bhat and Timasheff, 1992, Parsegian, 2006, Timasheff, 2002, Timasheff, 1993].

Macromolecular crowding strongly influences interparticle interactions. Many experimental studies on ternary systems composed of colloid-crowder-water report an attractive depletion interaction (see section 2.2.2) exerted on the colloidal particles (i.e. proteins) by the crowder (i.e. polymer [Ye et al., 1996, Kulkarni et al., 2000, Vivarès et al., 2002] or polysaccharide [Tuinier et al., 2003]).

Moreover, increasing the excluded volume of a single-component system can induce phase separation (see section 2.3.4), since the available volume is maximized when the two components phase separate. As a consequence, the translational entropy of the particles is increased, but at the expense of a decrease of the entropy of mixing [Adams and Fraden, 1998]. Dependent on the volume fraction, either the mixing entropy (low  $\Phi$ ) or the translational entropy dominates (high  $\Phi$ ). The addition of free non-adsorbing polymer to the system may alter the phase behavior of colloidal particles (i.e. proteins) [Atha and Ingham, 1981, Wang and Annunziata, 2007, Ramakrishnan et al., 2002, Annunziata et al., 2002, Bloustone et al., 2006, Bhat and Timasheff, 1992, Vergara et al., 2006]. At sufficiently high particle concentration and appropriate size asymmetry between colloid and crowder, the depletion attraction can induce a metastable liquid-liquid phase separation (LLPS) [Lekkerkerker et al., 1992, Vivarès and Bonneté, 2004, Tuinier et al., 2003] and eventually crystallization [McPherson, 1976, McPherson, 1985]. However, other research has shown that the influence of polymer addition on protein solutions may also be repulsive [Bloustone et al., 2006, Kozer et al., 2007], which indicates the presence of some sort of an effective repulsive force such as 'soft' polymer-protein attraction.

In all physiological fluid media, contributions of additional, longer-ranged, chemical, 'soft' non-specific interactions (enthalpically driven) between proteins and crowding agents must be taken into account in addition to the hard-core steric repulsion (entropically driven) [Gao et al., 2017b]. These pair-wise interactions like attractive hydrophobic interaction, hydrogen bonding, weak electrostatic repulsion/attraction depend on temperature as well as on global chemical properties of the biomolecules, crowder and solvent (i.e. net charge, solution dielectrics, dipol/multipol moment, macromolecular shape and polarity of surface residues) [Minton, 2001]. Thus, the always present enthalpic contributions to crowding may enhance or counteract the entropic excluded volume effect. The intermolecular interaction forces, originating from the presence of the 'background' molecules in solution, which modulate biological rates and/or equilibria might be rather weak in comparison to the specific interaction forces between reaction partners acting in solution. However, in presence of high concentrations of 'background' molecules, they can be collectively strong and induce order-of-magnitude changes.

Further, little to no "bulk-like" water is present within cellular environments [King et al., 2014]. As a consequence of the highly constrained water in crowded environments, hydration-mediated mechanisms are suggested to affect and modulate the intermolecular interactions (protein-specific) [Wang et al., 2017, Harada et al., 2012].

## Crowding Agents

Experiments on the so-called macromolecular crowding effect on biomolecular structures and functions are not easily accessible *in vivo* or in cell. As an alternative, artificially crowding environments are generally mimicked *in vitro* by adding high concentrations of inert synthetic or natural macromolecules to the systems, i.e. sugars, alcohols, polymers or stable proteins (e.g. lysozyme, ovalbumin, bovine serum albumin (BSA)) such as the well-studied crowding agents Ficoll PM 70/400 (a highly cross-linked sucrose-epichlorohydrin copolymer), dextran (a slightly branched polysaccharide) and the polymer polyethylene glycol (PEG) [Zimmerman and Minton, 1993, Ellis, 2001, Minton, 2006, Minton, 2001, Zhou, 2008, Zhou et al., 2011].

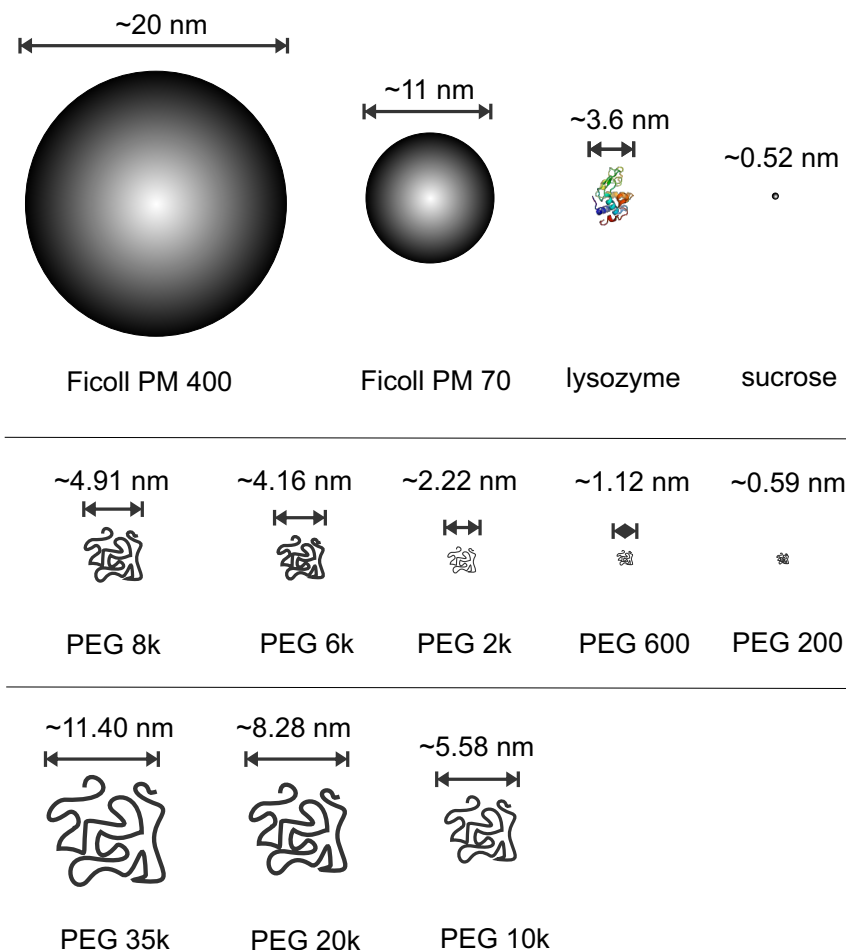


Figure 2.3: The model protein lysozyme and several synthetic crowding agents, employed in this thesis to mimic the highly crowded intracellular environment, shown together with the corresponding hydrodynamic diameters [Schultz and Solomon, 1961, Parmar and Muschol, 2009, Devanand and Selser, 1991].

In this thesis, the polar polysaccharide Ficoll PM 70/400 together with its subunit sucrose as well as the polymer PEG at more than three orders of magnitude of molecular weight ( $M_w \sim 200 - 35000 \text{ g mol}^{-1}$ ) are employed as crowding agents in order to study the impact of various crowding environments on the intermolecular interactions governing the spatial distribution of proteins in solution and the shape of the temperature and pressure dependent LLPS phase diagrams (see Figure 2.3). As the PEGs vary markedly in osmotic coefficients [Money, 1989, Stanley and Strey, 2003, Cohen et al., 2009] and size in this range of molecular weights, they allow for a thorough study of the impact of the interplay of hydrostatic pressure, osmotic pressure, and the excluded



volume effect as encountered intracellularly on the inter- and intramolecular interactions in crowded protein solutions. The synthetic, non-ionic straight chain polymer PEG  $(-(\text{CH}_2-\text{CH}_2-\text{O})_N-)$  exists in a random coil state in aqueous solution [Maxfield and Shepherd, 1975] and forms, similarly to Ficoll, network-like structures. Therefore, they both are well suited to mimic qualitative properties of an eukaryotic cell. The cytoskeleton forms a dynamic network of protein filaments in order to compartmentalize the cell into areas of cytoplasm where soluble proteins interact [Fink, 2005]. Globular macromolecules that may be present in real life biological settings may be adequately mimicked by Ficoll, which behaves like a semi-rigid sphere (radius of  $\sim 5.5$  nm for PM 70 and  $\sim 10$  nm for PM 400, respectively) [Luby-Phelps et al., 1987, Venturoli and Rippe, 2005]. The crowding agents have the capacity to exclude volume and also to dehydrate biopolymers at high concentrations through competition for hydration water. As we focus on the effect of crowding, the well characterized model protein hen egg-white lysozyme is used in the study on the influence of macromolecular crowders and cosolutes on the protein – protein interaction potential. Lysozyme is a monomeric globular protein with a molecular weight of 14.3 kDa and has a shape similar to a prolate ellipsoid of revolution with volume  $V = (\pi/6) 4.5 \times 3 \times 3 \text{ nm}^3$ . The crystal structure is displayed in Figure 2.4 (PDB entry: 1LYS [Harata, 1994]). The secondary structure is contrasting in color. Lysozyme has no symmetry and consists of 129 amino acid residues and is built of four  $\alpha$ -helices and three  $\beta$ -sheets [Voet and Voet, 1990]. The four disulfide bonds within the protein ensure the extraordinary stability of the protein against external stressors. The isoelectric point of the protein is  $\text{pI} = 11.2$  [Tanford and Roxby, 1972]. Under the solution condition selected in this thesis (pH 7), the protein has a net charge of  $+8 \pm 0.5$  electronic charges [Kuehner et al., 1999, Curtis et al., 1998, Yu et al., 2015]. It is thermally stable with a melting temperature of  $70.3 \pm 0.19$  °C at pH 7 [Venkataramani et al., 2013] and conformationally stable against pressures up to 5 kbar [Schroer et al., 2011a]. Lysozymes occur as part of the innate immune system in mammals and humans (e.g. in many secretions such as tears, saliva, airway surface liquid in the human respiratory system and human milk) and can also be found in plants, fungi and bacteria. Further, lysozyme is abundant in chicken egg white.

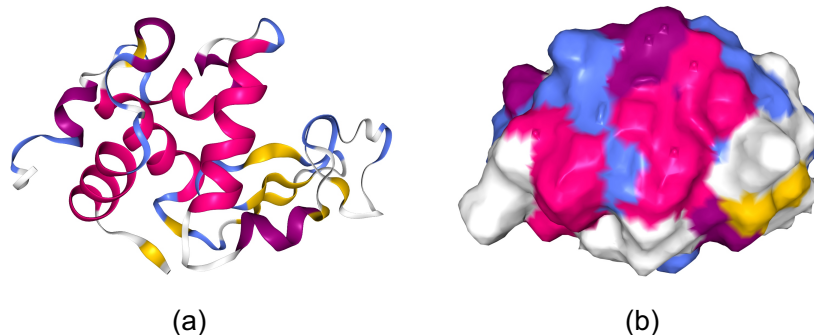


Figure 2.4: (a) Crystal structure (PDB entry: 1LYS [Harata, 1994]) of the monomeric protein lysozyme from hen egg-white and (b) its surface.

Under the assumption of a completely inert crowding agent, the behavior of a protein in a crowded environment can be described as completely entropic in terms of hard non-specific interaction between protein and crowder (i.e. excluded volume effect). However, the question of whether crowding agents are really chemically inert or make specific differential interactions with proteins and nucleic acids is still debated [Sharp, 2015]. For example, the highly soluble polymer PEG is hydrophobic in nature and can bind to the non-polar or hydrophobic side chains on the protein surface [Tubio et al., 2004, Crowley et al., 2008, Zhou, 2008, Du et al., 2006]. The usually repulsive protein-PEG interaction and entropically favorable preferential exclusion of PEG from the protein surface area due to the excluded volume effect can be reduced *via* soft attractive PEG-protein interactions, which are enhanced with increasing polymer concentration and size of the additive [Bhat and Timasheff, 1992, Timasheff, 2002], and upon minimization of the protein surface area exposed to the solvent. This is generally achieved through conformation changes,

precipitation or crystallization. However, as lysozyme is a small protein of hydrophilic nature, one may suggest that enthalpic contributions such as specific interactions like binding of the crowder to the hydrophobic residues on the protein surface, if present, are rather weak [Spelzini et al., 2008].

### 2.1.2 Organic Osmolytes - Cellular Adaption to Environmental Stresses

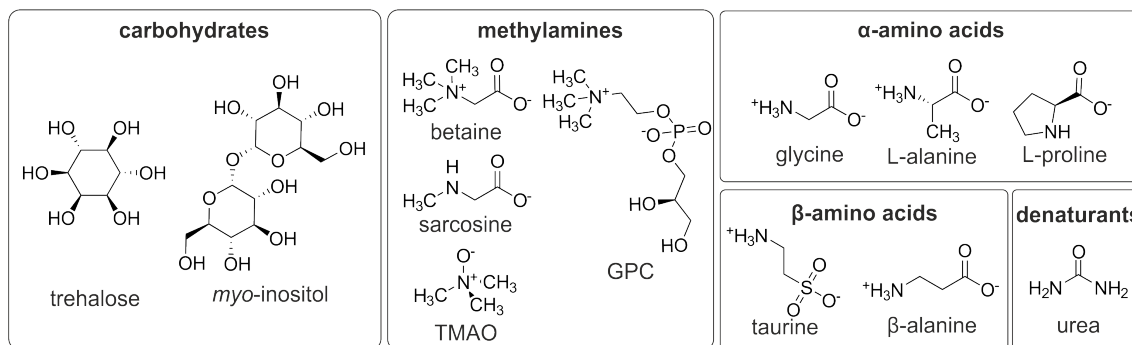


Figure 2.5: Structure of  $\alpha$ - and  $\beta$ -amino acids, the denaturant urea, carbohydrates and methylamines present as osmolytes in marine organisms. GPC = L- $\alpha$ -glycerophosphorylcholine. Reprinted with permission from [Julius et al., 2018b], Copyright © 2018 American Physical Society.

In osmoconforming marine organisms, small organic molecules like free amino acids (glycine, L-proline, L-alanine, taurine,  $\beta$ -alanine), methylamines (sarcosine, betaine, Trimethylamine N-oxide (TMAO), L- $\alpha$ -glycerophosphorylcholine (GPC)), sugars (sucrose, trehalose) and polyols (glycerol, *myo*-Inositol) as well as the denaturant urea are accumulated to high concentrations (up to  $\sim 600$  mM [Kelly and Yancey, 1999, Yancey et al., 2002]) by cells to maintain or adjust cell volume and osmotic pressure to the harsh extracellular environments (see Figure 2.5). The compositions of osmolytes used by the organisms vary considerably among marine taxa [Carr et al., 2014, Yancey et al., 2002]. By the up and down regulation of high levels of organic osmolytes, osmotic shrinkage and swelling in the course of changes in the osmotic concentration of the environment are prevented [Forster and Goldstein, 1976, Burg et al., 2007].

Aside from the osmoregulation, some of them act as cytoprotective agents for one by protecting metabolic reactions and on the other hand, by counteracting the destabilizing forces on cellular macromolecules [Yancey et al., 1982, Yancey, 2005]. For instance, some osmolytes serve as metabolic protectors by functioning as antioxidants (polyols), by redox balancing (glycerol), by enhancing the resistance against hydroxia (L-proline) and by supplying energy (trehalose) to an organism right after a period of dormancy induced by stress [Ansell et al., 1997, Cushman, 2001, Hanson et al., 1994, Shen et al., 1999, Orthén et al., 1994]. Also, since some of the organic osmolytes, particularly TMAO, betaine and urea, have densities less than seawater, they contribute to achieve neutral buoyancy by compensating the excess density of the cellular structural components [Withers et al., 1994a, Withers et al., 1994b].

Apart from that, significant amounts of strong stabilizing solutes are accumulated in organisms when there are stresses present to counteract like perturbing solutes, high temperature, freezing, anhydrobiosis or high hydrostatic pressure (HHP) as encountered in the deep sea up to the 1.1 kbar level [Hochachka and Somero, 2002]. Sugars and polyols are dominantly accumulated by organisms to increase thermostability [Back et al., 1979, Duman et al., 1991, Storey and Storey, 1988], as are trehalose and L-proline to protect membranes in freezing. The naturally occurring kosmotrope osmolyte trehalose is also known for the depression of protein aggregation [Jain and Roy, 2009, Ueda et al., 2001] and the replacement of water molecules within the hydration shell [Fedorov et al., 2011]. Moreover, deep sea microorganisms as well as the Mexican fruit fly in the larvae stadium seem to react to high pressure by an increased synthesis of trehalose [Vargas-Ortiz et al., 2013, Wang and Sun, 2017, Dong et al., 2007, Fujii et al., 1996].

Methylamines, including sarcosine, GPC, TMAO and betaine, are able to counteract salt [Pollard and Wyn Jones, 1979, Clark and Zounes, 1977] and urea inhibition [Burg and Peters, 1998, Burg et al., 1996, Zou et al., 2002, Bennion and Daggett, 2004] with the degree of counteraction depending

on the urea:methylamine ratio. TMAO counteracts the destabilizing effect of urea in an additive way, typically reaching full counteraction at a 2:1 concentration ratio [Schroer et al., 2011b, Wang and Bolen, 1997, Rezus and Bakker, 2009]. Interestingly, both osmolytes occur in most species at this physiological ratio [Yancey and Somero, 1979, Yancey and Somero, 1980, Yancey et al., 1982]. The underlying mechanism of the compensatory effect of TMAO and urea is still largely elusive. Theoretical and experimental work suggest an indirect, water-mediated mechanism. Direct interactions between the oxygen atom of the TMAO molecule and urea become relevant at higher concentrations than typically encountered in organisms, only [Meersman et al., 2011, Meersman et al., 2009]. Further, the methylamine TMAO is known to counteract the pressure-induced destabilization of several proteins by enhancing the ligand binding, protein folding and assembly [Yancey and Siebenaller, 1999, Yancey et al., 2001, Schroer et al., 2011b].

Correlating with habitat depths and thus hydrostatic pressure [Saunders and Fofonoff, 1976], a significant difference in the osmolyte compositions in muscle fluids of several deep-sea osmoconformers (e.g. shrimp, skate, crab) compared to their shallow-living relatives was reportedly found. High levels of methylamines, especially TMAO, are accumulated in deep-sea animals in the order shallow < bathyal (1600 - 2000 m) < abyssal (2850 m). Shallow-living species tend to be dominated by neutral amino acids; the rate of TMAO remains low concomitant with an increasing amount of amino acids like glycine in caridean shrimp and or of urea in rajid skates. In brachyuran crabs, osmoconformation is maintained by a decrease of the weaker protein stabilizers glycine, taurine and betaine at higher TMAO levels in bathyal trawl sites (see Figure 2.6) [Kelly and Yancey, 1999]. However, in deep-sea taxa where TMAO is absent (e.g. in snails, octopod and worms), the methylamines GPC and betaine as well as inositols are reported as significant osmotic components [Yancey et al., 2002].

In nature, these mixtures of counteracting osmolytes are more beneficial to cells than single stabilizers (or perturbants) alone. The absence of a perturbing component to offset stabilizers like methylamines at high concentrations can be detrimental to protein function. They lead to over-stabilization of the proteins, elevated rigidity of the enzymes and an enhanced formation of non-functional aggregates, whereas in presence of perturbants and other osmolytes flexibility and enzyme activity are restored.

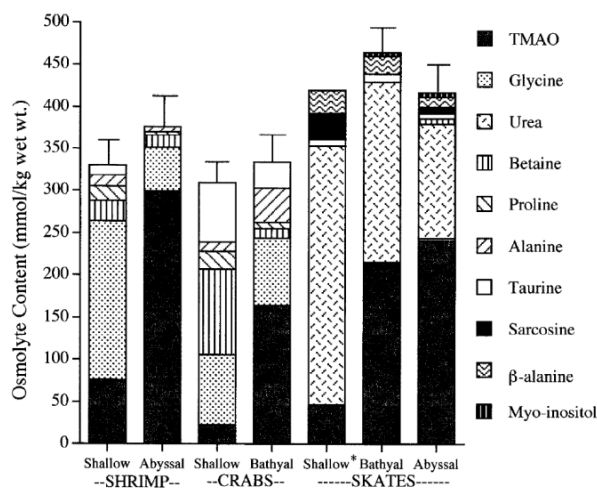


Figure 2.6: Osmolyte content in muscles of marine animals from shallow habitats and bathyal (1600 - 2000 m) and abyssal (2850 m) trawl sites. Reprinted with permission from [Kelly and Yancey, 1999], Copyright © 1999 Lancaster Press, Inc.

Apart from the perturbant urea, these organic solutes do not adversely affect function or structure of cellular macromolecules even at high concentrations [Clark and Zounes, 1977, Bowlus and Somero, 1979]. Since the negative charge of the amino acids at neutral pH is sufficiently small ( $\beta$ -alanine  $\ll$  proline  $<$  L-alanine and glycine  $<$  taurine); they can be considered as uncharged in good approximation for small concentrations. Therefore, all above-mentioned and generally most of organic osmolytes are neutral or lacking charges at physiological pH in order not to manipulate



the electrostatic balance. In addition to that, the zwitterionic polar amino acid types remain so over a wide pH range.

	$V_m / \text{cm}^3 \text{ mol}^{-1}$	
D(+)-trehalose dehydrate	244.03	[Banipal et al., 2002]
GPC	182.80	[Jackson-Atogi et al., 2013]
<i>myo</i> -Inositol	101.00	[Jackson-Atogi et al., 2013]
betaine	98.72	[Pitkänen et al., 2010]
L-proline	82.20	[Rodríguez-Arteche et al., 2012]
TMAO	73.40	[Rösgen and Jackson-Atogi, 2012]
taurine	71.20	[Jackson-Atogi et al., 2013]
L-alanine	60.46	[Rodríguez-Arteche et al., 2012]
sarcosine	62.48	[Gheorghe et al., 2016]
$\beta$ -alanine	58.90	[Rodríguez-Arteche et al., 2012]
urea	44.20	[Rösgen and Jackson-Atogi, 2012]
glycine	43.23	[Rodríguez-Arteche et al., 2012]
water	18.07	[Kell, 1977]

Table 2.1: Literature data of the partial molar volumes,  $V_m$ , of water and of the organic osmolytes at infinite dilution in water at 25°C .

Compared to the molecular volume of a water molecule, the partial molar volumes  $V_m$  of D(+)-trehalose dehydrate at infinite dilution in water at 25°C and GPC are rather large, followed by *myo*-Inositol and betaine. The amino acids  $\beta$ -alanine, L-alanine, L-proline, taurine and the methylamines TMAO, sarcosine are of comparable size. The smallest osmolytes studied in this thesis are urea and glycine (see Table 2.1).

As suggested by the variety of osmolytes and compositions occurring in organisms, their stabilizing effect might be universal and not depend on specific chemical interactions. Furthermore, the high concentrations of the agents required for solvent-mediated protein structure stabilization, denaturation and precipitation indicate, that the underlying mechanisms are neither strong nor specific but governed by the same weak interactions [Timasheff, 1993]. The osmolytes influence the proteins stability without breaking or making covalent bonds [Street et al., 2006]. So, if the observed stabilizing effect is not mainly arising from direct interaction between osmolyte and protein, structural modifications of water driven by the osmolytes and the osmolyte-water-protein interactions are likely to play an important role.

### Cosolvent Effects on the Folding Equilibria of Biomolecules

In a ternary biomolecule-cosolvent-buffer system, the stability and conformational dynamics of a biomolecule depends on the physico-chemical properties of the biomolecule itself (i.e. hydrophilic versus hydrophobic surface / polarity, surface charge distribution, compactness, packing defects/void volume, excluded volume), of the hydration water (e.g. hydrogen-bonding pattern, coordination number, density, dynamics) and of the cosolvent (e.g. charge, polarity, polarizability, volume, hydrogen-bonding capacity, concentration, conformational dynamics) in both the native and the denatured state [Gao et al., 2017b, Winter et al., 2007].

Possible (direct and indirect) interaction mechanisms in such ternary solutions are the adsorption of the cosolvent molecules to the protein surface, the exclusion of cosolvent molecules from the protein due to steric hindrance (i.e. cosolvent is significantly larger than the water molecules) and solvent reorganization (i.e. changes in the water structure). All three mechanism lead to changes in the numbers of water and cosolvent molecules and thereby to an excess population of one species in the protein phase compared to the bulk phase [Winter et al., 2007].

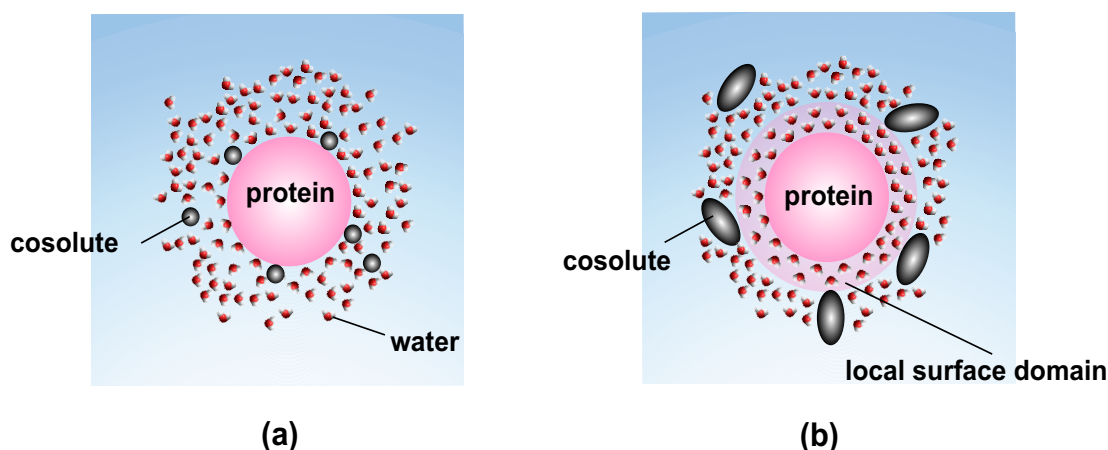


Figure 2.7: Model of (a) preferential binding of cosolutes to the protein surface and (b) preferential hydration of the protein. Picture modified from [Winter et al., 2007].

Two different, established models on the thermodynamics of the cosolvent effect are described in the following:

- We consider a system of biomolecule, cosolvent (i.e. salts, osmolytes, macromolecules) and water at constant pressure and temperature. The folding equilibrium of the biomolecules is perturbed upon addition of a cosolvent to the aqueous solution. The restoration of the chemical equilibrium requires an adaptation of chemical potential, here in the form of a change in the cosolvent concentration around the biomolecule [Timasheff, 2002]. Cosolvents which preferentially bind to the biomolecule are present in excess number in the local surface domain of the biomolecules over the bulk (see Figure 2.7 (a)). Conversely, a preferentially excluded cosolvent leads to an excess of water molecules around the biomolecule and, thereby, to its preferential hydration (see Figure 2.7 (b)). Thus, the mutual perturbation in the chemical potentials of cosolvents and biomolecules also affects that of the surrounding water [Timasheff, 2002, Timasheff, 1993, Parsegion et al., 2000, Record and Anderson, 1995]. In unfolding reactions, preferentially excluded osmolytes (stabilizers) favor the folded state [Canchi and García, 2013]. The preferential exclusion of the cosolvent from the protein stabilizes the conformation with the smallest solvent accessible surface area (SASA), and thereby favors the more compact native state of the protein over the more open structure of the denatured state with larger SASA. The neutral organic osmolytes L-proline, sarcosine, taurine, L-alanine,  $\beta$ -alanine, glycine, betaine and TMAO in concentrated state reportedly lead to a preferential hydration of the proteins lysozyme and bovine serum albumin and also to structural stabilization of the protein against thermal denaturation [Arakawa and Timasheff, 1983, Arakawa and Timasheff, 1985]. For sugars and polyols the source of conformational preservation was found also in the preferential hydration [Arakawa and Timasheff, 1982, Gekko and Timasheff, 1981b, Lee and Lee, 1981]. However, at very high concentration (generally > 50%), preferentially excluded cosolvents like glycerol and sucrose also might accumulate at the proteins surface.

Preferentially binding of cosolvents to the protein can result in a stabilization or destabilization of the protein, depending on whether the cosolvent molecules preferentially bind to the denatured or native state (or both). Perturbants like urea and guanidinium hydrochloride (GndHCl) preferentially interact with the poorly hydrated/apolar regions and accumulate at the proteins surface. Urea and GdmCl solvate the hydrophobic residues of the protein thereby reduce the effective hydrophobic reaction [Panuszko et al., 2009, Wallqvist et al., 1998]. This results in the extension of hydrated surface area (e.g. through ligand release, subunit dissociation and peptide unfolding), since for the protein the binding with the destabilizer is thermodynamically favorable [Simpson and Kauzmann, 1953, Cohn and Edsall, 1965, Tanford,

1964, Tanford, 1970]. At sufficiently high concentrations (typically  $\sim 6$  M), the preferentially binding eventually results in unfolding of the protein since a more open structure with more exposed hydrophobic groups favors the cosolvent-protein interactions [Timasheff and Xie, 2003].

- The Tanford Transfer Model accentuates the exclusive role of the protein peptide backbone in the energetics of cosolvent-induced protein folding and unfolding with only small contributions from side chains and negligible contributions from hydrophobic groups [Tanford, 1964, Bolen and Rose, 2008, Auton and Bolen, 2005]. This is in contrast to the model of preferential exclusion and preferential binding, where the major contribution comes from the protein side chains [Canchi and García, 2013]. In fact, the Tanford Transfer Model shows that shifts in protein stability are almost entirely controlled by protein backbone hydrogen bonding as a function of solvent quality. The degree to which a cosolvent either protects or destabilizes the protein structure relative to the pure buffer scenario depends on whether the cosolvent increases water solvent quality by favoring intramolecular peptide backbone-backbone hydrogen bonds (structure stabilizing), or diminish water solvent quality by increasing backbone-solvent hydrogen bonds in water (structure destabilizing) [Bolen and Rose, 2008, Auton and Bolen, 2005]. Previous studies have shown, that a repulsion between the stabilizers and the peptide-bond backbone results in a strong exclusion of the osmolyte from the protein surface and hence preferential hydration of the protein interface [Street et al., 2006]. Reducing the exposure of hydrated surface area and thus the entropically unfavorable interaction between cosolvent and backbones polar groups leads to a more compact protein folding and stabilization of the native protein folds against denaturation [Arakawa and Timasheff, 1985, Canchi and García, 2013].

### Cosolvent Effects on the Structure and Dynamics of Water

Changes in the hydrogen-bond network of the aqueous solvent can modulate hydrophobic interactions and intramolecular hydrogen bonding which represent the driving forces in conformational stability and dynamics of biomolecular systems. Cosolvents can perturbate and stabilize water structure and dynamics within and beyond the hydration shell of the solute. Water of hydration differs in many properties from those of bulk water, i.e. it is more ordered, has higher heat capacity and has reduced mobility compared to bulk water [Merzel and Smith, 2002].

Polyolic osmolytes like *myo*-Inositol, sucrose, trehalose and glycerol as well as the polymer PEG are strongly hydrophilic, contain hydrocarbon chains with multiple hydroxyl groups and therefore are structurally suited to fit the water lattice and to form hydrogen bonds with water. Here, this stronger affinity for the interaction with water than with the polar residues on the protein surface leads to a deficiency of the osmolyte in the vicinity of the protein and its preferential hydration [Gekko and Timasheff, 1981a, Lee and Lee, 1981, Sousa, 1995, Parsegion et al., 2000, Timasheff, 2002]. The consequences of this so-called **solvophobic effect** are the reinforcement of the water structure, the stabilization of the native protein conformation due to its smaller interaction interface and the decrease of intermolecular attractive interaction [Javid, 2007].

Preferential hydration might even prevent association of proteins as it is more difficult to remove hydration water from the interface between two proteins [Kozer et al., 2007]. The **(hydration-) repulsion** between the proteins increases, since the overlap and thus the partial destruction of the accumulated highly structured solvent layer near surface when two macromolecules approach each other, involves high costs in free energy [Belloni, 2000]. The hydration force reflects the required work to remove water from around the surface polar groups when two proteins approach each other and is suggested to play an important role in protein interactions [Edsall and McKenzie, 1983, Leikin et al., 1993, Broide et al., 1996]. Similar trends were reported by previous works on glycerol and sucrose in lysozyme and bovine pancreatic trypsin inhibitor (BPTI) solutions at ambient pressure and for glycerol at elevated pressures [Schroer et al., 2011b, Krywka et al., 2008, Farnum and Zukoski, 1999].

The denaturants urea and GdmCl are both weakly hydrated, since their  $-\text{NH}_2$  groups form only weak hydrogen bonds with water. The perturbant urea hardly affects the H-bond dynamics of

water beyond its first hydration shell [Rezus and Bakker, 2006] and fits well into the tetrahedral H-bond network of liquid water [Soper and Ricci, 2000]. Thus, the destabilizing effect of urea on protein structure is widely explained by its (direct) favorable interactions with the peptide backbone and amino acid side chains resulting in its preferential binding to the protein surface over water [Auton and Bolen, 2005, Stumpe and Grubmüller, 2007, Lee et al., 2010, Guinn et al., 2011, Guinn et al., 2013].

The hydration picture of the amphiphilic deep-sea osmolyte TMAO is more complex. Theoretical and experimental work report on the formation of strong hydrogen bonds in the hydration shell of the highly polar osmolyte in terms of shorter atomic distances, increased H-bond energy as well as a retardation of water dynamics reportedly increases the number of hydrogen bonds and thereby stabilizes the water structure [Street et al., 2006, Batchelor et al., 2004, Shikata and Itatani, 2002, Wei et al., 2010, Rezus and Bakker, 2009, Meersman et al., 2009, Panuszko et al., 2009, Kuffel and Zielkiewicz, 2010, Knake et al., 2015]. As TMAO strongly interacts with solvent molecules and its interactions with the peptide backbone of proteins and nucleic acids are unfavorable, the stabilizing effect of the deep-sea osmolyte on biomolecules may originate from an indirect mechanism of water structure enhancement [Wei et al., 2010, Zou et al., 2002, Arakawa and Timasheff, 1985, Bolen and Baskakov, 2001].

## 2.2 Model Systems and Intermolecular Interaction Potentials in Aqueous Biomolecular Systems

Biological macromolecules in solution interact with each other through medium-ranged (from a few Å to a few nm) interaction potentials, which control their spatial distribution in solution, liquid-liquid phase behavior as well as crystal growth and amorphous precipitation. These interactions include electrostatic and van der Waals contributions, osmotic attractive interactions due to the excluded volume effect, strong and short-ranged specific interactions such as hydrophobic bonds, hydrogen bonds and ionic bonds resulting in self-association as well as short-ranged repulsive hydration forces [Curtis et al., 1998, Narayanan and Liu, 2003, Molina-Bolívar et al., 1997]. Such repulsive hydration forces depend on the energy needed to dehydrate the surface of the protein and they arise whenever water molecules are highly structured or ordered around polar groups on the proteins surface [Israelachvili, 2011]. Small angle X-ray scattering (SAXS) is a powerful technique to follow the changes induced upon variation of the physico-chemical conditions such as protein concentration, pH, pressure, temperature, ionic strength and solvent additives like nano- and macromolecular crowder and organic osmolytes [Israelachvili, 2011, Hansen and McDonald, 2013]. SAXS yields the osmotic second virial coefficient,  $B_{22}$ , and by measuring the interaction parameters indirectly, it can get also an insight into the effective interaction potential and its single contributions.

$B_{22}$  is a convenient tool in studies of solutions containing biomolecules. It provides a measure of the strength of protein interactions and contains information on the stability of a protein solution. It is used to model and explain multiple pair-wise protein self-interactions like crystallization, liquid-liquid phase separation, folding/refolding and aggregation.  $B_{22}$  is defined via the osmotic virial expansion [Eisenberg, 1976],

$$\frac{\Pi(c)}{cRT} = \frac{1}{M_w} + B_{22} \cdot c + \mathcal{O}(c^2), \quad (2.2)$$

wherein,  $\Pi(c)$  is the osmotic pressure,  $R$  is the ideal gas constant,  $c$  is the particle concentration in units  $\text{g L}^{-1}$ ,  $T$  is the absolute temperature and  $M_w$  is the protein molecular weight in units  $\text{g mol}^{-1}$ . As a direct measure of the intermolecular forces between molecules,  $B_{22}$  can be calculated from the intermolecular pair-interaction potential,  $V(r)$ , via

$$B_{22} = 2\pi \frac{N_A}{M_w^2} \int_0^\infty \left( 1 - \exp\left(-\frac{V(r)}{k_B T}\right) \right) r^2 dr, \quad (2.3)$$

where  $N_A$  is the Avogadro constant and  $k_B$  is the Boltzmann constant.  $B_{22}$  serves as characteristic interaction parameter, allowing for the comparison of various biomolecular systems and

solution conditions independent of the model used for the effective interaction potential. The second osmotic virial coefficient reveals the predominantly attractive (-) or repulsive (+) nature of the two-body interaction simply by its sign [George and Wilson, 1994, Sedgwick et al., 2007, Quigley and Williams, 2015]. A general description of the intermolecular interactions between the macromolecules, depending neither on the protein type nor its size, can be obtained by factoring out the contribution of the hard sphere part,  $B_2^{\text{HS}} = 2\pi(\sigma_{\text{lys}} + \delta_b)^3/3$ , of the integral in Eq. (2.3) [Noro and Frenkel, 2000]:

$$b_2 = \frac{B_{22}M_w^2}{N_A B_2^{\text{HS}}} = 1 + \frac{3}{(\sigma + \delta_b)^3} \int_{\sigma + \delta_b}^{\infty} \left( 1 - \exp\left(-\frac{\tilde{V}(r)}{k_B T}\right) \right) r^2 dr. \quad (2.4)$$

The calculation of the excluded volume contribution,  $B_2^{\text{HS}}$ , takes an impenetrable layer of water into account. The thickness,  $\delta_b$ , describes the minimal approach of two lysozyme molecules and determines the lower limit of integration in Eq. (2.4). In order to remain consistent with literature,  $\delta_b$  is set to 0.1437 nm [Sedgwick et al., 2007, Möller et al., 2012, Poon et al., 2000]. For many different globular proteins and precipitants (including lysozyme/NaCl) a quasi-universal crystallization boundary is observed in the  $(\Phi_{\text{lys}}, b_2)$ -plane ( $\Phi_{\text{lys}}$ : protein volume fraction) [George and Wilson, 1994, Rosenbaum et al., 1996]. A normalized virial coefficient of  $b_2 < -1.5$  is reportedly needed in order to undergo liquid-liquid phase separation [Vliegthart and Lekkerkerker, 2000] and solution conditions conducive to crystallization correspond to a 'crystallization window' of  $-0.85 < b_2 < -3.2$  [George and Wilson, 1994, Poon et al., 2000]. Whilst for  $b_2$  values more positive than  $-0.85$ , the attractive interaction between the proteins is too weak to form stable protein crystals, the attraction is sufficiently strong for smaller values than  $-3.2$ . As a result, poorly ordered, amorphous agglomerates are formed rather than crystals, since the proteins have not sufficient time for proper mutual orientation as needed for crystallization [Bonneté et al., 1999, Wanka and Peukert, 2011]. Static and dynamic light scattering (SLS and DLS) are well-established techniques to probe the osmotic second virial coefficient,  $B_{22}$ , for dilute solutions [George and Wilson, 1994, Rosenbaum et al., 1996, Curtis et al., 1998, Velev et al., 1998, Petsev and Vekilov, 2000, Muschol and Rosenberger, 1995], whilst small angle neutron scattering (SANS) [Velev et al., 1998] and small angle X-ray scattering (SAXS) [Bonneté et al., 1999] are often employed for the study of denser solutions.

### 2.2.1 Lifshitz Theory - Van der Waals Interaction between Macroscopic Particles

Intermolecular van der Waals (vdW) dispersion forces play a significant role in all phenomena involving surface tension, physical adsorption, adhesion and structures of condensed macromolecules such as proteins and polymers. Even though vdW interactions are weak compared to electrostatic Coulomb or H-bonding interactions, they are always present and highly relevant both at short ( $\sim 0.2$  nm) and large ( $> 10$  nm) inter-particle distances. Dispersion forces between macromolecules may be repulsive or attractive and, in general, cannot be described by a simple power law function. Dispersion forces originate from quantum mechanics: The time averaged fluctuating dipole moment of a non-polar atom (e.g. helium) equals zero, but at any instant there exists a finite dipole moment which is determined by the positions of the electrons around the nuclear protons. The electric field, generated by such an instantaneous dipole, polarizes any neighboring neutral atom and induces a dipole moment in it. Thus, the dipole field is 'reflected back' by the other nearby atom which has been polarized by this field. This dipole-dipole interaction results in an instantaneous attractive force between the two atoms, whose time average is finite. [Israelachvili, 2011] The London expression for the vdW interaction energy,  $w(r)$ , of two identical small atoms or small molecules with diameter  $\sigma$  and center-to-center separation  $r \geq \sigma$  in vacuum is given by [London, 1937]

$$\begin{aligned} w(r) &= -\frac{3}{4} \frac{\alpha_0^2 h \nu}{(4\pi\epsilon_0)^2} \frac{1}{r^6} \\ &= -\frac{C}{r^6}. \end{aligned} \quad (2.5)$$

Here,  $h$  is the Planck constant,  $\nu$  the orbiting frequency of the electron ( $\nu = 3.3 \times 10^{15} \text{ s}^{-1}$  for a Bohr atom), and  $\alpha_0$  the electronic polarizability of the second atom.



For simplicity, we assume the vdW interactions between two atoms (molecules) being pair-wise *additive* and *non-retarded*<sup>1</sup>. Considering two macroscopic bodies of arbitrary geometries made up of like molecules, the effective 'two-body' potential of them will be the integral over the inter-atomic van der Waals pair potentials (Eq. 2.5) of the atoms in one body with the atoms in the other. For two interacting spheres with diameter  $\sigma$ , the resulting effective vdW pair-interaction potential in vacuum as a function of the center-to-center separation  $r$  reads [Israelachvili, 2011]

$$V_{\text{vdW}}(r) = -\frac{A}{12} \left( \frac{\sigma^2}{r^2 - \sigma^2} + \frac{\sigma^2}{r^2} + 2 \ln \left( 1 - \frac{\sigma^2}{r^2} \right) \right), \quad r > \sigma, \quad (2.6)$$

with  $V_{\text{vdW}}(r) \sim -(A\sigma^6/36)/r^6$  for large  $r$  and  $V_{\text{vdW}}(r) \sim -(A\sigma/24)/(r - \sigma)$  near the contact distance  $r = \sigma$ . The divergence of  $V_{\text{vdW}}(r)$  at contact distance, arising from the assumption of an ideally smooth surface of the spherical particles with two surface atoms overlapping [Nägele, 2008], is suppressed by an additional steric protection  $\sigma + \delta_b$ . The values reported in literature are within the range 0.1 - 0.3 nm. In concert with previous works, we set  $\delta_b = 0.1437$  nm [Poon et al., 2000, Sedgwick et al., 2007, Möller et al., 2012, Malfois et al., 1996]. In Eq. (2.6),  $A$  denotes the Hamaker constant, which is defined as

$$A = \pi^2 C \rho_1 \rho_2, \quad (2.7)$$

where  $\rho_1$  and  $\rho_2$  are the number of atoms per unit volume in the two bodies. The vdW interaction force,  $-dV_{\text{vdW}}/dr$ , is attractive when  $A$  positive and repulsive when  $A$  negative.

By making the assumption of pairwise additivity we omit the fact that the vdW pair-interaction between two atoms is influenced by the neighboring atoms. The effective polarizability of an atom changes in the presence of other atoms. Since all the atoms nearby are also polarized, the field emanating from one atom reaches a second atom both directly and by 'reflection' from other atoms. These multiple reflections lead to an additional contribution to the total vdW interaction potential. Within **Lifshitz theory** [Lifshitz, 1956, Dzyaloshinskii et al., 1961], the atomic structure of the particles is ignored and they are treated as homogeneous media, simply determined by bulk properties like the frequency dependent dielectric permittivity,  $\epsilon(i\nu)$ , and refractive indices,  $n$ . The dielectric permittivity of a medium exhibits much the same frequency dependence like the atomic polarizability of the atoms. A protein, dissolved in the solvent medium with dielectric permittivity  $\epsilon_s(i\nu)$ , can be modeled as a dielectric sphere of diameter  $\sigma$  and dielectric constant  $\epsilon_{\text{prot}}(i\nu)$  (see Fig. 2.8).

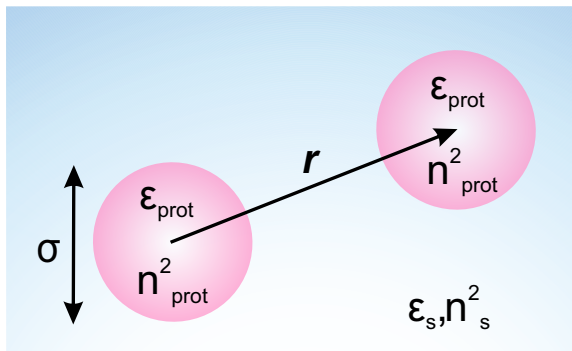


Figure 2.8: Identical Spheres of hard-sphere diameter  $\sigma$  interacting across a solvent medium.

As the expression for the vdW pair-interaction potential between two spheres (Eq. 2.6) is left unchanged, the non-retarded Hamaker constant,  $A$ , for two identical macroscopic bodies (e.g. proteins) interacting across another medium (e.g. water) is now calculated via [Israelachvili, 2011,

<sup>1</sup>Retardation effects occur for particles and molecules at large separations or interacting in a liquid medium, when the time taken for the electric field of the atom 1 to reach atom 2 becomes comparable with the period of the fluctuating dipole emanating the field.

Hunter, 2001]:

$$A = A_{\nu=0} + A_{\nu>0} \approx \frac{3}{4}k_B T \left( \frac{\epsilon_{\text{prot}} - \epsilon_r}{\epsilon_{\text{prot}} + \epsilon_r} \right)^2 + \frac{3h}{4\pi} \int_{\nu_1}^{\infty} \left( \frac{\epsilon_{\text{prot}}(i\nu) + \epsilon_s(i\nu)}{\epsilon_{\text{prot}}(i\nu) - \epsilon_s(i\nu)} \right)^2 d\nu \quad (2.8)$$

Here,  $\epsilon_r = \epsilon(0)$  denotes the static dielectric constant of the solvent and  $\nu_n = (2\pi k_B T/h)n = 4 \cdot 10^{13} \text{ s}^{-1}$  at 300 K with  $n$  being the refractive index of the medium in the visible ( $n^2 = \epsilon_{\text{vis}}(\nu)$ ). The first term,  $A_{\nu=0}$ , in Eq. (2.8) gives the zero-frequency energy of the vdW interaction and the second term,  $A_{\nu>0}$ , the dispersion energy of two protein phases across a water film. The dielectric permittivity of a medium,  $\epsilon(i\nu)$ , as a function of the frequency,  $\nu$ , is given by [Mahanty and Ninham, 1976, Parsegian, 2006]:

$$\epsilon(i\nu) = 1 + \frac{(\epsilon - n^2)}{1 - \nu/\nu_{\text{rot}}} + \frac{(n^2 - 1)}{1 + \nu/\nu_e}, \quad (2.9a)$$

$$\epsilon(0) = 1 + (\epsilon - n^2) + (n^2 - 1) = \epsilon_r, \quad (2.9b)$$

$$\epsilon(\infty) = 1. \quad (2.9c)$$

Here,  $\nu_{\text{rot}} < 10^{12} \text{ s}^{-1}$  is the molecular rotational relaxation frequency and  $\nu_e$  the media main electronic absorption frequency in the UV. Figure 2.9 depicts the dielectric permittivity of water and a typical hydrocarbon as a function of frequency. Since carbon chains with attached hydrogens are a key structural element in most macromolecules, here, the dielectric permittivity of hydrocarbon serves as a rough indication of the proteins dielectrics. Water exhibits a strong absorption at low frequencies and therefore has a high static dielectric constant of  $\epsilon_r = 78.36$  ( $T = 25^\circ\text{C}$ ) [Kaatze and Uhlendorf, 1981]. For the protein lysozyme,  $\epsilon_{\text{prot}} \approx 2$  [Dwyer et al., 2000]. Since  $\nu_1 \approx 4 \cdot 10^{13} \text{ s}^{-1} \gg \nu_{\text{rot}}$ , the frequency dependent dielectric permittivities  $\epsilon(i\nu)$  of both media, contributing to the integral in Eq. (2.8), are reduced to the second term in Eq. (2.9a):

$$\epsilon(i\nu) = 1 + \frac{n^2 - 1}{1 + \nu^2/\nu_e^2}. \quad (2.10)$$

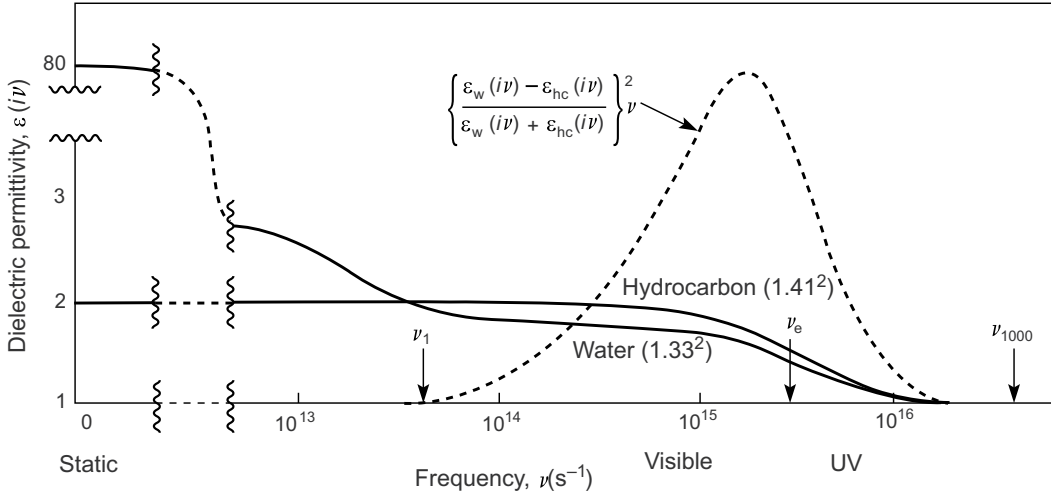


Figure 2.9: Dielectric permittivity  $\epsilon(i\nu)$  of water and hydrocarbon as a function of frequency  $\nu$ . Picture was adapted from [Israelachvili, 2011].

Under the assumption, that the absorption frequencies,  $\nu_e$ , of both particle and solvent are roughly the same (e.g. the characteristic UV electronic absorption frequency  $\nu_e = 3 \cdot 10^{15} \text{ s}^{-1}$ ), we obtain from inserting Eq. (2.10) in Eq. (2.8) the expression

$$A \approx \frac{3}{4}k_B T \left( \frac{\epsilon_{\text{prot}} - \epsilon_r}{\epsilon_{\text{prot}} + \epsilon_r} \right)^2 + \frac{3h\nu_e(n_{\text{prot}}^2 - n_s^2)^2}{16\sqrt{2}(n_{\text{prot}}^2 + n_s^2)^2}. \quad (2.11)$$

As clearly can be seen from Eqs. (2.6) and (2.11), the vdW dispersion force between two *identical* bodies (e.g. proteins) interacting across a medium described by the dielectrics  $(\epsilon_r, n_s)$  is always attractive ( $A$  positive). Non-identical particles can repel each other, however, when the dielectric permittivity of the solvent is between that of the interacting particles.

In this thesis, the solvents dielectrics  $\epsilon_r$  and  $n_s$  are taken from literature or from own dielectric spectroscopy (see section 3.5) and refractometry measurements (see section 3.4). Following [Farnum and Zukoski, 1999, Hand, 1934], the refractivity of the pure lysozyme molecule in the dissolved state,  $n_{\text{prot}} = 1.5176$ , is estimated from the specific refractive increment of pure aqueous lysozyme solutions ( $dn_{\text{prot,s}}/dc = 0.1943 \text{ mL g}^{-1}$  at pH 7) [Rickard et al., 2010, Fredericks et al., 1994] by extrapolating to solutions containing protein, only:

$$\epsilon_{\text{prot}} = \frac{M_w}{N_A \cdot \frac{4}{3}\pi(a^2b)} \cdot \frac{dn_{\text{prot,s}}}{dc} + n_s. \quad (2.12)$$

Here,  $M_w$  describes the molecular weight of lysozyme ( $14.300 \text{ g mol}^{-1}$ ),  $N_A$  the Avogadro constant and  $a = 1.57 \text{ nm}$  and  $b = 2.42 \text{ nm}$  the minor and major semi-axes of the prolate ellipsoid approximating the dimensions of a lysozyme molecules in solution (see section 2.4.2). Although the specific refractive increment varies with the refractivity of the solvent  $n_s$ , the extrapolated value  $n_{\text{prot}}$  for pure protein in solution is practically independent of the solvents studied here and characteristic for the protein, only [Hand, 1934]. The depth of the vdW potential is related, although in an indirect manner, to the Hamaker constant. We find, for large spherical particles in aqueous solution, the vdW potential is only relevant at short distances. Of note, since the time for adjustment between ions in the vicinity of a particles charged surface exceeds by far the correlation time of electronic fluctuations between atoms, the dispersion force is independent of the solutions ionic strength (e.g. presence of ions) as well as pH value [Israelachvili, 2011].

## 2.2.2 Depletion Theory and Osmotic Attraction Potential

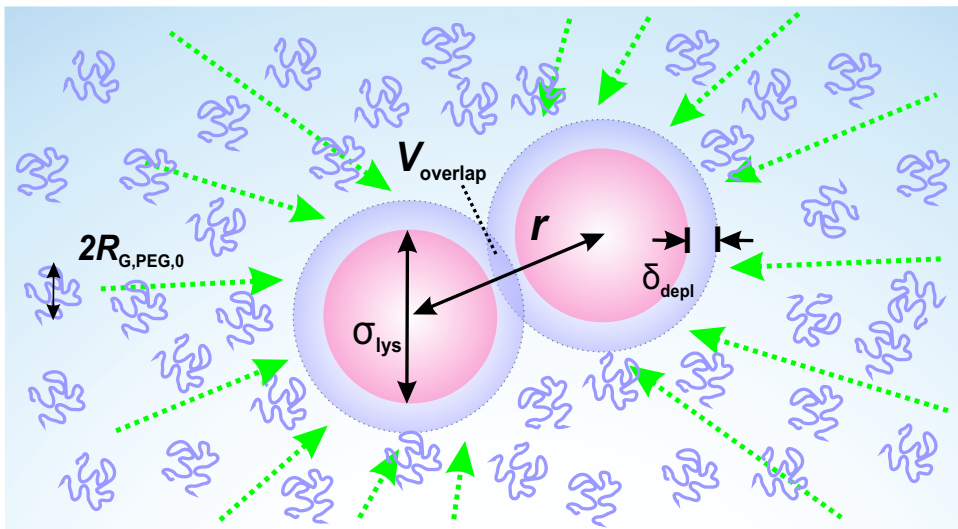


Figure 2.10: Basic principle of the depletion mechanism in a colloid-polymer mixture. Two globular proteins, here approximated by two homogeneous hard spheres of effective hard sphere diameter  $\sigma_{\text{lys}}$ , with centers separated by  $r$  are dispersed in an aqueous solution containing non-adsorbing polymers with radius of gyration  $R_{G,\text{PEG},0}$ . The polymers centers of mass are excluded from a region around the proteins with thickness  $\delta_{\text{depl}}$ . An overlap of these regions results in the exclusion of the polymers from the intermediate space between the proteins and thereby in an entropically favored attractive depletion interaction between the proteins.

High molecular weight PEGs exhibit properties of a quasi-random coil with some solvent-induced short-range ordering near the polymer backbone [Abbott et al., 1991]. The number of possible chain



conformations of the PEG polymer in solution increases with the degree of polymerization, i.e. polymer molecular weight  $M_w$ . The neighborhood of an impenetrable surface like a protein causes constraints on the conformational freedom of the polymer, i.e. is entropically unfavorable. Hence, the polymers are excluded from a sphere of radius  $\sigma_{\text{lys}}/2 + \delta_{\text{depl}}$  around the globular protein, where the depletion thickness,  $\delta_{\text{depl}}$ , is of the order of the characteristic length scale describing the polymer in solution (see Figure 2.10). If  $\delta_{\text{depl}}$  exceeds half of the protein’s surface-to-surface distance, the depletion zones surrounding the proteins overlap and the polymer is effectively excluded from the intermediate space of the protein [Poon et al., 1996, Lekkerkerker et al., 1992]. Because of the unbalanced osmotic pressure,  $\Pi$ , an attractive depletion potential of a range dependent on the effective polymer size and a strength dependent on polymer concentration, acts on the non-interpenetrating proteins. Since extra volume is recovered for the polymer when the depletion zones of the proteins overlap, the downsizing of the inaccessible space for the polymer is entropically favored and results in an effective attraction between the protein molecules [Vrij, 1976, Meijer and Frenkel, 1994]. Hence, for a sufficient amount of sufficiently large polymer, attractive protein-protein depletion interactions may be induced in a naturally repulsive polymer-protein mixture. Due to fluctuations of the coil shape in polymer solutions, the short-ranged depletion attraction is not cut off abruptly, but falls off slowly. The range of the depletion potential in protein-polymer mixtures depends strongly on the ratio of the protein size and the characteristic length scale describing the polymer in solution, which is highly correlated to the polymer concentration. To describe the interaction between the proteins, the particular length scales of the various polymer solutions need to be characterized. For the polymer’s radius of gyration in dependence of the relative molecular weight, a power-law behavior,  $R_{G,\text{PEG},0} = 0.0215 M_w^{(0.583 \pm 0.031)} / \text{nm}$  [Devanand and Selser, 1991] is reported, which corresponds to the conformation of a non-interacting swollen globule for a diluted polymer system (see Table 2.2.2). Beyond the polymer’s overlap concentration,  $c^*$ , which depends on the degree of polymerization (and hence  $M_w$ ), the volume excluded per polymer molecule diminishes due to shrinking and/or increasing compactness, according to  $R_{G,\text{PEG}} = R_{G,\text{PEG},0} \cdot (c_{\text{PEG}}/c^*)^{-1/8}$  [Teraoka, 2002].

	Molecular Weight $M_w / \text{g mol}^{-1}$	Hydrodynamic diameter $\sigma / \text{nm}$	Radius of gyration $R_{G,\text{PEG},0} / \text{nm}$	Overlap concentration $c^* / \% (\text{w/v})$
PEG 200	200	0.6	0.47	66.96
PEG 600	600	1.12	0.9	31.14
PEG 2k	2000	2.22	1.81	13.45
PEG 6k	6000	4.16	3.43	6.26
PEG 8k	8000	4.91	4.05	5.11
PEG 10k	10000	5.58	4.62	4.38
PEG 20k	20000	8.28	6.92	2.70
PEG 35k	35000	11.40	9.59	1.83
sucrose	342.30	0.52		
lysozyme	14300	$3.78 \pm 0.05$	$1.45 \pm 0.05$	

Table 2.2: Structural parameters describing the polymer PEG, sucrose and lysozyme in aqueous solution. Radii of gyration,  $R_{G,\text{PEG},0}$ , and hydrodynamic diameter,  $\sigma_{\text{PEG}}$ , for PEG are calculated from [Devanand and Selser, 1991]. The polymer overlap concentration,  $c^*$ , is calculated from the  $R_{G,\text{PEG},0}$  values shown in this table after [de Gennes, 1979b]. The hydrodynamic diameter,  $\sigma_{\text{lys}}$ , of lysozyme [Parmar and Muschol, 2009] and sucrose,  $\sigma_{\text{sucrose}}$ , [Schultz and Solomon, 1961] are taken from literature.

For example, the radius of gyration of a single PEG 3400 chain decreases with increasing polymer concentration from 1 to 30 wt.-% by about 6% [Gurnev et al., 2017]. At the cross-over from the dilute to the semi-dilute polymer regime, marked by  $c^* = M_w / (4/3\pi R_{G,\text{PEG},0}^3 N_A) / \text{mg mL}^{-1}$  [de Gennes, 1979b], an extensive entanglement of PEG molecules takes place and the entire volume is occupied by non-overlapping polymer coils (see Table 2.2.2). While for dilute solutions ( $c_{\text{PEG}} \ll c^*$ ) the identity of the individual polymer chain is preserved and determinant for the

solution properties, for  $c_{\text{PEG}} \geq c^*$  the system transitions from individually dispersed random coils to an entangled mesh of polymers [Mao et al., 1995], whose thermodynamic properties are being solely a function of the polymer's volume fraction,  $\Phi$ , which can be calculated from the protein concentration by using its partial specific volume ( $\tilde{V}^\circ = 0.825 / \text{mL g}^{-1}$  for PEG [Cohen et al., 2009]) [Abbott et al., 1991, de Gennes, 1979a]. As characteristic length scale, the polymer's radius of gyration is not suitable anymore, and has to be replaced by the correlation length (mesh size)  $\xi_b \approx a \cdot \Phi^{-3/4}$  of the entangled polymer net with the length scale of a monomer of  $a = 0.4 \text{ nm}$  [Mao et al., 1995, Cohen et al., 2009]. In terms of overlap concentration, the mesh size can be written as  $\xi_b \approx R_{G,\text{PEG},0} \cdot (c_{\text{PEG}}/c^*)^{-3/4}$  [Teraoka, 2002]. The mesh size decreases with increasing polymer concentration (volume fraction).

It was shown by a previous study on the osmotic pressure of aqueous polyethylene glycol of average molecular weights between ( $200 < M_w < 10000$ )  $\text{g mol}^{-1}$ , that low molecular weight PEG generate higher osmotic pressure than higher molecular weight PEGs at equivalent weight fraction (10% (w/v)  $< c_{\text{PEG}} < 30\%$  (w/v)) [Money, 1989]. For example, the curve fit by regression of the data for osmotic pressure in dependence of polymer molecular weight at 30% (w/v) PEG yields  $\Pi(M_w) = 419 \cdot (\log M_w)^{-2.4} / \text{bar}$  (e.g.  $\Pi(\text{PEG } 200) \sim 56.7 \text{ bar}$ ,  $\Pi(\text{PEG } 600) \sim 36.1 \text{ bar}$ ,  $\Pi(\text{PEG } 10000) \sim 15 \text{ bar}$ ). At a given number of polymers in solution, the increase of  $\Pi$  is reportedly steeper for large than for small  $M_w$ . Slightly above the overlap concentration  $c^*(M_w)$  of polyethylene glycol/water systems, [Cohen et al., 2009] identified a crossover concentration for osmotic pressure  $c^\#(M_w) = (1.78 \pm 0.03) \cdot c^*(M_w)$ , where the solutions of the neutral flexible polymers transfer from the dilute to the semi-dilute regime.

In terms of pure depletion theory, the depletion attraction between two proteins with radius of gyration  $R_{G,\text{lys}}$  in the protein-polymer mixtures depends on the concentration-dependent protein-to-blob size ratio in a non-monotonous manner. In the case  $\xi_b < R_{G,\text{lys}}$ , the polymer chains are depleted from the protein surface due to repulsive excluded volume interactions. The thickness of the depletion zone,  $\delta_{\text{depl}}$ , scales with  $\xi_b$  and shrinks with increasing polymer volume fraction [Abbott et al., 1992, Fuchs and Schweizer, 2001]. Strong attractive depletion forces between the proteins are only induced if the electrostatic repulsion due to the surface charge of the protein is small enough and the protein concentration high enough for the depletion zones of the proteins to overlap. Mesh sizes comparable to the protein's radius of gyration ( $\xi_b \approx R_{G,\text{lys}}$ ) lead to a minimal to no depletion attraction since the proteins fit perfectly into the polymer mesh spaces without distorting the network [Abbott et al., 1991, Fuchs and Schweizer, 2001]. If the size of the protein is significantly smaller than the blob size ( $\xi_b \ll R_{G,\text{lys}}$ ), the protein is capable of diffusing through the mesh.

To quantitatively explore the impact of the polymer on the attractive depletion interaction between two protein molecules with centers separated by  $r$ , the depletion potential,  $V_{\text{depl}}(r)$ , can be calculated in the framework of the analytic Polymer Reference Interaction Site Model (PRISM) [Poon et al., 1997, Ilett et al., 1995, Chatterjee and Schweizer, 1998b, Chatterjee and Schweizer, 1998a, Chatterjee and Schweizer, 1999]. PRISM is a two-component liquid-state approach based on the Percus-Yevick closure for describing polymer-induced attractive depletion forces between hard spheres. Within PRISM,  $V_{\text{depl}}(r)$  predicts the polymer-mediated protein-protein interaction for all polymer coil dimensions at polymer concentrations below and beyond  $c^*$  with no adjustable parameters, from

$$V_{\text{depl}}(r) = -k_B T \ln \left[ 1 + \frac{\pi z}{3} \left( \frac{R}{r} \right) \left( \frac{R}{\sigma} \right) \exp \left( \frac{1}{-\delta_{\text{depl}}} (r - 2R) \right) \right], \quad r > 2R \quad (2.13)$$

$$\sigma = \begin{cases} \sigma_0, & c_{\text{PEG}} < c^* \\ \sigma_0 \left( \frac{c_{\text{PEG}}}{c^*} \right)^{-1/8}, & c_{\text{PEG}} \geq c^* \end{cases} \quad (2.14)$$

$$R_{G,\text{PEG},0} = \sigma \sqrt{\frac{N}{6}}, \quad (2.15)$$

$$z = NN_A c_{\text{PEG}} \sigma^3, \quad (2.16)$$

$$\delta_{\text{depl}} = \sigma \frac{1}{\sqrt{12/N} + \pi z/3}. \quad (2.17)$$

Here,  $\sigma$  is the effective statistical segment length of the polymer chain with a monomer segment length of  $\sigma_0 = 0.4$  nm [Takahashi and Tadokoro, 1973].  $N \approx M_w / 44$  g mol<sup>-1</sup> defines the number of segments per chain. Fluctuations in polymer concentration are spatially correlated over a distance described by the depletion thickness,  $\delta_{\text{depl}}$  [de Gennes, 1979b].  $R$  describes the polymer segment-to-protein distance of closest approach, which equals the protein radius under the assumption of additivity of the hard core diameters [Chatterjee and Schweizer, 1998a, Biben and Hansen, 1997]; here, we set  $R \approx R_{G,\text{lys}} = 1.45$  nm.

### 2.2.3 Derjaguin Landau Verwey Overbeek (DLVO) - Theory of Colloidal Stability

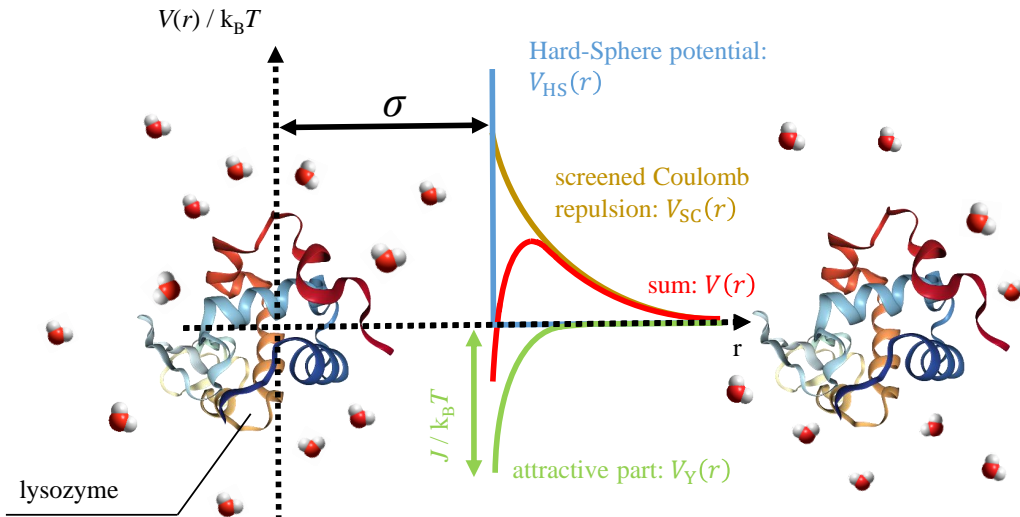


Figure 2.11: The Derjaguin Landau Verwey Overbeek (DLVO) - potential of two lysozyme molecules in aqueous solution and its single contributions.

The Derjaguin Landau Verwey Overbeek (DLVO)- theory [Derjaguin and Landau, 1993, Verwey and Overbeek, 1948] describes the stability of a colloidal suspension by the balance between an electrostatic coulombic force and the van der Waals force (see section 2.2.1), including a hard sphere (excluded volume) force. The DLVO effective potential is deduced within the one-component macrofluid model: The discrete nature of the polar solvent (e.g. water) is neglected and the solvent is approximated by a continuous dielectric medium with the static dielectric permittivity  $\epsilon_r$ . The interacting particles (e.g. proteins) are modeled by homogeneously charged hard spheres with diameter  $\sigma$ , uniform net surface charge,  $Z_{\text{eff}}$ , and number density  $n$ . Thus, anisotropy of particle shape and charge distribution are neglected. Dissolved salt ions are considered as point like charges (diameter  $\sigma = 0$ ) which formate as a counter ion cloud around the particle, effectively screening the particles surface charge towards a second particle and thereby decreasing their electrostatic repulsion (see Figure 2.12). As found in previous studies [Schroer et al., 2011b, Schroer et al., 2011a, Möller et al., 2012], the effective pair interaction potential of lysozyme molecules in solution,

which centers are separated by the distance  $r$ , is well described in the framework of the DLVO theory by the sum of a long-ranged repulsive screened Coulomb potential  $V_{\text{SC}}(r)$ , a short-ranged attractive Yukawian-like potential  $V_{\text{Y}}(r)$  and a hard-sphere (excluded-volume) potential  $V_{\text{HS}}(r)$ :

$$V(r) = V_{\text{HS}}(r) + V_{\text{SC}}(r) + V_{\text{Y}}(r). \quad (2.18)$$

The single contributions of  $V(r)$  are depicted in Figure 2.11 and discussed in detail in the following. The repulsive, hard-sphere potential

$$V_{\text{HS}}(r) = \begin{cases} \infty, & r \leq \sigma, \\ 0, & r > \sigma, \end{cases} \quad (2.19)$$

accounts for the fact that two particles with diameter  $\sigma$  are impenetrable and cannot occupy the same space. Since the shape of the protein lysozyme in solution can be approximated by an prolate ellipsoid of revolution with semi-axes  $a = 1.57$  nm and  $b = 2.42$  nm (see section 2.4.2), the effective hard-sphere diameter of the protein can be calculated from the ellipsoid axial parameters via  $\sigma = 2(a^2b)^{1/3}$  (see section 5.1).

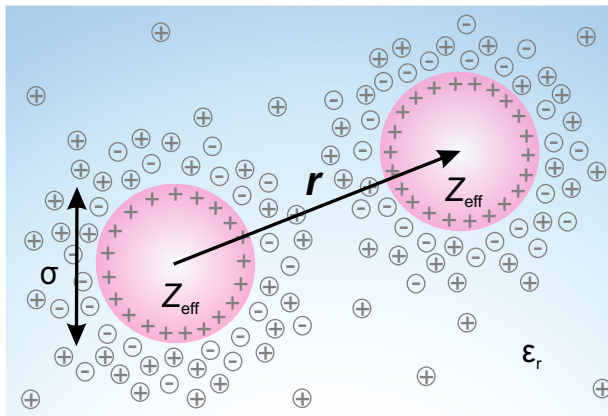


Figure 2.12: Two equally positive charged colloidal particles (diameter  $\sigma$ , effective surface charge  $Z_{\text{eff}}$ ) dissolved in a homogeneous media with dielectric permittivity  $\epsilon_r$ , and with centers separated by the distance  $r$ . The particles are surrounded by a distribution of 1:1 electrolytes (e.g. NaCl), which give rise to the screening of the long-ranged electrostatic Coulomb repulsion between the two colloids.

Proteins are composed of amino acid residues containing both amine ( $-\text{NH}_2$ ) and carboxyl ( $-\text{COOH}$ ) groups which carry positive and/ or negative charges upon ionizing in water. The effective surface net charge of a protein, determined by the charge of the different side chains of the amino acids on the protein surface, depends on the solutions pH value. The effective surface charge of the macromolecules in solution is responsible for intermolecular electrostatic repulsion or attraction as described by the long-ranged, screened Coulomb interaction potential,

$$V_{\text{SC}}(r) = \begin{cases} 0, & r \leq \sigma \\ \frac{Z_{\text{eff}}^2 e^2}{4\pi r \epsilon_0 \epsilon_r (1 + 0.5\sigma/\lambda_D)^2} \exp\left(\frac{-(r-\sigma)}{\lambda_D}\right), & r > \sigma. \end{cases} \quad (2.20)$$

The range typically varies from a few Å up to several nm. Here,  $\epsilon_0$  is the dielectric constant of vacuum,  $\epsilon_r$  is the pressure-dependent solvent's static relative dielectric permittivity, and  $e$  the elementary charge.  $Z_{\text{eff}}$  denotes the effective surface charge of the particles (e.g.  $Z_{\text{eff}} = +8$  for lysozyme at pH 7 [Yu et al., 2015, Kuehner et al., 1999]). The Debye-Hückel screening length of the solvent,  $\lambda_D$ , is defined by [Israelachvili, 2011]

$$\lambda_D = \sqrt{\frac{\epsilon_0 \epsilon_r k_B T}{2N_A e^2 I}}. \quad (2.21)$$

Here,  $k_B$  is the Boltzmann constant,  $T$  the absolute temperature,  $N_A$  the Avogadro constant and

$$I = \frac{1}{2} \sum_i e^2 z_i^2 \quad (2.22)$$

denotes the solutions ionic strength. The sum is taken over all ion types  $i$  with charge number  $z_i$ , which are present at a molar concentration  $c_i$  in solution. For the monovalent (1:1) electrolyte NaCl, we find with the ionic strength being equal to the molar salt concentration  $I = c_{\text{NaCl}}$  (here:  $z(\text{Na}^+) = 1$  and  $z(\text{Cl}^-) = -1$ ). The Debye length,  $\lambda_D$ , describes the 'thickness' of the ionic atmosphere near a charged surface and therefore characterizes the decay of the electrostatic interaction as a function of the distance  $r$ . As clearly can be seen from Eq. (2.21), its magnitude does not depend on the surface properties (e.g. surface charge, potential) but solely on the properties of the solution. In a monodisperse solution the resulting potential,  $V_{\text{SC}}(r)$ , is repulsive since all particles carry the same charge. Electrostatic repulsion becomes significant when two charged colloids approach beyond the point where their electric double layers interfere. The height of the pronounced maximum in the course of  $V(r)$ , as found for net repulsive intermolecular interactions, indicates the amount of energy which is required to force the particles together (see Figure 2.11). The energy barrier can be increased and decreased by changing the ionic strength, the solutions dielectric permittivity or the pH environment, affecting the surface charge of the colloid. In this thesis, the pressure dependence of the solvents dielectric constants,  $\epsilon_r$ , is reasonably adopted by the pressure dependence of  $\epsilon_r$  for pure water [Floriano and Nascimento, 2004] at 25°C with regard to the additives dielectric increment  $\delta = d\epsilon_r/dc$  with cosolvent concentration, partly taken from literature and partly obtained from own dielectric spectroscopy measurements (see section 3.5). The attractive Yukawian potential,  $V_Y(r)$ , given by

$$V_Y(r) = \begin{cases} 0, & r \leq \sigma \\ -J \left(\frac{\sigma}{r}\right) \exp\left(\frac{-(r-\sigma)}{d}\right), & r > \sigma, \end{cases} \quad (2.23)$$

accounts for the vdW interaction between the particles. For the width of the Yukawian potential  $d = 0.3$  nm is chosen in accord with previous work on the intermolecular interaction of lysozyme [Malfois et al., 1996, Schroer et al., 2011a, Möller et al., 2012]. This value corresponds to a layer of bound water between the proteins and determines the smallest distance of approach allowed between them. The only free parameter in the refinement of the effective structure factor from the SAXS intensities of dense protein solutions (see section 3.2.3) is depth of the attractive potential,  $J$ , at contact ( $r = \sigma$ ).<sup>2</sup>

Previous studies report that the DLVO model, described here, accounts well for all the small-angle scattering data on dense lysozyme solutions at ambient as well as at elevated pressures, in pure buffer and in the presence of additives like salts and organic osmolytes [Schroer et al., 2011a, Schroer et al., 2011b, Möller et al., 2012, Shukla et al., 2008]. Whilst the DLVO theory has appeared to work well for low salt concentrations ( $c \lesssim 0.05$  M) where the electrostatic force dominates, the assumption of point charges is poor for salt concentrations greater than  $\sim 0.1$  M [Boström et al., 2001, Velev et al., 1998, Broide et al., 1996, Narayanan and Liu, 2003]. Here, the anomalous stability of the systems at high ionic strength was attributed to the existence of the non-DLVO hydration repulsion resulting from the adsorption of the hydrated counter ions on the protein and dominating at short distances [Molina-Bolívar et al., 1997]. Moreover, the DLVO potential cannot resolve specific (an)ion effects (e.g. salt specificity of Hofmeister series) [Muschol and Rosenberger, 1995, Curtis et al., 1998, Tardieu et al., 1999] (see section 2.3.3).

---

<sup>2</sup>Of note: The effect of the attractive Yukawa potential on the protein-protein interaction is controlled by both the strength  $J$  and the width  $d$ . In order not to over-determine the system, one of them has to be set constant in the fitting procedure of the SAXS curves. For example, the width  $d$  might be modulated by hydration shell effects (e.g. hydrostatic pressure or preferential hydration, as imposed by the presence of cosolvents and crowder molecules). Since precise data on the hydration shell at every solution condition (and pressure) is out of reach up to this point, the width  $d$  is kept constant in this study and possible hydration effects will then be mirrored in the change of the only adjustable parameter  $J$  (i.e. an enhanced hydration shell is either modeled by an increased width at a fixed strength or an decreased strength at fixed width and thereby results in an effective reduction of the attractive interaction either way [Gögelein et al., 2012].)

In order to describe more complex systems (e.g. proteins in a crowded environment and/or in the presence of high levels of salt and organic osmolytes) the DLVO potential should be extended by an excluded volume / osmotic attraction potential, a square-well interaction to account for potential self-association of the protein, hydration repulsion and enthalpic effects between cosolute (e.g. crowder) and protein at short distances, next to the hard-sphere, Coulomb and vdW potential term [Javid, 2007, Curtis et al., 1998, Curtis et al., 2002, Boström et al., 2001, Boström et al., 2006, Ninham, 1999]. However, based on the experimental SAXS data, which ultimately only provides us with information of the spatial arrangement of the proteins in solution (see section 2.4.4), it is only possible to make limited statements about the potential landscape. Every extension of the DLVO potential by further parametrization would result in an over-determination of the system (and is also associated with further assumptions). Therefore, in this thesis we present this rather simple 2-Yukawa DLVO modeling approach in order to yield at least qualitative estimates of the (pressure-dependent) intermolecular interactions in complex solution systems, like proteins in a crowded environment and in the presence of high levels of cosolvents, in reference to the pure buffer scenario.

No self-association is observed in the experimental data (also in FTIR spectra as reported by [Schroer et al., 2011a]), so no need for further parametrization is needed in this respect. At low cosolvent concentrations, the contribution of an attractive osmotic interaction potential induced by the cosolutes is not important and can be neglected. However, in the presence of larger amounts of cosolvents, the attractive Yukawa potential necessarily includes, next to the vdW interaction, the osmotic attractive interaction due to the excluded volume effect induced by the cosolvent. However, the overall crowding-induced changes of the potential parameters in comparison to the pure buffer scenario are relatively small and can therefore be examined here approximately as a kind of perturbation of the model used, i.e. they are mirrored by the strength,  $J$ , of the attractive Yukawian part,  $V_Y(r)$ . In this simple model, all non-DLVO forces present in the system contributing to the effective protein pair interaction potential act as perturbations on the attractive Yukawian part.

In this study on lysozyme in a crowded environment and in the presence of high amounts of cosolvents, the refinement of the experimental scattering data is performed consistently with the same approach as employed for the pure buffer scenario. Principally, different and more complex potential models could be used, but the latter may not be useful with respect to the approximations needed for such complex solution mixture. Hence, we may regard the DLVO potential as used here sufficiently accurate to capture the impact of the cosolvents like organic osmolytes, salt and crowding agents on the relative changes of the potential parameters, at least in a qualitative way. To support these findings derived from the potential model used in the analysis of the scattering data on lysozyme in a crowded environment, in this thesis, this approach is complemented by two model-free add-ons, both providing information on the predominantly repulsive or attractive nature of the intermolecular interactions: First, complementary cloud point measurements were carried out, which, as reported in earlier studies [Möller et al., 2014a, Schulze et al., 2016] are directly related to the (pressure-dependent) protein-protein interaction potential, but are completely model-free (see section 2.3.4). Second, the estimation of the spatial arrangement and intermolecular distances of the proteins in solutions derive directly from the main peak position in the experimental static structure factor (see section 2.4.4). Hence, at any rate, we are sure that the potential model employed helps us to at least qualitatively understand the crowder-induced changes in molecular distances and shift of phase boundaries of the LLPS. Yet, some specific contributions to the protein-protein second virial coefficient in crowded solution need further attention and more in-depth theoretical treatment, including repulsive hydration forces and specific protein-polymer attraction forces.



## 2.3 High Hydrostatic Pressure Effects on Biomolecular Systems

High pressure is also a powerful tool for studying the thermodynamics and kinetics of biomolecules [Luong et al., 2015]. It serves as an important probe for mapping the conformational landscape of biomolecules and for delineating the proteins conformational subspace [Zwicker et al., 2017, Banani et al., 2017]. In general, pressure shifts chemical equilibria and redistributes the population of conformers by favoring the state of smallest partial molar volume. Hence, pressure is also a key variable for scrutinizing the roles of packing and hydration, both affecting the volumetric properties of biomolecules in solution markedly [Roche et al., 2012, Luong et al., 2015, Silva et al., 2014].

In contrast to temperature and detergents, pressure is a rather mild perturbing agent as it affects the density of the system only whilst thermal energy and chemical properties remain unchanged [Meersman et al., 2013].

Further, pressure perturbation has become a powerful tool for fine-tuning interparticle interactions in nanoparticle systems and in dense protein solutions [Möller et al., 2012, Schroer et al., 2016, Schroer et al., 2011a] and hence also for modulating LLPS phenomena in protein solutions [Möller et al., 2014a, Schulze et al., 2016, Cinar et al., 2018].

In this section, we will discuss the basic effects of pressure<sup>3</sup> on the thermodynamics and kinetic of biomolecules, intra- and intermolecular interactions in biomolecular systems including liquid-liquid phase separation phenomena and crystallization.

### 2.3.1 Temperature- and Pressure-Induced Unfolding and Denaturation

Biomolecular systems behave under pressure according to the *Le Chatelier principle*, which predicts the shift of an equilibrium in favor of the state with smallest overall volume [Atkins et al., 2018]. At high pressures, conformations occupying a smaller volume are favored as well as reactions with transition states for which the volume is smaller than in the ground state [Luong et al., 2015]. High hydrostatic pressure can be employed to characterize the equilibrium unfolding process as well as aggregation, since it allows to measure differences in partial molar volume between equilibrium species (e.g. differences in the apparent volume occupied by amino acids inside the protein and when exposed to water in an unfolded conformation.). For proteins, the partial molar volume,  $V$ , is defined by the sum of the intrinsic van-der-Waals volume of the constituent atoms,  $V_{\text{atoms}}$ , the volume of the interior voids which are water-inaccessible and evoked by packing inefficiencies,  $V_{\text{voids}}$ , and volume changes resulting from interactions between solvent-accessible atomic groups of the biomolecules and solvent molecules,  $\Delta V_{\text{hyd}}$ , [Kauzmann, 1959, Laidler, 1965, Heremans and Smeller, 1998]:

$$V = V_{\text{atoms}} + V_{\text{voids}} + \Delta V_{\text{hyd}}. \quad (2.24)$$

The largest (positive) changes of the partial molar volume upon protein unfolding originate from the presence of packing defects (voids) inside the biomolecule, whereas the (negative) volume changes due to hydration are relatively small (e.g. hydration processes may lead to a reduced partial molar volume since the density of hydration water is higher than the density of the bulk [Chalikian, 2001]) [Gao et al., 2017b]. Thus, the resulting total volume change upon unfolding,  $\Delta V$ , is relatively small and can be either positive or negative [Chen and Makhataдзе, 2017].

For a two-state physico-chemical process at equilibrium, the difference in partial molar volumes between equilibrium species,  $\Delta V / \text{mL mol}^{-1}$ , is related to the pressure-dependent equilibrium constant,  $K$ , by

$$\left( \frac{\partial \ln(K)}{\partial p} \right)_T = - \left( \frac{\Delta V}{RT} \right). \quad (2.25)$$

---

<sup>3</sup>The pressures employed for the study of biomolecular systems range from 1 bar up to 10 kbar and hence act predominantly on the supra-molecular structures (e.g. intermolecular distances) and affect conformations [Luong et al., 2015, Meersman et al., 2013]. Changing the covalent structure of low molecular mass molecules (e.g. covalent bond distances and bond angles) or the primary structure of macromolecules like proteins requires pressures of about 10-15 kbar (e.g. the primary structure of hen egg-white lysozyme was unperturbed by pressures higher than 10 kbar [Mozhaev et al., 1994, Gross and Jaenicke, 1994]). In order to affect the electronic structure of a molecule pressures in excess of 300 kbar are necessary [Drickamer and Frank, 1973].

Here,  $p$  is the pressure,  $R$  the gas constant and  $T$  the absolute temperature. Activity and stability of proteins depend on a variety of molecular interactions within proteins. However, according to Eq. (2.25) it is sufficient to consider the factors that contribute to  $\Delta V$  in order to describe and understand the molecular mechanisms underlying pressure-induced protein denaturation. The driving forces of pressure perturbation essentially include the increase in hydrophilic hydration of charged and polar atomic groups as well as the release of packing defects/voids - which all lead to a reduced partial molar volume of the protein [Boonyaratanakornkit et al., 2002, Frye and Royer, 1998, Roche et al., 2012, Chen and Makhatadze, 2017, Chalikian, 2001, Chalikian, 2003, Winter et al., 2007].

The tertiary and quaternary structure of the protein is stabilized by attractive, short-ranged ionic interactions between positively and negatively charged amino acid side chains within a range of  $\lesssim 4$  Å [Heremans and Heremans, 1989]. Interactions between ion pairs which are also hydrogen bonded are also termed salt-bridges [Creighton, 1992]. Salt bridges within the protein maintain the stability and specificity of the protein complex but also cause the solvent to be excluded from the inside of the protein [Heremans and Heremans, 1989]. Upon breakage of the ion pairs, the dipolar water molecules of the solvent are aligned in the electric field of the remaining exposed single charges, resulting in an effective contraction of the solvent. This mechanism is called **electrostriction**. Since this contraction corresponds to a decrease in volume [Abe et al., 1999], pressure promotes the disruption of salt bridges and ion pairs and thereby might induce protein dissociation and/or denaturation [Distèche, 1972, Boonyaratanakornkit et al., 2002].

**Hydrophobic interactions** cause the non-polar side chains to cluster within the protein and thereby are an important determinant of proper folding [Kauzmann, 1987]. As mentioned before, high pressure favors the hydration of charged groups and also of hydrophobic residues since it reduces the volume of the system and thereby weakens the hydrophobic interactions. At pressures up to  $\lesssim 2$  kbar, weakened hydrophobic interactions may lead to imperfect packing and cavity formation providing pathways for water to penetrate inside the protein. The solvation of the hydrophobic, unpolar groups upon unfolding of the protein leads to clathrate formation of the exposed groups. Water penetration into the interior of the native protein under pressure can likely induce the protein to adopt the conformation of a molten globule and, eventually, the unfolding of the protein.

The thermodynamic stability of a protein is a multidimensional function of temperature, pressure and solution conditions (pH, ionic strength, cosolute and cosolvent concentration). With the solution conditions kept constant, the corresponding multidimensional free energy landscape is reduced to a three-dimensional surface on the temperature-pressure plane with the free energy difference,  $d\Delta G$ , between native and denatured states as a vertical coordinate [Winter et al., 2007]. Under the assumption of a simple two-state (native  $\leftrightarrow$  unfolded) equilibrium behavior of the protein, the Gibbs free energy difference between the unfolded and native state,  $\Delta G = G_{\text{unfolded}} - G_{\text{native}}$ , is defined as

$$d\Delta G = -\Delta S dT + \Delta V dp, \quad (2.26)$$

with  $S$  and  $V$  being the entropy and the volume, respectively.  $\Delta$  denotes the change of the corresponding parameter during denaturation, that is, the value in the unfolded, denatured state, minus that in the native state. Integration of Eq. (2.26) from an arbitrary chosen reference point  $(T_0, p_0)$  to  $(T, p)$  yields [Hawley, 1971, Smeller, 2002, Lullien-Pellerin and Balny, 2002, Ravindra and Winter, 2003]

$$\begin{aligned} \Delta G = \Delta G_0 + \frac{\Delta \kappa'}{2} (p - p_0)^2 + \alpha' (p - p_0) (T - T_0) - \Delta C_p \left[ T \left( \ln \left( \frac{T}{T_0} \right) - 1 \right) + T_0 \right] \\ + \Delta V_0 (p - p_0) - \Delta S_0 (T - T_0). \end{aligned} \quad (2.27)$$

Herein,  $\Delta G_0$  the standard Gibbs free energy change of unfolding.  $\kappa'$  is the compressibility factor and  $\alpha'$  the thermal expansivity factor, correlated to the isothermal compressibility  $\kappa$  and the heat capacity  $C_p = T \cdot (\partial S / \partial T)_p$ , respectively, via  $\kappa' = -(\partial V / \partial p)_T = V \cdot \kappa$  and  $\alpha' = (\partial V / \partial T)_p = -(\partial S / \partial p)_T$ .



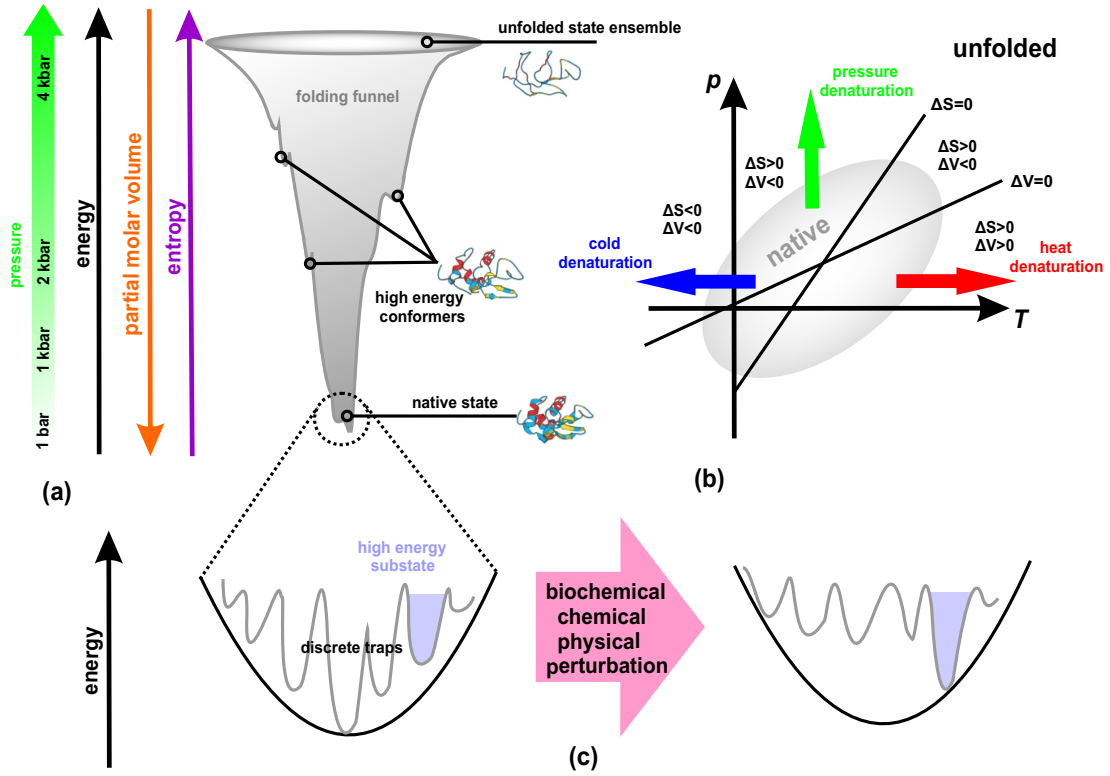


Figure 2.13: (a) Free-energy landscape (folding funnel) of a protein. (b) Theoretical  $(p-T)$ -stability phase diagram of a protein with a simple native  $\leftrightarrow$  unfolded (denatured) state equilibrium behavior. The respective signs of entropy and volume changing upon unfolding are depicted as well. (c) Energy landscape within the native state of the proteins and shift of the protein's conformational equilibria to higher energy conformations upon perturbation. Pictures modified from [Winter et al., 2007, Luong et al., 2015].

Assuming that  $\Delta C_p$ ,  $\Delta\kappa'$  and  $\Delta\alpha'$  are sufficiently independent of  $p$  and  $T$  around  $(T_0, p_0)$ , a second order Taylor expansion of  $\Delta G$  with respect to  $p$  and  $T$  around the reference point simplifies Eq. (2.27) to

$$\begin{aligned} \Delta G = \Delta G_0 + \frac{\Delta\kappa'}{2} (p - p_0)^2 + \alpha' (p - p_0) (T - T_0) - \Delta C_p \frac{(T - T_0)^2}{2T_0} \\ + \Delta V_0 (p - p_0) - \Delta S_0 (T - T_0), \end{aligned} \quad (2.28)$$

wherein

$$T \left( \ln \left( \frac{T}{T_0} \right) - 1 \right) + T_0 \approx \frac{(T - T_0)^2}{2T_0}, \quad (2.29)$$

is used [Clark, 1979]. The physically relevant solution of the function on the right hand side of Eq. (2.28) gives an elliptic paraboloid for  $\Delta G$ . The transition line,  $\Delta G = 0$ , defines where the protein denatures ( $\Delta G < 0$ ) or refolds ( $\Delta G > 0$ ), depending on the direction of crossing. The projection of this function to the  $(p-T)$ -plane yields an elliptic phase diagram as shown in Figure 2.13 (b). The protein is its native conformation inside the elliptically shaped phase boundary, and denatured outside the boundary. The actual shape, size and orientation of the elliptic phase diagram in the  $p-T$ -plane depends on the six thermodynamic parameters  $(\Delta\beta, \Delta\alpha, \Delta C_p, \Delta V_0, \Delta S_0, \Delta G_0)$ . As a rule of thumb,  $\Delta\alpha$  set predominantly the orientation of the ellipse in the plane and the decrease of  $\Delta C_p$  broadens the ellipse along the  $T$ -axis and the decrease of  $\Delta\beta$  along the  $p$ -axis, respectively.

Generally, proteins can unfold by pressure, heat and cold denaturation. Cold-induced denaturation

of proteins (in general between  $-30$  and  $0^\circ\text{C}$ ) is mainly driven by enthalpically favored hydrophobic hydration effects and results in partial unfolding, only, without affecting the secondary structure. In contrast, heat-induced denaturation leads to a largely unfolded conformation where the hydrophobic core of the protein is exposed to the solvent, as it is driven by entropy [Privalov, 1990, Beckett and Schellman, 1987, Winter et al., 2007]. During pressure-induced denaturation water penetrates into the interior of the protein, fills the voids and leads to a swelling of the core [Luong et al., 2015, Roche et al., 2012, Collins et al., 2005, Boonyaratankornkit et al., 2002, Meersman et al., 2013]. In molecular terms, pressure and temperature have antagonistic effects on equilibria and kinetics. As clearly can be seen from the  $(p-T)$ -stability phase diagram in Figure 2.13 (b), proteins can be stabilized against thermal inactivation by pressure. As follows from the principle of microscopic ordering, an increased pressure at constant temperature leads to an ordering of the molecules and decrease of entropy and increased temperature at constant pressure to disordering and increase of entropy. Pressure offsets the fluctuations and increased disorder arising from higher temperatures which are a major contributor to the thermal unfolding. The pressure at which the protein denatures at room temperature is usually lower than at elevated temperatures [Balny et al., 1997, Mozhaev et al., 1996].

However, the exact shape of the phase stability diagram is also strongly dependent on the individual secondary structure of the protein as well as on the interactions between protein and solvent. *In cellulo*, biomolecules naturally occur in a complex aqueous solution a variety of macromolecules, organic osmolytes and salts (see sections 2.1.1 and 2.1.2). Hence, Eq. (2.28) should be extended by two additional terms,  $\Delta G_{\text{cosolvent}}$  and  $\Delta G_{\text{crowder}}$ , to account for modulations of the folding energy landscape by cosolvent and crowding effects.

In general, the unfolding process of (especially large) proteins is more complicated and cannot be fully described in terms of such two discrete states but in a much more complex energy landscape picture (folding funnel) [Dobson et al., 1998, Onuchic et al., 1997, Chan and Dill, 1998] (see Figure 2.13 (a)). The energy landscape has a rough surface with several local minima corresponding to intermediate states in the un/folding process. Thus, the unfolded state is not represented by a single characteristic energy level but by a broad population of closely spaced energy levels, which are accessible upon changes in the chemical potential [Gao et al., 2017b]. As these nearly isoenergetic conformers could differ in their volumes, they are accessible upon pressure changes. This makes pressure a powerful tool to detect conformational fluctuations and to investigate protein dynamics and its functional role [Luong et al., 2015, Kapoor et al., 2012, Kalbitzer et al., 2009]. Pressure modifies the protein folding energy landscape surface by increasing its roughness and shifting the chemical equilibrium towards higher energy conformations. Further, functional transient conformational substates that are hardly accessible at ambient conditions can be populated upon compression as a consequence of the pressure-induced decrease of the conformational diffusion (see Figure 2.13 (c)) [Kalbitzer et al., 2009, Silva et al., 2001]. As for the kinetics of protein folding, the pressure is reported to mostly decrease the folding rate and increase the unfolding rate [Korzhev et al., 2006, Panick et al., 1998, Pappenberger et al., 2000, Gao et al., 2017b].

### 2.3.2 Pressure Induced Dissociation of Oligomeric Proteins

In general, molecular assemblages are dissociated by much lower hydrostatic pressures than those necessary for protein denaturation. Most small monomeric proteins unfold within the pressure range of 4 to 8 kbar reversibly, but oligomeric proteins and multi protein assemblies are rather fragile and often dissociate into individual subunits at much lower pressures of 0.5 to 2 kbar [Winter et al., 2007, Mozhaev et al., 1996, Robinson and Sligar, 1995, Meersman et al., 2013]. The different stages of pressure-induced dissociation of a native dimeric protein followed by further conformational changes of the subunits are lined out schematically in Figure 2.14 (a) - (d). The native dimeric protein contains cavities which are large enough to hold water molecules and water-inaccessible packing defects/voids both at the interface and within the monomeric subunits. The dissociation of the dimer occurs in the range  $0.5 \lesssim p \lesssim 2$  kbar. It is promoted by pressure since the breaking apart of the polar and ionic bonds in the inter-subunit region and the release of void volume arising from cavities and the imperfect packing of the atoms at the interfaces of the subunits leads to a negative volume change (*Le Chatelier principle*), meaning the dissociated protein occupies less space.

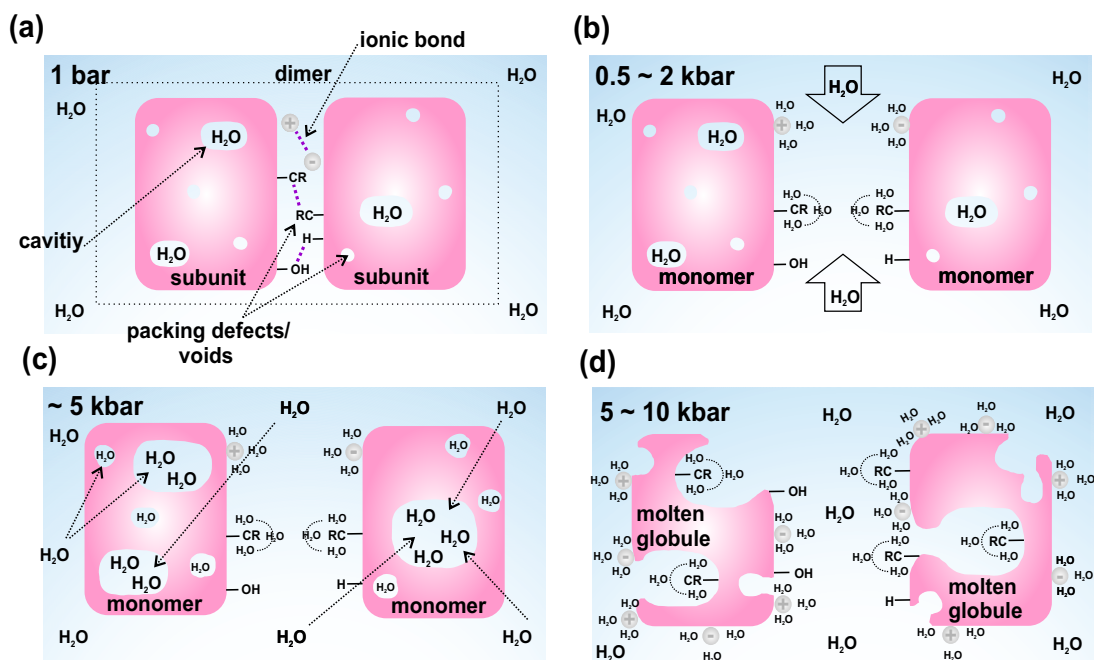


Figure 2.14: Sketch of the major mechanisms driving the pressure-induced dissociation of a dimeric proteins and subunit dissociation in solution. Picture modified from [Boonyaratanakornkit et al., 2002] and [Winter et al., 2007].

Water penetrates into the dimer interface and the dipolar water molecules arrange tightly around the newly formed charged solutes, hydrating the polar/ionic moieties with electrostriction, i.e. weakening the electrostatic contacts. The hydrophobic, unpolar groups (-CR) get hydrated as well (see Figure 2.14 (b)). Around  $\sim 5$  kbar, weakened hydrophobic interactions provide the pathway for water to penetrate into the cavities and voids in the subunits interior. An increased exposure of the protein to the solvent and increased hydration of the protein can lead to the (irreversible) loss of the tertiary/secondary structure [Gross and Jaenicke, 1994, Mozhaev et al., 1996]. By swelling of the hydrophobic core due to water, each monomer transitions to a molten-globule like state<sup>4</sup> (see Figure 2.14 (c)). At pressures between  $5 \lesssim p \lesssim 10$  kbar, the subunit eventually unfolds to a random coil<sup>5</sup>. The intramolecular hydrogen bonds, which help to maintain the secondary structure are destabilized by the water infiltrating the protein upon pressurization due to the formation of intermolecular hydrogen bonds with the water [Wroblowski et al., 1996]. This effect causes increased conformational fluctuations [Cioni and Strambini, 1994]. The secondary/tertiary structure is disrupted concomitant with the loss of the cavity volumes within the subunits and hydration of the residues (see Figure 2.14 (d)) [Boonyaratanakornkit et al., 2002].

Pressure-mediated dissociation of oligomeric proteins can also be accompanied by hysteresis or a conformational drift [King and Weber, 1986, Silva et al., 1986, Ruan and Weber, 1993, Weber, 1986, Ruan and Weber, 1989]. A re-association of the monomeric subunits to higher oligomers might follow the pressure-induced dissociation of a dimer. The formation of oligomeric aggregates depends on protein concentration, pressure, temperature as well as on the pH and cosolvents, as the extend of hysteresis increases with the number of protein subunits.

One way to counteract the pressure-induced dissociation of molecular assemblages is the application of osmotic pressure, e.g. by the addition of stabilizing osmolytes (see section 2.1.2) or small crowder molecules (see section 2.1.1) [Webb et al., 2001]. As mentioned before, the (stabilizing) cosolvents (e.g. glycerol, sucrose, PEG) are preferentially excluded from the protein surface. The

<sup>4</sup>A molten globule state is a compact, partially folded conformation lacking a specific tertiary structure. It is more hydrated than the native protein and therefore often referred to as 'swollen'.

<sup>5</sup>The unfolded protein exhibits no secondary or tertiary structure and the peptide bonds in the backbone are the only structuring elements left.

increase in the chemical potential upon addition of cosolutes due to the thermodynamically unfavorable interaction between protein and cosolute is minimized by the protein assuming the most compact state [Lee and Lee, 1981, Liu and Bolen, 1995, Kendrick et al., 1997, Timasheff, 1998, Gekko and Timasheff, 1981b]. Due to the osmotic stress, the water is sucked out from the internal voids and cavities of the protein and the core density increases both due to the compression of the protein and the reduction of the protein-solvent interface. Therefore, the pressure-mediated dissociation is counteracted by the decreased hydration of the protein as a result of the osmotic pressure produced by cosolutes [Boonyaratanakornkit et al., 2002].

Although the so-called molecular crowding effect on the stability of monomeric proteins is well understood, a deeper understanding of the effect of crowders, in particular the interplay of hydrostatic pressure, osmotic pressure and the reduced free space, on the structure and activity of oligomeric enzymes is largely lacking. Moreover, the effect of naturally occurring organic osmolytes on the pressure-dependent stability and activity of oligomeric enzymes is still largely *terra incognita*, although of high biological relevance. In this thesis, the connection between enzyme structure and function is investigated by the effect of pressure-induced dissociation/inactivation of the well-studied dimeric enzyme horse liver alcohol dehydrogenase (LADH) [Brändén et al., 1975, Winter et al., 2007, Trovaslet et al., 2003, Cioni and Strambini, 1996, Dalziel and Dickinson, 1966, Dallet and Legoy, 1996, Klinman, 1981, Eklund and Brändén, 1987, Petterson, 1987, Wang et al., 2000] in the presence of solution additives like crowder and (de) stabilizing organic osmolytes, mimicking conditions as encountered inside the biological cell (see section 6).

### 2.3.3 Pressure Effects on Protein Intermolecular Interactions

In the past years, protein-protein interaction have been studied extensively for several protein types (e.g.  $\alpha$ -crystallin, urate oxidase, lysozyme, bovine serum albumin (BSA), ovalbumin, bovine pancreatic trypsin inhibitor (BPTI)) as a function of protein concentration [Shukla et al., 2008, Cardinaux et al., 2007, Narayanan and Liu, 2003, Zhang et al., 2007, Ducruix et al., 1996], pH [Tardieu et al., 1999, Quigley and Williams, 2015], temperature [Tardieu et al., 1999, Bonneté et al., 1999], salt concentration and type [Curtis et al., 2002, Malfois et al., 1996, Zhang et al., 2007, Zhang et al., 2012b, Curtis et al., 1998, Quigley and Williams, 2015] as well as cosolvent effects like organic osmolytes [Javid, 2007, Farnum and Zukoski, 1999, Sedgwick et al., 2007], alcohols [Liu et al., 2004] and molecular crowding [Bonneté and Vivarès, 2002, Vivarès et al., 2002, Finet and Tardieu, 2001]. However, the influence of pressure on the structure and protein-protein interaction potential of dense protein solutions as a function of the above mentioned thermodynamic solution parameters is still largely unknown. Moreover, biophysical studies on pressure effects on protein temperature-pressure stability have mainly been carried out under dilute solution conditions and not under conditions as encountered in the intracellular environment where molecular crowding is prevailing, which has large effects on protein stability and folding rates [Ellis, 2001, Winter et al., 2007]. Thus, even though from highly importance, the underlying mechanisms of the solvent-mediated stabilization of macromolecules and, in particular, the linkage to the intermolecular interactions between proteins in a crowded environment (see section 2.1.1) as well as in presence of organic osmolytes (see section 2.1.2) as encountered in the living cell at ambient as well as at elevated pressures are still largely *terra incognita*.

Pressure modulation allows for fine tuning of the intermolecular distances in solution and thereby for exploring the intermolecular interactions governing the spatial arrangement of the proteins in solutions in detail. The studies carried out so far on the pressure dependence of intermolecular interaction between lysozyme<sup>6</sup> molecules, representing the starting point for this thesis, are summarized in this section. While first studies of the effect of single organic osmolytes and binary mixtures thereof on structural and dynamical properties of proteins in solution at high hydrostatic pressures show interesting features, data of the effects of more complex mixtures on the pressure-dependent protein-protein interaction potential are missing.

In this thesis, we focus on osmolyte mixtures mimicking cellular fluids encountered in deep-sea organisms, such as shallow- and deep-living crabs, skates and shrimps [Kelly and Yancey, 1999], in order to go one-step further towards a better understanding of ‘real’ biological intracellular fluids

---

<sup>6</sup>The monomeric protein lysozyme reportedly remains in its native conformation up to pressures of 5 kbar and is therefore well suited to investigate the changes in intermolecular interactions [Schroer et al., 2011a].

as they appear *in cellulo*, and reveal details and differential effects of their protecting properties (see section 5). Further, the effect of the crowded cellular environment is mimicked using the synthetic, biocompatible polymer polyethylene glycol (PEG), the macromolecular crowder Ficoll PM 70/400 as well as its subunit sucrose as crowding agents (see sections 4 and 7), to reveal how nano- and macromolecular crowding modulates the protein pair-interaction potential at high pressures.

### Impact of the Water Structure on the Pressure Dependent Protein Pair-Interaction

The structural properties of water at elevated pressures have significant implications for the intermolecular pair-interactions in dense protein solutions, since only a few water layers separate two adjacent protein molecules. In fact, pressures in the kbar-range modify transport properties of water, such as viscosity and diffusion coefficient, in a non-monotonically manner. The diffusion coefficient exhibits a maximum around  $\sim 2$  kbar [Ludwig, 2001, Wilbur et al., 1976] and for the shear viscosity a minimum at 1 - 2 kbar is reported [Debenedetti, 2003]. Within the limit of 5 kbar, marked structural changes are observed in the local water network, such as a rapid and monotonic increase of the coordination number of a water molecules starting at 2 kbar from 4 to 6.5 at 5 kbar, which is attributed to the penetration of non-hydrogen bonded water molecules into the first hydration shell (e.g. collapse of the second hydration shell) [Soper and Ricci, 2000, Weck et al., 2009, Katayama et al., 2010, Okhulkov et al., 1994]. As a consequence of the higher coordination number and increased density conformation of water surrounding another water molecule, a decreased mobility and increased structural order in the hydration shells are reported [Sciortino et al., 1991]. The average binding energy decreases and hydrophobic interactions are favored at elevated pressures, since the hydration costs of non-polar residues decrease [Meersman et al., 2013]. In a previous HHP SAXS study on dense lysozyme solutions in pure buffer solution [Schroer et al., 2011a], the protein pair-interaction potential was modeled in the framework of the Derjaguin-Landau-Verwey-Overbeek (DLVO) theory by a sum of a hard sphere potential, a repulsive screened Coulomb potential and an attractive Yukawian type part (see section 2.2.3). Leaving the first two parts unaltered, for lysozyme solutions a non-monotonic dependence of the attractive potential with rising pressure was found. The amplitude  $J$  of the attractive part shows a minimum at a pressure of  $\sim 1.6$  kbar, coinciding with the above mentioned structural changes in the solvent structure upon pressurization. A pressure increase up to  $\sim 1.6$  kbar results in a decrease of the mean intermolecular distance of the proteins in the compressed solution,  $d_{\text{lys}}$ , and concomitantly the strength,  $J$ , of the attractive part of the pair-interaction potential [Ortore et al., 2009], followed by a trend reversal upon further pressurization [Schroer et al., 2011a] (see Figure 2.15, *dashed magenta line*). The origin of such an increase in attraction and growing intermolecular spacing upon further compression was suggested to be due to structural changes in the water H-bond network, notably a collapse of the second hydration shell of water [Soper and Ricci, 2000, Katayama et al., 2010, Ludwig, 2001, Weck et al., 2009]. The relaxation of the intermolecular repulsion at pressures above 2 kbar and hindrance of closest approach, prevents the proteins from aggregation [Schroer et al., 2011a].

### Impact of Organic Osmolytes on the Pressure Dependent Protein Pair-Interaction

A previous HHP Small angle X-ray study on the intermolecular interaction in dense lysozyme solutions in absence and presence of cosolvent mixtures of the deep-sea osmolyte TMAO and denaturant urea at different ratios revealed, that, in contrast to urea, TMAO shifts the minimum of the strength of the attractive Yukawian part,  $J$ , of the effective protein-protein interaction (DLVO) potential to higher pressures (see Figure 2.15 (a)+(b)) [Schroer et al., 2011b]. This effect, scaling with osmolyte concentration, was rationalized by the stabilizing effect of TMAO on the hydrogen bond network of the water structure against pressure effects by enhancing the number of strong H-bonds [Panuszko et al., 2009, Bennion and Daggett, 2004, Wei et al., 2010]. The influence of the urea-TMAO mixtures on the protein-protein interaction significantly depends on the mixing ratio. In accordance with the finding, that TMAO also counteracts perturbations by the denaturant urea in deep-sea organisms [Yancey, 2005], the counterbalancing effect on urea is greatest at a physiological urea:TMAO ratio of 2:1 (see Figure 2.15 (c)) [Yancey and Somero, 1979, Yancey and Somero, 1980]. Complementary thermodynamic DSC measurements report that the counteracting effect of both osmolytes on protein-protein interactions is also reflected in protein stability ( $T_m$ ).



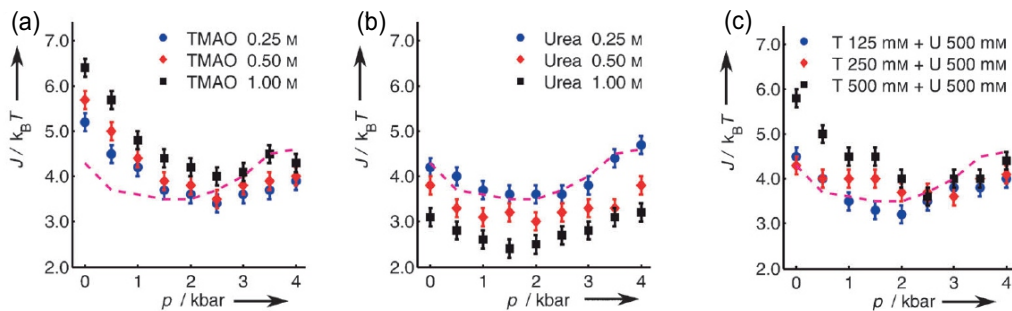


Figure 2.15: Pressure dependence of the attractive interaction of lysozyme molecules in pure buffer (*dashed magenta line*) and in single osmolyte solutions of (a) TMAO, (b) urea, as well as in mixtures thereof (c). Reprinted from [Schroer et al., 2011b] with permission of John Wiley & Sons, Inc., Copyright © 2011 Wiley-VCH Verlag GmbH & Co. KGaA, Weinheim.

Whilst the presence of the compatible osmolyte glycerol (*data not shown here*) as well as the denaturant urea induce an increased repulsion between the proteins which is also preserved at elevated pressures, they do not alter the pressure dependence of the pair-interaction found for the pure buffer system [Schroer et al., 2011b].

### Impact of Salt on the Pressure Dependent Protein Pair-Interaction

The Hofmeister series [Hofmeister, 1988, Kunz et al., 2004] (here: for anions)



ranks the relative impact of ions on physico-chemical processes in aqueous solution such as protein folding, colloidal assembly, protein crystallization, and enzymatic activity [Collins et al., 2007, Collins, 2006, Cacace et al., 1997, Tobias and Hemminger, 2008, Jungwirth and Winter, 2008, Zhang et al., 2006]. This behavior is more pronounced for anions than cations. Kosmotropic ions (Eq. (2.30), left from  $\text{Cl}^-$ ) are strongly hydrated and have the ability to precipitate proteins from aqueous solution and prevent protein unfolding, whilst chaotropic ions (Eq. (2.30), right from  $\text{Cl}^-$ ) are weakly hydrated, increase solubility and promote the denaturation of the proteins. It was originally believed that ions affect the physical properties of macromolecules in aqueous solution by making or breaking water structure. Kosmotropes (e.g. small, high charge-density cations and anions) reinforce the water hydrogen bond network whilst chaotropes (e.g. large cations and anions) exert the opposite effect [Marcus, 2009, Galamba, 2013, Ohtaki and Radnai, 1993, Collins and Washabaugh, 1985]. However, recent studies found that the ions have no long-ranged effects on bulk water structure and the hydrogen-bond network is not significantly changed upon addition of specific ions [Omta et al., 2003, Batchelor et al., 2004, Smith et al., 2007]. All the evidence suggests, that water structure making and breaking are not central in the phenomena related to the Hofmeister series. Instead, they might be explained by direct interactions between the ions and macromolecules as well as with the water molecules in their adjacent hydration shells [Zhang et al., 2006, Zhang and Cremer, 2010, Zhang et al., 2005].

In the recent years, the impact of specific ions on the protein-protein interactions in aqueous solution at ambient pressure has been extensively studied under several solution conditions [Le Brun et al., 2009, Curtis et al., 2002, Curtis et al., 1998, Tardieu et al., 1999, Ducruix et al., 1996]. [Curtis et al., 1998, Curtis et al., 2002, Muschol and Rosenberger, 1995] report that the forces contributing to the effective protein pair-interaction in salt-containing solutions cannot be described by simple DLVO theory and an extension in form of an osmotic attraction potential, since specific interactions like ion binding to the protein surface as well as hydration forces are supposed to be operative. A previous study on the impact of specific anion effects on the pressure dependent spatial organization and intermolecular interaction potential of the protein lysozyme in salt ( $\text{Cl}^-$ ,  $\text{SO}_4^{2-}$ ,  $\text{PO}_4^{3-}$ ) solutions, reveals a strong dependency on salt identity and their location within Hofmeister series, in particular upon compression (the counter ion being  $\text{Na}^+$  for all salts) [Möller et al., 2014b].

Notably, for sodium chloride (NaCl), being in the middle of the Hofmeister series, no detectable changes of the non-linear pressure dependence are observed in protein solutions at high NaCl concentrations [Möller et al., 2012]. Here, the main effect of the salt on the intermolecular interactions can be explained by electrostatic charge screening and the concomitant decrease of the effective electrostatic repulsion between the proteins [Zhang et al., 2007, Zhang et al., 2012b, Tardieu et al., 1999]. Consequently, sodium chloride was employed in this thesis for the purpose of simply fine-tuning the long-ranged electrostatic Coulomb repulsion and, thereby, the mean intermolecular spacing between the proteins dissolved in aqueous solutions of molecular crowding agents.

### **Impact of Protein Concentration (Self-Crowding) on the Pressure Dependent Protein Pair-Interaction**

Enhanced with increasing strength ( $I = 0 - 100$  mM NaCl), an increase of the protein concentration ( $c = 5 - 20\%$  (w/v)) was found to render the protein pair-interaction in dense lysozyme solutions more repulsive (i.e. reduces the strength  $J$  of the attractive part  $V_Y(r)$ ) [Möller et al., 2012], concomitant with the decrease of intermolecular distances between the proteins in the more crowded environment. The pressure dependence of the effective pair interaction reportedly remains unaltered by self-crowding, however [Möller et al., 2012, Schroer et al., 2011a].

### **Impact of Temperature on the Pressure Dependent Protein Pair-Interaction**

A previous HHP small-angle X-ray study on dense lysozyme solutions of elevated ionic strength ( $I = 0 - 100$  mM NaCl) as a function of temperature ( $T = 8 - 45$  C°), reports that temperature does not lead to marked changes of the non-linear pressure dependence of the intermolecular interactions [Möller et al., 2012, Schroer et al., 2011a]. An increased attractivity is observed upon temperature decrease, only [Tardieu et al., 1999]. Again, the pressure dependence of the intermolecular forces seems to be dominated by changes in the water structure.

## **2.3.4 Pressure Effects on Protein Liquid-Liquid Phase Behavior and Crystallization**

The formation of a LLPS in protein aqueous solutions has received tremendous recognition in recent years [Cardinaux et al., 2007]. The physics of LLPS are highly relevant for the understanding of the assembly and disassembly, composition and physical properties of biomolecular condensates as found in cellulo [Banani et al., 2017, Long et al., 2005], as well as their implications on cellular function in presence of external stresses like high hydrostatic pressure (HHP) or molecular crowding. Spatiotemporal control of biological processes is vitally important for cellular function. Either intracellular membrane-less organelles or membrane-bound vesicles were found to further compartmentalize the cell, achieving the necessary physical separation of the cellular compounds and processes. Recent studies suggest that these membrane-less organelles are multicomponent viscous liquid droplets, which form via segregation of molecules from complex mixtures by spontaneous liquid-liquid phase separation (LLPS) [Brangwynne et al., 2015]. Moreover, the propagation by division and subsequent growth of such active self-organized liquid droplets (coacervates) may even serve as model for prebiotic protocells [Keating, 2012].

Whilst the macromolecular diversity in cytoplasm abounds and the effective concentration of biological macromolecules in cell is high as  $80 - 400$  mg mL<sup>-1</sup>, the concentration of the individual species are generally too low for phase separation to occur [Luby-Phelps, 1999] (i.e. protein liquid-liquid phase separation generally does not occur at concentrations below 7 - 10%, which are seldom achieved by a single macromolecular species *in cellulo*). Still, solutions of different macromolecule species tend to phase separate upon mixing above certain concentrations. The requirements for multi phase separation in the liquid phase of the cytoplasm are met by both the diversity of proteins present at high concentrations in the liquid phase *and* macromolecular crowding [Walter and Brooks, 1995, Walter, 1999]. In presence of inert 'background' molecules the volume available for a single molecule is significantly reduced and the local concentration of the solutes can be effectively increased. Thereby, phase separation can take place at concentrations much lower than in absence of uninvolved species (crowding) [Johansson et al., 1999].

Due to the strong correlation of the phase boundaries for metastable liquid-liquid and solid-liquid



phase transitions [Broide et al., 1996], optimum solution conditions for the protein nucleation and crystal growth process can also be efficiently developed from the LLPS [Ten Wolde and Frenkel, 1997, Lutsko and Nicolis, 2006, Vekilov, 2004]. Next to electrostatic forces in the case of salt, entropic excluded volume effects/osmotic depletion forces are also widely used as protein-precipitant interaction in obtaining protein crystals for X-ray crystallography. Here, polymeric precipitants such as PEG ( $200 < M_w < 20000$  Da) are often employed in order to determine the structure of higher molecular weight (generally  $> 30$  kDa) biomolecules [Vergara et al., 2006, Tardieu et al., 2001]. Thus, understanding of the underlying mechanisms and the structural biochemistry of proteins is important for protein crystallography [Zhang et al., 2012b].

At high protein concentrations, metastable liquid-liquid phase separation into coexisting dilute and dense protein-rich liquid phases have been revealed for different proteins (e.g. lysozyme,  $\gamma$ -crystallin, hemoglobin, bovine serum albumin (BSA), horse spleen apoferritin) as a function of pH [Taratuta et al., 1990], protein concentration [Broide et al., 1996, Zhang et al., 2012c] as well as in the presence of additives such as salts [Möller et al., 2014a, Schulze et al., 2016, Muschol and Rosenberger, 1997, Taratuta et al., 1990, Zhang and Cremer, 2009, Broide et al., 1996] and polymers [Vivarès and Bonneté, 2004, Annunziata et al., 2002, Annunziata et al., 2003, Wang and Annunziata, 2007, Tanaka and Ataka, 2002, Galkin and Vekilov, 2000]. Whilst is a broad consensus, that transition into the liquid phase is driven by attractive interactions between the protein molecules [Dumetz et al., 2008], specific details on these interaction, especially in a crowded environment remain elusive. In this thesis, we explore the effect of high concentration of 'background' molecules on the LLPS boundaries at ambient and at elevated pressures.

Of note, in this thesis we consider the phase behavior of native proteins that do not undergo any significant conformational changes in the formation of native precipitates during LLPS, physical phenomena like the formation of gels and of amorphous aggregates are beyond the scope of this work [Cardinaux et al., 2007, Gibaud and Schurtenberger, 2009, Gibaud et al., 2012, Poon et al., 1997].<sup>7</sup>

## Experimental Phase Diagram

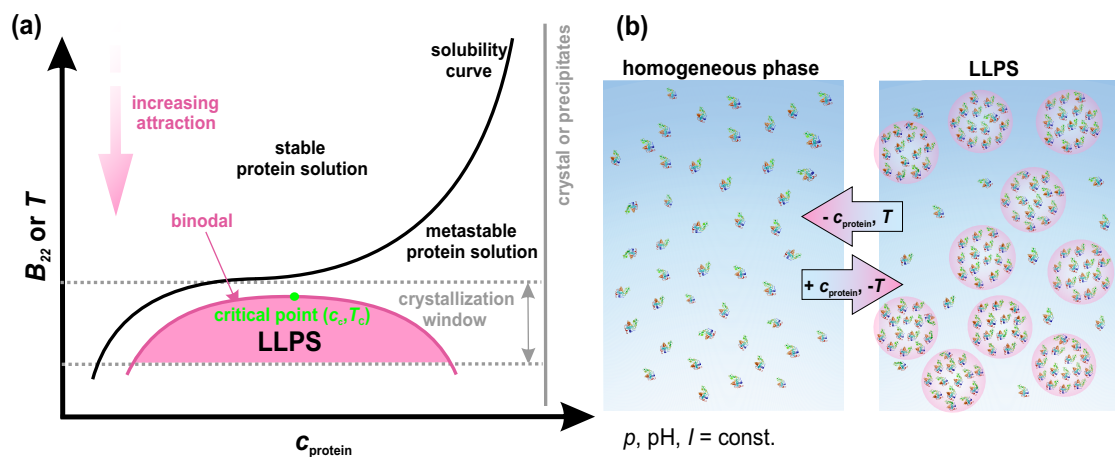


Figure 2.16: (a) Schematic representation of a typical phase diagram observed for short-ranged ( $d \sim 3$  Å) attractive interactions. The protein solution exhibits a critical point at the temperature and protein concentration pair  $(c_c, T_c)$ . (b) Sketch of the temperature- and protein concentration-dependent liquid-liquid phase transition at ambient pressure.

A typical protein phase diagram as observed for lysozyme [Ishimoto and Tanaka, 1977, Taratuta et al., 1990, Muschol and Rosenberger, 1997] and  $\gamma$ -crystallins [Thomson et al., 1987, Berland et al., 1992, Lomakin et al., 1996, Liu et al., 1996] in the protein concentration - temperature

<sup>7</sup>Of note, aggregation (i.e. the assembly of proteins into amorphous clusters) is no phase transition, since no macroscopic phase forms [Asherie, 2004]

$(c_{\text{protein}}, T)$ -plane is depicted in Figure 2.16 (a). Here, the decreasing temperature  $T$  is equivalent to increasing the attraction between proteins, i.e. repulsive interactions increase the solubility whilst increasing attraction promotes crystal growth. Different regions can be distinguished in the phase diagram. Above the solubility curve, the proteins are soluble in an under-saturated solution. The region below the solubility line is thermodynamically metastable with respect to crystallization [Broide et al., 1996, Asherie et al., 1996]. Density fluctuations near LLPS reduce the free energy barrier of crystallization (i.e. regions of high protein concentration correspond to a large supersaturation), resulting in an enhanced crystal nucleation rate by many orders of magnitude [Ten Wolde and Frenkel, 1997, Vekilov, 2004, Lutsko and Nicolis, 2006, Rosenbaum et al., 1996, Asherie et al., 1996]. The metastable, dense liquid-liquid phase emerges spontaneously from the gas-like phase in absence of crystal nucleation upon cooling below the critical temperature (i.e. cloud-point temperature),  $T_{\text{cloud}}$ , and denotes a critical intermediate on the path towards crystallization [Berland et al., 1992, Muschol and Rosenberger, 1997]. Below the binodal, strong and long-lived density fluctuations and long-range spatial correlations between the particles occur ( $\xi$ : *correlation length*). A dense liquid rich in protein is formed in equilibrium with its supernatant. The reversible white precipitate can be separated by ultracentrifugation into two clear phases delimited by a sharp meniscus [Dumetz, 2007]. In the LLPS two liquid protein phases coexist in form of microscopic droplets (*coacervates*) of highly concentrated protein dispersed in a solution of lower protein concentration (see Figure 2.16 (b)). As the size of these region approach the wavelength of visible light, the scattering at the droplets renders the solution opaque for visible light (so called: *critical opalescence*) [Nägele, 2008]. Over time, the metastable liquid phase decays into the solid phase. For lysozyme, the crystallization process from LLPS is slow and the LLPS is reported to be reversible without hysteresis [Galkin and Vekilov, 2000]. The effects of protein concentration, temperature and the characteristics of the solvent (i.e. pH, ionic strength, concentration and identity of buffer and any additives like polymer or organic compounds) on the liquid-liquid phase behavior of various proteins have been subject of thorough investigations. The phase diagrams reported for different proteins quantitatively differ, revealing that simple mutations can have huge effects on the phase behavior [Liu et al., 1996].

### Theoretical Phase Diagram

The effective shape of the phase diagram and the position of stable and metastable phase separations/transitions are the direct consequence of the forces acting on proteins in solution and also can vary considerably with changes in solution conditions and in the composition of the solvent. Despite its apparent complexity, some aspects of the protein phase behavior (i.e. the occurrence of a metastable LLPS region for lysozyme and  $\gamma$ -crystallins) can be explained in terms of theoretical colloid physics of critical phenomena using simple interaction potentials [Schurtenberger et al., 1989, Manno et al., 2003, Yeomans, 1992]. An atomic material such as Argon can form gas, liquid and solid phases by variations of temperature and pressure. It can exist as a single state or coexists in 2 - 3 of these phases. Figure 2.17 (a) depicts the schematic density( $\rho$ )-temperature( $T$ ) and pressure( $p$ )- temperature( $T$ )-diagrams of such a system together with the corresponding Lennard-Jones-type interatomic interaction potential [Poon et al., 1996, Nägele, 2008]. The gas-liquid coexistence line terminates in the critical point,  $(p_c, T_c)$ . Beyond the critical temperature, the system is in the fluid phase and there is no distinction between the gas and liquid state as the density difference between liquid and gas phase cease to exist [Poon et al., 1996]. The critical point marks the location of a continuous (i.e. 2nd order) phase transition. The critical point lies above the triple point, where all three phases coexist, indicating the presence of a stable liquid phase ( $T_c > T_p$ ). The liquid state only exists between the critical temperature and the temperature at the triple-point. The critical temperature,  $T_c$ , approximately denotes the temperature at which the thermal energy of the atoms is equal to the energy associated to the minimum of the interatomic interaction potential:  $\epsilon \sim k_B T_c$ . Now, we consider a one-component system of hard-sphere-like particles. In the simplest case, the system involves only entropic excluded volume interactions, i.e. as described by a repulsive hard-sphere potential,  $V_{\text{HS}}$ . The particles feel an infinite repulsive force when touching but no force otherwise [Poon et al., 1996] (see Figure 2.17 (b)). In a colloidal suspension of hard particles, the interaction energy,  $U$ , is zero.

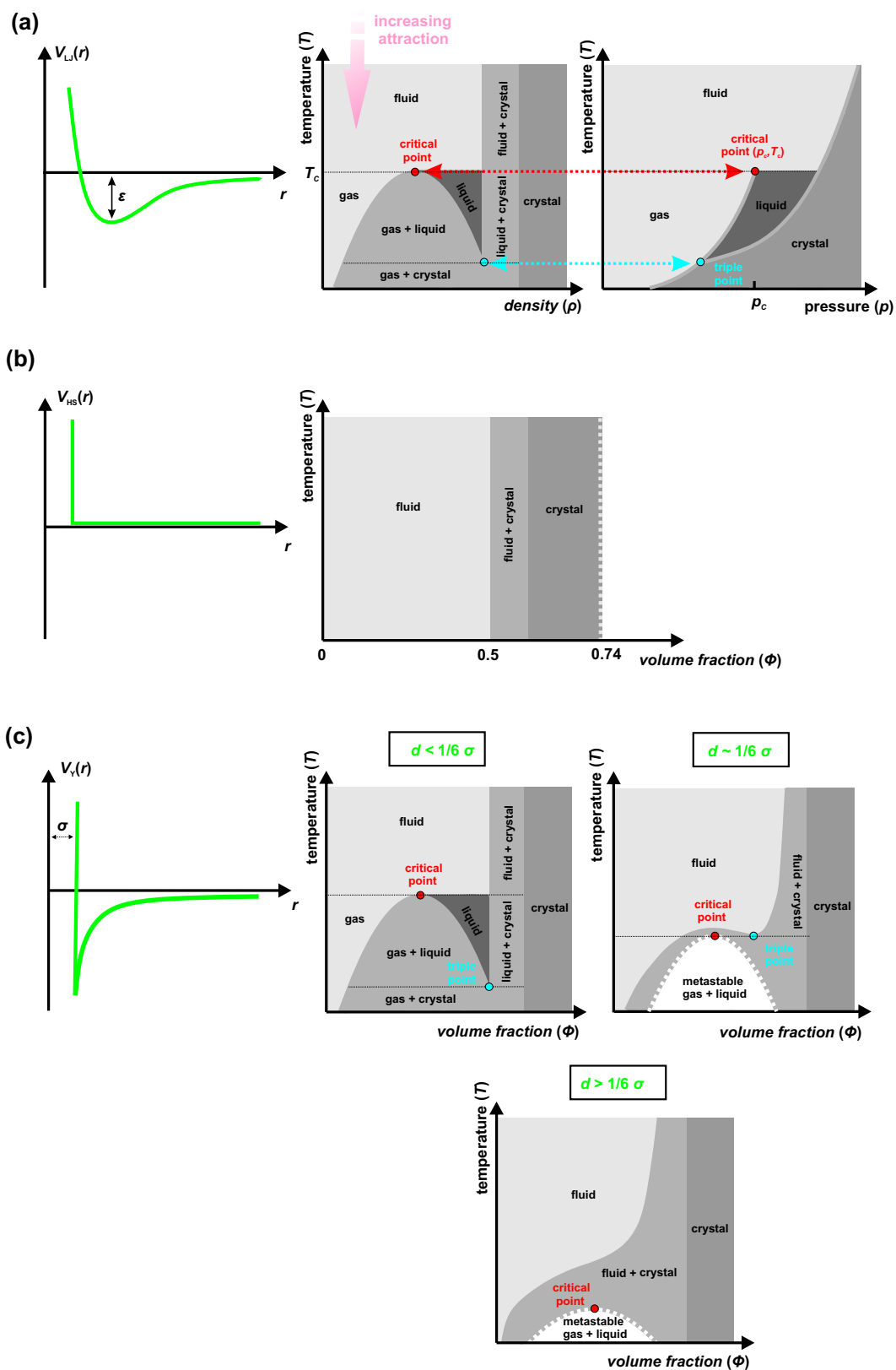


Figure 2.17: Schematic representation of interaction potentials and phase diagrams. (a) Lennard Jones interaction potential for two particles with centers separated by the distance  $r$ , and the theoretical phase diagram featuring a triple point. (b) Phase diagram for a purely repulsive hard-sphere potential,  $V_{HS}(r)$ . There is no liquid phase. (c) Typical phase diagrams for short-range attractive potentials in Yukawa form for different values of the potential range  $d$ .

Since the phase behavior of the system is determined by minimizing the free energy  $F = U - TS$ , of the system, it is determined by maximizing the entropy  $S$ . The absence of interparticle attraction implies that the critical temperature equals zero. Thus, a system of hard-spheres should exhibit a phase behavior similar to the one of a simple atomic substance (e.g. Argon, see Figure 2.17 (a)) above its critical point. There is no liquid state, but the low-density fluid freezes directly to a high-density crystalline solid [Poon et al., 1996]. At high colloid volume fraction (typically  $\sim 50\%$ ), the crystallization of hard spheres is entropically favored over the metastable fluid phase at the same density, since the particles have more freedom of movement in the crystal phase. Hence, the entropy-driven phase behavior of a simple system of  $N$  hard spheres with radius  $R$  is independent of the temperature and only controlled by the colloids volume fraction,  $\Phi = \frac{4}{3}\pi R^3 \left(\frac{N}{V}\right)$ . Here,  $V$  is the volume of the system.

To provide the cohesive energy for the transition into the stable liquid phase, attractive interparticle forces with a sufficiently large spatial range  $d$  have to be present, since the gap between  $T_c$  and the triple point temperature, where the liquid state exists, decreases with the range of the interparticle attraction. [Hagen and Frenkel, 1994] and [Foffi et al., 2002] investigated the phase behavior of particles interacting through short-range attractive potential in Yukawa form for different values of the potential range  $d$ . As depicted in Figure 2.17 (c), the ratio of range of the interaction to the diameter of the particle is the main parameter in describing the phase diagram. If the range of attraction is long in comparison to the hard core diameter of the colloid,  $d > \sigma/6$ , the critical point is well above the triple point temperature and the phase diagram of the colloidal suspension resembles that of an atomic substance (e.g. Argon, see Figure 2.17 (a)). The two characteristic temperatures coincide when the range of attraction equals roughly one sixth of the range of repulsion (i.e. effective hard-core diameter  $\sigma$ ). The gas-liquid coexistence region survives by moving underneath the fluid-crystal coexistence curve, forming a metastable state [Muschol and Rosenberger, 1997]. For  $d < \sigma/6$  the critical point has crossed the sublimation line and no stable liquid phase can exist [Hagen and Frenkel, 1994]. Only the fluid and crystal phases are found as the triple point vanishes and the liquid region ceases to exist [Poon et al., 1996, Hagen and Frenkel, 1994, Foffi et al., 2002]. By reducing the range of the attractive interaction, the gas-liquid phase transition becomes more and more hindered by the solid-liquid coexistence line [Hagen and Frenkel, 1994, Rosenbaum et al., 1996, Noro and Frenkel, 2000, Foffi et al., 2002]. To conclude, the occurrence of a metastable liquid-gas region in the  $\Phi$ - $T$ -phase diagram is the direct consequence of the short-ranged nature of the forces acting on the particles and crucially depends on the range of the attractive interaction potential relative to the particles diameter [Hagen and Frenkel, 1994, Foffi et al., 2002].

Hence, theoretical predictions of the protein phase behavior in a completely charge-screened system can be made with a simple model of colloidal particles displaying short-ranged attractive pair-interactions [Rosenbaum et al., 1996] as proteins can be considered as colloids in many aspects. For small proteins, the van der Waals interaction potential (including other contributions such as hydrogen bonding, hydration forces, etc.) tend to be short ranged in comparison to the protein size and can be modeled by an attractive short-ranged Yukawian potential (see section 2.2.3) [Malfois et al., 1996, Tardieu et al., 1999]. Van der Waals interactions quantified by Hamaker constants in the order of a few  $k_B T$  become significant at surface-to-surface separations of  $\sim \sigma/10$ . Solvation and structural forces act over the range of 1-5 solvent diameters, whilst hydrogen bonds and salt bridges become relevant at separations of one solvent layer, only. The phase diagram shown in Figure 2.17 (c) ( $d \sim 1/6 \sigma$ ) is most appropriate to describe protein phase behavior qualitatively. In full analogy to molecular fluid phase behavior, the fluid-crystal equilibrium (sublimation line) corresponds to the equilibrium of the protein crystals with their supernatant (i.e. crystal solubility line) and the liquid-liquid binodal can be understood as the gas-liquid coexistence curve (see Figure 2.16 (a)). In the LLPS region, a dense liquid rich in protein (the theoretical liquid) separates from a liquid dilute in protein (the theoretical gas<sup>8</sup>) [Dumetz et al., 2008].

As stated earlier, there is a close linkage between the existence of a liquid state and the range of interparticle attraction relative to the hard-sphere repulsion. The range of the effective protein-protein interaction can be changed by changing the pH and the salt concentration. Further, in

<sup>8</sup>The theoretical gas phase corresponds to a liquid in which protein motion shares characteristics of the Brownian motion of gas molecules [Dumetz, 2007].

binary system such as a size-asymmetric dispersion of colloid hard spheres or mixtures of colloids and non-adsorbing polymer (i.e. polyethylene glycol) a liquid-gas demixing transition may occur due to the entropy-driven depletion mechanism [Nägele, 2008, Ilett et al., 1995, Poon et al., 1997]. In the case of a polymer-colloid mixture, the entropically favored depletion of polymer from the intermediate region of two colloidal particles induces an attractive interaction between the colloids, whose range is determined by the effective polymer size and strength is set by the polymer concentration (see section 2.2.2) [Asakura and Oosawa, 1958, Vrij, 1976]. Under suitable conditions (i.e. the range of the depletion attraction exceeds  $\sim 25 - 30\%$  of the particle's radius) the colloid-polymer mixtures can undergo phase separation into colloid-rich and colloid poor regions [Poon et al., 1996, Ilett et al., 1995].

In this thesis, by employing more than three orders of magnitude of the polymer's molecular weight ( $M_w \sim 200 - 35000 \text{ g mol}^{-1}$ ) at concentrations crossing from the dilute to the semi-dilute polymer regime and the polysaccharide Ficoll PM 70, we explore their effect the protein's phase behavior by the impact of the size and shape of the crowding agent (see chapter 4 and 7). Changes in the phase boundaries reveal modulations in the intermolecular interaction forces, which drive the phase transition.

### Pressure Effects on the Protein Phase Behavior

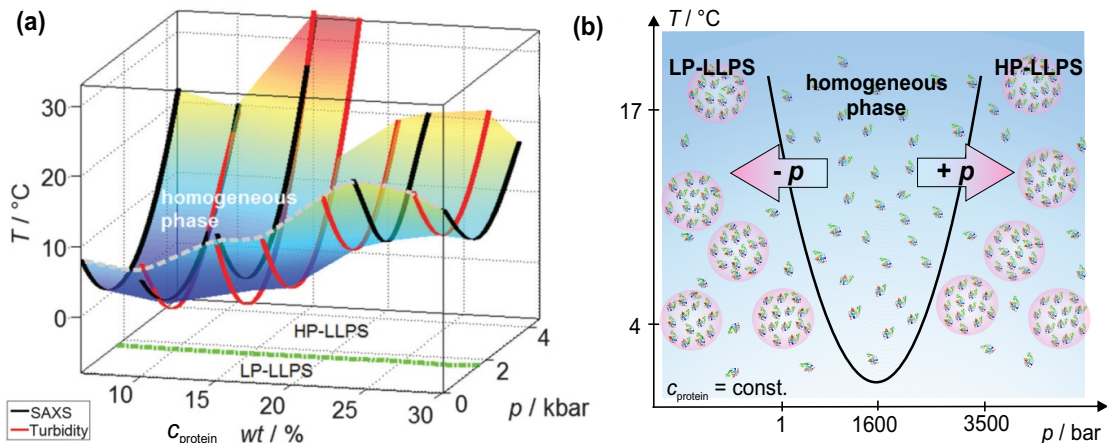


Figure 2.18: (a)  $p$ - $T$ - $c$  phase diagram for the monomeric protein lysozyme in the LLPS region. Picture reprinted with permission from [Schulze et al., 2016]. (b) Sketch of the Pressure dependent re-entrant liquid-liquid phase separation at constant protein concentration,  $c_{\text{protein}}$ , and temperature,  $T$ .

Crystallization requires the protein's chemical potential to exceed the chemical potential of the protein crystal (e.g. by temperature, protein concentration, salt concentration, addition of cosolutes, pressure) whilst not reaching the level where amorphous precipitates are formed. Previous studies have shown, that an increase of the protein solubility and the concomitant decrease of chemical potential of the protein upon pressurization reduces the proteins activity coefficient [Webb et al., 1999, Waghmare et al., 2000, Gross and Jaenicke, 1994]. The pressure-induced linear increase of lysozyme solubility at  $\sim 2500$  bar averages 40% over that at atmospheric pressure [Webb et al., 1999, Lorber et al., 1996, Takano et al., 1997]. *In situ*-observations on the crystallization of hen egg white lysozyme report a non-linear decrease in crystal growth rate with increasing pressure to value of nearly zero at  $\sim 1$  kbar, arresting upon further pressurization in a wide pressure range until crystal dissolution into the solvent occurs [Takano et al., 1997, Suzuki et al., 1994].

Previous HHP small-angle X-ray studies on the effect of pressure on the liquid-liquid phase separation boundaries of dense lysozyme solutions [Möller et al., 2014a, Schulze et al., 2016], report a re-entrant HHP-LLPS region at elevated pressures. For temperatures right below room temperature and ambient pressure, lysozyme solutions at intermediate protein concentration and high ionic strength ( $I = 500 \text{ mM}$ ) enter the LLPS region. An increase in pressure causes a phase



transition to the homogeneous phase and upon further pressurization this effect is reversed. This non-monotonous phase behavior is consistent with the finding that pressure has a increasing repulsive effect on the intermolecular interactions of proteins [Ortore et al., 2009, Russo et al., 2013], followed by a solvent-mediated rise in attractivity of the protein-protein effective interaction potential at kbar pressures [Schroer et al., 2011a]. This pressure-induced modulation of the intermolecular interactions was shown to persist even at high ionic strength [Möller et al., 2012] (see section 2.3.3). Notably, the non-monotonous pressure dependence of the LLPS boundaries with a turnover pressure from the low pressure LLPS to the high pressure LLPS at  $\sim 1.6$  kbar, has been found to persist even at a high level of self crowding (see Figure 2.18, *dashed green line*), i.e. the pressure effect is essentially solvent-mediated. The shift of the phase boundaries to higher temperatures with increasing lysozyme concentration, as already found for ambient pressure [Muschol and Rosenberger, 1997, Taratuta et al., 1990, Broide et al., 1996, Cardinaux et al., 2007], is preserved upon pressurization.

These studies provide valuable insight into the effects of hydrostatic pressure and self-crowding on the phase behavior of highly concentrated protein solutions. However, the intracellular environment is rather multicomponent and better described by a 'crowded' rather than 'concentrated' milieu, as, in general, no individual species may be present at high concentrations [Minton, 1997, Minton, 2000]. Little is known about the intermolecular interactions governing LLPS in more complex biomolecular systems. Especially their role in maintaining cellular function facing internal and external stresses factors, such as high osmotic pressure induced by the high fractional occupancy ( $> 30\%$ ) of 'background' molecules, extreme temperatures or high hydrostatic pressures as encountered in the deep sea, is still largely *terra incognita*. In this thesis, we have quantified the effect of multiple crowding scenarios, as encountered in the heterogeneous biological cell, on the protein-protein interaction potential and the protein's phase behavior over a wide range of temperatures and pressures (see section 4 and 7).



## 2.4 Small Angle X-ray Scattering (SAXS)

(Ultra) small-angle X-ray scattering is a well established, non-invasive method for analyzing structures of systems with random arrangement at the mesoscopic scale (1 nm to 1  $\mu\text{m}$ ), yielding physical quantities averaged over the whole sample with almost no approximation or model. This section introduces the small-angle X-ray experiment as applied to the investigation of soft condensed matter as well as the main concepts and methods for the interpretation of SAXS data of biological macromolecules in solution. The basic principle of small-angle X-ray scattering is, that charge density fluctuations in the medium (e.g. proteins in solution, inclusions in porous materials, etc.) give rise to X-ray scattering at small angles ( $\leq 5^\circ$ ). Thus, the measurement of the averaged scattered intensity in dependency of the scattering angle yields so-called 'low-resolution' structural information on the medium under investigation. As described in the following sections, in dependency of the wave vector transfer  $q$ , various levels of structural organization in the sample can be resolved from the scattered intensity,  $I(q)$  (see Figure 2.19). In a dilute system, this includes the shape, size and specific surface of the individual particles as well as the spatial arrangement of material within them. In concentrated systems, we learn from the so-called structure factor about the mean spatial arrangement of macromolecules in solution and thereby the intermolecular interaction forces governing them. In this work, small angle X-ray scattering is applied for probing the tertiary structure of dissolved oligomeric and monomeric proteins, like shape and size, as well as their spatial arrangement in dense solutions, correlated to the intermolecular forces acting in solution.

This section is oriented on [Lindner and Zemb, 2002], [Feigin and Svergun, 1987] and [Schroer et al., 2011b].

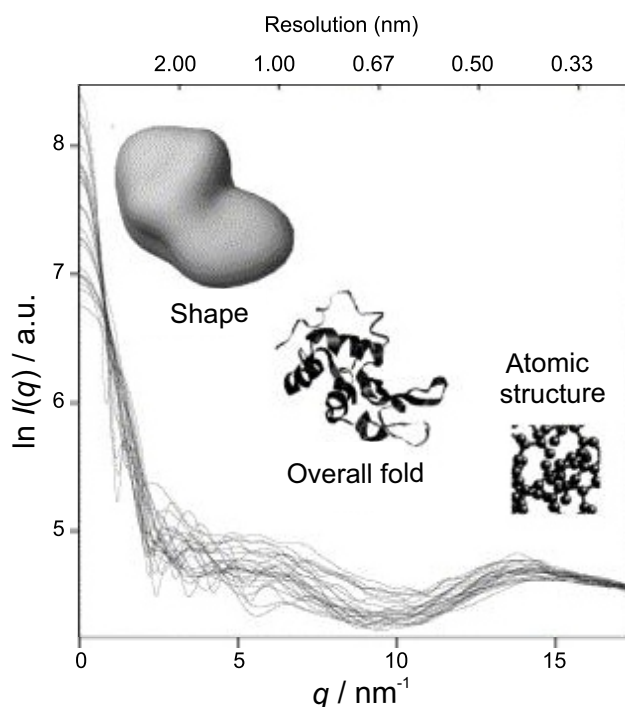


Figure 2.19: Theoretical small-angle X-ray scattering intensities,  $I(q)$ , computed for various proteins with molecular weights,  $M_w$ , ranging from 10 to 300 kDa. The upper axis displays the spatial resolution  $\Delta = 2\pi/q$  in real space. Picture adapted from [Svergun and Koch, 2002].

### 2.4.1 X-ray Scattering from Discrete Particles in Dilute and Concentrated Suspensions

Figure 2.20 shows the sketch of a typical small-angle X-ray experiment. A plane monochromatic electromagnetic wave,

$$\mathbf{E}_I(\mathbf{R}', t) \equiv \mathbf{E}_0 \cdot \exp(i(\mathbf{k}_0 \cdot \mathbf{R}' - \omega t)), \quad (2.31)$$

characterized by angular frequency  $\omega$  and wave vector  $\mathbf{k}_0$ , is incident on the system of interest (e.g. suspension of colloids or a solution of proteins or polymers) at position  $\mathbf{R}'$ . The wave vector  $\mathbf{k}_0$  specifies the direction of wave propagation. For the remainder, we consider the electric vector  $\mathbf{E}_0$  being polarized perpendicular to the scattering plane (plane of the paper). Inhomogeneities within the medium, associated with (electric charge) density fluctuations, cause some of the radiation to scatter (with the same polarization) away from the incident direction. The intensity of the scattered wave with wave vector  $\mathbf{k}_S$  is recorded at the scattering angle  $2\Theta$  by a detector, which is separated from the sample by the distance  $L$ . In the experiment, the part of the beam not interacting with the medium is removed by a beamstop (see section 3.2.1). The wave vector transfer,  $\mathbf{q}$ , is defined as the difference between the wave vectors of the incident and the scattered wave

$$\mathbf{q} = \mathbf{k}_S - \mathbf{k}_0. \quad (2.32)$$

We assume a 'quasi-elastic' scattering process with only very small changes in the incident beams wavelength,  $\lambda$ , by the medium. Hence, the moduli of the wave vectors of both incident,  $\mathbf{k}_0$ , and scattered wave,  $\mathbf{k}_S$ , are described by

$$|\mathbf{k}_S| = |\mathbf{k}_0| = k = \frac{2\pi}{\lambda}. \quad (2.33)$$

The magnitude,  $q$ , of the wave-vector transfer (Eq. (2.32)) results in

$$q = |\mathbf{q}| = \frac{4\pi}{\lambda} \sin(2\Theta/2). \quad (2.34)$$

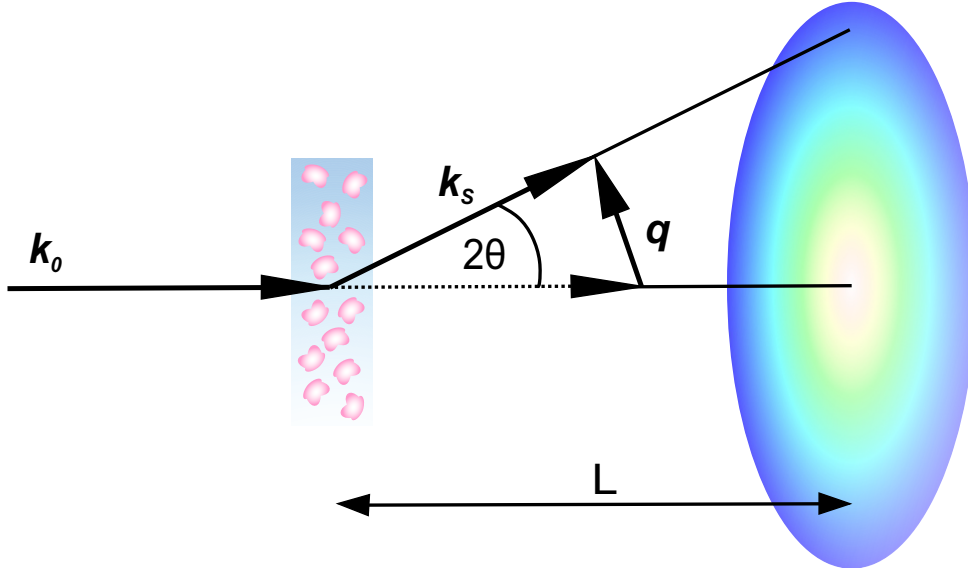


Figure 2.20: Scattering geometry of a typical small-angle X-ray scattering experiment.

We now consider a sample of  $N$  discrete particles (e.g. proteins, polymers or colloids) with Volume  $V_j$  suspended in a liquid (see Fig. 2.21). The center of mass of a particle  $j$  in the overall

scattering volume  $V$ , relative to an arbitrary origin  $O$ , is described by the position vector  $\mathbf{R}_j(t)$ . In general, the X-ray scattering ability of a sample is related to its direct structure, described by the local electric charge density,  $\rho(\mathbf{R}', t)$ , at the position  $\mathbf{R}'$  relative to the average electric charge density,  $\rho_0$ , of the medium. As the incident plane wave propagates through the medium, its alternating electric field (Eq. (2.31)) induces a dipole moment of the strength  $E_0[\rho(\mathbf{R}', t) - \rho_0]dV$  in the infinitesimal volume element  $dV$  [Als-Nielsen and McMorrow, 2011]. The elementary dipole oscillates with frequency  $\omega$  and emits (scatters) a spherical secondary wave propagating in all directions. For weak scattering fields it can be assumed that the incident wave is only scattered once and the probability of higher-order scattering of the secondary waves is negligible. The superposition of the secondary waves gives the first approximation to the scattering wave (first Born approximation) [Landau and Lifshitz, 1985]. Hence, the amplitude of the electric field,  $E_S(\mathbf{R}, t)$ , of the radiation scattered by a sample of volume  $V$  to a observation point at position  $\mathbf{R}$  in the far field, corresponds to the sum of the amplitudes of the electric fields,  $dE_S(\mathbf{R}, t)$ , scattered by the volume elements  $dV$  placed at  $\mathbf{R}'$ .

$$E_S(\mathbf{R}, t) = \int_V dE_S(\mathbf{R}, t) \quad (2.35a)$$

$$\begin{aligned} dE_S(\mathbf{R}, t) &= -\frac{k^2 E_0}{4\pi} \cdot \frac{\exp[i(\mathbf{k}_S \cdot (\mathbf{R} - \mathbf{R}') - \omega t)]}{|\mathbf{R} - \mathbf{R}'|} \cdot \left[ \frac{\rho(\mathbf{R}', t) - \rho_0}{\rho_0} \right] dV \cdot \exp(i\mathbf{k}_0 \cdot \mathbf{R}') \\ &= -\frac{k^2 E_0}{4\pi} \cdot \frac{\exp(i(kR - \omega t))}{L} \cdot \left[ \frac{\rho(\mathbf{R}', t) - \rho_0}{\rho_0} \right] dV \cdot \exp(-i\mathbf{q} \cdot \mathbf{R}'). \end{aligned} \quad (2.35b)$$

Here, we used Eq. (2.32) and the 'far field approximation'  $|\mathbf{R} - \mathbf{R}'| \approx |\mathbf{R}| = L$ , which is appropriate for a large distance between sample and observation point in comparison to the dimensions of the scattering volume.

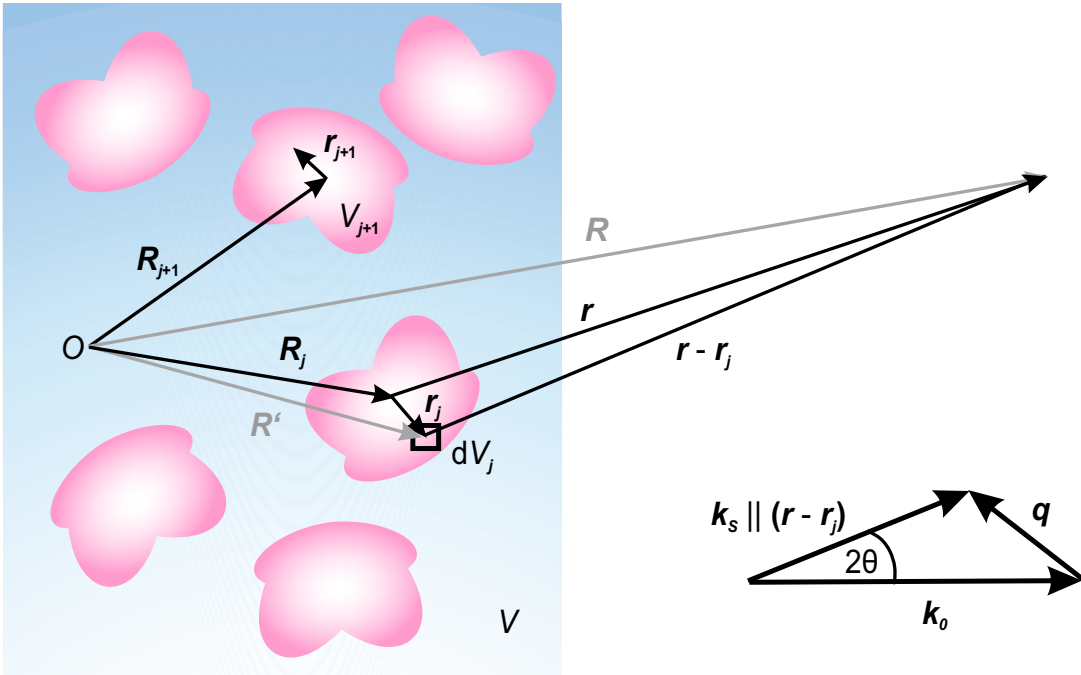


Figure 2.21: Coordinates for discrete scatterers suspended in a liquid. Relative to an arbitrary origin  $O$ ,  $\mathbf{R}_j(t)$  is the position of the center of mass of the particle  $j$  and  $\mathbf{R}' = \mathbf{R}_j(t) + \mathbf{r}_j$  the position of the volume element  $dV_j (= d^3r_j)$  in particle  $j$ . The scattered radiation emanating from  $dV_j$  is detected at the observation point at the position  $\mathbf{R}$  with  $|\mathbf{R}| = L$ .

In a totally homogeneous medium with constant electric charge density,  $\rho(\mathbf{R}', t) = \rho_0$ , the radiation would pass the sample undeviated. For particles with dimensions much larger than

internal structural inhomogeneities, the scattering ability of a single particle  $j$  by X-rays can be characterized by a continuous electric charge density distribution  $\rho^{(P)}(\mathbf{R}', t)$  [Porod, 1982]. In a solution of  $N$  particles in the scattering volume  $V$ , the scattering arises from three contributing parts [Pusey, 2002]:

$$\begin{aligned}\rho(\mathbf{R}', t) - \rho_0 &= \rho^{(P)}(\mathbf{R}', t) - \rho^{(L)} && (\mathbf{R}' \text{ inside any particle}) \\ &+ \rho^{(L)}(\mathbf{R}', t) - \rho^{(L)} && (\mathbf{R}' \text{ outside all particle}) \\ &+ \rho^{(L)} - \rho_0 && (\mathbf{R}' \text{ anywhere in } V).\end{aligned}\quad (2.36)$$

The first term in Eq. (2.36) accounts for the scattering by the difference between the electric charge density of the particle,  $\rho^{(P)}(\mathbf{R}', t)$ , and that of the liquid in which the particle is suspended,  $\rho^{(L)}$ . The second contribution arises from density and/or concentration fluctuations in the suspension medium itself,  $\rho^{(L)}(\mathbf{R}', t)$ , as found for mixtures of liquids or solutions of small molecules. For solvent molecules much smaller than the particle, as being the case for water molecules in aqueous protein solutions, the signal is constant in the relevant  $q$ -range and is simply proportional to the isothermal compressibility [Orthaber et al., 2000]. In the further course of this section, the intensity of this 'background' scattering is assumed to be negligible. Inserting the third term of Eq. (2.36) in Eq. (2.35), results in a contribution proportional to  $\int_V \exp(-i\mathbf{q} \cdot \mathbf{R}') dV$ , since  $(\rho^{(L)} - \rho_0)$  does not depend on the position  $\mathbf{R}'$ :<sup>9</sup>

$$(\rho^{(L)} - \rho_0) \int_V \exp(i\mathbf{q} \cdot \mathbf{R}') dV = (\rho^{(L)} - \rho_0) \delta(\mathbf{q}). \quad (2.37)$$

This integral describes the diffraction of the beam by the entire scattering volume,  $V$ . For scattering volume dimensions much larger than the wavelength of the incident radiation, Eq. (2.37) peaks at  $\mathbf{q} = 0$  and therefore this contribution can be neglected [Goodisman and Brumberger, 1973]. The local electric charge distribution at position  $\mathbf{r}_j$  in particle  $j$  can be described by

$$\rho^{(P)}(\mathbf{R}', t) = \sum_{j=1}^N \delta[\mathbf{R}' - (\mathbf{R}_j(t) + \mathbf{r}_j)] \rho^{(P)}(\mathbf{r}_j, t) dV_j. \quad (2.38)$$

The total electric field, scattered by the particle  $j$  to the observation point  $\mathbf{R}$ , emerges to

$$\begin{aligned}E_j(\mathbf{R}, t) &= -\frac{k^2 E_0}{4\pi} \cdot \frac{\exp(i(kR - \omega t))}{L} \cdot \left[ \int_{V_j} \left[ \frac{\rho^{(P)}(\mathbf{r}_j, t) - \rho^{(L)}}{\rho_0} \right] \exp(-i\mathbf{q} \cdot \mathbf{r}_j) d^3 r_j \right] \exp(-i\mathbf{q} \cdot \mathbf{R}_j(t)) \\ &= -E_0 \cdot \frac{\exp(i(kR - \omega t))}{L} \cdot \left[ \int_{V_j} \Delta\rho^{(P)}(\mathbf{r}_j, t) \exp(-i\mathbf{q} \cdot \mathbf{r}_j) d^3 r_j \right] \exp(-i\mathbf{q} \cdot \mathbf{R}_j(t)).\end{aligned}\quad (2.39)$$

For a given orientation, the normalized amplitude scattered by the particle  $j$ , is given by

$$F_j(\mathbf{q}, t) = \int_{V_j} \Delta\rho^{(P)}(\mathbf{r}_j, t) \exp(i\mathbf{q} \cdot \mathbf{r}_j) d^3 r_j. \quad (2.40)$$

Thus, the scattering amplitude,  $F_j(\mathbf{q}, t)$ , of the particle  $j$  is the Fourier transform of its electric charge distribution,  $\Delta\rho^{(P)}(\mathbf{r}_j, t)$ , characterizing its shape and size. Expanding to a system of  $j = 1 \dots N$  particles, the sum of the fields,  $E_j(\mathbf{R}, t)$ , scattered by the individual particles  $j$  yields the total scattered electric field

$$\begin{aligned}E_S(\mathbf{R}, t) &= \sum_{j=1}^N E_j(\mathbf{R}, t) \\ &= -E_0 \cdot \frac{\exp(i(kR - \omega t))}{L} \sum_{j=1}^N F_j(\mathbf{q}, t) \exp(-i\mathbf{q} \cdot \mathbf{R}_j(t)).\end{aligned}\quad (2.41)$$

---

<sup>9</sup>Basic properties of  $\delta$ -distribution:

$$\int_{-\infty}^{\infty} \delta(x) dx = 1 \quad \text{and} \quad \delta(x - a) = 0 \quad \text{when} \quad x \neq a$$

In the experiment, the intensity of the scattered radiation is measured rather than the electric field. Intensity and electric field of the wave scattered to the observation point  $\mathbf{R}$  are related by

$$\begin{aligned} I(\mathbf{q}, t) &= |E_S(\mathbf{q}, t)|^2 \\ &= \frac{I_0}{L^2} \sum_{j=1}^N \sum_{k=1}^N F_j(\mathbf{q}, t) F_k^*(\mathbf{q}, t) \exp(-\mathbf{q} \cdot (\mathbf{R}_j(t) - \mathbf{R}_k(t))), \end{aligned} \quad (2.42)$$

wherein  $I_0 = E_0^2$  is the intensity of the incident beam. Squaring the scattering amplitudes,  $E_S(\mathbf{q}, t)$ , cancels out the imaginary part specifying the phase relations. The scattering intensity,  $I(\mathbf{q}, t)$ , recorded in a scattering experiment is a real number and cannot be simply inverted to yield the electron distribution within the sample [Als-Nielsen and McMorrow, 2011]. Moreover, the sign of the scattering contrast  $\Delta\rho^{(P)}$  in (Eq. (2.40)) is lost. As a consequence, two complementary structures with electron densities equal according to amount and of opposite sign produce the same scattering signal. This is also referred to as the *Babinet Principle* in optics [Spalla, 2002]. Due to Brownian dynamics, the particles are diffusing in time through the volume within in sample exposed to the beam. Since the scattering intensity changes for the different positions and orientations of the particles, the average in time is the measured quantity. For an ergodic system, the time average is equal to the statistical average<sup>10</sup>  $\langle \dots \rangle_\Omega$  over the available positions and orientations of the particles [Spalla, 2002]. This applies to an assembly of discrete particles in a liquid, which is spatially isotropic on average, and the average intensity scattered by this kind of system is generally described by

$$\begin{aligned} I(q) &:= \langle I(\mathbf{q}) \rangle_\Omega \\ &= \frac{I_0}{L^2} \left\langle \sum_{j=1}^N \sum_{k=1}^N F_j(\mathbf{q}) F_k^*(\mathbf{q}) \exp(-\mathbf{q} \cdot (\mathbf{R}_j - \mathbf{R}_k)) \right\rangle_\Omega. \end{aligned} \quad (2.43)$$

Assuming an isotropic system, the average scattering intensity is written as a function of the modulus  $q = |\mathbf{q}|$  of the scattering vector. Concomitant with  $I(q)$  not being dependent on the orientation of  $\mathbf{q}$ , the information on the spatial order of the particles is lost. In the general case of polydisperse and non-spherical particles, the form factors  $F_j(\mathbf{q})$  vary from particle to particle. To simplify the description, only identical (non-spherical) particles are treated in the remainder of this section, only differing in their spatial location and orientation. We assume the relative orientation of the particles is not influenced by their separating distance. Thus, the form amplitudes,  $F_j(\mathbf{q})$ , are uncorrelated. Within this so-called *decoupling approximation*, which is valid for not too high particle concentrations, Eq. (2.43) can be written as

$$I(q) = \frac{I_0}{L^2} \left\langle \sum_{j=1}^N \sum_{k=1}^N \langle F_j(\mathbf{q}) F_k^*(\mathbf{q}) \rangle_\Omega \exp(-\mathbf{q} \cdot (\mathbf{R}_j - \mathbf{R}_k)) \right\rangle_\Omega. \quad (2.44)$$

The average of the form amplitudes  $\langle F_j(\mathbf{q}) F_k^*(\mathbf{q}) \rangle_\Omega$ , weighted by the distribution of particle orientations, can be decomposed to<sup>11</sup>

$$\langle F_j(\mathbf{q}) F_k^*(\mathbf{q}) \rangle_\Omega = [\langle |F(\mathbf{q})|^2 \rangle_\Omega - \langle F(\mathbf{q}) \rangle_\Omega \langle F^*(\mathbf{q}) \rangle_\Omega] \delta_{jk} + |\langle F(\mathbf{q}) \rangle_\Omega|^2. \quad (2.45)$$

The terms with index ( $j = k$ ), correspond to scattering contributions from only one particle as the terms ( $j \neq k$ ) describe scattering contributions from two different particles. Inserting Eq. (2.45)

<sup>10</sup> Statistical average,  $\langle \dots \rangle_\Omega$ , over all orientations for a given function  $F(\mathbf{q})$ :

$$\langle F(\mathbf{q}) \rangle_\Omega = \frac{1}{4\pi} \int_0^{2\pi} \int_0^\pi F(q, \Theta, \Phi) \sin(\Theta) d\Theta d\Phi,$$

wherein  $\Theta$  and  $\Phi$  denote the solid angles.

<sup>11</sup>Basic properties of the Kronecker delta:

$$\delta_{jk} = \begin{cases} 0 & \text{if } j \neq k, \\ 1 & \text{if } j = k. \end{cases}$$

in Eq. (2.44) and introducing the average interparticle **structure factor**,  $S(q)$ , defined by

$$S(q) = N \left\langle \sum_{j \neq k}^N \sum_{j=1}^N \exp(-\mathbf{q} \cdot (\mathbf{R}_j - \mathbf{R}_k)) \right\rangle_{\Omega}. \quad (2.46)$$

yields for the intensity scattered by monodisperse solutions of non-spherical particles [Kotlarchyk and Chen, 1983]:

$$\begin{aligned} I(q) &= \frac{I_0}{L^2} \left[ N [\langle |F(\mathbf{q})|^2 \rangle_{\Omega} - |\langle F(\mathbf{q}) \rangle_{\Omega}|^2] + N |\langle F(\mathbf{q}) \rangle_{\Omega}|^2 \cdot \left\langle \sum_{j \neq k}^N \sum_{j=1}^N \exp(-\mathbf{q} \cdot (\mathbf{R}_j - \mathbf{R}_k)) \right\rangle_{\Omega} \right] \\ &= \frac{I_0}{L^2} [N [\langle |F(\mathbf{q})|^2 \rangle_{\Omega} - |\langle F(\mathbf{q}) \rangle_{\Omega}|^2] + N |\langle F(\mathbf{q}) \rangle_{\Omega}|^2 \cdot S(q)]. \end{aligned} \quad (2.47)$$

The structure factor, depending on the distance  $\mathbf{R}_j - \mathbf{R}_k$  between the particles  $j$  and  $k$ , represents the modification of the scattering intensity due to the particles spatial correlation. The suppression of the oscillations in the course of the structure factor,  $S(q)$ , caused by orientation averaging, is described by the  $q$ -dependent factor

$$\beta(q) = \frac{|\langle F(\mathbf{q}) \rangle_{\Omega}|^2}{\langle |F(\mathbf{q})|^2 \rangle_{\Omega}} \quad \text{with } (0 < \beta(q) < 1). \quad (2.48)$$

Introducing the *effective* structure factor,

$$S_{\text{eff}}(q) = 1 + \beta(q)[S(q) - 1], \quad (2.49)$$

yields a more compact notation of Eq. (2.47):

$$I(q) = \frac{I_0}{L^2} N \langle |F(\mathbf{q})|^2 \rangle_{\Omega} S_{\text{eff}}(q). \quad (2.50)$$

In the case of scattering from monodisperse spheres ( $\beta(q) = 1$ ), Eq. (2.50) is reduced to

$$I(q) = \frac{I_0}{L^2} N \langle |F(\mathbf{q})|^2 \rangle_{\Omega} S(q). \quad (2.51)$$

As can be seen, the general overall scattering intensity (Eq. (2.50)) is proportional to the product of two  $q$ -dependent scattering contributions: The square of the Fourier transform of the particles electric charge distribution averaged over all orientations,  $\langle |F(\mathbf{q})|^2 \rangle_{\Omega}$ , yielding information about size and shape of the scattering particles, and the (effective) structure factor,  $S_{\text{eff}}(q)$ , sensitive to the spatial arrangement of the particles and therefore the intermolecular interactions between them.

## 2.4.2 Dilute solutions

In the dilute limit, the particles spatial separation is sufficiently large for them to be entirely uncorrelated. Over time, the particle  $j$  can take up any position in the sample and is unaffected by any other particle  $k$ . At diminishing correlations between the particles cross terms ( $j \neq k$ ) vanish and  $S(q) \rightarrow 1$ . The average intensity (Eq. (2.50)) can be written as the sum of averaged intensities scattered by the individual particles in the solution. Thus, the measured intensity, scattered by a monodisperse solution of  $N$  identical particles, yields the particles shape, size and structure averaged over orientation. The intensity,  $I(q)$ , is given by

$$\begin{aligned} I(q) &= \frac{I_0}{L^2} N \cdot \langle |F(\mathbf{q})|^2 \rangle_{\Omega} \\ &= \frac{I_0}{L^2} N \cdot P(q), \end{aligned} \quad (2.52)$$



introducing the particles **form factor**,

$$P(q) = \langle |F(\mathbf{q})|^2 \rangle_{\Omega}. \quad (2.53)$$

Using Eq. (2.40), the form factor can be written out as:

$$\begin{aligned} P(q) &= \langle F(\mathbf{q}) \cdot F^*(\mathbf{q}) \rangle_{\Omega} \\ &= \left\langle \int \int_{V_P} \Delta\rho^{(P)}(\mathbf{r}_1) \Delta\rho^{(P)}(\mathbf{r}_2) \exp(i\mathbf{q} \cdot (\mathbf{r}_1 - \mathbf{r}_2)) d\mathbf{r}_1 d\mathbf{r}_2 \right\rangle_{\Omega} \\ &= \left\langle \int \int_{V_P} \Delta\rho^{(P)}(\mathbf{r}_1) \Delta\rho^{(P)}(\mathbf{r}_1 - \mathbf{r}) \exp(i\mathbf{q} \cdot \mathbf{r}) d\mathbf{r}_1 d\mathbf{r} \right\rangle_{\Omega}. \end{aligned} \quad (2.54)$$

Here, the relations  $\mathbf{r}_1 - \mathbf{r}_2 = \mathbf{r}$  and  $\mathbf{r}_2 = \mathbf{r}_1 - \mathbf{r}$  were used. Introducing the convolution square  $\Delta\tilde{\rho}^2(\mathbf{r})$  of the density fluctuations ( $\equiv$  **auto-correlation function**  $\gamma(\mathbf{r})$ ) [Glatter, 2002, Debye and Bueche, 1949],

$$\gamma(\mathbf{r}) \equiv \Delta\tilde{\rho}^2(\mathbf{r}) = \int_{V_P} \Delta\rho^{(P)}(\mathbf{r}_1) \Delta\rho^{(P)}(\mathbf{r}_1 - \mathbf{r}) d\mathbf{r}_1, \quad (2.55)$$

into Eq. (2.55) gives

$$P(q) = \left\langle \int_{V_P} \gamma(\mathbf{r}) \exp(i\mathbf{q} \cdot \mathbf{r}) d\mathbf{r} \right\rangle_{\Omega}. \quad (2.56)$$

For a particle fixed in space with electron density contrast,  $\Delta\rho^{(P)}(\mathbf{r})$ , the convolution square  $\gamma(\mathbf{r}) = \Delta\tilde{\rho}^2(\mathbf{r})$  describes the overlapping volume between the particle itself and its identical *ghost* with centers shifted by  $\mathbf{r}$  (see Figure 2.22 (a)). Clearly, for non-spherical particles the overlap volume depends on the mutual orientation of the particles. Consequently, the spatially averaged convolution square,  $\gamma(r) = \langle \Delta\tilde{\rho}^2(\mathbf{r}) \rangle_{\Omega}$ , accounts for all possible directions in space the ghost can be shifted to by the distance  $r = |\mathbf{r}|$  and thus for all possible mutual particle orientations (see Figure 2.22 (b)) [Glatter, 2002].

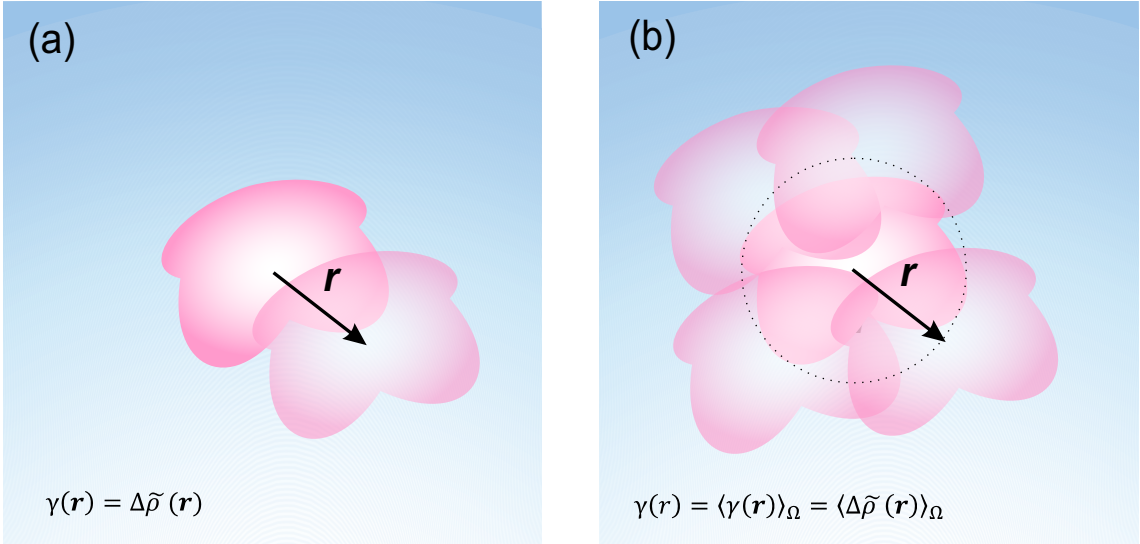


Figure 2.22: (a) For a particle fixed in space with electron density contrast,  $\Delta\rho^{(P)}(\mathbf{r})$ , the convolution square  $\Delta\tilde{\rho}^2(\mathbf{r})$  describes the overlapping volume between the particle itself and its identical *ghost* with centers shifted by  $\mathbf{r}$ . (b) The spatially averaged convolution square averages over all possible directions in which the ghost can be moved by the distance  $r = |\mathbf{r}|$  [Glatter, 2002].

By averaging over all orientations [Debye, 1915], information about the system gets lost, as the auto-correlation function only remains dependent on the magnitude of the distance  $r = |\mathbf{r}|$  and

the scattering intensity on the magnitude of the scattering vector  $q = |\mathbf{q}|$ , respectively:

$$P(q) = 4\pi \int_0^\infty \gamma(r) \cdot r^2 \cdot \frac{\sin(qr)}{qr} dr. \quad (2.57)$$

As mentioned above (see Eq. (2.40)), the scattering amplitude,  $F(\mathbf{q})$ , is the Fourier transformation of the particles electron density fluctuation,  $\Delta\rho^{(P)}(\mathbf{r})$ . Now we find (see Eq. (2.57)), that the scattering intensity,  $P(q) = \langle F(\mathbf{q}) \cdot F^*(\mathbf{q}) \rangle_\Omega$ , is the Fourier transform of the auto-correlation function,  $\gamma(r)$ , averaged over all directions in space.

By introducing the **pair distance distribution function**,  $p(r)$ , with

$$p(r) := \gamma(r) \cdot r^2, \quad (2.58)$$

in Eq. (2.57) the form factor is given as

$$P(q) = 4\pi \int_0^\infty p(r) \cdot \frac{\sin(qr)}{qr} dr. \quad (2.59)$$

Conversely,  $\gamma(r)$  and  $p(r)$  can, in principle, be obtained from the inverse Fourier transformation of the scattering intensity:

$$\gamma(r) = \frac{1}{2\pi} \int_0^\infty P(q) q^2 \frac{\sin(qr)}{qr} dq, \quad (2.60)$$

$$p(r) = \frac{1}{2\pi^2} \int_0^\infty P(q) qr \sin(qr) dq. \quad (2.61)$$

If the electron density is constant inside the particle ( $\Delta\rho^{(P)}(\mathbf{r}_1) \equiv \Delta\rho^{(P)}$ ) we find [Glatter, 2002]

$$\begin{aligned} \gamma(r=0) &= \langle \Delta\tilde{\rho}^2(\mathbf{r}=\mathbf{0}) \rangle_\Omega \\ &= \left\langle \int_{V_P} \Delta\rho^{(P)}(\mathbf{r}_1) \Delta\rho^{(P)}(\mathbf{r}_1 - \mathbf{0}) d\mathbf{r}_1 \right\rangle_\Omega \\ &= \left( \Delta\rho^{(P)} \right)^2 \cdot V_P. \end{aligned} \quad (2.62)$$

Correspondingly, for homogeneous particles the normalized auto-correlation function  $\gamma_0(r) = \gamma(r)/V_P$  can be geometrically interpreted as the probability to find at a distance  $r$ , starting from an arbitrary point inside the particle volume, again another point inside the particle. To obtain the number of distances from the probability, the volume of a spherical shell,  $V_{\text{shell}} = \frac{4}{3}\pi r^2 dr$ , with radius  $r$  and thickness  $dr$  is multiplied with  $\gamma(r)$ , yielding

$$4\pi \gamma(r) r^2 dr = 4\pi p(r) dr. \quad (2.63)$$

Herein, we employed Eq. (2.58). Accordingly, the pair distance distribution function,  $p(r)$ , can be interpreted as a distance histogram if the particle is homogeneous. The height of  $p(r)$  is proportional to the number of connection lines between two points inside a particle with a length between  $r$  and  $r + dr$  [Glatter, 2002]. For homogeneous particles, Eq. (2.59) is reduced to

$$P(q) = 4\pi \int_0^{D_{\max}} p(r) \cdot \frac{\sin(qr)}{qr} dr, \quad (2.64)$$

since  $\gamma_0(r=0) = 1$  and  $\gamma_0(r > D_{\max}) = 0$  for distances exceeding the maximum particle extension,  $D_{\max}$ .

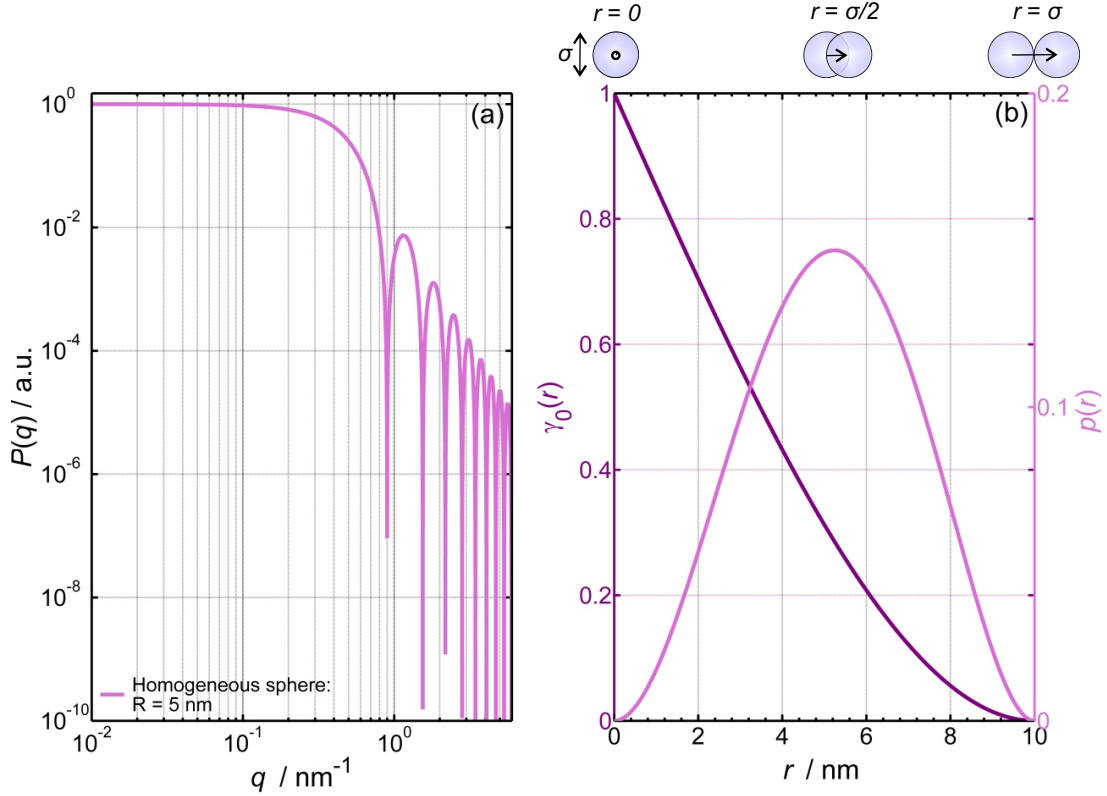


Figure 2.23: (a) Form factor,  $P(q)$ , of a homogeneous sphere with radius  $R (= \sigma/2) = 5$  nm, shown together with (b) the corresponding normalized auto-correlation function,  $\gamma_0(r)$ , and radial pair-distance distribution function,  $p(r)$ . The geometrical interpretation is depicted as well.

Exemplarily, the case of an homogeneous sphere of radius  $R = 5$  nm is shown in Figure 2.23. The normalized auto-correlation function for an homogeneous sphere is given by [Glatter, 2002]

$$\gamma_0(r) = \left( 1 - \frac{3}{4} \frac{r}{R} + \frac{1}{16} \frac{r^3}{R^3} \right). \quad (2.65)$$

and correspondingly

$$p(r) = \frac{3}{4\pi^2} \frac{r^2}{R^2} \left( 2 - \frac{3}{2} \frac{r}{R} + \frac{r^3}{8R^3} \right) \quad (2.66)$$

As shown in Figure 2.23 (b), at  $r = 0$  the overlap volume equals the overall volume and thus  $\gamma_0(r) = 1$ . With increasing distance of the particles centers, the overlap volume decreases till it is completely vanished for distances exceeding the maximal particle extension  $D_{\max}$  (here: the diameter  $\sigma = 2R$ ). The shape of the radial pair distribution function is nearly symmetric, exhibiting a pronounced maximum at a distance,  $r_{\max}$ , comparable to the radius of the sphere. With increasing asphericity (e.g. prolate/oblate ellipsoid of revolution, rod) the ratio  $D_{\max}/r_{\max}$  increases and the maximum of  $p(r)$  shifts to smaller  $r_{\max}$  values.

In Figure 2.24, the scattering intensity curves for various simple geometric bodies (e.g. a homogeneous sphere (red), a long rod (green), a flat disc (yellow), a hollow sphere (blue) and a dumbbell (magenta)) are shown in semi-logarithmic representation (left side) together with the corresponding pair distance distribution function (right side). Even though the information content of the displayed functions  $P(q)$  and  $p(r)$  is, in principle, the same, the particles shape can be much more easily accessed from the pair distribution function than the form factor: The maximal extension of each object can be obtained directly from the  $p(r)$  functions as  $p(r \geq D_{\max}) = 0$ .

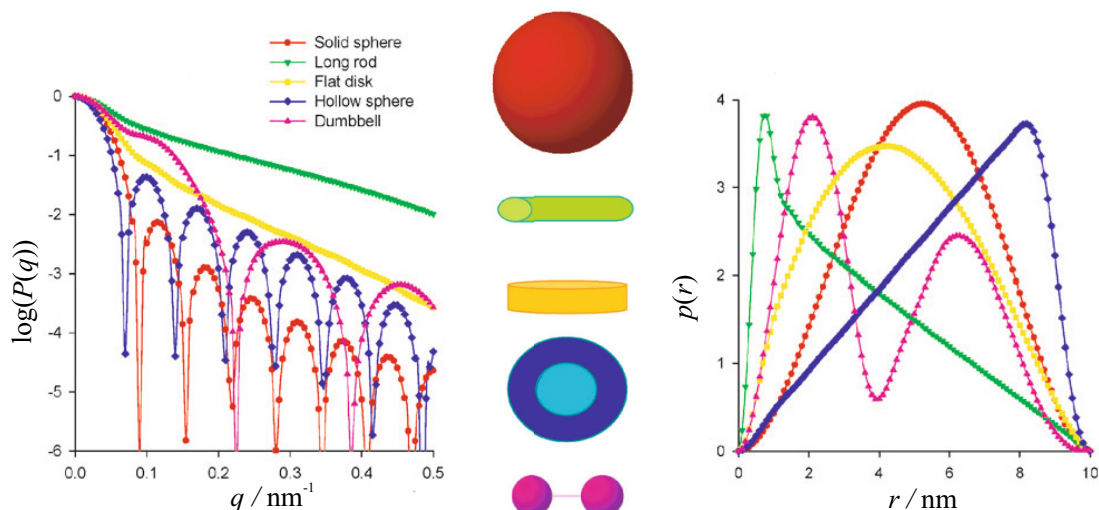


Figure 2.24: Scattering intensities,  $P(q)$ , (left) and radial pair-distance distribution functions,  $p(r)$ , (right) of various geometrical bodies with maximal dimension  $D_{\max} = 10$  nm. Picture adapted from [Svergun and Koch, 2003].

The sharp minima in the form factors of the sphere, the hollow sphere as well as the dumbbells (see Figure 2.24, left side) are typical for central-symmetric bodies. The location of the first minimum,  $q_c$ , is correlated with the maximal dimension of the particle,  $D_{\max}$ , via

$$q_c = \frac{2\pi}{D_{\max}}. \quad (2.67)$$

Due to the finite resolution obtainable in a SAXS experiment on e.g. proteins, these pronounced minima are not detectable.

In the following we shall focus on the problem to extract structural information on the particle in real space from the measured scattering signal  $P(q)$ . Equation (2.64) implies that  $P(q)$  is measured as a continuous function over the whole  $q$ -range. However, in a real scattering experiment the accessible  $q$ -range is limited as well as the spatial resolution of the detector providing only discrete data sets. Thus, instead of performing the direct Fourier transformation (Eq. 2.64), often a so-called indirect Fourier transformation is carried out [Glatter and Kratky, 1982]. Here, the exact radial pair distance distribution function,  $p(r)$ , is approximated by the finite sum  $p_A(r) = \sum_i c_i S_i(r)$  of discrete splines,  $S_i(r)$ , weighted by the coefficients,  $c_i$ . The theoretical scattering intensity, calculated from  $p_A(r)$ , is refined to the experimental data,  $P(q)$ , by adjusting the coefficients,  $c_i$ . The grand advantage is that this analysis method is model-free in respect of the shape of the scattering object, only an initial guess of the particles maximum extension,  $D_{\max}$ , is needed to obtain reasonable results. In this thesis, this approach was chosen for the data analysis of dilute protein solutions employing the program GNOM [Svergun et al., 1988, Svergun, 1992].

If the refinement of the whole scattering curve is not possible, still information on the structure of the sample can be obtained from the asymptotic behavior of the form factor at small wave vector transfer *via* the **Guinier approximation** and at large wave-vector transfer *via* the **Porod Law**.

### Guinier Approximation: The Radius of Gyration $R_G$

To examine the behavior of the form factor,  $P(q)$ , at very low angles, one can substitute the first two terms of the *Maclaurin series*

$$\frac{\sin(qr)}{qr} = 1 - \frac{q^2 r^2}{6} + \frac{q^4 r^4}{120} - \dots, \quad (2.68)$$

into Eq. (2.64), yielding

$$\begin{aligned} P(q) &\approx P(0) \cdot \left(1 - q^2 \frac{R_G^2}{3}\right) \\ &\approx P(0) \cdot \exp\left(-q^2 \frac{R_G^2}{3}\right) \end{aligned} \quad (2.69)$$

in the low  $q$  limit<sup>12</sup>. This is the so-called **Guinier approximation** for the scattering intensity of dilute solutions of non-interacting particles [Feigin and Svergun, 1987]. Herein,

$$P(0) = 4\pi \int_0^{D_{\max}} p(r) dr \quad (2.70)$$

denotes the scattering intensity at vanishing  $q$  and

$$R_G^2 = \frac{\int_0^{D_{\max}} p(r) r^2 dr}{2 \int_0^{D_{\max}} p(r) dr} \quad (2.71)$$

the squared radius of gyration,  $R_G$ . When all the secondary waves, scattered from a particle in solution, are in phase, the constructive interference develops the scattering intensity to the maximum at vanishing  $q$ . For homogeneous particles in solution the radial pair distribution function reads  $p(r) = (\Delta\rho^{(P)})^2 \cdot V_P \cdot r^2$  (see Eqs. (2.58) and (2.62)). Inserting this expression in Eq. (2.70), yields the parameter

$$P(0) = (\Delta\rho^{(P)} V_P)^2, \quad (2.72)$$

which characterizes the total amount of scattering matter. In a real SAXS experiment the forward scattering cannot be measured since it is superimposed by the primary beam and eventually masked by the beam stop. A more general expression for the radius of gyration,  $R_G$ , of a particle about its center of mass is given by [Feigin and Svergun, 1987]

$$R_G^2 = \frac{\int_{V_P} \Delta\rho^{(P)}(\mathbf{r}) r^2 d\mathbf{r}}{\int_{V_P} \Delta\rho^{(P)}(\mathbf{r}) d\mathbf{r}}. \quad (2.73)$$

In full analogy to the radius of inertia in mechanics,  $R_G$ , bears information on the particles distribution and electronic extend with respect to its center of mass [Kataoka et al., 1995]. Employing Eq. (2.69), the radius of gyration,  $R_G$ , can be determined with the so-called *Guinier plot* ( $\ln P(q)$  vs.  $q^2$ ) from the slope,  $(R_G^2/3)$ , in the low  $q$  limit ( $R_G \cdot q_{\max} \leq 1$ ) [Guinier and Fournet, 1955]. In case of proteins, this range can reportedly be extended to  $R_G \cdot q_{\max} \leq 1.3$  [Svergun and Koch, 2003]. As an example, the form factor of an homogeneous sphere with radius  $R = 5$  nm and the refinement made within the Guinier approximation are shown in Figure 2.25 together with the corresponding Guinier plot (*inset*).

Since  $R_G$  describes only the electronic extend of the particle (e.g. size) and not its shape, two different bodies (e.g. sphere and cube) with equal radius of gyration, give rise to the same scattering in the Guinier regime. The Guinier plot can also be employed to detect polydispersity, which induces an increase in scattering intensity at small  $q$  values, deviating from the linear course distinctive of monodisperse systems [Guinier and Fournet, 1955]. For diluted solutions of native protein, the assumption of monodispersity is reportedly valid as long as the solution is clear of aggregates [Svergun and Koch, 2003]. Thus, the radius of gyration is a powerful probe in the investigation of proteins, since the unfolding of a protein as well as the presence of aggregates give rise to an increased scattering at low angles e.g. increase of  $R_G$ .

---

<sup>12</sup>The *Maclaurin series* of  $\exp(x)$ :

$$\exp(x) = \sum_{k=0}^{\infty} \frac{x^k}{k!} = 1 + x + \frac{x^2}{2!} + \frac{x^3}{3!} + \frac{x^4}{4!} + \dots$$

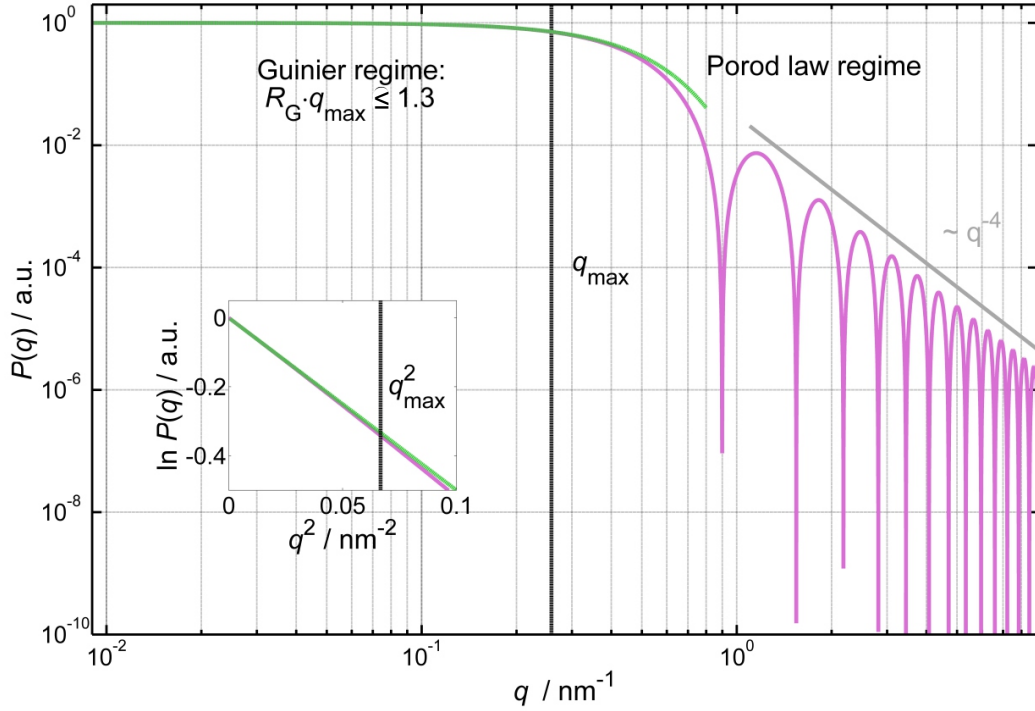


Figure 2.25: Form factor,  $P(q)$ , of an homogeneous sphere ( $R = 5$  nm, *solid violet line*), shown together with the results of the refinement made within the Guinier approximation (*light green line*) and the power law decay  $P(q) \sim q^{-\alpha}$  with  $\alpha = 4$  (*solid grey line*) at large  $q$  values. The inset shows the corresponding Guinier fit ( $\ln P(q)$  vs.  $q^2$ ).

### The Porod law

The **Porod law** [Porod, 1951, Debye and Bueche, 1949],

$$\lim_{q \rightarrow \infty} I(q) = \frac{2\pi (\Delta\rho^{(P)})^2 S}{q^4 V_P} \quad (2.74)$$

allows the measurement of the surface of objects,  $S$ , in diluted and concentrated solutions as well as in bi-continuous phases with no distinguishable particles. The Porod law only deals with the existence of an 'interface' regardless its distribution over the scattering medium. When we consider an object with uniform density which is bounded by a surface of area  $S$ , the interface displays simply a discontinuity of the electron density distribution. In principle, one can always go to larger  $q$  values to meet the assumption of part of the surface being plane, isolated and uncorrelated to other parts [Spalla, 2002]. In the so-called **Porod limit** of sharp (in normal direction) and smooth (in any parallel direction) surface with negligible curvature, the scattering intensity is simply decreasing as

$$I(q) \propto q^{-\alpha}, \quad (2.75)$$

with  $\alpha = 4$  in the large  $q$  range. Exemplarily, the Porod law regime is shown in Figure 2.25 for an homogeneous sphere with radius  $R = 5$  nm. Besides the oscillations, the form factor shows a power law decay of  $\propto q^{-4}$  at large  $q$  values (*gray straight line*).

However, the exponent  $\alpha$  is related to the structure of the scattering medium. Hence, the analysis of the scattering signals power law dependence  $\propto q^{-\alpha}$  at large scattering angles gives a deeper insight into the particle and solution structure when a suitable model is not available (e.g for an entangled polymer or polysaccharide network, surface fractals, mass fractals etc.). Surface and mass fractals correspond each to a characteristic power law exponent  $\alpha$ : For mass fractals



$1 < \alpha < 3$  and for surface fractals  $3 < \alpha < 4$  [Martin and Hurd, 1987]. A mass fractal can be employed to describe e.g. an entangled polymer mesh, as surface fractals correspond to rough interfaces and surfaces of e.g. biochemical materials. Figure 2.26 (a) depicts exemplarily the form

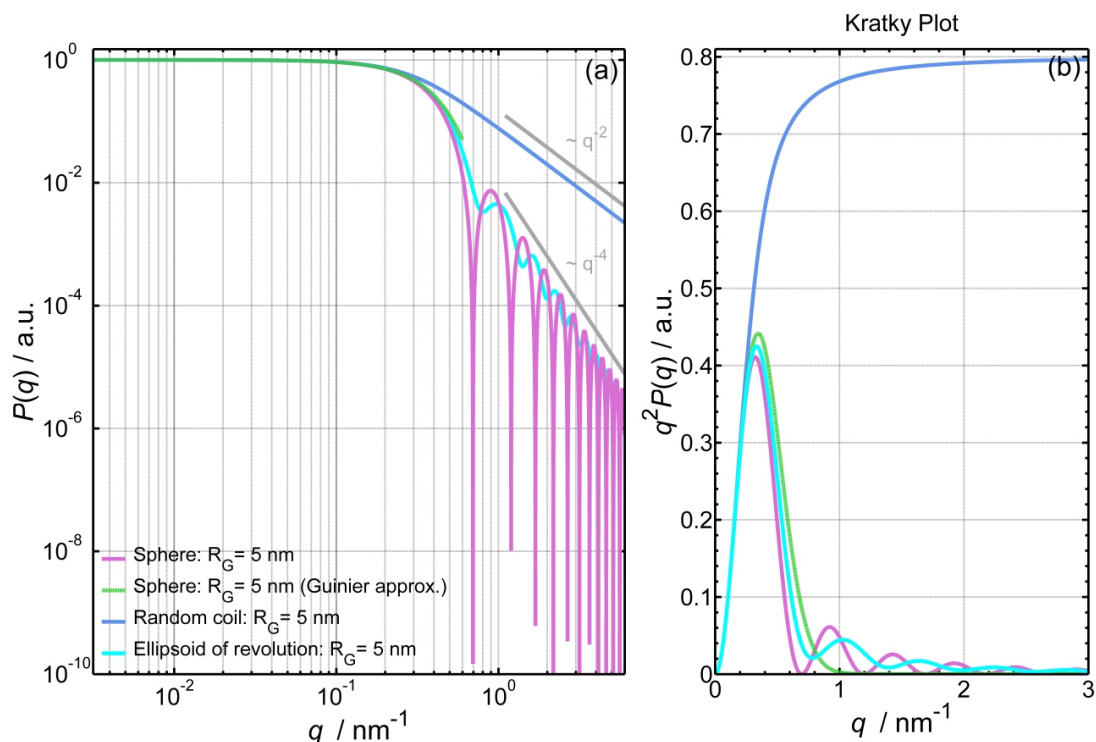


Figure 2.26: (a) Form factors,  $P(q)$ , of a homogeneous sphere (+ Guinier fit (light green line)), an ellipsoid of revolution (axial ratio  $b/a \sim 1.54$ ) and of a random coil (all  $R_G = 5$  nm). The power law decays  $\sim q^{-\alpha}$  (sphere, ellipsoid:  $\alpha = 4$ , random coil:  $\alpha = 2$ ) are shown as well (solid gray lines). (b) The corresponding Kratky plot ( $q^2 P(q)$  vs.  $q$ ) comprising the scattering intensities of all objects.

factors of a homogeneous sphere, a prolate ellipsoid of revolution and a random coil with radius of gyration  $R_G = 5$  nm together with the corresponding power law decays in double-logarithmic representation. The refinement to the form factor of the homogeneous sphere made within the Guinier approximation is depicted as well.

Since the scattering signal of a random coil exhibits a power law decay with the exponent  $\alpha = 2$  at large  $q$  values, in Kratky representation ( $q^2 P(q)$  vs.  $q$ ) the form factor appears as a plateau (see Figure 2.26 (b)). As more compact objects (e.g. colloids, proteins, etc.) have an asymptotic behavior with stronger decay ( $\alpha > 2$ ), they can easily be distinguished from more open structures (e.g. polymers, unfolded proteins, etc.) in this representation. The Kratky plots of a sphere and an ellipsoid of revolution exhibit one pronounced maximum at  $q_K$  followed by higher order maxima at large  $q$ . The first maximum can be linked to the radius of gyration,  $R_G$ , via

$$q_K = \frac{\sqrt{3}}{R_G}, \quad (2.76)$$

and, hence, yield a first estimate of the particles dimension, considering the Guinier approximation being valid in the corresponding wave vector transfer range (see Figure 2.26 (b) for the example of an homogeneous sphere).

### Modeling the form factors of simple geometrical bodies

With the coordinates of all atoms within a particle being given, the form factor can be calculated by the Debye formula for discrete scatterers [Debye, 1915]. The averaged intensity scattered by an

isolated particle then reads

$$P(q) = \sum_j \sum_k f_j f_k \frac{\sin(qr_{jk})}{qr_{jk}}. \quad (2.77)$$

Here, the sum is taken over all the atoms in the particle and  $r_{jk} = |\mathbf{r}_i - \mathbf{r}_j|$  denotes the distance between two atomic point scatterers  $j$  and  $k$  with scattering lengths  $f_j$  and  $f_k$  within the particle. However, often the scattering medium is described by continuous charge density distributions,  $\rho(\mathbf{r})$ , instead from a set of discrete atomic scatterers and the Debye equation takes the form

$$P(q) = \int \int_{V_P} \rho(\mathbf{r}_1) \rho(\mathbf{r}_2) \frac{\sin(qr_{12})}{qr_{12}} d\mathbf{r}_1 d\mathbf{r}_2. \quad (2.78)$$

The experimental scattering intensities of macromolecules like proteins or polymers in solution are often modeled by the theoretical form factors computed for simple geometrical objects (e.g. homogeneous sphere, tri-axial ellipsoid, ellipsoid of revolution, rod, cylinder, etc. (see Figure 2.24)) using their specific features of shape and structural organization. Here, it is sufficient to employ an averaged homogeneous charge density  $\Delta\rho^{(P)}(\mathbf{r}) = \Delta\rho^{(P)}$  to describe the scattering of the particle at small angles. In the modeling, the object dimensions serve as fitting parameters. The form factors of the geometric bodies, employed in this thesis to model the protein lysozyme, the polysaccharide Ficoll and the polymer polyethylene glycol are presented in the following.

**Homogeneous sphere:** The radius of gyration,  $R_G$ , for an homogeneous sphere with radius  $R$  is given by

$$R_G = \sqrt{\frac{3}{5}}R. \quad (2.79)$$

For a sphere with radius  $R$  and homogeneous charge density fluctuations  $\Delta\rho^{(P)}(\mathbf{r}) = \Delta\rho^{(P)}$  the form factor (Eq. 2.57) reads using (Eq. 2.62):

$$\begin{aligned} P(q) &= 4\pi \int_0^\infty \gamma(r) \cdot r^2 \cdot \frac{\sin(qr)}{qr} dr \\ &= 4\pi \left(\Delta\rho^{(P)}\right)^2 V_P \int_0^{2R} r^2 \cdot \frac{\sin(qr)}{qr} dr \\ &= \left(\Delta\rho^{(P)}\right)^2 V_P^2 \cdot \left[ \frac{3(\sin(qR) - qR \cos(qR))}{(qR)^3} \right]^2 \\ &= \left(\Delta\rho^{(P)}\right)^2 V_P^2 P_0(q). \end{aligned} \quad (2.80)$$

Herein, the normalized form factor,

$$P_0(q) = \left[ \frac{3(\sin(qR) - qR \cos(qR))}{(qR)^3} \right]^2, \quad (2.81)$$

is the square of the Bessel function of order  $3/2$   $J_{3/2}(qR)$ . Therefore, under the assumption of an homogeneous sphere, the relation for the position of the Bessel functions minima  $qR = 4.493, 7.725, \dots$  can be employed to estimate the size of the sphere [Guinier and Fournet, 1955, Glatter, 2002]. Assuming a plane surface, the form factor of an homogeneous sphere follows the power law decay  $P(q) \propto q^{-\alpha}$  with  $\alpha = 4$  at large wave vector transfer  $q$ . The polysaccharide Ficoll (PM 70 / PM 400) is reportedly a particle with spherical symmetry, however, since Ficoll has a fractal surface, the asymptotic behavior at large  $q$  will deviate from the standard (see Figure 2.27).

## Ficoll PM 70 / PM 400

- neutral, highly branched copolymer of sucrose and epichlorohydrin
- shaped like a sphere with **fractal** surface
- Stokes radius  $R_s$ 
  - ~ 5.1 nm (PM 70)
  - ~ 10 nm (PM 400)
- Molecular weight  $M_w$ 
  - ~ 70 kDa (PM 70)
  - ~ 400 kDa (PM 400)

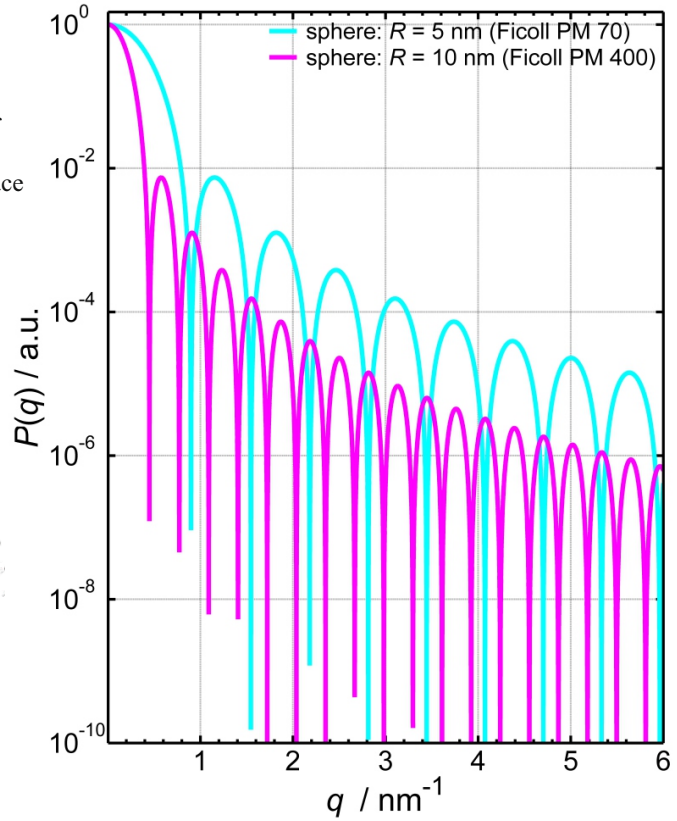
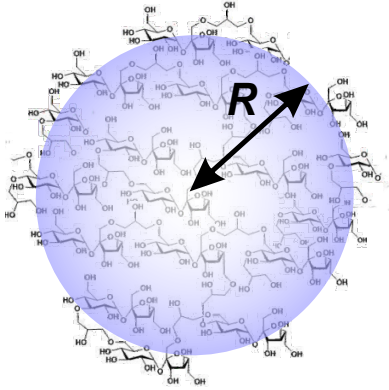


Figure 2.27: Sucrose-epichlorohydrin copolymer Ficoll PM 70 and Ficoll PM 400, approximated by the form factors of homogeneous spheres with radii  $R = 5$  nm and 10 nm.

**Ellipsoid of revolution:** The radius of gyration,  $R_G$ , and form factor,  $P(q)$ , for an ellipsoid of revolution with semi-axes  $a$ ,  $b$  are described by

$$R_G = \sqrt{\frac{2a^2 + b^2}{5}} \quad (2.82)$$

and

$$\begin{aligned} P(q) &= \int_0^1 P_0^2(q\sqrt{a^2 + x^2(b^2 - a^2)}) dx \\ &= \int_0^1 \frac{J_1(q\sqrt{a^2 + x^2(b^2 - a^2)})}{(q\sqrt{a^2 + x^2(b^2 - a^2)})^4}, \end{aligned} \quad (2.83)$$

wherein  $J_1$  denotes the first order Bessel function [Guinier, 1939, Mittelbach and Porod, 1962]. In contrast to the form factor of a sphere (Eq. (2.80)), the form factor of the ellipsoid of revolution is only numerical solvable. Figure 2.28 depicts the form factor,  $P(q)$ , of a homogeneous ellipsoid of revolution with semi-axes  $a = 1.57$  nm and  $b = 2.42$  nm, which provides a good model for the monomeric protein lysozyme ( $R_{G,lys} = 1.45 \pm 0.05$  nm) [Svergun et al., 1998]. The sharp minima as observed for monodisperse spheres (see Figure 2.27) are smeared out in the form factor of monodisperse ellipsoids due to its anisotropy and the orientational averaging. The same effect can be observed for shape and size polydispersity. As SAXS reflects the proteins global shape and size, the scattering at wider angles (Wide-angle X-ray scattering (WAXS)) yields more detailed structural features in the protein (e.g. information on the quaternary, tertiary or secondary structure). Thus, for macromolecules like proteins, the density fluctuations within the particle give rise to an additional scattering contribution in the high  $q$  range which leads to deviations from the Porod limit  $\alpha = 4$  [Fischetti et al., 2003, Sobry and Ciccariello, 2002].

## hen egg-white lysozyme

- Monomeric protein
- Molecular weight  $M_w$   
14.3 kDa
- shaped like a prolate ellipsoid of revolution with semi-axes  $a, b$ :  
 $V = (\pi/6) 4.5 \times 3 \times 3 \text{ nm}^3$
- Hydrodynamic diameter  
 $\sigma_{\text{lys}} = 3.78 \pm 0.05 \text{ nm}$
- Radius of gyration:  
 $R_{G,\text{lys}} = 1.45 \pm 0.05 \text{ nm}$

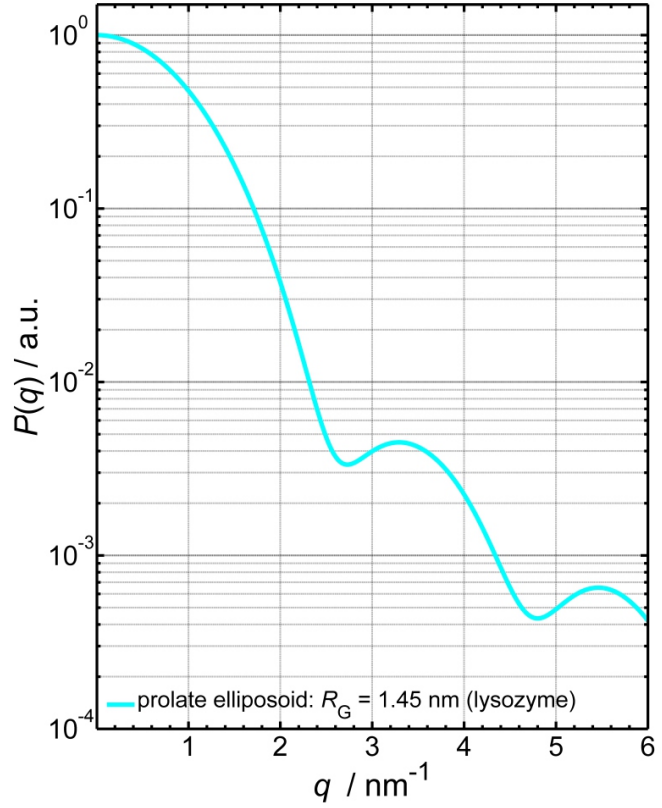
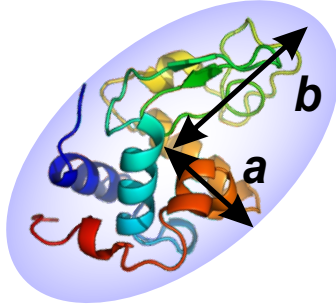


Figure 2.28: Tertiary structure of the monomeric protein hen egg-white lysozyme (PDB: 1AKI, [Artymiuk et al., 1982]), approximated by a prolate ellipsoid of revolution with semi-axes  $a, b$  [Broide et al., 1996]. The value for the protein hydrodynamic diameter,  $\sigma_{\text{lys}}$ , was obtained from [Parmar and Muschol, 2009] and the protein radius of gyration,  $R_{G,\text{lys}}$ , from our own SAXS measurements.

**Random coil:** The form factor and radius of gyration of a Gaussian random coil are given by

$$R_G = \sqrt{\frac{N}{6}} a, \quad (2.84)$$

and

$$P(q) = \frac{2}{q^4 R_G^4} (\exp(-q^2 R_G^2) - 1 + q^2 R_G^2). \quad (2.85)$$

Herein,  $N$  denotes the number of monomer chain segments (e.g. degree of polymerization) and  $a$  the length of the monomeric subunit [Debye, 1947]. Figure 2.29 depicts the theoretical form factors of Gaussian random coils approximating the polymer polyethylene glycol of various radii of gyrations [Devanand and Selser, 1991], corresponding to the molecular weights  $200 < M_w < 35000 \text{ g mol}^{-1}$ . The monomer segment length of the polymer PEG is  $a = 0.4 \text{ nm}$  and its molecular weight  $M_{w,\text{monomer}} = 44 \text{ g mol}^{-1}$ . Consequently,  $N \approx M_w/44 \text{ g mol}^{-1}$  defines the number of segments per chain [Takahashi and Tadokoro, 1973]. For the random coil, the power law exponent is  $\alpha = 2$ . Changes in the polymer solution structure are mirrored in the power law exponent: e.g.  $\alpha < 2$  corresponds to a swollen polymer chain and  $\alpha > 2$  to a collapsed chain [Kirste and Oberthür, 1982, Beaucage, 1996, Israelachvili, 2011]. Therefore, fractals are often used to describe polymers like polyethylene glycol.

## Poly (ethylene glycol)

- Polyether compound  
( $-(\text{CH}_2-\text{CH}_2-\text{O})_N-$ )  
 $N$ : degree of polymerization
- behaves like a swollen globule in dilute solutions
- monomeric subunit length:  
 $a = 0.4 \text{ nm}$
- Hydrodynamic radius:  
 $R_H = 0.0145 M_w^{(0.571 \pm 0.009)} \text{ nm}$
- Radius of gyration:  
 $R_{G,\text{PEG},0} = 0.0215 M_w^{(0.583 \pm 0.031)} \text{ nm}$

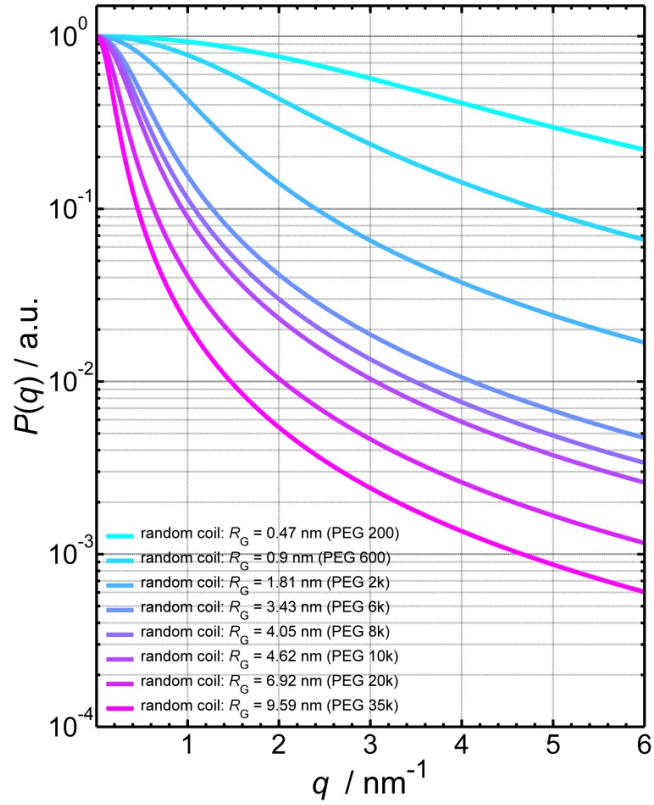
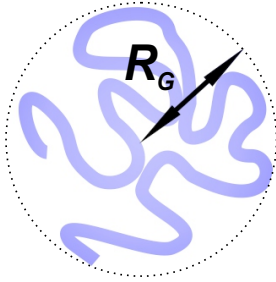


Figure 2.29: Synthetic polymer polyethylene glycol, approximated by a Gaussian random coil with a monomeric subunit of the length  $a$  and a degree of polymerization  $N$ . The experimentally derived relations between polymer molecular weight,  $M_w$ , hydrodynamic radius,  $R_H$  and radius of gyration,  $R_{G,\text{PEG},0}$ , are obtained from [Devanand and Selser, 1991].

### 2.4.3 Dilute polydisperse solutions

Now we consider a polydisperse mixture of  $K$  species of *non-interacting* particles which distinctly differ in shape and size. A typical system of this type of are oligomeric mixtures (e.g. monomer-dimer equilibrium). As in a system consisting of different types of non-interacting particles interference effects can be neglected and all particles scatter independently, the scattering intensity can be written as a linear combination of the form factors,  $P_k(q)$ , from the  $k$ th component (type of particle), weighted by their number concentration,  $n_k$ :

$$I(q) = \sum_{k=1}^K n_k P_k(q). \quad (2.86)$$

Introducing the volume fraction,  $\Phi_k = n_k V_k$ , of the  $k$ th species with particle volume  $V_k$ , Eq. (2.86) can be rewritten as

$$I(q) = \sum_{k=1}^K \Phi_k \frac{P_k(q)}{V_k}. \quad (2.87)$$

The volume fractions,  $\Phi_k$ , of the species can be obtained by the refinement of the experimental intensity scattered by the mixture if the form factors  $P_k(q)$  are known [Svergun et al., 2013].



#### 2.4.4 Concentrated solutions

We have shown, that the product  $N \cdot P(q)$  describes the scattering by  $N$  uncorrelated particles in dilute solutions, whilst spatial correlations between the particles at high concentrations give rise to a modification of the scattering intensity, represented by the structure factor (Eq. 2.50).

The microstructure of a system can also be described by means of the **radial distribution function**,  $g(r)$ , which is related to the probability of finding any particles center of mass at a distance  $r$  from the center of a given particle. Specifically, out of  $N$  particles in the overall volume  $V$ , a number of  $(N/V)g(r)dV$  particles are comprised in the volume element  $dV$  at the distance  $r$  from a given particle. In homogeneous and isotropic systems, like central-symmetric particles dispersed at moderate concentrations in a liquid, the structure factor is related to the radial distribution function,  $g(r)$ , by

$$S(q) = 1 + 4\pi \frac{N}{V} \int_0^\infty r^2 (g(r) - 1) \frac{\sin(qr)}{qr} dr \quad (2.88)$$

[Hansen and McDonald, 2013, Spalla, 2002]. As mentioned above, for anisotropic as well as for polydisperse particles, the *decoupling approximation* [Kotlarchyk and Chen, 1983] has to be considered additionally. The Fourier inversion of Eq. (2.88) gives the radial distribution function in terms of the structure factor:

$$g(r) = 1 + \frac{V}{2\pi^2 N} \int_0^\infty q^2 (S(q) - 1) \frac{\sin(qr)}{qr} dq. \quad (2.89)$$

To calculate the pair correlation function,  $g(r)$ , of dense liquids for a given pair interaction potential,  $V(r)$ , one uses the so-called **Ornstein-Zernike (OZ)** integral equation. The OZ equation of a homogeneous and isotropic system is given by [Hansen and McDonald, 2013, Klein, 2002]

$$h(r_{12}) = c(r_{12}) + n \int c(r_{13}) h(r_{23}) d\mathbf{r}_3, \quad (2.90)$$

and defines the direct correlation function,  $c(r)$ , in terms of the total correlation function,  $h(r) = g(r) - 1$ , of two particles separated by the distance  $r = r_{12}$ . Here,  $n = N/V$  describes the particle number density. The OZ equation states, that the correlation of two particles depends also on the contributions of the other  $(N - 2)$  particles. The identities of these indirect particle correlations, contributing to the total correlations,  $h(r_{12})$ , between the two particles 1 and 2 positioned at  $\mathbf{r}_1$  and  $\mathbf{r}_2$ , become more apparent when Eq. (2.90) is recursively solved for  $h(r_{12})$  [Nägele, 2008]:

$$h(r_{12}) = c(r_{12}) + n \int c(r_{13}) c(r_{23}) d\mathbf{r}_3 + n^2 \int c(r_{13}) c(r_{24}) c(r_{34}) d\mathbf{r}_3 d\mathbf{r}_4 + \mathcal{O}(c^4). \quad (2.91)$$

The total correlation between the particles 1 and 2 is composed of the direct correlation between themselves,  $c(r_{12})$ , the direct correlation,  $c(r_{13})$ , of the particle at  $\mathbf{r}_1$  with an intermediate one at  $\mathbf{r}_3$  and its correlation with the particle at  $\mathbf{r}_2$ , etc. That way, the indirect correlation is propagated by direct correlations via an increasingly large numbers of intermediate particles. In order to make Eq. (2.90) a closed integral equation for  $h(r)$ , it is necessary to interrelate the direct correlation  $c(r)$ , the pair correlation  $g(r)$  (and accordingly  $h(r)$ ) as well as the pair interaction potential  $V(r)$  in some physically appealing manner, by the so-called **closure relations**. From the resulting closed integral equation for  $h(r)$ , combined with computer simulation results and scattering data, the full  $r$ -dependence of  $g(r)$  and the thermodynamic properties of dense liquids can be calculated. When the direct correlation function,  $c(r)$ , is known *via* a closure relation, it can be used to calculate the static structure factor,  $S(q)$ . In order to relate  $S(q)$  to  $c(r)$ , the OZ equation (2.90) is rewritten in terms of  $\mathbf{r} = \mathbf{r}_{12}$ ,  $\mathbf{r}' = \mathbf{r}_{23}$  and  $|\mathbf{r} - \mathbf{r}'| = \mathbf{r}_{13}$ , yielding

$$h(r) = c(r) + n \int c(|\mathbf{r} - \mathbf{r}'|) h(r') d\mathbf{r}'. \quad (2.92)$$

Taking the Fourier transformation<sup>13</sup> of both sides of Eq. (2.92), one obtains

$$\begin{aligned}\tilde{h}(q) &= \tilde{c}(q) + n \tilde{c}(q) \tilde{h}(q) \\ &= \frac{\tilde{c}(q)}{1 - n\tilde{c}(q)}.\end{aligned}\tag{2.93}$$

From noting that  $S(q) = 1 + n\tilde{h}(q)$ , the result for the static structure factor,  $S(q)$ , in terms of  $c(r)$  is

$$S(q) = \frac{1}{1 - n\tilde{c}(q)} \geq 0.\tag{2.94}$$

This entails that  $n\tilde{c}(q) \leq 1$ .

In the modeling of the structure factor, the choice of the closure relation depends on the particle density as well as strength and range of the intermolecular interaction potential governing the spatial distribution of the particles in solution. These relations can be obtained by diagrammatic and density functional theory methods [Nägele, 2008].

For a system described by an effective interaction potential,  $V(r)$ , comprising a repulsive hard-core excluded-volume part,  $V_{\text{HS}}$  (see Eq. (2.19)), any closure relation should be consistent with

$$\begin{aligned}h(r < \sigma) &= -1; \\ g(r < \sigma) &= 0,\end{aligned}\tag{2.95}$$

since two spheres of diameter  $\sigma$  can not interpenetrate. For a wide class of pair potentials the asymptotic closure relation

$$c(r) = -\beta V(r), \quad \text{with } r \rightarrow \infty \text{ and } n \rightarrow 0,\tag{2.96}$$

is valid for large separations (e.g. vanishing number density). This exact asymptotic form for  $c(r)$  forms the basis for the **mean-spherical approximation (MSA)** [Lebowitz and Percus, 1966]. In the MSA, the direct correlation function is assumed to be approximately described by

$$c_{\text{MSA}}(r) \approx -\beta V(r), \quad r > \sigma,\tag{2.97}$$

yielding analytical solutions for various, even many-component, pair potential models. These include the square well potential, hard and sticky hard-sphere potentials, the Coulomb potential as well as attractive and repulsive Yukawa-type potentials [Hansen and McDonald, 2013, Nägele, 2008]. The MSA closure is well suited for mid-range interaction potentials and moderate particle densities. Whilst the **hypernetted-chain (HNC) closure**,

$$c_{\text{HNC}} = -\beta V(r) + h(r) - \ln[1 + h(r)],\tag{2.98}$$

reportedly shows a better accuracy for systems with a strong, short ranged attraction, the structural properties of predominantly repulsive systems measured in SAXS experiments can be modeled satisfactory by both the numerically HNC method and the analytical MSA approximation [Chen et al., 2007, Broccio et al., 2006]. Since the systems investigated in this thesis fulfill this condition, the simple analytical MSA approximation is employed in computing the static structure factor to capture the relative changes of the potential parameters in complex protein-cosolvent systems as studied here, allowing us to semi-quantitatively assess the impact of the cosolutes identity and concentration.

Within the **Percus-Yewick (PY) closure relation** [Percus and Yevick, 1958],

$$c_{\text{PY}}(r) = (1 - \exp(V(r))) g(r),\tag{2.99}$$

---

<sup>13</sup> Convolution theorem for the convolution,  $f_1 * f_2$ , of two integrable functions  $f_1(r)$ ,  $f_2(r)$  [Nägele, 2008]:

$$\begin{aligned}\int (f_1 * f_2)(r) \exp(iq \cdot r) dr &= f_1(q) f_2(q). \\ (f_1 * f_2)(r) &:= \int f_1(r') f_2(r - r') dr' = \int f_2(r') f_1(r - r') dr'.\end{aligned}$$

an analytical solution can be calculated for the important case of hard spheres, which serves as a reference system in the theory of uncharged liquid. For moderate volume fractions ( $\Phi \leq 0.35$ ), the PY approximation

$$c_{\text{PY,HS}}(r) = \begin{cases} (1 - \exp(V(r))) g(r), & r > \sigma, \\ 0, & r \leq \sigma, \end{cases} \quad (2.100)$$

provides a good representation of the static structure factor,  $S(q)$ , and radial distribution function,  $g(r)$ , of hard spheres.

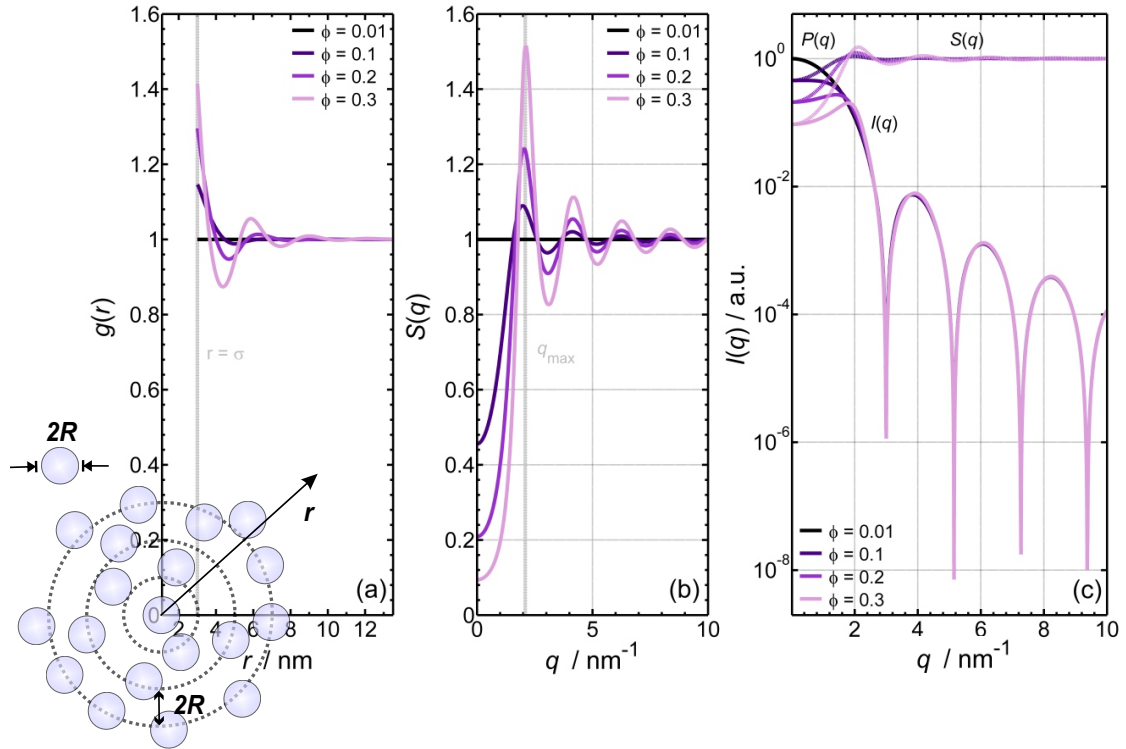


Figure 2.30: (a) Radial distribution function  $g(r)$  for a suspension of hard-sphere colloids with radius  $R = 1.5$  nm at various volume fractions,  $\Phi$ , calculated by using the PY approximation. The geometrical interpretation is depicted as well. (b) The corresponding structure factor,  $S(q)$ . (c) The resulting scattering intensity,  $I(q)$ , which is proportional to the product of the form factor,  $P(q)$  and the structure factor,  $S(q)$ .

The radial distribution function,  $g(r)$ , and structure factor,  $S(q)$ , for a suspension of strongly interacting hard spheres with radius  $R = 1.5$  nm at various particle volume fractions,  $\Phi$ , calculated using the PY approximation, are displayed in Fig. 2.30. As two impenetrable spheres cannot occupy the same space, the radial distribution function,  $g(r)$ , equals zero for center-to-center separations below the particles diameter ( $r < \sigma = 2R$ ) (Fig. 2.30 (a)). The main peak in  $g(r)$  at  $r = \sigma$  describes the nearest-neighbor shell of particles surrounding a given particle. In disordered systems like liquids exists no long range order. For two particles, separated by distances larger than the correlation length  $r > \xi$  of the suspension, there is no spatial correlation anymore and  $g(r) \rightarrow 1$ . Concomitantly,  $S(q) \rightarrow 1$  for large  $q$ .

The corresponding intermolecular structure factors,  $S(q)$ , are depicted in (Fig. 2.30 (b)). The information on the structure factor,  $S(q)$ , at a particular momentum transfer  $q$  is stored in the oscillations of  $g(r)$  at all  $r$  (see Eq. (2.88)). However, as a 'rule of thumb', a scattering experiment operating at the momentum transfer  $q$ , measures structural organizations with spatial resolution of  $\Delta = 2\pi/q$ . In this sense, approximating the first peak of the structure factor,  $S(q = q_{\text{max}})$ , by a 'Bragg reflection' from planes of particles separated by the distance  $r$  equal to the center-to-center

distance,  $d_p$ , of the nearest neighbors, yields the 'Bragg condition'  $q_{\max} \cdot d_p \approx 2\pi$  for the positions of the main peaks of  $g(r = d_p)$  and  $S(q = q_{\max})$  [Pusey, 2002]. The extrema of  $S(q)$  (and  $g(r)$ ) are more pronounced and shift to higher  $q$  (smaller  $r$ ) values as the volume fraction increases. Concomitantly, the limit for small  $q$  values

$$\lim_{q \rightarrow 0} S(q) = nk_B T \kappa_T, \quad (2.101)$$

decreases in magnitude due to the change of the isothermal compressibility,  $\kappa_T$ , of the system [Hansen and McDonald, 2013].

As shown in Fig. 2.30 (c), the resulting structure factor of the suspension of hard-spheres at volume fraction  $\Phi$  modulates the scattering signal,  $I(q)$ , which is proportional the product of the theoretical form factor,  $P(q)$ , and structure factor,  $S(q)$  (see Eq. (2.51)). The structure factor causes the presence of a so-called *correlation peak* in the scattering signal at the wave vector transfer  $q_{\text{corr}}$ , which is most pronounced for large volume fractions. The lowest particle concentration,  $\Phi = 0.01$ , allows a measure of the form factor,  $P(q)$ , since at this level the interparticle interactions and ordering are very weak:

$$\lim_{n \rightarrow 0} S(q) \rightarrow 1, \quad (2.102a)$$

$$\lim_{n \rightarrow 0} g(r) \rightarrow 1. \quad (2.102b)$$

In a real SAXS experiment, the effective structure factor, describing the spatial correlation of the proteins in solution, is implicitly given by the scattering intensity

$$I(q) \propto \Delta\rho^2 \cdot n \cdot V_p^2 \cdot P(q) \cdot S_{\text{eff}}(q). \quad (2.103)$$

The form factor,  $P(q)$ , can be determined by measuring the scattering of a diluted solution and modeled by a simple geometrical body. In this thesis, the theoretical effective structure factors,  $S_{\text{eff}}(q)$ , are calculated in MSA using the MATLAB<sup>®</sup> code of [Liu et al., 2005b] and refined to the experimental data by a model based on a 2-Yukawa (DLVO) potential (see section 2.2.3, Eq. (2.18)), which accounts for the attractive and repulsive pair-interactions between spherical colloidal particles. From the potential parameters, obtained from the refinement of the SAXS data, the osmotic second virial coefficient,  $B_{22}$ , can be calculated employing Eq. (2.3).

### Triplet correlation function

Correlation functions of more than two particles play a significant part in many macroscopic properties like thermal expansion, specific heat as well as thermal pressure coefficient. Three-body correlations are described by the triplet correlation function (TCF)  $g_3(\mathbf{r}_1, \mathbf{r}_2, \mathbf{r}_3)$ , which defines the probability of finding three particles simultaneously in space at the positions  $\mathbf{r}_1$ ,  $\mathbf{r}_2$  and  $\mathbf{r}_3$ . Since TCFs are largely contributing to the above-mentioned properties, they may not be evaluated without reasonable knowledge of that function [Egelstaff, 1973]. The understanding of TCFs is also crucial to describe the structure of a complex liquid like water adequately (e.g. the local tetrahedral order) [Dhabal et al., 2014, Dhabal et al., 2017].

We already showed for the case of an homogeneous, isotropic liquid, that the Fourier transform pairs,  $S(q) - 1$  and  $g(r) - 1$ , are related as (Eq. 2.88) and (Eq. 2.89). Hence, the pair correlation function,  $g(r)$ , can be calculated straight-forward from the structure factor,  $S(q)$ , and *vice versa*. However, unlike the pair correlation function, the triplet correlation function cannot be measured directly in X-ray scattering experiments since the radiation scattering cross sections of higher-order correlations are too small. Still, information about the importance of the triplet correlation functions can be obtained through measurements of the isothermal pressure derivative of the pair correlation function,  $g(r)$ , or its experimentally determined Fourier-transform, the structure factor,  $S(q)$  [Egelstaff et al., 1969, Egelstaff et al., 1971]. The basic principle of this method will be described in the following.

For a homogeneous, isotropic fluid, the triplet correlation function can be written as a function of the relative distances  $r = |\mathbf{r}| = |\mathbf{r}_2 - \mathbf{r}_1|$ ,  $s = |\mathbf{s}| = |\mathbf{r}_3 - \mathbf{r}_1|$  and  $t = |\mathbf{t}| = |\mathbf{s} - \mathbf{r}|$ , yielding  $g_3(\mathbf{r}_1, \mathbf{r}_2, \mathbf{r}_3) = g_3(r, s, t)$ . For a canonical ensemble of  $N$  particles the pair and triplet correlation

functions are related as [Hansen and McDonald, 2013, Egelstaff, 1994]

$$n \int g_3(r, s, t) d\mathbf{s} = (N - 2) g(r). \quad (2.104)$$

Here,  $n$  denotes the particle number density. According to [Schofield, 1966], in the grand canonical ensemble Eq. (2.104) can be rewritten as

$$n \int [g_3(r, s, t) - g(r)] d\mathbf{s} + 2g(r) = n_p k_B T \left( \frac{\partial g(r)}{\partial p} \right)_T. \quad (2.105)$$

Thus, the three-body correlations, integrated over the coordinates of the third particle,  $\mathbf{s}$ , are linked to the isothermal pressure derivative of the radial pair distribution function,  $g(r)$ . Following [Egelstaff et al., 1971, Egelstaff, 1973, Egelstaff et al., 1969], we define a function  $H(r, s, t)$  as

$$H(r, s, t) = g(r)g(s)g(t) - g_3(r, s, t), \quad (2.106)$$

which expresses the deviation from the superposition approximation,  $g(r)g(s)g(t)$ , as proposed by [Kirkwood, 1935]. On using Eq. (2.106) in Eq. (2.105) and Fourier transforming we obtain

$$\begin{aligned} \tilde{H}(q) &= n \int \exp(i\mathbf{q} \cdot \mathbf{r}) d\mathbf{r} \int H(r, s, t) d\mathbf{s} \\ &= \frac{1}{(2\pi)^3 n} [S(q) - 1] * [S(q) - 1]^2 + [S(q) - 1][S(0) + S(q) - 1] - nk_B T \left( \frac{\partial S(q, p)}{\partial p} \right)_T. \end{aligned} \quad (2.107)$$

Here, the limiting value  $S(0)$  for  $q \rightarrow 0$  is related to the isothermal compressibility,  $\kappa_T$ , via Eq. (2.101) and the star \* indicates the convolution of the two terms. We find, the quantity  $\tilde{H}(q)$  can be directly obtained from the information of the structure factor,  $S(q)$ , and its isothermal pressure derivative,  $(\partial S(q, p)/\partial p)_T$ , both accessible through neutron or X-ray diffraction experiments [Egelstaff et al., 1971, Egelstaff, 1973, Egelstaff et al., 1969].

It was recently shown, that this method can also be applied to complex systems like aqueous protein solutions. Following [Schroer et al., 2012], the experimentally derived effective structure factor of proteins in solution, even though it contains only information on the pair correlations of the proteins (see Eq. (2.88)), can provide insight into three-body correlations between the particles through its isothermal pressure derivative. The analysis of  $(\partial S_{\text{eff}}(q, p)/\partial p)_T$  allows to disclose changes in intermolecular interactions that are hardly visible in the corresponding static effective structure factor,  $S_{\text{eff}}(q, p)$ .

Detailed structural features of liquids of small molecules (e.g. water) are obtained from the scattering at much wider angles (WAXS) than for the larger protein molecules and, in this thesis, the accessible  $q$ -range in the SAXS experiment ( $0.03 \lesssim q \lesssim 6.6 \text{ nm}^{-1}$ , see section 3.2.2) does not allow the investigation of the solvents structure factor. Furthermore, biological macromolecules like proteins modulate the scattering at wider angles due to internal structural fluctuations (e.g. secondary structure). However, since the intermolecular pair-interactions between proteins are assumed to be solvent-mediated to a great extent [Schroer et al., 2011a, Schroer et al., 2011b, Julius et al., 2018b], the experimental isothermal pressure derivative of the protein structure factor can still be indicative of changes in the solvents structure and used to differentiate protein solution structures with different three-body correlations in dependency of the solvent properties (e.g. the impact of additives). Moreover, it can be used in gauging structural rearrangements in the water structure close to biological interfaces under pressure and the effects of cosolvents thereon.

Considering the experimental effective structure factors recorded at two different pressures, say  $p_1$  and  $p_2$ , the effective structure factor at the intermediate pressure,  $p_m = (p_1 + p_2)/2$ , can be calculated *via*

$$S_{\text{eff}}(q, p_m) \approx \frac{S_{\text{eff}}(q, p_m + \Delta p/2) + S_{\text{eff}}(q, p_m - \Delta p/2)}{2}. \quad (2.108)$$

Its derivative at the mean value  $p_m$  can then be calculated by the central difference approximation as

$$\left( \frac{\partial S_{\text{eff}}(q, p_m)}{\partial p} \right)_T = \frac{S_{\text{eff}}(q, p_m + \Delta p/2) - S_{\text{eff}}(q, p_m - \Delta p/2)}{\Delta p}, \quad (2.109)$$



where  $\Delta p = p_2 - p_1$ . [Egelstaff et al., 1971]

## Chapter 3

# Experimental Setup

### 3.1 Materials and Sample Preparation

#### Chapter 4: Impact of Macromolecular Crowding and Compression on Protein-Protein Interactions and Liquid-Liquid Phase Separation Phenomena

The protein, buffer and crowder used in the experiments were purchased from Sigma Aldrich, St. Louis, MO, USA. Before each measurement, the monomeric protein lysozyme from chicken egg white (14.3 kDa, pI = 11, dialyzed, lyophilized, powder,  $\sim 100000$  U/mg (product code: 62970 SIGMA-ALDRICH)) was freshly dissolved at the concentrations 1 – 10% (w/v) in 25 mM or 50 mM Bis-Tris buffer at pH 7 (B4429 SIGMA) to ensure a stable pH value at all pressure conditions studied. For some SAXS measurements, sodium chloride (NaCl) (S7653 SIGMA-ALDRICH) was added to the buffer at the molarity 75 mM. The polymer polyethylene glycol (PEG) of the sizes PEG 200 ( $M_w \sim 190 - 210$  g mol $^{-1}$  (88440 SIGMA)), PEG 600 ( $M_w \sim 570 - 630$  g mol $^{-1}$  (87333 SIGMA)), PEG 2000 ( $M_w \sim 1900 - 2200$  g mol $^{-1}$  (84797 SIGMA)), PEG 4000 ( $M_w \sim 3500 - 4500$  g mol $^{-1}$  (95904 SIGMA)), PEG 6000 ( $M_w \sim 5000 - 7000$  g mol $^{-1}$  (81255 SIGMA)), PEG 8000 ( $M_w \sim 7000 - 9000$  g mol $^{-1}$  (89510 SIGMA)), PEG 10000 ( $M_w \sim 8500 - 11500$  g mol $^{-1}$  (92897 SIGMA)), PEG 20000 ( $M_w \sim 16000 - 24000$  g mol $^{-1}$  (95172 SIGMA)), PEG 35000 ( $M_w \sim 35000$  g mol $^{-1}$  (94646 SIGMA)) and the disaccharide sucrose (S7903 SIGMA) were added to the solution at various concentrations:

**10% (w/v) lysozyme + 25 mM Bis-Tris (pH 7)**

+ 5 – 50% (w/v) sucrose

**1% (w/v) lysozyme + 25 mM Bis-Tris (pH 7)**

+ 15% (w/v) PEG 200

+ 15% (w/v) PEG 600

+ 15% (w/v) PEG 2000

+ 15% (w/v) PEG 35000

**10% (w/v) lysozyme + 25 mM Bis-Tris + 75 mM NaCl (pH 7)**

+ 5, 10% (w/v) PEG 200

+ 10% (w/v) PEG 600

+ 5, 10% (w/v) PEG 2000

+ 1 – 10% (w/v) PEG 6000

+ 5, 10% (w/v) PEG 10000

+ 10% (w/v) PEG 20000

+ 5, 10% (w/v) PEG 35000

**10% (w/v) lysozyme + 50 mM Bis-Tris (pH 7)**

+ 5 – 30% (w/v) PEG 200

+ 5 – 50% (w/v) PEG 600

+ 10 – 30% (w/v) PEG 2000

+ 20% (w/v) PEG 6000

+ 10 – 30% (w/v) PEG 8000

+ 20% (w/v) PEG 10000

+ 20% (w/v) PEG 20000  
+ 20% (w/v) PEG 35000

The Light transmission experiments (see section 3.3) were carried out at a higher protein concentration. In the case of the protein lysozyme, dialysis is necessary in order to generate protein concentrations beyond  $\sim 150 \text{ mg mL}^{-1}$ . The dialysis cassettes (Slide-A-Lyzer G2, 15 mL, Thermo Scientific) were filled with 15% (w/v) lysozyme, dissolved in 25 mM Bis-Tris buffer (pH 7), and placed into a  $250 \text{ g L}^{-1}$  PEG 35k + 25 mM Bis-Tris (pH 7) bath at  $25^\circ\text{C}$  for  $\sim 14 \text{ h}$  under constant steering. To determine and adjust the final protein concentration after dialysis to  $240 \text{ mg mL}^{-1}$ , a Nanovue Plus Spectrometer (Biochrom, Cambridge, UK) was employed. Protein-free salt-crowder stock solutions are prepared of 7.5% (w/v), 15% (w/v), 30% (w/v) PEG ( $M_w \sim 200, 600, 2000, 4000, 6000, 8000, 10000, 20000, 35000 \text{ g mol}^{-1}$ ), and 3 M NaCl + 25 mM Bis-Tris (pH 7). Before each turbidity measurement, the protein and salt-PEG stock solutions were mixed to obtain  $200 \text{ mg mL}^{-1}$  + 25 mM Bis-Tris (pH 7) + 0.5 M NaCl solutions in the presence of 1.25% (w/v), 2.5% (w/v) and 5% (w/v) PEG of various sizes and  $100 \text{ mg mL}^{-1}$  lysozyme + 25 mM Bis-Tris (pH 7) + 1 M NaCl solutions in the presence of 5% (w/v) PEG, respectively.

## Chapter 5: Water-Mediated Protein-Protein Interactions at High Pressures are Controlled by a Deep-Sea Osmolyte

The protein, buffer and cosolvents used in the experiments were purchased from Sigma Aldrich, St. Louis, MO, USA. 10% (w/v) ( $\sim 102.6 \text{ mg mL}^{-1}$ ) and 1% (w/v) ( $\sim 10 \text{ mg mL}^{-1}$ ) lysozyme from chicken egg white (14.3 kDa, pI = 11, dialyzed, lyophilized, powder, 100000 U/mg, (product code: 62970 SIGMA-ALDRICH)) was dissolved freshly before each measurement in 25 mM Bis-Tris buffer at pH 7 (B4429 SIGMA). The organic osmolytes TMAO (Trimethylamine N-oxide dihydrate (92277 SIGMA-ALDRICH)), urea (U5378 SIGMA), trehalose (1673715 USP), L-alanine (05129 SIGMA), glycine (50046 SIGMA), sarcosine (S7672 SIGMA), betaine (61962 SIGMA),  $\beta$ -alanine (05160 SIGMA), taurine (86329 SIGMA), L- $\alpha$ -glycerophosphorylcholine (GPC) (G5291 SIGMA), *myo*-Inositol (57570 SIGMA-ALDRICH) and L-proline (81709 SIGMA) were added at various molar concentrations and compositions.

**Shallow living crabs (1 M mixture):** 227 mM taurine, 38 mM L-alanine, 67 mM L-proline, 329 mM betaine, 268 mM glycine, and 71 mM TMAO.

**Crabs at bathyal (1850 m, 185 bar) trawl sites (1 M mixture):** 94 mM taurine, 120 mM L-alanine, 24 mM L-proline, 35 mM betaine, 236 mM glycine, and 492 mM TMAO.

**Abyssal (2900 m, 290 bar) shrimp (0.63 M mixture):** 500 mM TMAO, 87 mM glycine, 24 mM betaine, 7 mM L-proline, 9 mM L-alanine.

**Shallow living shrimp (0.63 M mixture):** 144 mM TMAO, 360 mM, 45 mM betaine, L-proline 32 mM, 25 mM L-alanine, and 22 mM taurine.

**Abyssal skate (0.63 M mixture):** 8 mM betaine, 18 mM *myo*-inositol, 12 mM  $\beta$ -alanine, 10 mM sarcosine, 10 mM taurine, 204 mM urea and 369 mM TMAO.

**Shallow living skates (0.63 M mixture):** 43 mM  $\beta$ -alanine, 47 mM sarcosine, 12 mM taurine, 459 mM urea, and 70 mM TMAO.

## Chapter 6: The Effect of Osmolytes and Crowding on the Pressure-Induced Dissociation and Inactivation of Dimeric Horse Liver Alcohol Dehydrogenase

The protein, buffer and cosolvents used in the experiment were purchased from Sigma Aldrich, St. Louis, MO, USA. Alcohol Dehydrogenase equine powder (recombinant, expressed in *E. coli*,  $\geq 0.5 \text{ U/mg}$ , 80 kDa, pI 6.8, (product code: 55689 SIGMA)) was dissolved in 10 mM Tris-HCl buffer solution (Trizma<sup>®</sup> Base (T1503 SIGMA)) in order to keep the pH value constant at pH 8.5 at all pressure conditions studied. In order to remove aggregates, the freshly prepared protein solution was filtered through  $0.2 \mu\text{m}$  membrane filter. The concentration after filtration was determined using a Nanovue Plus Spectrometer (Biochrom, Cambridge, UK), to be approximately 0.7% (w/v). The cosolvents TMAO (92277 SIGMA-ALDRICH), urea (U5378 SIGMA) and PEG 200 ( $M_w \sim 190 - 210 \text{ g mol}^{-1}$  (88440 SIGMA)) were added to the 0.7% (w/v) LADH buffer solutions at various concentrations:

**0.7% (w/v) LADH + 10 mM Tris-HCl (pH 8.5)**

+ 5, 15% (w/v) PEG 200

+ 500 mM TMAO

+ 500 mM Urea

+ 250 mM TMAO + 500 mM Urea

## Chapter 7: Macromolecular Crowding of Protein Solutions by the Polysaccharide Ficoll

The protein, buffer and crowder used in the experiments were purchased from Sigma Aldrich, St. Louis, MO, USA. Before each measurement, the monomeric protein lysozyme from chicken egg white (14.3 kDa, pI = 11, dialyzed, lyophilized, powder, 100000 U/mg (product code: 62970 SIGMA-ALDRICH)) was freshly dissolved at the concentrations 5 – 15 % (w/v) in aqueous buffer-crowder mixtures composed of 25 mM Bis-Tris buffer (pH 7) (B4429 SIGMA) and various amounts,  $1 < c_{\text{Ficoll}} < 30$  % (w/v), of the polysaccharides Ficoll PM 70 (F2878 SIGMA) or Ficoll PM 400 (F4375 SIGMA).

For the light transmission experiment (see section 3.3), protein-free salt-Ficoll stock solutions are prepared of 7.5% (w/v) Ficoll PM 70 and 3 M NaCl + 25 mM Bis-Tris (pH 7). To generate salt-free protein stock solutions, dialysis was applied as described above. Before each turbidity measurement, the protein and salt-Ficoll stock solutions were mixed, yielding solutions of 285 mg mL<sup>-1</sup> lysozyme + 25 mM Bis-Tris (pH 7) + 0.5 M NaCl with 1.25% (w/v) Ficoll PM 70.

$c_{\text{lys}} / \% \text{ (w/v)}$	$c_{\text{lys}} / \text{mg mL}^{-1}$	$\Phi_{\text{lys}} / \%$
0.5	5.01	0.37
1	10.03	0.75
5	50.75	3.77
10	103.00	7.65
15	156.75	11.65
20	212.00	15.75
25	268.75	19.97
30	327.00	24.30

Table 3.1: Lysozyme concentration,  $c_{\text{lys}}$ , unit conversion and the corresponding volume fraction,  $\Phi_{\text{lys}}$ , calculated using the partial specific volume of lysozyme  $\bar{V}_{\text{lys}}^{\circ} = 0.743 \text{ mL g}^{-1}$  [Orthaber et al., 2000, Sophianopoulos et al., 1962, Mylonas and Svergun, 2007].

## 3.2 (High-Pressure) Small Angle X-ray Scattering Experiment

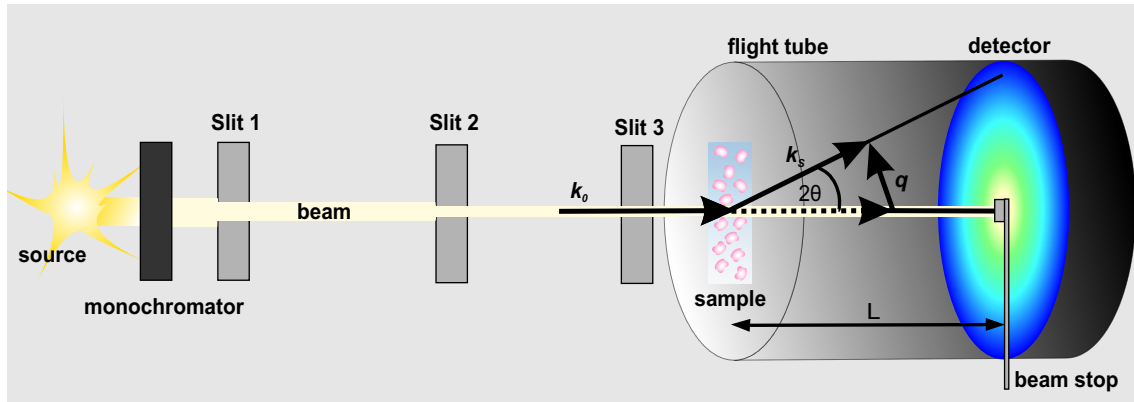


Figure 3.1: Typical experimental SAXS setup with the elementary components.

In order to perform a successful measurement of the intensity scattered of biomolecular solutions at small-angles to gain information on the shape and size of the single components as well as their spatial arrangement and thus interactions in solution, the experimental setup and the sample have to meet several technical requirements, which are discussed in the following.

The schematic layout of a typical SAXS experiment with its basic elements is shown in Figure 3.1. The X-ray source can be a laboratory X-ray tube or an insertion device at a synchrotron radiation facility. Since a monochromatic beam is required, a monochromator is employed to select a wavelength of the emitted synchrotron radiation spectrum.

In order to obtain a collimated, well defined beam profile, the beam passes through a system of optics, tailor-made for the particular beamline. Essentially, two slits are needed for a properly collimated beam: At each slit, the beam profile is defined *via* an arrangement of knife edges made of a material with high absorbency. However, the knife edges can become source of parasitic scattering themselves which is most pronounced at small angles near the primary beam. Thus, for SAXS a third slit is generally located close to the sample holder in order to remove this scattering which otherwise would superimpose the weak signal scattered of the sample.

In general, the scattering at small angles of an electromagnetic wave by a medium is frequency dependent. For X-rays with an energy close to the characteristic absorption edge of an atom, effects of anomalous small-angle X-ray scattering (ASAXS) become significant, modulating the scattering signal. However, the absorption edges for the light atoms frequently found in soft condensed matter (i.e. carbon, hydrogen, nitrogen, sulfur and oxygen) occur at very low X-ray energies and, hence, outside the accessible photon energy range. Thus, the contribution of ASAXS effects to the scattering signal of the biomolecular systems, studied in this thesis, can be neglected [Schurtenberger, 2002].

However, generic X-ray attenuation also takes place at frequencies far from the matters characteristic absorption edges and the transmitted intensity of monochromatic X-rays of a constant wavelength,  $\lambda$ , is proportional to

$$I \propto d \cdot \exp(-\mu(\lambda) d), \quad (3.1)$$

wherein  $d$  is the thickness of the sample and  $\mu(\lambda)$  the linear absorption coefficient [Lindner, 2002]. A maximal amount of the signal is transmitted through the sample when the relation  $\mu(\lambda) = 1/d$  is fulfilled. Since the average electron density of proteins ( $\sim 0.420$  electrons/ $\text{\AA}^3$ ) does not differ largely from the electron density of water ( $\sim 0.334$  electrons/ $\text{\AA}^3$ ), the scattering contrast and accordingly the signal-to-background ratio are small [Svergun and Koch, 2003]. For example, protein systems containing sugar as additive especially suffer from a weak scattering contrast (50% (w/v) sucrose  $\sim 0.400$  electrons/ $\text{\AA}^3$  [Svergun and Koch, 2003]). The statistics of the measurement can be increased by choosing a larger sample thickness and therefore a larger number of particles in the

beam. At the same time the sample cannot be too thick as otherwise the approximation of a single scattering event loses validity and the absorption increases (see Eq. (3.1)). Since in the case of aqueous protein solutions the absorption is mainly due to the solvent, the effective transmission of the sample can be approximated by using the absorption coefficient for water. Essentially, in a real SAXS experiment all components along the beam path give rise to an additional scattering contribution and attenuation of the incoming beam (e.g. diamond windows of the pressure cell, sample carrier, air). The attenuation can be accounted for by increasing the photon energy (Another benefit: The beam damage of the sample system declines at photon energies in the range 20 - 30 keV.), by increasing the measurement time as well as by the usage of X-rays of high flux.

Also, the signal strength and the signal-to-noise ratio can be increased by employing a two-dimensional area detector and by azimuthally averaging over the isotropic SAXS pattern produced by aqueous biomolecular systems. Moreover, one of the great advantages of the appliance of two-dimensional resolving area detectors in small-angle X-ray scattering experiments on aqueous biomolecular solutions is, that the scattering signal is recorded over the whole  $q$ -range in one single detector image. Thereby, the sample exposure time and, hence, beam damage are minimized and any anisotropy of the signal can be disclosed.

Signal loss due to air scattering and X-ray absorption by the air is prevented by evacuated flight paths between source and sample as well as between the sample and the detector. The weakness of the SAXS signal commands highly sensitive detectors which are protected by a beam stop against destructive overexposure by the much stronger transmitted primary beam.

To summarize, in a real SAXS experiment the recorded scattering intensity (Eq. (2.103)) depends on the sample transmission, the beam properties as well as on the experimental setup:

$$I(q) = \frac{I_0}{L^2} \cdot T \cdot A \cdot d \cdot \Delta\rho^2 \cdot n \cdot V_p^2 \cdot P(q) \cdot S_{\text{eff}}(q), \quad (3.2)$$

with  $A$  being the spot size of the X-ray beam (e.g. beam size),  $d$  the sample thickness and  $T$  the transmission. At a fixed wavelength, the detectable  $q$ -range is determined by the sample-to-detector distance and detector size.

### 3.2.1 High-Pressure SAXS Setup

In order to perform SAXS experiments on the proteins shape and size as well as on the protein intermolecular interactions in ternary protein-cosolute-buffer systems under high hydrostatic pressure conditions, two different custom built HHP sample cells, constructed by C. Krywka [Krywka, 2008] and J. Möller [Möller et al., 2016], were employed. Both sample cells were also used for temperature- and pressure-dependent light transmission (turbidity) measurements to map metastable liquid-liquid phase diagrams of protein-cosolute-buffer solutions in the ( $p$ - $T$ )-plane (see section 3.3). The two different HHP SAXS setups will be presented in the following.

#### HHP SAXS - Setup I

The pressure cell constructed by J. Möller was originally developed for time-resolved solution SAXS studies of kinetic processes induced by sub-ms HHP jumps [Möller et al., 2016]. However, in this thesis it was employed for static pressure SAXS measurements and also for temperature- and pressure-dependent light transmission measurements (see section 3.3) in the pressure range ( $1 < p < 1250$ ) bar and at temperatures ranging from 4 to 26°C. The HHP SAXS setup at beamline ID02 of the ESRF (see section 3.2.2) as well as the technical drawings of the pressure cell are depicted in Figure 3.2. The body of the pressure cell is machined from F16PH stainless steel with two openings for the X-ray beam, one opening for the exchange of the sample holder and two further openings for pressurizing the cell. The X-ray entrance and exit windows are sealed by two transparent disk-shaped diamonds with 1 mm thickness and 3 mm diameter, which are mounted on a diamond support and fixed using epoxy glue. Due to the high absorption by the diamonds<sup>1</sup>, only hard X-rays, small beam size and with a sufficiently high flux are applicable with the pressure

---

<sup>1</sup>A diamond of 2 mm thickness absorbs 40% of the incoming photons at the photon energy  $E = 15$  keV (absorption is strongly energy dependent) [Henke et al., 1993].



setup in order to record a meaningful scattering curve within a short time. The effective beam path throughout the sample has a diameter of 1 mm and the window opening angle measures  $20^\circ$ .

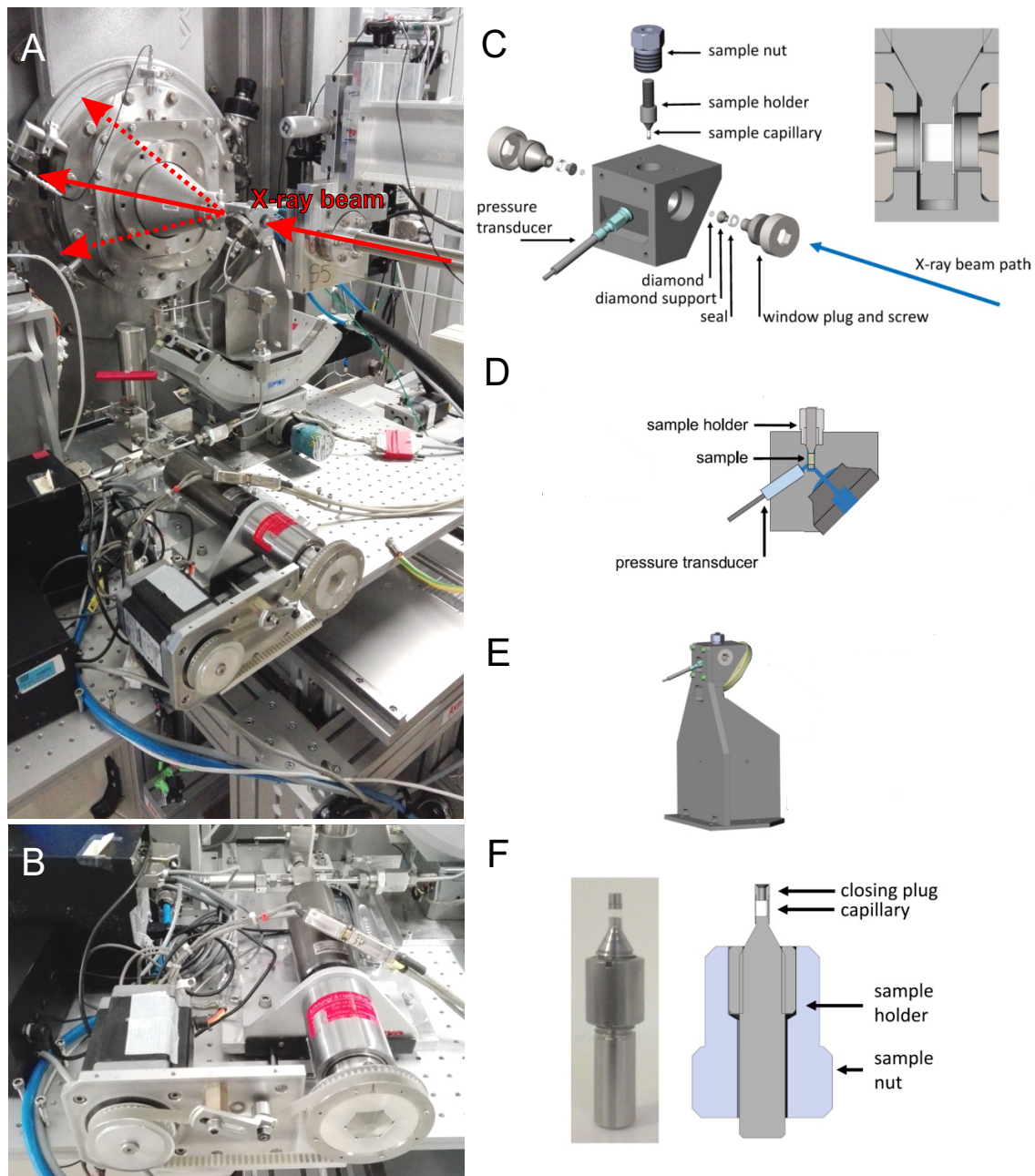


Figure 3.2: (A) HHP SAXS setup I at beamline ID02 (ESRF) (see section 3.2.2) featuring the pressure cell by J. Möller mounted on the sample holder in the beam path and connected *via* high pressure pipes to a (B) motor-driven pressure pump system. The temperature within the cell is regulated by a HUBER<sup>TM</sup> Ministat 230. (C) Exploded view of the X-ray beam path components and the sample holder. The inset depicts the capillary of the sample holder positioned in the beam path between the two diamond windows. (D) Sketch of the cross section of the cell from the top. (E) The sample cell mounted on the setup holder. (F) Sample holder with a polycarbonate capillary and a closing plug. Pictures of the pressure cell are adapted from [Möller et al., 2016].

The sample holder (see Figure 3.2 (F)), consists of either a polycarbonate capillary (Enki Microtubes S.r.l. Italy) or a polyimide (Kapton, MicroLumen, Inc. USA) capillary, mounted on the sample carrier, which also serves as a seal of the pressure cell body. The capillary has a length

of 4 mm, an inner diameter of 1.9 mm and a wall thickness of 50  $\mu\text{m}$  for the polycarbonate and 40  $\mu\text{m}$  for the polyimide, respectively. Before use, the ends of the empty capillaries are glued to the sample holder and a closing plug, respectively. The sample (5 - 10  $\mu\text{l}$  volume) is filled into the prepared capillary through a small channel in the closing plug, which is then closed by a small M1 screw. The filled sample holder is placed from the top in the cell body between the two diamond windows as shown in Figure 3.2 (C). Tightening the sample nut seals the pressure cell. Remote temperature control of the sample environment is implemented *via* a water-circulating temperature jacket around the cell, which is connected to a refrigerated heating circulator bath with water-cooled cooling machine (HUBER<sup>TM</sup> Ministat 230). The cell is connected *via* a standard 1/4 in. high pressure connection to an external motor-driven pressure generating pump (Nova Swiss<sup>®</sup> 550.0301). As pressurizing medium inside the cell (internal cell volume 55  $\mu\text{l}$ ) deionized water is used. With the HHP SAXS setup I, static pressures up to 1.5 kbar can be generated in the sample environment.

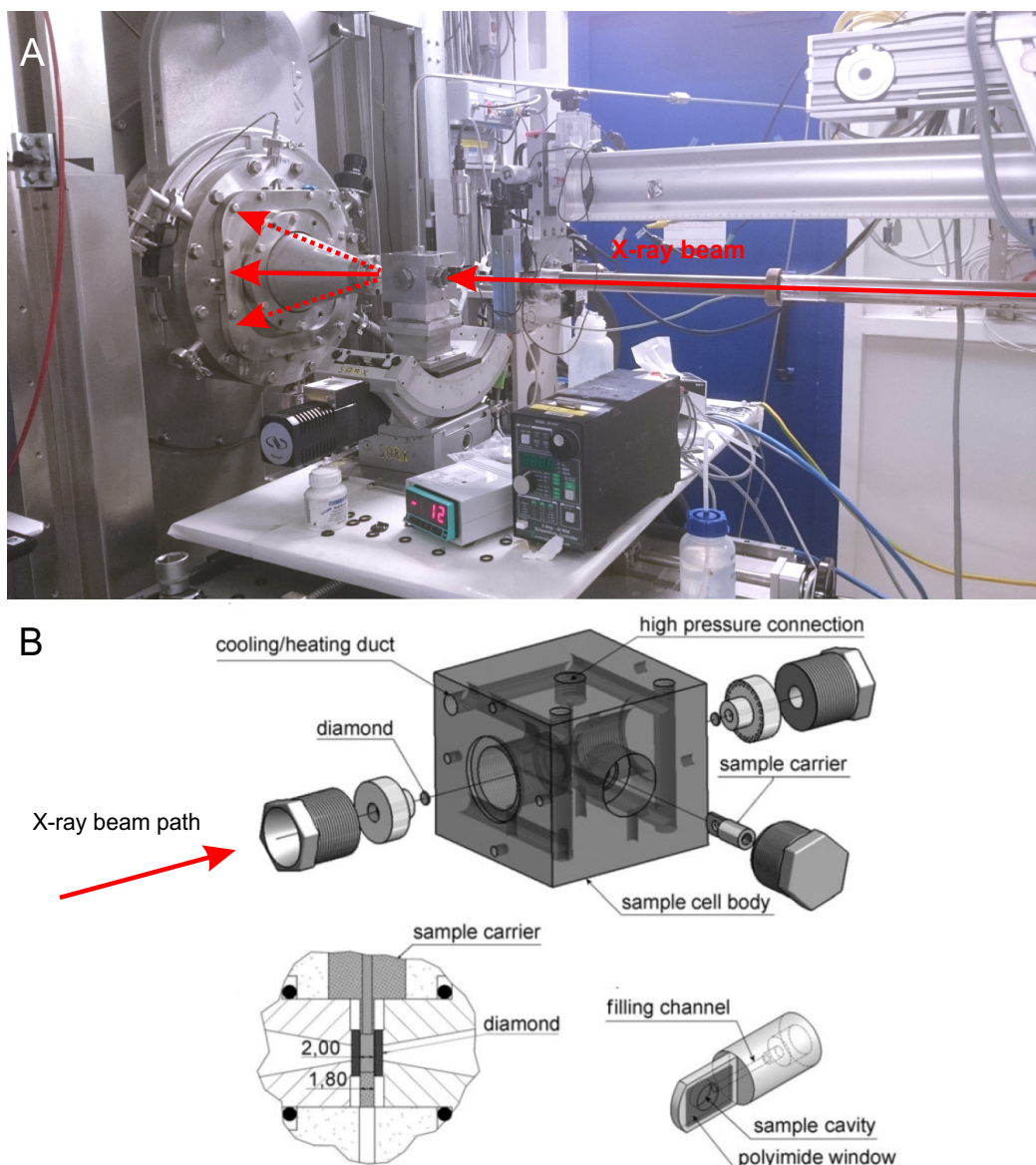


Figure 3.3: (A) HHP SAXS setup II at beamline ID02 (ESRF) (see section 3.2.2) featuring the pressure cell by C. Krywka (B) Exploded view of the X-ray beam path components and the sample holder. Reprinted with permission from [Krywka, 2008]. Copyright © 2008 WILEY-VCH Verlag GmbH & Co. KGaA, Weinheim.

## HHP SAXS - Setup II

The design principle of the second setup is similar to the HHP SAXS - Setup I, but the custom-built high pressure sample cell by C. Krywka [Krywka, 2008] can be employed to generate hydrostatic pressures up to 5 kbar in the sample environment. Figure 3.3 depicts a photography of the HHP SAXS setup at beamline ID02 (ESRF) (see section 3.2.2) as well as an exploded view of the pressure cell. The cell body, made from stainless steel (Inconel 718, 2.4668) is sealed with two flat diamond windows (type IIa, 1 mm thickness, 6 mm diameter) for entering and exit of the X-ray beam. The diamonds are mounted with epoxy glue on the window holders, to fix them in place at low pressures. At elevated pressures, these so-called Poulter-type windows are fixed and sealed by the pressure [Poulter, 1932]. The diamond window holders are equipped with  $\varnothing$  13.00 x 3.00 NBR 90 Shore A precision O-rings to seal the cell at high hydrostatic pressures. Next to the two diamond windows for the X-ray beam passage, an additional front opening serves the fast exchange of the actual sample carrier which is placed in the pressure cell body in the beam path between the two diamond windows, which are separated by a distance of 2 mm (see inset in Figure 3.3 (B)). The area around the sample carrier's window has a thickness of 1.8 mm and is, before usage, glued with polyimide foil (Kapton<sup>®</sup>, thickness 25  $\mu$ m). The sample carrier can be filled through a thin channel by a needle and sealed with a M2.5 polyamind screw (TOOLCRAFT<sup>®</sup> 830415). The sample carrier holds a sample volume of 55  $\mu$ l. The seal the sample entrance,  $\varnothing$  11.00 x 3.00 NBR 70 Shore A precision O-rings of RALICKS GmbH<sup>®</sup> are employed. Again, as pressure transmitting medium ionized water is used. A hand spindle pump (Nova Swiss<sup>®</sup>), connected *via* a special valve and tubing to a water reservoir as well as to the pressure cell, is used to increase the pressure (not shown in Figure 3.3). The pressure is measured at the pump as well as at the cell by two pressure detectors.

### 3.2.2 Beamlines

Within this thesis, the HHP SAXS experiments were performed at various synchrotron light sources to meet the above mentioned special demands of a high pressure setup as well as at one laboratory X-ray instrument for measurements at ambient conditions. The different end stations at which the experiments were carried out as well as the experimental procedure are described shortly in the following.

#### Laboratory SAXS Instrument GALAXI, Forschungszentrum Jülich (Jülich, Germany)

The high brilliance laboratory Gallium Anode Low-Angle X-ray Instrument (GALAXI) at the Forschungszentrum Jülich, Germany, is based on the JUSFIA anomalous SAXS instrument, which was formerly operating at beamline B1 at the storage ring DORIS (HASYLAB, DESY Hamburg, Germany).

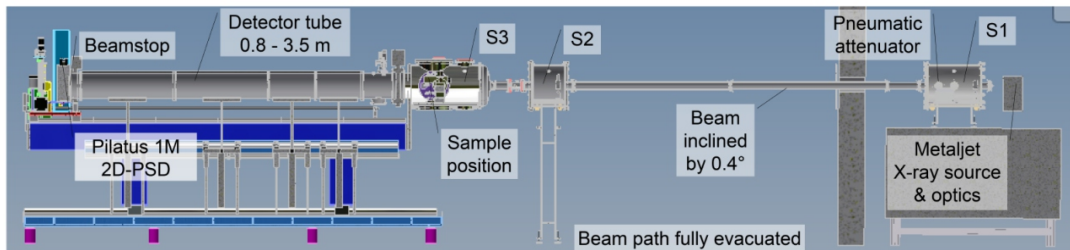


Figure 3.4: Sketch of the X-ray source GALAXI (Forschungszentrum Jülich, Jülich, Germany) with its main components. Picture adapted from [Kentzinger et al., 2016].

The laboratory X-ray scattering instrument GALAXI is equipped with a METALJET source by Bruker AXS, utilizing a liquid metal jet of a GaInSn alloy as anode, which provides Ga  $K_{\alpha}$  radiation at  $\lambda = 0.134$  nm ( $E = 9243$  eV photon energy).



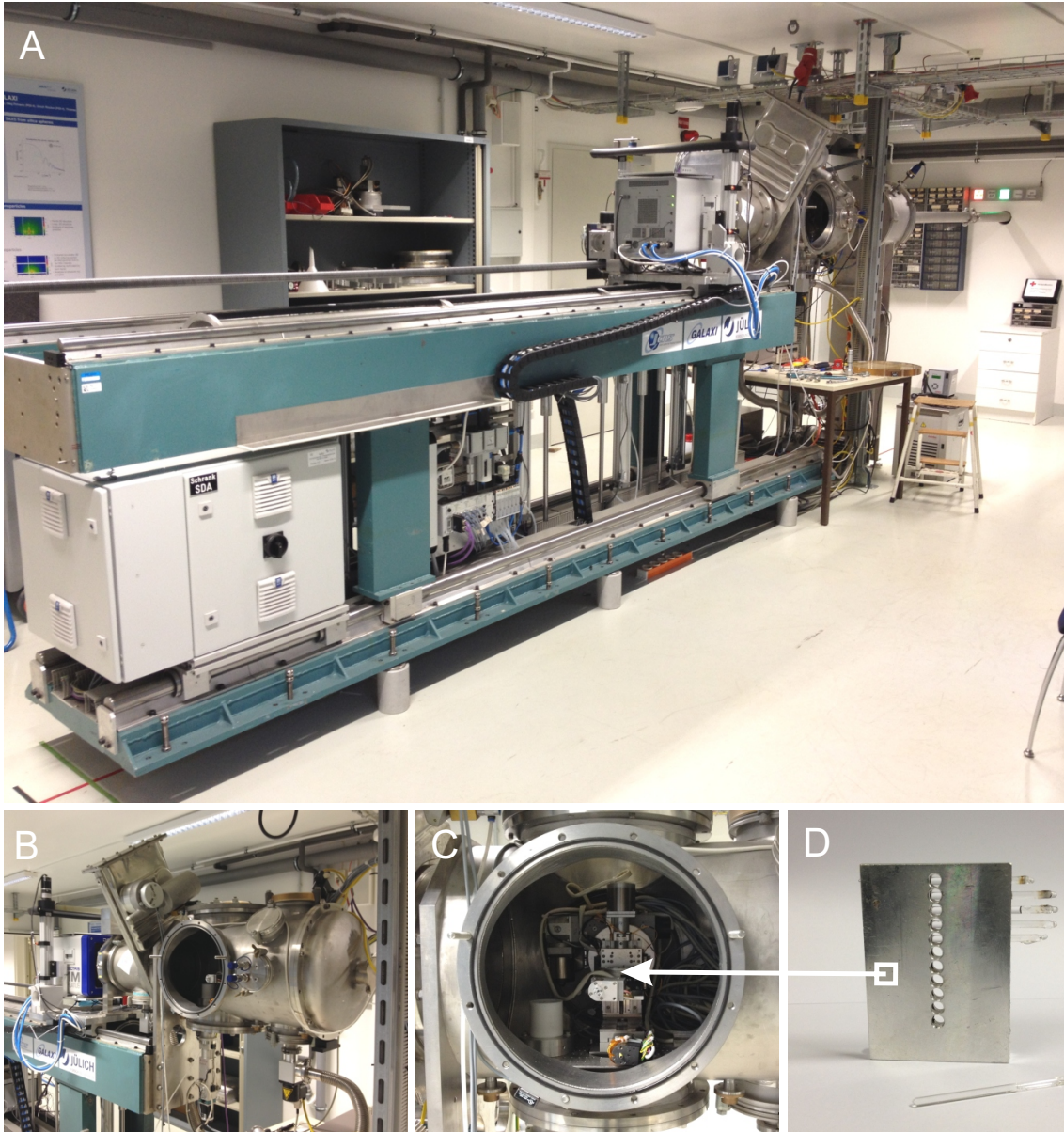


Figure 3.5: (A) GALAXI diffractometer with shortest detector distance available. The X-ray source (GaInSn liquid anode) is located behind the wall. (B) Pilatus 1M 2D-position sensitive detector located in the SAXS region and the sample position. (C) Close-up of the evacuated sample position. (D) Standard sample holder for sealed capillaries with outer diameter ranging from 1.5 to 2.1 mm.

Five different sample-to-detector distances can be adjusted between 0.835 and 3.535 m, yielding an overall accessible  $q$ -range of  $0.04 < q < 8 \text{ nm}^{-1}$ . Owing to the small X-ray source ( $20 \mu\text{m}$  diameter projected to beam direction), the intrinsic divergence is 0.3 mrad at parallel beam size of  $2.4 \times 2.4 \text{ mm}^2$ . At the evacuated sample position, a flux of  $1 \times 10^9 \frac{\text{photons}}{\text{s} \cdot \text{mm}^2}$  is received. As detector a 2D position sensitive Pilatus 1M detector with an active area of  $169 \text{ (H)} \times 179 \text{ (V)} \text{ mm}^2$  and single pixel size  $172 \times 172 \mu\text{m}^2$  is employed [Kentzinger et al., 2016]. The schematic layout of the instrument is shown in Figure 3.4.

In the framework of the project 'Macromolecular Crowding of Protein Solutions by the Polysaccharide Ficoll' (see chapter 7), the SAXS measurements were performed at a sample-to-detector distance of 0.834 m and 3.534 m, corresponding to a  $q$ -range of  $0.0400 < q < 2.0234 \text{ nm}^{-1}$  and  $0.1481 < q < 7.905 \text{ nm}^{-1}$ , respectively. The liquid samples were measured at ambient pressure

and at 25°C in borosilicate glass capillaries with 2.1 mm diameter and 0.05 mm wall thickness and sealed with hot glue, using the in-house sample holder (see Figure 3.5). The exposure time was 1 h. The 15% (w/v) lysozyme + 25 mM Bis-Tris (pH 7) solutions and the corresponding background solvent scattering were measured for the crowder Ficoll PM 70 added to the solution at various concentrations (see section 3.1).

#### Beamline SWING, Soleil (Saint-Aubin, France)

At the Small-angle and Wide-angle scatterING beamline SWING at the storage ring SOLEIL in Saint-Aubin, France, a U20 in-vacuum undulator provides a beam of the size 20  $\mu\text{m}$  x 20  $\mu\text{m}$  and divergence 14.5 (H) x 4.6 (V)  $\mu\text{rad}$ . The accessible energy range is 5 - 17 keV (Si(111) double crystal monochromator) with energy resolution of  $\Delta E \simeq 2$  eV. The typical flux on the sample is of the order  $10^{12}$   $\frac{\text{photons}}{\text{s}}$  at 16 keV. For a SAXS setup, the detectors Eiger 4M (Dectris) and PCCD170170 (AVIEX) are available [Beamline SWING, 2018].

In the SAXS experiment, performed within the framework of the project 'Water-Mediated Protein-Protein Interactions at High Pressures are Controlled by a Deep-Sea Osmolyte' (see chapter 5), a  $q$ -range of  $0.070 < q < 6.389$   $\text{nm}^{-1}$  was obtained at a sample-to-detector (AVIEX PCCD170170) distance of 2.175 m and with a photon wavelength of  $\lambda = 0.8266$  Å. The exposure time was 1 s. The temperature was held constant at 25°C and the high hydrostatic pressures in the range 1 - 4000 bar were generated in the sample environment employing the HHP SAXS - Setup II described in section 3.2.1. The 10% (w/v) and 1% (w/v) lysozyme + 25 mM Bis-Tris (pH 7) solutions and the corresponding background solvent scattering were measured at 25°C in 500 bar steps in an overall pressure range from 1 to 4000 bar for single organic osmolytes at various concentrations,  $c$ , and mixtures thereof (see section 3.1).

#### Beamline I22, DLS (Didcot, United Kingdom)

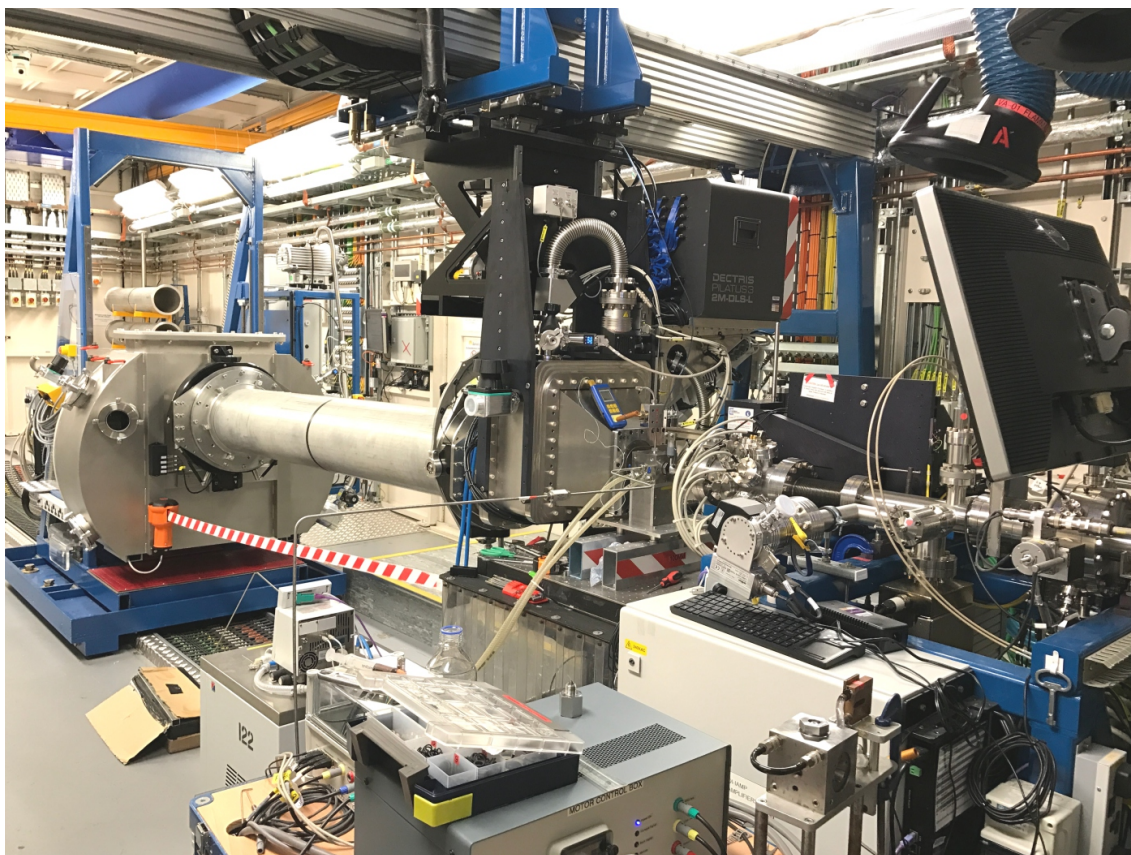


Figure 3.6: Experimental SAXS setup at beamline I22 (DLS, Didcot, United Kingdom).



The beamline I22 at the storage ring **Diamond Light Source (DLS)** in Didcot, United Kingdom, dedicated to small- and wide-angle scattering and diffraction, operates at an energy range from 3.7 to 20 keV with an energy resolution of  $(\Delta E/E) = 1.2 \times 10^{-4}$ , employing a Si(111) double crystal monochromator. The flux at 12.4 keV on sample is  $6 \times 10^{12} \frac{\text{photons}}{\text{s}}$ . The beam size at the sample measures 320 (H)  $\times$  80 (V)  $\mu\text{m}^2$  and with micro-focusing 10 (H)  $\times$  8 (V)  $\mu\text{m}^2$ . The source of the beam is an in-vacuum U25 undulator and detection of the SAXS signal is achieved using a Pilatus-P3-2M (DECTRIS) with an active area of 253.7 (W)  $\times$  288.8 (H)  $\text{mm}^2$  made of 1475 (W)  $\times$  1679 (H) total pixels (single pixel size 172  $\times$  172  $\mu\text{m}^2$ ) [Beamline I22, 2018]. The schematic layout of the beamline is depicted in Figure 3.7 and the experimental SAXS setup in in Figure 3.6.

For the SAXS experiments serving the projects 'Impact of Macromolecular Crowding and Compression on Protein-Protein Interactions and Liquid-Liquid Phase Separation Phenomena' (see chapter 4), 'Water-Mediated Protein-Protein Interactions at High Pressures are Controlled by a Deep-Sea Osmolyte' (see chapter 5) and 'The Effect of Osmolytes and Crowding on the Pressure-Induced Dissociation and Inactivation of Dimeric Horse Liver Alcohol Dehydrogenase' (see chapter 6), the distance of the detector to the sample was set to 3.752 m. The wavelength of the incident photon beam was  $\lambda = 0.6888 \text{ \AA}$  and the wave vector transfer covered a range of  $0.070 < q < 6.600 \text{ nm}^{-1}$ . The exposure time was 1 s. The measurements were performed at a constant temperature of 25°C employing the HHP SAXS setup II lined out in section 3.2.1 and motor driven high pressure pump (SITEC-Sieber, Zürich, Switzerland) installed at the beamline [Brooks et al., 2010]. The 10% (w/v), 1% (w/v) lysozyme + 25 mM (50 mM) Bis-Tris (pH 7) (+ 75 mM NaCl) solutions, the 1% (w/v) LADH + 10 mM Tris-HCl (pH 8.5) solutions and the corresponding background solvent scattering were measured in 250 bar steps in an overall pressure range from 1 to 3500 bar for several cosolvents and crowders added at various concentrations,  $c$ , and mixtures thereof (see section 3.1).

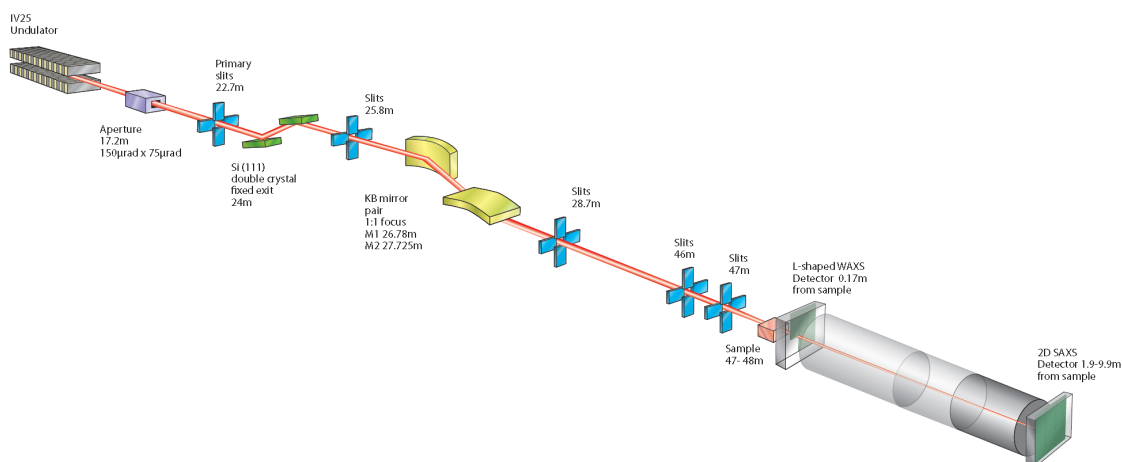


Figure 3.7: Schematic layout of beamline I22 (DLS, Didcot, United Kingdom). Picture adapted from [Beamline I22, 2018].

### Beamline ID02, ESRF (Grenoble, France)

At the WAXS and (U)SAXS beamline ID02 at the storage ring **European Synchrotron Radiation Facility (ESRF)** in Grenoble, France, the X-ray radiation is delivered by two phased U21.4 undulators or a single U35 undulator. As the U35 device covers the full energy range of the beamline (8-29 keV), the two U21.4 undulators are primarily operated at a energy between 12.4 - 15.2 keV, providing a monochromatic flux of the order  $6 \times 10^{13} \frac{\text{photons}}{\text{s}}$  at the sample position. The beamline is equipped with a liquid-nitrogen-cooled Si(111) crystal monochromator ( $\Delta E/E \simeq 2 \times 10^{-4}$ ) and three detectors for high resolution USAXS (FReLoN 4M), time-resolved SAXS (Pilatus 300K, Dectris) and workhouse SAXS/USAXS (Rayonix MX 170 HS). The Rayonix MX-170HS CCD detector has an overall size of 170  $\times$  170  $\text{mm}^2$  and a spatial resolution of  $\sim 85 \mu\text{m}$  [Narayanan et al., 2018]. The schematic layout of the beamline is depicted in Figure 3.8.



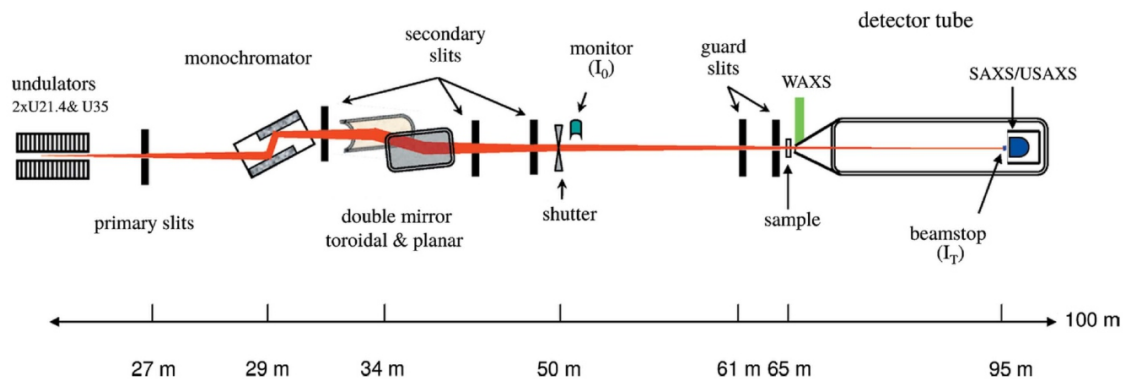


Figure 3.8: Sketch of beamline ID02 (ESRF, Grenoble, France). Picture adapted from [Narayanan et al., 2018].

In the SAXS experiment dedicated to the project '**Macromolecular Crowding of Protein Solutions by the Polysaccharide Ficoll**' (see chapter 7), the incident photon wavelength was set to  $\lambda = 0.7232 \text{ \AA}$  and the sample-to-detector (Rayonix MX-170HS CCD) distance to 2.4 m, yielding the wave vector transfer range  $0.0396 < q < 4.412 \text{ nm}^{-1}$ . To generate HHP ( $1 < p < 4000 \text{ bar}$ ) in the sample environment, the high-pressure setup lined out in section 3.2.1 (HHP SAXS setup II) was employed at a constant temperature of  $25^\circ\text{C}$ . The sample was exposed to the radiation for 0.5 s.

During beam time allocated to the project '**Water-Mediated Protein-Protein Interactions at High Pressures are Controlled by a Deep-Sea Osmolyte**' (see chapter 5), an incident photon wavelength of  $\lambda = 0.7293 \text{ \AA}$  and a sample-to-detector (Rayonix MX-170HS CCD) distance of 2.3999 m yielded an wave-vector-transfer ranging from  $0.0396 < q < 0.7022 \text{ nm}^{-1}$ . The experiment was performed using the high-pressure setup section as mentioned above (see section 3.2.1 (HHP SAXS setup II)). The exposure time was 1 s.

For the SAXS experiment, performed during the RESOLV GSS international internship at beamline ID02 serving the project '**Impact of Macromolecular Crowding and Compression on Protein-Protein Interactions and Liquid-Liquid Phase Separation Phenomena**' (see chapter 4), an in-house high pressure cell was used (see section 3.2.1 (HHP SAXS setup I)). The distance between the detector (Rayonix MX-170HS CCD) and the sample was 2 m and the wavelength of the incoming beam was  $\lambda = 0.7490 \text{ \AA}$ . The SAXS curves were recorded over range  $0.0519 < q < 4.9837 \text{ nm}^{-1}$ . The exposure time was 0.25 s.

During the experimental sessions, the 10% (w/v) and 1% (w/v) lysozyme + 25 mM Bis-Tris (pH 7) solutions and the corresponding background solvent scattering were measured at  $25^\circ\text{C}$  in 100 or 500 bar steps in an overall pressure range from 1 to 4000 bar for single organic osmolytes and crowders at various concentrations,  $c$ , and mixtures thereof (see section 3.1).

### Beamline 9, DELTA (Dortmund, Germany)

At beamline 9 at the storage ring **Dortmunder ELekTronenspeicherringAnlage (DELTA)** in Dortmund, Germany, a superconducting asymmetric wiggler (SAW) provides the synchrotron radiation. The schematic outline of beamline 9 is depicted in Figure 3.9. The beamline is equipped with a MAR345 2D image plate detector with an active diameter of 345 mm and a pixel size of  $100 \times 100 \mu\text{m}^2$ . The evacuated flight tube between sample and detector has a length of 1.1 m and a diameter of 200 mm, effectively limiting the active area of the detector. Employing a Si(311) double crystal monochromator, the beamline can be operated at X-ray energies between 4 - 30 keV. At a photon energy of 10 keV, the photon flux is  $5 \times 10^7 \frac{\text{photons}}{\text{s mm}^2 \text{ mA}}$ . The beam size is typically 1 (H)  $\times$  2 (V)  $\text{mm}^2$  [Krywka et al., 2007].

In the SAXS experiment performed within the framework of the project '**Impact of Macromolecular Crowding and Compression on Protein-Protein Interactions and Liquid-Liquid Phase Separation Phenomena**' (see chapter 4), the measurements were performed employing

the MAR345 image plate detector at a distance of 1.103 m from the sample at an incident photon wavelength of  $\lambda = 1.2399 \text{ \AA}$ . Here, the HHP SAXS setup II described in section 3.2.1 was employed without the diamond windows and the accessible momentum transfer was  $0.238 < q < 5.769 \text{ nm}^{-1}$  (see Figure 3.10). The exposure time was 10 min. The 1% (w/v) lysozyme + 25 mM Bis-Tris (pH 7) solutions and the corresponding background solvent scattering were measured at 25°C in 500 and 1000 bar steps in an overall pressure range from 1 to 3500 bar for 15% (w/v) PEG of various molecular weights (see section 3.1).

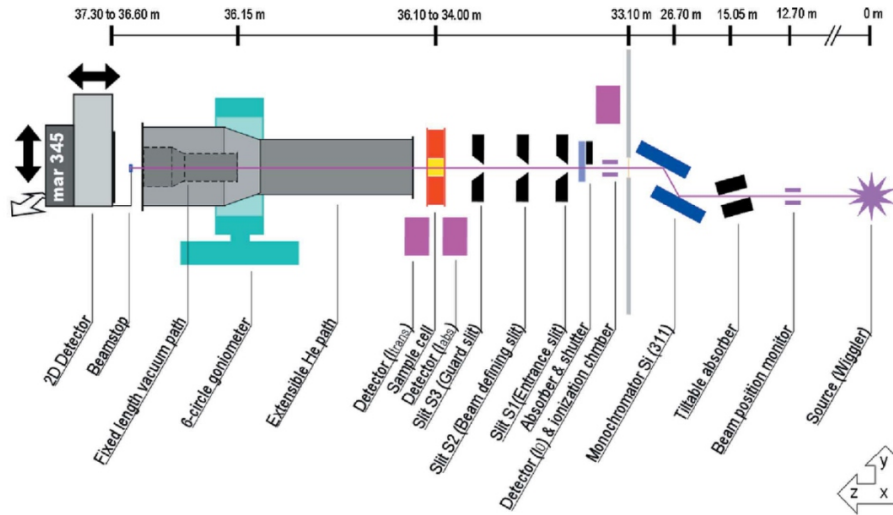


Figure 3.9: Schematic outline of the SAXS/WAXS setup at beamline 9 (DELTA, Dortmund, Germany). Picture adapted from [Krywka et al., 2007].

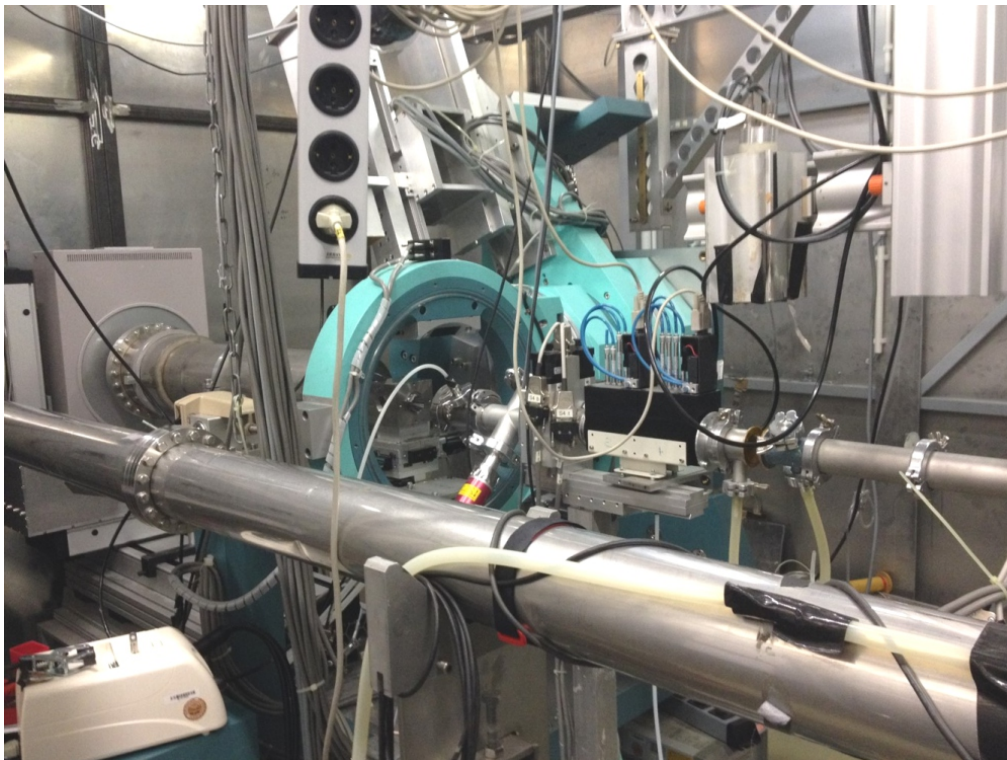


Figure 3.10: Experimental SAXS Setup at beamline 9 (DELTA, Dortmund, Germany).

### Beamline P03, Petra III (Hamburg, Germany)

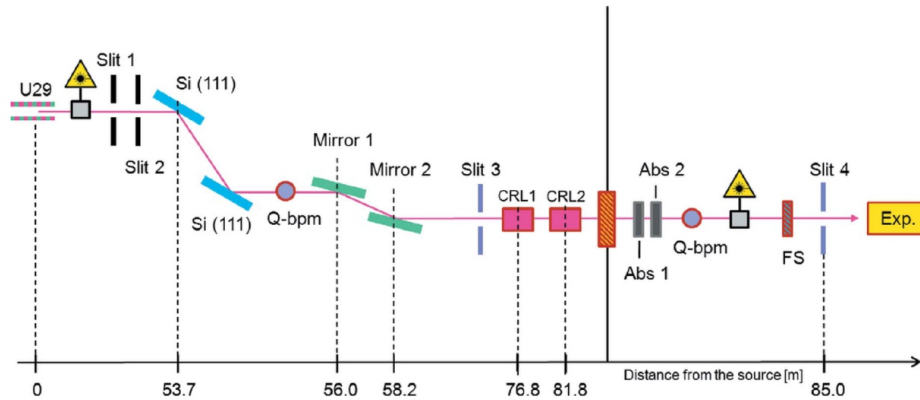


Figure 3.11: Sketch of beamline P03 (PETRA III (DESY), Hamburg, Germany). Picture adapted from [Buffet et al., 2012].

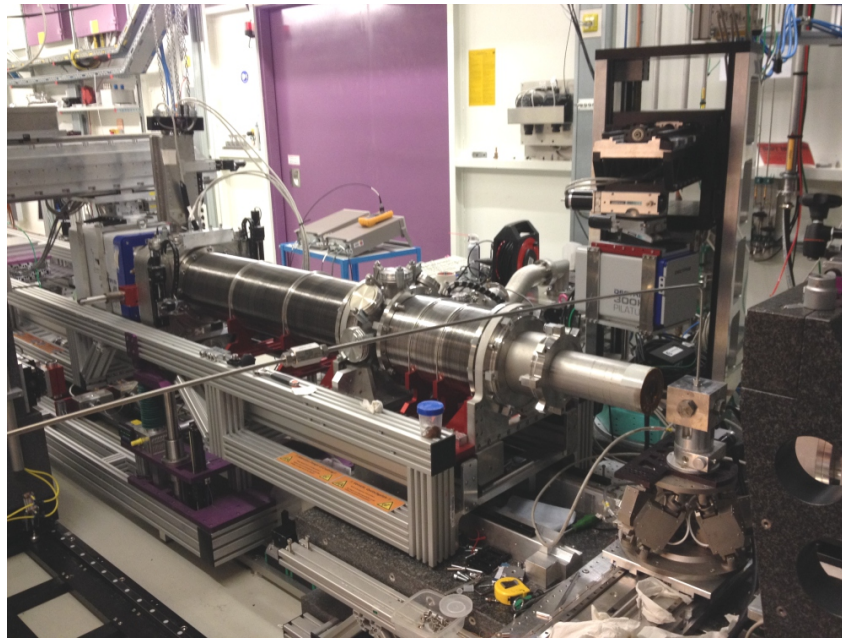


Figure 3.12: Experimental SAXS Setup at P03 (PETRA III, Hamburg, Germany).

The **Microfocus and Nanofocus X-ray Scattering (MiNaXS)** beamline P03 at the storage ring PETRA III in Hamburg, Germany, exploits one of a high- $\beta$  canted 2 m undulator pairs. The monochromator is equipped with a cryocooled Si(111) double crystal and provides a micro-focused ( $H \times V \geq 23 \mu\text{m} \times 13 \mu\text{m}$ ) monochromatic X-ray beam in the energy range 8 - 23 keV with a resolution of  $\Delta E/E \simeq 10^{-4}$  and a photon flux of  $\geq 10^{11} \frac{\text{photons}}{\text{s}}$  [Buffet et al., 2012]. A sketch of the beamline is depicted in Figure 3.11.

In the SAXS experiment performed within the framework of the two projects '**Impact of Macromolecular Crowding and Compression on Protein-Protein Interactions and Liquid-Liquid Phase Separation Phenomena**' (see chapter 4) and '**Macromolecular Crowding of Protein Solutions by the Polysaccharide Ficoll**' (see chapter 7), a  $q$ -range of  $0.070 < q < 6.389 \text{ nm}^{-1}$  was obtained at a sample-to-detector (Pilatus 1M pixel detector) distance of 1.630 m and with a photon wavelength of  $\lambda = 0.9480 \text{ \AA}$ . The exposure time was 0.1 s. The HHP SAXS



setup II described in section 3.2.1 was employed to generate pressures up to 3.5 kbar in the sample environment. The temperature was held constant at  $T = 25^\circ\text{C}$  (see Figure 3.12). The 10% (w/v) lysozyme + 50 mM Bis-Tris (pH 7) solutions and the corresponding background solvent scattering were measured at  $25^\circ\text{C}$  in 250 bar steps in an overall pressure range from 1 to 3500 bar for the crowder Ficoll PM 70 (PM 400) and PEG of various molecular weights at various concentrations (see section 3.1).

### 3.2.3 Basic Data Treatment and Refinement

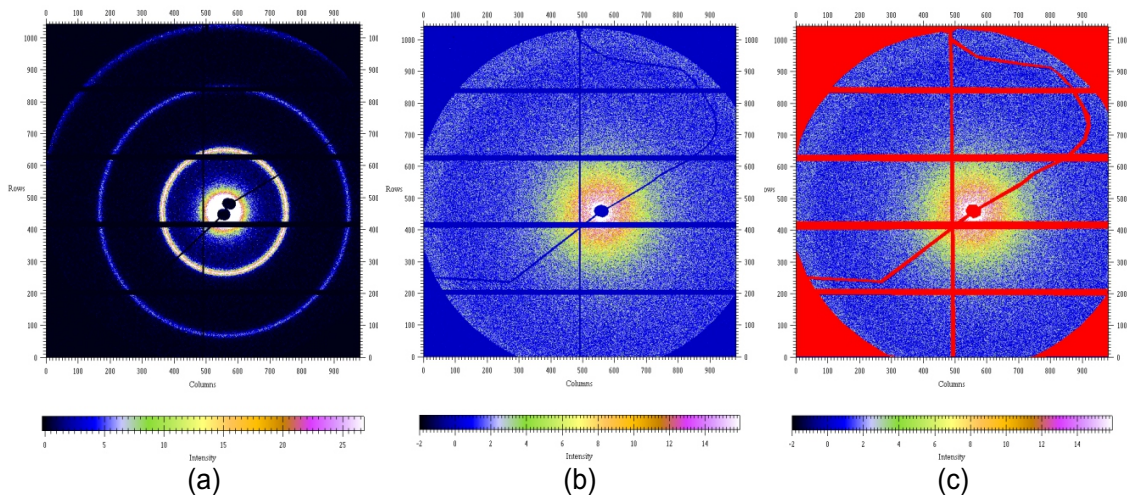


Figure 3.13: (a) Scattering image of the calibrant silver behenate ( $\text{AgC}_{22}\text{H}_{43}\text{O}_2$ ) (b) Raw scattering image recorded with a Pilatus 1M detector of an aqueous 10% (w/v) Ficoll PM 70 solution. (c) The same image with the corresponding mask (*red*) made by the program FIT2D [Hammersley et al., 1996]. All images were recorded at beamline P03 at PETRA III (see section 3.2.2).

Although the software employed for the detector calibration and raw data treatment of the SAXS patterns recorded with a 2D area detector differs from beamline to beamline (e.g. FIT2D [Hammersley et al., 1996] at P03 (PETRA III) and bl9 (DELTA), Foxtrott at SWING (SOLEIL), DAWN at I22 (DLS), SAXSutilities at ID02 (ESRF)), the basic principle is the same and will be discussed in the following. The first step is the calibration of the sample-to-detector distance and the position of the primary beam on the detector with the low-angle diffraction standard silver behenate ( $\text{AgC}_{22}\text{H}_{43}\text{O}_2$ ,  $M_w = 447.2287 \text{ g mol}^{-1}$ ) [Huang et al., 2007]. It has been shown that silver behenate has a set of well defined and regularly spaced ( $00l$ ) diffraction peaks at  $2\Theta \leq 20^\circ$  with  $d_{001} = 58.380(3) \text{ \AA}$ . Figure 3.13 (a) shows the corresponding small-angle section of the powder diffraction pattern of silver behenate recorded with a Pilatus 1M detector at beamline P03 at PETRA III. In the next step, the two-dimensional scattering pattern of the sample is azimuthally averaged whereby various areas of the detector are excluded by a so-called mask. This includes parts of the area that are shadowed by the beam stop and anisotropies like the so-called Pseudo-Kossel lines, which emerge from X-ray reflection of the lattice planes of the diamond windows. Figure 3.13 (b) and (c) show the (un)masked detector image of the scattering pattern.

Then, in order to extract the weak scattering contribution, originating from the proteins, to the measured SAXS signal of an aqueous protein solution, a background correction is performed. Since the main focus is on the proteins tertiary and/or quaternary structure as well as the protein-protein interaction, the solvents signal is treated as background next to the parasitic scattering contributions from slits, air, the Kapton foil ('Kapton peak' at  $q = 3.8 \text{ nm}^{-1}$ ), the diamond windows, etc. The SAXS signal of the proteins is obtained by measuring the scattering of a sample carrier filled with the solvent of the same composition as that used for the protein solution, and subtracting it from the signal of the corresponding protein solution. For an exact background subtraction, an accurate normalization of the experimental scattering signals,  $I^{(\text{exp})}(q)$ , to the incoming flux

of the X-ray beam,  $I_0$ , and the transmission of the sample,  $T$ , is required. Both quantities differ significantly from measurement to measurement due to the pressure dependence of the sample transmission. In general, they are measured by diodes or ion chambers. Alternatively, the integrated scattering signal, recorded with a 2D resolving detector, can be used as well. The normalized scattering signal is given by

$$I^{(\text{norm})}(q) \cong \frac{I^{(\text{exp})}(q)}{I_0} \cdot \frac{1}{T} = \frac{I^{(\text{exp})}(q)}{I_0} \cdot \frac{I_0}{I^{(T)}} = \frac{I^{(\text{exp})}(q)}{I^{(T)}}. \quad (3.3)$$

Here, it is used that the transmission of the sample is the ratio of the incoming,  $I_0$ , and the transmitted, attenuated beam,  $I^{(T)}$ . However, a proper background subtraction generally cannot be obtained by the simple normalization, but scaling the normalized signals from the protein solution,  $I_{\text{prot+solv+bkg}}^{(\text{norm})}(q)$ , as well as the solvent scattering,  $I_{\text{solv+bkg}}^{(\text{norm})}(q)$ , by an additional factor,  $g$ , yields the scattering signal emerging solely from the proteins

$$I(q) = \frac{I_{\text{prot+solv+bkg}}^{(\text{exp})}(q)}{I_{\text{prot+solv+bkg}}^{(T)}} - g \cdot \frac{I_{\text{solv+bkg}}^{(\text{exp})}(q)}{I_{\text{solv+bkg}}^{(T)}}. \quad (3.4)$$

The factor  $g$  is close to unity and the quality of the background subtraction can be evaluated by the Kratky plot (see section 2.4.2) for dilute solutions. For example, the Kratky plot of a dilute lysozyme solution should exhibit a sharp maximum as well as a minimum close to zero. For concentrated solutions, the choice of the value  $g$  should be coincidental with the high  $q$ -limit,  $S(q) \rightarrow 1$ , of the structure factor (see section 2.4.4).

### 3.3 Liquid-Liquid Phase Separation (LLPS)-Turbidity Measurement

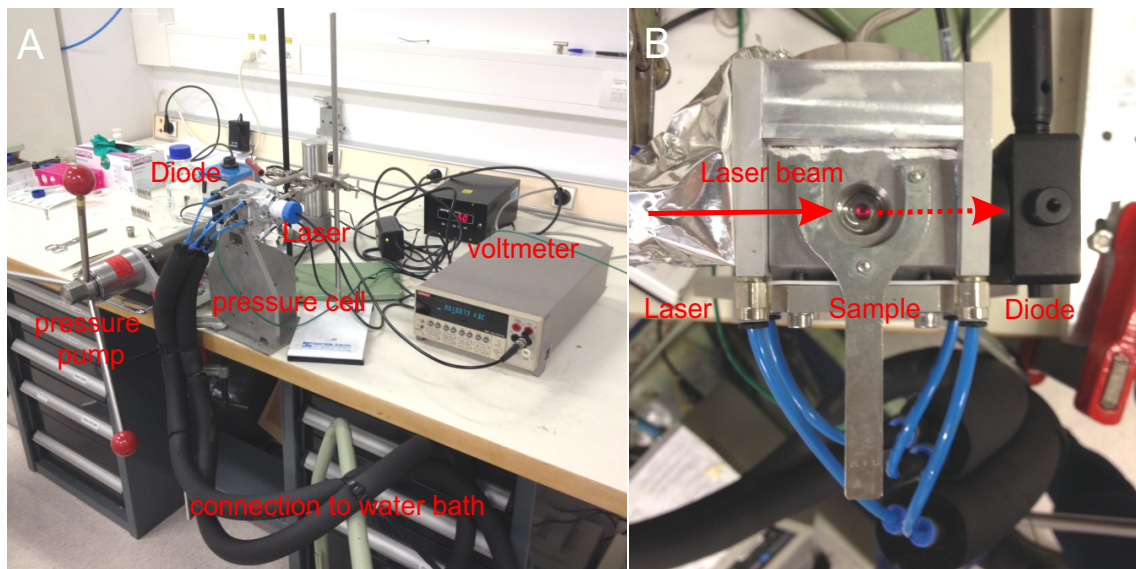


Figure 3.14: (A) Experimental setup for temperature- and pressure-dependent light transmission measurements featuring the HHP setup I (see section 3.2.1). The pressure cell is connected to a pressure pump as well as to a refrigerated heating circulator bath with water-cooled cooling machine (HUBER<sup>TM</sup> Ministat 230) for temperature control. (B) Beam path of the laser beam passing the sample. The intensity of the laser is recorded by a diode and converted to a voltage signal. The signal is reproduced with a voltmeter.

For temperature- and pressure-dependent light transmission measurements of the protein-crowder solutions, the HHP setups I and II [Möller et al., 2016, Krywka et al., 2007] (see section 3.2.1) were

employed together with a laser and diode mounted alongside the optical path of the cell's diamond windows. Figure 3.14 depicts the experimental setup for light transmission measurements featuring the pressure cell by [Möller et al., 2016], exemplarily. Entering the LLPS region, the transparent homogeneous protein solution becomes turbid due to formation of droplets of higher protein concentration dispersed in the lower concentrated bulk solution. A pressure-, temperature- and/or crowder-induced transition to the liquid-liquid phase separation (LLPS) region of the protein-crowder solutions and the concomitant increase of the solutions' turbidity are quantified by the reduction of laser light transmission in a temperature range from 6 to 28°C and a pressure range from 1 to 4500 bar. A detailed description of this 'cloud-point'-determination can be found in [Liu et al., 1996, Asherie, 2004].

### 3.4 Refractometry

The refractive indices,  $n_s$ , of the cosolvent solutions at various concentrations were measured with an accuracy of  $\pm 0.0002$  at ambient pressure and  $T = 25^\circ\text{C}$  employing a Brix/RI-Check Refractometer (RI Range 1.3330 – 1.4465; 589 nm LED) from Reichert Technologies.

### 3.5 Dielectric Spectroscopy

In this thesis, the static dielectric constants for the cosolvent solutions of protein systems were determined with two devices, the Dekameter DK 03 (with kind support of the Chemical Practical Course, TU Dortmund) and the Agilent E4991A RF Impedance/Material Analyzer (with kind support of the Chair of Experimental Physics E III, AG Böhmer, TU Dortmund), which will be described in the following.

#### Calibration

With both the Agilent E4991A RF Impedance/Material Analyzer and the Dekameter DK 03, the effective capacity of the actual measuring space of the cell cannot be calculated with sufficient accuracy from the geometric dimensions. For this reason, each cell is calibrated with liquids which are characterized by a dielectric constant known as precisely as possible, chemically stable and of a low conductivity. For the calibration of the instruments, measurements of ethanol ( $\epsilon_r = 25.43$  [Barthel et al., 1983]), dimethyl sulfoxide ( $\epsilon_r = 46.48$  [Barthel et al., 1990]) and ultra-pure water ( $\epsilon_r = 78.36$  [Kaatze and Uhlendorf, 1981]) were carried out at 25°C and ambient pressure, which cover a large area of the measuring range. The literature values of the static dielectric constant of the three calibration substances are plotted against the corresponding read off scale values. From the linear regression results the conversion formula of the scale value  $x$  into the dielectric constant  $\epsilon'(1.8 \text{ MHz}) \simeq \epsilon_r$ .

#### Dekameteter Type DK 03

The Dekameteter Type DK 03 made by the Wissenschaftlich - Technische Werkstätten (WTW) GmbH (Welheim Oberbayern, Deutschland) with the sample cell for liquids Type MFL 3/s is based on the compensation method and provides the real part of the frequency-dependent dielectric permittivity at a constant measuring frequency of  $\nu = 1.8 \text{ MHz}$ . At this frequency for aqueous solutions at room temperature the area of anomalous dispersion is not reached and thus the quasi-static dielectric constant  $\epsilon_r$  is measured. Generally, this setup can be employed for liquids with static dielectric permittivities between  $21 < \epsilon_r < 90$  at ambient pressure [Oehme, 1962]. Figure 3.15 depicts the device together with its block diagram as well as the sample cell and its cross-section. The sample cell Z is a cylindrical capacitor with capacity  $C_Z$ , made from metal and with an sample volume of  $\sim 10 \text{ ml}$ . The sample is filled in the capacitor Z and operates as dielectric medium. The sample cell is connected in parallel to an adjustable capacitor MK with capacity  $C_{MK}$  without dielectric medium. The total capacity of both is given by  $C_{1,2} = C_{MK} + C_Z$ . The resonant circuit of the capacitor MK and the inductivity  $L$  resonates when tuning  $C_{MK}$  to the



constant normal frequency

$$\nu_N = \nu_E = \frac{1}{2\pi} \sqrt{\frac{1}{LC_{MK}}}, \quad (3.5)$$

equal to the eigenfrequency,  $\nu_E$ , of the resonant circuit. By switching on the capacitor Z, the capacity is increased to  $C_{1,2}$  and the eigenfrequency of the extended resonant circuit reads

$$\nu'_E = \frac{1}{2\pi} \sqrt{\frac{1}{LC_{1,2}}} \neq \nu_N. \quad (3.6)$$

The resonance condition in Eq. (3.6) can be restored by decreasing the capacity  $C_{MK}$  by the same amount as the capacitor Z has increased the capacity of the resonant circuit. Consequently, changes in the dielectric permittivity  $\epsilon'$  (1.8 MHz) of the sample results in a detuned generator resonant circuit (see Figure 3.15 (D)). The change in capacity via the dielectric medium can be compensated by adjusting  $C_{MK}$ . A luminescent quartz (see Figure 3.15 (C)) serves as resonance display and for fine tuning. The scale value is read off the display and converted into an absolute value  $\epsilon'$  (1.8 MHz)  $\simeq \epsilon_r$  using the above mentioned calibration diagram.

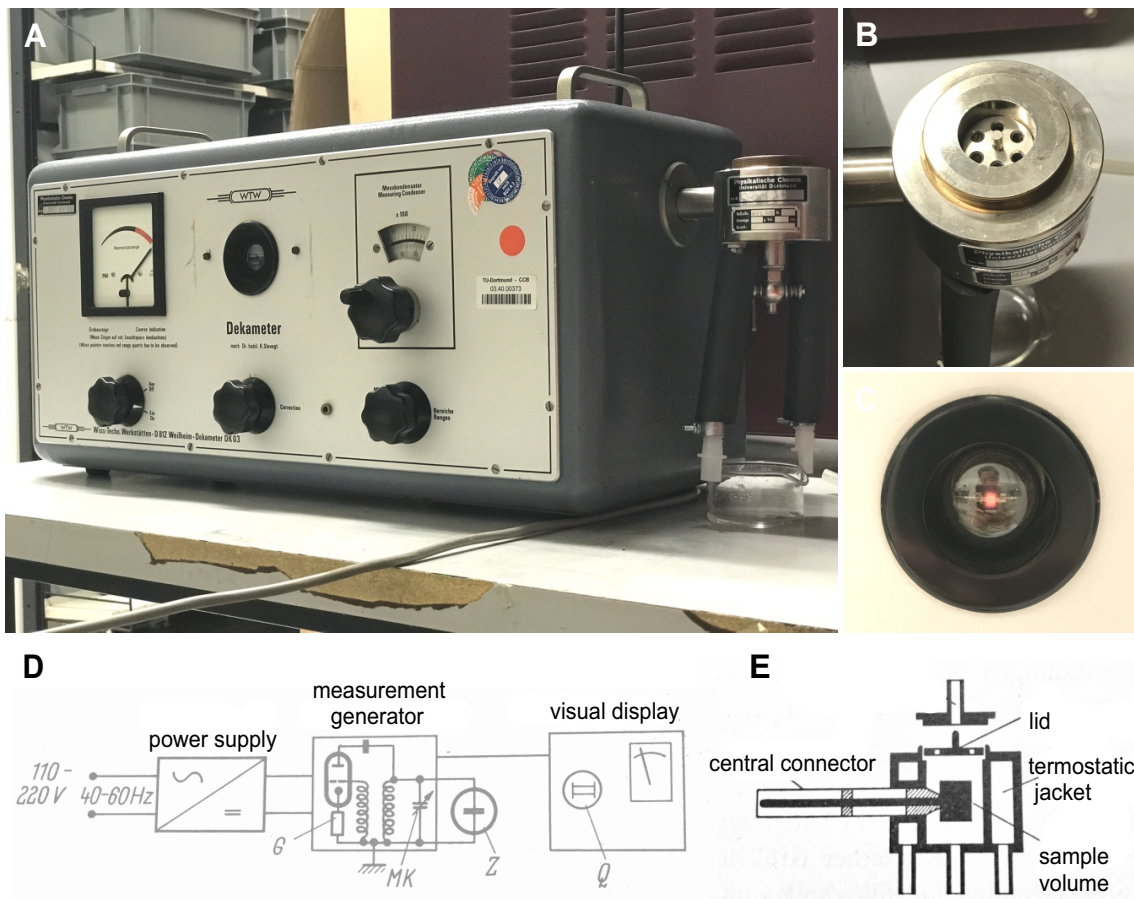


Figure 3.15: (A) Dekameter Type DK 03 (WTW Weilheim) with internal calibration means. (B) Sample cell for liquids, Type MFL 3/s for a measuring range  $21 < \epsilon_r < 90$ . (C) Luminescent quartz for fine tuning. (D) Block diagram of the device with G: closed-loop gain, MK: measuring capacitor, Z: sample cell and Q: luminescent quartz. Picture modified from [Oehme, 1962]. (E) Cross-section of the sample cell. Picture modified from [Oehme, 1962].

## Agilent E4991A RF Impedance/Material Analyzer

The Agilent E4991A RF Impedance/Material Analyzer is based on the RF (Radio Frequency) I-V method (see Figure 3.16 (C)). The grand advantages of this method are a high accuracy (1% typ.) and a high resistance range at high frequencies. The Agilent E4991A Analyzer determines the dielectric permittivity  $\epsilon'$ , the dielectric absorption coefficient,  $\epsilon''$ , and the loss factor,  $\tan(\delta)$ , at a variable measuring frequency in a range from 1 MHz to 3 GHz. With this setup the range beyond  $\epsilon_r > 90$  is accessible. The measurements of the dielectric permittivity,  $\epsilon'(\nu)$ , are preceded by a calibration program specified by the manufacturer [Agilent Technologies, 2016]. Figure 3.16 (D) depicts the plate capacitor of the measuring cell in open state. A Kapton membrane with 80  $\mu\text{m}$  thickness and a circular section of 6 mm diameter is located between the parallel plates of the capacitor. One to two drops of the sample liquid to be examined are pipetted into the center of the circular section. The two capacitor plates are guided to each other and adjusted with a screw so that the circuit is closed for measurement. For further analysis, the value of  $\epsilon'$  at a frequency of 1.8 MHz was used from each spectrum.

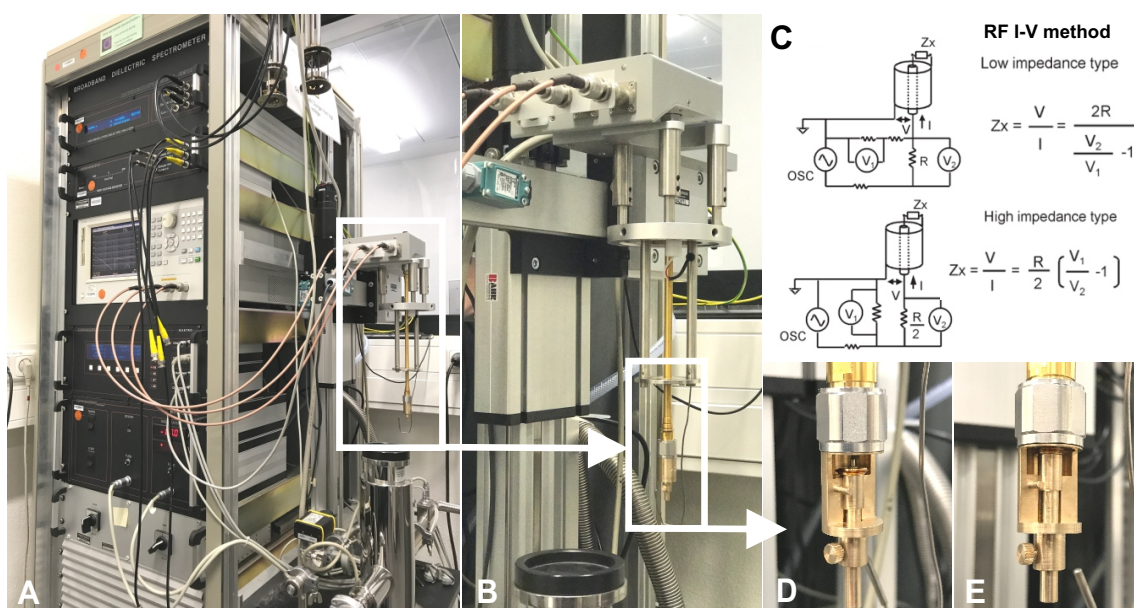


Figure 3.16: (A) Agilent E4991A RF Impedance/Material Analyzer for the measurement of the dielectric permittivity,  $\epsilon'(\nu)$ , in a frequency range  $1 \text{ MHz} < \nu < 3 \text{ GHz}$  [Agilent Technologies, 2011] [Agilent Technologies, 2016]. (B) Close-up of the sample holder. (C) Schematic circuit diagram representing the RF I-V method [Agilent Technologies, 2009]. (D) Open and (E) closed measuring plate capacitor.

## 3.6 High-Pressure Isothermal Solvent Compressibility Measurement

Within the framework of the two projects 'Impact of Macromolecular Crowding and Compression on Protein-Protein Interactions and Liquid-Liquid Phase Separation Phenomena' (see chapter 4) and 'Water-Mediated Protein-Protein Interactions at High Pressures are Controlled by a Deep-Sea Osmolyte' (see chapter 5) a X-ray transmission experiment was performed at DELTA beamline 8 [Lützenkirchen-Hecht et al., 2009] to investigate the impact of crowder molecules, like the polymer polyethylene glycol (PEG) of the molecular weights  $\sim 200 \text{ g mol}^{-1}$ ,  $\sim 600 \text{ g mol}^{-1}$ ,  $\sim 2000 \text{ g mol}^{-1}$ ,  $\sim 4000 \text{ g mol}^{-1}$  and  $\sim 8000 \text{ g mol}^{-1}$  and sucrose on the compressibility of aqueous 10% (w/v) lysozyme solutions at pressures up to 4500 bar (see section 3.1 for materials and sample preparation.). With the compressibility data, the volume fraction,  $\Phi_{\text{lys}}$ , of the protein in solution can be calculated as a function of pressure, crowder identity and crowder concentration.

## DELTA (Dortmund, Germany), Beamline 8

The hard X-ray beamline 8 at the Dortmund **E**LeK**T**ronenspeicherring**A**nlage (**DELTA**) storage ring in Dortmund, Germany, is installed at the superconducting asymmetric wiggler (SAW) and accommodates a pair of Si(311) crystals for the spectral range of 8 to  $\sim 30$  keV as well as a pair of Si(111) crystals plus an additional pair of YB<sub>66</sub>(400) crystals for the low-energy range 2.1 - 14 keV. The flux at the sample position for the Si(111) at 9 keV is  $\sim 10^7 \frac{\text{photons}}{\text{s mA mrad}}$  and for the Si(311) at 20 keV accordingly  $\sim 3 \times 10^6 \frac{\text{photons}}{\text{s mA mrad}}$  [Lützenkirchen-Hecht et al., 2009]. The layout of the beamline is shown in Figure 3.17. In the experiment described in the following, the beam size was 1 (H) x 0.5 (V) mm<sup>2</sup>.

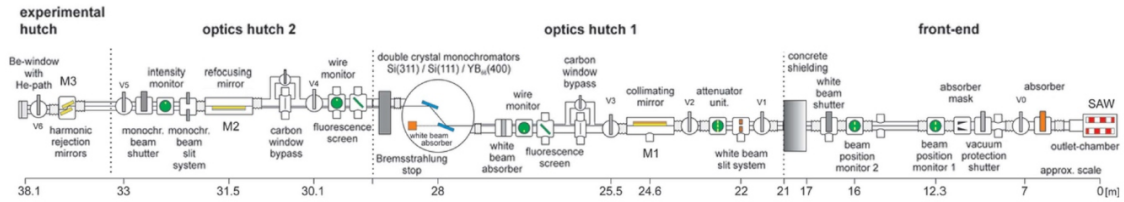


Figure 3.17: Schematic outline of the material science X-ray beamline 8 (DELTA, Dortmund, Germany). Picture adapted from [Lützenkirchen-Hecht et al., 2009].

## High-Pressure X-ray Transmission Setup

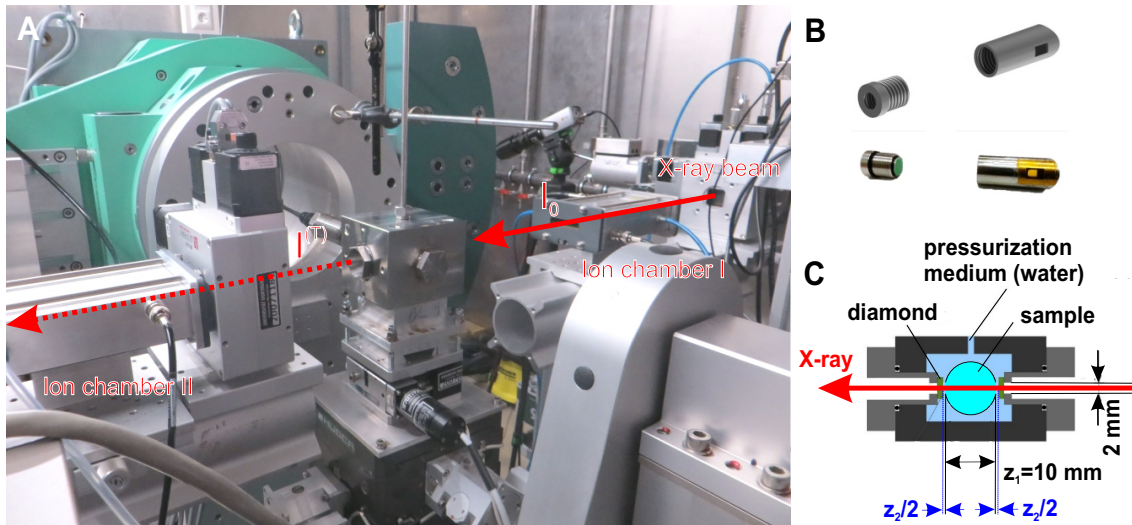


Figure 3.18: (A) Experimental setup of the HHP X-ray transmission experiment at beamline 8 (DELTA) employing a custom-built high-pressure cell by [Wirkert et al., 2014]. (B) Sample holders. Picture modified from [Wirkert, 2015]. (C) Cross section of the sample cell and sketch of the beam path. Picture modified from [Wirkert et al., 2014].

The HHP X-ray transmission setup at beamline 8 (DELTA) is depicted in Figure 3.18. For the pressure dependent X-ray transmission measurements, a custom-built high-pressure cell (developed for X-ray reflectivity measurements of liquid/solid interfaces under high hydrostatic pressure conditions by [Wirkert et al., 2014]) was employed (see Figure 3.18). With a layout similar to the HHP setup II (see section 3.2.1), it was modified to carry larger sample cells with an inner volume of about 375  $\mu\text{l}$  and a diameter of 1 mm in direction of the beam path (see Figure 3.18) (B)+(C). The windows for beam entry and exit are sealed with Kapton foil with 25  $\mu\text{m}$  thickness. After the filling, the sample carrier is closed by a M3 grub screw covered by a rubber membrane to compensate for the volume and pressure changes. The experiment has been carried out in a



pressure range from 50 to 4500 bar in 500 bar steps at a sample temperature of 25°C. For an energy range from 16.86 to 16.91 keV with an increment of 1 eV and a counting rate of 5 s, the radiant flux received and transmitted by the sample of thickness  $d$  was measured, employing ion chambers filled with Ar and Xe at 1 atm. Absorption spectra of 10% (w/v) aqueous lysozyme solutions in 25 mM Bis-Tris buffer at pH 7 containing polymer polyethylene glycol (PEG) or sucrose were recorded for crowder concentrations ranging from 0 to 45% (w/v).

### Data Treatment and Refinement

The linear absorption coefficient<sup>2</sup>,  $\mu$ , and accordingly the mass density,  $\rho$ , of a sample with thickness  $z_1$  can be determined by **Lambert-Beer's law** [Swinehart, 1962] from the X-ray transmission through the sample:

$$\begin{aligned} I^{(T)}(z) &= I_0 \exp(-\mu \cdot z) \\ \Leftrightarrow \ln \left( \frac{I_0}{I^{(T)}(z)} \right) &= \mu \cdot z \\ \Leftrightarrow \ln \left( \frac{I_0}{I^{(T)}(z)} \right) &\propto \rho \cdot z. \end{aligned} \quad (3.7)$$

Here,  $I_0$  is the incident beam intensity at  $z = 0$  and  $I^{(T)}(z)$  the intensity of the attenuated X-ray beam due to absorption after covering the distance  $z$  within the sample. In the calculation of the pressure dependent X-ray transmission through the sample holder with thickness  $z_1$ , the whole distance,  $z_2$ , the beam travels within the pressure transmitting liquid (water) between the inner sample cell and each diamond window (see Figure 3.7 (C)) must also be taken into account. Normalization to the transmission at ambient pressure yields for the pressure dependent X-ray transmission. Using the relation between mass density and attenuation coefficient yields

$$\rho_{\text{sample}}(p) = \frac{\ln \left( \frac{I_0(1\text{bar})}{I^{(T)}(1\text{bar})} \right)}{\ln \left( \frac{I_0(p)}{I^{(T)}(p)} \right)} \cdot \rho_{\text{sample}}(1\text{bar}). \quad (3.8)$$

The relative mass densities of the samples,  $\rho_{\text{sample}}(p)$ , are normalized by Eq. (3.8) to an absolute scale by complementary density measurements at ambient pressure employing an Anton Paar DSA 5000 densitometer.

Based on the finding that lysozyme is pressure resistant over the whole pressure range covered [Schroer et al., 2011a], the volume fraction,  $\Phi_{\text{lys}}$ , of lysozyme in solution at elevated pressures can be calculated directly from the partial specific volume of lysozyme  $\bar{V}^\circ$  [Orthaber et al., 2000, Sophianopoulos et al., 1962, Mylonas and Svergun, 2007], the protein concentration and the measured mass density,  $\rho(p)$ , of the solution *via*

$$\Phi_{\text{lys}}(p) = \bar{V}_{\text{lys}}^\circ \cdot \frac{m_{\text{lys}} \rho(p)}{m_{\text{sol}}}. \quad (3.9)$$

Here,  $m_{\text{lys}}$  and  $m_{\text{sol}}$  describe the mass of the protein powder dissolved in buffer and of the whole protein solution, respectively, and  $\rho(p)$  the experimentally derived pressure dependent density of the protein solution. At 25°C and ambient pressure, the partial specific volume of lysozyme at infinite dilution was found to be  $\bar{V}_{\text{lys}}^\circ = 0.743 \text{ mL g}^{-1}$  [Orthaber et al., 2000, Sophianopoulos et al., 1962, Mylonas and Svergun, 2007, Millero et al., 1976].

<sup>2</sup>For a composite material with several kinds of atoms  $j$ , the absorption coefficient,

$$\mu = \sum_j \left( \frac{\rho N_A}{M} \right)_j \cdot \sigma_j,$$

is determined by the product of number density,  $n_j = \left( \frac{\rho N_A}{M} \right)_j$ , and cross section,  $\sigma_j$ , summed over all atom types  $j$  present in the sample. Here,  $N_A$  is the Avogadro constant,  $M$  the molar mass and  $\rho$  the mass density [Als-Nielsen and McMorrow, 2011].

## Chapter 4

# Impact of Macromolecular Crowding and Compression on Protein-Protein Interactions and Liquid-Liquid Phase Separation Phenomena

Inside cells, the conformational stability of biomolecules as well as equilibria and rates of biochemical reactions are strongly influenced by the high fractional occupancy ( $> 30\%$ ) of ‘background’ species like proteins, osmolytes, nucleic acids and other biopolymers [Ellis and Minton, 2003, Zimmerman and Trach, 1991] (see section 2.1.1). Moreover, the size, shape and concentration of such crowder molecules modulate the intermolecular interactions between biomolecules such as proteins and hence affect their dynamics, phase behavior and spatiotemporal organization. Spatiotemporal control of biological processes is vitally important for cellular function. Recently, next to lipid vesicles also membrane-less organelles were found to play a major role in compartmentalizing the cell, thereby achieving the necessary physical separation of the cellular compounds and processes.

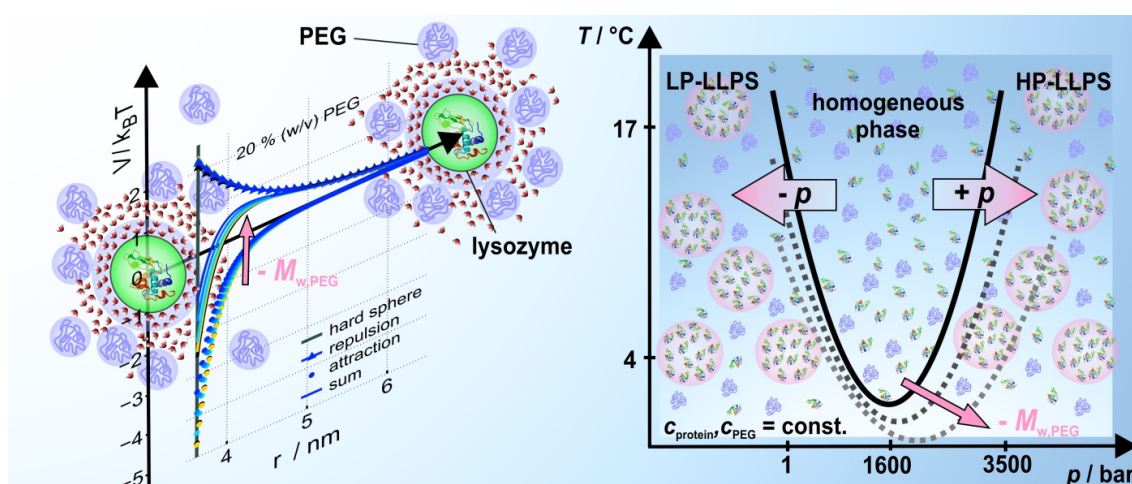


Figure 4.1: The intermolecular interaction potential,  $V(r)$ , of dense lysozyme solutions (*left side*), which governs the spatial distribution of the protein molecules in solution and the location of the (pressure-dependent) liquid-liquid phase separation (LLPS) region (*right side*), in various crowding environments (i.e. 20% (w/v) PEG solutions of various molecular weights,  $M_{w,PEG}$ ).

These membrane-less organelles consist of multicomponent viscous liquid droplets (coacervates) formed *via* segregation of molecules from complex protein or protein-nucleic acid mixtures by spontaneous liquid-liquid phase separation (LLPS) [Brangwynne et al., 2015]. The occurrence of a metastable LLPS region of coexisting dilute and protein rich liquid phases has been reported for highly concentrated protein solutions at low temperatures and in the presence of precipitating additives such as salt [Muschol and Rosenberger, 1997, Möller et al., 2014a, Schulze et al., 2016] or polymers [Annunziata et al., 2002, Annunziata et al., 2003, Wang and Annunziata, 2007] (see section 2.3.4). The propagation by division and subsequent growth of such active self-organized liquid droplets may also have served as prebiotic protocells [Zwicker et al., 2017]. By studying the physics of LLPS phenomena we gain insights into mechanisms underlying the assembly and disassembly of such biomolecular condensates present in the living cell [Banani et al., 2017, Long et al., 2005] and into their particular role for cellular function when exposed to internal and external stressors, such as high osmotic pressure due to high osmolyte and crowder concentrations (see section 2.1), extreme temperatures or high hydrostatic pressure (see section 2.3). The intermolecular interactions and microscopic structure of ternary protein-cosolute-buffer systems and their effects on the temperature- and pressure-dependent phase behavior of crowded protein solutions are still largely unknown. In addition to direct intermolecular interactions resulting from electrostatic, van der Waals or hydrophobic forces, the entropically driven excluded volume effect can induce attractive forces between proteins in the presence of crowder molecules (see section 2.1.1).

In this chapter we investigate the intermolecular interactions that govern the spatial arrangement of proteins in solution and their effects on the temperature- and pressure-dependent boundaries of the (metastable) liquid-liquid phase separation region in various crowding environments. Since we focus on the crowding effect, the well-characterized monomeric protein lysozyme of chicken egg white is employed as a model protein. The conditions prevailing in the crowded cellular environment are mimicked by macro- and nanomolecular crowding agents such as the synthetic, biocompatible polymer polyethylene glycol (PEG) and the disaccharide sucrose. To investigate to what extent the polymer properties play a role in the description of crowding by smallest polymer molecules, sucrose was chosen for reference as an inert nanomolecular crowder only, with a similar molecular weight, size and osmotic coefficient as PEG 200 and PEG 600. The non-ionic straight chain polymer PEG  $(-(\text{CH}_2-\text{CH}_2-\text{O})_N-)$  exists in a random coil state in aqueous solution [Maxfield and Shepherd, 1975] and is often employed in biochemical and pharmaceutical applications [Harris, 1992]. PEG has the capacity to exclude volume and dehydrates biopolymers at high concentrations through competition for hydration water. By applying small angle X-ray scattering (SAXS) in combination with a liquid theoretical approach we obtain the intermolecular protein-protein interaction potential  $V(r)$  and the second osmotic virial coefficient,  $B_{22}$ , as a function of crowder concentration and identity and, in combination with complementary light transmission measurements (turbidity), further insight into the effect of different crowding environments on the phase behavior of dense lysozyme solutions in the metastable LLPS region. We investigate the influence of the crowder's shape, size and concentration on  $V(r)$  and the phase boundaries in the  $p$ - $T$ -plane by employing more than three orders of magnitude of the polymer's molecular weight ( $M_w \sim 200 - 35000 \text{ g mol}^{-1}$ ) and concentrations crossing from the dilute to the semi-dilute polymer regime, thereby mimicking crowding scenarios as they occur in heterogeneous biological cells. In addition to their biological relevance, these studies also provide a deeper understanding of the forces controlling the  $B_{22}$  region, which is prone to lead to protein crystallization [Durbin and Feher, 1996, Tardieu et al., 2001, Bonneté and Vivarès, 2002].

This chapter is structured as follows: In section 4.1, the protein's conformational stability upon pressurization and in the presence of the polymer is investigated by SAXS measurements of diluted lysozyme solutions, yielding size and shape of the protein in solution. In section 4.2 we analyze the pressure-dependent intermolecular interaction potential,  $V(r)$ , governing the spatial distribution of proteins in solution, in various crowding environments employing SAXS in combination with a liquid state theoretical approach. In section 4.3, we explore the effects of PEG on the shape of the protein liquid-liquid phase separation (LLPS) region in the  $p$ - $T$ -plane over a wide range of temperatures and pressures for various polymer molecular weights and concentrations. Finally, the results are summarized in section 4.4.



The content of this chapter is published in the following original publication and has been rephrased for this thesis:

Julius, K., Weine, J., Gao, M., Latarius, J., Elbers, M., Paulus, M., Tolan, M., and Winter, R. (2019). Impact of Macromolecular Crowding and Compression on Protein-Protein Interactions and Liquid-Liquid Phase Separation Phenomena, *Macromolecules*, 52(4):1772-1784 (Copyright © 2019 American Chemical Society)

## 4.1 Pressure Dependence of the Protein’s Radius of Gyration in the Presence of PEG

Information on the proteins shape and size under particular solution conditions can be derived from the small- angle scattering of a single lysozyme molecule averaged over its orientation,  $\langle |F(\mathbf{q})|^2 \rangle_\Omega$  (see section 2.4.2). The protein form factor  $\langle |F(\mathbf{q})|^2 \rangle_\Omega$  is provided experimentally by the SAXS intensity of a dilute solution of non-interacting lysozyme molecules ( $\sim 1\%$  (w/v)) and can be successfully refined by the scattering calculated from the atomic coordinates (+ hydration) of lysozyme (crystal structure PDB entry: 1LYZ [Harata, 1994]) employing the program CRY SOL [Svergun et al., 1995].

In order to exclude potential pressure-dependent changes in the protein’s native folded state, high-pressure SAXS measurements were performed on diluted 1% (w/v) lysozyme in 25 mM Bis-Tris buffer (pH 7) at pressures from 1 to 3500 bar. Moreover, the system was checked for crowder-induced conformational changes at ambient and at elevated pressures ( $p = 1 - 3500$  bar) by adding 15% (w/v) of small (PEG200, PEG 600), medium (PEG 2000) and large (PEG 35000) polymer to the buffer solution. Figure 4.2 (a) depicts the experimental SAXS curves of 1% (w/v) lysozyme dissolved in 25 mM Bis-Tris + 15% (w/v) PEG 2000 aqueous solution (pH 7) for selected pressures. The refinements of the scattering intensities of the diluted lysozyme solutions (*solid lines*), made by employing the inverse Fourier-transformation program GNOM [Svergun et al., 1988, Svergun, 1992], yield an approximation of the major dimension  $D_{\max}$  of the protein in solution, the pair distance distribution function  $p(r)$  (see Figure 4.2 (c)), as well as the protein’s radius of gyration,  $R_{G,\text{lys}}$ . The pronounced maximum in the experimental data when plotted in the Kratky presentation ( $q^2 I(q)$  vs.  $q$ ) for selected pressures, indicates a globular shape of the protein present at all solution conditions (see Figure 4.2 (b)). Further, the protein’s radius of gyration,  $R_{G,\text{lys}}$ , was determined from the low- $q$  Guinier region of the scattering data [Guinier, 1939], for  $R_{G,\text{lys}} < 1.3$  (see section 2.4.2), employing the program PRIMUS [Konarev et al., 2003]. Figure 4.2 (e)-(h) display the Guinier plots of the 1% (w/v) lysozyme + 15% (w/v) PEG (200, 600, 2k, 35k) solution scattering intensities for 1 bar, 2 kbar and 3.5 kbar, with the corresponding refinements (*solid lines*). Figure 4.2 (d) depicts the radii of gyration,  $R_{G,\text{lys}}$ , found for lysozyme in pure 25 mM Bis-Tris buffer solution (pH 7, 25°C) as well as in the presence of 15% (w/v) polymer of various molecular weights as a function of pressure. In accordance with literature data [Schroer et al., 2011a], we find that lysozyme is conformational stable with a constant radius of gyration of  $R_{G,\text{lys}} = 1.45 \pm 0.05$  nm in the whole pressure range covered and regardless the respective crowding additive.

For the combined form and structure factor analysis of the scattering from dense lysozyme solutions, the lysozyme form factor was approximated by the radially averaged scattering function of a prolate ellipsoid [Shukla et al., 2008, Liu et al., 2005b]. The lysozyme form factor can be successfully modeled from the SAXS intensity curves from the diluted 1% (w/v) lysozyme solutions by the radially averaged analytical scattering function,  $P(q)$  of an prolate ellipsoid of revolution with the semi-axes  $a = 1.57$  nm and  $b = 2.42$  nm, effective hard-sphere diameter  $\sigma_{\text{lys}} = 2(a^2b)^{1/3}$  and volume  $V_p = 4/3\pi(a^2b)$  (see section 2.4.2), in good agreement with previous works [Shukla et al., 2008, Schroer et al., 2011a, Schroer et al., 2011b, Liu et al., 2005b]. The analytic form factor  $P(q)$  calculated by this method is in good agreement with the scattering calculated from the crystal structure (+ hydration) of lysozyme employing CRY SOL [Svergun et al., 1995], except that a small additive constant background ( $0.0105 \cdot P(q)|_{q=0}$ ) is needed in order to describe the data at high  $q$  [Shukla et al., 2008].

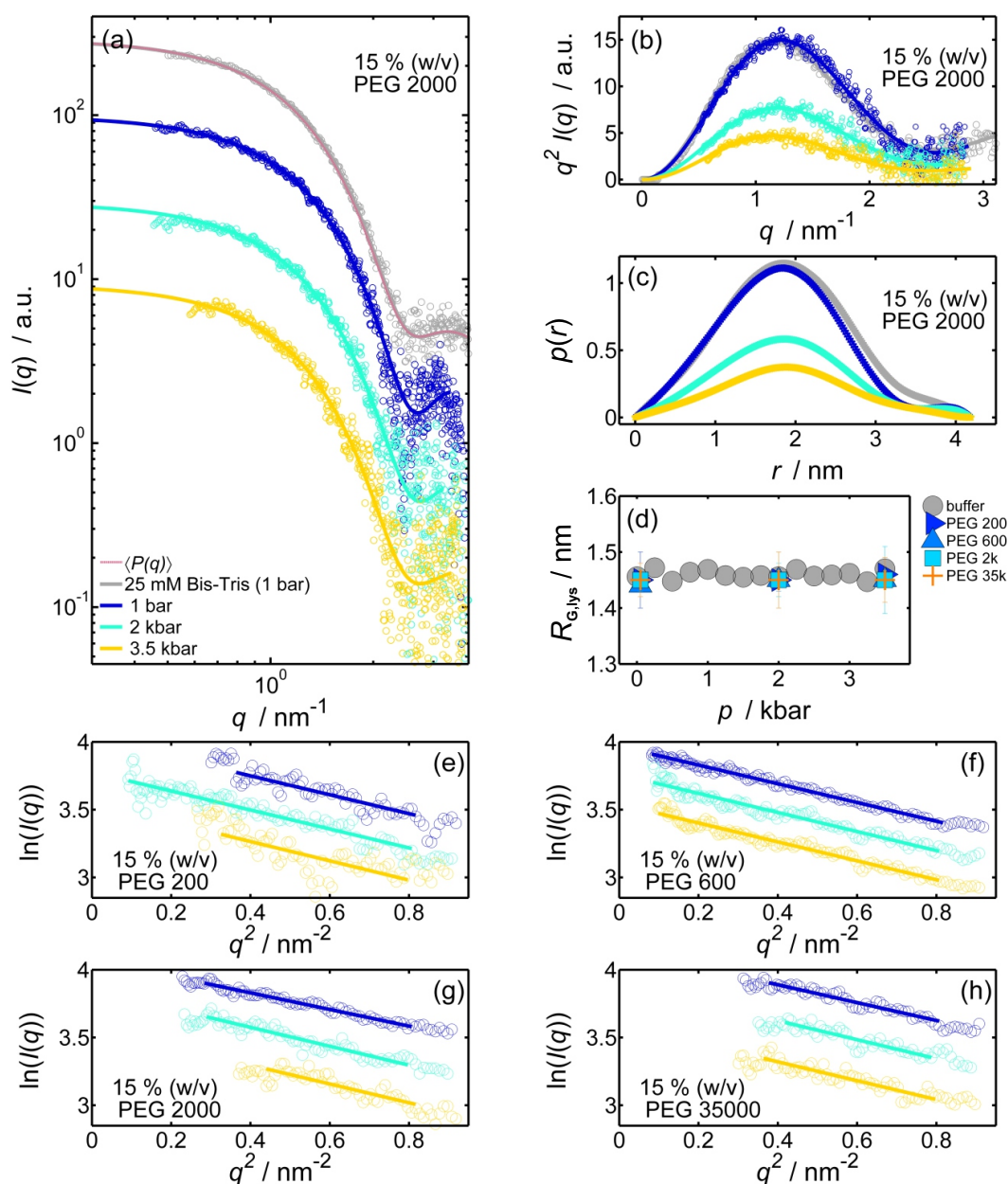


Figure 4.2: (a) Experimental SAXS curves of 1% (w/v) lysozyme dissolved in 25 mM Bis-Tris + 15% (w/v) PEG 2000 aqueous solution (pH 7), collected at 25°C in a pressure range from 1 – 3500 bar. The scattering data and the corresponding refinements made by employing the inverse Fourier transformation program GNOM [Svergun et al., 1988, Svergun, 1992] (*solid lines*) are shifted for reasons of clarity. The refined scattering intensity of the polymer-free 1% (w/v) lysozyme solution at ambient pressure (*grey marker*) as well as the theoretical scattering of a prolate ellipsoid of revolution,  $P(q)$ , (*magenta*) are depicted as well for reference. (b) SAXS data and refinement plotted in the Kratky presentation ( $q^2 I(q)$  vs.  $q$ ) for selected pressures. (c) Radial pair-distance distribution function,  $p(r)$ , as a function of pressure. (d) Pressure dependence of the protein's radius of gyration,  $R_{G,lys}$ , in pure 25 mM Bis-Tris buffer solution (pH 7, 25°C) and in the presence of 15% (w/v) polymer of various molecular weights, derived from the scattering data. (e)-(h) Guinier plot of the 1% (w/v) lysozyme + 15% (w/v) PEG (200, 600, 2k, 35k) solution scattering intensities for 1 bar, 2 kbar and 3.5 kbar, with the corresponding refinements (*solid lines*) obtained by PRIMUS [Konarev et al., 2003]. Reprinted with permission from [Julius et al., 2019]. Copyright © 2019 American Chemical Society.

The refined scattering intensity of the polymer-free 1% (w/v) lysozyme solution at ambient pressure (*grey marker*) as well as the theoretical scattering of a prolate ellipsoid of revolution  $P(q)$  (*magenta*) are depicted in Figure 4.2 (a) for reference.

## 4.2 Influence of Macro- and Nanomolecular Crowders on the Protein-Protein Interaction

To explore the effects of different levels of nano- and macromolecular crowding on the pressure-dependent protein pair-interaction potential, high pressure SAXS data of dense aqueous lysozyme-crowder mixtures were recorded in a pressure range from 1 to 4000 bar at 25°C. The polymer polyethylene glycol with different molecular weights ( $200 \leq M_w \leq 35000$ ) g mol<sup>-1</sup> and the compatible disaccharide sucrose ( $M_w = 342.30$  g mol<sup>-1</sup>) serve as crowding agents and were used in concentrations of  $c_{\text{crowder}} = 1$  to 50% (w/v), the solubility limit of PEG [Bončina et al., 2008].

The total scattering intensity,  $I(q)$ , of a ternary mixture consisting of lysozyme and the polymer polyethylene glycol dissolved in aqueous buffer solution, includes, next to the scattering from the protein,  $I_{\text{lys-lys}}(q)$ , and the polymer,  $I_{\text{PEG-PEG}}(q)$ , an additional scattering cross-term,  $I_{\text{lys-PEG}}(q)$ , emerging from correlations between the lysozyme and PEG molecules [Tong et al., 1990], i.e.

$$I(q) \propto I_{\text{lys-lys}}(q) + I_{\text{lys-PEG}}(q) + I_{\text{PEG-PEG}}(q). \quad (4.1)$$

Owing to chain flexibility, interpenetration and polydispersity in polymer shape and size, the scattering intensity of the neat aqueous PEG solutions shows no significant wave vector dependency within the range of momentum transfer covered here and is simply proportional to the polymer concentration. Moreover, at ambient conditions, the electron density contrast between water ( $\rho_{\text{el,H}_2\text{O}} = 0.334$  electrons Å<sup>-3</sup>) and polyethylene glycol (e.g.,  $\rho_{\text{el,PEG}}(20\% \text{ w/v PEG } 200) = 0.336$  electrons Å<sup>-3</sup>) [Tyree et al., 2018] is much smaller than for the protein ( $\rho_{\text{el,protein}} = 0.43$  electrons Å<sup>-3</sup>) [Crick, 1957]. Consequently, the forward scattering,  $I(q \rightarrow 0) = n\Delta\rho^2V_p^2$  of the polymer [Svergun and Koch, 2003] is suppressed and we find that the scattering contributions of the protein-protein interaction structure factor and protein form factor exceed the polymer solution scattering by almost two orders of magnitude even at high polymer concentrations (see Figure 4.2 and Appendix A, Figure A.3). At higher polymer concentrations, increasing correlations between the polymer coils and the protein emerge and manifest in form of a polymer size specific structure factor,  $S_{\text{lys-PEG}}(q)$ , which also contributes to the scattering intensity. However,  $S_{\text{lys-PEG}}(q)$  is weighted by the particles form factors, particle-buffer electron density contrasts and particle number densities. Moreover, since PEG consists of flexible and polydisperse random coils in aqueous solution, the interaction potential for protein-polymer interactions is much softer and longer ranged than a typical hard-sphere potential. Hence, the oscillations in the structure factor  $S_{\text{lys-PEG}}(q)$ , describing these weak correlations, are damped and do not have to be taken into account in this work in order to extract the effective intermolecular pair-interaction potential of the protein [D'Aguanno and Klein, 1991]. Under these conditions, the polymer solution can be treated as a solvent and can be subtracted from the total scattering intensity of the protein-polymer mixture,  $I(q)$ , to obtain  $I_{\text{lys-lys}}(q)$  (i.e., Eq. (4.2)). We approximate the ternary protein-polymer-buffer solution by an effective two-component system in which the non-adsorbing polymer-buffer solution is treated as background solvent and the influence of the polymer is simply expressed by an effective intermolecular pair interaction potential in the coordinates of the protein.

Under the assumptions made, the scattering profiles,  $I(q)$ , of aqueous solutions of interacting monodisperse globular lysozyme molecules in the presence of sucrose or the polymer PEG can be modeled by

$$I(q) \propto n \cdot \Delta\rho^2 \cdot V_p^2 \cdot P(q) \cdot S_{\text{eff}}(q) \quad (4.2)$$

within the decoupling approximation [Kotlarchyk and Chen, 1983, Liu et al., 2005b] (see section 2.4.4). Here,  $n$  denotes the number density of particles in solution, which is related to the protein's volume fraction  $\Phi_{\text{lys}}$ .  $\Delta\rho$  describes the electron density contrast and  $V_p$  the volume of

the particle. The protein’s form factor,  $P(q)$  is modeled theoretically by the radially averaged scattering function of a prolate ellipsoid of revolution (see section 4.1). The effective structure factor,  $S_{\text{eff}}(q)$ , represents an additional scattering contribution for solutions with higher protein concentrations and is sensitive to the spatial order and thus the intermolecular interactions of the scattering particles.  $S_{\text{eff}}(q)$  is linked to the proteins effective intermolecular interaction potential,  $V(r)$ , within the mean-spherical approximation (MSA) [Liu et al., 2005b, Hansen and McDonald, 2013] (see section 2.4.4). The effective protein pair interaction potential,  $V(r)$ , which acts on lysozyme molecules in solution whose centers are separated by the distance  $r$ , is modeled in the framework of the Derjaguin-Landau-Verwey-Overbeek (DLVO) theory as the sum of a long-ranged screened Coulomb potential,  $V_{\text{SC}}(r)$ , a repulsive hard-sphere potential,  $V_{\text{HS}}(r)$ , and a short-ranged attractive Yukawian-like potential,  $V_{\text{Y}}(r)$  [Möller et al., 2012, Schroer et al., 2011a] (see section 2.2.3). It should be noted that the following potential factors that may contribute to the protein-protein interaction in dense protein-crowder mixtures are not included in the parametrization of DLVO potential: Steric / depletion forces, hydrogen bonding, soft crowder-protein interactions or liquid-like ordering of the solute and hydration repulsion at short distances. The effective net charge of the protein is set to a constant value of  $Z_{\text{eff}} = +8e$  at pH 7 when calculating  $V_{\text{SC}}(r)$  (see Eq. (2.20)), which applies to all solution conditions examined here [Kuehner et al., 1999]. The pH value is neither affected by the presence of PEG nor sucrose [McPherson, 1990]. In accordance with previous works [Möller et al., 2012, Schroer et al., 2011a], the width of the attractive part of the potential is fixed at  $d = 0.3$  nm, which corresponds to one hydration layer, only, regardless of the presence of crowders (see section 2.2.3). The DLVO potential, describing the lysozyme interaction in the crowded environment, is determined by the refinement of the experimental effective structure factor,  $S_{\text{eff}}(q)$ , which is extracted from the experimental scattering intensities of dense protein-crowder mixtures,  $I(q)$ , by dividing them by the analytical protein form factor,  $P(q)$ . The only free parameter in refining the experimental data is the strength of the attractive Yukawian-like part of the total interaction potential,  $J$ . In order to describe the total protein pair-interaction, the osmotic second virial coefficient,  $B_{22}$ , and its normalized dimensionless value,  $b_2$ , are calculated from the DLVO potential using Eqs. (2.3) and (2.4).

### Changes of the Solutions Compressibility by the Crowding Agents

In SAXS data analysis, a further parameter is the volume fraction,  $\Phi_{\text{lys}}$ , occupied by the protein in the sample volume. The conformation of the protein lysozyme was found to be stable in pure buffer in a pressure range up to 5 kbar [Schroer et al., 2011a]. However, applying pressure leads to a reduction of the volume of the surrounding solvent and hence an increase of the volume fraction of the protein. At a given protein concentration, the isothermal compressibility of the solution at high pressures is strongly dependent on the crowding level. Our own high-pressure X-ray transmission measurements on highly concentrated 10% (w/v) lysozyme + 25 mM Bis-Tris (pH 7, 25°C) solutions reveal the impact of crowder molecules of various sizes and chemical properties (sucrose, PEG of molecular weight  $M_w \sim 200 - 8000$  g mol<sup>-1</sup>) at concentration ranging from 0 to 45% (w/v) on the solutions compressibility and allowed us to calculate the protein volume fraction,  $\Phi_{\text{lys}}$ , at pressures up to 4500 bar (see section 3.1 for more details on the sample preparation and section 3.6 for additional information on the experimental setup and data analysis). Based on the finding of a pressure resistant conformation of lysozyme and given that the protein is dissolved in the same volume regardless of the crowder concentration, the volume fraction of lysozyme in solution,  $\Phi_{\text{lys}}$ , at elevated pressures and at different crowding conditions can be calculated directly from the partial specific volume of lysozyme,  $\bar{V}^0$ , and the measured mass density,  $\rho(p)$ , of the solution employing Eq. (3.9). The experimentally derived mass densities of the crowder solutions and protein-crowder mixtures at ambient pressure,  $\rho(c)$ , are shown in Figure 4.3. The crowder-induced modulation of the pressure dependence of the proteins volume fraction,  $\Phi_{\text{lys}}(p)$ , is shown in Figure 4.4 as a function of crowder concentration and crowder identity (i.e., molecular weight,  $M_w$ ). For other PEG molecular weights, the pressure dependence of  $\Phi_{\text{lys}}$  was estimated by extrapolating the values obtained from the transmission experiment.

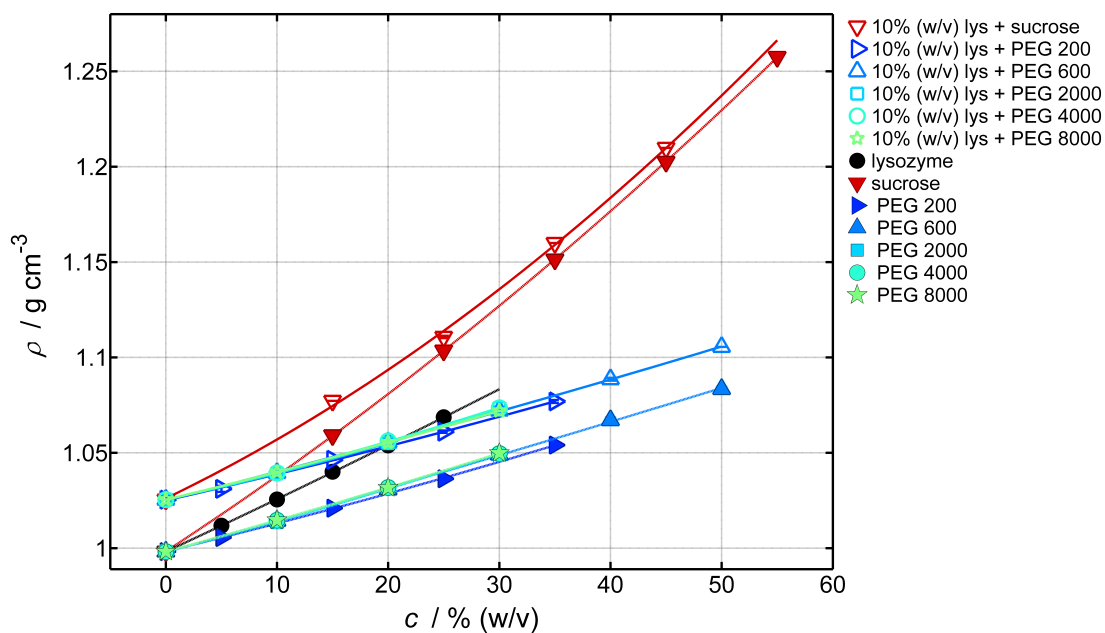


Figure 4.3: Mass densities,  $\rho$ , of 10% (w/v) lysozyme, polyethylene glycol (PEG 200, PEG 600, PEG 2000, PEG 4000, PEG 8000) and sucrose dissolved in 25 mM Bis-Tris (pH 7) solution and protein-crowder mixtures thereof at 25°C and ambient pressure as a function of crowder concentration,  $c$ , displayed together with the corresponding polynomial refinements (*lines*). Reprinted with permission from [Julius et al., 2019]. Copyright © 2019 American Chemical Society.

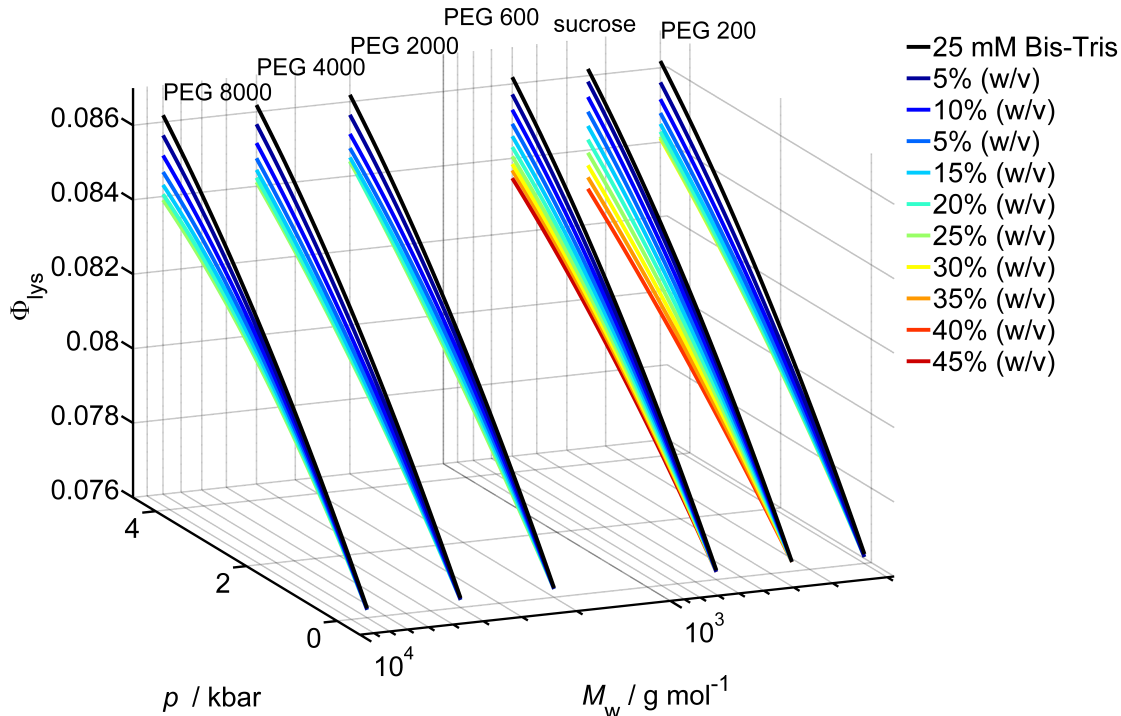


Figure 4.4: Volume fraction,  $\Phi_{\text{lys}}$ , of 10% (w/v) lysozyme in 25 mM Bis-Tris (pH 7) solution in a pressure range from 1 – 4500 bar at 25°C as a function of the molecular weight,  $M_w$ , of the crowding agent ( $M_{w,\text{sucrose}} = 342.3 \text{ g mol}^{-1}$ ) for various crowder concentrations,  $c$ . Reprinted with permission from [Julius et al., 2019]. Copyright © 2019 American Chemical Society.



## Changes of the Solutions Dielectrics by the Crowding Agents

The screened Coulomb potential,  $V_{SC}(r)$ , contributing to the DLVO potential (see Eq. (2.20)) is modulated by changes of the solutions static dielectric permittivity,  $\epsilon_r$ . This occurs both upon pressurization and upon addition of the crowding agents. Here, the pressure dependence of the solutions dielectric permittivity in presence of the crowders is reasonably well approximated by the pressure dependence of  $\epsilon_r(p)$  of water [Floriano and Nascimento, 2004]. The change in the relative dielectric permittivity of water with the concentration,  $c$ , of the solute (i.e. PEG, sucrose) is described by the dielectric increment,  $\delta = d\epsilon_r/dc$ , which is obtained for all solution conditions by our own dielectric spectroscopy experiments (see section 3.5 for experimental details) or from literature. Figure 4.5 displays the relative static dielectric permittivity,  $\epsilon_r$ , of the polymers in 25 mM Bis-Tris buffer (pH 7) as well as of aqueous sucrose solution [Malmberg and Maryott, 1950] at 25°C and ambient pressure as a function of concentration,  $c$ .

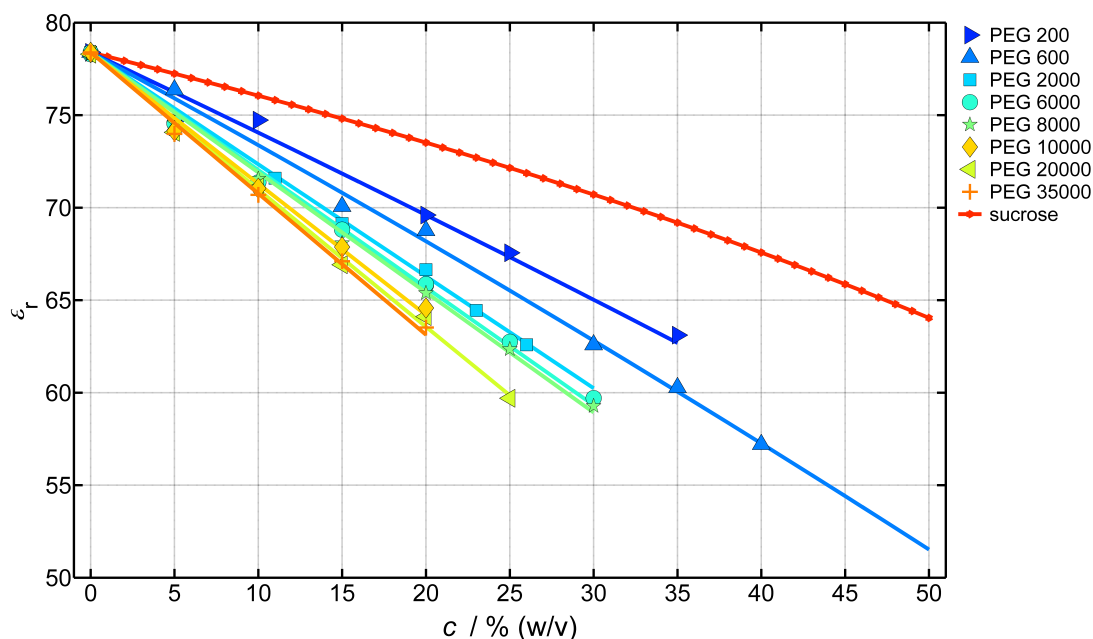


Figure 4.5: Relative static dielectric permittivity,  $\epsilon_r$ , of polyethylene glycol (PEG) + 25 mM Bis-Tris (pH 7) solutions at ambient pressure and 25°C for various PEG sizes as a function of polymer concentration,  $c$ . Data is shown together with the corresponding refinements (*solid lines*). The data for sucrose solutions at 25°C and ambient pressure were calculated from [Malmberg and Maryott, 1950]. The dielectric increments,  $\delta = d\epsilon_r/dc$ , of the polymers in buffer at 25°C: PEG 200 ( $\delta = -4.33$  (10% w/v) $^{-1}$ , this relation is not linear); PEG 600 ( $\delta = -5.01$  (10% w/v) $^{-1}$ , this relation is not linear); PEG 2000 ( $\delta = -6.1$  (10% w/v) $^{-1}$ ); PEG 6000 ( $\delta = -6.4$  (10% w/v) $^{-1}$ ); PEG 8000 ( $\delta = -6.5$  (10% w/v) $^{-1}$ ); PEG 10000 ( $\delta = -7.1$  (10% w/v) $^{-1}$ ); PEG 20000 ( $\delta = -7.4$  (10% w/v) $^{-1}$ ); PEG 35000 ( $\delta = -7.6$  (10% w/v) $^{-1}$ ); sucrose ( $\delta = -1.19$  (10% w/v) $^{-1}$ , this relation is not linear [Malmberg and Maryott, 1950]). Reprinted with permission from [Julius et al., 2019]. Copyright © 2019 American Chemical Society.



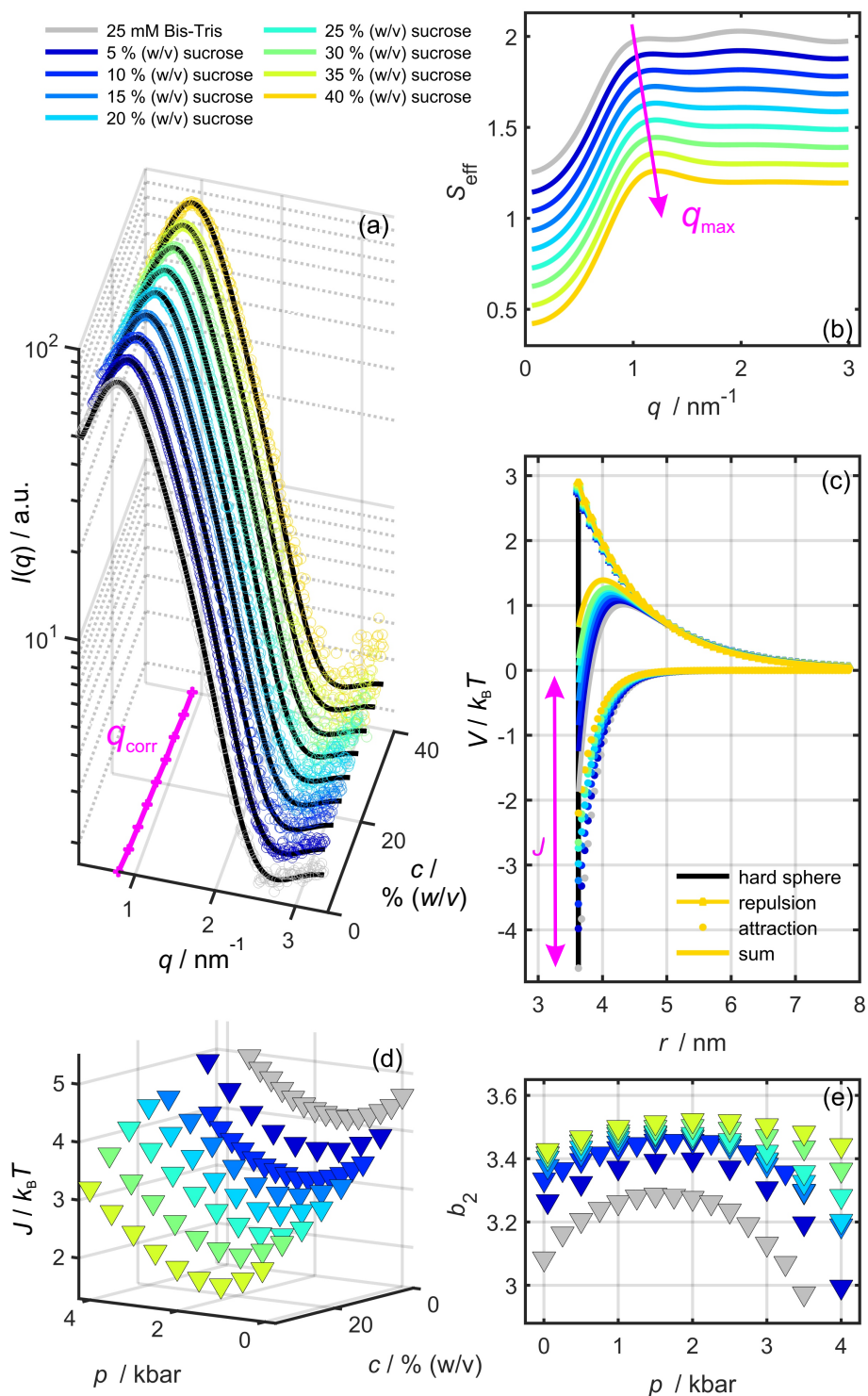


Figure 4.6: (a) SAXS data of 10% (w/v) lysozyme dissolved in 25 mM Bis-Tris (pH 7) at various sucrose concentrations,  $c$ , at ambient pressure and 25°C together with the corresponding refinements (*solid black lines*). (b) Refinements for the effective structure factor,  $S_{\text{eff}}(q)$ , as a function of sucrose concentration (*curves are shifted for clarity, see Appendix A, Figure A.1 for non-shifted representation*). (c) Total effective pair-interaction potential with its contributing parts for various amounts of sucrose at ambient pressure. (d) Strength of the attractive part of the pair-interaction potential,  $J$ , as a function of pressure,  $p$ , and sucrose concentration,  $c$ . (e) Pressure dependence of the normalized osmotic second virial coefficient,  $b_2$ , for various sucrose concentrations. Reprinted with permission from [Julius et al., 2019]. Copyright © 2019 American Chemical Society.

## Influence of Sucrose on the Protein-Protein Interaction

Figure 4.6 shows the analysis of the SAXS intensities of dense protein-crowder mixtures by the example of 10% (w/v) lysozyme in 25 mM Bis-Tris (pH 7, 25°C) in the presence of the nanomolecular crowder sucrose at concentrations,  $c$ , in the range of 5 to 40% (w/v). Figure 4.6 (a) depicts the refinements for the scattering intensities,  $I(q)$ , displayed as *solid black lines*, and (b) the corresponding refinements for the effective structure factors,  $S_{\text{eff}}(q)$  (see also Appendix A, Figure A.1). The pronounced correlation peak in the SAXS intensity curves,  $I(q_{\text{corr}})$ , is a direct consequence of a repulsive short-range ordering of the globular protein in solution, and the mean intermolecular distance between adjacent lysozyme molecules can be estimated by the relation  $d_{\text{lys}} \simeq 2\pi/q_{\text{max}}$  from the position of the first maximum,  $q_{\text{max}}$ , of the effective structure factor,  $S_{\text{eff}}(q)$ . As can be seen from the rise of  $S_{\text{eff}}(q_{\text{max}})$  and  $q_{\text{max}}$  with increasing sucrose concentration, the mean distance between the proteins is gradually reduced by adding sucrose to the buffer solution (see Figure 4.8). This can be rationalized by the growing excluded volume imposed by the nano-crowder. The DLVO potential,  $V(r)$ , determined by refining the experimental effective structure factors, is shown in Figure 4.6 (c) together with its contributing parts for various sucrose concentrations,  $c$ . The effective protein-protein pair-interaction potential exhibits a maximal value (energy barrier) at all crowding levels, followed by a rapid decline at greater distances, while generally remaining repulsive. The decrease of the solvent's static dielectric permittivity with rising sucrose concentration, as described by the decrement [Malmberg and Maryott, 1950]  $d\epsilon_r/dc = -1.19$  (10% w/v) $^{-1}$  (see Figure 4.5), leads to a reduced range of the repulsive Coulomb potential,  $V_{\text{SC}}(r)$ , due to a decreasing Debye Hückel screening length,  $\lambda_D$ , but also to an increased strength. As shown in Figure 4.6 (d), the attractive interaction (i.e.  $J(c, p)$ ) decreases monotonously with increasing sucrose concentration as compared to the pure buffer system, while the non-monotonic behavior under pressure, as observed in previous studies on dense lysozyme solutions in neat buffer [Schroer et al., 2011a] as well as in the presence of salts [Möller et al., 2014a, Möller et al., 2012] and various organic osmolytes [Julius et al., 2018b, Schroer et al., 2011b], remains essentially unchanged. A pressure increase up to  $\sim 1.6$  kbar leads to a reduction of the mean intermolecular distance of the proteins,  $d_{\text{lys}}$ , in the compressed solution and also to a decrease of the attractive interaction (i.e., the strength  $J$ ), followed by a trend reversal upon further pressurization. The increasing attraction and growing intermolecular distances at further compression were attributed to structural changes in the bulk water and increased hydration repulsion [Soper and Ricci, 2000, Katayama et al., 2010]. The nano-crowder sucrose renders the effective pair-interaction slightly more repulsive, which is also reflected in the increase of the normalized second osmotic virial coefficient  $b_2$  with sucrose concentration (see Figure 4.6 (e)).

## Influence of PEG on the Protein-Protein Interaction

As described in section 2.2.2, the structure of the polymer solution and its properties strongly depend on the polymer's degree of polymerization (i.e.,  $M_w$ ) and its concentration in solution. In order to investigate the effect of the macromolecular crowder PEG of various molecular weights (sizes) on the pressure-dependent protein pair-interaction in both the dilute and the semi-dilute polymer concentration regime, SAXS measurements were performed on dense lysozyme-PEG mixtures at 25°C in a pressure range from 1 up to 3500 bar. In Figure 4.7 (a) the SAXS data for 10% (w/v) lysozyme dissolved in 50 mM Bis-Tris (pH 7) aqueous solution containing 20% (w/v) PEG 20k, 2k, 600 and 200, are shown together with the corresponding refinements (*solid lines*) of the effective structure factor,  $S_{\text{eff}}(q)$ , and the protein form factor,  $P(q)$  (see also Appendix A, Figure A.2). Significant changes in the position and magnitude of the first maximum of the effective structure factor,  $q_{\text{max}}$ , as well as changes in potential parameters with varying polymer size are clearly visible (see Figure 4.7 (b)). Regardless of the additive's identity, the repulsive energy barrier in  $V(r)$  is persistent, however, and effectively does not fall below the value found for the pure buffer solution. The positive values for the second osmotic virial coefficient,  $B_{22}$ , reflect the repulsive nature of  $V(r)$  (see Figure 4.7 (c)). Here, the transition to the semi-dilute regime ( $c_{\text{PEG}} \geq c^*(M_w)$ ), whose value is specific to the molecular weight of the polymer (see section 2.2.2), is visualized by empty symbols. In accordance with literature data for similar buffer conditions [Liu et al., 2004], the osmotic second virial coefficient,  $B_{22}$ , for 10% (w/v) lysozyme in the neat 50 mM Bis-Tris

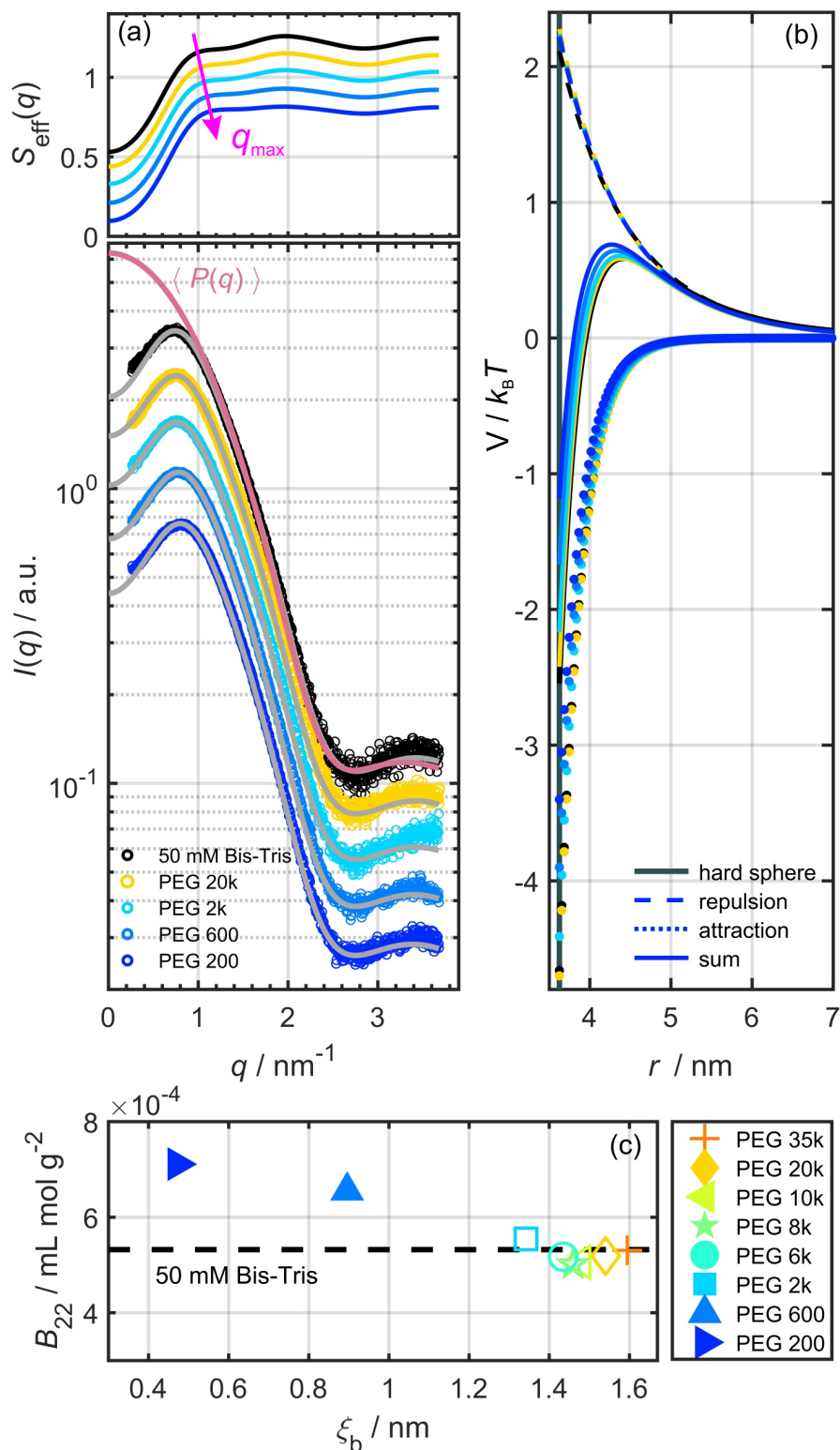


Figure 4.7: (a) Experimental SAXS intensities of 10% (w/v) lysozyme dissolved in 50 mM Bis-Tris (pH 7, 25°C) and 20% (w/v) PEG of selected  $M_w$  at ambient pressure, shown together with the refinements for the scattering intensities ( $I(q)$  and  $P(q)$ ), and the effective structure factors,  $S_{\text{eff}}(q)$  (curves are shifted for clarity, see Appendix A, Figure A.2 for non-shifted representation of  $S_{\text{eff}}(q)$ ). (b) The corresponding effective pair-interaction potential with its contributing parts and (c) osmotic second virial coefficients,  $B_{22}$ , as a function of the spatial correlation length  $\xi_b$ . Empty symbols visualize the  $B_{22}$  values for PEG concentrations exceeding  $c^*$ . Reprinted with permission from [Julius et al., 2019]. Copyright © 2019 American Chemical Society.

(pH 7) buffer solution amounts to  $5.32 \cdot 10^{-4} \text{ mL mol g}^{-2}$ . Scaling to the excluded volume contribution,  $B_2^{\text{HS}}$ , yields the corresponding reduced osmotic second virial coefficient  $b_2 = 1.61$ . At ambient conditions, the value of  $B_{22}$  decreases from  $7.15 \cdot 10^{-4}$  to  $4.92 \cdot 10^{-4} \text{ mL mol g}^{-2}$ , upon addition of 20% (w/v) polymer with molecular weights between 200 and 6000  $\text{g mol}^{-1}$ . In solutions of higher molecular weight polymer, the second osmotic virial coefficient,  $B_{22}$ , levels off near the pure buffer value, most likely due to changes in the PEG structure from single dispersed chains to an entangled polymer network [Abbott et al., 1991]. At a concentration of 20% (w/v) polymer, the volume fraction of the polymers is  $\Phi \sim 0.17$ , regardless of the degree of polymerization. Still, we observe strong differences between polymers in their effect on protein pair interaction depending on polymer molecular weight,  $M_w$ . Even though the volume fraction remains constant, the changing nature of the polymer's solution structure with concentration, as described by the mesh (blob) size,  $\xi_b(c_{\text{PEG}}, M_w)$ , is able to modulate the protein pair-interaction.

#### 4.2.1 Spatial Distribution of the Protein Molecules

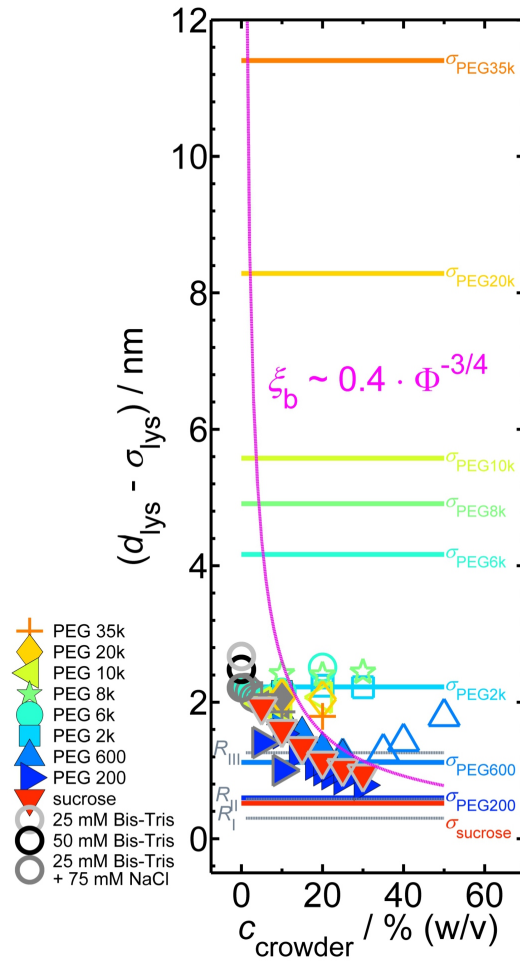


Figure 4.8: Experimentally derived separation of protein surfaces,  $d_{\text{lys}} - \sigma_{\text{lys}}$ , in a 10% (w/v) lysozyme in 50 mM Bis-Tris (pH 7, 25°C), 25 mM Bis-Tris + 75 mM NaCl (*tagged dark grey*) and 25 mM Bis-Tris (*tagged light grey*) buffer solutions as a function of crowder identity and concentration,  $c_{\text{crowder}}$ , in comparison to the crowders' hydrodynamic diameters,  $\sigma_{\text{PEG}}$  and  $\sigma_{\text{sucrose}}$ , (see section 2.2.2, Table 2.2.2) and the dimensions of the three hydration shells of lysozyme ( $R_{\text{I-III}}$ ). The polymer mesh size<sup>2</sup>,  $\xi_b(\Phi)$ , is depicted as well for reference (*solid magenta line*). *Empty symbols* visualize the  $d_{\text{lys}} - \sigma_{\text{lys}}$  values for PEG concentrations exceeding  $c^*$ . Reprinted with permission from [Julius et al., 2019]. Copyright © 2019 American Chemical Society.

An estimate of the intermolecular distances of proteins in solutions at various crowding levels can be derived directly from the main peak position in the experimental static effective structure factor,  $S_{\text{eff}}(q)$ . Figures 4.8 and 4.9 depict the mean protein-protein surface separation,  $d_{\text{lys}} - \sigma_{\text{lys}}$ , as a function of crowder concentration,  $c_{\text{crowder}}$ , for various crowding agents (see section 3.1 for detailed sample compositions). The influence on the mean spacing between protein surfaces compared to the corresponding crowder-free buffer system depends strongly on the crowder identity (size). The most pronounced effect is observed with solutions containing the similarly sized nano-crowders PEG 200 and sucrose. The mean distance between protein surfaces decreases from  $d_{\text{lys}} - \sigma_{\text{lys}} \approx 2.48$  nm in 50 mM Bis-Tris buffer to  $\sim 0.78$  nm upon addition of 30% (w/v) of the polymer PEG 200. Adding 30% (w/v) sucrose to the 25 mM Bis-Tris buffer induces a decrease from  $\sim 2.67$  to  $\sim 0.95$  nm. A study of the properties of hydration water around hen egg lysozyme using FTIR spectroscopy and molecular dynamics simulations [Panuszko et al., 2012], revealed three distinct water hydration shells for the protein in aqueous solution. The first (I) and second (II) hydration shells are located, starting from the protein's surface, at  $R_{\text{I}} = 0.0 - 0.3$  nm and  $R_{\text{II}} = 0.3 - 0.58$  nm. The third hydration shell at  $R_{\text{III}} = 0.58 - 1.26$  nm may almost be considered as bulk water-like. In this respect, the effect of the crowders on the mean intermolecular spacing of the proteins levels off when the proteins approach each other sufficiently close for their second hydration shells to penetrate.

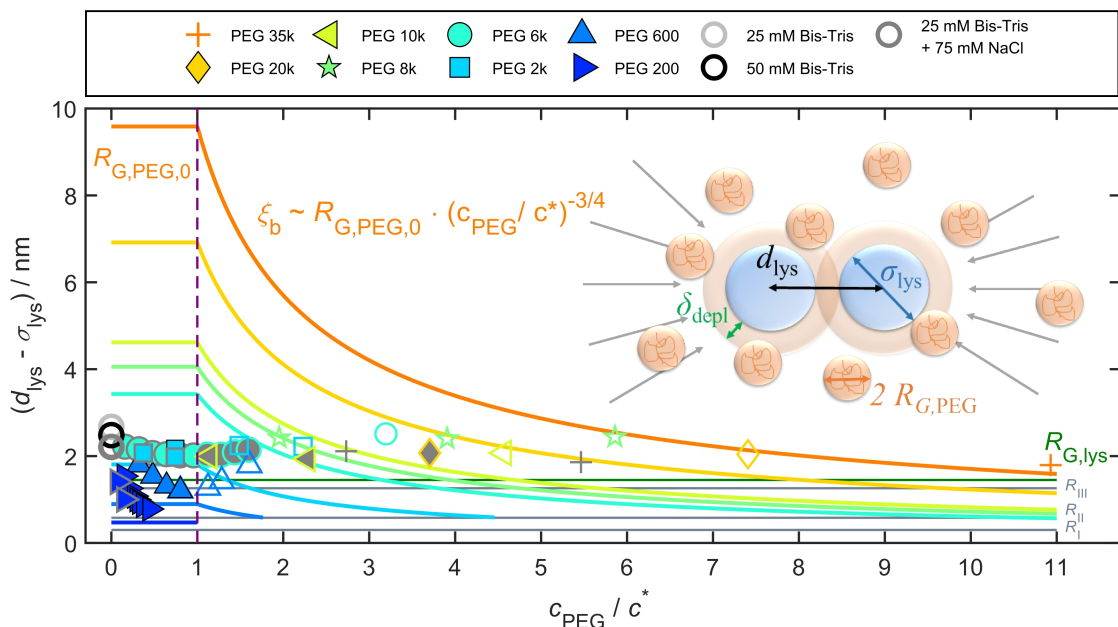


Figure 4.9: Experimentally derived protein surface separation,  $d_{\text{lys}} - \sigma_{\text{lys}}$ , for 10% (w/v) lysozyme dissolved in 50 mM Bis-Tris and 25 mM Bis-Tris + 75 mM NaCl (*tagged dark gray*) buffer solutions (pH 7, 25°C) as a function of the polymer concentration ratio  $c_{\text{PEG}}/c^*$ , depicted together with the particular length scales of the polymer solution in the dilute ( $R_{\text{G,PEG},0}$ ) and semi-dilute ( $\xi_b$ ) regime. The dimensions of the three hydration shells of lysozyme ( $R_{\text{I-III}}$ ) and the proteins radius of gyration ( $R_{\text{G,lys}}$ ) are depicted as well for reference. The  $d_{\text{lys}} - \sigma_{\text{lys}}$  values for PEG concentrations exceeding  $c^*$  are visualized by *empty symbols* (50 mM Bis-Tris buffer) and *symbols with dark gray filling* (25 mM Bis-Tris + 75 mM NaCl buffer), respectively. Reprinted with permission from [Julius et al., 2019]. Copyright © 2019 American Chemical Society.

This effect can be further tested by increasing the ionic strength of the solutions. In the aqueous 10% (w/v) lysozyme solutions the increase of the ionic strength of the solution with the addition

<sup>2</sup>The correlation length (mesh size),  $\xi_b \approx a \cdot \Phi^{-3/4}$ , of the entangled polymer network with the length scale of a monomer of  $a = 0.4$  nm is solely a function of the polymer's volume fraction,  $\Phi$ , which can be calculated from the polymer concentration by using its partial specific volume ( $V^\circ = 0.825$  mL g<sup>-1</sup> for PEG) [Cohen et al., 2009, de Gennes, 1979a, Abbott et al., 1991].



of NaCl results in a significant screening of the long-ranged Coulomb repulsion (e.g.  $B_{22} = 3.07 \cdot 10^{-4} \text{ mL mol g}^{-2}$  in 25 mM Bis-Tris + 75 mM NaCl,  $T = 25^\circ\text{C}$ ) between the proteins, since the net surface charge of the protein at pH 7 is effectively screened by  $\sim 100 \text{ mM NaCl}$  [Liu et al., 2004]. This reduces the mean protein-protein distance prior to the addition of the crowder molecules to a value at which the hydration shells of the proteins begin to touch each other ( $d_{\text{lys}} - \sigma_{\text{lys}} \approx 2.21 \text{ nm}$  in 25 mM Bis-Tris + 75 mM NaCl,  $T = 25^\circ\text{C}$ ). However, the comparison of the crowder concentration dependence of the average protein surface-to-surface distance for 50 mM Bis-Tris, 25mM Bis-Tris + 75 mM NaCl (*tagged dark grey*) and 25 mM Bis-Tris buffer solutions (*tagged light grey*), shows that the crowder-effect is consistent for all buffer compositions in the investigated concentration regime (see Figures 4.8 and 4.9). Thus, the increased attraction upon the addition of salt only seems to cause an offset. Figure 4.9 shows the influence of the molecular weight specific transition from the dilute to the semi-dilute region at  $c_{\text{PEG}} = c^*(M_w)$  on the protein surface-to-surface distance,  $d_{\text{lys}} - \sigma_{\text{lys}}$ , as well as on the polymer correlation length,  $\xi_b$ . Below the threshold  $c_{\text{PEG}}/c^* < 1$ , the polymers can be considered as single dispersed polymer chains (i.e.  $\xi_b \approx R_{G,\text{PEG},0}$ ). In this dilute regime, the addition of polymers to the solution leads to a decrease of the mean intermolecular spacing of the proteins as the crowder concentration increases. This effect depends markedly on the polymer size and is enhanced as the polymer/protein size ratio decreases. For smaller polymer such as PEG 200, the transition from single dispersed polymer chains to an entangled network takes place at significantly higher concentrations than those investigated here. The distance between the protein surfaces,  $d_{\text{lys}} - \sigma_{\text{lys}}$ , shows a non-monotonic dependence on the polymer concentration: Around  $c_{\text{PEG}}/c^* = 1$ , where the polymer chains build up an extensive entanglement, the mean intermolecular distance of the proteins in the polymer solution begins to rise again until it reaches a plateau value comparable to that of the polymer-free buffer system deep in the semi-diluted region where  $c_{\text{PEG}}/c^* \gg 1$ .

#### 4.2.2 Depletion Interaction

The attractive forces between proteins resulting from the entropically driven excluded volume (depletion) effect in the presence of crowder molecules (see section 2.2.2) are not explicitly included in the parametrization of the DLVO potential (see 2.2.3). Their contribution to the modeled effective proteins' pair-interaction is comprised – among others - in the attractive Yukawian part,  $V_Y(r)$ . In order to quantitatively investigate the influence of the polymer on the effective intermolecular interactions between two protein molecules in a dense protein-polymer mixture, we will now consider the contribution made by the entropically driven excluded volume (depletion) effect separately as well as in conjunction with the other DLVO forces. In the framework of the Polymer Reference Interaction Site Model (PRISM) [Poon et al., 1997, Ilett et al., 1995, Chatterjee and Schweizer, 1998b], the depletion potential,  $V_{\text{depl}}(r)$ , predicts polymer-induced attractive depletion interactions between proteins with centers separated by  $r$  for all polymer coil dimensions at polymer concentrations below and beyond  $c^*$  with no adjustable parameters. Within the parametrization of  $V_{\text{depl}}(r)$ , the depletion thickness,  $\delta_{\text{depl}}(M_w)$ , describes the spatial distance over which fluctuations in polymer concentration are correlated [de Gennes, 1979b] (see section 2.2.2, Eq. (2.17)). Bases on earlier work on the intermolecular protein pair-interactions in lysozyme-PEG solutions [Kulkarni et al., 1999, Kulkarni and Zukoski, 2001], we assume that the standard DLVO and depletion interactions are additive [Chandler and Andersen, 1972]. Combining Eqs. (2.13) and (2.18) yields the effective protein-protein interaction potential,  $V^*(r)$ , of lysozyme molecules in the polymer solution:

$$V^*(r) = (V_{\text{HS}}(r) + V_Y^{\text{buffer}}(r) + V_{\text{SC}}^{\text{PEG-buffer}}(r))_{\text{DLVO}} + V_{\text{depl}}^{\text{PEG-buffer}}(r). \quad (4.3)$$

For  $V_Y^{\text{buffer}}(r)$  and  $V_{\text{HS}}^{\text{buffer}}(r)$ , the potential parameters determined by the refinement of the effective structure factor for polymer-free systems are applied.

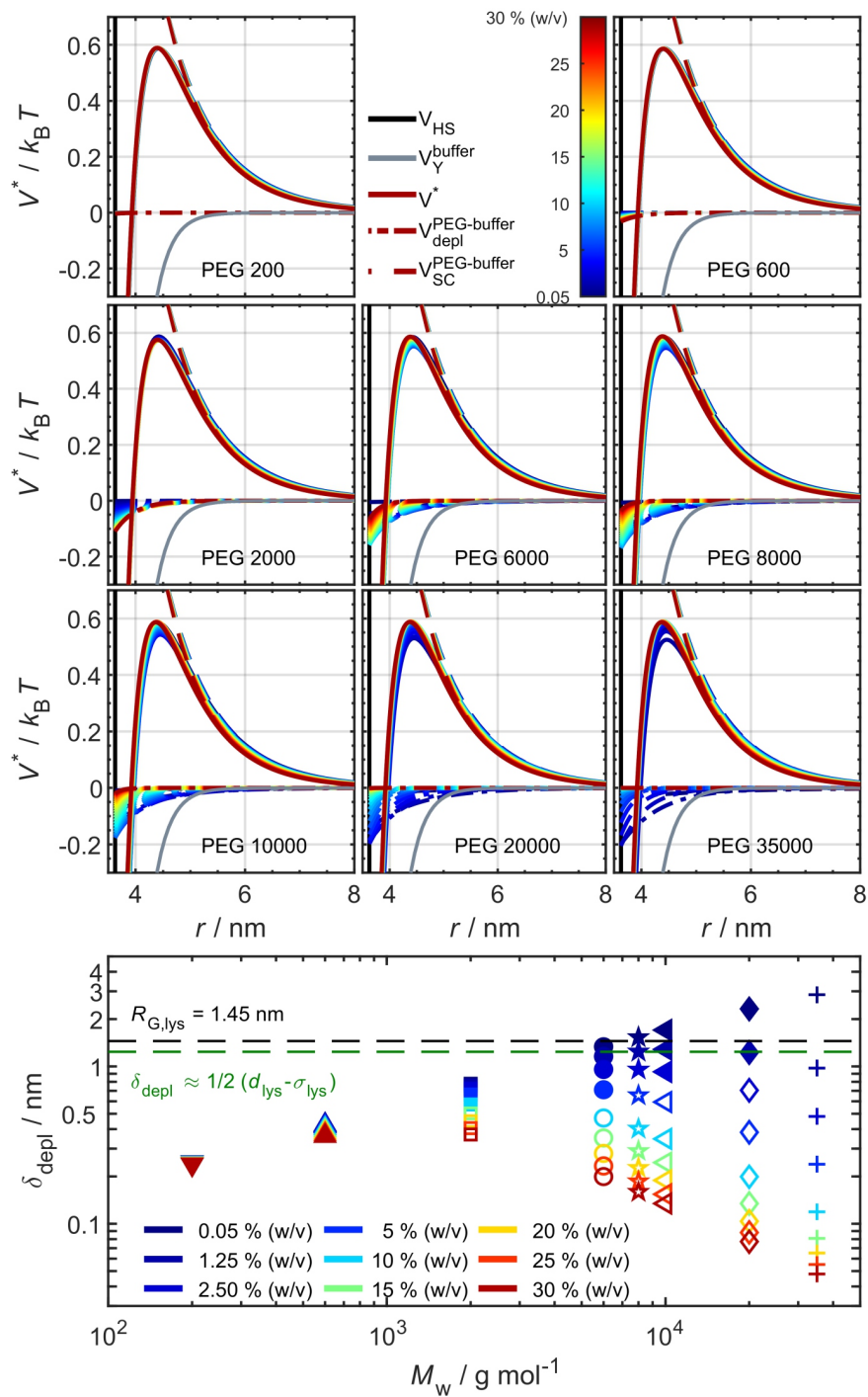


Figure 4.10: (*top half*) Effective protein pair-interaction potential,  $V^*(r)$ , calculated from Eq. (4.3), as a function of polymer concentration for various PEG sizes, shown together with its contributing parts.  $V_Y^{buffer}$  and  $V_{HS}$  are obtained by the refinement of the SAXS curves of polymer-free 10% (w/v) lysozyme + 50 mM Bis-Tris aqueous solution (pH 7,  $T = 25^\circ C$ ,  $p = 1\ bar$ ) carried out in the framework of the DLVO theory, just as  $V_{SC}^{PEG-buffer}$ , which is modified for the polymer solution's dielectrics.  $V_{depl}^{PEG-buffer}$  is calculated from Eq. (2.13) applying the PRISM model [Poon et al., 1997, Ilett et al., 1995, Chatterjee and Schweizer, 1998b]. (*bottom half*) Corresponding depletion thickness,  $\delta_{depl}(c_{PEG}, M_w)$ , calculated from Eq. (2.17), as a function of polymer molecular weight for various polymer concentrations. Empty symbols visualize the  $\delta_{depl}$  values for PEG concentrations exceeding  $c^*$ . Reprinted with permission from [Julius et al., 2019]. Copyright © 2019 American Chemical Society.

The Coulomb part,  $V_{SC}^{\text{PEG-buffer}}(r)$ , takes into account the changes of the dielectric constant  $\epsilon_r(M_w, c_{\text{PEG}})$  (see Figure 4.5) and the Debye-Hückel inverse screening length  $\kappa(\epsilon_r(M_w, c_{\text{PEG}}))$ , caused by the polymer in solution. The *top half* of Figure 4.10 depicts the predictions for the modulated effective protein pair-interaction potential,  $V^*(r)$ , in 10% (w/v) lysozyme + 50 mM Bis-Tris (pH 7) solutions upon addition of PEG with molecular weights between  $200 \text{ g mol}^{-1} < M_w < 35\,000 \text{ g mol}^{-1}$  at concentrations in the range of  $0.05\% \text{ (w/v)} < c_{\text{PEG}} < 30\% \text{ (w/v)}$ . Clearly, the depletion interaction induced by the polymer is too weak and short-ranged to generate a significant attraction between the proteins when the blob size of the polymer is much smaller than the lysozyme molecule ( $\xi_b \ll R_{G,\text{lys}}$ ). As shown in the *bottom half* of Figure 4.10, the depletion thickness,  $\delta_{\text{depl}}$ , and thus also the range of the depletion potential, decreases significantly with increasing polymer concentration, which is most pronounced for large polymers in the investigated concentration range.

For dilute polymer systems, the depletion thickness scales with the polymer's molecular weight (i.e. size) by a power law function. Due to the increasing entanglement of the polymer chains, this dependency gradually breaks down at higher polymer concentrations. The break point in  $\delta_{\text{depl}}(c_{\text{PEG}}, M_w)$  occurs at a particular molecular weight-specific concentration. For 5% (w/v) PEG, it is located at a molecular weight around  $6000 \text{ g mol}^{-1}$ , for 10% (w/v) PEG around  $2000 \text{ g mol}^{-1}$ , and for 20% (w/v) PEG around  $600 \text{ g mol}^{-1}$ .

Remarkably, in the dilute regime  $c_{\text{PEG}}/c^* < 1$ , the dependence of the strength,  $J$ , of the attractive interactions in lysozyme-polymer mixtures on the molecular weight,  $M_w$ , of the polymer (and depletion thickness  $\delta_{\text{depl}}(M_w, c_{\text{PEG}})$ ) can be described at ambient conditions by the power laws  $J(c_{\text{PEG}} < c^*, M_w) \propto \alpha(M_w)^m \propto \mu(\delta_{\text{depl}}(M_w, c_{\text{PEG}}))^k$  (see Figure 4.11). Within the experimental error, the increment  $dk/dc_{\text{PEG}}$  (relation is not linear) is essentially independent of the buffer composition (i.e. ionic strength) and is therefore not affected by the screening of the protein's surface charge (see Appendix A, Figure A.4). The reduced Coulomb repulsion is reflected in an increase of the parameter value  $\mu$  (i.e. shift of  $J$  to larger values), only. At elevated ionic strength of the buffer solution, the addition of PEG to the system leads to an even more repulsive protein-protein interaction.

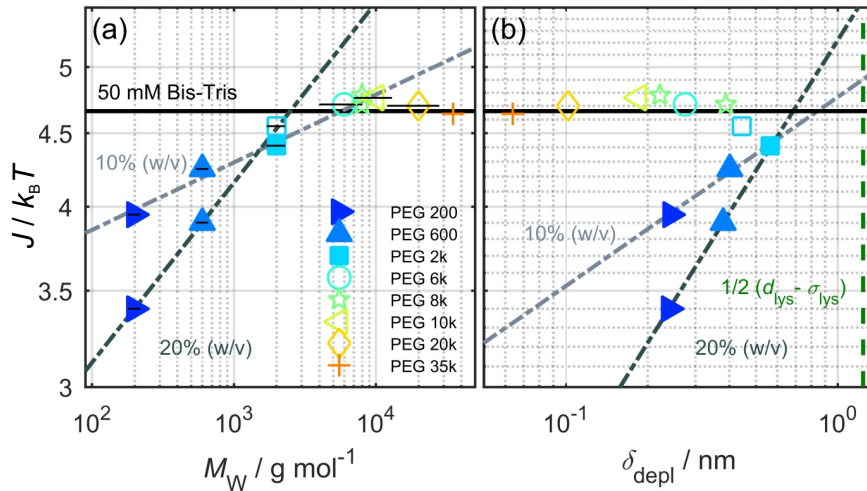


Figure 4.11: (a) Double-logarithmic representation of the strength of the attractive part,  $J$ , in 10% (w/v) lysozyme in 50 mM Bis-Tris (pH 7) solution at ambient pressure and  $25^\circ\text{C}$  as a function of the PEGs molecular weight,  $M_w$ , and (b) depletion thickness,  $\delta_{\text{depl}}$ , for 10 and 20% (w/v) of the polymer. The corresponding power-law trend-lines  $J(c_{\text{PEG}} < c^*) \propto \alpha(M_w)^m$  and  $J(c_{\text{PEG}} < c^*) \propto \mu(\delta_{\text{depl}})^k$  are depicted as well. *Empty symbols* visualize the  $J$  values for PEG concentrations exceeding  $c^*$ . Reprinted with permission from [Julius et al., 2019]. Copyright © 2019 American Chemical Society.

In contrast to the salt-free protein-polymer mixtures, the strength of attraction,  $J$ , in solutions containing  $c_{\text{NaCl}} = 75 \text{ mM}$  does not again correspond to the pure buffer value at polymer concentrations  $c_{\text{PEG}} < c^*$  and  $c_{\text{PEG}} \geq c^*$ . This increased degree of repulsion may be due to a modulation of

the protein's (preferential) hydration in the presence of additives such as polyethylene glycol [Bhat and Timasheff, 1992], affecting the protein pair interaction particularly at small protein distances, as under these conditions hydration repulsion becomes effective. As shown in Figure 4.11 (b) and Appendix A, Figure A.5 (f) for both buffer compositions, the depletion thickness,  $\delta_{\text{depl}}$ , levels off at high polymer concentrations before reaching a sufficiently high value to induce a significant attraction between protein molecules. The theoretical normalized second osmotic virial coefficient,  $b_2^*$ , predicted by PRSIM theory is calculated from the overall effective pair-interaction potential  $V^*(r)$  by employing Eq. (2.4). The results are shown in Figure 4.12 as a function of  $c_{\text{PEG}}/c^*$  for various polymer molecular weights in comparison to the experimental data. For all PEG molecular weights and concentrations investigated in this work, the polymer-induced attractive depletion interaction is predicted to be too weak and short ranged to induce an attractive (negative) value for the normalized second osmotic virial coefficient  $b_2^*$ .

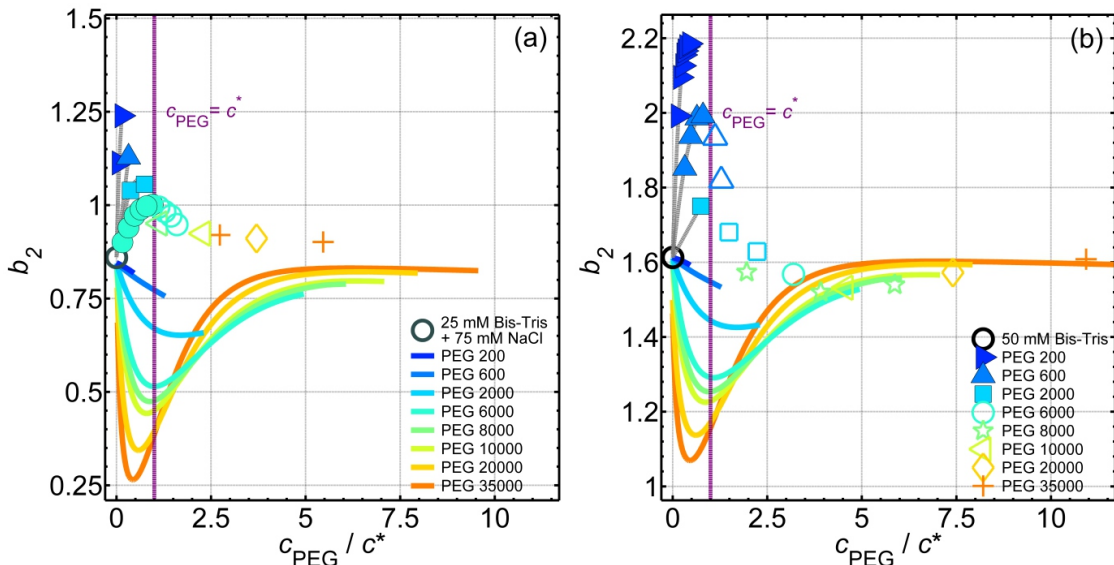


Figure 4.12: Experimentally derived reduced second osmotic virial coefficient,  $b_2$ , for 10% (w/v) lysozyme dissolved in (a) 25 mM Bis-Tris + 75 mM NaCl and (b) 50 mM Bis-Tris (pH 7, 25°C), respectively, as a function of  $c_{\text{PEG}}/c^*$  for various polymer molecular weights. Data is shown together with the theoretical value of  $b_2^*$  predicted by PRSIM theory (solid lines).  $b_2^*$  is calculated from the overall effective pair-interaction potential,  $V^*(r)$ , consisting of the DLVO and the athermal PRISM depletion potential using (Eq. 4.3). Empty symbols visualize the experimental  $b_2$  values for PEG concentrations exceeding  $c^*$ . Reprinted with permission from [Julius et al., 2019]. Copyright © 2019 American Chemical Society.

The impact of the depletion mechanism on the protein-protein interaction is not strong enough to significantly overcome the repulsive contributions that dominate the experimental data for  $b_2$ . For solutions with polymers of higher molecular weight ( $M_w > 600 \text{ g mol}^{-1}$ ), the course of  $b_2^*$  shows a pronounced non-monotonic behavior in the form of an attractive minimum around the overlap concentration  $c^*$ . As polymer concentration increases, the competing effects of a decreasing polymer mesh size  $\xi_b(c_{\text{PEG}}, M_w)$ , which reduces the range of attractive depletion force, and an increasing gradient of osmotic pressure  $\Pi(c_{\text{PEG}}, M_w)$  between the bulk solution and the depletion region, which increases the strength of the attraction, lead to a trend reversal. When the polymer coils penetrate each other, there is a much steeper increase in osmotic pressure with concentration. [Cohen et al., 2009]. Thus, the depletion force is even more suppressed as the steep osmotic pressure gradient between the bulk solution and the depletion region impedes polymer transport out of the depletion region [Feigin and Napper, 1980]. Furthermore, the polymers tend to mutual avoidance to maintain coil conformational entropy, which is most pronounced just below the overlap concentration [Mao et al., 1995]. The depletion attraction between the proteins is attenuated by repulsive polymer-polymer interactions, as they occur at sufficiently high polymer concentra-

tions, which stabilizes the system [Feigin and Napper, 1980, Ye et al., 1996].

At high polymer levels, the protein solution is stabilized by the decreasing polymer-induced depletion attraction and the proteins keep such a large distance that the depletion forces are completely dampened. Figure 4.12 depicts the comparison of the theoretically predicted normalized second osmotic virial coefficients,  $b_2^*$ , with the experimentally derived values,  $b_2$ , for 10% (w/v) lysozyme in (a) 25mM Bis-Tris + 75 mM NaCl buffer and (b) 50 mM Bis-Tris buffer. The large discrepancy in the concentration dependence of the theoretical  $b_2^*$  and experimental  $b_2$  data for  $c_{\text{PEG}} < c^*$  suggests that although protein-protein interactions in these polymer-protein mixtures might be modulated by the depletion mechanism, additional (repulsive) forces must be operative at small protein distance, thereby stabilizing the protein against strong attractive depletion interaction in the presence of polymer.

In the semi-dilution regime, protein-protein interaction no longer depends on the identity of the polymers, but only on the polymer concentration. The experimentally derived normalized second osmotic virial coefficient,  $b_2$ , decreases rapidly with increasing amount of polymer at concentrations above the threshold  $c^*(M_w)$  (see Figure 4.12).

### 4.2.3 van der Waals Interactions

The van der Waals (vdW) interaction between protein is comprised in the attractive Yukawian part,  $V_Y(r)$ , of the DLVO potential. The vdW attraction between two lysozyme molecules across another medium (see section 2.2.1) can be either suppressed or enhanced by cosolute-induced changes of the solution's dielectric constant,  $\epsilon_r(M_w, c_{\text{crowder}})$ , and refractivity  $n_s(M_w, c_{\text{crowder}})$ .

The refractive index,  $n_s(M_w, c_{\text{PEG}})$ , increases with the mole fraction of PEG in a non-linear manner, and is correlated with the growing non-ideality of the polymer-water mixture [Kolská et al., 2016]. For smaller PEGs the increment  $dn_s(M_w, c_{\text{PEG}})/dc_{\text{PEG}}$  increases (and  $d\epsilon_r/dc_{\text{PEG}}$  decreases, see Figure 4.5) significantly with the molecular weight of the polymer,  $M_w$ , until this effect diminishes for larger PEG [Mohsen-Nia et al., 2005]. In the total concentration range from 0.1 to 50% (w/v), the refractive index of aqueous solutions of polyethylene glycol with a molecular weight as high as  $6\text{k} < M_w < 2\text{M g mol}^{-1}$  is no longer dependent on the molecular weight of the polymer [Ziebacz et al., 2011]. Accordingly, the vdW interactions, as represented by the Hamaker constant,  $A(\epsilon_r, n_s)$ , scale in this case with the polymer concentration, only [Ziebacz et al., 2011]. The Hamaker constant was calculated exemplarily for  $c_{\text{PEG}} = 20\%$  (w/v) of small ( $M_w = 200 \text{ g mol}^{-1}$ ) and a large ( $M_w = 10000 \text{ g mol}^{-1}$ ) PEG as well as for 20% (w/v) sucrose employing Eq. (2.11). The static dielectric constants for the aqueous PEG solutions,  $\epsilon_r(M_w, c_{\text{PEG}})$ , are obtained from our own measurements (see Figure 4.5 and section 3.5 for experimental details) and for aqueous sucrose from [Malmberg and Maryott, 1950]. The refractive indices of the solvent,  $n_s(\text{PEG}200, 20\% \text{ (w/v)}) \approx 1.3585$ ,  $n_s(\text{PEG}10\text{k}, 20\% \text{ (w/v)}) \approx 1.3617$  and  $n_s(\text{sucrose}, 20\% \text{ (w/v)}) \approx 1.3639$ , are taken from [Kolská et al., 2016, Mohsen-Nia et al., 2005] for aqueous PEG 200 and 10k solutions and for aqueous sucrose solutions from [Lide, 2003], respectively.

Under all conditions, the addition of polymer suppresses the attractive van der Waals interaction, rendering the system overall more repulsive in comparison to the pure buffer system. The degree of repulsion caused by the decrease of the Hamaker constant (e.g.  $A_{\text{sucrose}} = 2.15 k_B T < A_{\text{PEG}10\text{k}} = 2.18 k_B T < A_{\text{PEG}200} = 2.25 k_B T < A_{\text{buffer}} = 2.84 k_B T$  for  $c_{\text{crowder}} = 20\%$  (w/v)) is much lower than in the experimental data. Further, the observed trend in crowder identity at a given crowder concentration does not coincide with the experimental results, hence, we suggest that other mechanisms, such as enthalpic attractive polymer-protein interactions, volume exclusion due to strong preferential protein hydration or hydration repulsion, are responsible for the observed effect.

### 4.2.4 Protein-Polymer Interactions

Any attractive interaction between protein and polymer is expected to translate into protein repulsion and steric stabilization at high polymer concentrations. Previous studies on the weak hydrophobic interactions between polyethylene glycol and lysozyme in aqueous solution revealed that the interactions are enhanced with increasing polymer concentration and that they are most pronounced for polymer of high molecular weight, which was mainly attributed to the change of hydrophilicity to amphiphilicity of PEG with increasing polymer chain length [Wu et al., 2014b, Wu



et al., 2014a, Arakawa and Timasheff, 1985, Baskir et al., 1989]. The data show, that smaller polymer render the effective protein-protein interaction more repulsive than the larger ones. The effect of attractive protein-PEG interactions on the protein pair-interaction, owing to (transient) hydrophobic interactions between lysozyme and crowders would in particular operate when the small PEG molecules are able to reside between protein molecules:

We consider the association free energy  $\Delta F$  of two lysozyme molecules, representing the attraction that offsets the repulsion due to unscreened charges when two lysozyme make a contact (i.e. when the distance between their surfaces,  $d_{\text{lys}} - \sigma_{\text{lys}}$ , is decreased to zero corresponding to dry (or almost dry) interface). Unlike in the close-contact associated state of the proteins, in the dissociated state crowder molecules may be located in the space between proteins. Due to geometrical constraints, this can only happen for small enough crowder molecules, whose radius of gyration is  $R_{\text{G,PEG},0} \lesssim 1/2(d_{\text{lys}} - \sigma_{\text{lys}})$  (i.e., PEG 200, PEG 600 and sucrose). In crowded solution, weak hydrophobic interactions between the polymer and lysozyme induce a reduction of the proteins free energy in the dissociated state by  $\Delta F_{\text{h}}$  (see Figure 4.13).

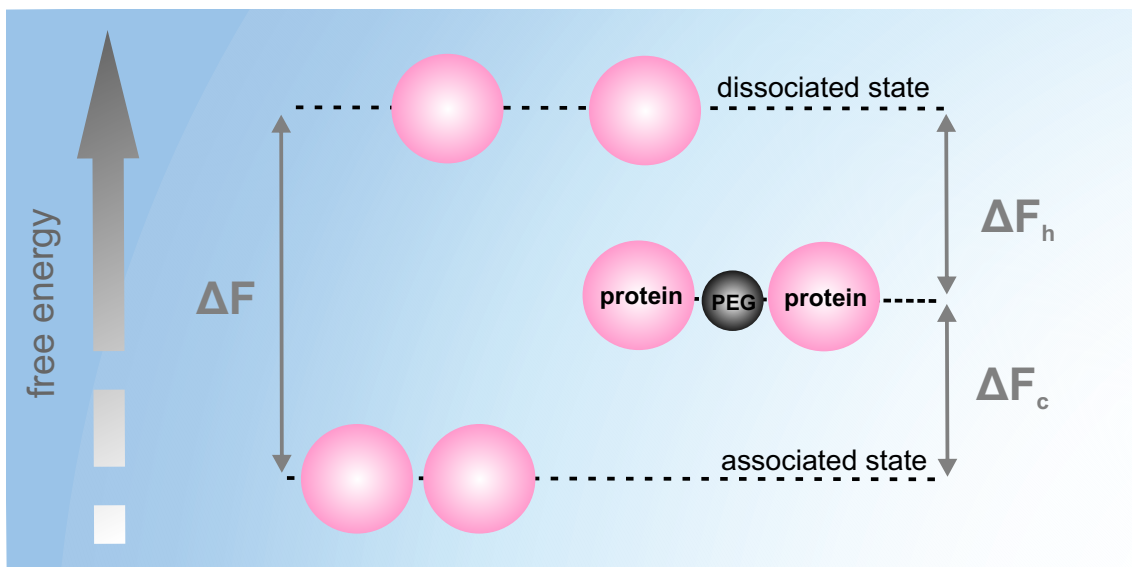


Figure 4.13: The association free energy  $\Delta F$  of two lysozyme molecules in the presence of PEG.

As a consequence, the association cost is reduced to  $\Delta F_{\text{c}} = \Delta F - \Delta F_{\text{h}}$ . Hence, when a PEG molecule is residing between two protein molecules an additional repulsion between proteins is induced. This in turn is roughly proportional to the number density of PEG at small concentrations, where all locations of the crowder molecules in solution are equally probable. Therefore, the strength of the additional repulsion is expected to grow linearly with the PEG concentration. As the concentration is increased to the point where interactions between PEG molecules become important, roughly at  $c^*$ , the effect will begin to die down, as proteins will start to compete for the intercalating PEGs with other PEGs (see Figure 4.14 (a)). This is observed for PEG 600, but not for PEG 200, for which the overlap concentration has not been reached.

At a fixed polymer volume fraction, the decrease in the strength of the attractive interaction potential,  $J$ , is most pronounced for small polymers with molecular weights of 200 and 600  $\text{g mol}^{-1}$  (see Figure 4.14 (a) and Appendix A, Figure A.5 (b)), possibly due to their ability to intercalate between adjacent protein molecules. So it appears that the model in which crowding agents are able to induce additional repulsion between proteins by interacting favorably with them via weak hydrophobic forces may indeed explain, at least in part, the reported results. We therefore assume that in addition to hydration repulsion, which is effective at very short protein distances, weak attractive protein-polymer interactions with small crowder molecules may also contribute to the net repulsive effect on protein-protein interaction [Bhat and Timasheff, 1992].

### 4.2.5 Hydration Effects

The exclusion of compatible osmolytes such as sucrose from the vicinity of proteins leads to an excess of water in the protein's surface area and thus to a preferential hydration of the protein [Ajito et al., 2018, Arakawa and Timasheff, 1982, Timasheff, 1993] (see section 2.1.2). The preferential hydration of the proteins caused by polyethylene glycols is reinforced with increasing molecular weight of the polymers [Bhat and Timasheff, 1992, Arakawa and Timasheff, 1985, Lee and Lee, 1981]. The preferential hydration effect is due to a solvophobic effect, i.e., to the inability of the solutes to form as many hydrogen bonds when close to the solute's surface as opposed to the bulk. A steric barrier in the form of a strong hydration layer surrounds the protein molecules and effectively represents an additional excluded volume. The protein's native state is stabilized in the presence of the cosolute, since the more compact native fold with a smaller solvent accessible surface area is thermodynamically favored over the extended conformation of the denatured protein. Thus, even in the presence of polymer sizes that do not meet the conditions for the depletion mechanism, a reduction in the intermolecular distance of proteins can still be induced, the driving force being the excluded volume effect due to preferential hydration of the protein surface [Adams and Fraden, 1998]. In very confined spaces, where the hydration shells of the protein molecules begin to overlap, a strong hydration repulsion may be operative, however.

### 4.2.6 HHP Effects on the Protein-Protein Interaction

The results of the refinement of the high-pressure SAXS intensities of 10% (w/v) lysozyme + 50 mM Bis-Tris (pH 7) solutions containing sucrose and polymer of various molecular weights at various concentrations are shown in Figure 4.14 (and Appendix A, Figure A.5 for the case of elevated ionic strength,  $c_{\text{NaCl}} = 75$  mM). As already reported for 10% (w/v) lysozyme dissolved in pure Bis-Tris buffer (pH 7) [Schroer et al., 2011a, Julius et al., 2018b], the mean intermolecular distance of the proteins,  $d_{\text{lys}}$ , decreases at pressures up to 1.6 kbar, accompanied by an increasing repulsion in the protein-protein interactions (i.e. increase of  $b_2$ ). This trend is reversed by further pressurization; the mean intermolecular distance of the protein gradually increases again, whereby the normalized second osmotic virial coefficient,  $b_2$ , drops significantly below the value found for ambient conditions. At ambient conditions and for polymer-free protein solutions,  $b_2$  reportedly changes its sign from positive to negative values only at high ionic strength, i.e. effectively screened surface charges of the lysozyme molecule, as it occurs at 0.1 M NaCl [Voet and Voet, 1990]. Owing to the pressure effect, negative  $b_2$  values are observed already at 75 mM NaCl at high pressures both in the pure protein solution and in the presence of 10% (w/v) PEG 35k (see Appendix A, Figure A.5). In solutions containing polymer of lower molecular weight ( $< 35000$  g mol<sup>-1</sup>), the increase in attraction is suppressed, however, and  $b_2$  remains positive for all pressures. Notably, the trend of increasing protein-protein repulsive interactions for smaller PEG sizes and at polymer concentrations below  $c_{\text{PEG}} < c^*$ , as found at ambient pressure, is also reflected in the pressure dependence of the normalized second osmotic virial coefficient,  $b_2$ . Within the concentration limit  $c_{\text{PEG}} < c^*$ , the peculiarity of the non-monotonous pressure-dependencies  $J(p)$  and  $b_2(p)$  weakens with decreasing polymer size and increasing degree of crowding and changes significantly around the overlap concentration. For concentrations exceeding  $c_{\text{PEG}} \gg c^*$ , the strength of the attractive part of the effective protein pair-interaction,  $J$ , revisits the value found for ambient conditions already at pressures below 1.6 kbar (see Figure 4.14 and Appendix A, Figure A.5, *empty symbols*). In fact, the increase in the strength of the protein-protein attractive interaction at high pressures is significantly sharper for the protein-polymer mixtures containing PEGs with high molecular weights than in the polymer-free buffer case. A static light scattering study on the pressure dependence of the effective polymer radius in aqueous 8% (w/v) PEG 6000 solutions revealed a decrease of the effective radius and thus of the volume excluded by PEG of about  $\sim 20\%$  with a pressure increase from 1 bar to 2.5 kbar [Crisman and Randolph, 2010]. The compression of the polymer chains results in a downsizing of the depletion forces, which might be the reason for the relaxation of the repulsive forces upon pressurization and the increase of the protein intermolecular distance.

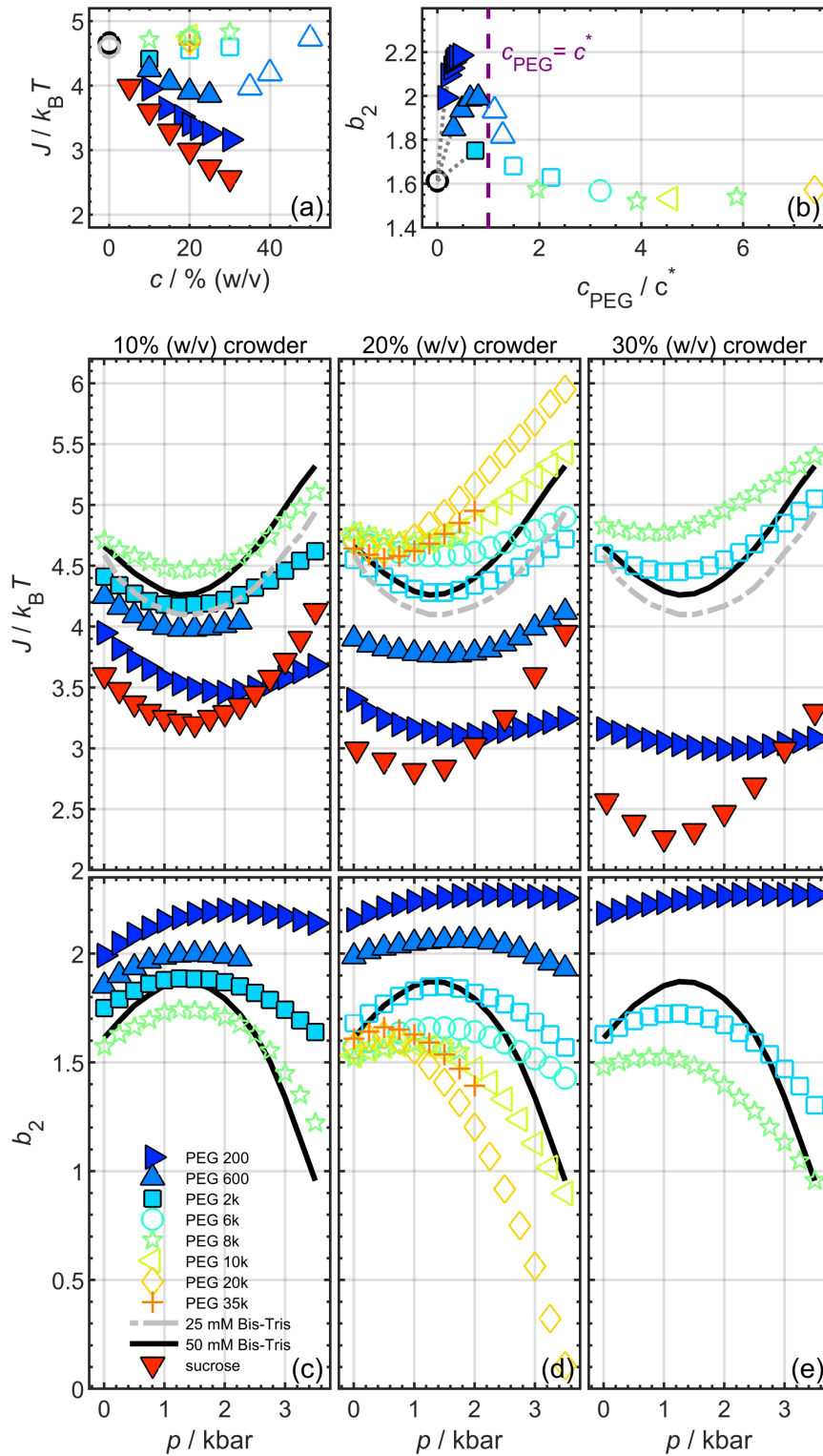


Figure 4.14: (a) Strength of the attractive interaction,  $J$ , in 10% (w/v) lysozyme + 50 mM (25 mM) Bis-Tris (pH 7) solution as a function of crowder (PEG, sucrose) concentration at ambient pressure and 25°C. (b) Normalized second osmotic virial coefficient,  $b_2$ , as a function of the polymer concentration, normalized to the overlap concentration, i.e.  $c_{PEG}/c^*$ . (c)–(e) Pressure dependence of  $J$  and  $b_2$  for 10% (w/v), 20% (w/v) and 30% (w/v) crowder of various sizes added to the buffer solution at 25°C. *Empty symbols* visualize the  $J$  and  $b_2$  values for PEG concentrations exceeding  $c^*$ . Reprinted with permission from [Julius et al., 2019]. Copyright © 2019 American Chemical Society.

### 4.3 Liquid-Liquid Phase Separation of Lysozyme

The limits of the liquid-liquid phase separation (LLPS) region for the protein lysozyme have been found to be sensitive to changes in solution conditions such as pH, ionic strength and protein concentration, as well as to changes in temperature and pressure [Muschol and Rosenberger, 1997, Taratuta et al., 1990, Broide et al., 1996]. Remarkably, a reentrant liquid-liquid phase coexistence region has been discovered at elevated pressures in an earlier work on the  $p$ - $T$  phase behavior of dense lysozyme-salt solutions, which originates in the pressure dependence of the solvent-mediated protein pair-interactions [Möller et al., 2014a]. Generally, LLPS of proteins is induced by strong attractive protein-protein interactions with a range much shorter than the size of the particles, which are quantified in this work by the strength,  $J$ , of the attractive Yukawian-part,  $V_Y(r)$ , of the effective protein pair interaction potential (see section 2.3.4). Therefore, the effects of PEG polymers of different size and concentration on  $V(r)$  should also be reflected in the temperature and pressure values marking the transition to the metastable liquid-liquid phase region. Following our previous works [Möller et al., 2014a, Schulze et al., 2016], the LLPS phase diagrams for the protein-polymer mixtures were determined in the  $p$ - $T$ -plane by high-pressure laser transmission (turbidity) measurements, where the temperature is gradually lowered at various pressures to determine cloud point temperatures,  $T_{\text{cloud}}$ , and pressures,  $p_{\text{cloud}}$ , respectively (see section 3.1 and 3.6 for more details on the sample preparation and the experimental setup). The LLPS phase boundaries (binodals) in 200 and 100 mg mL<sup>-1</sup> lysozyme solutions, buffered by 25 mM Bis-Tris (pH 7) and with an ionic strength of 0.5 M and 1 M NaCl, respectively, were determined in the presence of 1.25, 2.5 and 5% (w/v) PEG of various molecular weights for hydrostatic pressures up to 4500 bar (see Figure 4.15). Within the limits of the polymer overlap concentration,  $c_{\text{PEG}} < c^*(M_w)$ , the LLPS phase separation in the ternary protein-polymer-buffer solution is markedly modulated by the molecular weight of the polymer, visible as a decrease of the cloud point temperature,  $T_{\text{cloud}}(c_{\text{PEG}}, M_w)$ , relative to the pure buffer case. The effect is enhanced by a decrease in the molecular weight of the polymer and an increase in the concentration of PEG (see Figure 4.15 (a), (b)). In general, it is predicted that polymers, whose centers of mass are excluded from a sphere of radius  $R + \delta_{\text{depl}}$  around a non-adsorbing colloid of radius  $R$ , can induce LLPS in polymer-colloid mixtures via the depletion mechanism when  $\delta_{\text{depl}}/R > 0.3$  [Lekkerkerker et al., 1992]. Even though all PEG sizes  $M_w > 600$  g mol<sup>-1</sup> meet this criterion for  $c_{\text{PEG}} < c^*(M_w)$ , the attractive depletion interaction between the proteins appears to be too weak to induce LLPS at room temperature at polymer concentrations in the range of 1.25 to 5.00% (w/v) PEG. The phase transition temperature in the ternary lysozyme-PEG-buffer mixtures is even shifted to lower values compared to the pure buffer system (see Figure 4.15 (a), (b)). The effect can be quantified by a power-law trend line  $T_{\text{cloud}}(M_w, p = 1 \text{ bar}, c_{\text{lys}}, c_{\text{PEG}} < c^*, I) \propto \eta (M_w)^s$ , characterizing the dependency of the cloud point temperature,  $T_{\text{cloud}}$ , on the polymer molecular weight,  $M_w$ , at ambient pressure in the dilute polymer concentration regime. In the double-logarithmic representation, the slope,  $s$ , of the power-law trend line for the 100 mg mL<sup>-1</sup> lysozyme + 1 M NaCl + 5% (w/v) PEG solution corresponds to that of the 200 mg mL<sup>-1</sup> lysozyme + 1 M NaCl + 2.5% (w/v) PEG system within the experimental error. Clearly, the influence of lysozyme concentration on the polymer-polymer interaction and the conformation of the polymer chain cannot be neglected at this degree of crowding. If the proteins take up less volume in the system, more polymer is required to induce phase separation. As reported by previous works [Möller et al., 2014a, Schulze et al., 2016], the LLPS boundary is shifted to slighter lower temperatures with a decrease of protein concentration from 20% to 10% (w/v) lysozyme in 25 mM Bis-Tris + 0.5 M NaCl (pH 7) aqueous solution. Due to the surface charge screening of the protein, an increase in ionic strength leads to a shift of the binodal to higher temperatures, which is reflected in an increased value of  $\eta$ . For polymer concentrations  $c_{\text{PEG}} < 5\%$  (w/v), we are well below the threshold for polymer-polymer interpenetration,  $c^*$ , the polymers can be regarded as single dispersed spheres of radius  $R_{G,\text{PEG},0}$ . In the dilute regime ( $c_{\text{PEG}} < c^*(M_w)$ ), the extrapolated power-law trend lines  $T_{\text{cloud}} \propto \gamma(\delta_{\text{depl}})^b$  coincide (i.e. are independent of protein concentration and ionic strength) in the  $p$ - $T$  plane with the respective cloud point temperature found for the pure buffer ( $T_{\text{cloud}}$  of 17.5°C and 26°C for 0.5 and 1 M NaCl, respectively) at ambient pressure for a depletion thickness,  $\delta_{\text{depl}}$ , comparable to the hydrodynamic radius of the protein,  $R_{\text{lys}} = 1.72$  nm (see Figure 4.15 (c), (d)) [Sophianopoulos et al., 1962].

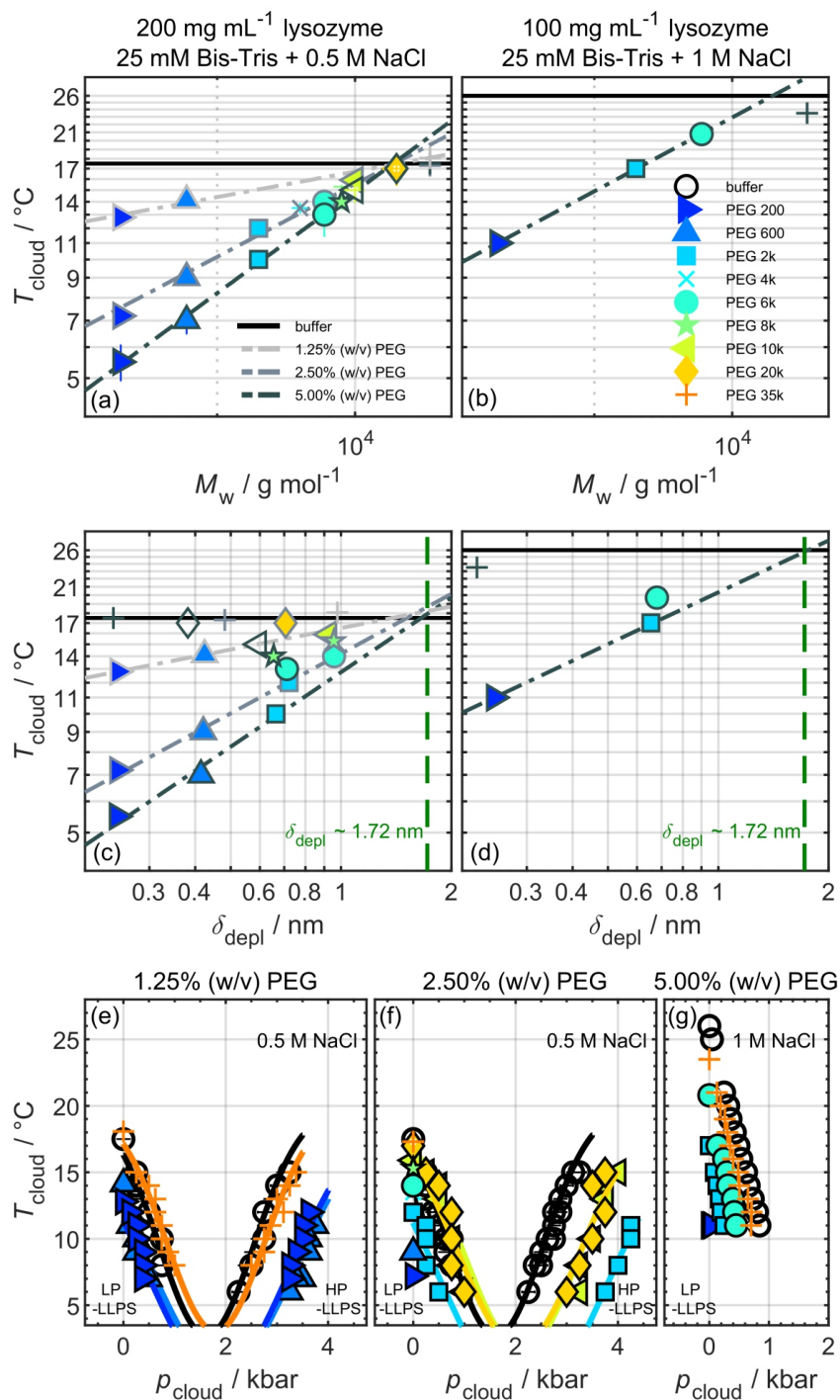


Figure 4.15: Temperature of the cloud point,  $T_{\text{cloud}}$ , of 200 mg mL<sup>-1</sup> lysozyme in 0.5 M NaCl + 25 mM Bis-Tris (pH 7) and 100 mg mL<sup>-1</sup> lysozyme in 1 M NaCl + 25 mM Bis-Tris (pH 7) solution at ambient pressure for various polymer concentrations as a function of the polymer molecular weight,  $M_w$ , (a)+(b), and depletion thickness,  $\delta_{\text{depl}}$ , (c)+(d). The data is refined by power-law functions,  $T_{\text{cloud}}(M_w) \propto \eta(M_w)^s \propto \gamma(\delta_{\text{depl}}(M_w, c_{\text{PEG}}))^b$  (dashed grey lines) as well as compared to the pure buffer system (solid black line). ( $p$ - $T$ )-LLPS phase diagrams of 200 mg mL<sup>-1</sup> lysozyme in 0.5 M NaCl + 25 mM Bis-Tris (pH 7) in the presence of (e) 1.25 and (f) 2.5% (w/v) PEG of various molecular weights,  $M_w$ , in a pressure range from 1 to 4500 bar. (g) ( $p$ - $T$ )-LLPS phase diagrams of 100 mg mL<sup>-1</sup> lysozyme in 1 M NaCl + 25 mM Bis-Tris (pH 7) in the presence of 5% (w/v) PEG of various molecular weights,  $M_w$ , in a pressure range from 1 to 1100 bar. Empty symbols visualize the  $T_{\text{cloud}}$  values for PEG concentrations exceeding  $c^*$ . Reprinted with permission from [Julius et al., 2019]. Copyright © 2019 American Chemical Society.



In Figure 4.15 (e)-(g) the cloud point temperatures,  $T_{\text{cloud}}$ , of the ternary protein-polymer-buffer mixtures are depicted as a function of pressure for three polymer concentrations and for various PEG molecular weights. The reentrant liquid-liquid coexistence region (HP-LLPS) found at elevated pressures for dense polymer-free protein solutions reflects the increasing attractiveness of the solvent-mediated protein-protein interaction upon pressurization, likely due to pressure-induced changes in the water network structure [Möller et al., 2014a]. The decrease of  $T_{\text{cloud}}$  observed at ambient pressure in the presence of PEG also persists at high hydrostatic pressures. The pressure dependence of the phase boundary at low pressures (LP-LLPS), as found for the clean buffer system, remains largely unaffected by the addition of polymers, which is most likely due to a release of the void-volume of the closed-packed protein system. In contrast, the phase boundary of the HP-LLPS region is significantly shifted to higher pressures, most pronounced for small polymer sizes. The limits of the metastable LLPS region at both ambient and elevated pressures are modulated by the presence of the polymer in a similar way to the strength,  $J$ , of the attractive part of the protein-protein interaction potential derived from the SAXS signals of the complementary low-ionic strength protein-polymer mixtures. In the presence of polymers, the attractive part of the protein pair interaction potential,  $V_Y$ , in protein-polymer mixtures becomes more repulsive, leading to a decrease of the cloud point temperature and a shift of the HP-LLPS region to higher pressures. This effect is enhanced by a decreasing effective size ratio between the single polymer chain and the protein and by an increasing polymer concentration within the  $c_{\text{PEG}} < c^*$  boundary.

## 4.4 Conclusions

The effective protein-protein interaction potential,  $V(r)$ , governing the spatial distribution of lysozyme molecules in solution, as well as the boundaries of the temperature- and pressure-dependent (metastable) liquid-liquid phase coexistence region of dense lysozyme solutions were analyzed over a wide range of temperatures and pressures under various crowding conditions. Employing the disaccharide sucrose and the non-adsorbing polymer polyethylene glycol (PEG) with molecular weights within more than three orders of magnitude, we studied macro- and nanomolecular crowding scenarios, both occurring in the heterogeneous biological cell, and a wide range of crowder concentrations, crossing from dilute to semi-dilute polymer regime. The synthetic linear polymer PEG forms network-like structures beyond a polymer molecular weight specific crossover concentration and thereby mimics aspects of a eukaryotic cell, such as the dynamic cytoskeleton network.

We find that the influence of the crowder concentration on the mean distance between the protein molecules strongly depends on the size of the crowder. The strongest effect is observed in solutions containing small PEG molecules and sucrose, both leading to a significant decrease in the mean intermolecular distance of the protein molecules with increasing crowder concentration. Interestingly, the effect diminishes at intermolecular distances that are small enough for the second hydration shells of the proteins to penetrate each other. Conversely, the increase in polymer concentration beyond the polymer-size specific threshold ( $c_{\text{PEG}}/c^* \geq 1$ ), where the polymer solution structure changes from single dispersed polymers to an entangled network, leads to the recovery of the system where the proteins eventually maintain a distance comparable to that in the polymer-free system.

Furthermore, in the dilute polymer regime ( $c_{\text{PEG}}/c^* < 1$ ), the net effect of polymer size and concentration on the protein pair-interactions in protein-polymer mixtures, quantified by the protein's normalized second osmotic virial coefficient  $b_2$ , is strongly correlated with the position of the phase boundaries of the liquid-liquid coexistence region in the  $p$ - $T$ -plane. The effective protein-protein interactions become more repulsive in the presence of the polymer PEG, resulting in an increase of  $b_2$ . The effect is enhanced by a decreasing ratio of protein to polymer chain size and amplified with increasing polymer concentration. Accordingly, the entry into the high pressure liquid-liquid phase coexistence (HP-LLPS) region is shifted to higher pressures with the binodal being shifted to lower temperatures,  $T_{\text{cloud}}$ , over the entire pressure range. Under ambient conditions and within the limits of the dilute polymer regime ( $c_{\text{PEG}}/c^* < 1$ ), the impact of the polymer molecular weight (size) on both the strength,  $J$ , of the attractive interactions and the cloud point

temperature,  $T_{\text{cloud}}$ , exhibits a power law behavior. The dependence of the polymer’s radius of gyration,  $R_{G,\text{PEG},0}(M_w)$ , on the polymer molecular weight,  $M_w$ , is similarly described by a power law, indicating that (steric) excluded volume and depletion forces, both scaling with polymer size, are able to strongly modulate the protein-protein interactions.

The DLVO description is extended by the polymer-mediated depletion interaction potential between two lysozyme molecules to quantify its influence on the effective protein-protein interaction in dense protein-polymer mixtures. We find the depletion forces between the protein molecules are enhanced by increasing the polymer concentration, but level off at  $c_{\text{PEG}}/c^* \geq 1$  due to their decreasing range upon the formation of polymer network structures, before sufficient attraction (i.e. negative  $b_2$  values) could be induced. However, especially at  $c_{\text{PEG}}/c^* < 1$ , we observe a strong discrepancy between the theoretically predicted and experimental  $b_2$  values. This suggests that additional non-DLVO repulsive forces must be operative that control intermolecular protein-protein interactions at short distances, thereby stabilizing the densely packed protein solution against depletion-induced aggregation. Hydration repulsion, which only occurs when the protein molecules come close together and their hydration spheres start to overlap, is very likely to become important here. However, net attractive (transient) hydrophobic interactions between protein and polymer may be important as well, especially when the small PEG molecules are able to reside in the space between two protein molecules.

The application of hydrostatic pressures is a powerful tool for fine-tuning intermolecular distances in aqueous biomolecular systems and for the investigation of intermolecular interaction forces. In polymer-free buffer solution, the approach of lysozyme molecules upon compression and the concomitant increase of the normalized second virial coefficient,  $b_2$ , level off around  $\sim 1.6$  kbar, most likely due to changes of the water hydrogen-bond network structure, which eventually leads to a trend reversal upon further pressurization [Schroer et al., 2011a]. This non-monotonous pressure dependence of the proteins’ mean intermolecular distance and effective pair-interaction is affected by PEG-induced depletion forces, which gradually decline as the depletion thickness decreases owing to the decreasing polymer size upon compression, however. Hence, pressurization reduces the protein distance,  $d_{\text{lys}}$ , but also the depletion thickness,  $\delta_{\text{depl}}$ , of the crowder i.e. HHP counteracts the attractive depletion interaction in crowded solutions. In this sense, high hydrostatic pressures, as encountered in the deep sea up to the 1.1 kbar level, may alleviate the attractive forces between biomolecules induced by macromolecular crowding and thereby help to prevent the proteins from approaching each other too closely under compression, which could lead to protein aggregation.

Finally, since the metastable liquid-liquid phase separation is strongly correlated with the solid-liquid phase transition [Broide et al., 1996] (i.e. protein crystallization, see section 2.3.4), we envisage to optimize the solution conditions and the kinetics for protein nucleation and crystal growth using both variables, PEG and high hydrostatic pressure. Our study highlights the important, yet unexplored role of hydrostatic pressure in controlling and fine-tuning intermolecular distances and hence crystal growth in addition to the excluded volume (osmotic pressure) effect imposed by the polymer PEG [Crisman and Randolph, 2009, Gross and Jaenicke, 1994].

## Chapter 5

# Water-Mediated Protein-Protein Interactions at High Pressures are Controlled by a Deep-Sea Osmolyte

Cosolvents or osmolytes, such as free amino acids, methylamines, sugars, and polyols as well as the denaturant urea (see Figure 2.5) can be accumulated to rather high concentrations by cells to adjust cell volume and osmotic pressure to harsh extracellular environments, such as high temperature, freezing, and anhydrobiosis or to high hydrostatic pressure (HHP) as encountered in the deep sea up to the 1 kbar level (see section 2.1.2) [Hochachka and Somero, 2002]. In correlation with habitat depth and thus hydrostatic pressure, significant differences occur in the osmolyte compositions of cellular fluids compared to their shallow-living relatives. Under abyssal conditions, highest levels of methylamines, especially Trimethylamine-N-oxide (TMAO), are accumulated [Yancey et al., 2001, Kelly and Yancey, 1999]. TMAO is known to counteract the temperature- and pressure-induced destabilization of proteins [Yancey et al., 2001, Schroer et al., 2011a, Gao et al., 2017b, Arakawa and Timasheff, 1985] as well as the salt and urea inhibition of enzymes [Yancey, 2005]. Previous studies have shown, that a repulsion between stabilizers such as TMAO and the peptide-bond backbone of the protein leads to a strong exclusion of the cosolvent from the protein surface (depending on the protein charge [Canchi and García, 2013, Canchi et al., 2012, Su et al., 2017]) and thus to a preferential hydration of the protein's surface. Reducing the exposure of hydrated surface area and thus the entropically unfavorable interaction between cosolvent and backbone stabilizes native protein folds against denaturation [Canchi and García, 2013, Timasheff and Xie, 2003]. Conversely, perturbants such as urea are accumulated at the proteins surface and destabilize proteins at high concentrations by interacting preferentially with the protein backbone and amino acid side chains [Canchi and García, 2013, Timasheff and Xie, 2003] (see section 2.1.2).

In nature, mixtures of counteracting osmolytes are often found to be more beneficial for cells than individual ones. The absence of a perturbing component to offset stabilizers like methylamines at high concentrations may be detrimental to protein function. The latter may lead to over-stabilization of the proteins, elevated rigidity of enzymes and enhanced formation of non-functional aggregates. The underlying mechanisms of protein stabilization and, in particular, the linkage to the intermolecular interactions between proteins in such cosolvent mixtures both at ambient and elevated pressure are still largely unknown.

In this chapter, we focus on the impact of different types of organic osmolytes and biologically relevant osmolyte mixtures on the pressure dependent intermolecular pair-interaction potential,  $V(r)$ , of highly concentrated protein solutions (mimicking cell-like crowding conditions) applying small-angle X-ray scattering (SAXS) in combination with a liquid-state theoretical approach. To probe protein-protein interactions in such natural cosolvent solutions, the well-characterized monomeric protein lysozyme is employed, which is conformationally stable up to 5 kbar, and has successfully

been used before for this purpose [Schroer et al., 2011b, Möller et al., 2012, Schroer et al., 2011a]. By focusing on osmolyte mixtures that mimic cellular fluids of deep-sea organisms, such as shallow- and deep-living crabs, skates, and shrimps [Kelly and Yancey, 1999], we are able to go one step further in understanding the “real” biological intracellular fluids in nature and learn more details about their protective properties as well as and their differential effects.

This chapter is structured as follows: To investigate pressure-dependent protein-protein interactions in solution, the employed protein needs to remain in its folded state in the whole pressure range and at all solution conditions covered. Hence, in section 5.1, the pressure stability of the protein structure is checked by high-pressure SAXS measurements carried out on diluted lysozyme solutions for all solution conditions yielding shape and size of the protein. In Section 5.2, the DLVO theory in concert with SAXS measurements of the intermolecular structure factor and liquid state theoretical approaches have been used in determining the influence of single osmolytes and natural osmolyte mixtures on the pressure-dependent protein pair-interaction potential of dense protein solutions. In section 5.4, we disclose water-mediated changes of the protein-protein interactions, hardly visible in the associated average static structure factors, by the analysis of its isothermal pressure derivatives which reflect changes in three-body correlations in the liquid and are sensitive to changes in the solvent-mediated intermolecular interaction. Finally, section 5.5 summarizes the results.

**The content of this chapter is published in the following original publication and has been rephrased for this thesis:**

Julius, K., Weine, J., Berghaus, M., König, N., Gao, M., Latarius, J., Paulus, M., Schroer, M.A., Tolan, M., and Winter, R. (2018). Water-Mediated Protein-Protein Interactions at High Pressures are Controlled by a Deep-Sea Osmolyte, *Phys. Rev. Lett.*, 121(3):038101 (Copyright © 2018 American Physical Society)

## 5.1 Pressure Dependence of the Protein’s Radius of Gyration at Various Solution Conditions

First, to reveal potential pressure-dependent changes in the structure of the lysozyme molecule, high-pressure SAXS measurements were carried out on diluted 1% (w/v) ( $\sim 10 \text{ mg mL}^{-1}$ ) lysozyme solutions with an amount of up to 1 M organic osmolytes in a pressure range from 1 to 3500 kbar (see sections 3.1 and 3.2 for more details on sample preparation and the experimental SAXS setup, respectively). For the analysis of the azimuthally averaged and background corrected scattering intensities,  $I(q)$ , the inverse Fourier-transformation program GNOM [Svergun et al., 1988, Svergun, 1992] was employed, yielding the radial pair-distance distribution,  $p(r)$ , the maximum dimension of the protein in solution,  $D_{\text{max}}$  and the proteins radius of gyration,  $R_G$ .

In Figure 5.1, the analysis is lined out exemplarily for the 1% (w/v) lysozyme in 25 mM Bis-Tris + 1 M L-proline ( $T = 25^\circ\text{C}$ , pH 7) solution. Figure 5.1 (a) depicts the scattering intensities,  $I(q)$ , as a function of pressure together with the corresponding refinements (*black solid lines*). The Kratky representation of the data, ( $q^2 I(q)$  vs.  $q$ ), exhibits a pronounced maximum for all solution conditions and pressures studied. The Kratky plots together with the shapes of the corresponding  $p(r)$  curves, depicted in (c), indicate that the globular shape of the protein is preserved and no unfolding is induced. In good agreement with literature data [Schroer et al., 2011a, Maeno et al., 2009], the protein exhibits, within the experimental error, a constant radius of gyration of  $R_G = 1.45 \pm 0.02 \text{ nm}$  in the whole pressure range and for all cosolvents studied (see Figure 5.1 (d)). Of note, at high osmolyte concentrations an increase of the solvents electron density leads to a reduction of the scattering contrast of the proteins, accompanied by a decline of the signal-to-noise ratio. This is mirrored in a greater variance in the obtained  $R_G$  values.

The results are consistent with the findings of earlier work, that osmolytes, selected by nature for the purpose of maintaining osmotic pressure at high concentrations, reportedly lead to a stabilization of the native protein structure by being preferentially excluded from the protein surface,

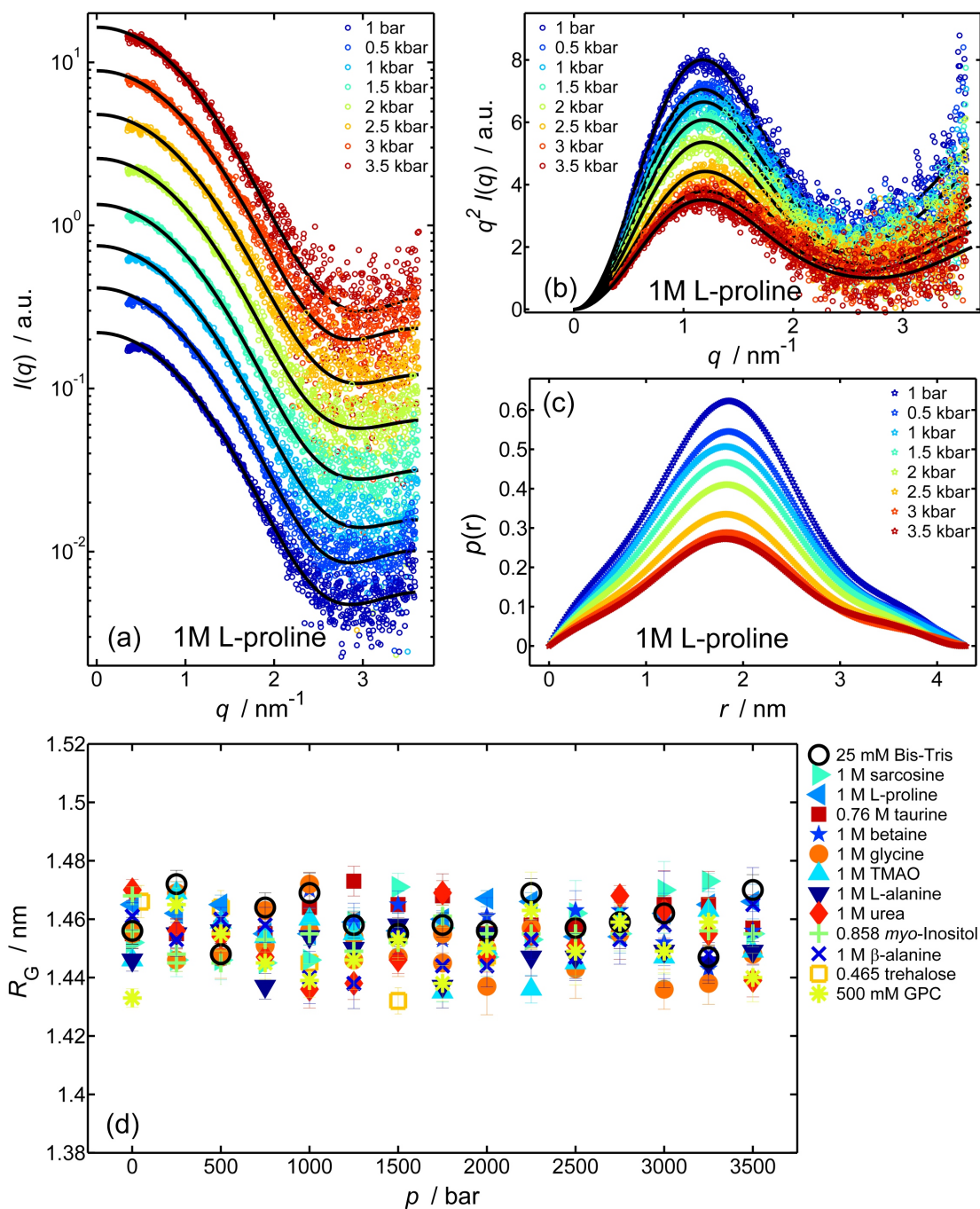


Figure 5.1: Experimental SAXS data of 1% (w/v) lysozyme + 25 mM Bis-Tris (pH 7) with 1 M L-proline at 25°C in a pressure range from 1 - 3500 bar and the corresponding refinements (*solid black lines*), generated with the inverse Fourier-transformation program GNOM of the ATSAS 2.8 package [Svergun et al., 1988, Svergun, 1992]. The scattering signals were shifted for reasons of clarity. (b) Kratky plot ( $q^2 I(q)$  vs.  $q$ ) of the experimental data and the corresponding refinements (*solid black lines*). (c) Radial pair distance distribution function,  $p(r)$ , as a function of pressure. (d) Comparison of the experimentally derived radii of gyration,  $R_G$ , for all osmolyte species at high concentration as a function of pressure. Reprinted from [Julius et al., 2018b]. Copyright © 2018 American Physical Society.



or if so bind very weakly to the protein, since they should not perturb enzyme or other cellular components (see section 2.1.2). The scattering of a single lysozyme molecule averaged over its orientation,  $\langle |F(\mathbf{q})|^2 \rangle_\Omega$ , is provided experimentally by the lowest protein concentrations for each solution condition and can be successfully refined by the scattering calculated from the atomic coordinates (+ hydration) of lysozyme (crystal structure PDB entry: 1LYZ [Harata, 1994]) employing the program CRY SOL [Svergun et al., 1995]. However, for the combined form and structure factor analysis from the scattering from dense lysozyme solutions, the lysozyme form factor was approximated by the radially averaged scattering function of a prolate ellipsoid [Shukla et al., 2008, Liu et al., 2005b]. The lysozyme form factor can be successfully modeled from the SAXS intensity curves from the diluted 1% (w/v) lysozyme solutions by the radially averaged analytical scattering function,  $P(q)$  of an prolate ellipsoid of revolution with the semi-axes  $a = 1.57$  nm and  $b = 2.42$  nm, effective hard-sphere diameter  $\sigma_{\text{lys}} = 2(a^2b)^{1/3}$  and volume  $V_p = 4/3\pi(a^2b)$  (see section 2.4.2), in good agreement with previous works [Shukla et al., 2008, Schroer et al., 2011a, Möller et al., 2012, Schroer et al., 2011b, Liu et al., 2005b]. The analytic form factor,  $P(q)$ , calculated by this method is in good agreement with the scattering calculated from the crystal structure (+ hydration) of lysozyme employing CRY SOL [Svergun et al., 1995], except that a small additive constant background ( $0.0105 \cdot P(q)|_{q=0}$ ) is needed in order to describe the data at high  $q$  values [Shukla et al., 2008].

## 5.2 Effects of Single Cosolvents on the Pressure-Dependent Protein-Protein Interaction Potential

As described in section 2.4.4, the small-angle scattering profiles,  $I(q)$ , of a solution of interacting monodisperse globular particles like lysozyme molecules can be modeled by

$$I(q) \propto n \cdot \Delta\rho^2 \cdot V_p^2 \cdot P(q) \cdot S_{\text{eff}}(q) \quad (5.1)$$

within the so-called decoupling approximation [Liu et al., 2005b, Kotlarchyk and Chen, 1983, Shukla et al., 2008]. Here,  $\Delta\rho$  denotes the electron density contrast,  $V_p$  the volume of the particle and  $P(q)$  the protein's form factor, determined by the shape and size of a single lysozyme molecule averaged over its spatial orientation (see section 5.1). The average number density of particles in the sample  $n$  is related to the protein's volume fraction *via*  $\Phi_{\text{lys}} = nV_p$ . Since the volume fraction occupied by the protein in the sample volume increases upon compression, high-pressure X-ray transmission measurements on dense aqueous 10% (w/v) lysozyme solutions were carried out yielding  $\Phi_{\text{lys}}(p)$  for all pressure conditions (see Figure 4.4 and section 3.6 for more details on the experimental setup and the data analysis). The effective structure factor,  $S_{\text{eff}}(q)$ , an additional scattering contribution arising for solutions of higher protein concentration, is sensitive to the spatial arrangement and thus the intermolecular interactions of the scattering particles. The position  $q_{\text{max}}$  of the main peak of  $S_{\text{eff}}(q)$  can be linked to the mean distance  $d_{\text{lys}} \simeq 2\pi/q_{\text{max}}$  between neighboring protein molecules in solution in real space. Within the mean-spherical approximation (MSA),  $S_{\text{eff}}(q)$  is linked to the proteins effective intermolecular interaction potential,  $V(r)$  [Liu et al., 2005b, Hansen and McDonald, 2013] (see section 2.4.4). Following previous works [Schroer et al., 2011a, Schroer et al., 2011b, Möller et al., 2012], the effective pair interaction potential,  $V(r)$ , of lysozyme molecules in solution, with centers separated by the distance  $r$ , is modeled in the framework of the Derjaguin-Landau-Verwey-Overbeek (DLVO) theory as the sum of a long-ranged screened Coulomb potential,  $V_{\text{SC}}(r)$ , a repulsive hard-sphere potential,  $V_{\text{HS}}(r)$ , and a short-ranged attractive Yukawian-like potential,  $V_{\text{Y}}(r)$  (see section 2.2.3). The DLVO potential is determined by fitting the effective structure factor to the experimental scattering intensity employing the MATLAB<sup>®</sup> package from [Liu et al., 2005a]. The only free parameter in the modeling of the experimental data is the strength of the attractive Yukawian-like part of the effective pair interaction potential,  $J$ .

As a measure of the overall pair-interaction potential, the normalized protein-protein osmotic second virial coefficient,  $b_2$ , has been calculated from the DLVO potential parameters employing Eq. (2.4).

Figure 5.2 depicts exemplarily the model-based data analysis procedure for the experimental SAXS intensities,  $I(q)$ , of 10% (w/v) lysozyme in 25 mM Bis-Tris (pH 7) buffer as a function of

trehalose concentration,  $c$ , and pressure,  $p$ , at  $T = 25^\circ\text{C}$ . A pronounced intermolecular correlation peak is observed at momentum transfer  $q_{\text{corr}}$ , indicating a repulsive short-range order of lysozyme molecules, that shifts to a higher  $q$ -value with increasing trehalose concentration (Figure 5.2 (a)).

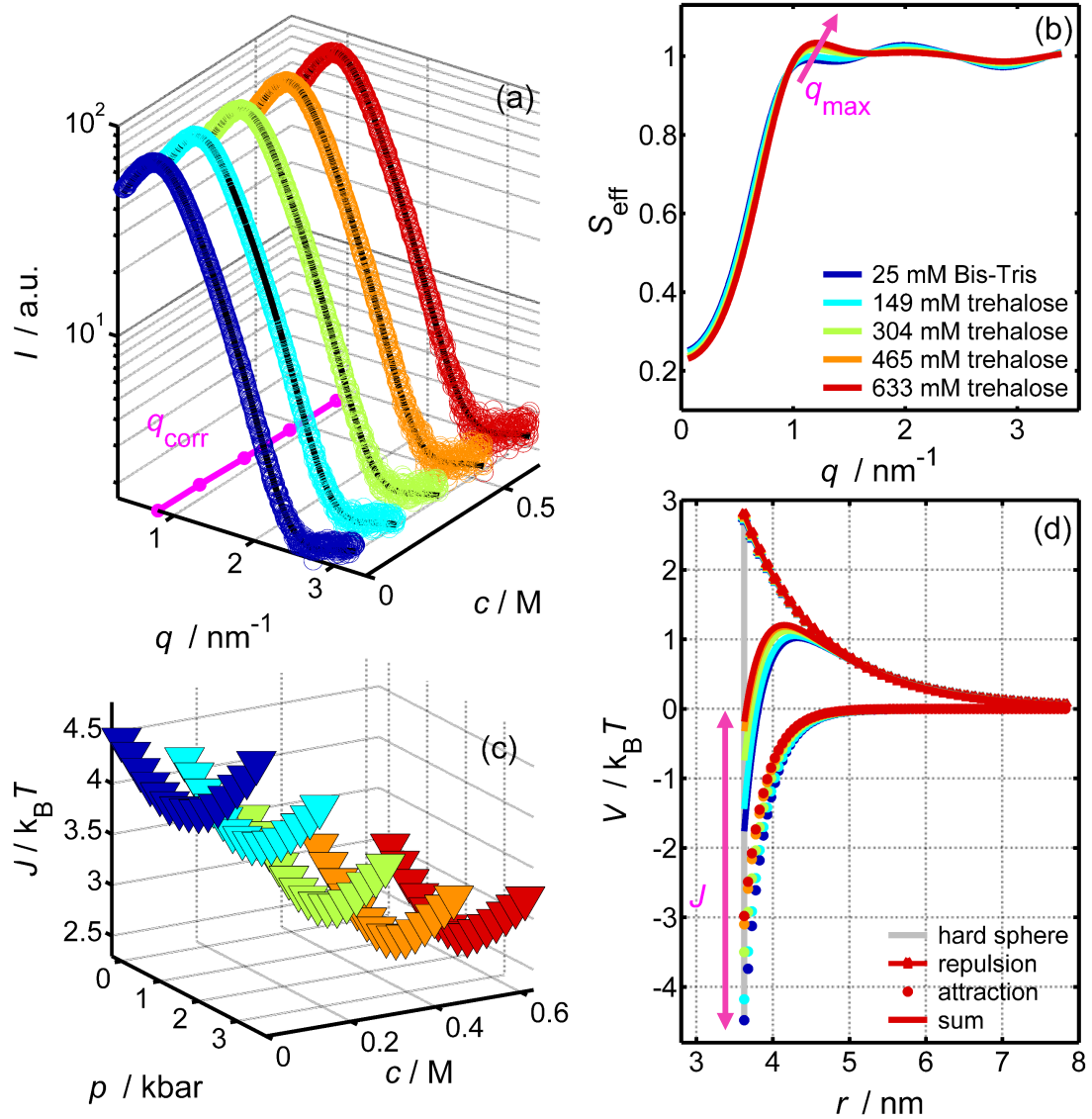


Figure 5.2: (a) Experimental SAXS data,  $I(q)$ , for a 10% (w/v) lysozyme in 25 mM Bis-Tris solution at  $25^\circ\text{C}$  and ambient pressure for various trehalose concentrations,  $c$ . *Solid black lines* display the refinement of the data. (b) Results of the refinement for the effective structure factor,  $S_{\text{eff}}(q)$ , at various trehalose concentrations,  $c$  and pressures,  $p$ . (c) Strength of the attractive interaction,  $J(c, p)$ . (d) Total protein-protein interaction potential,  $V(r)$ , (*sum*) displayed together with its contributing parts for various trehalose concentrations. Reprinted from [Julius et al., 2018b]. Copyright © 2018 American Physical Society.

Division of the scattering intensities by the analytical form factor,  $\langle P(q) \rangle$ , obtained by refining the scattering intensities of a dilute lysozyme solution with the model presented above (see section 5.1), yields the effective structure factor,  $S_{\text{eff}}(q)$ . The refinements of  $S_{\text{eff}}(q)$  to extract the effective protein-protein interaction potential,  $V(r)$ , are displayed in Figure 5.2 (b) and the consequent fits of the scattering intensities in (a) as solid black lines. The height of the first maximum of the effective structure factor,  $S_{\text{eff}}(q)$ , increases with the trehalose concentration and its position shifts to slightly higher  $q$ -values, concomitantly (*marked by arrow*). The increase of  $q_{\text{max}}$  reflects a slight decrease of the mean intermolecular distance between adjacent lysozyme molecules,  $d_{\text{lys}} \simeq 2\pi/q_{\text{max}}$

(see Appendix B, Figure B.1). The resulting DLVO effective pair interaction potential is depicted in Figure 5.2 (d) together with its single contributions for all trehalose concentrations and the pure buffer case. The decrease in dielectric permittivity of the solution at 25°C upon addition of trehalose ( $d\epsilon_r/dc = -7.53 \text{ M}^{-1}$ ) was taken into account in the calculation of the repulsive (screened) long-range Coulomb contribution,  $V_{SC}(r)$  (Eq. (2.20)). By reducing the solvents permittivity, trehalose enhances the strength of the electrostatic repulsion between the proteins with constant like charge  $+8e$  and concomitantly reduces the Debye-Hückel screening length,  $\lambda_D$ , (Eq. (2.21)). The increase in repulsive Coulomb interaction is accompanied by a marked decrease of the short-range attractive part with increasing trehalose concentration. Still, a slight decrease of  $d_{lys}$  is observed (see Appendix B, Figure B.1), which might be rationalized by the excluded volume effect imposed by the compatible cosolvent (see section 2.1.1). Among other osmolytes, trehalose was reportedly found to be most excluded from the proteins surface [Timasheff, 2002, Xie and Timasheff, 1997]. The effect of trehalose, and sugars in general, on the protein conformation was found to be very weak [Lerbret et al., 2007]. As reported elsewhere [Paul and Paul, 2015, Sapir and Harries, 2011, Lerbret et al., 2005], an increase in trehalose concentration results in a growth of the average number of trehalose-trehalose hydrogen bonds, the consequence being an enhanced trehalose-trehalose interaction and development of trehalose clusters. However, for the trehalose concentration range considered here ( $c \leq 0.633 \text{ M}$ ), the actual formation of an extended trehalose hydrogen-bond network and its potential influence on the protein-protein interaction can be neglected.

Subsequently, HHP SAXS measurements were performed on the 10% (w/v) ( $\sim 102.7 \text{ mg mL}^{-1}$ ) lysozyme solutions to reveal changes in the intermolecular interaction due to combined pressure-cosolvent effects. Figure 5.2 (c), depicts the strength of the attractive part of the pair interaction potential,  $J$ , as a function of trehalose concentration,  $c$ , and pressure,  $p$ . First, a monotonous decrease of  $J$  compared to the pure buffer system with increasing trehalose concentration is visible and second, the non-monotonous pressure dependence of  $J(p)$ , as observed in previous studies on the pure dense lysozyme solution [Schroer et al., 2011a], is present at all cosolvent concentrations. With continuous compression of the solution, intermolecular spacing,  $d_{lys}$ , is slightly reduced and the intermolecular interaction potential,  $V(r)$ , is affected by a decrease of  $J$  (see Appendix B, Figure B.1). It is remarkable that with a pressure rise above  $\sim 1.6 \text{ kbar}$ , this effect is reversed. In earlier studies [Schroer et al., 2011a, Schroer et al., 2011b] such a trend reversal was attributed to an incipient change in the water structure upon pressurization [Soper and Ricci, 2000, Katayama et al., 2010, Schroer et al., 2011a].

In order to systematically investigate the effects of individual osmolytes on intermolecular interactions in dense lysozyme solutions, high-pressure SAXS measurements on 10% (w/v) lysozyme in osmolyte solutions were performed over the whole concentration range from 0 to 1 M for all species. Figure 5.3 (a) displays the experimentally determined strength,  $J(c)$ , of the attractive part of the interaction potential and the normalized second virial coefficient,  $b_2(c)$ , for a 10% (w/v) lysozyme + 25 mM Bis-Tris solution (pH 7) at ambient pressure and  $T = 25^\circ\text{C}$  in dependence of the osmolyte species and concentration,  $c$ . Further, the effect of pressure is depicted exemplarily for mid-level (Figure 5.3 (b)) and high concentration (Figure 5.3 (c)) of each species. It can be clearly seen that especially at high concentrations a pronounced osmolyte concentration dependence of the potential parameters is recognizable. In terms of species, two distinct cosolvent classes with contrasting effects on  $J(c)$  and  $b_2(c)$  emerge. One class is solely formed by TMAO and the second class essentially comprises all other osmolytes investigated in this study. In accordance with data from literature [Schroer et al., 2011b], TMAO significantly increases the attractive interactions between proteins. Remarkably, the other osmolytes are nearly completely interchangeable in their impact on the strength,  $J$ , of the attractive part of the pair-interaction potential up to mid-level concentrations. Since the additives belong to chemically disparate classes, the underlying process ought to be universal. These osmolytes similarly cause the effective pair interaction potential,  $V(r)$ , to become more repulsive, i.e., the strength of the Yukawian part,  $J$ , decreases in a linear manner with increasing osmolyte concentration. Here, differences only become apparent at higher osmolyte concentrations ( $\gtrsim 0.5 \text{ M}$ ), i.e. in the region where changes in the (pressure-dependent) dielectric solution properties become more prominent. The corresponding normalized second osmotic virial coefficient,  $b_2$ , includes the contribution of the screened coulomb repulsion and, thus,

monitors the total effective pair-interaction (see Figure 5.3 (a)).

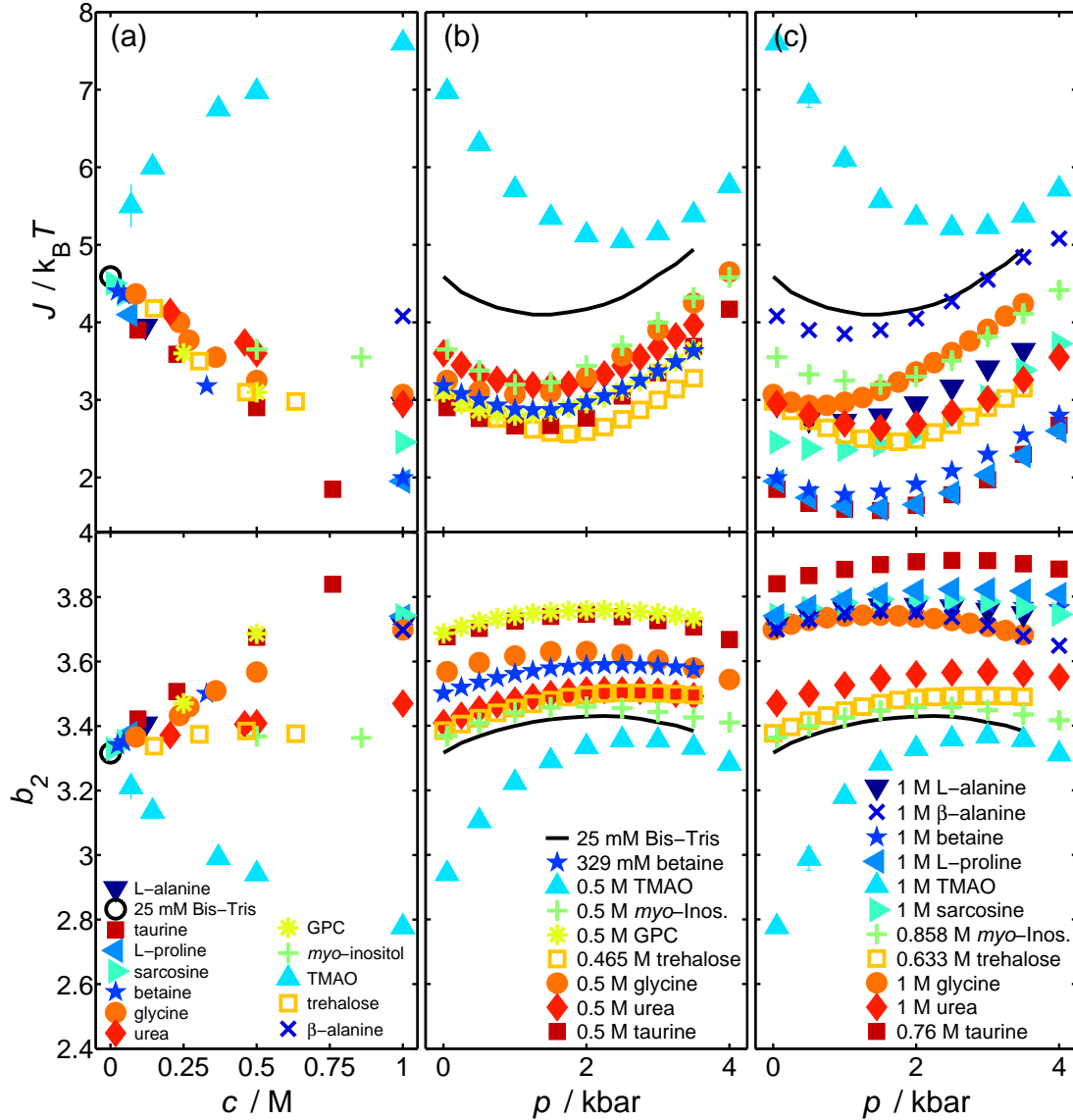


Figure 5.3: (a) Results of the refinement for the strength of the attractive part of the protein-protein interaction potential,  $J$ , and the normalized second virial coefficient,  $b_2$ , as a function of osmolyte concentration,  $c$ , at 25°C and ambient pressure, and as a function of pressure for mid-level (b) and highest (c) osmolyte concentrations. For comparison, the pure buffer system (10% (w/v) lysozyme, 25 mM Bis-Tris, pH 7) is depicted as well (black circle, solid line). Reprinted from [Julius et al., 2018b]. Copyright © 2018 American Physical Society.

As clearly can be seen from the theoretical expression for the screened Coulomb interaction potential,  $V_{SC}(r)$ , in Eq. (2.20) and from the Debye-Hückel screening length,  $\lambda_D$ , in Eq. (2.21), the strength as well as the range of electrostatic interactions in solution depend crucially on the solutions dielectrics (i.e.  $\epsilon_r$ ) as well as the effective net charge of the protein,  $Z_{eff}$ . To reveal if cosolvent-induced changes in the electrostatics could explain the different cosolvent effects, measurements of the solution pH and static dielectric permittivity were carried out for all solution conditions (For more details on the sample preparation see section 3.1 and for further information on the experimental setup see section 3.5) and the results will be discussed in the following:

**Cosolvent-Induced Changes of the Solutions pH** The effective net charge of the protein,  $Z_{\text{eff}}$ , is determined by the pH of the solution and has in pure 25 mM Bis-Tris buffer (pH 7) the effective net positive value  $Z_{\text{eff}} = +8e$  [Yu et al., 2015].

Pushing the pH-value towards the proteins isoelectric point ( $\text{pI}_{\text{lys}}=11$ ) and thus shifting the effective net charge of lysozyme towards smaller positive values  $Z_{\text{eff}} < +8e$  [Rodríguez-Arteche et al., 2012] results in a reduced Coulomb repulsion between the proteins. Furthermore, proteins are least hydrated at their pI and the increase of pH would result in binding more water.

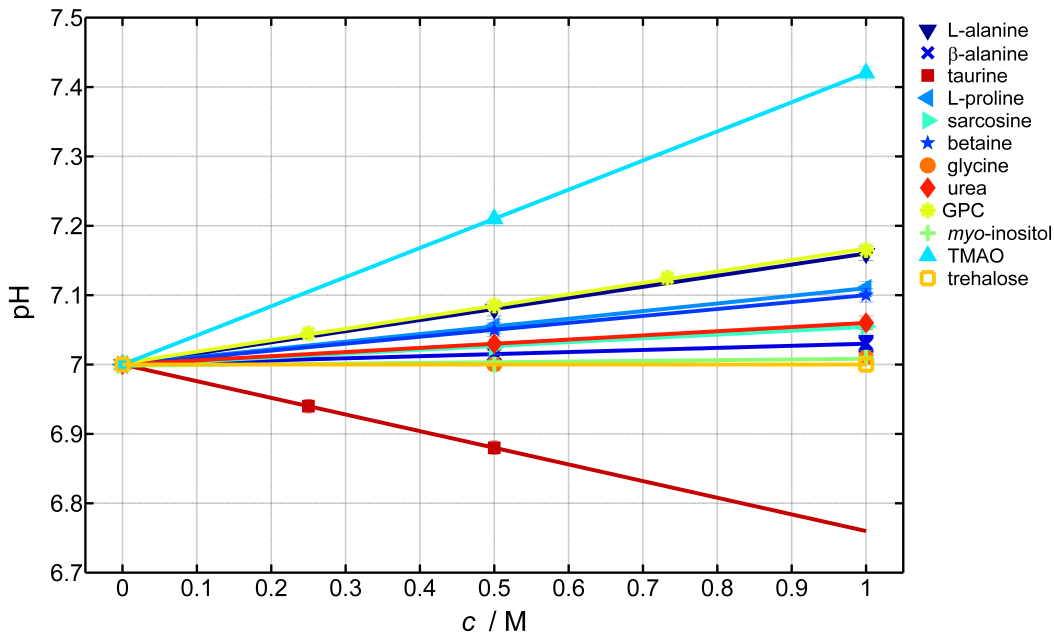


Figure 5.4: Experimentally derived pH dependence of the aqueous 25 mM Bis-Tris (pH 7) buffer solutions with dissolved osmolytes at molar concentration  $c$  at ambient pressure and  $T = 25^\circ\text{C}$ . Data is shown together with the corresponding linear refinements (*solid lines*). Reprinted from [Julius et al., 2018b]. Copyright © 2019 American Physical Society.

The molecular structures of the organic osmolytes investigated in this thesis are displayed in section 2.1.2, Figure 2.5. The  $\alpha$ -amino acids L-alanine ( $\text{pK}_a(-\text{COOH})=2.34$ ,  $\text{pK}_a(-\text{NH}_3^+)=9.69$ ;  $\text{pI} = 6.02$ ), L-proline ( $\text{pK}_a(-\text{COOH})=1.99$ ,  $\text{pK}_a(-\text{NH}_3^+)=10.60$ ;  $\text{pI} = 6.30$ ), glycine ( $\text{pK}_a(-\text{COOH})=2.34$ ,  $\text{pK}_a(-\text{NH}_3^+)=9.60$ ;  $\text{pI} = 5.97$ ) and the  $\beta$ -amino acids taurine ( $\text{pK}_a(-\text{SO}_3\text{H})=1.5$ ,  $\text{pK}_a(-\text{NH}_3^+)=8.74$ ;  $\text{pI} = 5.12$ ) and  $\beta$ -alanine ( $\text{pK}_a(-\text{COOH})=3.60$ ,  $\text{pK}_a(-\text{NH}_3^+)=10.19$ ;  $\text{pI} = 6.895$ ), are of zwitterionic nature with acidic isoelectric points [Jencks and Regenstein, 1968]. Depending on the ionization/protonation of the amino acids characteristic functional groups  $-\text{COOH}$  ( $-\text{SO}_3\text{H}$ ) and  $-\text{NH}_3^+$  at a particular pH, the amino acids can be present in different equilibrium forms. Regarding the  $\text{pK}_a$  values of the functional groups, the amino acids under study are all expected to be in their zwitterionic form at physiological pH.

The pH values of the dissolved osmolytes in aqueous 25 mM Bis-Tris (pH 7) buffer at concentrations ranging from  $c = 0$  to 1 M were measured with an accuracy of  $\pm 0.01$  at ambient pressure and  $T = 25^\circ\text{C}$ . The obtained results for the pH values as a function of osmolyte concentration reveal that the pH is constant within 0.5 pH units, i.e. the effective net positive value  $Z_{\text{eff}} = +8e$  of lysozyme can be considered to be constant for all solution conditions [Yu et al., 2015, McNeil-Watson and Kaszuba, 2011] (see Figure 5.4).

**Cosolvent-Induced Changes of the Solutions Static Dielectric Permittivity** The long-range Coulomb electrostatic pair interaction potential,  $V_{\text{SC}}(r)$ , between two proteins with effective net charge  $Z_{\text{eff}}$  is screened by solvents of high permittivity  $\epsilon_r$  surrounding the proteins. The reduction in strength of the long-range Coulomb interaction of the proteins occurs due to the polarization of the cosolvent molecules in the bulk water.



Figure 5.5 depicts the relative static dielectric permittivities  $\epsilon_r$  obtained from our own measurements and from literature (see Appendix B for the exact values for the dielectric increments,  $\delta = d\epsilon_r/dc$ , of the solitary osmolyte solutions and the dielectric permittivities,  $\epsilon_r$ , of the osmolyte mixtures of the shallow and deep-living species).

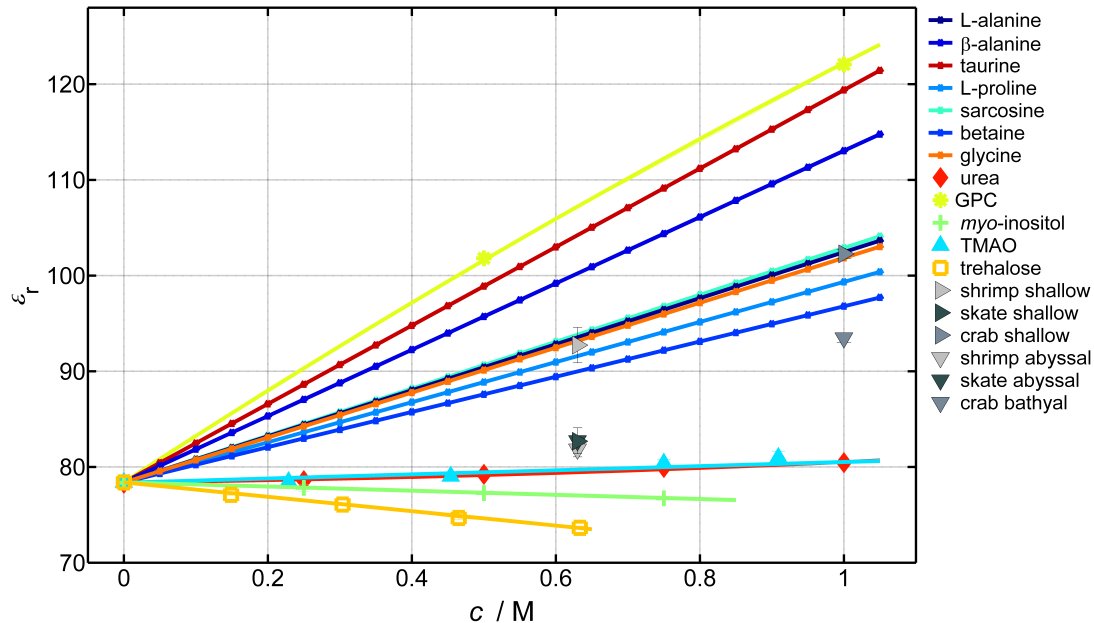


Figure 5.5: Experimentally derived values for the relative static dielectric permittivity,  $\epsilon_r$ , of the aqueous cosolvent mixtures found in shallow-living and deep-sea shrimp, crab and skate as well as of solitary osmolyte solutions (urea, TMAO, *myo*-inositol, GPC, and trehalose) in dependence of molar concentration,  $c$ . For comparison, this figure also includes  $\epsilon_r(c)$  data from literature for aqueous osmolyte solutions containing L-proline [Cohn and Edsall, 1965], sarcosine [Cohn and Edsall, 1965], betaine [Edsall and Wyman, 1964], taurine [Cohn and Edsall, 1965],  $\beta$ -alanine [Wyman and McMeekin, 1933], L-alanine [Wyman and McMeekin, 1933], and glycine [Wyman and McMeekin, 1933]. All data are valid for 25°C and ambient pressure. Reprinted from [Julius et al., 2018b]. Copyright © 2018 American Physical Society.

Previous dielectric spectroscopy studies on aqueous solutions of L-alanine, glycine,  $\beta$ -alanine and L-proline revealed that despite the huge dipole moment of the zwitterions, the tendency towards dipolar alignment is very weak in the concentration range investigated in this work. Solute-solute interactions are mainly screened by water and the zwitterions remain as isolated hydrated monomers in solution and if so, a weak decrease of the effective dipole moment of the solute is detected, due to anti-parallel dipole-dipole alignment when the solute molecules come closer with increasing concentration [Rodríguez-Arteche et al., 2012, Sato et al., 2005, Mcmeekin et al., 1964]. The fact that the osmolytes make no direct solute-solute interactions at moderate concentrations is in concert with our finding that the dielectric permittivities of the mixtures for the deep-sea species of water-structure stabilizing and destabilizing solutes seem to follow an additivity rule (see Figure 5.5). The experimentally derived static dielectric increments,  $\delta = d\epsilon_r/dc$ , of the individual cosolvents in aqueous solution can be placed in the order  $\delta(\text{trehalose}) = -7.53 \text{ M}^{-1} < \text{myo-inositol}$  (negative)  $< \text{water} < (\text{positive}) \text{ urea} \sim \text{TMAO} \ll \text{betaine} < \text{L-proline} < \text{glycine} \sim \text{L-alanine} \sim \text{sarcosine} \ll \beta\text{-alanine} < \text{taurine} \sim \delta(\text{GPC}) = +43.8 \text{ M}^{-1}$  (see Appendix B for exact values and Figure 5.5). In contrast to the other osmolytes, the carbohydrates trehalose and *myo*-Inositol lower the permittivity of the water (i.e. the dielectric screening) and as a result the Coulomb repulsion rises. The increase of  $\epsilon_r$  with increasing osmolyte concentration is strongest for taurine and GPC, which should lead to stronger screening and hence a reduction of Coulomb repulsion. As seen by the strong increase of  $b_2$  with  $c$  in Figure 5.3 (a), the increased dielectric screening cannot offset the increasing repulsion brought about by the decrease of the short-range attractive Yukawa

part of the effective pair-interaction potential:  $J(c)$  exhibits a strong negative gradient, indicating increasing repulsion. Hence, again, an excluded volume effect seems to dominate over electrostatics, which leads to slight decrease of the intermolecular distance,  $d_{\text{lys}}$  (see Appendix B, Figure B.1).

A completely different scenario can be observed with the stabilizing osmolyte TMAO, which, similar to the perturbant urea, changes the relative static dielectric permittivity of the solvent,  $\epsilon_r$ , only very little ( $\delta = d\epsilon_r/dc = +2.16 \text{ M}^{-1}$ ). In contrast to all other osmolytes, even concentrations of 0.5 M TMAO lead to a drastic increase of the attractivity, i.e.  $J$ . Such a strong rise of  $J$  must have another origin. The large variations in the concentration dependence of  $J(c)$  and  $b_2(c)$  among osmolytes may be due to a cosolvent-induced change in the van der Waals (vdW) potential (see section 2.2.1), which contributes to the attractive Yukawa part,  $V_Y(r)$ , of the DLVO potential (see section 2.2.3). This can be estimated using the Hamaker constant, as explained below.

**Van der Waals Forces** The Hamaker constant is, although in an indirect manner, related to the depth of the vdW potential and depends on the refractive and dielectric properties of the interacting proteins and on those of the surrounding medium (i.e.  $\epsilon_r, n_s$ ) (see section 2.2.1).

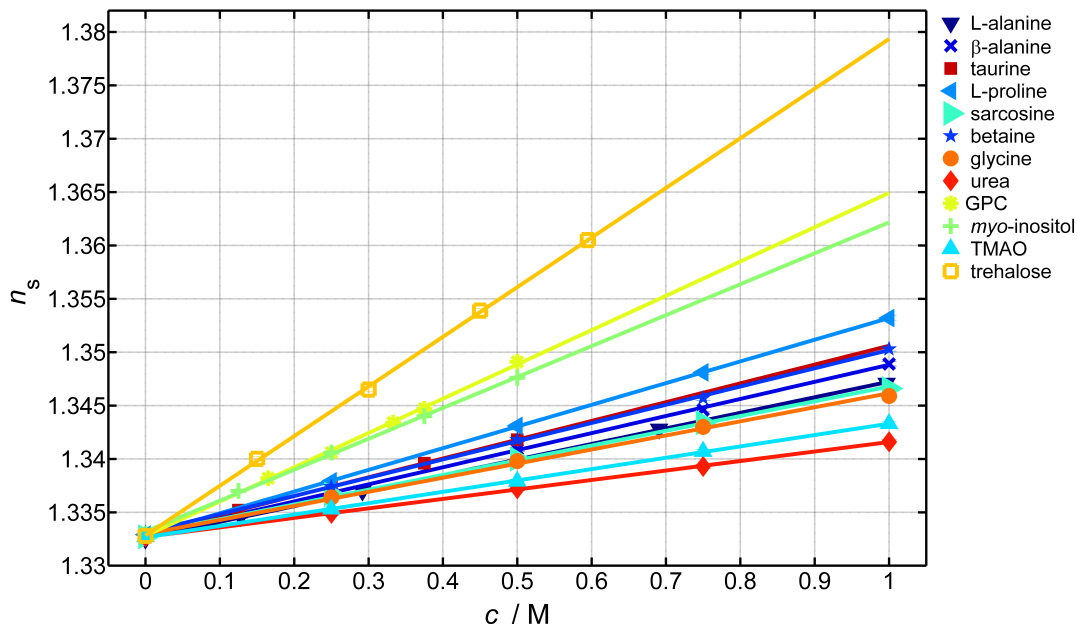


Figure 5.6: Experimentally derived refractive indices,  $n_s$ , of various aqueous 25 mM Bis-Tris (pH 7) osmolyte solutions in dependence of the osmolyte concentration,  $c$ , at ambient pressure and  $T = 25^\circ\text{C}$ . Data is shown together with the corresponding linear (extrapolated) refinements (*solid lines*). Reprinted from [Julius et al., 2018b]. Copyright © 2018 American Physical Society.

In theory, since the lysozyme molecules interact across a polarizable medium (water) containing also polarizable dissolved additives (osmolytes), the dipole field created by quantum fluctuations in one lysozyme molecule is many-times reflected back by each component of the condensed media that has been polarized by this field. Thereby, the classical van der Waals interaction between two proteins dissolved in pure water is strongly modified by these additionally generated electrodynamic (dispersion) forces due to the presence of the osmolytes. Sign and magnitude of these forces depend on the frequency-dependent polarizability of the components.

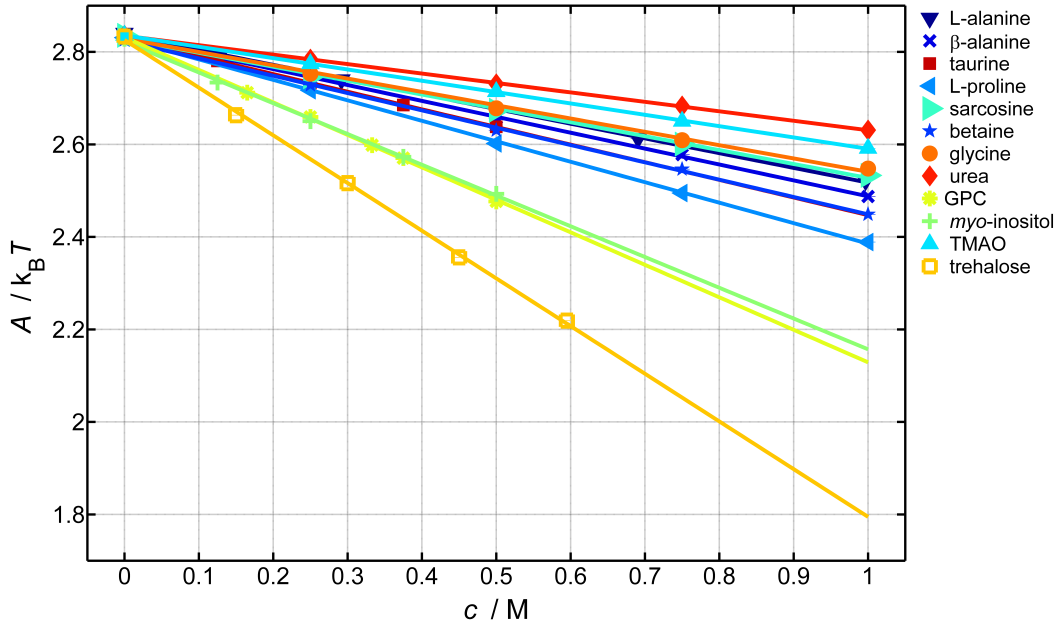


Figure 5.7: Calculated Hamaker Constant,  $A$ , of various aqueous osmolyte solutions containing 25 mM Bis-Tris (pH 7) in dependence of the osmolyte concentration,  $c$ , at ambient pressure and  $T = 25^\circ\text{C}$ . Data is shown together with the corresponding (extrapolated) linear refinements (*solid lines*). Reprinted from [Julius et al., 2018b]. Copyright © 2018 American Physical Society.

Here, the Hamaker constant was calculated for all solution conditions in the framework of the Lifshitz theory (see section 2.2.1) employing Eq. (2.11) with the solvents refractive indices  $n_s$  (see Figure 5.6) and static dielectric permittivities  $\epsilon_r$  (see Figure 5.5) obtained from our own measurements and from literature. For more details on the sample preparation see section 3.1 and for further information on the experimental setups for refractometry and dielectric spectroscopy see sections 3.4 and 3.5, respectively.

Figure 5.7 displays the calculated Hamaker constant for all solution conditions. At equal concentrations, the weakest attractive interaction should be observed in trehalose solution and the strongest in solutions with urea or TMAO, which is not consistent with the experimental data showing increased attractive interactions only in TMAO solutions (see Figure 5.3 (a)). As a result, solvent-induced changes of the Hamaker constant are not able to explain the particular effects of TMAO on the protein-protein interaction.

The impact of Coulomb repulsion on the effective pair interaction should become significant upon compression owing to a decrease of interatomic spacing (see Appendix B Figure B.1) and the monotonic increase of water permittivity,  $\epsilon_r$ , with pressure [Floriano and Nascimento, 2004]. As shown in Figure 5.3 (b) and (c), a decrease in  $J(p)$  and a concomitant increase of the normalized virial coefficient,  $b_2(p)$ , is in fact observed upon compression. However, this effect is noticeable up to about 1.6 kbar, only, where a trend reversal emerges. Remarkably, adding the osmolytes modulates the curves  $J(p)$  and  $b_2(p)$  only, but does not change their general shape, i.e. the mechanism underlying this effect ought to be universal. Next to the 1 M glycine solution, significant deviations in the pressure dependence of the intermolecular interactions from the pure buffer scenario occur only in TMAO solutions, which cause a much stronger pressure dependence of  $J(p)$  and  $b(p)$  as well as a shift of the minimum to  $J(p)$  and a maximum of  $b_2(p)$  to  $\sim 1$  kbar higher pressures. This effect may be due to significant changes in the solvent structure and/or a very strong thermodynamically favored exclusion of the additive from the protein surface, i.e. a pronounced solvophobic effect (see section 2.1.2) that reduces intermolecular distances and apparently enhances intermolecular attractive interactions.

### 5.3 Cosolvent Mixtures Mimicking Deep-Sea Conditions

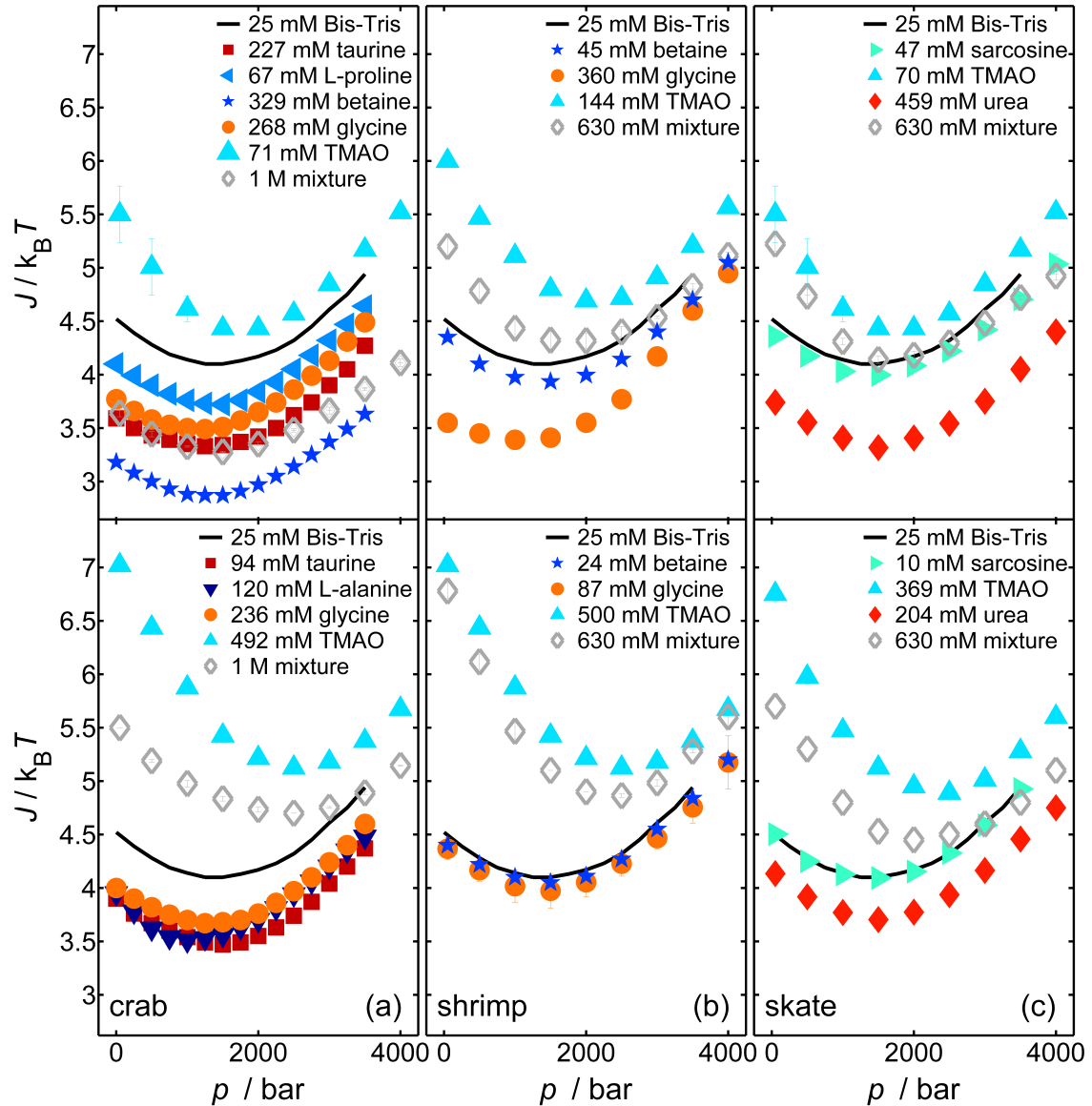


Figure 5.8: Pressure dependence of the strength of the attractive protein-protein interaction,  $J$ , in 10% (w/v) lysozyme + 25 mM Bis-Tris (pH 7) at 25°C with osmolyte mixtures added as found for shallow-living (*top half*) and deep-living (*bottom half*) crabs (a), shrimps (b), and skates (c) [Kelly and Yancey, 1999]. The results for the pure buffer (*solid black line*) and for the contributing single cosolvent solutions are shown as well. Reprinted from [Julius et al., 2018b]. Copyright © 2018 American Physical Society.

The next step was to record HHP SAXS data of 10% (w/v) lysozyme in natural cosolvent mixtures that mimic the cellular conditions found in marine organisms such as shallow and deep living crabs, skates and shrimps [Kelly and Yancey, 1999]. The cosolvent mixtures were calculated from [Kelly and Yancey, 1999], estimating a total concentration of 630 mM for skates, shrimps and 1 M for crab osmolyte mixtures based on typical values for cell solute concentrations [Yancey, 2005] (see section 3.1 for detailed sample compositions). Remarkably, in all species the TMAO content rises with increasing sea depth, i.e. hydrostatic pressure, accompanied by a decrease of the overall amount of amino acids, inositols, urea and methylamines. The amount and kind of osmolytes employed depend strongly on the species, however. Figure 5.8 shows the correspond-

ing potential parameter  $J(p)$  together with the data of the main contributing osmolytes of deep (bathyal/abyssal)-living and shallow living species. For comparison, the pure puffer system is shown as well (*solid black line*). The data unambiguously show that the cosolvents other than TMAO are largely interchangeable. This is probably due to the fact that the osmolytes do not interact directly at moderate concentrations [Canchi et al., 2012, Rodríguez-Arteche et al., 2012, Jackson-Atogi et al., 2013], i.e. the net effect on the protein-protein interaction seems to follow largely an additivity rule. In fact, the addition of the other solvents to the solution causes the effect of TMAO to be attenuated to varying degrees depending on the cosolute structure. As a consequence, the pronounced effect of TMAO on the potential parameters is reduced and the shift of the minimum in  $J(p)$  to higher pressures is reversed, not only by the denaturant urea [Niebuhr and Koch, 2005, Schroer et al., 2011b], but also by the presence of compatible cosolvents such as glycine (as exemplarily demonstrated in section 5.3.1, Figure 5.9). Since TMAO is also known to stabilize proteins and other biomolecules most effectively [Canchi and García, 2013], it appears that natural osmolyte mixtures are composed to compensate for TMAO-induced overstabilization and overattractiveness, which may be necessary to maintain normal cellular functionality.

### 5.3.1 Counteracting the Effect of TMAO

Figure 5.9 (a) depicts the contrasting effects of glycine and TMAO on the effective structure factor,  $S_{\text{eff}}(q)$ , of 10% (w/v) lysozyme in 25 mM Bis-Tris (pH 7, 25°C) solution at various osmolyte concentrations and ambient pressure. As can be seen from the shift of the position of the structure factors main peak,  $q_{\text{max}}$ , towards smaller  $q$ -values, TMAO increases the intramolecular distance,  $d_{\text{lys}} \cong 2\pi/q_{\text{max}}$ , between the protein molecules as it is reduced by glycine relative to the pure buffer system (see also Appendix B, Figure B.1). The corresponding effective protein-protein interaction potential is shown in Figure 5.9 (c) as well. As depicted in Figure 5.9 (b), the pressure dependence of the strength of the Yukawa part,  $J$ , for the TMAO and glycine systems of concentrations in the range of  $\sim 0.07$  to 1 M shows a different effect of both osmolytes on the pressure sensitivity of  $J$  below  $\sim 3$  kbar, both in terms of shape and magnitude of  $J(p)$ . Figure 5.9 (d) and (e) show that in mixtures of TMAO and glycine the pressure dependence of  $J$  is dominated by the strong cosmotropic stabilizer TMAO. Even in a TMAO-glycine mixture with a molar ratio of 1:2, the effect of TMAO on the pressure sensitivity of  $J$  is only slightly compensated by glycine. Of note, it was found that the ratio 1(TMAO):2(urea) is most effective in the counteraction of urea and TMAO at the same protein concentration [Schroer et al., 2011b, Yancey et al., 2002]. Since there seems to be no specific direct interaction between glycine (and the other osmolytes) and TMAO in bulk, the observed effect has to be mediated indirectly via the water hydrogen-bonded network [Pollard and Wyn Jones, 1979].



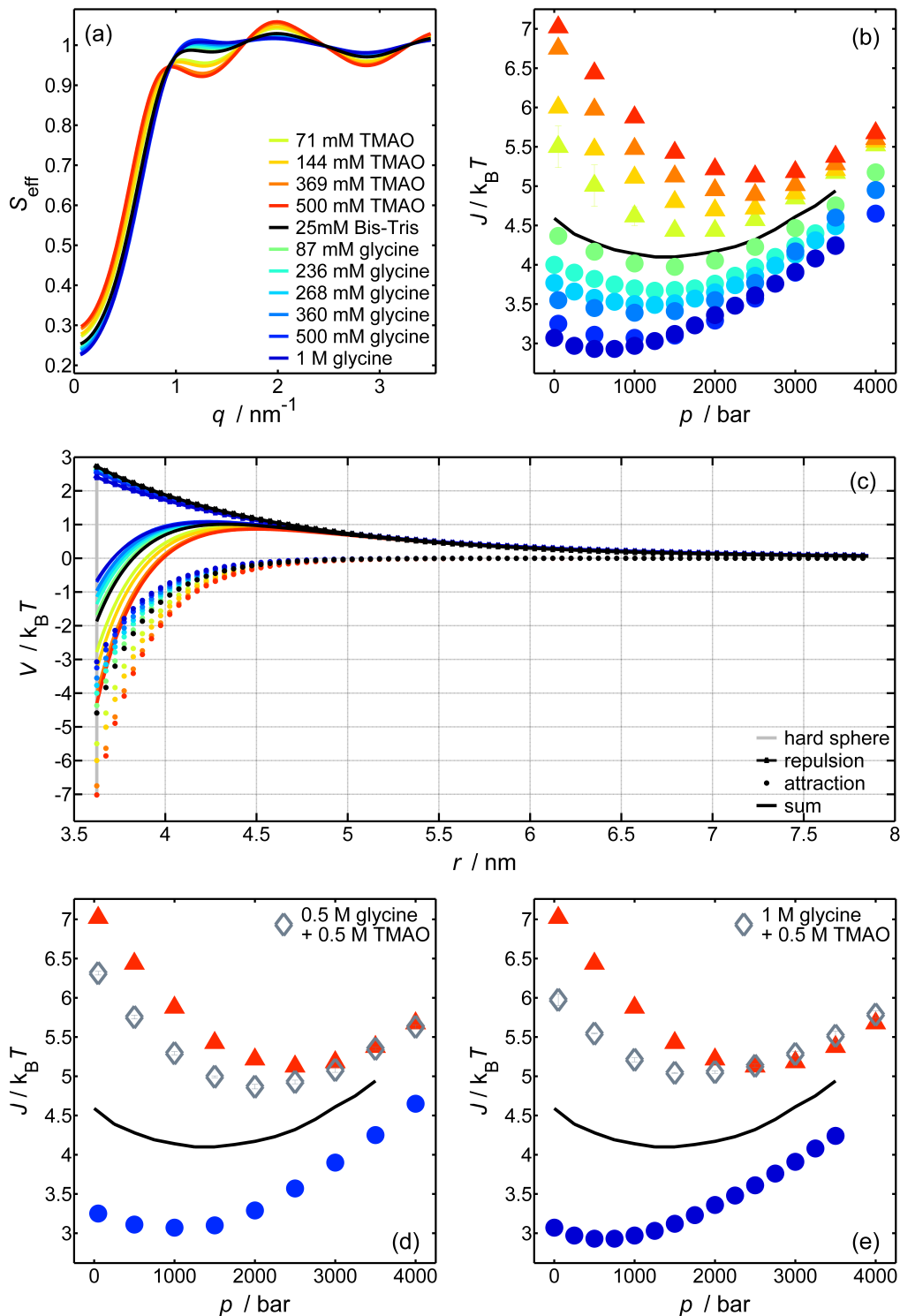


Figure 5.9: (a) Effective structure factor,  $S_{\text{eff}}(q)$ , of a 10% (w/v) lysozyme solution with 25 mM Bis-Tris (pH 7) at 25°C and ambient pressure for TMAO concentrations of 71 to 500 mM and glycine concentrations of 87 mM to 1 M. (b) Results of the refinement for the strength of the attractive part of the protein-protein interaction potential,  $J(c)$ , as a function of pressure,  $p$ , for various osmolyte concentrations. (c) Total interaction potential,  $V(r)$ , and its different contributions. (d) Pressure dependence of the attractive interaction of lysozyme solutions in glycine-TMAO mixtures at the ratio 1:1 and (e) 2:1. Reprinted from [Julius et al., 2018b]. Copyright © 2018 American Physical Society.

## 5.4 Water-Mediated Changes of the Protein-Protein Interactions

The particular role played by TMAO is clearly evident and might be attributed to its ability to compensate for pressure effects by strengthening and increasing water-water-hydrogen bonds and by inducing a strong spatial order of the hydrogen bonding network [Zou et al., 2002, Canchi and García, 2013]. Seeking to reveal an additional proof for such water-mediated effect, information on many-body structural correlations is expected to be helpful. In fact, for the description of hydrogen-bound liquids, such as water itself or protein solutions, triplet correlation functions (TCFs),  $g_3(\mathbf{r}_1, \mathbf{r}_2, \mathbf{r}_3)$ , seem play an important role in addition to the pair distribution functions [Dhabal et al., 2017, Egelstaff et al., 1971, Schroer et al., 2012] (see section 2.4.4).

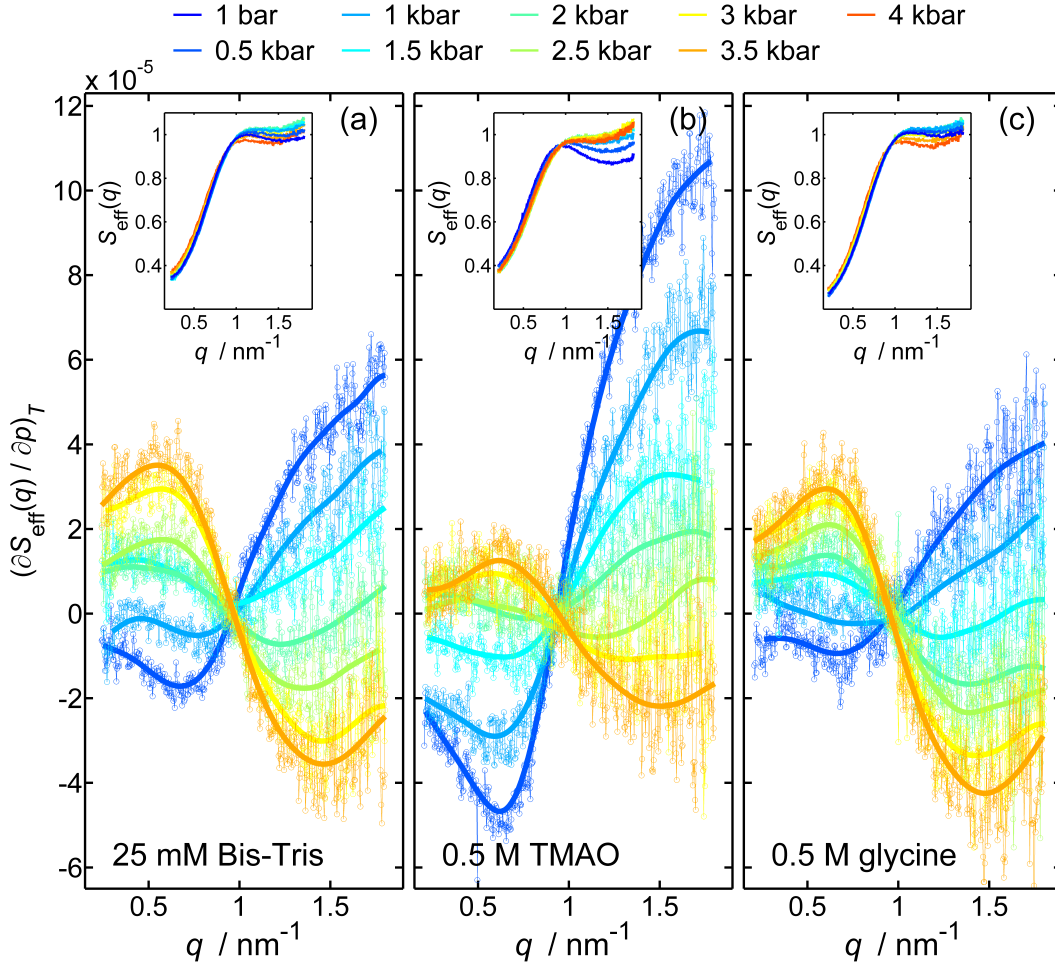


Figure 5.10: Isothermal pressure derivative of the experimental effective protein structure factor,  $S_{\text{eff}}(q)$ , for (a) 10% (w/v) lysozyme dissolved in pure buffer (25 mM Bis-Tris, pH 7,  $T=25^\circ\text{C}$ ), and buffer solutions containing (b) 0.5 M TMAO and (c) 0.5 M glycine. *The lines are a guide to the eye. The insets show the underlying experimentally derived structure factors for different pressures.* Reprinted from [Julius et al., 2018b]. Copyright © 2018 American Physical Society.

In order to obtain information on the TCFs, the isothermal pressure derivative of the static (effective) structure factor,  $(\partial S_{\text{eff}}(q, p_m)/\partial p)_T$ , of dense protein solutions at the mean value  $p_m$  was calculated from the experimental data by numerical differentiation employing Eq. (2.109). Here, we employ the pressure interval  $\Delta p = 0.5$  kbar, since the experimental data was collected in pressure steps of 250 bar at  $T = 25^\circ\text{C}$ . Changes in the shape and sign of  $(\partial S_{\text{eff}}(q, p_m)/\partial p)_T$  reflect changes in the three-body correlations in the liquid [Dhabal et al., 2017], and are sensitive

to changes in the solvent-mediated intermolecular interaction potential. The essential features describing the structure of the liquid via inter-protein correlations are located in the  $q$ -range around the correlation peak in the SAXS pattern. Hence, in the analysis of  $(\partial S_{\text{eff}}(q, p_m)/\partial p)_T$  we mainly focus on the region  $q \lesssim 1.72 \text{ nm}^{-1}$ . Figure 5.10 shows  $(\partial S_{\text{eff}}(q, p_m)/\partial p)_T$  for aqueous 10 % (w/v) lysozyme solutions at three different buffer conditions (e.g. 25 mM Bis-Tris buffer (pH 7), 25 mM Bis-Tris + 0.5 M TMAO, 25 mM Bis-Tris + 0.5 M glycine). At ambient pressure, the addition of 0.5 M TMAO to the protein solution results in a decreased height of the static effective structure factors first maximum and its shift to lower  $q$ -values in comparison to the pure buffer system as 0.5 M glycine has the opposite effect (see insets in Figure 5.10 and Figure 5.9 (a)). A decreasing first peak corresponds to a damping of the oscillations in the pair correlation function,  $g(r)$ , and therefore to less localized particles and a less ordered system. The shift of the main peak of  $S_{\text{eff}}(q)$  to lower  $q$ -values, mirrors an increasing mean intermolecular spacing of the proteins at the corresponding solution condition (first minimum in  $g(r)$  shifts outwards). Independent of the solutions additive, the application of pressures up to  $\sim 1.6$  kbar results in a simple isotropic compression of the system and therefore in a decreasing mean intermolecular spacing,  $d_{\text{lys}}$ . In pure buffer solution and 0.5 M glycine,  $(\partial S_{\text{eff}}(q, p_m)/\partial p)_T$  changes shape and sign around  $\sim 2$  kbar, indicating significant changes in the intermediate-range order of the hydrogen-bonded liquid in this pressure range. This may be due to the rearrangement of neighboring water molecules (e.g. changes in the tetrahedral network structure, collapse of the second coordination shell of water) [Schroer et al., 2012]. Interestingly,  $(\partial S_{\text{eff}}(q, p_m)/\partial p)_T$ , of lysozyme in the 0.5 M TMAO solution exhibits more pronounced maxima and minima in the region of the structure factor maxima, which indicates a different solution structure already under ambient conditions. In addition, changes in the shape of  $(\partial S_{\text{eff}}(q, p_m)/\partial p)_T$  and thus in the three-body correlation function are shifted to about  $\sim 1$  kbar higher pressures, indicating that the water-mediated protein-protein interaction potential in the TMAO solution differs significantly from the pure buffer case. A more quantitative analysis of these higher-ordered correlations and cosolvent-induced changes in structure and dynamics of dense protein solutions would require detailed molecular dynamics simulations of the system with appropriate pressure-adjusted force fields, which are out of reach at this time.

## 5.5 Conclusions

The influence of natural cosolvent mixtures on the pressure-dependent structure and protein-protein interaction potential of dense protein solutions was studied and analyzed using small-angle X-ray scattering in combination with a liquid-state theoretical approach. At conditions where intermolecular distances between proteins are of the order of a few water layers (i.e. under cell-like crowding conditions), a change in the second coordination shell of water and an increased hydration repulsion between the proteins seem to lead to the reversal of attractive interaction and intermolecular spacing upon compression. Changes in the interactions between cosolvent and water can modulate this behavior. These may include effects such as an inward shift of the pair-correlation function of oxygen atoms in water,  $g_{\text{O}_w\text{O}_w}(r)$ , by TMAO [Towey et al., 2013]; a cross-interaction between cosolvents, such as that of TMAO and urea observed at ambient pressure [Ganguly et al., 2015, Hunger et al., 2015]; or changes in protein-cosolvent-water interactions.

We find, that natural cosolvents are able to modulate the protein-protein interaction potential and its pressure dependence to variable extents. The addition of the deep-sea osmolyte TMAO leads to a pronounced exclusion volume and affects  $V(r)$  most strongly. This is due to its particular structure: TMAO is a rather small solute offering both highly hydrophilic and hydrophobic solvation regions. It has a strong dipole moment ( $\sim 5$  D) and excellent H-bonding performance. In addition, it shows a predominantly repulsive self-interaction [Canchi et al., 2012]. The other osmolytes seem to act essentially only as osmoregulators.

Not only does the presence of TMAO guarantee sustainability of the native protein's folded state under harsh environmental conditions [Yancey et al., 2001, Schroer et al., 2011a, Gao et al., 2017b, Arakawa and Timasheff, 1985], it also controls water-mediated intermolecular interactions at elevated pressure, preventing contact formation and protein aggregation. In fact, Embedded Cluster Reference Interaction Site Model (EC-RISM) theory in concert with ab initio molecular dynamics simulations and FT-IR data have recently revealed a charge redistribution upon compres-

sion of TMAO. Increased solvent-related polarization and a locally enhanced H-bonding network are both proposed as key elements for high-pressure adaptation [Hölzl et al., 2016, Imoto et al., 2016].

## Chapter 6

# The Effect of Osmolytes and Crowding on the Pressure-Induced Dissociation and Inactivation of Dimeric Horse Liver Alcohol Dehydrogenase

The study of the relationship between structure and activity of oligomeric enzymes under high pressure is essential for understanding the intermolecular interactions and reactivity of proteins in the cells of organisms thriving under harsh environmental conditions as well as for applications in biotechnology such as high-pressure enzymology. The effect of pressure on the assembly of oligomeric proteins and larger multi-subunit aggregates has already been discussed in detail, and the pressure-induced dissociation of oligomeric proteins is a well-described phenomenon [Daniel et al., 2006, Boonyaratanakornkit et al., 2002, Gross and Jaenicke, 1994, Silva and Weber, 1993, Weber, 1993, Silva et al., 2001, Silva et al., 1996, Ruan and Weber, 1993, Peng et al., 1993, Peng et al., 1994, Silva et al., 1992, Jaenicke, 1981, Mozhaev et al., 1996, King and Weber, 1986, Knorr et al., 2006, Lullien-Pellerin and Balny, 2002, Tang and Ruan, 1996, Silva et al., 1986, Ruan and Weber, 1989] (see section 2.3.2). Conversely, the effect of naturally occurring compatible, counteracting and (de)stabilizing osmolytes (see section 2.1.2) on the stability and enzymatic activity of oligomeric enzymes within the biologically relevant pressure range is largely unknown. Although the influence of macro- and nanomolecular crowding, as it occurs within the biological cell, on the stability of monomeric proteins is reasonably well understood (see section 2.1.1), there is a lack of knowledge about the interplay of temperature, hydrostatic pressure, osmotic pressure and the reduced free space (excluded volume effect) and its effects on oligomeric proteins, albeit of high biological relevance.

The HHP SAXS study presented here was performed within a collaboration between the groups of Prof. M. Tolan (Experimental Physics E IA / DELTA, TU Dortmund University) and Prof. R. Winter (Physical Chemistry I - Biophysical Chemistry, TU Dortmund University), set out to explore the relationship between enzyme stability, structure and function through the effect of pressure on horse liver alcohol dehydrogenase (LADH) in physiologically relevant solution conditions like crowding and the presence of cosolvents. In a combined experimental effort, the HHP SAXS measurements, yielding pressure-induced conformational changes of LADH on the quaternary and tertiary structure, were complemented by pressure-dependent FT-IR and fluorescence spectroscopy, monitoring changes on the secondary structural level. In addition, HHP-stopped flow kinetic measurements were performed to reveal the influence of high hydrostatic pressure [Luong et al., 2015, Luong et al., 2016], crowding and cosolvents [Yancey, 2005, Luong et al., 2015, Yancey and Somero, 1980, Yancey et al., 1982] on the enzymatic activity of the horse LADH, which is also effectively modulated by changes in the oligomerization state [Shallom et al., 2004, Ottosen et al.,



2002, Beernink and Tolan, 1996].

The chapter is structured as follows: At first, the studied dimeric enzyme horse liver alcohol dehydrogenase (LADH) is introduced in section 6.1. The results of the theoretical modeling of the small-angle X-ray scattering of monodisperse dimeric and monomeric LADH solutions as well as mixtures thereof, mimicking the solution conditions during the dissociation process of the dimeric enzyme in pure buffer, are lined out in section 6.2. Section 6.3 reports on the experimental HHP-SAXS data on diluted LADH in pure buffer solution in a pressure range of 1 - 3500 bar as well as on the results of the refinement of the SAXS signals on the structural changes of LADH under pressure. Section 6.4 reports on how the oligomerization reactions and hydrostatic pressure dependence of the dissociation rate of LADH are effectively modified by changes in the solution conditions upon addition of crowding agents and cosolvents. The results of the complementary experimental studies (i.e. pressure-dependent FT-IR, fluorescence spectroscopy and HHP-stopped flow measurements) carried out within the framework of the cooperation will be summarized shortly at the end of this chapter and discussed together with the SAXS data (see section 6.5).

**The content of this chapter is published in the following original publication and has been rephrased for this thesis:**

Julius, K., Al-Ayoubi, S.R., Paulus, M., Tolan, M., and Winter, R. (2018). The effects of osmolytes and crowding on the pressure-induced dissociation and inactivation of dimeric LADH, *Phys. Chem. Chem. Phys.*, 20(10):7093-7104

## 6.1 Horse Liver Alcohol Dehydrogenase (LADH)

In the biological metabolism of alcohols and hydroxysteroids, alcohol dehydrogenases (ADH) of various origins constitute a central element. Alcohol dehydrogenases catalyze the oxidation of various primary and secondary alcohols to the corresponding aldehydes or ketones and vice versa in the presence of the cofactor nicotinamide-adenine-dinucleotide ( $\text{NAD}^+$ ) by the reduction of  $\text{NAD}^+$  to NADH [Dalziel and Dickinson, 1966, Dallet and Legoy, 1996, Klinman, 1981, Silverstein and Boyer, 1964, Brändén et al., 1973]. ADHs play a key role in the alcoholic fermentation as well as in the ethanol metabolism and also have been employed as biocatalysts in chemical syntheses that involve ethanol oxidation [Galletti et al., 2010b, Giacomini et al., 2007, Galletti et al., 2010a]. This makes understanding the protein's stability and reactivity not only relevant for research purposes but also for technological applications. The well-studied enzyme horse liver alcohol dehydrogenase (LADH) is a dimeric protein of two identical subunits [Brändén et al., 1975, Klinman, 1981, Pettersson, 1987, Eklund and Brändén, 1987, Wang et al., 2000]. Each subunit's peptide chain is composed of 374 amino acid residues and features a catalytic and a coenzyme binding domain with two firmly bound tetracoordinated zinc atoms [Eklund et al., 1974, Ramaswamy et al., 1994]. The enzyme is not active in the monomeric state [Theorell, 1970, Sund and Theorell, 1963, Kornblatt et al., 1998], thus, the dissociation of the dimer is accompanied by the failure of the enzymatic activity. The dimeric protein has a molecular weight of  $M_w \simeq 80$  kDa and the monomeric subunit  $M_w \simeq 40$  kDa. The overall shape of the dimer corresponds to a prolate ellipsoid with the approximate dimensions  $45 \times 55 \times 100 \text{ \AA}^3$  [Eklund et al., 1974, Eklund et al., 1976, Brändén et al., 1973, Eklund et al., 1981, Eklund and Ramaswamy, 2008, Al-Karadaghi et al., 1994, Meijers et al., 2001, Meijers et al., 2007, De Smidt et al., 2008, Sturgis et al., 2001].

Earlier studies on horse liver alcohol dehydrogenase, based mainly on the fluorescence and phosphorescence properties of the tryptophan residues of the protein, have already reported that the protein is markedly affected by high hydrostatic pressures. However, pressure-induced structural changes such as dissociation and unfolding of the protein have not yet been investigated in detail [Trovaslet et al., 2003, Cioni and Strambini, 2002, Cioni and Strambini, 1996]. Conformational changes of the monomeric subunit, referred to as conformational drift, are generally reported to accompany the pressure-induced dissociation process of proteins. [King and Weber, 1986, Silva et al., 1986, Ruan and Weber, 1993, Weber, 1986, Ruan and Weber, 1989].

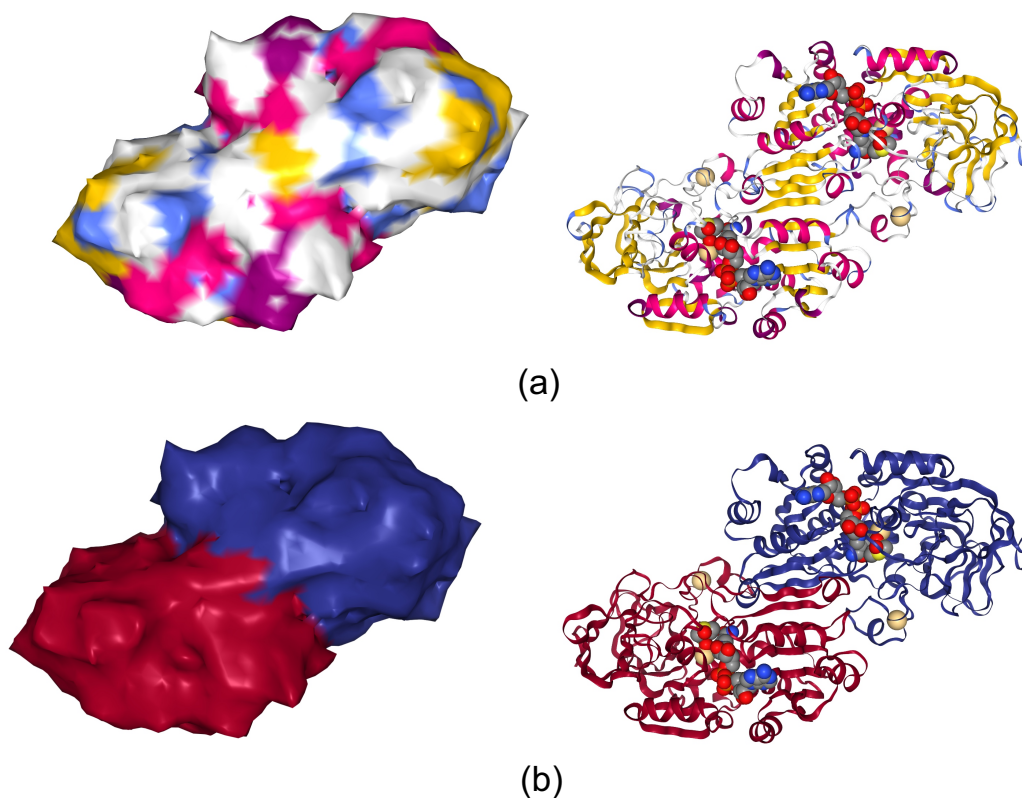


Figure 6.1: (a) Crystal structure (PDB entry: 2JHF [Meijers et al., 2007]) of the dimeric apoenzyme horse liver alcohol dehydrogenase (LADH). The dimer has the overall shape of a prolate ellipsoid with the approximate dimensions  $45 \times 55 \times 110 \text{ \AA}^3$  and a molecular weight of  $M_w \simeq 80 \text{ kDa}$  [Brändén et al., 1973]. Here, the individual components of the secondary structure are color-coded and the cofactors  $\text{NAD}^+$  (*gray*) and the Zinc ions (*beige*) are displayed in space filling model. The surface of the protein is depicted as well. In panel (b), the two monomeric subunits are separated in color for reasons of clarity.

## 6.2 Quantitative Estimation of the Monomer-Dimer Ratio in LADH Solutions from the Theoretical SAXS Profiles

The acquisition of information about the low resolution structure of a particle in ideal monodisperse systems is quite simple, since the measured intensity is directly related to the single-particle scattering (see section 2.4.2). As a rule, a dilute solution of purified biological macromolecules meets this requirement of monodispersity. It becomes more complicated in polydisperse systems where particles differ in shape, size or conformation, though. The reconstruction of the shape or modeling of the structure of a single particle from a mixture of different types of particles with arbitrary structures is extremely difficult. However, such systems can still be characterized in terms of their composition: In a system containing non-interacting particles with distinctly different shapes and sizes (shape polydispersity), where interference effects can be neglected and all particles scatter independently, the fraction of the components in the mixture can be determined under the condition that the single-particle scattering intensities of the different particle types in solution are known [Svergun et al., 2013] (see section 2.4.3).

Typically, weakly bound oligomeric complexes dissociate into individual subunits upon pressurization between 0.5 - 2 kbar (see section 2.3.2). In the following, we assume that a dilute solution of dimeric protein is monodisperse at ambient pressure and the corresponding scattering signal can be completely represented by the form factor of the dimer. Once the pressure at which the

protein dissociates has been exceeded, we obtain a mixture of dimers and monomers in a pressure-dependent mixing ratio and, concomitantly, pressure-dependent level of shape polydispersity. Under the assumption that the native conformations of monomer and dimer are preserved and that no unfolding occurs under pressure, the ratio of dimer and monomer is gradually shifted to the monomeric species with increasing pressure until the solution finally becomes monodisperse again when all dimers are dissociated. In theory, based on this information the dissociation constant can be determined.

Even though in many practical cases the monodisperse approximation of the dimeric solution at ambient pressure is not applicable due to the formation of loose higher-order oligomer and pressure-related conformational changes of the monomeric subunit after dissociation (e.g. transition to a molten globule state or unfolding), this theoretical treatment of the ideal case of the dissociation process still represents a valuable reference for the analysis of the scattering profiles in non-ideal situations.

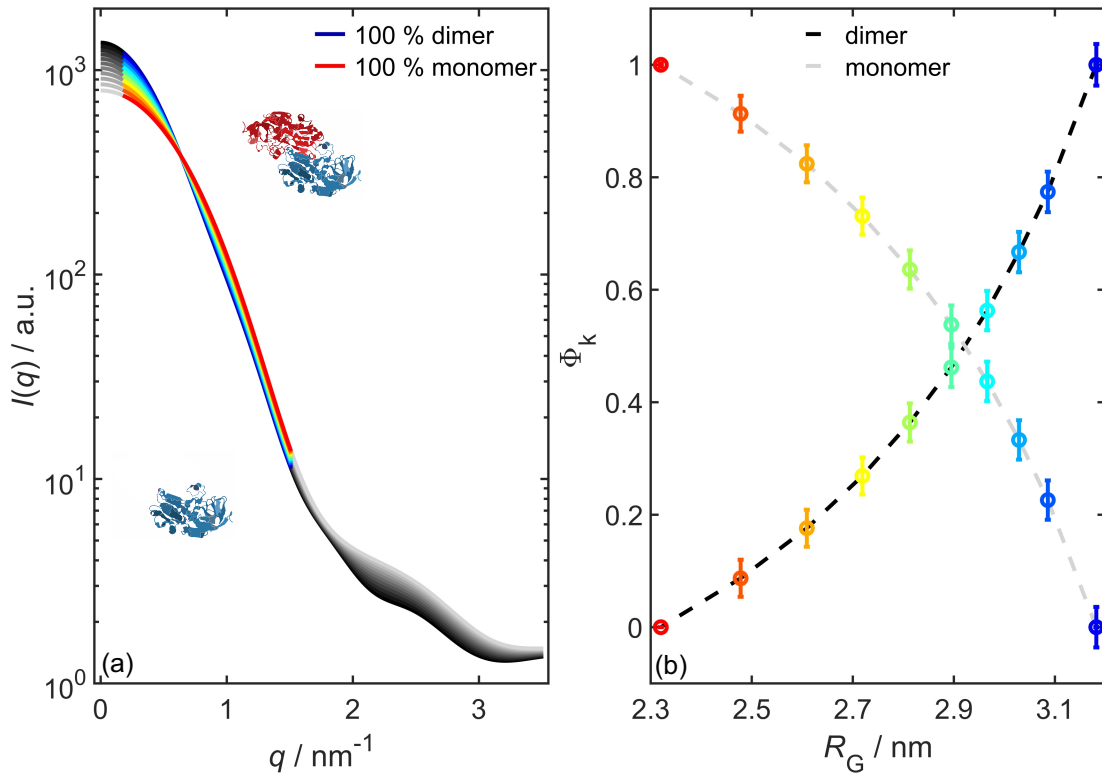


Figure 6.2: (a) Theoretical SAXS intensities,  $I(q)$ , of a monomeric and dimeric LADH molecule as well as of mixtures thereof at various molar ratios, calculated from the monomer and dimer crystal structures (PDB entry: 2JHF [Meijers et al., 2007]) employing the program CRY SOL [Svergun et al., 1995]. (b) The corresponding radii of gyration,  $R_G$ , obtained from  $I(q)$  in the  $q$ -range  $0 < q < 2.51 \text{ nm}^{-1}$  (dashed lines) as well as for the experimentally accessible  $q$ -range  $0.23 < q < 1.5 \text{ nm}^{-1}$  (circles), using the program OLIGOMER [Franke et al., 2017], for all solution compositions characterized by the dimeric and monomeric volume fractions,  $\Phi_k$ .

Figure 6.2 (a) depicts the theoretical scattering intensity of a mixture composed of monomeric ( $k=1$ ) and dimeric ( $k=2$ ) LADH,

$$I(q) = \sum_{k=1}^2 \Phi_k \frac{P_k(q)}{V_k}, \quad \text{with } \Phi_1 + \Phi_2 = 1, \quad (6.1)$$

computed at various mixing ratios from the linear combination of the appropriately renormalized scattering intensities from the single species,  $P_k(q)/V_k$ , weighted by its volume fractions,  $\Phi_k$ . The

theoretical solution scattering curves,  $P_k(q)$ , of the components  $k$  with particle volumes  $V_k$  are modeled from the corresponding crystal structures using the program CRY SOL [Svergun et al., 1995]. For this purpose, the high-resolution structures of the monomeric and dimeric LADH were taken from the Protein Data Bank (accession number 2JHF [Meijers et al., 2007]). Assuming a hydration shell width of 3 Å, the model structure leads to the theoretical radius of gyration  $R_{G,\text{dimer}} = 3.183$  nm, envelope diameter  $D_{\text{max}} = 11.02$  nm, envelope volume  $V_1 = 57.38$  nm<sup>3</sup> and molecular mass  $M_w = 79.61$  kDa for the dimeric LADH and  $R_{G,\text{monomer}} = 2.286$  nm,  $D_{\text{max}} = 7.431$  nm,  $V_2 = 121.20$  nm<sup>3</sup> and  $M_w = 39.81$  kDa for the monomeric LADH. The model was checked on the experimental X-ray scattering signals of monodisperse dimeric solutions. The scattering from the mixtures (see Figure 6.2 (a)) represents a 'blended' scattering from dimers and monomers. For the mixture analysis, the application OLIGOMER of the ATSAS 2.8 package [Franke et al., 2017] was used, yielding the corresponding radii of gyration and the dimeric and monomeric volume fractions  $\Phi_k$ . The structure parameters derived from the scattering signals of the mixtures (i.e. radii of gyration,  $R_G$ ) lie between the values found for the individual components. Here, the radius of gyration is to be understood as an average radius of gyration of all particles, of different shape and size, present in the solution. However, as shown in Figure 6.2 (b), it is not possible to read the state of the dimer dissociation directly from the value of the radius of gyration. For equimolar monomer-dimer mixtures, the mean radius of gyration resulting from the solution scattering is not the mid-level value between the  $R_G$  for monodisperse dimeric and monodisperse monomeric solutions, since the dimeric proteins result in a stronger increase in forward scattering and thus a larger  $R_G$  than the monomer species.

In the real SAXS experiment the accessible  $q$ -space is limited to the range  $0.23 \lesssim q \lesssim 1.5$  nm<sup>-1</sup> (see section 6.3). In Figure 6.2 (a) this region of the scattering curves is visualized by color. In order to estimate the inaccuracy caused by the limited  $q$ -range, the analysis described above was additionally performed for the reduced  $q$ -range, yielding the results (*circles*) displayed with error bars above the ones obtained from the analysis on the entire range (*dashed lines*) in Figure 6.2 (b). We find, even in the limited  $q$ -range the fractions of the components in the mixture can be determined with sufficient accuracy.

### 6.3 The Dissociation of LADH under Pressure in Pure Buffer Solution

HHP SAXS measurements of 0.7% (w/v) LADH + 10 mM Tris-HCl solutions (pH 8.5,  $T = 25^\circ\text{C}$ ) were performed to investigate the structural changes of the dimeric protein LADH upon pressurization in the range from 1 - 3500 bar. For more details on the sample preparation and experimental setup see sections 3.1 and 3.2, respectively. The experimental data reveal that the LADH solution is not completely monodisperse at ambient conditions, but contains higher-order loose oligomeric complexes. In the presence of higher oligomers, the experimental data cannot be refined by linear combinations of the scattering of monomers and dimers as described in section 6.2 and as the conformation (shape, size) of these larger oligomers is not known, the exact composition of the solution remains elusive. However, the average radius of gyration,  $R_G$ , representing the mean dimension of all particles of different shapes and sizes present in the solution can be derived from the low  $q$ -range ( $qR_G < 1.3$  [Feigin and Svergun, 1987]) of the total scattering signals by using the Guinier approximation [Guinier, 1939] employing the program PRIMUS [Konarev et al., 2003] (see section 2.4.2). The (dissociation) behavior of these oligomers under pressure can also be derived from these data. In order to be as insensitive as possible to larger non-functional aggregates, the inner part of the data ( $q \leq 0.23$  nm<sup>-1</sup>) is omitted from the Guinier analysis and the radius of gyration  $R_G$  is estimated on the basis of the outer part, only. Further, in a model-free approach, the real space distance distribution functions,  $p(r)$ , are refined to the scattering data in the range  $q \leq 0.23$  nm<sup>-1</sup> using the inverse indirect Fourier transformation program GNOM [Svergun et al., 1988, Svergun, 1992]. Next to  $p(r)$ , the analysis yields an approximation of the particle's maximum dimension,  $D_{\text{max}}$ , in solution, and the average radius of gyration,  $R_G$ .



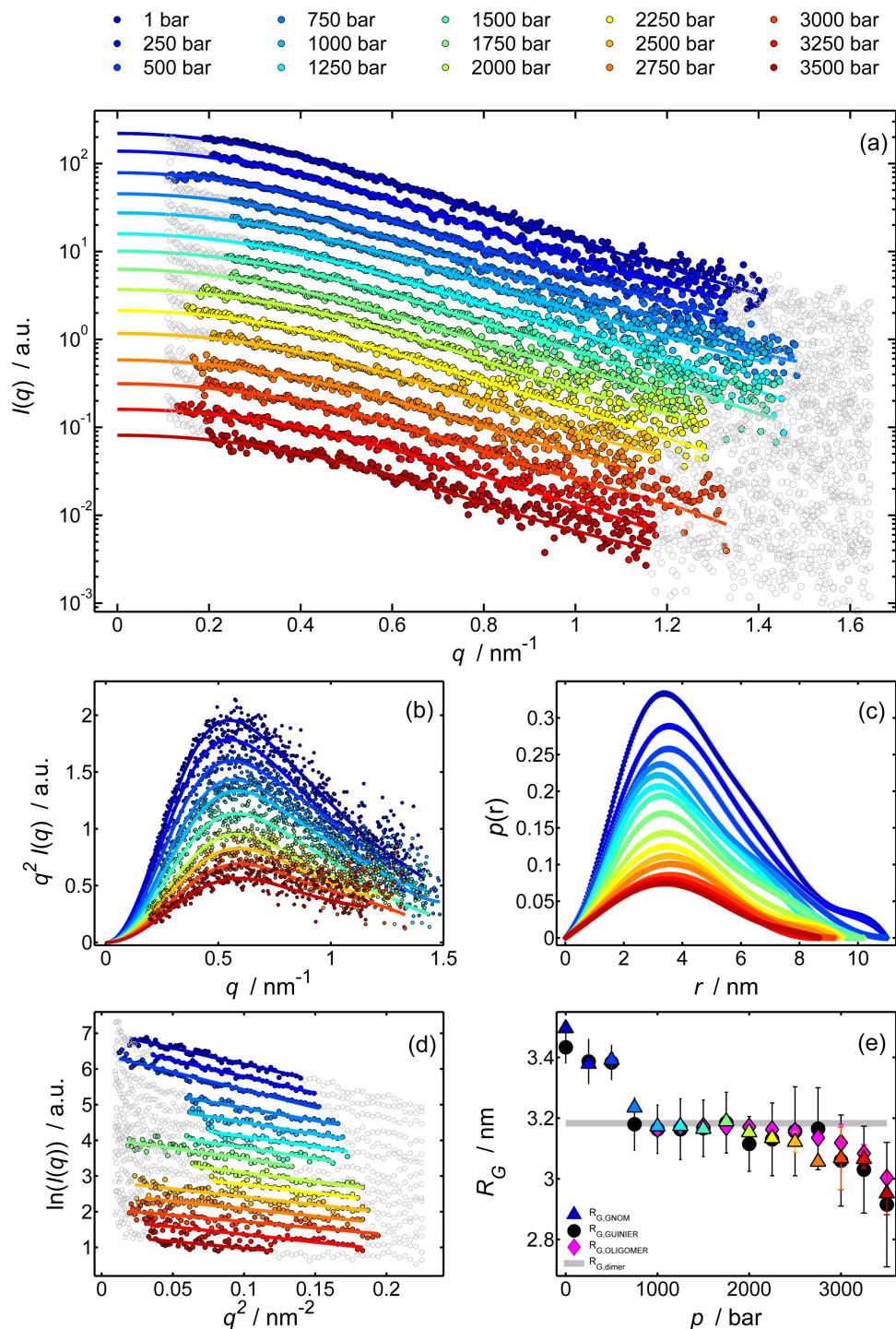


Figure 6.3: (a) Experimental SAXS data of the 0.7% (w/v) LADH + 10mM Tris-HCl solution (pH 8.5), collected at 25°C in a pressure range of 1 – 3500 bar and the corresponding refinements (*solid lines*) made with GNOM [Svergun et al., 1988, Svergun, 1992]. The scattering signals were shifted for reasons of clarity. The data range not taken into account in the analysis is marked in gray. (b) Kratky plot ( $q^2 I(q)$  vs.  $q$ ) of the experimental data and the corresponding refinements (*solid lines*) for selected pressures. (c) Radial pair-distance distribution function,  $p(r)$ , as a function of pressure. (d) Guinier plot of the 0.7% (w/v) LADH solution scattering, obtained by PRIMUS [Konarev et al., 2003]. (e) Comparison of the experimentally derived radii of gyration,  $R_G$ , for the different analysis methods in comparison with the theoretical value for dimeric LADH,  $R_{G,dimer}$ , calculated with CRY SOL (*solid gray line*). Reprinted from [Julius et al., 2018a].



At elevated pressures ( $p > 1000$  bar) where the weakly bound, higher-order oligomers are dissociated, the volume fractions of the monomers and dimers of the 0.7% (w/v) LADH + 10 mM Tris-HCl solutions can be determined using OLIGOMER of the ATSAS 2.8 package [Franke et al., 2017]. The experimental data is fitted by a linear combination of the monomer and dimer scattering curves and an additional constant corresponding to the resolution of the experiment (see section 2.4.3):

$$I(q) = \sum_{k=1}^2 \Phi_k \frac{P_k(q)}{V_k} + \text{const.} \quad (6.2)$$

This approach was successfully chosen in a recent SAXS study on the transthyretin (TTR) self-assembly mechanism into fibrils [Groenning et al., 2015].

The influence of increasing pressure on the SAXS data of 0.7% (w/v) LADH in 10 mM Tris-HCl is shown in Figure 6.3 (a) together with the corresponding refinements (*solid lines*) made by GNOM [Svergun et al., 1988, Svergun, 1992]. As can be seen clearly from the Kratky representation ( $q^2 I(q)$  vs.  $q$ ) of the SAXS data and the associated pair-distance distribution functions,  $p(r)$ , the overall globular, folded shape of the protein persists over the entire pressure range investigated (see Figure 6.3 (b)+(c)). However, the gradual shift of the maximum of  $p(r)$  to smaller  $r$  values with increasing pressure and the concomitant decrease of the mean maximum expansion,  $D_{\max}$ , of the dissolved particles indicate a dissociation of the oligomeric protein. The pressure dependence of the mean radius of gyration  $R_G$ , depicted in Figure 6.3 (e), was determined from the scattering intensities,  $I(q)$ , using three different analysis approaches: By the analysis in the small  $q$ -range within the Guinier approximation employing the program PRIMUS [Konarev et al., 2003] (see Figure 6.3 (d)), by the refinement of the pair-distance distribution function,  $p(r)$ , to the scattering data using GNOM [Svergun et al., 1988, Svergun, 1992] and by the refining a linear combination of the monomer and dimer scattering contributions (and a constant) to the scattering data using OLIGOMER [Franke et al., 2017]. As can be clearly seen, the models used provide comparable results. The solutions exhibit shape polydispersity, caused both by the presence of higher oligomers at lower pressures and by dissociation into monomeric subunits at higher pressures. Still, we find that the analysis with GNOM [Svergun et al., 1988, Svergun, 1992] can be successfully applied to all solution conditions and that it yields refinements of good quality.

The dissociation of higher oligomers can be recognized by the strong reduction of the radius of gyration at pressures below 1000 bar until the dimeric conformation is reached. This type of pressure sensitivity of loosely bound protein clusters (higher-order oligomers) is a well-known phenomenon (see section 2.3.2). In 10 mM Tris-HCl buffer, the dimeric conformation of the protein LADH remains stable under pressure until the dissociation into monomeric species sets in at 2000 bar. Upon further pressurization, the volume fraction of the dimer gradually decreases down to  $0.63 \pm 0.05$  at 3500 bar. The population of the monomeric species increases concomitantly and finally occupies about 34% of the volume at 3500 bar.

## 6.4 The Effect of Crowders and Organic Osmolytes on the Dissociation of LADH upon Pressurization

In the following, we report SAXS data on the effect of pressure on the protein LADH in the presence of the hydrophilic polymer and nanocrowder PEG 200, the compatible osmolyte TMAO and the chaotropic agent urea. Since TMAO is reported to counteract the perturbation by the destabilizing waste product urea in deep sea organisms most efficiently at a 1(TMAO):2(urea) molar ratio (see section 2.1.2), an analogous molar mixture thereof is investigated as well.

Figure 6.4 depicts the average radii of gyration,  $R_G$ , derived from the HHP SAXS signals of 0.7% (w/v) LADH in pure aqueous 10 mM Tris/HCl buffer solution (pH 8.5,  $T = 25^\circ$ ) as well as in presence of the crowder and osmolytes as a function of pressure. The experimental results are compared to the theoretical values  $R_{G,\text{dimer}}$  and  $R_{G,\text{monomer}}$  for monomeric and dimeric LADH, respectively, which are computed from the crystal structure with the program CRY SOL [Svergun et al., 1995] (see section 6.2). If the mean radius of gyration exceeds the value found for the dimeric conformation,  $R_G > R_{G,\text{dimer}}$ , higher oligomers are present in the corresponding solution.

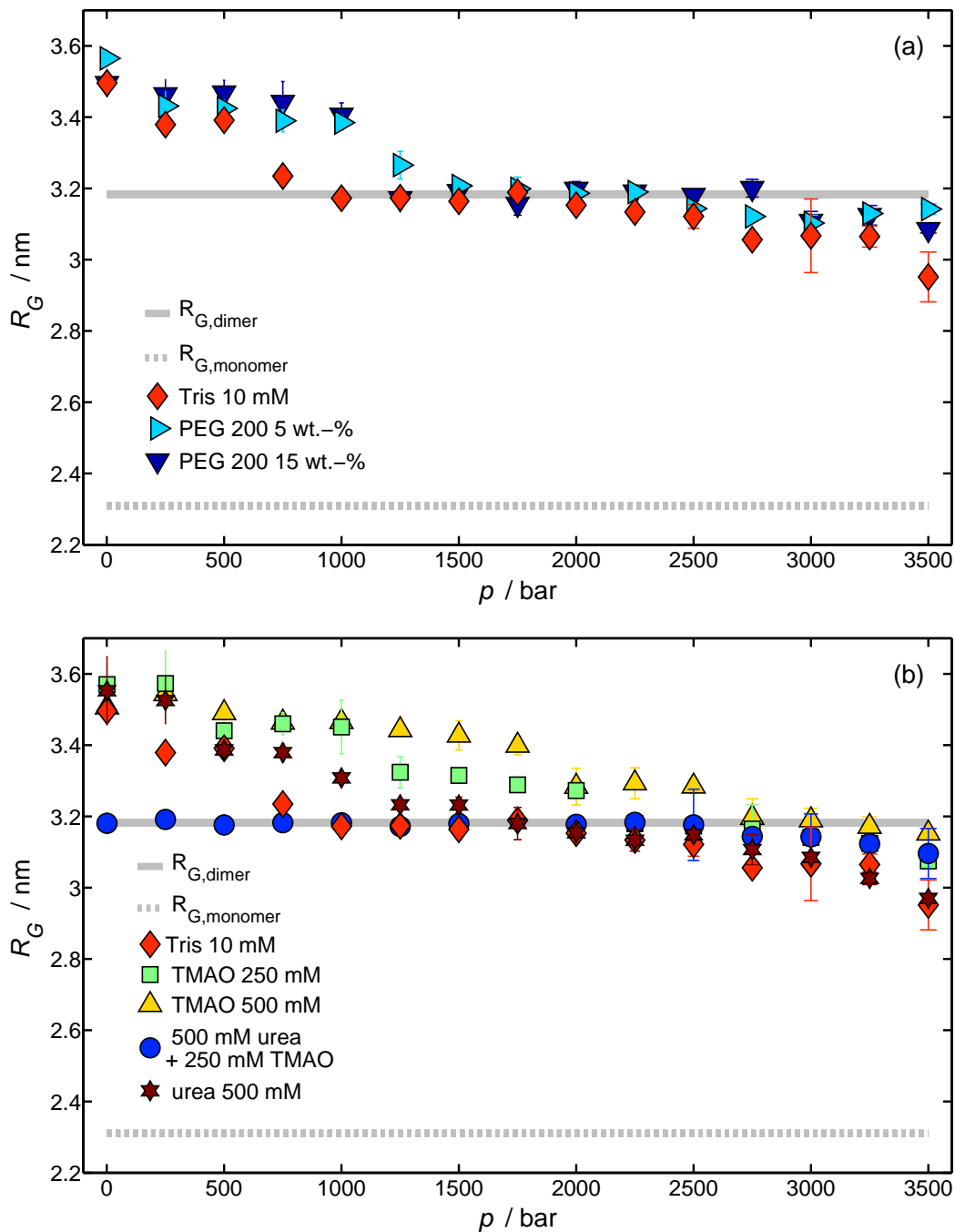


Figure 6.4: Pressure-induced reduction of the radius of gyration,  $R_G$ , of a 0.7% (w/v) + 10 mM Tris-HCl (pH 7) LADH solution in (a) 5 and 15% (w/v) PEG 200 and (b) in 250 mM TMAO, 500 mM urea, and 250 mM TMAO + 500 mM urea at 25°C. The experimentally determined radii of gyration evaluated with GNOM [Svergun et al., 1988, Svergun, 1992] are depicted in comparison with the theoretical values for dimeric LADH,  $R_{G,dimer}$  (solid gray line), and monomeric LADH,  $R_{G,monomer}$  (dashed gray line) calculated with CRY SOL [Svergun et al., 1995]. Reprinted from [Julius et al., 2018a].

We find, in solutions containing the nanomolecular crowder PEG 200, the oligomers exhibit increased pressure stability. The higher oligomers dissociate for the most part at a pressure of 1250 bar and form dimers. Further compression from 1500 bar to 3500 bar does not result in significant conformational changes and the protein remains mostly its dimeric conformation. At 3500 bar, the volume fraction of the dimers is  $0.95 \pm 0.01$  at a crowder concentration of 5% (w/v) and  $0.98 \pm 0.01$  at 15% (w/v) PEG 200.

Further, we investigate the influence of trimethylamine-N-oxide (TMAO), known to enhance water structure (see section 2.1.2), on the dissociation behavior of LADH. As shown in Figure 6.4. (b), the addition of the stabilizing osmolyte TMAO to the 0.7% (w/v) LADH + 10 mM Tris-HCl (pH 8.5) solution results in an increased pressure stability of the oligomers compared to the pure buffer. In the presence of 500 mM TMAO, pressures up to 2750 bar are required to dissociate the higher oligomers and obtain a monodisperse solution of dimers. At a concentration of 250 mM TMAO, this point is attained already at 2250 bar and in the pure buffer at 1000 bar. Further, the osmolyte TMAO shifts the dissociation of the dimer to higher pressures. Whilst the dimer dissociation in pure 10 mM Tris-HCl buffer already takes place at 2000 bar, it shifts upon addition of 250 mM TMAO to 2750 bar and to pressures beyond 3500 bar in the presence of 500 mM TMAO. Finally, we study the impact of the chaotropic agent urea on the system as well as the counteraction between TMAO and urea by a mixture composed of the two in the physiological ratio 1:2. There are no drastic deviations from the pure 10 mM Tris/HCl buffer system when adding 500 mM urea. Remarkably, the 0.7% (w/v) LADH + 10 mM Tris-HCl (pH 8.5) + 250 mM TMAO + 500 mM urea solution is already monodisperse under ambient conditions. Since the protein only occurs in its native dimeric conformation, the scattering signal is adequately described by the scattering form factor of the dimer in a pressure range from 1 bar to 2500 bar before it dissociates on further pressure increase. At a pressure of 3500 bar, the total volume is occupied by dimers to a fraction of  $0.86 \pm 0.01$  and with monomers to a fraction of  $0.14 \pm 0.01$ . This case is comparable to the 250 mM TMAO mixture at the same pressure. At pressures above approximately 2500 bar, the dimer dissociates for all solution conditions, with the extent depending on the respective cosolvent mixture.

## 6.5 Conclusions

We report SAXS studies on LADH solutions as a function of pressure to reveal the dissociation/association process of horse LADH in the presence of the hydrophilic polymer polyethylene glycol PEG 200, the water structure enhancing osmolyte TMAO and the denaturant urea. We show that the application of hydrostatic pressure up to 3.5 kbar leads to marked changes in the oligomeric state of LADH and that the conformational state of the protein can be significantly altered by changing the solution conditions (i.e. solvent composition). In the absence of larger oligomers, the refinement of the SAXS curves by the model of a mixture of the dimeric and its monomeric subunit can be successfully applied leading to a thorough insight on the mixtures composition.

At ambient conditions and in pure buffer, the LADH dimers coexist with larger, multi-subunit and loosely bound oligomers. Although these higher-order oligomers (clusters) are very pressure-sensitive and dissociate at pressures below about 1 kbar, we find their pressure stability can be significantly increased by adding the compatible solute TMAO and the polymer PEG 200. This enhanced protein self-association can be explained by the excluded volume theory, as suggested in previous studies on the impact of nano- and macromolecular crowding on self-association of proteins under ambient conditions [Cole and Ralston, 2006, Rivas et al., 1999, Lindner and Ralston, 1995, Minton, 2000] (see section 2.1.1). The system with the least excluded volume is entropically favored, and since when proteins form oligomers less volume is excluded for the predominant background type than for an equal number of subunits, self-association is facilitated in the presence of crowder molecules. In addition, the exclusion of the cosolvents from the immediate vicinity of the protein peptide backbone results in preferential hydration of the protein and an enhanced stability by an entropic stabilization mechanism [Pincus et al., 2008, Street et al., 2006] (see section 2.1.2). While higher order oligomers dissociate at lower pressures, dimeric LADH dissociates into its subunits at higher pressures between 2 and 4 kbar, depending on the solution condition. In general,

the dissociation of oligomers under pressure is based on a significant amount of void volume at the contact interface of the constituting subunits. After dissociation, the void volume fills with solvent, resulting in a reduction of the total volume as preferred under pressure (*Le Chatelier principle*, see section 2.3.2). Among all additives studied, the osmolyte TMAO causes the most pronounced shift of the onset of the oligomer's dissociation to higher pressures. Notably, both the polymer PEG 200 and the osmolyte TMAO stabilize the native dimeric conformation of LADH against pressure once this conformation is reached and cause a shift of the dissociation of the dimer into its monomeric subunits to higher pressures in comparison to the pure buffer scenario. This shift of the dissociation to higher pressures can also be explained by the excluded volume effect and partly by the osmotic pressure increase induced by the cosolvent [Canchi et al., 2012, Money, 1989]. The comparison of the results for the 250 mM TMAO solution with those for the 250 mM TMAO + 500 mM urea 1:2 mixture shows a clear suppression of oligomerization at lower pressures and a high pressure stability of the native dimeric state up to the highest investigated pressure. It is remarkable that the presence of the chaotropic agent urea suppresses the over-stabilization of the oligomeric state caused by TMAO.

Within the framework of the project [Julius et al., 2018a], the high pressure small-angle X-ray scattering study described herein on the pressure dependent conformational changes in the quaternary and ternary structure of the dimeric enzyme horse liver alcohol dehydrogenase in presence of solution additives like crowder and osmolytes was complemented by FT-IR and fluorescence spectroscopy as well as HHP stopped flow measurements carried out by the research group of Prof. R. Winter, Physical Chemistry I - Biophysical Chemistry, TU Dortmund University. FT-IR difference spectra monitor pressure-dependent conformational changes of the secondary structure of the protein in the presence of the different cosolvents (and crowder) and the HHP stopped flow measurements yield information about the relationship between enzyme structure and functionality. The dissociation process and the associated structural changes of the enzyme were further investigated by means of high-pressure intrinsic tryptophan fluorescence as well as the pressure-dependent fluorescence of the LADH-bound fluorophore 1-anilino-naphthalene-8-sulfonate (ANS) [Hawe et al., 2008], an established method for the investigation of the dissociation behavior of oligomeric protein complexes [Tian et al., 2000, Torrent et al., 2015, Cioni and Strambini, 1996, Tang and Ruan, 1996]. Since the fluorophore ANS binds to hydrophobic patches on the protein surface as well as to hydrophobic pockets, which are supposed to get exposed to the fluorophore upon dissociation, an increased ANS fluorescence intensity is expected upon pressure-induced dissociation. More details about these techniques and the data analysis can be found in the corresponding publication [Julius et al., 2018a]. As described therein, the complementary FT-IR measurements showed that pressure-induced dissociation of the oligomers leads to small changes in the secondary structure, probably due to rehydration of the interface of the subunit. In accordance with the SAXS data, we observed a significant shift towards higher dissociation pressures in the presence of 0.5 M TMAO and 5 - 15% (w/v) PEG 200, but no distinct effects for 0.5 M urea or the 1:2 mixture of TMAO and urea. ANS fluorescence measurements revealed small conformational changes in the binding pocket of the coenzyme already at approx. 600 - 800 bar, which may be responsible for the significant reduction of the kinetic parameters observed in high-pressure stop-flow measurements of enzymatic activity in the same pressure range. The initial reaction rate as well as the pressure-dependent kinetic properties of the LADH-catalyzed ethanol oxidation are significantly reduced by the addition of urea. Although 0.5 M TMAO does not significantly affect the kinetic properties of the enzyme, it was found that the destabilizing effect of 0.5 M urea is compensated by 0.25 M TMAO.

In summary, the combined experimental approach employed here revealed three different phases in the reaction of the oligomeric LADH to the increase in hydrostatic pressure. The dissociation of loosely bound protein clusters (i.e. higher-order oligomers) takes place at moderate pressures below 800 bar. Above 600 - 800 bar, small conformational changes occur in the binding pocket of the coenzyme, probably related to its pronounced compressibility. Following an increase in enzymatic activity at lower pressures, the loss of enzyme activity occurs at 600-800 bar. Higher-order oligomers dissociate at low pressures, whereas the dissociation of the LADH dimer only starts at approximately 2000 bar, which is accompanied by small changes in the secondary structure of

the protein. Conformational changes such as oligomerization and dissociation into multimeric and monomeric subunits are modified by the addition of cosolvents such as urea or trimethylamine N-oxide (TMAO) and macromolecular crowding agents such as polyethylene glycol PEG, as they tend to bind to the interface of the protein or act via their excluded volume effect, respectively. In general, the enzymatic activity of many oligomeric enzymes depends on their oligomerization state, which, like the dissociation of the subunits, is influenced not only by hydrostatic pressure but also by cosolvents and cosolutes. Osmolytes can therefore be regarded as effective means of marine organisms to modulate the oligomeric state of enzymes and thus their activity. Enzymes in the cells of deep living organisms may exhibit some intrinsic adaptations to extreme temperatures and pressures, but extrinsic adaptations such as the use of stabilizing osmolytes such as TMAO also appear to be required, which act on proteins in a rather universal way through non-specific, solvent-mediated interactions.



## Chapter 7

# Macromolecular Crowding of Protein Solutions by the Polysaccharide Ficoll

The synthetic macromolecular crowding agents Ficoll PM 70 and Ficoll PM 400 are compact and highly internally-crosslinked and branched copolymers of sucrose and epichlorohydrin, which in solution behave like semi-rigid spheres [Bohrer et al., 1984, Lavrenko et al., 1987, Deen et al., 1981]. As the impact of Ficolls subunit sucrose on the protein pair-interaction has already been described in section 4, the comparison of the effects of both Ficoll and its subunit sucrose on protein interaction may reveal the particular effects of macro vs. nanomolecular crowding on protein intermolecular interactions [Pielak and Miklos, 2010] (see section 2.1.1). Further, it can be tested whether the effect of Ficoll on protein interaction is purely entropic (excluded volume effect) or more likely to result from a favored interaction between polymer and native protein [Miklos et al., 2010] or from a solvophobic effect [Auton and Bolen, 2005].

This chapter is organized as follows: In section 7.1, the synthetic polysaccharide Ficoll PM 70/400 is introduced, which is widely used in biochemical applications as a macromolecular crowding agent to mimic intracellular crowded solution conditions and thus to investigate the influence of excluded volume on biomolecular systems *in vitro* [Zimmerman and Minton, 1993] (see also section 2.1.1). In order to characterize the conformation of the single Ficoll molecule in solution and the microscopic structure of the solutions as a function of Ficoll concentration and hydrostatic pressure, HHP small-angle X-ray scattering experiments were performed on aqueous Ficoll PM 70/400 solutions at concentrations ranging from the dilute to the semi-dilute regime ( $0.5 < c_{\text{Ficoll}} < 30\%$  (w/v)) and at pressures up to 4 kbar (see section 7.2). Section 7.3 reports on high pressure small angle X-ray scattering measurements carried out on aqueous lysozyme-Ficoll mixtures of different compositions. Further, complementary liquid-liquid phase separation measurements were performed, providing (model-free) insight on the crowder-induced effects. At the end of the chapter the results are summarized (see section 7.4).

### 7.1 Macromolecular Crowding Agent: Ficoll PM 70/400

Both Ficoll PM 70 and PM 400 have analogous structures (see Figure 7.1), but differ in molecular weight. The manufacturer-quoted averaged molecular weight is  $M_{w, \text{PM70}} \sim 70$  kDa and  $M_{w, \text{PM400}} \sim 400$  kDa, respectively. Ficoll is inert, polar and does not contain any ionized groups, so that the structure under physiological conditions hardly reacts nor interacts with proteins. Ficoll is very hydrophilic. The abundance of hydroxyl groups leads to very good solubility in aqueous media. Therefore, concentrations of 50% (w/v) can be attained in water, covering a density range with a maximum of  $\sim 1.2 \text{ g mL}^{-1}$ . At equivalent concentration, aqueous solutions of Ficoll have much lower osmotic pressure than aqueous solutions of its subunit sucrose. Further, Ficoll was found to reduce the dielectric permittivity of aqueous Ficoll solutions with increasing concentra-

tion. The dielectric decrement  $\delta = d\epsilon_r/dc_{\text{Ficoll}} = -0.71 \pm 0.03 (\% \text{ w/v})^{-1}$  describes the decrease of the solutions static dielectric constant,  $\epsilon_r$ , as a function of Ficoll PM 400 concentration,  $c_{\text{Ficoll}}$  [Zaslavsky et al., 1989]. In addition to its function as crowding agent, the highly soluble, uncharged polymer Ficoll PM 70/400 is widely used for applications in blood preservation and renal filtration [Palit and Yethiraj, 2017, Wang et al., 2012, Wong et al., 2016, Groszek et al., 2010, Fissell et al., 2007, Venturoli and Rippe, 2005, Dhar et al., 2010, Wenner and Bloomfield, 1999, Galán et al., 2001, Lavrenko et al., 1987, Tokuriki et al., 2004, Wang et al., 2012].

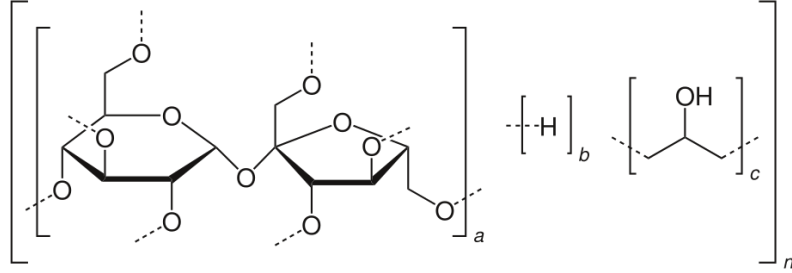


Figure 7.1: Structural formula of Ficoll (PM 70/400): A branched copolymer of sucrose and epichlorohydrin.

## 7.2 Effect of Concentration and Hydrostatic Pressure on the Conformation of Ficoll PM 70 / PM 400 in Aqueous Solution

Crowder size and shape are key factors determining the net effect of macromolecular crowding on proteins. It is therefore crucial to characterize the structural properties of the crowding agent in solution in order to understand crowding effects. In essence, the ability of the crowder to reduce the volume available for the protein molecules in the system is determined by its fractional volume occupancy,  $\Phi_F$ , which can be derived from the Ficoll concentration,  $c_{\text{Ficoll}} / \text{g mL}^{-1}$ , and the partial specific volume  $\bar{V}_{\text{Ficoll}}^\circ = 0.667 \text{ mL g}^{-1}$  (water, 26°C) [Lavrenko et al., 1987] (see table 7.1):

$$\Phi_F = c_{\text{Ficoll}} \cdot \bar{V}_{\text{Ficoll}}^\circ. \quad (7.1)$$

Inside cells, proteins are surrounded by different macromolecules, including proteins themselves, which cover approximately 30% of the available volume (see section 2.1.1). This level of occupied space as found in 'real' biological systems can be reached in Ficoll aqueous solutions for concentrations as high as a 40% (w/v) (see Table 7.1).

Another possible way to determine the volume occupied by the crowder molecule is through its hydrodynamic radius  $R_H$ , which describes the effective size of a molecule in a physiological and aqueous environment<sup>1</sup>.  $R_H$  can be experimentally derived by dynamic light scattering (DLS), which is known for being a powerful tool to derive low and medium resolution information on molecular structures in solution. For Ficoll PM 400, an approximate hydrodynamic radius of  $R_{H,\text{PM400}} \sim 8 - 13.6 \text{ nm}$  is reported [Chen et al., 2011, Harve et al., 2006] and for Ficoll PM 70  $R_{H,\text{PM70}} \sim 4.5 - 5.5 \text{ nm}$  [Chen et al., 2011, Wenner and Bloomfield, 1999, Georgalis et al., 2012, Luby-Phelps et al., 1987, Sörensson et al., 1998], respectively.

Based on the assumption that Ficoll has a spherical shape, the volume of a single molecule is given by  $V_{\text{Ficoll}} = 4/3\pi R_H^3$ . The fractional volume occupancy of the Ficoll molecules with molecular

<sup>1</sup>It is important to remember that the net charge of an anionic molecule and the partial charge of a neutral but polar-hydrophilic molecules such as Ficoll, respectively, strongly influence  $R_H$  in physiological salt solutions at pH 7.4. The surface charge creates intermolecular electrostatic repulsion, amplifying steric exclusion effects, and large hydration shells around the molecules. Solvent structuring may be involved as well. All these effects influence  $R_H$  [Chen et al., 2011, Palit and Yethiraj, 2017].

weight  $M_w$  in an aqueous Ficoll solution with density  $\rho$  and concentration  $c_{\text{Ficoll}}$  can then be approximated by the product of the crowders number density,  $n_{\text{Ficoll}} = N_A \cdot \rho \cdot c_{\text{Ficoll}} / M_w$ , and the volume of the single Ficoll molecule,  $V_{\text{Ficoll}}$ , (see table 7.1):

$$\tilde{\Phi}_F = \frac{4}{3}\pi R_H^3 N_A \cdot \rho \cdot c_{\text{Ficoll}} / M_w. \quad (7.2)$$

However, the polymeric crowder Ficoll is not completely impenetrable [Lavrenko et al., 1987]. Whilst Ficoll acts in dilute solution as individual molecule and the hydrodynamic radius presents a constant mean value of  $R_{H,\text{PM70}} \sim 5.1$  nm and  $R_{H,\text{PM70}} \sim 10$  nm, respectively, it exhibits for Ficoll concentrations  $c_{\text{Ficoll}} \geq c^*$  a dramatic decrease. The overlap concentrations  $c_{\text{PM400}}^* \sim 10$  mg mL<sup>-1</sup> for Ficoll PM 400 [Gtari et al., 2017, Harve et al., 2006] and  $c_{\text{PM70}}^* \sim 12.5$  mg mL<sup>-1</sup> for Ficoll PM 70 [Harve et al., 2006] indicate the passage into the semi-diluted regime where the Ficoll molecules penetrate and/or are compressed, i.e. the volume occupied by a single Ficoll molecule decreases. By employing Eq. (7.2), we find for a Ficoll PM 400 concentration of 40 mg mL<sup>-1</sup> an volume occupancy of  $\sim 17\%$  [Gtari et al., 2017], which is much larger than the value computed by Eq. (7.1) even though the decrease of  $R_{H,\text{PM400}}$  with concentration was considered. In this model, the physiological volume occupancy of  $\sim 30\%$  is already reached at  $c_{\text{Ficoll}} \sim 7\%$  (w/v). Hence, at high concentrations the analogy between a hard-packed sphere and Ficoll PM 70/400 is not valid anymore, which may result in an overestimation of the excluded volume,  $\tilde{\Phi}_{F,\text{PM400}}$  [Lavrenko et al., 1987] (see Table 7.1).

$c_F$ / % (w/v)	$c_F$ / mg mL <sup>-1</sup>	$\Phi_{\text{Ficoll}}$ / %	$R_{H,\text{PM400}}$ / nm	$\tilde{\Phi}_{F,\text{PM400}}$ / %
0.5	5.01	0.34		
1	10.04	0.68	10	6.3
2	20.16	1.36	9.45	8.05
3.5	35.46	2.40	8.57	13.3
5	50.93	3.45	8.06	20.3
7	71.8	4.86	7.91	28.7
10	103.65	7.02		
15	158.16	10.71		
20	214.47	14.52		
25	272.57	18.45		
30	332.46	22.51		
35	394.14	26.68		
40	457.61	30.98		

Table 7.1: Ficoll PM 70 concentration,  $c_{\text{Ficoll}}$ , and the corresponding volume fraction,  $\Phi_F$ , as a percentage of total volume.  $\Phi_F$  was calculated by Eq. (7.1) using the partial specific volume  $\bar{V}_{\text{Ficoll}}^0 = 0.677$  mL g<sup>-1</sup> [Lavrenko et al., 1987] (The values for Ficoll PM 400 match the values for Ficoll PM 70 within a relative error of  $\lesssim 1\%$ ). The data for the hydrodynamic radius,  $R_{H,\text{PM400}}$ , and excluded volume,  $\tilde{\Phi}_{F,\text{PM400}}$ , for Ficoll PM 400 were taken from [Gtari et al., 2017].

The single molecules entangle and form a network-like structure as their concentration increases and mutual interactions trigger intra-chain-folding transitions within the macromolecules [Gtari et al., 2017, Harve et al., 2006]. Furthermore, aqueous Ficoll solutions are polydisperse. There is a range of shapes of Ficoll as there is also a broad dispersion in molecular weights [Fissell et al., 2010]. For Ficoll PM 70 the polydispersity as represented by the ratio,  $M_w/M_n$ , of the weight-average molecular weights,  $M_w$ , and the number-average molecular weights,  $M_n$ , was found within a range of 1.08 - 1.63 [Bohrer et al., 1984].

To conclude, it is difficult to make accurate statements about the volume effectively excluded for the proteins due to the strong changes in the solution structure and the conformation of the Ficoll molecule as a function of concentration. Since Ficoll has a soft surface and can deform, it may not

be a large steric barrier to the protein and thereby not be particularly effective as crowding agent. Moreover, it has been indicated elsewhere [Palit and Yethiraj, 2017] that in aqueous Ficoll solutions with a partial volume fraction of  $\Phi_F = 30\%$  as much as  $\sim 60\%$  of the water is surface-associated. This suggests that Ficoll is highly porous and lots of additional volume may be excluded by the hydration water.

### 7.2.1 Dilute Regime

In order to derive the structure of the single Ficoll PM 70/400 molecules in solution and to reveal potential pressure-dependent conformational changes, high-pressure SAXS measurements were carried out on diluted (0.5 - 1% (w/v)) aqueous Ficoll in 25 mM Bis-Tris buffer solution (pH 7) at 25°C and at pressures ranging from 1 to 4000 bar (see sections 3.1 and 3.2 for more details on sample preparation and the experimental SAXS setup, respectively). For the analysis of the background corrected scattering intensities of the dilute Ficoll PM 70/400 solutions,  $I(q)$ , the inverse indirect Fourier transformation program GNOM [Svergun et al., 1988, Svergun, 1992] is employed, yielding an approximation of the major dimension,  $D_{\max}$ , of the crowder in solution, the real space distance distribution  $p(r)$ , as well as the averaged radius of gyration of the molecule,  $R_G$ . The analysis is lined out for Ficoll PM 70 in Figure 7.2 and for Ficoll PM 400 in Figure 7.3, respectively.

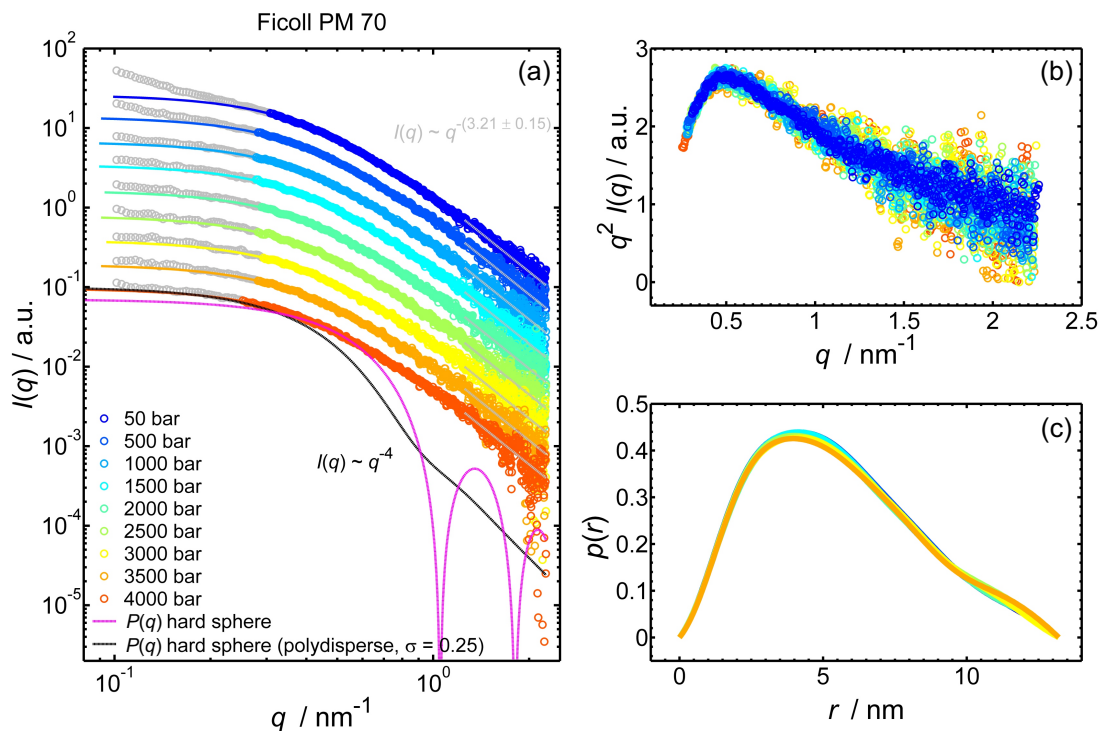


Figure 7.2: (a) Experimental SAXS intensities,  $I(q)$ , of 0.5 % (w/v) Ficoll PM 70 in 25 mM Bis-Tris solution (pH 7,  $T = 25^\circ\text{C}$ ) collected in a pressure range from 1 to 4000 bar with the corresponding refinements (*same-colored solid lines*) made with the program GNOM [Svergun et al., 1988, Svergun, 1992]. Fits to the power law decay,  $I(q) \propto q^{-\alpha}$ , in the Porod limit at large  $q$  are shown as *solid gray lines*. The theoretical form factor,  $P(q)$ , of a hard-sphere with radius of gyration  $R_{G,PM70} = 4.27 \text{ nm}$  ( $R \sim 5.5 \text{ nm}$ ) with (*solid black line*) and without (*solid magenta line*) polydispersity (polydispersity index: 0.25) are shown for comparison as well. (b) The corresponding Kratky plot ( $q^2 I(q)$  vs.  $q$ ) comprising the scattering intensities at all pressures. (c) Radial pair distribution function,  $p(r)$ , derived by the analysis of the scattering data.

In both Figures, panel (a) depicts the scattering intensities,  $I(q)$ , in double-logarithmic representation as a function of pressure together with the corresponding refinements (*same-colored solid*

lines), (b) the Kratky representation,  $q^2 I(q)$  vs.  $q$ , of the data and (c) the corresponding radial pair-distance distributions,  $p(r)$ . The Kratky-plots exhibit a pronounced maximum indicating a globular shape, which is preserved for all solution conditions and pressures studied. For both Ficoll sizes the slope,  $\alpha$ , obtained by the refinement of the experimental scattering intensity in the Porod limit by the power-law function  $I(q) \sim q^{-\alpha}$ , is smaller than predicted by theory for a hard sphere ( $\alpha=4$ ) (see Figures 7.2 (a) and 7.3 (a)). Even though the highly cross-linked polymer is more compact than a random coil ( $\alpha=2$ ), it is much less compact than a protein [Minton, 2005, Axelsson et al., 2011] and rather behaves as a relatively open structure [Wenner and Bloomfield, 1999].

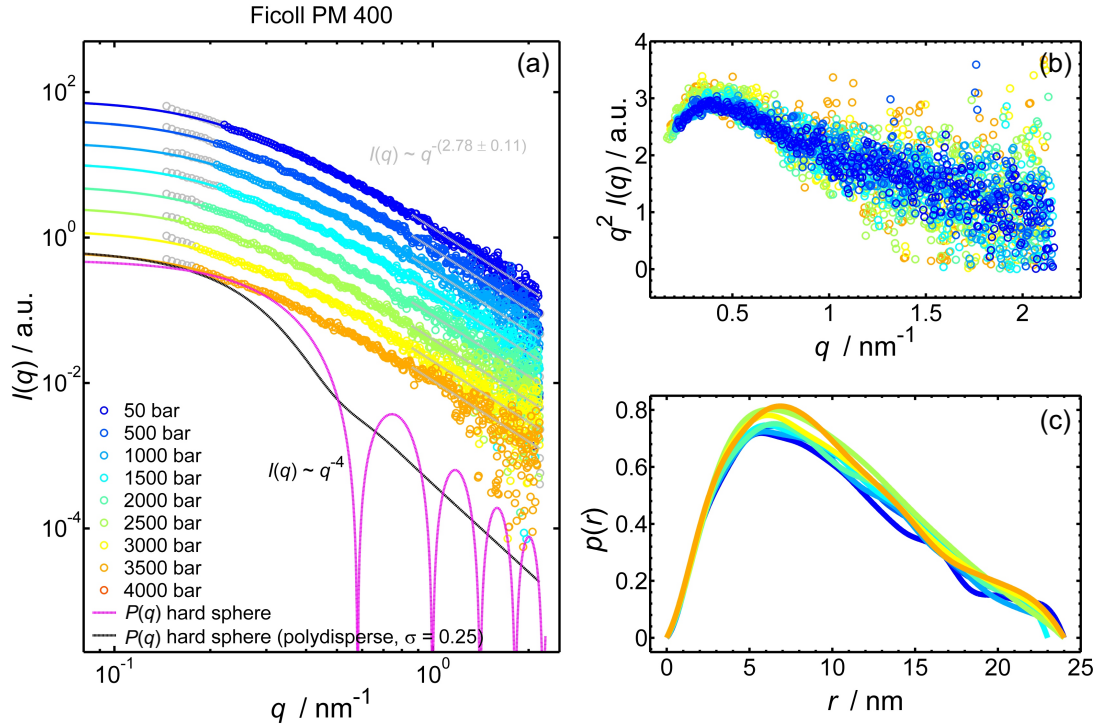


Figure 7.3: (a) Experimental SAXS intensities,  $I(q)$ , of 1% (w/v) Ficoll PM 400 in 25 mM Bis-Tris solution (pH 7,  $T = 25^\circ\text{C}$ ) collected in a pressure range from 1 to 4000 bar with the corresponding refinements (*same-colored solid lines*) made with the program GNOM [Svergun et al., 1988, Svergun, 1992]. Fits to the power law decay,  $I(q) \propto q^{-\alpha}$ , in the Porod limit at large  $q$  are shown as *solid gray lines*. The theoretical form factor,  $P(q)$ , of a hard-sphere with radius of gyration  $R_{G, \text{PM400}} = 7.76$  nm ( $R \sim 10$  nm) with (*solid black line*) and without (*solid magenta line*) polydispersity (polydispersity index: 0.25) are shown for comparison as well. (b) The corresponding Kratky plot ( $q^2 I(q)$  vs.  $q$ ) comprising the scattering intensities at all pressures. (c) Radial pair distribution function,  $p(r)$ , derived by the analysis of the scattering data.

However, the power law behavior found at ambient conditions remains essentially unchanged upon pressurization for both Ficolls. Averaged over all pressures, we find Ficoll PM 400 with an exponent,  $\alpha = 2.78 \pm 0.11$ , corresponding to a mass fractal ( $1 < \alpha < 3$ ) being softer than the smaller Ficoll PM 70 with  $\alpha = 3.21 \pm 0.15$ , corresponding to a surface fractal ( $3 < \alpha < 4$ ) (see Figure 7.5). The finding that Ficoll has no spherical conformation but some rigid intermediate shape, agrees closely with reported data on the molecular mass dependence of the intrinsic viscosity of Ficoll PM 70/400, classifying both Ficoll sizes mid-way between a solid sphere and a random coil [Fissell et al., 2010]. The true Ficoll potential is certainly not a hard-sphere one but far softer than that, hence, Ficoll might be less effective in excluding volume than i.e. protein crowding agents. As clearly can be seen in Figures 7.2 (a) and 7.3 (a) by the upturn of the scattering intensity in the small  $q$ -range and by the comparison with the computed form factors,  $P(q)$ , of monodisperse hard spheres with radii  $R = 5.5$  nm and 10 nm (*solid magenta lines*), the diluted Ficoll PM 70/400



solutions are highly polydisperse. The theoretical form factors,  $P(q)$ , taking polydispersity into account (polydispersity index: 0.25 [Georgalis et al., 2012]) are also presented for comparison (*solid black lines*). [Palit and Yethiraj, 2017] and [Georgalis et al., 2012] report an increasing fraction of Ficoll PM 70 clusters from  $\sim 5\%$  at onset up to  $\sim 60\%$  in the crowded regime at packing fraction  $\Phi_F \sim 30\%$ . However, the cluster-to-monomer size ratio of  $\sim 2.37$  is reported to remain unchanged with increasing concentration. We find, the self-clusters dissociate under pressure (see Figures 7.2 (a) and 7.3 (a)).

Despite the apparent polydispersity, an analysis of the data was performed by assuming an arbitrary monodisperse solution and a maximal dimension for the polysaccharide Ficoll PM 70 of  $D_{\max} = 13.2$  nm and  $D_{\max} = 24$  nm for Ficoll PM 400, in order to detect possible pressure-induced conformational changes of the molecule. The refinement of the scattering data was performed by neglecting the very small  $q$ -range corresponding to larger oligomeric structures using the program GNOM [Svergun et al., 1988, Svergun, 1992]. Averaged over all pressures, the analysis yields for Ficoll PM 70 a radius of gyration of  $R_{G,PM70} = 4.29 \pm 0.02$  nm and, correspondingly, for Ficoll PM 400  $R_{G,PM400} = 7.78 \pm 0.05$  nm. Under the assumptions made, the structure of the Ficoll PM 70/400 molecules remains essentially unchanged upon pressurization on the nm-scale. We find modeling Ficoll as individual hard spheres is not an accurate assessment of physical reality. This accounts not only for systems where the polysaccharide is present in excess of the overlap concentration, but also for the dilute regime. The idea that Ficoll is somewhat 'squishy' is also supported by studies on its diffusion through nanosized pores [Fissell et al., 2010]: Ficoll PM 70 was found to be able to penetrate through silicon slit nanopore membranes even when the Stokes-Einstein radius is greater than the slit width, implying deformability.

## 7.2.2 Concentrated Regime

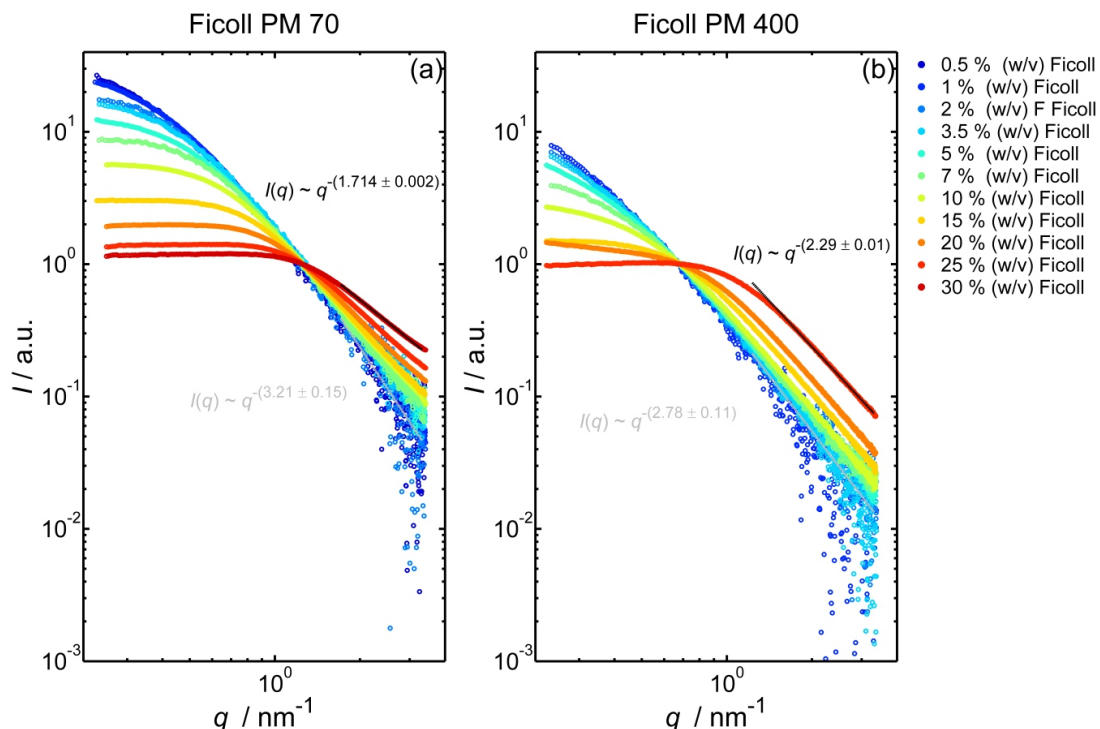


Figure 7.4: Experimental SAXS curves of aqueous (a) Ficoll PM 70 and (b) Ficoll PM 400 + 25 mM Bis-Tris (pH 7,  $T = 25^\circ\text{C}$ ) solutions as a function of Ficoll concentration at ambient pressure. Fits to the power law decay,  $I(q) \propto q^{-\alpha}$ , in the Porod limit at large  $q$  are shown for the highest and lowest concentration as *dashed gray lines* and *dashed black lines* together with the corresponding expressions for  $I(q)$ . The scattering signals were shifted for reasons of clarity.

In order to explore the effects of different levels of macromolecular (self-)crowding on the structure of aqueous Ficoll PM 70/400 solutions at ambient as well as elevated pressures, HHP SAXS data of up to 25% (w/v) Ficoll PM 70/400 in 25 mM Bis-Tris buffer (pH 7) solutions were recorded in a pressure range from 1 – 4000 bar at 25°C (see Figure 7.4). Exceeding the threshold concentration,  $c^*$ , the SAXS curves exhibit a well pronounced Ficoll-Ficoll structure factor,  $S_{\text{Ficoll-Ficoll}}(q)$ , which is a measure for direct or indirect correlations between the Ficoll molecules in dense solutions. As the Ficoll volume fraction increases, the scattering intensity at small  $q$  decreases in magnitude due to changes of the isothermal compressibility of the system. Due to the fact that Ficoll loses its spherical shape during the formation of network-like structures, the scattering intensities show no correlation peak but a broad maximum, which is characteristic of highly branched polymer of high segment density. Figure 7.5 (*top half*) depicts the pressure dependence of the exponent  $\alpha$ , obtained by the refinement of the power law function,  $I(q) \propto q^{-\alpha}$ , to the scattering intensity at large  $q$  for (a) Ficoll PM 70 and (b) Ficoll PM 400 at various concentrations in a pressure range from 1 to 4000 bar. The impact of the excluded volume effect on the solution structure is strongly pronounced. Upon entering the semi-dilute concentration regime ( $c_{\text{Ficoll}} > c^*$ ), where intermolecular interactions increase markedly, the exponent,  $\alpha$ , gradually decreases down to values as reported for mass fractals or even random coils in case of Ficoll PM 70, indicating a highly entangled network topology. However, the application of pressures of up to 4 kbar leads to minor changes in the shape of the scattering curve, and thereby solution structure, only. Figure 7.5 (*bottom half*) shows the exponent  $\alpha$  averaged over all pressures as a function of concentration. The pressure-averaged exponents decrease for  $c_{\text{Ficoll}}$  in a linear manner, whereby the slope of the decrease is much steeper for the smaller polysaccharide Ficoll PM 70 (c) than for Ficoll PM 400 (d). Clearly, Ficoll PM 70 is particularly good at branching out, which might be rationalized by its smaller size which allows a more optimal packing. When the polysaccharides form a network structure, the identity of the individual molecule, in particular the difference between Ficoll PM 70 and PM 400, should diminish. In this semi-dilute regime, the properties of the solution should be determined solely by the crowder concentration. Still, we observe differences in the scattering data for the two crowding agents. However, it has to be considered that at equal concentration [% (w/v)], the number density of the smaller Ficoll PM 70 with lower molecular weight is always larger than for Ficoll PM 400. In a previous SAXS study on the structure of aqueous Ficoll PM 70 solutions in the semi-dilute concentration regime at concentrations up to  $c_{\text{Ficoll}} = 30$  wt.%, the correlation length,  $\xi$  of the transient network of entangled chains was derived *via* an Ornstein Zernicke analysis from the SAXS curves [Erlkamp, 2014, Erlkamp et al., 2014]. The correlation length was found to decrease from  $\xi(c_{\text{Ficoll}}=15 \text{ wt.}\%) = 4.9 \pm 0.1$  nm to  $\xi(c_{\text{Ficoll}}=30 \text{ wt.}\%) = 3.2 \pm 0.1$  nm at ambient pressure and to be independent of pressure.

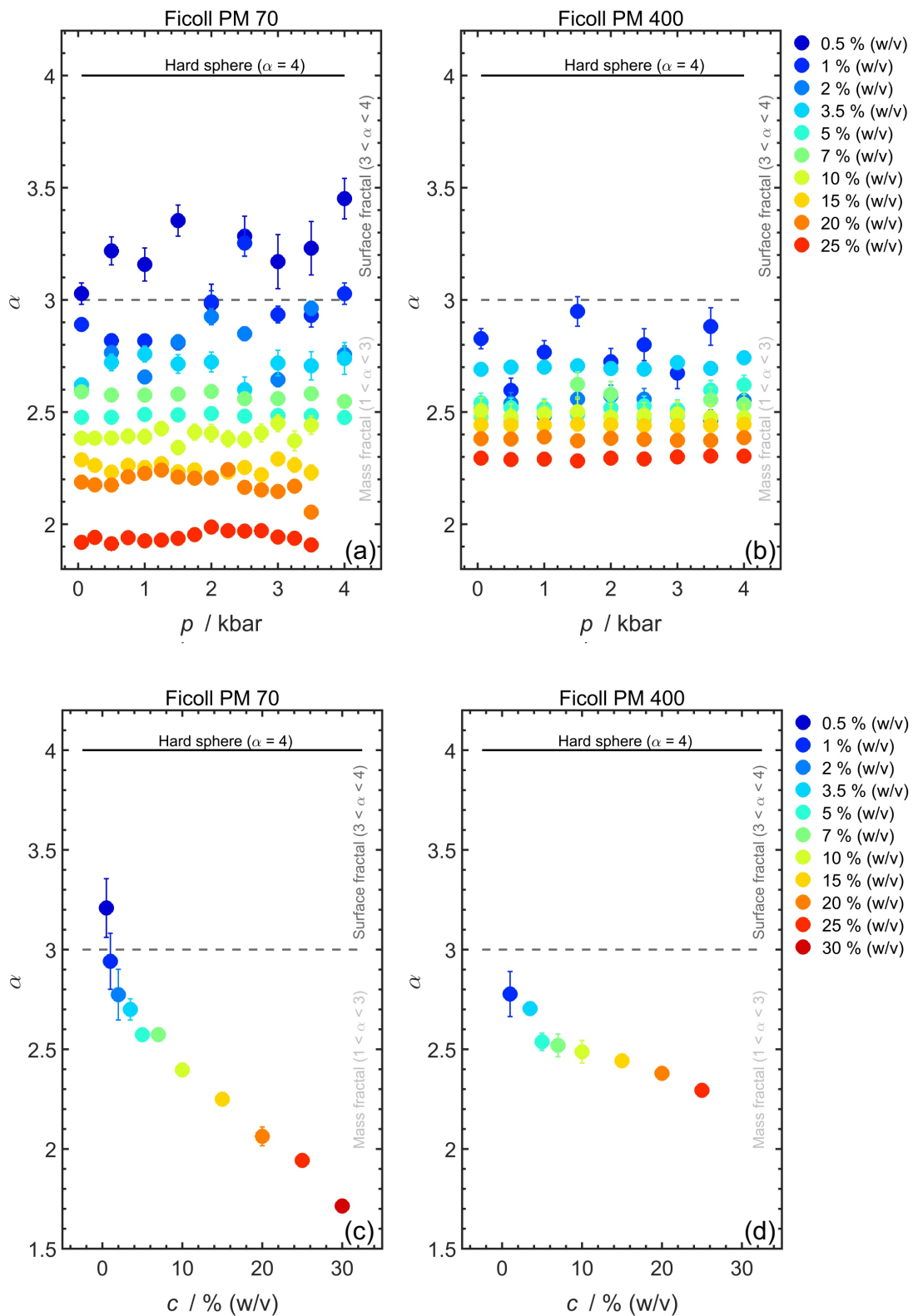


Figure 7.5: Exponent  $\alpha$  of the power law decay in the Porod limit,  $I(q) \propto q^{-\alpha}$ , derived from the fits to the experimental SAXS intensities of aqueous (a) Ficoll PM 70 and (b) Ficoll PM 400 + 25 mM Bis-Tris solutions (pH 7,  $T=25^\circ\text{C}$ ) at various Ficoll concentrations as a function of pressure and (c)+(d) averaged over all pressures.

### 7.3 Impact of Ficoll PM 70 / 400 on the Pressure-Dependent Protein Pair-Interaction

As already mentioned in section 2.1.1, macromolecular crowding in a binary protein-crowder mixture is most effective if protein and crowder are of similar size [Tokuriki et al., 2004, Minton, 2001]. However, we find that Ficoll PM 70 is  $\sim 3$  times larger than lysozyme and Ficoll PM 400  $\sim 6$  times, respectively. In theory, the ability of hard spheres of this size to exclude volume in lysozyme solutions should be small, as the protein should be able to reside unaffected in the spaces between the large spheres at all packing fractions. However, Ficoll is not adequately described by a rigid sphere but is largely porous, deformable and tends to form network-like structures and, most importantly, bounds a significant amount of the accessible bulk water. The impact of such complex solution conditions on the protein-protein interactions similar to the conditions as encountered in the living cell are still largely *terra incognita*.

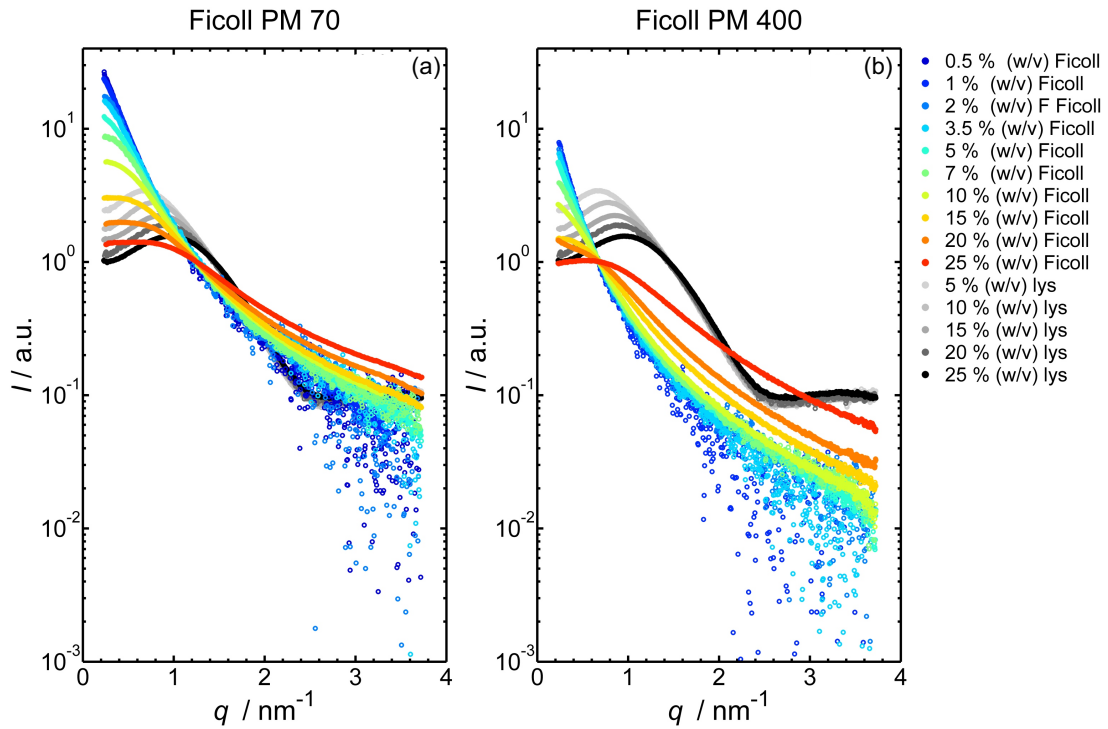


Figure 7.6: Experimental SAXS curves of pure aqueous 5 - 25% (w/v) lysozyme + 25 mM Bis-Tris (pH 7,  $T = 25^\circ\text{C}$ ) solutions in comparison to pure aqueous (a) Ficoll PM 70 and (b) Ficoll PM 400 + 25 mM Bis-Tris (pH 7,  $T = 25^\circ\text{C}$ ) solutions at various concentrations and at ambient pressure. The scattering signals were shifted for reasons of clarity.

The total scattering intensity,  $I(q)$ , of a dense ternary lysozyme-Ficoll-buffer mixture includes next to the scattering from the protein,  $I_{\text{lys-lys}}(q)$ , and the polysaccharide,  $I_{\text{Ficoll-Ficoll}}(q)$ , an additional scattering cross-term,  $I_{\text{lys-Ficoll}}(q)$ , emerging from correlations between the lysozyme and Ficoll molecules, i.e.

$$I(q) \propto I_{\text{lys-lys}}(q) + I_{\text{lys-Ficoll}}(q) + I_{\text{Ficoll-Ficoll}}(q). \quad (7.3)$$

In order to investigate how the protein-protein interaction is modulated by the presence of the macromolecular crowder Ficoll, the structure factor,  $S_{\text{lys-lys}}(q)$ , needs to be extracted from the total scattering intensity as described by Eq. (7.3). However, the removal of the background scattering contributions  $I_{\text{Ficoll-Ficoll}}(q)$  and  $I_{\text{lys-Ficoll}}(q)$  from the total scattering of the mixture,  $I(q)$ , is not possible for the following reasons:

As shown in Figure 7.6, the scattering intensity of the pure aqueous Ficoll solutions shows for

both Ficoll sizes a significant wave-vector dependency within the range of momentum transfer,  $q \lesssim 1.7 \text{ nm}^{-1}$ , which is critical for the proteins structure factor,  $S_{\text{lys-lys}}(q)$ . Moreover, the scattering contribution of the Ficoll-Ficoll interaction structure factor,  $S_{\text{Ficoll-Ficoll}}(q)$ , and Ficoll form factor exceeds the protein solution scattering significantly up to the point where the scattering contribution of the protein cannot be identified anymore in the total scattering signal,  $I(q)$ , of the mixture (see Figure 7.7 for the example of 5% (w/v) aqueous Ficoll PM 70/400 in the presence of 5 - 25% (w/v) lysozyme). The superposition of the protein and crowder scattering contributions makes an extraction of the lysozyme structure factor impossible, as the removal of the  $q$ -dependent Ficoll background would greatly alter the protein scattering signal.

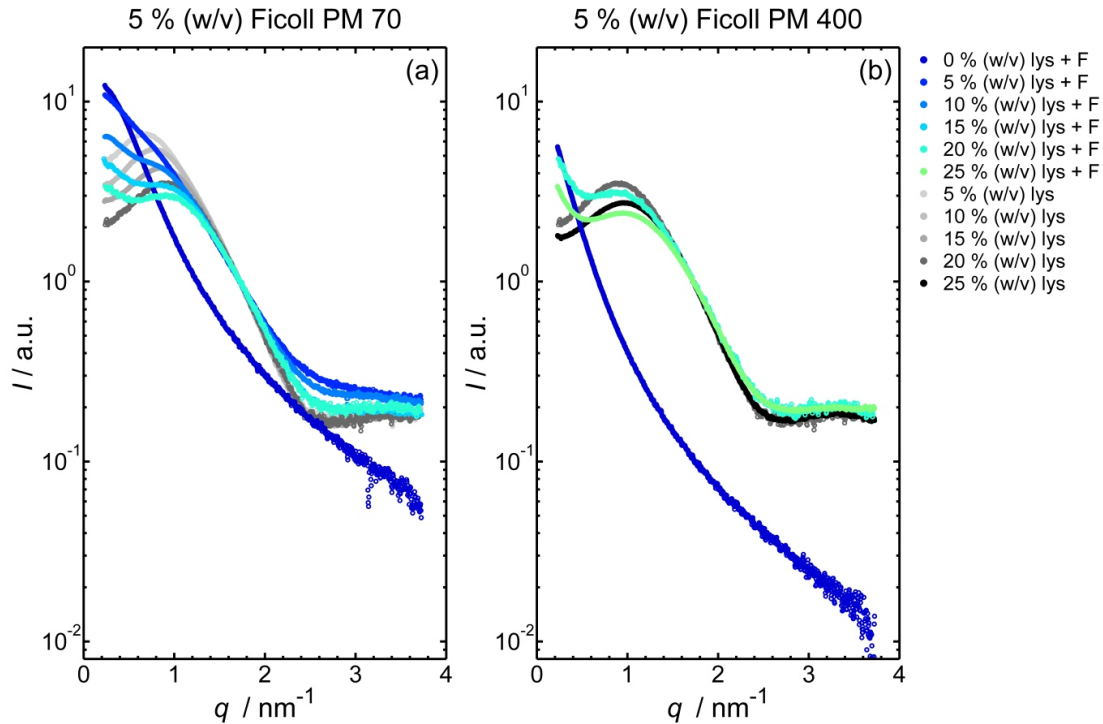


Figure 7.7: SAXS intensities of pure aqueous 5 - 25% (w/v) lysozyme + 25 mM Bis-Tris (pH 7,  $T = 25^\circ\text{C}$ ) solutions in comparison to pure aqueous (a) 5 % (w/v) Ficoll PM 70 and (b) 5 % (w/v) Ficoll PM 400 + 25 mM Bis-Tris (pH 7,  $T = 25^\circ\text{C}$ ) solutions and mixtures thereof, at ambient pressure. Data are shifted along the ordiante for clarity.

Considering the strong dependency of the Ficoll solution structure on the level of excluded volume, either produced by an increased Ficoll concentration or by the presence of large amounts of protein, the structure factor,  $S_{\text{Ficoll-Ficoll}}(q)$ , is not likely to be the same in the Ficoll-lysozyme mixture as in the pure Ficoll solution - even at equal crowder mass concentration. This means that the deduction of the Ficoll scattering contribution  $I_{\text{Ficoll-Ficoll}}(q)$ , as for example derived from the SAXS signal of a pure Ficoll solution, from the total scattering signal,  $I(q)$ , is already invalid in principle.

Moreover, at higher concentrations the increasing correlations between the Ficoll molecules and the proteins should result in an (effective) Ficoll concentration specific structure factor,  $S_{\text{lys-Ficoll}}(q)$ , contributing also to the total scattering intensity  $I(q)$  of the protein-Ficoll mixture. Both structure factors,  $S_{\text{Ficoll-Ficoll}}(q)$  and  $S_{\text{lys-Ficoll}}(q)$ , cannot be measured separately by means of small-angle X-ray scattering and therefore remain elusive. Here, SANS scattering experiments with isotopically mixed solvents (i.e. deuterated Ficoll) would eliminate the undesirable scattering from the polysaccharide. However, SANS data on such systems is up to this point out of reach.

However, the interpretation of the SAXS data is not only complicated due to the unwanted scattering from the polysaccharide but also due to the reduction in scattering contrast as sucrose,



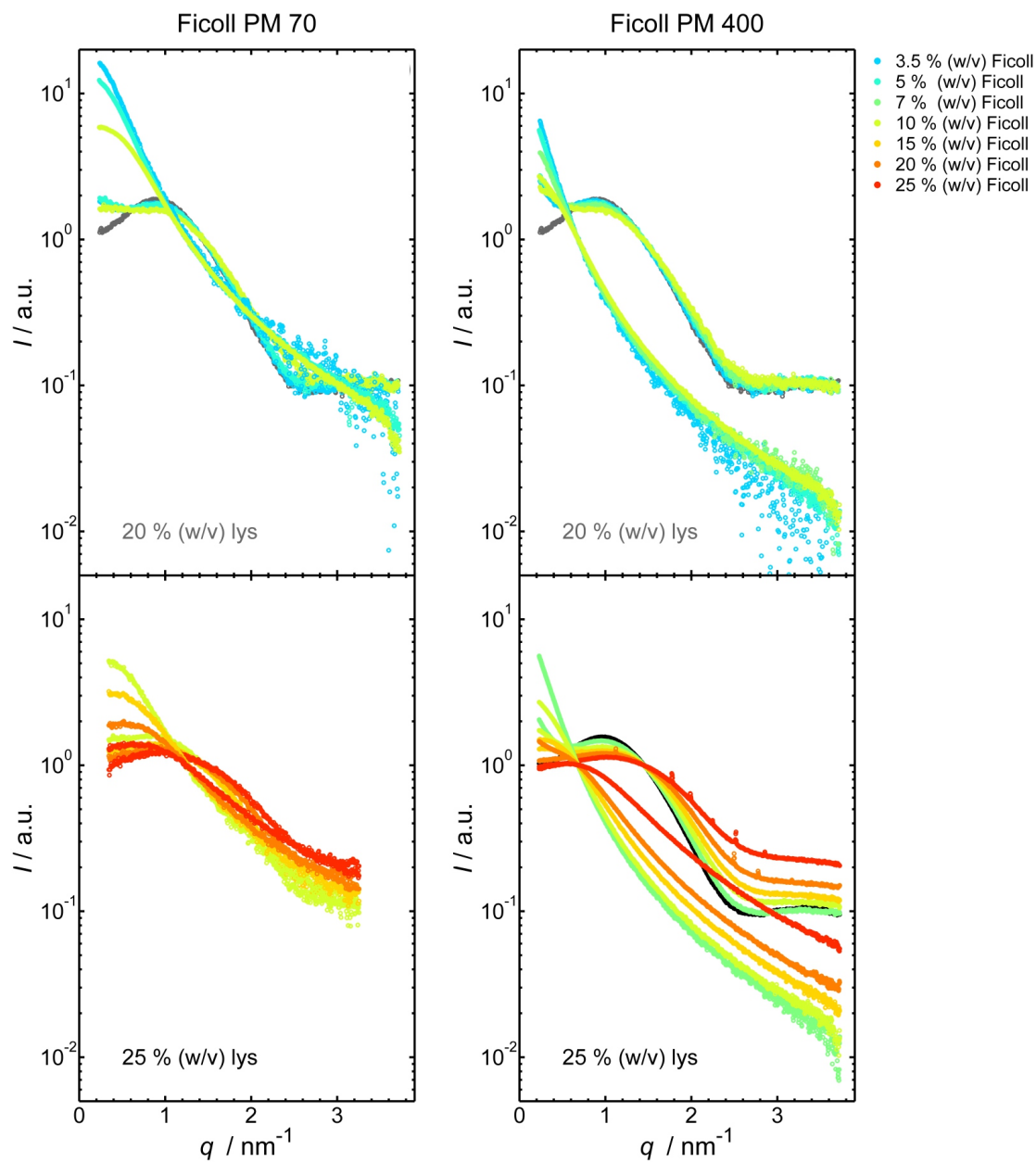


Figure 7.8: SAXS intensities of 20 and 25 % (w/v) lysozyme dissolved in 25 mM Bis-Tris (pH 7) and 3.5 - 25 % (w/v) Ficoll PM 70 (*left*) and Ficoll PM 400 (*right*) at ambient pressure and  $T = 25^\circ\text{C}$ , shown together with the corresponding scattering of the protein-free crowder solutions and crowder-free protein solutions. The SAXS patterns are all corrected for the background solution scattering of the pure buffer and shifted along the ordinate for clarity.

the subunit of the macromolecule Ficoll, has a very similar average electron density ( $\sim 0.400$  electrons/ $\text{\AA}^3$  at 50% (w/v) sucrose) to proteins ( $\sim 0.420$  electrons/ $\text{\AA}^3$ ) [Svergun and Koch, 2003]. For comparison: water has an electron density of 0.334 electrons/ $\text{\AA}^3$  [Svergun and Koch, 2003]. The SAXS spectra of 20 and 25 % (w/v) lysozyme dissolved in 25 mM (50 mM) Bis-Tris (pH 7) and 3.5 - 25 % (w/v) Ficoll PM 70 (*left*) and Ficoll PM 400 (*right*) were recorded at  $T = 25^\circ\text{C}$  in a pressure range from 1 - 4000 bar. The data collected at ambient conditions are shown together with the corresponding scattering of the protein-free crowder solutions and crowder-free protein solutions in Figure 7.8. Here, the SAXS curves are all corrected for the background solution scattering of the pure buffer and shifted along the ordinate for clarity. At  $\Phi_{\text{lys}} \sim 20\%$  volume occupancy by lysozyme, we observe an onset of crystallization at a crowding level of  $\Phi_{\text{Ficoll}} \sim 14\%$  Ficoll PM 400, indicating that the solubility limit is reached at this point.

### 7.3.1 Modulation of the Reentrant LLPS-Boundaries at High Pressures by Ficoll PM 70

The liquid-liquid phase separation (LLPS) is particularly suitable to gain a (model-free) insight into the effects of crowding on the protein intermolecular interactions in complex ternary protein-crowder-buffer solutions, as the solutions microscopic structure, and thereby the protein structure factor  $S_{\text{lys-lys}}(q)$ , are inaccessible to scattering techniques due to contrast issues or interference effects. Here, we utilize the fact that the protein intermolecular interactions also underlie the phase behavior (see section 2.3.4). Hence, the effects of the macromolecular crowder on the magnitude and nature of pressure-dependent intermolecular interactions in low-ionic strength lysozyme-Ficoll aqueous solution, should also be mirrored in the phase transition temperature and pressure, termed cloud point, in complementary near-critical solutions. Aside from the insight into the proteins intermolecular interactions provided by LLPS, it is also of high interest as a fundamental biological phenomena and as a prerequisite for the formation of protein crystals as already lined out in section 2.3.4.

To support the findings derived by the SAXS data (see section 7.3), the phase boundaries (binodals) for metastable liquid-liquid phase separation in  $285 \text{ mg mL}^{-1}$  lysozyme + 25 mM Bis-Tris solutions with an ionic strength of 0.5 M NaCl were determined at hydrostatic pressures up to 3.5 kbar for pure buffer as well as upon addition of 1.25% (w/v) Ficoll PM 70 to the solution (see Figure 7.9). The LLPS ( $p$ - $T$ )-phase diagrams for the protein-buffer and protein-Ficoll-buffer systems was determined in high-pressure laser transmission (turbidity) measurements (see section 3.3 for more details on sample preparation and experimental setup).

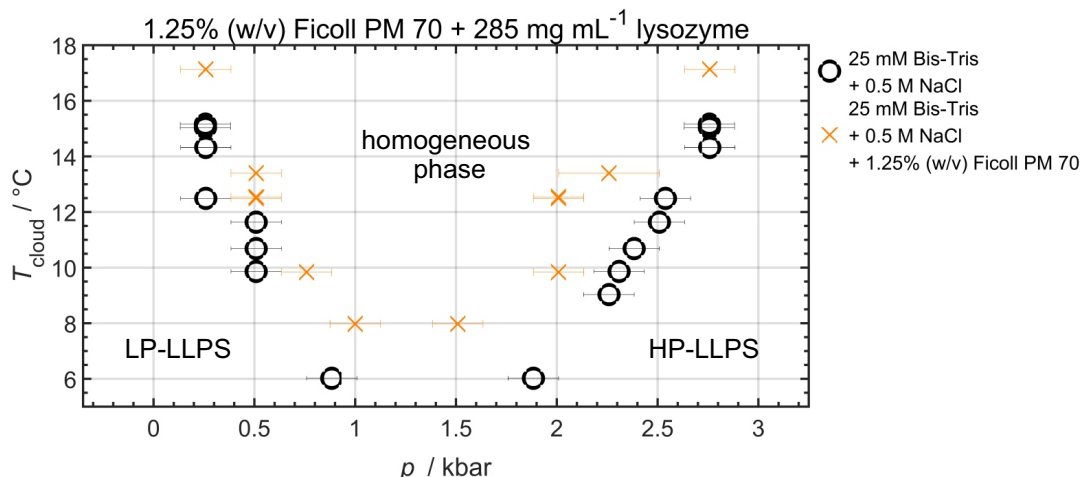


Figure 7.9: Temperature cloud point,  $T_{\text{cloud}}$ , of  $285 \text{ mg mL}^{-1}$  lysozyme in 0.5 M NaCl + 25 mM Bis-Tris (pH 7) (*black circles*) and with addition of 1.25% (w/v) Ficoll PM 70 to the buffer (*orange crosses*) in a pressure range from 1 - 3500 bar.

Clearly, the LP- and HP-LLPS boundaries in the  $p$ - $T$ -phase diagram are shifted to higher

temperatures in the presence of Ficoll PM 70, as also observed upon increasing the protein concentration [Cardinaux et al., 2007, Möller et al., 2014a, Schulze et al., 2016]. Thus, Ficoll seems to simply act by excluding the available volume to the protein, effectively increasing the protein concentration. This enables a phase transition of the protein solution already at higher temperatures, which would otherwise only have been possible at higher protein concentrations. Background molecules (i.e. crowder) fulfill exactly this purpose in the cell, they facilitate LLPS where the concentration of the individual species are generally too low for phase separation to occur [Luby-Phelps, 1999, Walter and Brooks, 1995, Walter, 1999] (see section 2.3.4).

The reentrant liquid-liquid phase transition found for dense protein solutions in neat buffer at kbar pressures mirrors the increasing attractivity of the protein pair interaction upon pressurization due to pressure-induced structural changes in the water network (i.e. collapse of the 2nd water hydration shell) [Schroer et al., 2011a, Möller et al., 2014a, Schulze et al., 2016]. The turnover pressure from the low pressure (LP-)LLPS to the high pressure (HP-)LLPS region is independent of the crowding level, since this effect is essentially solvent-mediated.

## 7.4 Conclusions

We report SAXS studies on pure Ficoll PM 70/400 solutions as a function of concentration and pressure as well as on ternary lysozyme-Ficoll-buffer mixtures at various compositions to reveal the structure of the Ficoll molecule in solution upon changes in the solution conditions (i.e. solvent composition) and upon compression as well as its effect as macromolecular crowding agent on the pressure-dependent protein-protein interactions at various crowding levels.

The recorded SAXS data show that the structure of Ficoll PM 70/400 in solution deviates from a compact ideal sphere as it exhibits both signs of softness and polydispersity. With increasing concentrations, the formation of a stable suspension of monomers and clusters becomes likely, eventually merging into a network-like structure at high concentrations. Whilst the structure of Ficoll is strongly modulated by the excluded volume effect at increasing crowder number densities, it remains essentially unchanged upon pressurization up to the 4 kbar level.

Due to the increase of background scattering in case of the macromolecular crowding agent Ficoll PM 70/400, the protein-protein structure factor,  $S_{\text{lys-lys}}(q)$ , cannot be derived from the total scattering intensity of Ficoll-lysozyme mixtures. Here, small-angle neutron scattering (SANS) in combination with the contrast matching technique (i.e. changing the hydrogen/deuterium content of the polysaccharide) would be the more suitable method to elucidate the crowder's influence on the protein pair-interaction.

Complementary LLPS cloud point measurements reveal a shift of the LLPS phase boundaries in the  $p$ - $T$ -plane to higher temperatures. Hence, we find the LLPS is promoted upon addition of the macromolecular crowder Ficoll PM 70 due to the increased effective protein concentration by the excluded volume effect. The solvent-mediated non-monotonous pressure-dependence of the effective protein pair-interactions, i.e. the boundaries of the reentrant LLPS region at elevated pressures, remain unaffected by the macromolecular crowder Ficoll PM 70, however.

Based on the current data, the comparison of the impact of the polysaccharide Ficoll and its subunit sucrose (see section 4) on the protein interaction reveals a significant difference in the particular effects of macro- vs. nanomolecular crowding. We find that sucrose renders the effective protein pair-interaction more repulsive with increasing sucrose concentration, as reflected in the increase of the normalized second osmotic virial coefficient,  $b_2$ . Conversely, Ficoll PM 70 shifts the LLPS to higher temperatures, i.e. increases the attractive interaction between the protein molecules. However, the comparison of the two systems is only circumstantially, since the ionic strength in the second system is much larger, screening the proteins surface charge entirely.

## Chapter 8

# General Conclusions and Outlook

In this thesis, the influence of natural cosolvent mixtures occurring within cells of organisms that thrive under extreme environmental conditions and the cellular effect of molecular crowding on the pressure-dependent structure and effective protein-protein interaction potential,  $V(r)$ , of dense protein solutions was studied for the model protein lysozyme and analyzed using small-angle X-ray scattering (SAXS) in combination with a liquid-state theoretical approach. The protein pair-interactions govern the spatial distribution of lysozyme molecules in solution, as well as the boundary of the temperature- and pressure-dependent (metastable) liquid-liquid phase coexistence region. Liquid-liquid phase separation (LLPS) phenomena of biomolecules such as proteins are highly relevant for the self organization and spatiotemporal control of biological processes *in cellulo*. We explored the effect of the polysaccharide Ficoll PM 70 and the non-adsorbing polymer polyethylene glycol (PEG) on the phase behavior of dense lysozyme solutions over a wide range of temperatures and pressures. Employing more than three orders of magnitude of the polymer's molecular weight ( $M_w \approx 200 - 35000 \text{ g mol}^{-1}$ ), we investigated the effects of molecular crowding by the impact of the size and shape of the crowding agent at concentrations crossing from the dilute to the semi-dilute polymer regime, thereby mimicking all crowding scenarios encountered in the heterogeneous biological cell. Moreover, in a combined experimental effort employing small-angle X-ray scattering (this work), FT-IR and fluorescence spectroscopy as well as stopped-flow enzyme kinetics in concert with high-pressure techniques (see [Julius et al., 2018a]), we revealed the effects of cosolutes and crowding agents on the pressure-induced conformational changes of the dimeric enzyme horse liver alcohol dehydrogenase (LADH) on the quaternary, secondary and tertiary structural level.

### Effects of Molecular Crowding on the Protein-Protein Interaction Potential:

We observe, that the pressure-dependent protein pair-interaction potential,  $V(r)$ , and, hence, the protein-protein distances and the phase boundary of the LLPS region markedly depend on the polymer-to-protein size ratio and the polymer concentration. The strongest effect is observed for small PEG molecules and sucrose, both leading to a marked decrease of the mean intermolecular spacing of the protein molecules with increasing crowder concentration. The effect levels off at intermolecular distances where the proteins' second hydration shells start to penetrate each other. Conversely, increasing the polymer concentration beyond the polymer size specific threshold ( $c_{\text{PEG}}/c^* \geq 1$ ), where the structure of the polymer solution changes from single dispersed polymers to an entangled network, results in the recovery of the system. Eventually, the proteins maintain a distance comparable to that of the polymer-free system.

In order to quantify the influence of the polymer-mediated depletion interaction between two lysozyme molecules on the effective protein-protein interaction in dense protein-polymer mixtures, the DLVO description was extended by an attractive depletion interaction potential, which was calculated in the framework of PRISM theory. We find that the depletion forces between the protein molecules are enhanced by an increase in the polymer concentration. At  $c_{\text{PEG}}/c^* \geq 1$ , they decrease in range due to the formation of polymeric network structures before sufficient attraction (i.e. negative values for the second osmotic virial coefficient) could be induced. We observe a

strong discrepancy between the theoretically predicted and experimental  $b_2$  values, especially at  $c_{\text{PEG}}/c^* < 1$ . This suggests that additional non-DLVO repulsive forces must be present that control protein-protein interactions at short distances and stabilize the densely packed protein solution against depletion-induced aggregation, even at pressures as high as in the deep sea.

We observe increased repulsive interaction between proteins when they are forced to come very close (i.e. in the presence of small crowder molecules). This effect is mirrored in the decrease of the depth of the attractive Yukawa potential refined from the experimental SAXS data as well as in the shift of the liquid-liquid phase boundary to lower temperatures in the presence of small PEGs. Thus, the cause for the increased repulsion of the system is sought in forces that are always present, but only relevant at very short distances. At short distances ( $\lesssim 10$  Å [Luby-Phelps, 1999]) between the molecular surfaces, as encountered in the highly crowded cytoplasm [Fulton, 1982], short-ranged interactions such as hydrophobic interactions, electrostatic attraction/repulsion, specific binding and solvent structuring are enhanced [Kuehner et al., 1999, Leckband and Israelachvili, 2001, Fersht, 1999]. We find, net-attractive weak (transient) hydrophobic interactions between protein and polymer may at least partially explain the reported results, as such soft enthalpic protein-PEG interactions would cause an additional repulsion between proteins and become particularly important, when the crowder molecules are able to reside in the space between two protein molecules (i.e. small PEG,  $M_w \sim 200, 600$  g mol $^{-1}$ ). Further, hydration-shell repulsion, which acts at intermolecular distances small enough for the second hydration shells of the proteins to penetrate each other, is very likely to become important here.

Pressure modulation is a convenient means to fine tune intermolecular distances in aqueous biomolecular systems as well as to explore the intermolecular interaction forces. In polymer-free buffer solution, the pressure-induced reduction of the intermolecular distances between lysozyme molecules and the concomitant increase of the normalized second virial coefficient,  $b_2$ , level off around  $\sim 1.6$  kbar, most likely due to structural changes of the water H-bond network, which eventually leads to a trend reversal upon further pressurization [Schroer et al., 2011a]. This non-monotonic pressure dependence of the mean intermolecular distance and the effective intermolecular interaction between proteins are affected by polymer-mediated depletion forces, which gradually decline with decreasing depletion thickness as the polymer size decreases upon compression. Therefore the application of pressure reduces the protein distance, but also the depletion thickness of the crowder, i.e. HHP counteracts the depletion interaction. In this sense, high hydrostatic pressures, as they occur in the deep sea where organisms thrive at pressures up to 1.1 kbar, may attenuate the crowding-induced attraction between proteins and thereby help prevent the protein molecules from getting too close to each other during compression, which could cause protein aggregation.

Based on small-angle X-ray scattering data of ternary lysozyme-Ficoll-buffer mixtures, no statement could be made about the effect of the polysaccharides Ficoll PM 70/400 as macromolecular crowding agents on the pressure-dependent protein-protein interaction potential in dense lysozyme solutions at different crowding levels due to the increased background scattering of the crowders. The analysis of the SAXS data on binary Ficoll PM 70/400-buffer solutions as a function of concentration and pressure shows that the structure of the Ficoll molecule in solution deviates from a compact, ideal sphere as it exhibits both signs of softness and polydispersity and, hence, changes markedly by the excluded volume effect at increasing crowder number density. With increasing concentrations, the formation of a stable suspension of monomers and clusters becomes likely, eventually merging into a network-like structure at high concentrations. The structure of Ficoll remains essentially unchanged upon pressurization up to the 4 kbar level, however. Such findings about the effect of (self-)crowding and increased excluded volume on 'soft', net-forming polymers, which are abundantly present in living cells, are of high relevance in the research on the cellular crowding effect and, in particular, on its role in guaranteeing and improving mechanical strength of the cell under high pressure conditions as encountered in the deep-sea.

### Effects of Molecular Crowding the Protein Liquid-Liquid Phase Separation Boundary in the ( $p$ - $T$ )-Plane:

In the dilute polymer regime ( $c_{\text{PEG}}/c^* < 1$ ) we find a strong correlation between the position of the phase boundary of the liquid-liquid coexistence region in the ( $p$ - $T$ )-plane and the protein



pair-interactions in protein-polymer mixtures with respect to the net effect of polymer size and concentration. The effective protein-protein interactions, quantified by the normalized second osmotic virial coefficient of the protein, become more repulsive in the presence of the polymer PEG (i.e. increase of  $b_2$ ). The effect is enhanced by a decreasing ratio of protein-to-polymer chain size and an increasing polymer concentration. Accordingly, the entry into the HP-LLPS region is shifted to higher pressures, whereby the binodal is shifted to lower temperatures,  $T_{\text{cloud}}$ , over the entire pressure range. Under ambient conditions and within the limits of the dilute polymer regime, both the strength of the attractive interactions and the cloud point temperature are influenced by the polymer molecular weight (size) in a way that can be described by a power law. The dependence of the polymer's radius of gyration on the polymer molecular weight is similarly described by a power law, which indicates that (steric) excluded volume and depletion forces, both scaling with polymer size, are able to strongly modulate protein-protein interactions.

The comparison of the impact of the polysaccharide Ficoll PM 70 and its subunit sucrose (and small PEG) on the protein interaction reveals a significant difference between the particular effects of macro- vs. nanomolecular crowding. We find that sucrose and small polymer render the effective protein pair-interaction more repulsive with increasing crowder concentration, as reflected in the increase of the normalized second osmotic virial coefficient,  $b_2$ , and in a shift of the LLPS boundaries to lower temperatures for the polymer. Conversely, we find the entrance into the LLPS region is promoted upon addition of the macromolecular crowder Ficoll PM 70 (i.e. shift of the LLPS phase boundary in the ( $p$ - $T$ )-plane to higher temperatures), most likely due to the increased effective protein concentration by the excluded volume effect. The shift of the phase boundaries to higher temperatures, as already found for increasing lysozyme concentration [Muschol and Rosenberger, 1997, Taratuta et al., 1990, Broide et al., 1996, Cardinaux et al., 2007] at ambient conditions, is preserved upon pressurization. The solvent-mediated non-monotonous pressure-dependence of the effective protein pair-interactions, i.e. the boundaries of the reentrant LLPS region at elevated pressures [Möller et al., 2014a, Schulze et al., 2016], remain unaffected by the macromolecular crowder Ficoll PM 70, however.

Finally, since the metastable liquid-liquid phase separation is strongly correlated with the solid-liquid phase transition [Broide et al., 1996] (i.e. protein crystallization), such findings may also be applied in the optimization of the solution conditions and the kinetics for protein nucleation and crystal growth using both variables, PEG and high hydrostatic pressure [Crisman and Randolph, 2009, Gross and Jaenicke, 1994].

### Effects of Natural Cosolvent Mixtures on the Protein-Protein Interaction Potential:

We investigated the effect of individual cosolvents, such as the carbohydrates trehalose and *myo*-inositol, the methylamines betaine, TMAO, sarcosine and GPC, the  $\alpha$ -amino acids glycine, L-proline and L-alanine, the  $\beta$ -amino acids taurine and  $\beta$ -alanine and the denaturant urea, on intermolecular interactions in dense protein solutions over the entire concentration range from 0 to 1M. We find that natural cosolvents modulate the protein-protein interaction potential and its pressure dependence to varying degrees. Two different cosolvent classes with contrasting effects on the pressure-dependent protein-protein interactions emerge: Whilst TMAO significantly increases the attractive interaction between the lysozyme molecules, all the other cosolvents, even though of different chemical make-up, render the overall pair-interaction potential more repulsive. Nonetheless, a slight decrease of the intermolecular distance can be observed for the latter. Such an effect might be rationalized invoking an excluded volume effect imposed by the cosolvents. The strength of the attractive interaction,  $J(c)$ , decreases linearly with increasing osmolyte concentration,  $c$ , and differences become visible at higher cosolvent concentrations, only, i.e. in the region where changes in dielectric solvent properties become more prominent.

Remarkably, the addition of all osmolytes only modulates the non-monotonic pressure dependence of the protein pair-interaction found for the pure buffer system, but leaves its general form essentially unchanged, i.e. the mechanism underlying this effect should be universal. Significant differences only arise for TMAO, meaning a much stronger pressure dependency and a shift of the minimum in  $J(p)$  and the maximum of  $b_2(p)$  to  $\sim 1$  kbar higher pressures. Such an effect may be due to significant structural changes of the solvent and/or to a very strong thermodynamically favored exclusion of the additive from the protein surface, i.e., a strong solvophobic effect, which

reduces intermolecular distances and apparently increases intermolecular attractive interactions.

High-pressure SAXS data on protein solutions containing cosolvent mixtures, which mimic conditions encountered in deep-sea organisms (i.e. shallow and deep-living crabs, skates and shrimps [Kelly and Yancey, 1999]), clearly show that all cosolvents other than TMAO are largely interchangeable and that their presence leads to attenuation of the effects of TMAO in varying degrees depending on the cosolute structure. Consequently, the marked effect of TMAO on the interaction potential is reduced and the shift of the minimum in  $J(p)$  to higher pressures is reversed, not only by the denaturant urea, but also by the presence of other cosolvents. Since TMAO is also known to stabilize proteins and other biomolecules most effectively [Canchi and García, 2013], it appears that natural osmolyte mixtures are composed in a way that compensates for TMAO-induced overstabilization and too strong attractivity, which might be necessary to maintain normal cellular functionality. The unique role played by TMAO is clearly evident and could be attributed to its ability to counter pressure effects by strengthening and increasing the amount of water-water-hydrogen bonds as well as by a strong spatial ordering of the solution's hydrogen bond network [Canchi and García, 2013, Zou et al., 2002].

Under cell-like crowding conditions, the intermolecular distances between the proteins are in the order of a few water layers, only. Here, an increased hydration repulsion between the proteins and a change in the second coordination shell of water at a pressure of  $\sim 1.6$  kbar seem to lead to a trend reversal in the attractive interaction and the intermolecular distances, which until then have decreased with increasing pressure. This behavior is modulated by changes in the interactions between cosolvent and water. These may include effects such as an inward shift of the pair-correlation function of oxygen atoms in water,  $g_{\text{OwOw}}(r)$ , by TMAO [Towey et al., 2013] and a cross-interaction between cosolvents as observed for TMAO and urea at ambient pressure [Ganguly et al., 2015, Hunger et al., 2015]. In addition, changes in protein-cosolvent-water interactions may contribute.

The deep-sea osmolyte TMAO has been shown to play an outstanding and unique role. The addition of TMAO to the protein solution leads to a pronounced excluded volume and affects the protein-protein interactions most strongly. This is due to the special structure of the deep sea osmolyte. TMAO is a rather small solute offering both highly hydrophilic and hydrophobic solvation regions. It has a strong dipole moment ( $\sim 5$  D) and excellent H-bonding capability. In addition, it shows a predominantly repulsive self-interaction [Canchi et al., 2012]. Not only does the presence of TMAO guarantee sustainability of the native protein's folded state under harsh environmental conditions [Yancey et al., 2001, Schroer et al., 2011a, Gao et al., 2017b, Arakawa and Timasheff, 1985], it also controls water-mediated intermolecular interactions at elevated pressure, thereby preventing contact formation and hence protein aggregation. In fact, Embedded Cluster Reference Interaction Site Model (EC-RISM) theory in concert with *ab initio* molecular dynamics simulations and FT-IR data have recently revealed a charge redistribution of TMAO upon compression. Increased solvent-induced polarization and a locally enhanced H-bonding network are both proposed being key ingredients to high-pressure adaptation [Hözl et al., 2016, Imoto et al., 2016].

### Impact of Cosolvents and Molecular Crowding on the Pressure-Induced Dissociation/Inactivation of Oligomeric Enzymes

The combined experimental approach employed here [Julius et al., 2018a] revealed three different phases in the reaction of the oligomeric LADH to the increase in hydrostatic pressure. Our results show that beyond an increase of enzymatic activity at low pressures, the loss of enzyme activity occurs around 600 – 800 bar, i.e. in a pressure regime where small conformational changes take place in the coenzyme's binding pocket, only, probably related to its pronounced compressibility. Whereas higher-order oligomers dissociate at low pressures ( $\lesssim 800$  bar), the dissociation of dimeric LADH into subunits takes place between 2000 and 4000 bar, depending on the solution conditions. Cosolvents such as urea or Trimethylamine N-oxide (TMAO) and the nanocrowder PEG 200 modulate conformational changes such as oligomerization and dissociation into multimeric and monomeric subunits as they tend to bind to the interface of the protein or to act *via* the excluded volume effect. In general, the enzymatic activity of many oligomeric enzymes depends on their oligomerization state, which is influenced not only by hydrostatic pressure but also by cosolvents

and crowders, as is the dissociation of the subunits. Osmolytes can therefore be regarded as effective means of marine organisms to modulate the oligomeric state of enzymes and thus their activity. Enzymes in the cells of deep-living organisms may exhibit some intrinsic adaptations to extreme temperatures and pressures, but extrinsic adaptations such as the use of stabilizing osmolytes like TMAO seem necessary, which have a rather universal effect on proteins through non-specific, solvent-mediated interactions.

## Outlook

Through this thesis, we reinforce the notion that the DLVO model for protein pair-interaction fails at extreme crowding conditions. Ideally, the DLVO potential should be extended by an excluded volume / osmotic attractive potential as a function of cosolute concentration and identity (i.e. size), a square-well interaction to account for potential self-association of the protein due to strong, short-range interactions (i.e. *via* hydrophobic bonds, hydrogen bonds, ionic bonds), hydration repulsion and enthalpic effects between crowder and protein at short distances, next to the hard-sphere, Coulomb and van der Waals potential terms [Narayanan and Liu, 2003, Curtis et al., 1998]. At present, the effects of the non-adsorbing polymer PEG on the lysozyme pair-interaction cannot be described by simple DLVO theory or an osmotic interaction potential but repulsive hydration forces and other specific protein-polymer attraction forces are contributing significantly to the total pair-interaction potential and are controlling intermolecular protein-protein interactions at short distances. In order to yield a more quantitative description of the potential landscape of proteins interacting in complex solutions, these specific contributions need further attention and more in-depth theoretical treatment in order to accurately account for the experimental SAXS data.

In all physiological fluid media, contributions of additional, longer-ranged, chemical, 'soft' interactions (enthalpically driven) between proteins and crowding agents must be taken into account in addition to the hard-core steric repulsion (entropically driven) [Gao et al., 2017b]. These pair-wise interactions like attractive hydrophobic interaction, hydrogen bonding, weak electrostatic repulsion/attraction depend on temperature as well as on global chemical properties of the biomolecules, crowder and solvent (i.e. net charge, solution dielectrics, dipol/multipol moment, macromolecular shape and polarity of surface residues) [Minton, 2001]. The always present enthalpic contributions to crowding may enhance or counteract the entropic excluded volume effect *in cellulo*. In order to investigate more precisely to what extent the simple entropically excluded volume effect is effectively modulated by such enthalpic contributions, we propose to investigate the influence of non-inert biological crowder molecules (i.e. other protein types, e.g. BSA) with well characterized chemical properties compared to inert crowding agents of similar shape and size for various solution conditions (e.g. pH, solution dielectrics).

With our study on ternary protein-crowder-solvent systems, we have taken another step towards understanding the modulation of conformational stability, intermolecular interactions and phase behavior by biological nano- and macromolecular crowding, a typical generic phenomenon of the cellular environment. However, the intracellular environment is rather multicomponent [Minton, 1997, Minton, 2000]. Since in general no individual species may be present in high concentrations, crowding studies with a single species of equally sized crowding agents do not fully represent the composition and size heterogeneity found in living cells [Batra et al., 2009, Ando et al., 2016]. Hence, we propose to investigate more complex multi-component systems of crowding agents of various identities and concentrations. However, since macromolecular crowding agents give rise to an increased  $q$ -dependent background scattering, which impedes the extraction protein-protein structure factor from the total scattering intensity of crowder-protein mixtures (as observed in this work for the polysaccharides Ficoll PM 70/400), small-angle X-ray scattering is not the right experimental method for this. Here, small-angle neutron scattering (SANS) in combination with the contrast matching technique (i.e. changing the hydrogen/deuterium content of the crowder molecules) would be the more suitable method to elucidate the crowder's influence on the protein pair-interaction.

According to theoretical colloid physics of critical phenomena, the occurrence of a metastable liquid-liquid phase region in the protein ( $\Phi_{\text{lys}}-T$ )-phase diagram is the direct consequence of the short-ranged nature of the forces acting on the particles and crucially depends on the range of

the attractive interaction potential relative to the particles diameter (i.e. the hard-sphere repulsion) [Hagen and Frenkel, 1994, Foffi et al., 2002]. The range of the effective protein-protein interaction can be modulated by changing the pH and the salt concentration. Further, in mixtures of colloidal particles (i.e. proteins) and non-adsorbing polymer (i.e. polyethylene glycol) a liquid-liquid demixing transition may occur due to the entropy-driven depletion mechanism [Nägele, 2008, Ilett et al., 1995, Poon et al., 1997]. Here, the entropically favored depletion of polymer from the intermediate region of two colloidal particles induces an attractive interaction between the colloids, whose range is determined by the effective polymer size [Asakura and Oosawa, 1958, Vrij, 1976]. Under suitable conditions (i.e. the range of the depletion attraction exceeds  $\sim 25 - 30\%$  of the particle's radius) the colloid-polymer mixtures can undergo phase separation into colloid-rich and colloid poor regions [Poon et al., 1996, Ilett et al., 1995]. We propose employing a potential model with an adjustable parameter for the range,  $d$ , of the attractive interaction (i.e. the controlling LLPS parameter) in the analysis of the small-angle X-ray scattering data, in order to achieve better comparability to the LLPS phenomena. Further, in case of ternary protein-cosolute-water solutions, it would help resolve the modulation of total pair-interactions by hydration shell effects (e.g. preferential hydration, as imposed by the presence of the crowding agents and organic osmolytes [Gögelein et al., 2012]) and also by attractive osmotic depletion interactions with a range scaling by the crowder size. Complementary high-resolution SAXS experiments (e.g. in a capillary at ambient pressure) on dilute protein-cosolute solutions as a function of cosolute concentration and a thorough form factor analysis with the program CRY SOL [Svergun et al., 1995] to detect modulations in the protein hydration by changes in the scattering contrast (i.e. forward scattering) between the bulk phase (+cosolute) and the pure hydration water of the protein might be helpful to highlight hydration shell effects as well. Up to now it has been remained unresolved to what extent such hydration shell effects on the protein pair-interactions are modulated upon compression due to the different compressibilities of the bulk and the hydration shell water. Detailed molecular dynamics simulations of the system with appropriate pressure-adjusted force fields would help to elucidate the pressure- and cosolvent-induced changes in structure and dynamics of hydration shell water of dense protein solutions and their effects on protein-protein interaction.

## Appendix A

# Supplementary Information for Chapter 4

Refinements for the Effective Structure Factor,  $S_{\text{eff}}(q)$ , as a Function of Sucrose Concentration

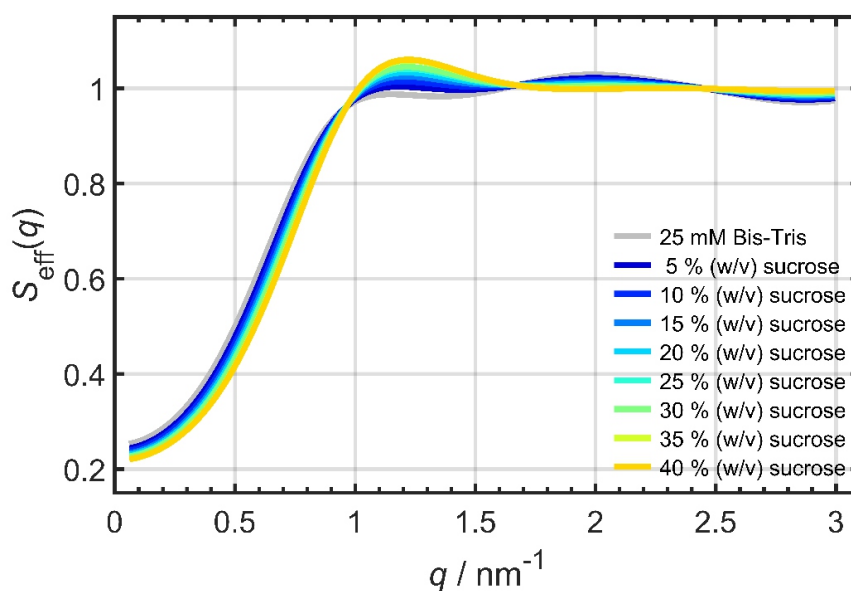


Figure A.1: Refinements for the effective structure factor,  $S_{\text{eff}}(q)$ , of 10% (w/v) lysozyme dissolved in 25 mM Bis-Tris (pH 7) at various sucrose concentrations,  $c$ , at ambient pressure and 25°C. Reprinted with permission from [Julius et al., 2019]. Copyright © 2019 American Chemical Society.



## Refinements for the Effective Structure Factor, $S_{\text{eff}}(q)$ , as a Function of Polymer Molecular Weight

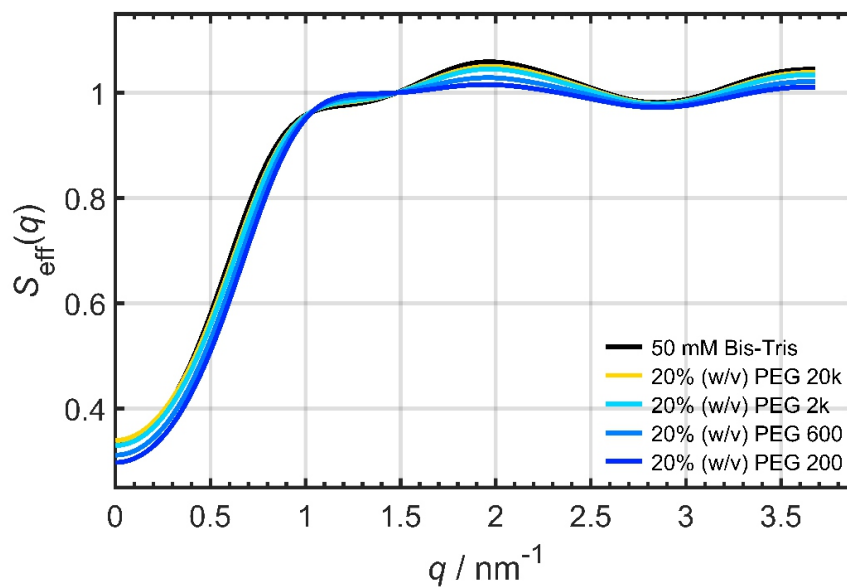


Figure A.2: Refinements for the effective structure factor,  $S_{\text{eff}}(q)$ , of 10% (w/v) lysozyme dissolved in 50 mM Bis-Tris (pH 7, 25°C) and 20% (w/v) PEG of selected  $M_w$  at ambient pressure. Reprinted with permission from [Julius et al., 2019]. Copyright © 2019 American Chemical Society.

## SAXS Data Refinement

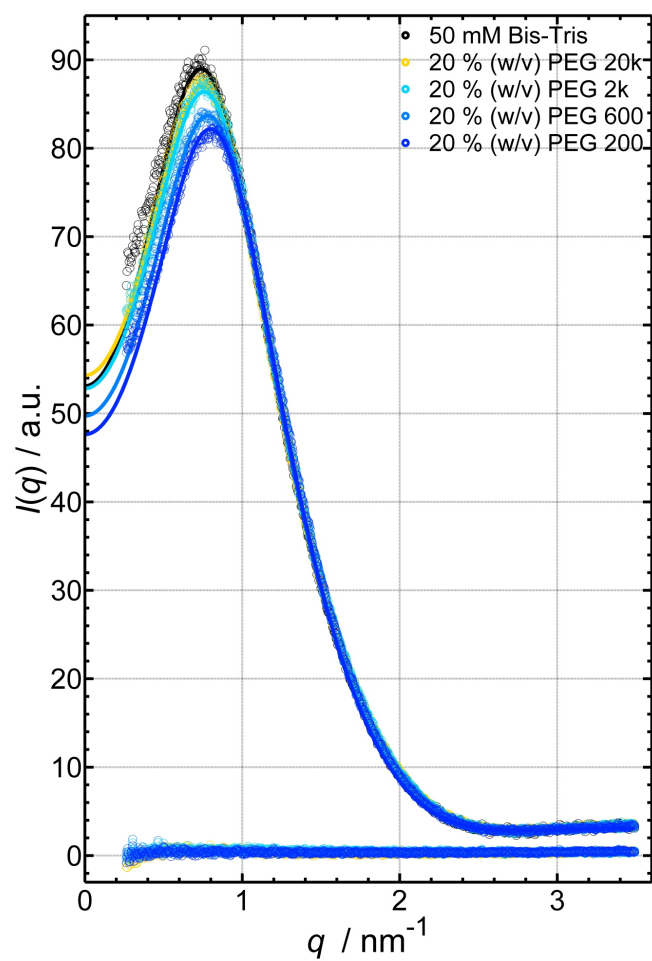


Figure A.3: Background-corrected experimental SAXS curves of 10% (w/v) lysozyme dissolved in 25 mM Bis-Tris (pH 7) + 20% (w/v) PEG of selected polymer sizes (200, 600, 2k, 20k) and of the neat polymer (*flat curves*). Data were recorded at ambient pressure and 25°C and are displayed together with the refinements (*solid lines*) for the protein solution scattering intensities,  $I(q)$ . Reprinted with permission from [Julius et al., 2019]. Copyright © 2019 American Chemical Society.

## Potential Parameters $J(c, p)$ and $b_2(c, p)$ for Various PEG Molecular Weights and Degrees of Crowding at Elevated Ionic Strength

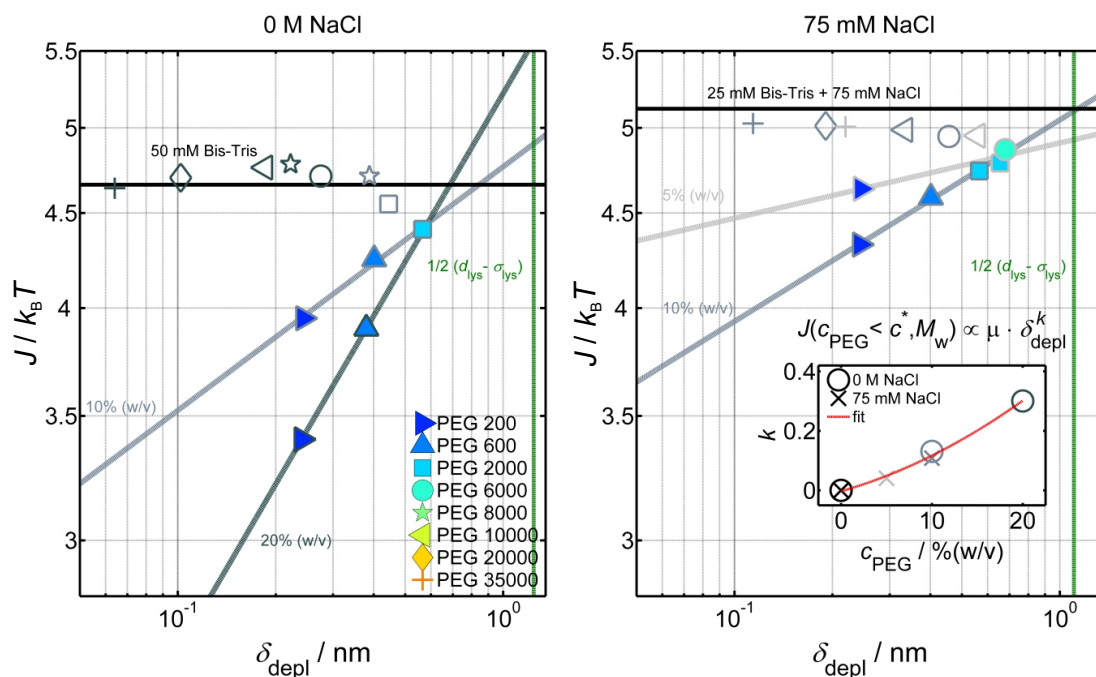


Figure A.4: Impact of ionic strength on the power-law relation  $J(c_{\text{PEG}} < c^*) \propto \mu(\delta_{\text{depl}})^k$  (grey lines) for 10% (w/v) lysozyme dissolved in (left side) 50 mM Bis-Tris and (right side) 25 mM Bis-Tris + 75 mM NaCl (solid black lines), respectively, and 5 – 20% (w/v) polymer of various molecular weights at ambient pressure and 25°C (double-logarithmic representation). Inset: Slope  $k$  as a function of polymer concentration,  $c_{\text{PEG}}$ , for both buffer compositions, shown together with the corresponding polynomial refinement (solid red line). Empty symbols visualize the  $J$  values for PEG concentrations exceeding  $c^*$ . Reprinted with permission from [Julius et al., 2019]. Copyright © 2019 American Chemical Society.

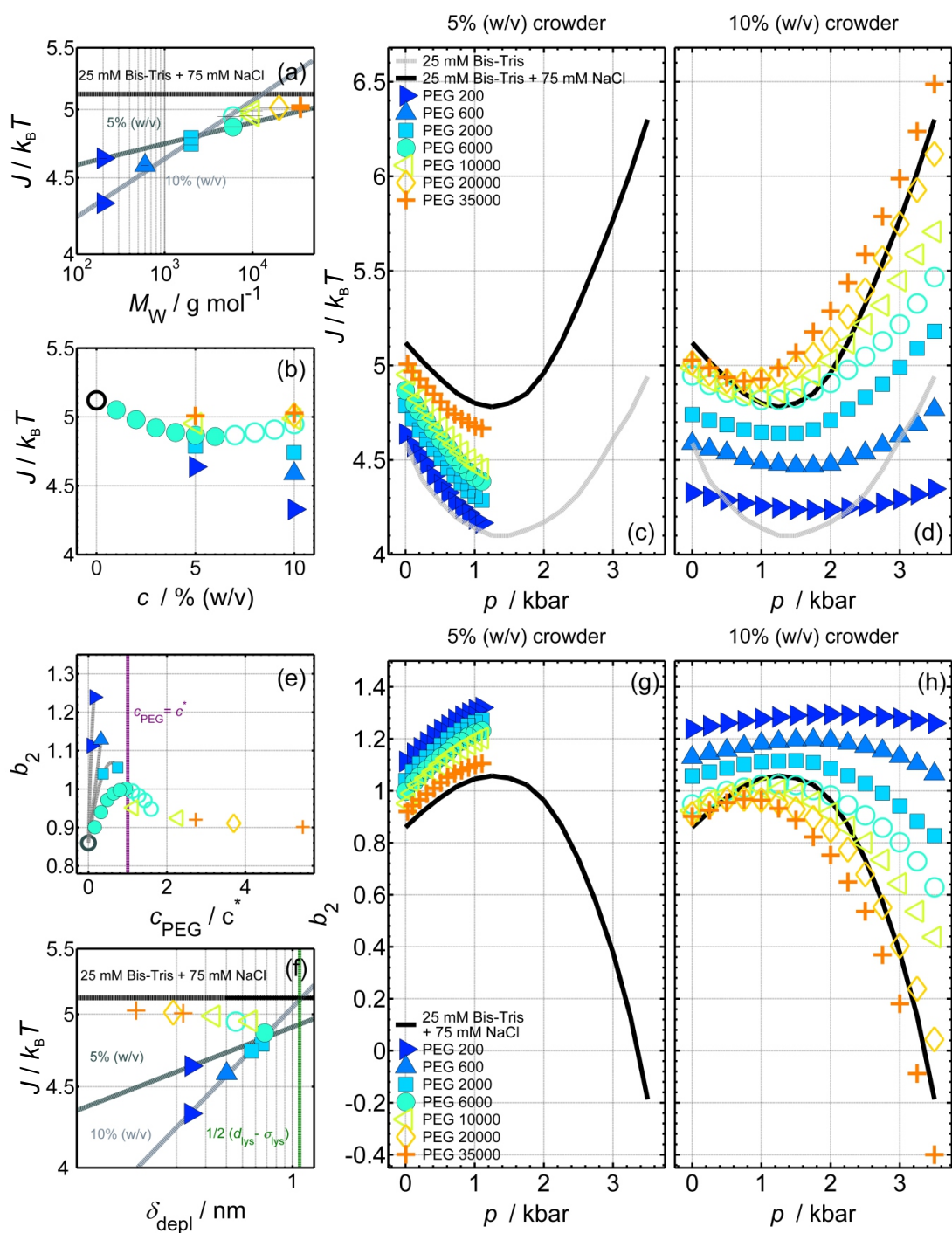


Figure A.5: (a)+(f) Double-logarithmic plots of the strength of the attractive part,  $J$ , in 10% (w/v) lysozyme in 25 mM Bis-Tris + 75 mM NaCl (pH 7, 25°C) solution at ambient pressure as a function of the PEGs molecular weight,  $M_w$ , and depletion thickness,  $\delta_{\text{depl}}$ , for 5, 10% (w/v) amount of the polymer. The corresponding power-law trend-lines  $J(c_{\text{PEG}} < c^*) \propto \alpha(M_w)^m$  and  $J(c_{\text{PEG}} < c^*) \propto \mu(\delta_{\text{depl}})^k$  are depicted as well. (b)  $J$  as a function of PEG concentration at ambient pressure and 25°C. (f) Normalized second osmotic virial coefficient,  $b_2$ , as a function of the polymer concentration normalized to the overlap concentration, i.e.  $c_{\text{PEG}}/c^*$ . (c)+(d) Pressure dependence of  $J$  and (g)+(h)  $b_2$  for 5% (w/v) and 10% (w/v) PEG of various sizes added to the buffer solution at 25°C. *Empty symbols* visualize the  $J$  and  $b_2$  values for PEG concentrations exceeding  $c^*$ . Reprinted with permission from [Julius et al., 2019]. Copyright © 2019 American Chemical Society.

## Pressure Dependence of the Potential Parameters $J$ and $b_2$ for Various PEG Molecular Weights and Degrees of Crowding

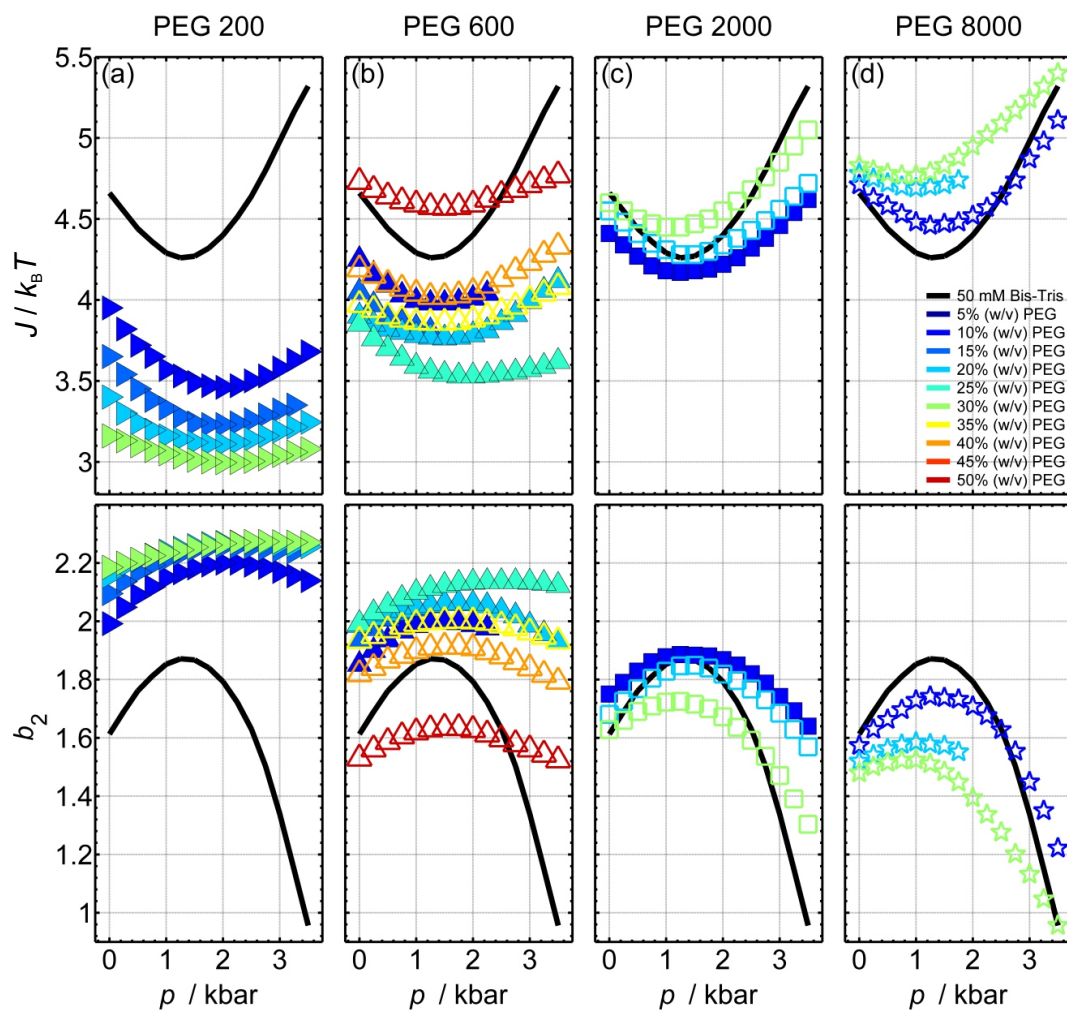


Figure A.6: Pressure dependence of the strength of the attractive part of the effective pair-interaction potential,  $J$ , (*top half*) and the normalized second osmotic virial coefficient,  $b_2$ , (*bottom half*) for 10% (w/v) lysozyme in 50 mM Bis-Tris (pH 7) solution as a function of polymer concentration,  $c$ , for various PEG molecular weights. *Empty symbols* visualize the  $J$  and  $b_2$  values for PEG concentrations exceeding  $c^*$ . Reprinted with permission from [Julius et al., 2019]. Copyright © 2019 American Chemical Society.



## Appendix B

# Supplementary Information for Chapter 5

### Average Intermolecular Distances between Protein Molecules

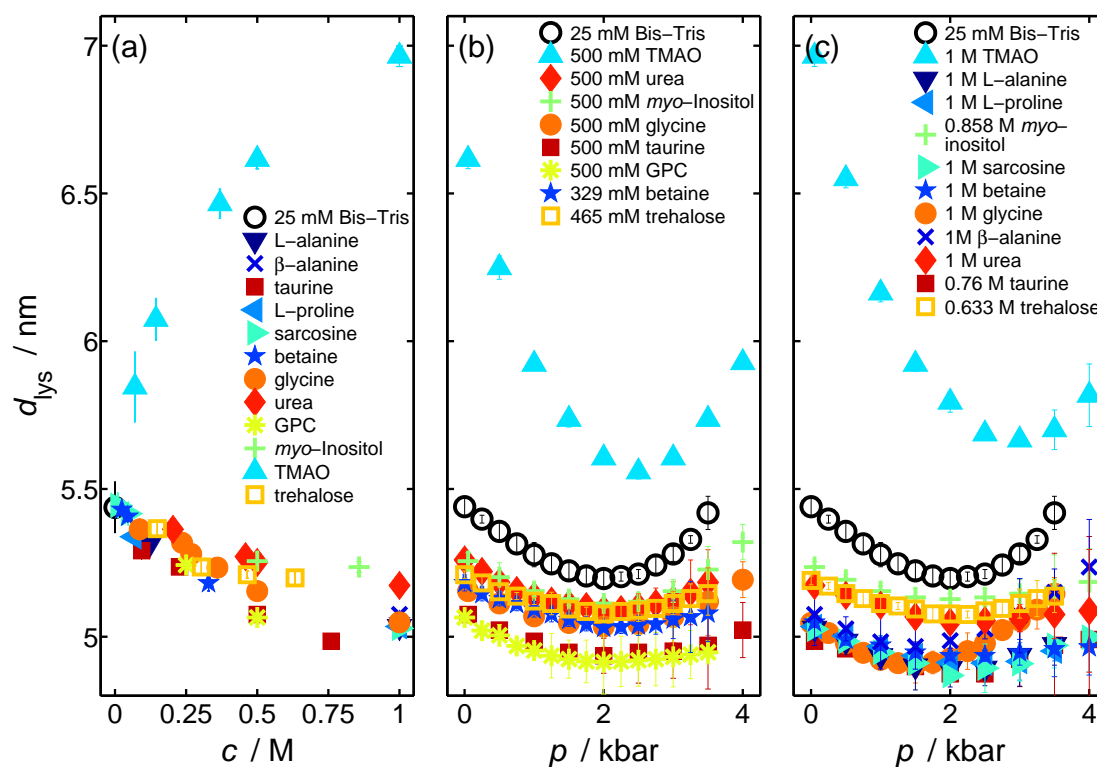


Figure B.1: (a) Mean intermolecular spacing,  $d_{\text{lys}}$ , of lysozyme molecules, derived from the first maximum of the effective structure factor,  $S_{\text{eff}}(q)$ , in a 10% (w/v) lysozyme solution with 25 mM Bis-Tris (pH 7) at 25°C as a function of osmolyte species and concentration,  $c$ , at ambient pressure and as a function of pressure,  $p$ , for selected osmolytes at mid-level (b) and highest (c) concentrations. Reprinted with permission from [Julius et al., 2018b]. Copyright © 2019 American Physical Society.

## Cosolvent-Induced Changes of the Solutions Static Dielectric Permittivity $\epsilon_r$

The dielectric increments,  $\delta = \frac{d\epsilon_r(c)}{dc}$ , of the amino acids and cosolvents in water at 25°C amount to: L-alanine ( $\delta = 23.16 \text{ M}^{-1}$ ) [Wyman and McMeekin, 1933], L-proline ( $\delta = 21 \text{ M}^{-1}$ ) [Cohn and Edsall, 1965], glycine ( $\delta = 22.58 \text{ M}^{-1}$ ) [Wyman and McMeekin, 1933],  $\beta$ -alanine ( $\delta = 34.5 \text{ M}^{-1}$ ) [Wyman and McMeekin, 1933], taurine ( $\delta = 41 \text{ M}^{-1}$ ) [Cohn and Edsall, 1965], sarcosine ( $\delta = 24.5 \text{ M}^{-1}$ ) [Cohn and Edsall, 1965], betaine ( $\delta = 18.2 \text{ M}^{-1}$ ) [Edsall and Wyman, 1964], *myo*-inositol ( $\delta = -2.17$ ) [Franks et al., 1973], TMAO ( $\delta = 2.16 \text{ M}^{-1}$ ) [Hunger et al., 2012], trehalose ( $\delta = -7.53 \text{ M}^{-1}$ ) [Sajadi et al., 2010], GPC ( $\delta = 43.8 \pm 0.5 \text{ M}^{-1}$ ) and urea ( $\delta = 3.4 \text{ M}^{-1}$ , this relation is not linear) [Wyman, 1936]. For the osmolyte mixtures for shallow living species, relative static dielectric permittivities of  $102.0 \pm 0.5$  (1 M crab),  $89.5 \pm 1.8$  (630 mM shrimp) and  $82.2 \pm 0.2$  (630 mM skate) were found and for the deep-sea species  $92.3 \pm 0.5$  (1 M crab),  $82.0 \pm 0.8$  (630 mM shrimp) and  $80.2 \pm 1.3$  (630 mM skate).

# Bibliography

- [Abbott et al., 1991] Abbott, N. L., Blankschtein, D., and Alan Hatton, T. (1991). Protein Partitioning in Two-Phase Aqueous Polymer Systems. 1. Novel Physical Pictures and a Scaling-Thermodynamic Formulation. *Macromolecules*, 24(15):4334–4348.
- [Abbott et al., 1992] Abbott, N. L., Blankschtein, D., and Hatton, T. A. (1992). Protein Partitioning in Two-Phase Aqueous Polymer Systems. 4. Proteins in Solutions of Entangled Polymers. *Macromolecules*, 25(20):5192–5200.
- [Abe et al., 1999] Abe, F., Kato, C., and Horikoshi, K. (1999). Pressure-regulated metabolism in microorganisms. *Trends Microbiol.*, 7(11):447–453.
- [Adams and Fraden, 1998] Adams, M. and Fraden, S. (1998). Phase Behavior of Mixtures of Rods (Tobacco Mosaic Virus) and Spheres (Polyethylene Oxide, Bovine Serum Albumin). *Biophys. J.*, 74(1):669–677.
- [Agilent Technologies, 2009] Agilent Technologies (2009). Agilent Impedance Measurement Handbook A guide to measurement technology and techniques.
- [Agilent Technologies, 2011] Agilent Technologies (2011). Agilent E4991A RF Impedance / Material Analyzer Data Sheet.
- [Agilent Technologies, 2016] Agilent Technologies (2016). Agilent E4991A RF Impedance/Material Analyzer - Service Manual.
- [Ai et al., 2006] Ai, X., Zhou, Z., Bai, Y., and Choy, W. Y. (2006). <sup>15</sup>N NMR Spin Relaxation Dispersion Study of the Molecular Crowding Effects on Protein Folding under Native Conditions. *J. Am. Chem. Soc.*, 128(12):3916–3917.
- [Ajito et al., 2018] Ajito, S., Iwase, H., Takata, S.-i., and Hirai, M. (2018). Sugar-Mediated Stabilization of Protein Against Chemical or Thermal Denaturation. *J. Phys. Chem. B*, 122(37):8685–8697.
- [Al-Karadaghi et al., 1994] Al-Karadaghi, S., Cedergren-Zeppezauer, E. S., Hövmöller, S., Petratos, K., Terry, H., and Wilson, K. S. (1994). Refined Crystal Structure of Liver Alcohol Dehydrogenase-NADH Complex at 1.8 Angstroms Resolution. *Acta Crystallogr., Sect D: Biol. Crystallogr.*, 50(6):793–807.
- [Als-Nielsen and McMorrow, 2011] Als-Nielsen, J. and McMorrow, D. (2011). *Elements of Modern X-ray Physics*. John Wiley & Sons Ltd., London, 2nd edition.
- [Ando et al., 2016] Ando, T., Yu, I., Feig, M., and Sugita, Y. (2016). Thermodynamics of Macromolecular Association in Heterogeneous Crowding Environments: Theoretical and Simulation Studies with a Simplified Model. *J. Phys. Chem. B*, 120(46):11856–11865.
- [Annunziata et al., 2002] Annunziata, O., Asherie, N., Lomakin, A., Pande, J., Ogun, O., and Benedek, G. B. (2002). Effect of polyethylene glycol on the liquid-liquid phase transition in aqueous protein solutions. *Proc. Natl. Acad. Sci. USA*, 99(22):14165–14170.

- [Annunziata et al., 2003] Annunziata, O., Ogun, O., and Benedek, G. B. (2003). Observation of liquid-liquid phase separation for eye lens  $\gamma$ S-crystallin. *Proc. Natl. Acad. Sci. USA*, 100(3):970–974.
- [Ansell et al., 1997] Ansell, R., Granath, K., Hohmann, S., Thevelein, J. M., and Adler, L. (1997). The two isoenzymes for yeast NAD<sup>+</sup>-dependent glycerol 3-phosphate dehydrogenase encoded by GPD1 and GDP2 have distinct roles in osmoadaptation and redox regulation. *EMBO J.*, 16(9):2179–2187.
- [Arakawa and Timasheff, 1982] Arakawa, T. and Timasheff, S. N. (1982). Stabilization of Protein Structure by Sugars. *Biochemistry*, 21(25):6536–6544.
- [Arakawa and Timasheff, 1983] Arakawa, T. and Timasheff, S. N. (1983). Preferential Interactions of Proteins with Solvent Components in Aqueous Amino Acid Solutions. *Arch. Biochem. Biophys.*, 224(1):169–177.
- [Arakawa and Timasheff, 1985] Arakawa, T. and Timasheff, S. N. (1985). Mechanism of Poly(ethylene glycol) Interaction with Proteins. *Biochemistry*, 24(24):6756–6762.
- [Artymiuk et al., 1982] Artymiuk, P. J., Blake, C. C. F., Rice, D. W., and Wilson, K. S. (1982). The structures of the Monoclinic and Orthorhombic Forms of Hen Egg-White Lysozyme at 6 Å Resolution. *Acta Cryst. B*, 38:778–783.
- [Asakura and Oosawa, 1958] Asakura, S. and Oosawa, F. (1958). Interaction between Particles Suspended in Solutions of Macromolecules. *J. Polym. Sci.*, 33(126):183–192.
- [Asherie, 2004] Asherie, N. (2004). Protein crystallization and phase diagrams. *Methods*, 34(3):266–272.
- [Asherie et al., 1996] Asherie, N., Lomakin, A., and Benedek, G. (1996). Phase Diagram of Colloidal Solutions. *Phys. Rev. Lett.*, 77(23):4832–4835.
- [Atha and Ingham, 1981] Atha, D. H. and Ingham, K. (1981). Mechanism of Precipitation of Proteins by Polyethylene Glycols. *J. Biol. Chem.*, 256(23):12108–12117.
- [Atkins et al., 2018] Atkins, P., de Paula, J., and Keeler, J. (2018). *Atkins' Physical Chemistry*. Oxford University Press, New York, 11 edition.
- [Auton and Bolen, 2005] Auton, M. and Bolen, D. W. (2005). Predicting the energetics of osmolyte-induced protein folding/unfolding. *Proc. Natl. Acad. Sci. USA*, 102(42):15065–15068.
- [Axelsson et al., 2011] Axelsson, J., Sverrisson, K., Rippe, A., Fissell, W., and Rippe, B. (2011). Reduced diffusion of charge-modified, conformationally intact anionic Ficoll relative to neutral Ficoll across the rat glomerular filtration barrier in vivo. *Am. J. Physiol.-Renal Physiol.*, 301(4):F708–F712.
- [Back et al., 1979] Back, J. F., Oakenfull, D., and Smith, M. B. (1979). Increased Thermal Stability of Proteins in the Presence of Sugars and Polyols. *Biochemistry*, 18(23):5191–5196.
- [Ball, 2008] Ball, P. (2008). Water as an Active Constituent in Cell Biology. *Chem. Rev.*, 108(1):74–108.
- [Balny et al., 1997] Balny, C., Mozhaev, V., and Lange, R. (1997). Hydrostatic Pressure and Proteins: Basic Concepts and New Data. *Comp. Biochem. Physiol. A*, 116(4):299–304.
- [Banani et al., 2017] Banani, S. F., Lee, H. O., Hyman, A. A., and Rosen, M. K. (2017). Biomolecular condensates: Organizers of cellular biochemistry. *Nat. Rev. Mol. Cell Biol.*, 18(5):285–298.
- [Banipal et al., 2002] Banipal, T. S., Kaur, D., Singh, G., Lark, B. S., and Banipal, P. K. (2002). Partial molar volumes of transfer of some disaccharides from water to aqueous guanidine hydrochloride solutions at 298.15 K. *Indian J. Chem. A*, 41(6):1131–1138.

- [Barthel et al., 1990] Barthel, J., Bachhuber, K., Buchner, R., and Hetzenauer, H. (1990). Dielectric spectra of some common solvents in the microwave region. Water and lower alcohols. *Chem. Phys. Lett.*, 165(4):369–373.
- [Barthel et al., 1983] Barthel, J., Gores, H., Schmeer, G., and Wachter, R. (1983). Non-Aqueous Electrolyte Solutions in Chemistry and Modern Technology. In Barthel, J., editor, *Physical and Inorganic Chemistry. Topics in Current Chemistry*, volume 111, pages 33–144. Springer, Berlin, 1 edition.
- [Bartlett, 2002] Bartlett, D. H. (2002). Pressure effects on in vivo microbial processes. *Biochim. Biophys. Acta*, 1595(1-2):367–381.
- [Baskir et al., 1989] Baskir, J. N., Hatton, T. A., and Suter, U. W. (1989). Thermodynamics of the partitioning of biomaterials in two-phase aqueous polymer systems: comparison of lattice model to experimental data. *J. Phys. Chem.*, 93(5):2111–2122.
- [Batchelor et al., 2004] Batchelor, J. D., Olteanu, A., Tripathy, A., and Pielak, G. J. (2004). Impact of Protein Denaturants and Stabilizers on Water Structure. *J. Am. Chem. Soc.*, 126(7):1958–1961.
- [Batra et al., 2009] Batra, J., Xu, K., Qin, S., and Zhou, H. X. (2009). Effect of macromolecular crowding on protein binding stability: Modest stabilization and significant biological consequences. *Biophys. J.*, 97(3):906–911.
- [Beamline I22, 2018] Beamline I22 (2018). Technical Specifications - Small Angle Scattering - Diamond Light Source. Available at <https://www.diamond.ac.uk/Instruments/Soft-Condensed-Matter/small-angle/I22/specs.html> (Accessed: 14th February 2019).
- [Beamline SWING, 2018] Beamline SWING (2018). Technical Data - SOLEIL. Available at <https://www.synchrotron-soleil.fr/en/beamlines/swing> (Accessed: 14th February 2019).
- [Beaucage, 1996] Beaucage, G. (1996). Small-Angle Scattering from Polymeric Mass Fractals of Arbitrary Mass-Fractal Dimension. *J. Appl. Cryst.*, 29(2):134–146.
- [Becktel and Schellman, 1987] Becktel, W. J. and Schellman, J. A. (1987). Protein Stability Curves. *Biopolymers*, 26(11):1859–1877.
- [Beernink and Tolan, 1996] Beernink, P. T. and Tolan, D. R. (1996). Disruption of the aldolase A tetramer into catalytically active monomers. *Proc. Natl. Acad. Sci. USA*, 93(11):5374–5379.
- [Belloni, 2000] Belloni, L. (2000). Colloidal interactions. *J. Phys.: Condens. Matter*, 12(46):R549–R587.
- [Benedek, 1997] Benedek, G. B. (1997). Cataract as a protein condensation disease: The Proctor lecture. *Investig. Ophthalmol. Vis. Sci.*, 38(10):1911–1921.
- [Bennion and Daggett, 2004] Bennion, B. J. and Daggett, V. (2004). Counteraction of urea-induced protein denaturation by trimethylamine N-oxide : A chemical chaperone at atomic resolution. *Proc. Natl. Acad. Sci. USA*, 101(17):6433–6438.
- [Berland et al., 1992] Berland, C. R., Thurston, G. M., Kondo, M., Broide, M. L., Pande, J., Ogun, O., and Benedek, G. B. (1992). Solid-liquid phase boundaries of lens protein solutions. *Proc. Natl. Acad. Sci. USA*, 89(4):1214–1218.
- [Bhat and Timasheff, 1992] Bhat, R. and Timasheff, S. N. (1992). Steric exclusion is the principal source of the preferential hydration of proteins in the presence of polyethylene glycols. *Protein Sci.*, 1(9):1133–1143.
- [Biben and Hansen, 1997] Biben, T. and Hansen, J. P. (1997). Osmotic depletion, non-additivity and phase separation. *Physica A*, 235(1-2):142–148.



- [Bloustine et al., 2006] Bloustine, J., Virmani, T., Thurston, G. M., and Fraden, S. (2006). Light Scattering and Phase Behavior of Lysozyme-PEG Mixtures. *Phys. Rev. Lett.*, 96(8):087803.
- [Bohrer et al., 1984] Bohrer, M. P., Patterson, G. D., and Carroll, P. J. (1984). Hindered Diffusion of Dextran and Ficoll in Microporous Membranes. *Macromolecules*, 17(6):1170–1173.
- [Bolen and Baskakov, 2001] Bolen, D. W. and Baskakov, I. V. (2001). The Osmophobic Effect: Natural Selection of a Thermodynamic Force in Protein Folding. *J. Mol. Biol.*, 310(5):955–963.
- [Bolen and Rose, 2008] Bolen, D. W. and Rose, G. D. (2008). Structure and Energetics of the Hydrogen-Bonded Backbone of Protein Folding. *Annu. Rev. Biochem.*, 77(10):339–362.
- [Bončina et al., 2008] Bončina, M., Reščič, J., and Vlachy, V. (2008). Solubility of Lysozyme in Polyethylene Glycol-Electrolyte Mixtures: The Depletion Interaction and Ion-Specific Effects. *Biophys. J.*, 95(3):1285–1294.
- [Bonneté et al., 1999] Bonneté, F., Finet, S., and Tardieu, A. (1999). Second virial coefficient: variations with lysozyme crystallization conditions. *J. Cryst. Growth*, 196(2-4):403–414.
- [Bonneté and Vivarès, 2002] Bonneté, F. and Vivarès, D. (2002). Interest of the normalized second virial coefficient and interaction potentials for crystallizing large macromolecules. *Acta Cryst. D*, 58(10 I):1571–1575.
- [Boonyaratanakornkit et al., 2002] Boonyaratanakornkit, B. B., Park, C. B., and Clark, D. S. (2002). Pressure effects on intra- and intermolecular interactions within proteins. *Biochim. Biophys. Acta*, 1595(1-2):235–249.
- [Boström et al., 2006] Boström, M., Deniz, V., Franks, G. V., and Ninham, B. W. (2006). Extended DLVO theory: Electrostatic and non-electrostatic forces in oxide suspensions. *Adv. Colloid Interface Sci.*, 123-126:5–15.
- [Boström et al., 2001] Boström, M., Williams, D. R., and Ninham, B. W. (2001). Specific ion effects: Why DLVO theory fails for biology and colloid systems. *Phys. Rev. Lett.*, 87(16):168103.
- [Bowlus and Somero, 1979] Bowlus, R. D. and Somero, G. N. (1979). Solute Compatibility with Enzyme Function and Structure: Rationales for the Selection of Osmotic Agents and End-products of Anaerobic Metabolism in Marine Invertebrates. *J. Exp. Zool.*, 208:137–152.
- [Brändén et al., 1973] Brändén, C. I., Eklund, H., Nordström, B., Boiwe, T., Söderlund, G., Zeppezauer, E., Ohlsson, I., and Akeson, A. (1973). Structure of liver alcohol dehydrogenase at 2.9-Angstrom resolution. *Proc. Natl. Acad. Sci. USA*, 70(8):2439–2442.
- [Brändén et al., 1975] Brändén, C.-I., Jörnvall, H., Eklund, H., and Furugren, B. (1975). Alcohol dehydrogenases. In *The Enzymes Vol. 11*, chapter 3, pages 103 – 190. Academic Press, New York, 3 edition.
- [Brangwynne et al., 2015] Brangwynne, C. P., Tompa, P., and Pappu, R. V. (2015). Polymer physics of intracellular phase transitions. *Nat. Phys.*, 11(11):899–904.
- [Broccio et al., 2006] Broccio, M., Costa, D., Liu, Y., and Chen, S. H. (2006). The structural properties of a two-Yukawa fluid: Simulation and analytical results. *J. Chem. Phys.*, 124(8):084501.
- [Broide et al., 1996] Broide, M. L., Tominc, T. M., and Saxowsky, M. D. (1996). Using phase transitions to investigate the effect of salts on protein interactions. *Phys. Rev. E*, 53(6):6325–6335.
- [Brooks et al., 2010] Brooks, N. J., Gauthe, B. L. L. E., Terrill, N. J., Rogers, S. E., Templer, R. H., Ces, O., and Seddon, J. M. (2010). Automated high pressure cell for pressure jump x-ray diffraction. *Rev. Sci. Instrum.*, 81(6):064103.

- [Buffet et al., 2012] Buffet, A., Rothkirch, A., Döhrmann, R., Körstgens, V., Abul Kashem, M. M., Perlich, J., Herzog, G., Schwartzkopf, M., Gehrke, R., Müller-Buschbaum, P., and Roth, S. V. (2012). P03, the microfocus and nanofocus X-ray scattering (MiNaXS) beamline of the PETRA III storage ring: The microfocus endstation. *J. Synchrotron Radiat.*, 19(4):647–653.
- [Burg et al., 2007] Burg, M. B., Ferraris, J. D., and Dmitrieva, N. I. (2007). Cellular Response to Hyperosmotic Stresses. *Physiol. Rev.*, 87(4):1441–1474.
- [Burg et al., 1996] Burg, M. B., Kwon, E. D., and Peters, E. M. (1996). Glycerophosphocholine and betaine counteract the effect of urea on pyruvate kinase. *Kidney Int Suppl.*, 57:S100–S104.
- [Burg and Peters, 1998] Burg, M. B. and Peters, E. M. (1998). Effects of glycine betaine and glycerophosphocholine on thermal stability of ribonuclease. *Am. J. Physiol.*, 274(4 II):F762–F765.
- [Cacace et al., 1997] Cacace, M. G., Landa, E. M., and Ramsden, J. J. (1997). The Hofmeister series : salt and solvent effects on interfacial phenomena. *Q. Rev. Biophys.*, 30(3):241–277.
- [Canchi and García, 2013] Canchi, D. R. and García, A. E. (2013). Cosolvent Effects on Protein Stability. *Annu. Rev. Phys. Chem.*, 64:273–293.
- [Canchi et al., 2012] Canchi, D. R., Jayasimha, P., Rau, D. C., Makhatadze, G., and Garcia, A. E. (2012). Molecular Mechanism for the Preferential Exclusion of TMAO from Protein Surfaces. *J. Phys. Chem. B*, 116(40):12095–12104.
- [Cardinaux et al., 2007] Cardinaux, F., Stradner, A., Schurtenberger, P., Sciortino, F., and Zaccarelli, E. (2007). Modeling equilibrium clusters in lysozyme solutions. *EPL*, 77(4):48004.
- [Carr et al., 2014] Carr, W. E. S., Netherton, J. C., Gleeson, R. A., and Charles, D. D. (2014). Stimulants of Feeding Behavior in Fish: Analyses of Tissues of Diverse Marine Organisms. *Biol. Bull.*, 190(2):149–160.
- [Chalikian, 2001] Chalikian, T. V. (2001). Structural thermodynamics of hydration. *J. Phys. Chem. B*, 105(50):12566–12578.
- [Chalikian, 2003] Chalikian, T. V. (2003). Volumetric Properties of Proteins. *Annu. Rev. Biophys. Biomol. Struct.*, 32(1):207–235.
- [Chan and Dill, 1998] Chan, H. S. and Dill, K. A. (1998). Protein folding in the landscape perspective: Chevron plots and non-Arrhenius kinetics. *Proteins*, 30(1):2–33.
- [Chandler and Andersen, 1972] Chandler, D. and Andersen, H. C. (1972). Optimized cluster expansions for classical fluids. II. Theory of molecular liquids. *J. Chem. Phys.*, 57(5):1930–1937.
- [Chatterjee and Schweizer, 1998a] Chatterjee, A. P. and Schweizer, K. S. (1998a). Liquid-State Theory of Semidilute and Concentrated Polymer Solutions. *Macromolecules*, 31(7):2353–2367.
- [Chatterjee and Schweizer, 1998b] Chatterjee, A. P. and Schweizer, K. S. (1998b). Microscopic theory of polymer-mediated interactions between spherical particles. *J. Chem. Phys.*, 109(23):10464–10476.
- [Chatterjee and Schweizer, 1999] Chatterjee, A. P. and Schweizer, K. S. (1999). Influence of Solvent Quality and Thermal Fluctuations on Polymer-Mediated Depletion Interactions. *Macromolecules*, 32(3):923–934.
- [Chen et al., 2011] Chen, C., Loe, F., Blocki, A., Peng, Y., and Raghunath, M. (2011). Applying macromolecular crowding to enhance extracellular matrix deposition and its remodeling in vitro for tissue engineering and cell-based therapies. *Adv. Drug Deliv. Rev.*, 63(4):277–290.
- [Chen and Makhatadze, 2017] Chen, C. R. and Makhatadze, G. I. (2017). Molecular determinant of the effects of hydrostatic pressure on protein folding stability. *Nat. Commun.*, 8(14561):1–9.

- [Chen et al., 2007] Chen, S. H., Broccio, M., Liu, Y., Fratini, E., and Baglioni, P. (2007). The two-Yukawa model and its applications: The cases of charged proteins and copolymer micellar solutions. *J. Appl. Cryst.*, 40(s1):s321–s326.
- [Cheung et al., 2005] Cheung, M. S., Klimov, D., and Thirumalai, D. (2005). Molecular crowding enhances native state stability and refolding rates of globular proteins. *Proc. Natl. Acad. Sci. USA*, 102(13):4753–4758.
- [Cinar et al., 2018] Cinar, H., Cinar, S., Chan, H. S., and Winter, R. (2018). Pressure-Induced Dissolution and Reentrant Formation of Condensed, Liquid–Liquid Phase-Separated Elastomeric  $\alpha$ -Elastin. *Chem. Eur. J.*, 24(33):8286–8291.
- [Cioni and Strambini, 1994] Cioni, P. and Strambini, G. (1994). Pressure Effects on Protein Flexibility Monomeric Proteins. *J. Mol. Biol.*, 242(3):291–301.
- [Cioni and Strambini, 1996] Cioni, P. and Strambini, G. B. (1996). Pressure effects on the structure of oligomeric proteins prior to subunit dissociation. *J. Mol. Biol.*, 263(5):789–799.
- [Cioni and Strambini, 2002] Cioni, P. and Strambini, G. B. (2002). Tryptophan phosphorescence and pressure effects on protein structure. *Biochim. Biophys. Acta*, 1595(1-2):116–130.
- [Clark and Zounes, 1977] Clark, M. E. and Zounes, M. (1977). The effects of selected cell osmolytes on the activity of lactate dehydrogenase from the euryhaline polychaete, *neris succinea*. *Biol. Bull.*, 153(3):468–484.
- [Clark, 1979] Clark, N. (1979). Thermodynamics of the re-entrant nematic-bilayer smectic a transition. *J. Phys. Colloq.*, 40(C3):345–349.
- [Cohen et al., 2009] Cohen, J. A., Podgornik, R., Hansen, P. L., and Parsegian, V. A. (2009). A phenomenological one-parameter equation of state for osmotic pressures of PEG and other neutral flexible polymers in good solvents. *J. Phys. Chem. B*, 113(12):3709–3714.
- [Cohn and Edsall, 1965] Cohn, E. J. and Edsall, J. T. (1965). *Proteins, amino acids and peptides*. Hafner, New York.
- [Cole and Ralston, 2006] Cole, N. and Ralston, G. B. (2006). Enhancement of self-association of human spectrin by polyethylene glycol. *Int. J. Biochem.*, 26(6):799–804.
- [Collins, 2006] Collins, K. D. (2006). Ion hydration: Implications for cellular function, polyelectrolytes, and protein crystallization. *Biophys. Chem.*, 119(3):271–281.
- [Collins et al., 2007] Collins, K. D., Neilson, G. W., and Enderby, J. E. (2007). Ions in water: Characterizing the forces that control chemical processes and biological structure. *Biophys. Chem.*, 128(2-3):95–104.
- [Collins and Washabaugh, 1985] Collins, K. D. and Washabaugh, M. W. (1985). The Hofmeister effect and the behaviour of water at interfaces. *Q. Rev. Biophys.*, 18(4):323–422.
- [Collins et al., 2005] Collins, M. D., Hummer, G., Quillin, M. L., Matthews, B. W., and Gruner, S. M. (2005). Cooperative water filling of a nonpolar protein cavity observed by high-pressure crystallography and simulation. *Proc. Natl. Acad. Sci. USA*, 103(12):16668–16671.
- [Creighton, 1992] Creighton, T. (1992). *Proteins: Structures and Molecular Properties*. W. H. Freeman, New York, 2nd edition.
- [Crick, 1957] Crick, F. H. C. (1957). X-Ray Diffraction of Protein Crystals. *Methods in Enzymology*, 4:127–146.
- [Crisman and Randolph, 2009] Crisman, R. L. and Randolph, T. W. (2009). Refolding of proteins from inclusion bodies is favored by a diminished hydrophobic effect at elevated pressures. *Biotechnol. Bioeng.*, 102(2):483–492.

- [Crisman and Randolph, 2010] Crisman, R. L. and Randolph, T. W. (2010). Crystallization of recombinant human growth hormone at elevated pressures: Pressure effects on PEG-induced volume exclusion interactions. *Biotechnol. Bioeng.*, 107(4):663–672.
- [Crowley et al., 2008] Crowley, P. B., Brett, K., and Muldoon, J. (2008). NMR spectroscopy reveals cytochrome c-poly(ethylene glycol) interactions. *Chem. Bio. Chem.*, 9(5):685–688.
- [Curtis et al., 1998] Curtis, R., Prausnitz, J., and Blanch, H. (1998). Protein-Protein and Protein-Salt Interactions in Aqueous Protein Solutions Containing Concentrated Electrolytes. *Biotechnol. Bioeng.*, 57(1):11–21.
- [Curtis et al., 2002] Curtis, R. A., Ulrich, J., Montaser, A., Prausnitz, J. M., and Blanch, H. W. (2002). Protein-protein interactions in concentrated electrolyte solutions: Hofmeister-series effects. *Biotechnol. B*, 79(4):367–380.
- [Cushman, 2001] Cushman, J. C. (2001). Osmoregulation in Plants : Implications for Agriculture. *Amer. Zool.*, 41(4):758–769.
- [D’Aguanno and Klein, 1991] D’Aguanno, B. and Klein, R. (1991). Structural Effects of Polydispersity in Charged Colloidal Dispersions. *J. Chem. Soc. Faraday Trans.*, 87(3):379–390.
- [Dallet and Legoy, 1996] Dallet, S. and Legoy, M. D. (1996). Hydrostatic pressure induces conformational and catalytic changes on two alcohol dehydrogenases but no oligomeric dissociation. *Biochim. Biophys. Acta*, 1294(1):15–24.
- [Dalziel and Dickinson, 1966] Dalziel, K. and Dickinson, F. (1966). The Kinetics and Mechanism of Liver Alcohol Dehydrogenase with Primary and Secondary Alcohols as Substrates. *Biochem. J.*, 100(1):34–46.
- [Daniel et al., 2006] Daniel, I., Oger, P., and Winter, R. (2006). Origins of life and biochemistry under high-pressure conditions. *Chem. Soc. Rev.*, 35(10):858–875.
- [de Gennes, 1979a] de Gennes, P. G. (1979a). Colloid suspensions in a polymer solution. *C. R. Seances Acad. Sci., Ser. B*, 288(21):359–361.
- [de Gennes, 1979b] de Gennes, P. G. (1979b). *Scaling Concepts in Polymer Physics*. Cornell University Press, New York, 1 edition.
- [De Smidt et al., 2008] De Smidt, O., Du Preez, J. C., and Albertyn, J. (2008). The alcohol dehydrogenases of *Saccharomyces cerevisiae*: A comprehensive review. *FEMS Yeast Res.*, 8(7):967–978.
- [Debenedetti, 2003] Debenedetti, P. G. (2003). Supercooled and glassy water. *J. Phys. Condens. Matter*, 15(45):R1669–R1726.
- [Debye, 1915] Debye, P. (1915). Zerstreung von Röntgenstrahlen. *Ann. Phys.*, 46:809.
- [Debye, 1947] Debye, P. (1947). Molecular-weight determination by light scattering. *J. Phys. Coll. Chem.*, 51(1):18–32.
- [Debye and Bueche, 1949] Debye, P. and Bueche, A. M. (1949). Scattering by an inhomogeneous solid. *J. Appl. Phys.*, 20(6):518–525.
- [Deen et al., 1981] Deen, W. M., Bohrer, M. P., and Epstein, N. B. (1981). Effects of molecular size and configuration on diffusion in microporous membranes. *AIChE Journal*, 27(6):952–959.
- [Derjaguin and Landau, 1993] Derjaguin, B. and Landau, L. (1993). Theory of the stability of strongly lyophobic sols and of the adhesion of strongly charged particles in solution of electrolytes. *Prog. Surf. Sci.*, 43(1):30–59.
- [Devanand and Selser, 1991] Devanand, K. and Selser, J. C. (1991). Asymptotic Behavior and Long-Range Interactions in Aqueous Solutions of Poly(ethylene oxide). *Macromolecules*, 24(22):5943–5947.

- [Dhabal et al., 2014] Dhabal, D., Singh, M., Wikfeldt, K. T., and Chakravarty, C. (2014). Triplet correlation functions in liquid water. *J. Chem. Phys.*, 141(17):174504.
- [Dhabal et al., 2017] Dhabal, D., Wikfeldt, K. T., Skinner, L. B., Chakravarty, C., and Kashyap, H. K. (2017). Probing the triplet correlation function in liquid water by experiments and molecular simulations. *Phys. Chem. Chem. Phys.*, 19(4):3265–3278.
- [Dhar et al., 2010] Dhar, A., Samiotakis, A., Ebbinghaus, S., Nienhaus, L., Homouz, D., Gruebele, M., and Cheung, M. S. (2010). Structure, function, and folding of phosphoglycerate kinase are strongly perturbed by macromolecular crowding. *Proc. Natl. Acad. Sci. USA*, 107(41):17586–17591.
- [Distèche, 1972] Distèche, A. (1972). Effects of pressure on the dissociation of weak acids. *Symp. Soc. Exp. Biol.*, 26:27–60.
- [Dobson et al., 1998] Dobson, C. M., Sali, A., and Karplus, M. (1998). Proteinfaltung aus theoretischer und experimenteller Sicht. *Angew. Chem.*, 110(7):908–935.
- [Dong et al., 2007] Dong, Y., Yang, Q., Jia, S., and Qiao, C. (2007). Effects of high pressure on the accumulation of trehalose and glutathione in the *Saccharomyces cerevisiae* cells. *Biochem. Eng. J.*, 37(2):226–230.
- [Drickamer and Frank, 1973] Drickamer, H. and Frank, C. (1973). *Electronic Transition and the High Pressure Chemistry and Physics of Solids*. Chapman and Hall, London.
- [Du et al., 2006] Du, F., Zhou, Z., Mo, Z. Y., Shi, J. Z., Chen, J., and Liang, Y. (2006). Mixed Macromolecular Crowding Accelerates the Refolding of Rabbit Muscle Creatine Kinase: Implications for Protein Folding in Physiological Environments. *J. Mol. Biol.*, 364(3):469–482.
- [Ducruix et al., 1996] Ducruix, A., Guilloteau, J. P., Riès-Kautt, M., and Tardieu, A. (1996). Protein interactions as seen by solution X-ray scattering prior to crystallogenesis. *J. Cryst. Growth*, 168(1-4):28–39.
- [Duman et al., 1991] Duman, J. G., Wu, D. W., Xu, L., Tursman, D., and Olsen, T. M. (1991). Adaptions of Insects to Subzero Temperatures. *Q. Rev. Biol.*, 66(4):387–410.
- [Dumetz, 2007] Dumetz, A. C. (2007). *Protein Interactions and Phase Behavior in Aqueous Solutions: Effects of Salt, Polymer, and Organic Additives*. PhD thesis, University of Delaware.
- [Dumetz et al., 2008] Dumetz, A. C., Chockla, A. M., Kaler, E. W., and Lenhoff, A. M. (2008). Protein phase behavior in aqueous solutions: crystallization, liquid-liquid phase separation, gels, and aggregates. *Biophys. J.*, 94(2):570–583.
- [Durbin and Feher, 1996] Durbin, S. D. and Feher, G. (1996). Protein Crystallization. *Annu. Rev. Phys. Chem.*, 47:171–204.
- [Dwyer et al., 2000] Dwyer, J. J., Gittis, A. G., Karp, D. A., Lattman, E. E., Spencer, D. S., Stites, W. E., and García-Moreno E., B. (2000). High Apparent Dielectric Constants in the Interior of a Protein Reflect Water Penetration. *Biophys. J.*, 79(3):1610–1620.
- [Dzyaloshinskii et al., 1961] Dzyaloshinskii, I. E., Lifshitz, E. M., and Pitaevskii, L. P. (1961). The general theory of van der Waals forces. *Adv. Phys.*, 10(38):165–209.
- [Edsall and McKenzie, 1983] Edsall, J. T. and McKenzie, H. a. (1983). Water and proteins. II. The location and dynamics of water in protein systems and its relation to their stability and properties. *Adv. Biophys.*, 16:53–183.
- [Edsall and Wyman, 1964] Edsall, J. T. and Wyman, J. (1964). Studies in the Physical Chemistry of Betaines and Related Substances . I . Studies of Dielectric Constants and Apparent Molal Volume. *J. Am. Chem. Soc.*, 57(10):1964–1975.



- [Egelstaff, 1973] Egelstaff, P. (1973). The structure simple liquids. *Annu. Rev. Phys. Chem.*, 24:159–187.
- [Egelstaff et al., 1969] Egelstaff, P., Page, D., and Heard, C. (1969). Experimental study of the triplet correlation function for simple liquids. *Phys. Lett. A*, 30(7):376–377.
- [Egelstaff, 1994] Egelstaff, P. A. (1994). *An introduction to the liquid state*. Clarendon Press, Oxford, 2nd edition.
- [Egelstaff et al., 1971] Egelstaff, P. A., Page, D. I., and Heard, C. R. T. (1971). Experimental study of the triplet correlation function for simple liquids. *J. Phys. C: Solid St. Phys.*, 4:1453–1465.
- [Eisenberg, 1976] Eisenberg, H. (1976). *Biological Macromolecules and Polyelectrolytes in solution*. Clarendon Press, Oxford.
- [Eklund and Brändén, 1987] Eklund, H. and Brändén, C. (1987). Alcohol Dehydrogenase. In Jurnak, F. and McPherson, A., editors, *Biological Macromolecules and Assemblies*. Wiley, New York.
- [Eklund et al., 1974] Eklund, H., Nordström, B., Zeppezauer, E., Söderlund, G., Ohlsson, I., Boiwe, T., and Brändén, C. I. (1974). The structure of horse liver alcohol dehydrogenase. *FEBS Lett.*, 44(2):200–204.
- [Eklund et al., 1976] Eklund, H., Nordström, B., Zeppezauer, E., Söderlund, G., Ohlsson, I., Boiwe, T., Söderberg, B. O., Tapia, O., Brändén, C. I., and Åkeson, Å. (1976). Three-dimensional structure of horse liver alcohol dehydrogenase at 2.4 Å resolution. *J. Mol. Biol.*, 102(1):27–59.
- [Eklund and Ramaswamy, 2008] Eklund, H. and Ramaswamy, S. (2008). Medium- and short-chain dehydrogenase/reductase gene and protein families : Three-dimensional structures of MDR alcohol dehydrogenases. *Cell. Mol. Life Sci.*, 65(24):3907–3917.
- [Eklund et al., 1981] Eklund, H., Samama, J. P., Wallén, L., Brändén, C. I., Åkeson, Å., and Jones, T. A. (1981). Structure of a triclinic ternary complex of horse liver alcohol dehydrogenase at 2.9 Å resolution. *J. Mol. Biol.*, 146(4):561–587.
- [Ellis, 1996] Ellis, R. (1996). *Deep Atlantic: Life, Death, and Exploration in the Abyss*. Lyons Press, New York.
- [Ellis and Minton, 2003] Ellis, R. and Minton, A. (2003). Join the Crowd. *Nature*, 425(4):27–28.
- [Ellis, 2001] Ellis, R. J. (2001). Macromolecular crowding: Obvious but underappreciated. *Trends Biochem. Sci.*, 26(10):597–604.
- [Ellis, 2007] Ellis, R. J. (2007). Protein misassembly: macromolecular crowding and molecular chaperones. In Csermely, P. and Vigh, L., editors, *Molecular Aspects of the Stress Response: Chaperones, Membranes and Networks*, pages 1–13. Springer New York, New York.
- [Erlkamp, 2014] Erlkamp, M. (2014). *Strukturbestimmung ausgewählter Protein- und Lipidsysteme mit nicht-typischem Aggregations- und Phasenverhalten*. PhD thesis, TU Dortmund.
- [Erlkamp et al., 2014] Erlkamp, M., Grobelny, S., and Winter, R. (2014). Crowding effects on the temperature and pressure dependent structure, stability and folding kinetics of Staphylococcal Nuclease. *Phys. Chem. Chem. Phys.*, 16(13):5965–5976.
- [Erlkamp et al., 2015] Erlkamp, M., Marion, J., Martinez, N., Czeslik, C., Peters, J., and Winter, R. (2015). Influence of Pressure and Crowding on the Sub-Nanosecond Dynamics of Globular Proteins. *J. Phys. Chem. B*, 119(14):4842–4848.
- [Everett, 1988] Everett, D. (1988). *Basic Principles of Colloid Science*. Royal Society of Chemistry, London.

- [Farnum and Zukoski, 1999] Farnum, M. and Zukoski, C. (1999). Effect of Glycerol on the Interactions and Solubility of Bovine Pancreatic Trypsin Inhibitor. *Biophys. J.*, 76(5):2716–2726.
- [Fedorov et al., 2011] Fedorov, M. V., Goodman, J. M., Nerukh, D., and Schumm, S. (2011). Self-assembly of trehalose molecules on a lysozyme surface: the broken glass hypothesis. *Phys. Chem. Chem. Phys.*, 13(6):2294–2299.
- [Feigin and Svergun, 1987] Feigin, L. A. and Svergun, D. I. (1987). *Structure Analysis by Small-Angle X-Ray and Neutron Scattering*. Press, Plenum, New York.
- [Feigin and Napper, 1980] Feigin, R. I. and Napper, D. H. (1980). Depletion stabilization and depletion flocculation. *J. Colloid Interface Sci.*, 75(2):525–541.
- [Fersht, 1999] Fersht, A. (1999). *Structure and mechanism in protein science*. W.H. Freeman, New York.
- [Finet and Tardieu, 2001] Finet, S. and Tardieu, A. (2001).  $\alpha$ -crystallin interaction forces studied by small angle X-ray scattering and numerical simulations. *J. Cryst. Growth*, 232(1):40–49.
- [Fink, 2005] Fink, A. L. (2005). Natively unfolded proteins. *Curr. Opin. Struc. Biol.*, 15(1):35–41.
- [Fischetti et al., 2003] Fischetti, R. F., Rodi, D. J., Mirza, A., Irving, T. C., Kondrashkina, E., and Makowski, L. (2003). High-resolution wide-angle X-ray scattering of protein solutions: Effect of beam dose on protein integrity. *J. Synchrotron Radiat.*, 10(5):398–404.
- [Fissell et al., 2010] Fissell, W. H., Hofmann, C. L., Smith, R., and Chen, M. H. (2010). Size and conformation of Ficoll as determined by size-exclusion chromatography followed by multiangle light scattering. *Am. J. Physiol.-Renal Physiol.*, 298(1):F205–F208.
- [Fissell et al., 2007] Fissell, W. H., Manley, S., Dubnisheva, A., Glass, J., Magistrelli, J., Eldridge, A. N., Fleischman, A. J., Zydney, A. L., and Roy, S. (2007). Ficoll is not a rigid sphere. *Am. J. Physiol.-Renal Physiol.*, 293(4):F1209–F1213.
- [Floriano and Nascimento, 2004] Floriano, W. B. and Nascimento, M. A. C. (2004). Dielectric Constant and Density of Water as a Function of Pressure at Constant Temperature. *Braz. J. Phys.*, 34(1):38–41.
- [Foffi et al., 2002] Foffi, G., McCullagh, G. D., Lawlor, A., Zaccarelli, E., Dawson, K. A., Sciortino, F., Tartaglia, P., Pini, D., and Stell, G. (2002). Phase equilibria and glass transition in colloidal systems with short-ranged attractive interactions: Application to protein crystallization. *Phys. Rev. E*, 65(3):031407.
- [Forster and Goldstein, 1976] Forster, R. P. and Goldstein, L. (1976). Intracellular osmoregulatory role of amino acids and urea in marine elasmobranchs. *Am. J. Physiol.*, 230(4):925–931.
- [Franke et al., 2017] Franke, D., Petoukhov, M. V., Konarev, P. V., Panjkovich, A., Tuukkanen, A., Mertens, H. D. T., Kikhney, A. G., Hajizadeh, N. R., Franklin, J. M., Jeffries, C. M., and Svergun, D. I. (2017). ATSAS 2.8: A comprehensive data analysis suite for small-angle scattering from macromolecular solutions. *J. Appl. Crystallogr.*, 50(4):1212–1225.
- [Franks et al., 1973] Franks, F., Reid, D. S., and Suggett, A. (1973). Conformation and Hydration of Sugars and Related Compounds in Dilute Aqueous Solution. *J. Solution Chem.*, 2(2-3):99–118.
- [Fredericks et al., 1994] Fredericks, W. J., Hammonds, M. C., Howard, S. B., and Rosenberger, F. (1994). Density, thermal expansivity, viscosity and refractive index of lysozyme solutions at crystal growth concentrations. *J. Cryst. Growth*, 141(1-2):183–192.
- [Frye and Royer, 1998] Frye, K. J. and Royer, C. A. (1998). Probing the contribution of internal cavities to the volume change of protein unfolding under pressure. *Protein Sci.*, 7(10):2217–2222.
- [Fuchs and Schweizer, 2001] Fuchs, M. and Schweizer, K. S. (2001). Macromolecular theory of solvation and structure in mixtures of colloids and polymers. *Phys. Rev. E*, 64(2):021514.

- [Fujii et al., 1996] Fujii, S., Obuchi, K., Iwahashi, H., Fujii, T., and Komatsu, Y. (1996). Saccharides protect yeast against pressure correlated to the mean number of equatorial OH groups. *Biotechnol. Prog.*, 13:245–252.
- [Fulton, 1982] Fulton, A. (1982). How Crowded Is the Cytoplasm? *Cell*, 30(2):345–347.
- [Galamba, 2013] Galamba, N. (2013). On the effects of temperature, pressure, and dissolved salts on the hydrogen-bond network of water. *J. Phys. Chem. B*, 117(2):589–601.
- [Galán et al., 2001] Galán, A., Sot, B., Llorcai, O., Carrascosai, J. L., Valpuestai, J. M., and Muga, A. (2001). Excluded volume effects on the refolding and assembly of an oligomeric protein. *J. Biol. Chem.*, 276(2):957–964.
- [Galkin and Vekilov, 2000] Galkin, O. and Vekilov, P. G. (2000). Control of protein crystal nucleation around the metastable liquid-liquid phase boundary. *Proc. Natl. Acad. Sci. USA*, 97(12):6277–6281.
- [Galletti et al., 2010a] Galletti, P., Emer, E., Gucciardo, G., Quintavalla, A., Pori, M., and Giacomini, D. (2010a). Chemoenzymatic synthesis of (2S)-2-arylpropanols through a dynamic kinetic resolution of 2-arylpropanals with alcohol dehydrogenases. *Org. Biomol. Chem.*, 8(18):4117.
- [Galletti et al., 2010b] Galletti, P., Pori, M., and Giacomini, D. (2010b). One-Step Oxidation of 2-Arylpropanols to 2-Arylpropionic Acids: Improving Sustainability in the Synthesis of Profens. *Synlett*, 17:2644–2648.
- [Ganguly et al., 2015] Ganguly, P., Hajari, T., Shea, J. E., and van Der Vegt, N. F. (2015). Mutual exclusion of urea and trimethylamine N-oxide from amino acids in mixed solvent environment. *J. Phys. Chem. Lett.*, 6(4):581–585.
- [Gao et al., 2017a] Gao, M., Arns, L., and Winter, R. (2017a). Modulation of the Thermodynamic Signatures of an RNA Thermometer by Osmolytes and Salts. *Angew. Chem. Int. Ed.*, 56(9):2302–2306.
- [Gao et al., 2016] Gao, M., Gnutt, D., Orban, A., Appel, B., Righetti, F., Winter, R., Narberhaus, F., Müller, S., and Ebbinghaus, S. (2016). RNA Hairpin Folding in the Crowded Cell. *Angew. Chem. Int. Ed.*, 55(9):3224–3228.
- [Gao et al., 2017b] Gao, M., Held, C., Patra, S., Arns, L., Sadowski, G., and Winter, R. (2017b). Crowders and Cosolvents—Major Contributors to the Cellular Milieu and Efficient Means to Counteract Environmental Stresses. *Chem. Phys. Chem*, 18(21):2951–2972.
- [Gekko and Timasheff, 1981a] Gekko, K. and Timasheff, S. N. (1981a). Mechanism of Protein Stabilization by Glycerol : Preferential Hydration in Glycerol-Water Mixtures. *Biochemistry*, 20(16):4667–4676.
- [Gekko and Timasheff, 1981b] Gekko, K. and Timasheff, S. N. (1981b). Mechanism of protein stabilization by glycerol: preferential hydration in glycerol-water mixtures. *Biochemistry*, 20(16):4667–4676.
- [Georgalis et al., 2012] Georgalis, Y., Philipp, M., Aleksandrova, R., and Krüger, J. K. (2012). Light scattering studies on Ficoll PM70 solutions reveal two distinct diffusive modes. *J. Colloid Interface Sci.*, 386(1):141–147.
- [George and Wilson, 1994] George, A. and Wilson, W. W. (1994). Predicting protein crystallization from a dilute solution property. *Acta Cryst. D*, 50:361–365.
- [Gheorghe et al., 2016] Gheorghe, I., Stoicescu, C., and Sirbu, F. (2016). Partial molar volumes, isentropic compressibilities, and partial molar expansibilities of N-Methylglycine and D-Glucose in aqueous environments at temperatures between (298.15 and 323.15)K. *J. Mol. Liq.*, 218(C):515–524.

- [Giacomini et al., 2007] Giacomini, D., Galletti, P., Quintavalla, A., Gucciardo, G., and Paradisi, F. (2007). Highly efficient asymmetric reduction of arylpropionic aldehydes by Horse Liver Alcohol Dehydrogenase through dynamic kinetic resolution. *Chem. Commun.*, 0(39):4038–4040.
- [Gibaud et al., 2012] Gibaud, T., Mahmoudi, N., Oberdisse, J., Lindner, P., Pedersen, J. S., Oliveira, C. L., Stradner, A., and Schurtenberger, P. (2012). New routes to food gels and glasses. *Faraday Discuss.*, 158:267–284.
- [Gibaud and Schurtenberger, 2009] Gibaud, T. and Schurtenberger, P. (2009). A closer look at arrested spinodal decomposition in protein solutions. *J. Phys.: Condens. Matter*, 21(32):322201.
- [Glatter, 2002] Glatter, O. (2002). The Inverse Scattering Problem in Small-Angle Scattering. In Lindner, P. and Zemb, T., editors, *Neutrons, X-rays and Light: Scattering Methods Applied to Soft Condensed Matter*, chapter 4, pages 73–102. Elsevier Science B.V, Amsterdam, 1st edition.
- [Glatter and Kratky, 1982] Glatter, O. and Kratky, O., editors (1982). *Small Angle X-ray Scattering*. Academic Press, London.
- [Gögelein et al., 2012] Gögelein, C., Wagner, D., Cardinaux, F., Nägele, G., and Egelhaaf, S. U. (2012). Effect of glycerol and dimethyl sulfoxide on the phase behavior of lysozyme: Theory and experiments. *J. Chem. Phys.*, 136(1):1–32.
- [Goodisman and Brumberger, 1973] Goodisman, J. and Brumberger, H. (1973). Über die Zulässigkeit der Subtraktion der Lösungsmittelstreuung von der Streuung der Lösungen bei Röntgenkleinwinkelstreuungsmessungen. *Monatsh. Chem.*, 104:598–606.
- [Groenning et al., 2015] Groenning, M., Campos, R. I., Hirschberg, D., Hammarström, P., and Vestergaard, B. (2015). Considerably Unfolded Transthyretin Monomers Precede and Exchange with Dynamically Structured Amyloid Protofibrils. *Sci. Rep.*, 5:11443.
- [Gross and Jaenicke, 1994] Gross, M. and Jaenicke, R. (1994). Proteins under pressure The influence of high hydrostatic pressure on structure , function and assembly of proteins and protein complexes. *Eur. J. Biochem.*, 221(2):617–630.
- [Groszek et al., 2010] Groszek, J., Li, L., Ferrell, N., Smith, R., Zorman, C. a., Hofmann, C. L., Roy, S., and Fissell, W. H. (2010). Molecular conformation and filtration properties of anionic Ficoll. *Am. J. Physiol.-Renal Physiol.*, 299(4):F752–F757.
- [Gtari et al., 2017] Gtari, W., Bey, H., Aschi, A., Bitri, L., and Othman, T. (2017). Impact of macromolecular crowding on structure and properties of pepsin and trypsin. *Mater. Sci. Eng. C*, 72:98–105.
- [Guinier, 1939] Guinier, A. (1939). La diffraction des rayons X aux très petits angles: Application à l'étude de phénomènes ultramicroscopiques. *Ann. Phys.*, 11(12):161–237.
- [Guinier and Fournet, 1955] Guinier, A. and Fournet, G. (1955). *Small-Angle Scattering of X-rays*. John Wiley & Sons, Inc., New York.
- [Guinn et al., 2011] Guinn, E. J., Pegram, L. M., Capp, M. W., Pollock, M. N., and Record, M. T. (2011). Quantifying why urea is a protein denaturant, whereas glycine betaine is a protein stabilizer. *Proc. Natl. Acad. Sci. USA*, 108(41):16932–16937.
- [Guinn et al., 2013] Guinn, E. J., Schweinfus, J. J., Cha, H. K., McDevitt, J. L., Merker, W. E., Ritzer, R., Muth, G. W., Engelskjerd, S. W., Mangold, K. E., Thompson, P. J., Kerins, M. J., and Record, M. T. (2013). Quantifying functional group interactions that determine urea effects on nucleic acid helix formation. *J. Am. Chem. Soc.*, 135(15):5828–5838.
- [Gurnev et al., 2017] Gurnev, P. A., Stanley, C. B., Aksoyoglu, M. A., Hong, K., Parsegian, V. A., and Bezrukov, S. M. (2017). Poly(ethylene glycol)s in Semidilute Regime: Radius of Gyration in the Bulk and Partitioning into a Nanopore. *Macromolecules*, 50(6):2477–2483.

- [Hagen and Frenkel, 1994] Hagen, M. H. and Frenkel, D. (1994). Determination of phase diagrams for the hard-core attractive Yukawa system. *J. Chem. Phys.*, 101(5):4093–4097.
- [Hammersley et al., 1996] Hammersley, A. P., Svensson, S. O., Hanfland, M., Fitch, A. N., and Häusermann, D. (1996). Two-dimensional detector software: From real detector to idealised image or two-theta scan. *High Pressure Res.*, 14(4-6):235–248.
- [Hand, 1934] Hand, D. B. (1934). Refractivity of Protein Solutions. *J. Biol. Chem.*, 108(3):703–708.
- [Hansen and McDonald, 2013] Hansen, J. P. and McDonald, I. R. (2013). *Theory of simple liquids*. Academic Press, Amsterdam, 4th edition.
- [Hanson et al., 1994] Hanson, A. D., Rathinasabapathi, B., Rivoal, J., Burnet, M., Dillon, M., and Gage, D. A. (1994). Osmoprotective compounds in the Plumbaginaceae : A natural experiment in metabolic engineering of stress tolerance. *Proc. Natl. Acad. Sci. USA*, 91(1):306–310.
- [Harada et al., 2012] Harada, R., Sugita, Y., and Feig, M. (2012). Protein crowding affects hydration structure and dynamics. *J. Am. Chem. Soc.*, 134(10):4842–4849.
- [Harata, 1994] Harata, K. (1994). X-ray structure of a monoclinic form of hen egg-white lysozyme crystallized at 313 K. Comparison of two independent molecules. *Acta Cryst. D*, 50(3):250–257.
- [Harris, 1992] Harris, J. (1992). *Poly(Ethylene Glycol) Chemistry: Biotechnical and Biomedical Applications*. Springer US, New York, 1 edition.
- [Harve et al., 2006] Harve, K. S., Raghunath, M., Lareu, R. R., and Rajagopalan, R. A. J. (2006). Macromolecular crowding in biological systems: Dynamic light scattering (DLS) to quantify the excluded volume effect (EVE). *Biophys. Rev. Lett.*, 1(3):317–325.
- [Hatters et al., 2002] Hatters, D. M., Minton, A. P., and Howlett, G. J. (2002). Macromolecular crowding accelerates amyloid formation by human apolipoprotein C-II. *J. Biol. Chem.*, 277(10):7824–7830.
- [Hausmann and Kremer, 1994] Hausmann, K. and Kremer, B., editors (1994). *Extremophile: Mikroorganismen in ausgefallenen Lebensräumen*. VHC, Weinheim, 2 edition.
- [Hawe et al., 2008] Hawe, A., Sutter, M., and Jiskoot, W. (2008). Extrinsic fluorescent dyes as tools for protein characterization. *Pharm. Res.*, 25(7):1487–1499.
- [Hawley, 1971] Hawley, S. A. (1971). Reversible Pressure-Temperature Denaturation of Chymotrypsinogen. *Biochemistry*, 10(13):2436–2442.
- [Henke et al., 1993] Henke, B., Gullikson, E., and Davis, J. (1993). X-ray interactions: Photoabsorption, scattering, transmission, and reflection at E=50-30000 eV, Z=1-92. *At. Data Nucl. Data Tables*, 54(2):181–342.
- [Heremans and Smeller, 1998] Heremans, K. and Smeller, L. (1998). Protein structure and dynamics at high pressure. *Biochim. Biophys. Acta*, 1386(2):353–370.
- [Heremans and Heremans, 1989] Heremans, L. U. C. and Heremans, K. (1989). Pressure Effects on the Raman Spectrum of Proteins: Stability of the Salt Bridge in Trypsin and Elastase. *J. Mol. Struct.*, 214(1-3):305–314.
- [Hochachka and Somero, 2002] Hochachka, P. W. and Somero, G. N. (2002). *Biochemical Adaptation: Mechanism and Process in Physiological Evolution*. Oxford University Press Inc.
- [Hofmeister, 1988] Hofmeister, F. (1988). Zur Lehre von der Wirkung der Salze. *Archiv für experimentelle Pathologie und Pharmakologie*, 25(1):1–30.
- [Hölzl et al., 2016] Hölzl, C., Kibies, P., Imoto, S., Frach, R., Suladze, S., Winter, R., Marx, D., Horinek, D., and Kast, S. M. (2016). Design principles for high-pressure force fields: Aqueous TMAO solutions from ambient to kilobar pressures. *J. Chem. Phys.*, 144(14):144104.



- [Homouz et al., 2008] Homouz, D., Perham, M., Samiotakis, A., Cheung, M. S., and Wittung-Stafshede, P. (2008). Crowded, cell-like environment induces shape changes in aspherical protein. *Proc. Natl. Acad. Sci. USA*, 105(33):11754–11759.
- [Hong and Gierasch, 2010] Hong, J. and Gierasch, L. M. (2010). Macromolecular crowding remodels the energy landscape of a protein by favoring a more compact unfolded state. *J. Am. Chem. Soc.*, 132(30):10445–10452.
- [Huang et al., 2017] Huang, H. W., Wu, S. J., Lu, J. K., Shyu, Y. T., and Wang, C. Y. (2017). Current status and future trends of high-pressure processing in food industry. *Food Control*, 72(12):1–8.
- [Huang et al., 2007] Huang, Y.-S., Jeng, U.-S., Shiu, Y.-J., Lai, Y.-H., and Sun, Y.-S. (2007). Charge interaction and temperature effects on the solution structure of lysozyme as revealed by small-angle X-ray scattering. *J. Appl. Cryst.*, 40(s1):s165–s169.
- [Hunger et al., 2015] Hunger, J., Ottosson, N., Mazur, K., Bonn, M., and Bakker, H. J. (2015). Water-mediated interactions between trimethylamine-N-oxide and urea. *Phys. Chem. Chem. Phys.*, 17(1):298–306.
- [Hunger et al., 2012] Hunger, J., Tielrooij, K. J., Buchner, R., Bonn, M., and Bakker, H. J. (2012). Complex formation in aqueous trimethylamine-N-oxide (TMAO) solutions. *J. Phys. Chem. B*, 116(16):4783–4795.
- [Hunter, 2001] Hunter, R. J. (2001). *Foundations of Colloid Science*. Oxford University Press Inc., New York, 2 edition.
- [Ikkai and Ooi, 1966] Ikkai, T. and Ooi, T. (1966). The effects of pressure on F-G transformation of actin. *Biochemistry*, 5(5):1551–1560.
- [Ilett et al., 1995] Ilett, S. M., Orrock, A., Poon, W. C. K., and Pusey, P. N. (1995). Phase behavior of a model colloid-polymer mixture. *Phys. Rev. E*, 51(2):1344–1352.
- [Imoto et al., 2016] Imoto, S., Kibies, P., Rosin, C., Winter, R., Kast, S. M., and Marx, D. (2016). Toward Extreme Biophysics : Deciphering the Infrared Response of Biomolecular Solutions at High Pressures. *Angew. Chem. Int. Ed.*, 55:9534–9538.
- [Ishimoto and Tanaka, 1977] Ishimoto, C. and Tanaka, T. (1977). Critical behaviour of a binary mixture of protein and salt water. *Phys. Rev. Lett.*, 39(8):474–477.
- [Israelachvili, 2011] Israelachvili, J. (2011). *Intermolecular and Surface Forces*. Academic Press, London, 3rd edition.
- [Jackson-Atogi et al., 2013] Jackson-Atogi, R., Sinha, P. K., and Rösger, J. (2013). Distinctive Solvation Patterns Make Renal Osmolytes Diverse. *Biophys. J.*, 105(9):2166–2174.
- [Jaenicke, 1981] Jaenicke, R. (1981). Enzymes under extremes of physical conditions. *Ann. Rev. Biophys. Bioeng.*, 10(1):1–67.
- [Jain and Roy, 2009] Jain, N. K. and Roy, I. (2009). Effect of trehalose on protein structure. *Protein Sci.*, 18:24–36.
- [Jannasch and Taylor, 1984] Jannasch, H. W. and Taylor, C. D. (1984). Deep-sea microbiology. *Ann. Rev. Microbiol.*, 38(1):487–514.
- [Javid, 2007] Javid, N. (2007). *Protein-Protein Interactions in Complex Cosolvent Solutions Revealed by Synchrotron Small-Angle X-ray Scattering*. PhD thesis, TU Dortmund.
- [Jencks and Regenstein, 1968] Jencks, W. and Regenstein, J. (1968). Ionization Constants of Acids and Bases. In Sober, M., editor, *Handbook of Biochemistry and Molecular Biology*, pages 595–635. Chemical Rubber Company, Cleveland, Ohio, 4 edition.

- [Johansson et al., 1999] Johansson, H.-O., Brooks, D., and Haynes, C. (1999). Macromolecular Crowding and Its Consequences. *Int. Rev. Cytol.*, 192:155–170.
- [Julius et al., 2018a] Julius, K., Al-Ayoubi, S. R., Paulus, M., Tolan, M., and Winter, R. (2018a). The effects of osmolytes and crowding on the pressure-induced dissociation and inactivation of dimeric LADH. *Phys. Chem. Chem. Phys.*, 20(10):7093–7104.
- [Julius et al., 2018b] Julius, K., Weine, J., Berghaus, M., König, N., Gao, M., Latarius, J., Paulus, M., Schroer, M. A., Tolan, M., and Winter, R. (2018b). Water-Mediated Protein-Protein Interactions at High Pressures are Controlled by a Deep-Sea Osmolyte. *Phys. Rev. Lett.*, 121(3):038101.
- [Julius et al., 2019] Julius, K., Weine, J., Gao, M., Latarius, J., Elbers, M., Paulus, M., Tolan, M., and Winter, R. (2019). Impact of Macromolecular Crowding and Compression on Protein-Protein Interactions and Liquid-Liquid Phase Separation Phenomena. *Macromolecules*, 52(4):1772–1784.
- [Jungwirth and Winter, 2008] Jungwirth, P. and Winter, B. (2008). Ions at Aqueous Interfaces: From Water Surface to Hydrated Proteins. *Ann. Rev. Phys. Chem.*, 59(1):343–366.
- [Kaatze and Uhlendorf, 1981] Kaatze, U. and Uhlendorf, V. (1981). The dielectric Properties of Water at Microwave Frequencies. *Z. Phys. Chem.*, 126(2):151–165.
- [Kalbitzer et al., 2009] Kalbitzer, H. R., Spoerner, M., Ganser, P., Hozsa, C., and Kremer, W. (2009). Fundamental link between folding states and functional states of proteins. *J. Am. Chem. Soc.*, 131(46):16714–16719.
- [Kapoor et al., 2012] Kapoor, S., Triola, G., Vetter, I., Erkamp, M., Waldmann, H., and Winter, R. (2012). Revealing conformational substates of lipidated N-Ras protein by pressure modulation. *Proc. Natl. Acad. Sci. USA*, 109(2):460–465.
- [Kataoka et al., 1995] Kataoka, M., Nishii, I., Fujisawa, T., Ueki, T., Tokunaga, F., and Goto, Y. (1995). Structural characterization of the molten globule and native states of apomyoglobin by solution x-ray scattering. *J. Mol. Biol.*, 249(1):215–228.
- [Katayama et al., 2010] Katayama, Y., Hattori, T., Saitoh, H., Ikeda, T., and Aoki, K. (2010). Structure of liquid water under high pressure up to 17 GPa. *Phys. Rev. B*, 81(1):014109.
- [Kauzmann, 1959] Kauzmann, W. (1959). Some Factors in the Interpretation of Protein Denaturation. *Adv. Protein Chem.*, 14(C):1–63.
- [Kauzmann, 1987] Kauzmann, W. (1987). Thermodynamics of unfolding. *Nature*, 325:763–764.
- [Keating, 2012] Keating, C. D. (2012). Aqueous phase separation as a possible route to compartmentalization of biological molecules. *Acc. Chem. Res.*, 45(12):2114–2124.
- [Kell, 1977] Kell, G. S. (1977). Effects of isotopic composition, temperature, pressure, and dissolved gases on the density of liquid water. *J. Phys. Chem. Ref. Data*, 6(4):1109–1131.
- [Kelly and Yancey, 1999] Kelly, R. H. and Yancey, P. H. (1999). High contents of trimethylamine oxide correlating with depth in deep-sea teleost fishes, skates, and decapod crustaceans. *Biological Bulletin*, 196(1):18–25.
- [Kendrick et al., 1997] Kendrick, B. S., Chang, B. S., Arakawa, T., Peterson, B., Randolph, T. W., Manning, M. C., and Carpenter, J. F. (1997). Preferential exclusion of sucrose from recombinant interleukin-1 receptor antagonist: Role in restricted conformational mobility and compaction of native state. *Proc. Natl. Acad. Sci. USA*, 94(22):11917–11922.
- [Kentzinger et al., 2016] Kentzinger, E., Krutyeva, M., and Rücker, U. (2016). GALAXI: Gallium anode low-angle x-ray instrument. *JLSRF*, 2(A61):1–5.
- [King et al., 2014] King, J., Arthur, E., Brooks, C., and Kubarych, K. (2014). Crowding induced collective hydration of biological macromolecules over extended distances. *J. Am. Chem. Soc.*, 136(1):188–194.

- [King and Weber, 1986] King, L. and Weber, G. (1986). Conformational Drift of Dissociated Lactate Dehydrogenases. *Biochemistry*, 25(12):3632–3637.
- [Kirkwood, 1935] Kirkwood, J. G. (1935). Statistical mechanics of fluid mixtures. *J. Chem. Phys.*, 3(5):300–313.
- [Kirste and Oberthür, 1982] Kirste, R. and Oberthür, R. (1982). Synthetic polymers in solution. In *Small Angle X-ray Scattering*, chapter 12, pages 387–431. Academic Press, New York.
- [Klein, 2002] Klein, R. (2002). Interacting Colloidal Suspensions. In Lindner, P. and Zemb, T., editors, *Neutrons, X-rays and Light: Scattering Methods Applied to Soft Condensed Matter*, chapter 14, pages 351–379. Elsevier Science B.V., Amsterdam.
- [Klinman, 1981] Klinman, J. P. (1981). Probes of mechanism and transition-state structure in the alcohol dehydrogenase reaction. *CRC Crit. Rev. Biochem.*, 10(1):39–78.
- [Knake et al., 2015] Knake, L., Schwaab, G., Kartaschew, K., and Havenith, M. (2015). Solvation Dynamics of Trimethylamine N-Oxide in Aqueous Solution Probed by Terahertz Spectroscopy. *J. Phys. Chem. B.*, 119(43):13842–13851.
- [Knorr et al., 2006] Knorr, D., Heinz, V., and Buckow, R. (2006). High pressure application for food biopolymers. *Biochim. Biophys. Acta*, 1764:619–631.
- [Kolská et al., 2016] Kolská, Z., Valha, P., Slepíčka, P., and Švorčík, V. (2016). Refractometric study of systems water-poly(ethylene glycol) for preparation and characterization of Au nanoparticles dispersion. *Arab. J. Chem.*, doi:10.101.
- [Konarev et al., 2003] Konarev, P. V., Volkov, V. V., Sokolova, A. V., Koch, M. H. J., and Svergun, D. I. (2003). PRIMUS: a Windows PC-based system for small-angle scattering data analysis. *J. Appl. Cryst.*, 36(5):1277–1282.
- [Koo et al., 1999] Koo, H., Lansbury, P., and Kelly, J. (1999). Amyloid diseases: Abnormal protein aggregation in neurodegeneration. *Proc. Natl. Acad. Sci. USA*, 96(18):9989–9990.
- [Kornblatt et al., 1998] Kornblatt, M. J., Lange, R., and Balny, C. (1998). Can monomers of yeast enolase have enzymatic activity? *Eur. J. Biochem.*, 251(3):775–780.
- [Korzhev et al., 2006] Korzhnev, D. M., Bezsonova, I., Evanics, F., Taulier, N., Zhou, Z., Bai, Y., Chalikian, T. V., Prosser, R. S., and Kay, L. E. (2006). Probing the transition state ensemble of a protein folding reaction by pressure-dependent nmr relaxation dispersion. *J. Am. Chem. Soc.*, 128(15):5262–5269.
- [Kotlarchyk and Chen, 1983] Kotlarchyk, M. and Chen, S. H. (1983). Analysis of small angle neutron scattering spectra from polydisperse interacting colloids. *J. Chem. Phys.*, 79(5):2461–2469.
- [Kozer et al., 2007] Kozer, N., Kuttner, Y. Y., Haran, G., and Schreiber, G. (2007). Protein-protein association in polymer solutions: From dilute to semidilute to concentrated. *Biophys. J.*, 92(6):2139–2149.
- [Krywka, 2008] Krywka, C. (2008). *Ein Aufbau für Röntgenkleinwinkelstreuung an Protein-Lösungen an der Synchrotronstrahlungsquelle DELTA*. PhD thesis, TU Dortmund.
- [Krywka et al., 2007] Krywka, C., Sternemann, C., Paulus, M., Javid, N., Winter, R., Al-Sawalmih, A., Yi, S., Raabe, D., and Tolan, M. (2007). The small-angle and wide-angle X-ray scattering set-up at beamline BL9 of DELTA. *J. Synchrotron Radiat.*, 14(3):244–251.
- [Krywka et al., 2008] Krywka, C., Sternemann, C., Paulus, M., Tolan, M., Royer, C., and Winter, R. (2008). Effect of osmolytes on pressure-induced unfolding of proteins: A high-pressure SAXS study. *Chem. Phys. Chem.*, 9(18):2809–2815.

- [Kuehner et al., 1999] Kuehner, D. E., Engmann, J., Fergg, F., Wernick, M., Blanch, H. W., and Prausnitz, J. M. (1999). Lysozyme Net Charge and Ion Binding in Concentrated Aqueous Electrolyte Solutions. *J. Phys. Chem. B*, 103(8):1368–1374.
- [Kuffel and Zielkiewicz, 2010] Kuffel, A. and Zielkiewicz, J. (2010). The hydrogen bond network structure within the hydration shell around simple osmolytes: Urea, tetramethylurea, and trimethylamine-N-oxide, investigated using both a fixed charge and a polarizable water model. *J. Chem. Phys.*, 133(3):035102.
- [Kulkarni et al., 1999] Kulkarni, A., Chatterjee, A., Schweizer, K., and Zukoski, C. (1999). Depletion Interactions in the Protein Limit: Effects of Polymer Density Fluctuations. *Phys. Rev. Lett.*, 83(22):4554–4557.
- [Kulkarni and Zukoski, 2001] Kulkarni, A. and Zukoski, C. (2001). Depletion interactions and protein crystallization. *J. Cryst. Growth*, 232(1):156–164.
- [Kulkarni et al., 2000] Kulkarni, A. M., Chatterjee, A. P., Schweizer, K. S., and Zukoski, C. F. (2000). Effects of polymer density fluctuations on depletion interactions. *J. Phys. Condens. Matter*, 12(8A):A301–A307.
- [Kunz et al., 2004] Kunz, W., Henle, J., and Ninham, B. W. (2004). 'Zur Lehre von der Wirkung der Salze' (about the science of the effect of salts): Franz Hofmeister's historical papers. *Curr. Opin. Colloid Interface Sci.*, 9(1-2):19–37.
- [Laidler, 1965] Laidler, K. (1965). *Chemical Kinetics*. McGraw-Hill, New York.
- [Landau and Lifshitz, 1985] Landau, L. and Lifshitz, E. (1985). *Classical Theory of Fields*. Pergamon Press., Oxford.
- [Lavrenko et al., 1987] Lavrenko, P. N., Mikriukova, O. I., and Okatova, O. V. (1987). On the separation ability of various ficoll gradient solutions in zonal centrifugation. *Anal. Biochem.*, 166(2):287–297.
- [Le Brun et al., 2009] Le Brun, V., Friess, W., Schultz-Fademrecht, T., Muehlau, S., and Garidel, P. (2009). Lysozyme-lysozyme self-interactions as assessed by the osmotic second virial coefficient: Impact for physical protein stabilization. *Biotechnol. J.*, 4(9):1305–1319.
- [Lebowitz et al., 1965] Lebowitz, J. L., Helfand, E., and Psaestgaakd, E. (1965). Scaled particle theory of fluid mixtures. *J. Chem. Phys.*, 43(3):774–779.
- [Lebowitz and Percus, 1966] Lebowitz, J. L. and Percus, J. K. (1966). Mean spherical model for lattice gases with extended hard cores and continuum fluids. *Phys. Rev.*, 144(1):251–258.
- [Leckband and Israelachvili, 2001] Leckband, D. and Israelachvili, J. (2001). Intermolecular forces in biology. *Q. Rev. Biophys.*, 34(2):105–267.
- [Lee and Lee, 1981] Lee, J. C. and Lee, L. L. Y. (1981). Preferential Solvent Interactions between Proteins and Polyethylene Glycols. *J. Biol. Chem.*, 256(2):625–631.
- [Lee et al., 2010] Lee, S., Shek, Y. L., and Chalikian, T. V. (2010). Urea interactions with protein groups: A volumetric study. *Biopolymers*, 93(10):866–879.
- [Leikin et al., 1993] Leikin, S., Parsegian, V. a., Rau, D. C., and Rand, R. P. (1993). Hydration forces. *Annu. Rev. Phys. Chem.*, 44:369–395.
- [Lekkerkerker et al., 1992] Lekkerkerker, H. N. W., Poon, W. C. K., Pusey, P. N., Stroobants, A., and Warren, P. B. (1992). Phase behavior of colloid + polymer mixtures. *Europhys. Lett.*, 20(6):559–564.
- [Lerbret et al., 2005] Lerbret, A., Bordat, P., Affouard, F., Descamps, M., and Migliardo, F. (2005). How Homogeneous Are the Trehalose, Maltose, and Sucrose Water Solutions? An Insight from Molecular Dynamics Simulations. *J. Phys. Chem. B*, 109(21):11046–11057.

- [Lerbret et al., 2007] Lerbret, A., Bordat, P., Affouard, F., Hédoux, A., Guinet, Y., and Descamps, M. (2007). How Do Trehalose, Maltose, and Sucrose Influence Some Structural and Dynamical Properties of Lysozyme? Insight from Molecular Dynamics Simulations. *J. Phys. Chem. B*, 111(31):9410–9420.
- [Lide, 2003] Lide, D. R., editor (2003). *CRC Handbook of Chemistry and Physics*. CRC Press LLC, Boca Raton, Fla., 84th edition.
- [Lifshitz, 1956] Lifshitz, E. M. (1956). The theory of molecular attractive forces between solids. *Soviet Physics JETP*, 2(1):73–83.
- [Lindner, 2002] Lindner, P. (2002). Scattering Experiments: Experimental Aspects, Initial Data Reduction and Absolute Calibration. In Lindner, P. and Zemb, T., editors, *Neutrons, X-rays and Light: Scattering Methods Applied to Soft Condensed Matter*, chapter 2, pages 23–48. Elsevier Science B.V., Amsterdam, 1st edition.
- [Lindner and Zemb, 2002] Lindner, P. and Zemb, T. (2002). *Neutrons, X-rays and Light: Scattering Methods Applied to Soft Condensed Matter*. Elsevier Science B.V, Amsterdam, 1st edition.
- [Lindner and Ralston, 1995] Lindner, R. and Ralston, G. (1995). Effects of dextran on the self-association of human spectrin. *Biophys. Chem.*, 57(1):15–25.
- [Liu et al., 1996] Liu, C., Asherie, N., Lomakin, A., Pande, J., Ogun, O., and Benedek, G. B. (1996). Phase separation in aqueous solutions of lens  $\gamma$ -crystallins: Special role of  $\gamma$ s. *Proc. Natl. Acad. Sci. USA*, 93(1):377–382.
- [Liu et al., 2004] Liu, W., Bratko, D., Prausnitz, J. M., and Blanch, H. W. (2004). Effect of alcohols on aqueous lysozyme-lysozyme interactions from static light-scattering measurements. *Biophys. Chem.*, 107(3):289–298.
- [Liu and Bolen, 1995] Liu, Y. and Bolen, D. W. (1995). The Peptide Backbone Plays Dominant Role in Protein Stabilization by Naturally Occurring Osmolytes. *Biochemistry*, 34(39):12884–12891.
- [Liu et al., 2005a] Liu, Y., Chen, W.-r., and Chen, H. (2005a). Manual for TYSQ21 Matlab Package. *Manual*.
- [Liu et al., 2005b] Liu, Y., Chen, W. R., and Chen, S. H. (2005b). Cluster formation in two-Yukawa fluids. *J. Chem. Phys.*, 122(4):044507.
- [Lomakin et al., 1996] Lomakin, A., Asherie, N., and Benedek, G. B. (1996). Monte Carlo study of phase separation in aqueous protein solutions. *J. Chem. Phys.*, 104(4):1646–1656.
- [London, 1937] London, F. (1937). The general theory of molecular forces. *J. Chem. Soc. Faraday Trans.*, 33:8–26.
- [Long et al., 2005] Long, M. S., Jones, C. D., Helfrich, M. R., Mangeney-Slavin, L. K., and Keating, C. D. (2005). Dynamic microcompartmentation in synthetic cells. *Proc. Natl. Acad. Sci. USA*, 102(17):5920–5925.
- [Lorber et al., 1996] Lorber, B., Jenner, G., and Giegé, R. (1996). Effect of high hydrostatic pressure on nucleation and growth of protein crystals. *J. Cryst. Growth*, 158(1-2):103–117.
- [Luby-Phelps, 1999] Luby-Phelps, K. (1999). Cytoarchitecture and Physical Properties of Cytoplasm: Volume, Viscosity, Diffusion, Intracellular Surface Area. *Int. Rev. Cytol.*, 192:189–221.
- [Luby-Phelps et al., 1987] Luby-Phelps, K., Castle, P. E., Taylor, D. L., and Lanni, F. (1987). Hindered diffusion of inert tracer particles in the cytoplasm of mouse 3T3 cells. *Proc. Natl. Acad. Sci. USA*, 84(14):4910–4913.
- [Ludwig, 2001] Ludwig, R. (2001). Water: From Clusters to the Bulk. *Angew. Chem. Int. Ed.*, 40(10):1808–1827.



- [Lullien-Pellerin and Balny, 2002] Lullien-Pellerin, V. and Balny, C. (2002). High-pressure as a tool to study some proteins' properties: conformational modification, activity and oligomeric dissociation. *Innov. Food Sci. Emerg. Technol.*, 3(3):209–221.
- [Luong et al., 2016] Luong, T. Q., Erwin, N., Neumann, M., Schmidt, A., Loos, C., Schmidt, V., Fändrich, M., and Winter, R. (2016). Hydrostatic Pressure Increases the Catalytic Activity of Amyloid Fibril Enzymes. *Angew. Chem. Int. Ed.*, 55(40):12412–12416.
- [Luong et al., 2015] Luong, T. Q., Kapoor, S., and Winter, R. (2015). Pressure - A Gateway to Fundamental Insights into Protein Solvation, Dynamics, and Function. *Chem. Phys. Chem.*, 16(17):3555–3571.
- [Lutsko and Nicolis, 2006] Lutsko, J. F. and Nicolis, G. (2006). Theoretical evidence for a dense fluid precursor to crystallization. *Phys. Rev. Lett.*, 96(4):046102.
- [Lützenkirchen-Hecht et al., 2009] Lützenkirchen-Hecht, D., Wagner, R., Haake, U., Watenphul, A., and Frahm, R. (2009). The materials science X-ray beamline BL8 at the DELTA storage ring. *J. Synchrotron Radiat.*, 16(pt2):264–272.
- [Maeno et al., 2009] Maeno, A., Matsuo, H., and Akasaka, K. (2009). The pressure-temperature phase diagram of hen lysozyme at low pH. *Biophysics*, 5:1–9.
- [Mahanty and Ninham, 1976] Mahanty, J. and Ninham, B. (1976). *Dispersion forces*. Academic Press, New York.
- [Malfois et al., 1996] Malfois, M., Bonneté, F., Belloni, L., and Tardieu, A. (1996). A model of attractive interactions to account for fluid-fluid phase separation of protein solutions. *J. Chem. Phys.*, 105(8):3290–3300.
- [Malmberg and Maryott, 1950] Malmberg, C. and Maryott, A. (1950). Dielectric constants of aqueous solutions of dextrose and sucrose. *J. Res. Natl. Bur. Stand.*, 45(4):299 – 303.
- [Manno et al., 2003] Manno, M., Xiao, C., Bulone, D., Martorana, V., and San Biagio, P. L. (2003). Thermodynamic instability in supersaturated lysozyme solutions: Effect of salt and role of concentration fluctuations. *Phys. Rev. E*, 68(1):011904.
- [Mao et al., 1995] Mao, Y., Cates, M. E., and Lekkerkerker, H. N. (1995). Depletion force in colloidal systems. *Physica A*, 222(1):10–24.
- [Marcus, 2009] Marcus, Y. (2009). Effect of Ions on the Structure of Water: Structure Making and Breaking. *Chem. Rev.*, 109(3):1346–1370.
- [Martin and Hurd, 1987] Martin, J. E. and Hurd, A. J. (1987). Scattering from fractals. *J. Appl. Cryst.*, 20(2):61–78.
- [Masson et al., 2001] Masson, P., Tonello, C., and Balny, C. (2001). High-pressure biotechnology in medicine and pharmaceutical science. *J. Biomed. Biotechnol.*, 1(2):85–88.
- [Maxfield and Shepherd, 1975] Maxfield, J. and Shepherd, I. W. (1975). Conformation of poly(ethylene oxide) in the solid state, melt and solution measured by Raman scattering. *Polymer*, 16(7):505–509.
- [Mcmeekin et al., 1964] Mcmeekin, T. L., Groves, M. L., and Hipp, N. J. (1964). Refractive Indices of Amino Acids, Proteins, and Related Substances. In Stekol, J., editor, *Advances in Chemistry*, volume 44, chapter 4, pages 54–66. American Chemical Society.
- [McNeil-Watson and Kaszuba, 2011] McNeil-Watson, F. and Kaszuba, M. (2011). A Novel Method for Measuring Zeta Potential of High-Concentration, Low-Volume Protein Samples. *Life Science Instruments*, 1:007.
- [McPherson, 1976] McPherson, A. (1976). Crystallization of Proteins from Polyethylene Glycol. *J. Biol. Chem.*, 251(20):6300–6303.

- [McPherson, 1985] McPherson, A. (1985). Use of polyethylene glycol in the crystallization of macromolecules. *Methods Enzymol.*, 114:120–125.
- [McPherson, 1990] McPherson, A. (1990). Current approaches to macromolecular crystallization. *Eur. J. Biochem.*, 189(1):1–23.
- [Meersman et al., 2009] Meersman, F., Bowron, D., Soper, A. K., and Koch, M. H. (2009). Counteraction of urea by trimethylamine N-oxide is due to direct interaction. *Biophys. J.*, 97(9):2559–2566.
- [Meersman et al., 2011] Meersman, F., Bowron, D., Soper, A. K., and Koch, M. H. (2011). An X-ray and neutron scattering study of the equilibrium between trimethylamine N-oxide and urea in aqueous solution. *Phys. Chem. Chem. Phys.*, 13(30):13765–13771.
- [Meersman et al., 2013] Meersman, F., Daniel, I., Bartlett, D. H., Winter, R., Hazael, R., and McMillan, P. F. (2013). High-Pressure Biochemistry and Biophysics. *Rev. Mineral. Geochem.*, 75(1):607–648.
- [Meijer and Frenkel, 1994] Meijer, E. J. and Frenkel, D. (1994). Colloids dispersed in polymer solutions. A computer simulation study. *J. Chem. Phys.*, 100(9):6873–6887.
- [Meijers et al., 2007] Meijers, R., Adolph, H. W., Dauter, Z., Wilson, K. S., Lamzin, V. S., and Cedergren-Zeppezauer, E. S. (2007). Structural evidence for a ligand coordination switch in liver alcohol dehydrogenase. *Biochemistry*, 46(18):5446–5454.
- [Meijers et al., 2001] Meijers, R., Morris, R. J., Adolph, H. W., Merli, A., Lamzin, V. S., and Cedergren-Zeppezauer, E. S. (2001). On the Enzymatic Activation of NADH. *J. Biol. Chem.*, 276(12):9316–9321.
- [Mentré and Hoa, 2001] Mentré, P. and Hoa, G. H. B. (2001). Effects of high hydrostatic pressures on living cells: A consequence of the properties of macromolecules and macromolecule-associated water. *Int. Rev. Cytol.*, 201:1–84.
- [Merzel and Smith, 2002] Merzel, F. and Smith, J. C. (2002). Is the first hydration shell of lysozyme of higher density than bulk water? *Proc Natl Acad Sci U S A*, 99(8):5378–5383.
- [Miklos et al., 2010] Miklos, A. C., Li, C., Sharaf, N. G., and Pielak, G. J. (2010). Volume exclusion and soft interaction effects on protein stability under crowded conditions. *Biochemistry*, 49(33):6984–6991.
- [Millero et al., 1976] Millero, F. J., Ward, G. K., and Chetirkin, P. (1976). Partial specific volume, expansibility, compressibility, and heat capacity of aqueous lysozyme solutions. *J. Biol. Chem.*, 251(13):4001–4004.
- [Minton, 1997] Minton, A. P. (1997). Influence of excluded volume upon macromolecular structure and associations in 'crowded' media. *Curr. Opin. Biotechnol.*, 8(1):65–69.
- [Minton, 2000] Minton, A. P. (2000). Implications of macromolecular crowding for protein assembly. *Curr. Opin. Struct. Biol.*, 10(1):34–39.
- [Minton, 2001] Minton, A. P. (2001). The Influence of Macromolecular Crowding and Macromolecular Confinement on Biochemical Reactions in Physiological Media. *J. Biol. Chem.*, 276(14):10577–10580.
- [Minton, 2005] Minton, A. P. (2005). Models for Excluded Volume Interaction between an Unfolded Protein and Rigid Macromolecular Cosolutes: Macromolecular Crowding and Protein Stability Revisited. *Biophys. J.*, 88(2):971–985.
- [Minton, 2006] Minton, A. P. (2006). How can biochemical reactions within cells differ from those in test tubes? *J. Cell Sci.*, 119(pt14):2863–2869.

- [Mittelbach and Porod, 1962] Mittelbach, P. and Porod, G. (1962). Zur Röntgenkleinwinkelstreuung verdünnter kolloider Systeme VII. Die Berechnung der Streukurven von dreiachsigen Ellipsoiden. *Acta Phys. Austriaca*, 15(15):122–147.
- [Mohsen-Nia et al., 2005] Mohsen-Nia, M., Modarress, H., and Rasa, H. (2005). Measurement and modeling of density, kinematic viscosity, and refractive index for poly(ethylene glycol) aqueous solution at different temperatures. *J. Chem. Eng. Data*, 50(5):1662–1666.
- [Molina-Bolívar et al., 1997] Molina-Bolívar, J. A., Galisteo-González, F., and Hidalgo-Álvarez, R. (1997). Colloidal stability of protein-polymer systems: A possible explanation by hydration forces. *Phys. Rev. E*, 55(4):4522–4530.
- [Möller et al., 2014a] Möller, J., Grobelny, S., Schulze, J., Bieder, S., Steffen, A., Erkamp, M., Paulus, M., Tolan, M., and Winter, R. (2014a). Reentrant liquid-liquid phase separation in protein solutions at elevated hydrostatic pressures. *Phys. Rev. Lett.*, 112(2):028101.
- [Möller et al., 2014b] Möller, J., Grobelny, S., Schulze, J., Steffen, A., Bieder, S., Paulus, M., Tolan, M., and Winter, R. (2014b). Specific anion effects on the pressure dependence of the protein-protein interaction potential. *Phys. Chem. Chem. Phys.*, 16(16):7423–7429.
- [Möller et al., 2016] Möller, J., Léonardon, J., Gorini, J., Dattani, R., and Narayanan, T. (2016). A sub-ms pressure jump setup for time-resolved X-ray scattering. *Rev. Sci. Instrum.*, 87(12):125116.
- [Möller et al., 2012] Möller, J., Schroer, M. A., Erkamp, M., Grobelny, S., Paulus, M., Tiemeyer, S., Wirkert, F. J., Tolan, M., and Winter, R. (2012). The effect of ionic strength, temperature, and pressure on the interaction potential of dense protein solutions: From nonlinear pressure response to protein crystallization. *Biophys. J.*, 102(11):2641–2648.
- [Money, 1989] Money, N. P. (1989). Osmotic Pressure of Aqueous Polyethylene Glycols. *Plant Physiol.*, 91(2):766–769.
- [Mozhaev et al., 1994] Mozhaev, V. V., Heremans, K., Frank, J., Masson, P., and Balny, C. (1994). Exploiting the effects of high hydrostatic pressure in biotechnological applications. *Trends Biotechnol.*, 12(12):493–501.
- [Mozhaev et al., 1996] Mozhaev, V. V., Heremans, K., Frank, J., Masson, P., and Balny, C. (1996). High pressure effects on protein structure and function. *Proteins*, 24(1):81–91.
- [Muschol and Rosenberger, 1995] Muschol, M. and Rosenberger, F. (1995). Interactions in Undersaturated and Supersaturated Lysozyme Solutions: Static and Dynamic Light scattering Results. *J. Chem. Phys.*, 103(24):10424.
- [Muschol and Rosenberger, 1997] Muschol, M. and Rosenberger, F. (1997). Liquid-liquid phase separation in supersaturated lysozyme solutions and associated precipitate formation/crystallization. *J. Chem. Phys.*, 107(6):1953–1962.
- [Mylonas and Svergun, 2007] Mylonas, E. and Svergun, D. I. (2007). Accuracy of molecular mass determination of proteins in solution by small-angle X-ray scattering. *J. Appl. Cryst.*, 40:s245–s249.
- [Nägele, 2008] Nägele, G. (2008). Theories of Fluid Microstructures. In *Soft Matter: From Synthetic to Biological Materials (39th IFF Spring School, Series: Key Technologies Vol. 31)*, chapter B2. Forschungszentrum Jülich Publishing.
- [Narayanan and Liu, 2003] Narayanan, J. and Liu, X. (2003). Protein Interactions in Undersaturated and Supersaturated Solutions: A Study Using Light and X-Ray Scattering. *Biophys. J.*, 84(1):523–532.

- [Narayanan et al., 2018] Narayanan, T., Sztucki, M., Van Vaerenbergh, P., L  onardon, J., Gorini, J., Claustre, L., Sever, F., Morse, J., and Boesecke, P. (2018). A multipurpose instrument for time-resolved ultra-small-angle and coherent X-ray scattering. *J. Appl. Cryst.*, 51:1–14.
- [Niebuhr and Koch, 2005] Niebuhr, M. and Koch, M. H. J. (2005). Effects of urea and trimethylamine-N-oxide (TMAO) on the interactions of lysozyme in solution. *Biophys. J.*, 89(3):1978–1983.
- [Ninham, 1999] Ninham, B. W. (1999). On progress in forces since the DLVO theory. *Adv. Colloid Interface Sci.*, 83(1):1–17.
- [Noro and Frenkel, 2000] Noro, M. G. and Frenkel, D. (2000). Extended corresponding-states behavior for particles with variable range attractions. *J. Chem. Phys.*, 113(8):2941–2944.
- [Oehme, 1962] Oehme, F. (1962). *Dielektrische Me  methoden*. Verlag Chemie, GmbH, Weinheim, 2nd edition.
- [Ohtaki and Radnai, 1993] Ohtaki, H. and Radnai, T. (1993). Structure and Dynamics of Hydrated Ions. *Chem. Rev.*, 93(3):1157–1204.
- [Okhulkov et al., 1994] Okhulkov, A. V., Demianets, Y. N., and Gorbaty, Y. E. (1994). X-ray scattering in liquid water at pressures of up to 7.7 kbar: Test of a fluctuation model. *J. Chem. Phys.*, 100(2):1578–1588.
- [Omta et al., 2003] Omta, A. W., Kropman, M. F., Woutersen, S., and Bakker, H. J. (2003). Negligible Effect of Ions on the Hydrogen-Bond Structure in Liquid Water. *Science*, 301:347–349.
- [Onuchic et al., 1997] Onuchic, J. N., Luthey-Schulten, Z., and Wolynes, P. G. (1997). Theory of protein folding: The Energy Landscape Perspective. *Ann. Rev. Phys. Chem.*, 48(1):545–600.
- [Orthaber et al., 2000] Orthaber, D., Bergmann, A., and Glatter, O. (2000). SAXS experiments on absolute scale with Kratky systems using water as a secondary standard. *J. Appl. Cryst.*, 33:218–225.
- [Orthen et al., 1994] Orthen, B., Popp, M., and Smirnov, N. (1994). Hydroxyl radical scavenging properties of cyclitols. *Proc. Royal Soc. B*, 102:269–272.
- [Ortore et al., 2009] Ortore, M., Spinozzi, F., Mariani, P., Paciaroni, A., Barbose, L., Amenitsch, H., Steinhart, M., Ollivier, J., and Russo, D. (2009). Combining structure and dynamics : non denaturing high-pressure effect on lysozyme in solution. *J. R. Soc. Interface*, 6:S619–S634.
- [Ottosen et al., 2002] Ottosen, M. B., Bj  rnberg, O., Norager, S., Larsen, S., Palfey, B., and Jensen, K. (2002). The dimeric dihydroorotate dehydrogenase A from *Lactococcus lactis* dissociates reversibly into inactive monomers. *Protein Sci.*, 11:2575–2583.
- [Palit and Yethiraj, 2017] Palit, S. and Yethiraj, A. (2017). Dynamics and complex formation in charged and uncharged Ficoll70 solutions. *J. Chem. Phys.*, 147(7):074901.
- [Pande et al., 2001] Pande, A., Pande, J., Asherie, N., Lomakin, A., Ogun, O., King, J., and Benedek, G. B. (2001). Crystal cataracts: Human genetic cataract caused by protein crystallization. *Proc. Natl. Acad. Sci. USA*, 98(11):6116–6120.
- [Panick et al., 1998] Panick, G., Malessa, R., Winter, R., Rapp, G., Frye, K. J., and Royer, C. A. (1998). Structural Characterization of the Pressure-Denatured State and Unfolding/refolding Kinetics of Staphylococcal Nuclease by Synchrotron Small-Angle X-Ray-Scattering and Fourier-Transform Infrared-Spectroscopy. *J. Mol. Biol.*, 275(2):389–402.
- [Panuszko et al., 2009] Panuszko, A., Bru  dziak, P., Zielkiewicz, J., Wyrzykowski, D., and Stangret, J. (2009). Effects of Urea and Trimethylamine- N -oxide on the Properties of Water and the Secondary Structure of Hen Egg White Lysozyme. *J. Phys. Chem. B*, 113(44):14797–14809.

- [Panuszko et al., 2012] Panuszko, A., Wojciechowski, M., Brudzdiak, P., Rakowska, P. W., and Stangret, J. (2012). Characteristics of hydration water around hen egg lysozyme as the protein model in aqueous solution. FTIR spectroscopy and molecular dynamics simulation. *Phys. Chem. Chem. Phys.*, 14(45):15765–15773.
- [Pappenberger et al., 2000] Pappenberger, G., Saudan, C., Becker, M., Merbach, A. E., and Kiefhaber, T. (2000). Denaturant-induced movement of the transition state of protein folding revealed by high-pressure stopped-flow measurements. *Proc. Natl. Acad. Sci. USA*, 97(1):17–22.
- [Parmar and Muschol, 2009] Parmar, A. S. and Muschol, M. (2009). Hydration and hydrodynamic interactions of lysozyme: Effects of chaotropic versus kosmotropic ions. *Biophys. J.*, 97(2):590–598.
- [Parsegian, 2006] Parsegian, V. (2006). *Van der Waals forces: a handbook for biologists, chemists, engineers, and physicists*. Cambridge University Press, New York.
- [Parsegian et al., 2000] Parsegian, V., Ranf, R., and Rau, D. (2000). Osmotic stress, crowding, preferential hydration, and binding: A comparison of perspectives. *Proc. Natl. Acad. Sci. USA*, 97(8):3987–3992.
- [Paul and Paul, 2015] Paul, S. and Paul, S. (2015). Molecular Insights into the Role of Aqueous Trehalose Solution on Temperature-Induced Protein Denaturation. *J. Phys. Chem. B*, 119(4):1598–1610.
- [Peng et al., 1993] Peng, X., Jonas, J., and Silva, J. L. (1993). Molten-globule conformation of Arc repressor monomers determined by high-pressure  $^1\text{H}$  NMR spectroscopy. *Proc. Natl. Acad. Sci. USA*, 90(5):1776–1780.
- [Peng et al., 1994] Peng, X., Jonas, J., and Silva, J. L. (1994). High-pressure NMR study of the dissociation of Arc repressor. *Biochemistry*, 33(27):8323–9.
- [Percus and Yevick, 1958] Percus, J. K. and Yevick, G. J. (1958). Analysis of Classical Statistical Mechanics by Means of Collective Coordinates. *Phys. Rev.*, 110(1):1–13.
- [Petsev and Vekilov, 2000] Petsev, D. N. and Vekilov, P. G. (2000). Evidence for Non-DLVO Hydration Interactions in Solutions of the Protein Apoferritin. *Phys. Rev. Lett.*, 84(6):1339–1342.
- [Petterson, 1987] Petterson, G. (1987). Liver Alcohol Dehydrogenas. *Crit. Rev. Biochem.*, 21(4):349–389.
- [Phillip et al., 2009] Phillip, Y., Sherman, E., Haran, G., and Schreiber, G. (2009). Common crowding agents have only a small effect on protein-protein interactions. *Biophys. J.*, 97(3):875–885.
- [Pielak and Miklos, 2010] Pielak, G. J. and Miklos, A. C. (2010). Crowding and function reunite. *Proc. Natl. Acad. Sci. USA*, 107(41):17457–17458.
- [Pincus et al., 2008] Pincus, D. L., Hyeon, C., and Thirumalai, D. (2008). Effects of Trimethylamine N-Oxide (TMAO) and Crowding Agents on the Stability of RNA Hairpins. *J. Am. Chem. Soc.*, 130(12):7364–7372.
- [Pitkänen et al., 2010] Pitkänen, I., Suuronen, J., and Nurmi, J. (2010). Partial Molar Volume, Ionization, Viscosity and Structure of Glycine Betaine in Aqueous Solutions. *J. Solution Chem.*, 39(11):1609–1626.
- [Pollard and Wyn Jones, 1979] Pollard, A. and Wyn Jones, R. G. (1979). Enzyme activities in concentrated solutions of glycinebetaine and other solutes. *Planta*, 144(3):291–298.
- [Poon et al., 1997] Poon, W. C., Pirie, A. D., Haw, M. D., and Pusey, P. N. (1997). Non-equilibrium behaviour of colloid-polymer mixtures. *Physica A*, 235(1-2):110–119.



- [Poon et al., 2000] Poon, W. C. K., Egelhaaf, S. U., Beales, P. a., Salonen, A., and Sawyer, L. (2000). Protein crystallization: scaling of charge and salt concentration in lysozyme solutions. *J. Phys.: Condens. Matter*, 12(35):L569–L574.
- [Poon et al., 1996] Poon, W. C. K., Pusey, P., and Lekkerkerker, H. N. W. (1996). Colloids in suspension. *Physics World*, 9(4):27–33.
- [Porod, 1951] Porod, G. (1951). Die Röntgenkleinwinkelstreuung von dichtgepackten kolloiden Systemen - I. Teil. *Kolloid Z.*, 124(2):83–114.
- [Porod, 1982] Porod, G. (1982). General Theory. In Glatter, O. and Kratky, O., editors, *Small-Angle X-ray Scattering*, chapter 2, pages 17–51. Academic Press, London.
- [Poulter, 1932] Poulter, T. (1932). Apparatus for Optical Studies at High Pressure. *Phys. Rev.*, 40(5):860–871.
- [Prieur, 1998] Prieur, D. (1998). Piezophily: Prokaryotes exposed to elevated hydrostatic pressure. In *Extremophiles*, volume III, pages 157–173. EOLSS, Oxford.
- [Privalov, 1990] Privalov, P. L. (1990). Cold denaturation of protein. *Crit. Rev. Biochem. Mol. Biol.*, 25(4):281–306.
- [Pusey, 2002] Pusey, P. (2002). Introduction to Scattering Experiments. In Lindner, P. and Zemb, T., editors, *Neutrons, X-rays and Light: Scattering Methods Applied to Soft Condensed Matter*, chapter 1, pages 3–21. Elsevier Science B.V., Amsterdam, 1 edition.
- [Quigley and Williams, 2015] Quigley, A. and Williams, D. R. (2015). The second virial coefficient as a predictor of protein aggregation propensity : A self-interaction chromatography study. *Eur. J. Pharm. Biopharm.*, 96:282–290.
- [Rajapaksha et al., 2015] Rajapaksha, A., Stanley, C. B., and Todd, B. A. (2015). Effects of macromolecular crowding on the structure of a protein complex: A small-angle scattering study of superoxide dismutase. *Biophys. J.*, 108(4):967–974.
- [Ralston, 1990] Ralston, G. B. (1990). Effects of "crowding" in protein solutions. *J. Chem. Educ.*, 67(10):857–860.
- [Ramakrishnan et al., 2002] Ramakrishnan, S., Fuchs, M., Schweizer, K. S., and Zukoski, C. F. (2002). Entropy driven phase transitions in colloid-polymer suspensions: Tests of depletion theories. *J. Chem. Phys.*, 116(5):2201–2212.
- [Ramaswamy et al., 1994] Ramaswamy, S., Eklund, H., and Plapp, B. V. (1994). Structures of horse liver alcohol dehydrogenase complexed with NAD<sup>+</sup> and substituted benzyl alcohols. *Biochemistry*, 33(17):5230–5237.
- [Ravindra and Winter, 2003] Ravindra, R. and Winter, R. (2003). On the temperature-Pressure free-energy landscape of proteins. *Chem. Phys. Chem*, 4(4):359–365.
- [Record and Anderson, 1995] Record, M. T. and Anderson, C. F. (1995). Interpretation of preferential interaction coefficients of nonelectrolytes and of electrolyte ions in terms of a two-domain model. *Biophys. J.*, 68(3):786–794.
- [Rezus and Bakker, 2006] Rezus, Y. L. A. and Bakker, H. J. (2006). Effect of urea on the structural dynamics of water. *Proc. Natl. Acad. Sci. USA*, 103(49):18417–18420.
- [Rezus and Bakker, 2009] Rezus, Y. L. A. and Bakker, H. J. (2009). Destabilization of the hydrogen-bond structure of water by the osmolyte trimethylamine N-oxide. *J. Phys. Chem. B*, 113(13):4038–4044.
- [Rickard et al., 2010] Rickard, D. L., Duncan, P. B., and Needham, D. (2010). Hydration potential of lysozyme: Protein dehydration using a single microparticle technique. *Biophys. J.*, 98(6):1075–1084.

- [Rivalain et al., 2010] Rivalain, N., Roquain, J., and Demazeau, G. (2010). Development of high hydrostatic pressure in biosciences: Pressure effect on biological structures and potential applications in Biotechnologies. *Biotechnol. Adv.*, 28(6):659–672.
- [Rivas et al., 1999] Rivas, G., Fernandez, J. A., and Minton, A. P. (1999). Direct Observation of the Self-Association of Dilute Proteins in the Presence of Inert Macromolecules at High Concentration via Tracer Sedimentation Equilibrium: Theory, Experiment, and Biological Significance. *Biochemistry*, 38(29):9379–9388.
- [Rivas et al., 2004] Rivas, G., Ferrone, F., and Herzfeld, J. (2004). Life in a crowded world. *EMBO reports*, 5(1):23–27.
- [Robinson and Sligar, 1995] Robinson, C. R. and Sligar, S. G. (1995). Hydrostatic and osmotic pressure as tools to study macromolecular recognition. *Methods in Enzymol.*, 259:395–427.
- [Roche et al., 2012] Roche, J., Caro, J. A., Norberto, D. R., Barthe, P., Roumestand, C., Schlessman, J. L., Garcia, A. E., Garcia-Moreno E., B., and Royer, C. A. (2012). Cavities determine the pressure unfolding of proteins. *Proc. Natl. Acad. Sci. USA*, 109(18):6945–6950.
- [Rodríguez-Arteche et al., 2012] Rodríguez-Arteche, I., Cervený, S., Alegría, Á., and Colmenero, J. (2012). Dielectric spectroscopy in the GHz region on fully hydrated zwitterionic amino acids. *Phys. Chem. Chem. Phys.*, 14(32):11352–11362.
- [Rosenbaum et al., 1996] Rosenbaum, D., Zamora, P. C., and Zukoski, C. F. (1996). Phase behavior of small attractive colloidal particles. *Phys. Rev. Lett.*, 76(1):150–153.
- [Rösgen and Jackson-Atogi, 2012] Rösgen, J. and Jackson-Atogi, R. (2012). Volume Exclusion and H-Bonding Dominate the Thermodynamics and Solvation of Trimethylamine-N-oxide in Aqueous Urea. *J. Am. Chem. Soc.*, 134(7):3590–3597.
- [Ruan and Weber, 1989] Ruan, K. and Weber, G. (1989). Hysteresis and Conformational Drift of Pressure-Dissociated Glyceraldehydephosphate Dehydrogenase. *Biochemistry*, 28(5):2144–2153.
- [Ruan and Weber, 1993] Ruan, K. and Weber, G. (1993). Physical heterogeneity of muscle glycogen phosphorylase revealed by hydrostatic pressure dissociation. *Biochemistry*, 32(24):6295–6301.
- [Russo et al., 2013] Russo, D., Ortore, M. G., Spinozzi, F., Mariani, P., Loupiac, C., Annighofer, B., and Paciaroni, A. (2013). The impact of high hydrostatic pressure on structure and dynamics of  $\beta$ -lactoglobulin. *Biochim. Biophys. Acta*, 1830(10):4974–4980.
- [Sajadi et al., 2010] Sajadi, M., Ajaj, Y., Ioffe, I., Weingärtner, H., and Ernsting, N. P. (2010). Terahertz Absorption Spectroscopy of a Liquid Using a Polarity Probe: A Case Study of Trehalose/Water Mixtures. *Angew. Chem. Int. Ed.*, 49(2):454–457.
- [Salmon, 1975] Salmon, E. D. (1975). Pressure-induced depolymerization of brain microtubules in vitro. *Science*, 189(4206):884–886.
- [San Biagio and Palma, 1991] San Biagio, P. L. and Palma, M. U. (1991). Spinodal lines and Flory-Huggins free-energies for solutions of human hemoglobins HbS and HbA. *Biophys. J.*, 60(2):508–512.
- [Sapir and Harries, 2011] Sapir, L. and Harries, D. (2011). Linking Trehalose Self-Association with Binary Aqueous Solution Equation of State. *J. Phys. Chem. B*, 115:624–634.
- [Sasaki et al., 2007] Sasaki, Y., Miyoshi, D., and Sugimoto, N. (2007). Regulation of DNA nucleases by molecular crowding. *Nucleic Acids Res.*, 35(12):4086–4093.
- [Sato et al., 2005] Sato, T., Buchner, R., Fernandez, S., Chiba, A., and Kunz, W. (2005). Dielectric relaxation spectroscopy of aqueous amino acid solutions: dynamics and interactions in aqueous glycine. *J. Mol. Liq.*, 117:93–98.

- [Saunders and Fofonoff, 1976] Saunders, P. M. and Fofonoff, N. P. (1976). Conversion of pressure to depth in the ocean. *Deep-Sea Res.*, 23:109–111.
- [Schellman, 2003] Schellman, J. A. (2003). Protein Stability in Mixed Solvents: A Balance of Contact Interaction and Excluded Volume. *Biophys. J.*, 85(1):108–125.
- [Schofield, 1966] Schofield, P. (1966). Wavelength-dependent fluctuations in classical fluids: I. The long wavelength limit. *Proc. Phys. Soc.*, 88(1):149–170.
- [Schroer et al., 2011a] Schroer, M. A., Markgraf, J., Wieland, D. C. F., Sahle, C. J., Möller, J., Paulus, M., Tolan, M., and Winter, R. (2011a). Nonlinear pressure dependence of the interaction potential of dense protein solutions. *Phys. Rev. Lett.*, 106(17):178102.
- [Schroer et al., 2016] Schroer, M. A., Schulz, F., Lehmkuhler, F., Möller, J., Smith, A. J., Lange, H., Vossmeier, T., and Grübel, G. (2016). Tuning the Interaction of Nanoparticles from Repulsive to Attractive by Pressure. *J. Phys. Chem. C*, 120(35):19856–19861.
- [Schroer et al., 2012] Schroer, M. A., Tolan, M., and Winter, R. (2012). Exploring the thermodynamic derivatives of the structure factor of dense protein solutions. *Phys. Chem. Chem. Phys.*, 14(26):9486–9491.
- [Schroer et al., 2011b] Schroer, M. A., Zhai, Y., Wieland, D. C. F., Sahle, C. J., Nase, J., Paulus, M., Tolan, M., and Winter, R. (2011b). Exploring the piezophilic behavior of natural cosolvent mixtures. *Angew. Chem. Int. Ed.*, 50(48):11413–11416.
- [Schultz and Solomon, 1961] Schultz, S. G. and Solomon, A. K. (1961). Determination of the Effective Hydrodynamic Radii of Small Molecules by Viscometry. *J. Gen. Physiol.*, 44(6):1189–1199.
- [Schulze et al., 2016] Schulze, J., Möller, J., Weine, J., Julius, K., König, N., Nase, J., Paulus, M., Tolan, M., and Winter, R. (2016). Phase behavior of lysozyme solutions in the liquid–liquid phase coexistence region at high hydrostatic pressures. *Phys. Chem. Chem. Phys.*, 18(21):14252–14256.
- [Schurtenberger, 2002] Schurtenberger, P. (2002). Contrast and contrast variation in neutron, X-ray and light scattering. In Lindner, P. and Zemb, T., editors, *Neutrons, X-rays and Light: Scattering Methods Applied to Soft Condensed Matter*, chapter 7, pages 145–170. Elsevier Science B.V, Amsterdam, 1 edition.
- [Schurtenberger et al., 1989] Schurtenberger, P., Chamberlin, R. A., Thurston, G. M., Thomson, J. A., and Benedek, G. B. (1989). Observation of critical phenomena in a protein-water solution. *Phys. Rev. Lett.*, 63(19):2064–2067.
- [Sciortino et al., 1991] Sciortino, F., Geiger, A., and Stanley, H. E. (1991). Effect of defects on molecular mobility in liquid water. *Nature*, 354:218–221.
- [Sedgwick et al., 2007] Sedgwick, H., Cameron, J. E., Poon, W. C. K., and Egelhaaf, S. U. (2007). Protein phase behavior and crystallization: Effect of glycerol. *J. Chem. Phys.*, 127(12):125102.
- [Selkoe, 1994] Selkoe, D. (1994). Alzheimer’s Disease: A Central Role for Amyloid. *J. Neuropathol. Exp. Neurol.*, 53(5):438–447.
- [Shallom et al., 2004] Shallom, D., Golan, G., Shoham, G., and Shoham, Y. (2004). Effect of dimer dissociation on activity and thermostability of the  $\alpha$ -glucuronidase from *Geobacillus stearothermophilus*: Dissecting the different oligomeric forms of family 67 glycoside hydrolases. *J. Bacteriol.*, 186(20):6928–6937.
- [Sharp, 2015] Sharp, K. A. (2015). Analysis of the size dependence of macromolecular crowding shows that smaller is better. *Proc. Natl. Acad. Sci. USA*, 112(26):7990–7995.

- [Shen et al., 1999] Shen, B., Hohmann, S., Jensen, R. G., and Bohnert, H. J. (1999). Roles of Sugar Alcohols in Osmotic Stress Adaptation . Replacement of Glycerol by Mannitol and Sorbitol in Yeast. *Plant Physiol.*, 121:45–52.
- [Shikata and Itatani, 2002] Shikata, T. and Itatani, S. (2002). Dielectric Relaxation of Aqueous Trimethylamineoxide Solutions. *J. Solution Chem.*, 31(10):823–844.
- [Shukla et al., 2008] Shukla, A., Mylonas, E., Di Cola, E., Finet, S., Timmins, P., Narayanan, T., and Svergun, D. I. (2008). Absence of equilibrium cluster phase in concentrated lysozyme solutions. *Proc. Natl. Acad. Sci. USA*, 105(13):5075–5080.
- [Silva et al., 1996] Silva, J. L., Foguel, D., Da Poian, A. T., and Prevelige, P. E. (1996). The use of hydrostatic pressure as a tool to study viruses and other macromolecular assemblages. *Curr. Opin. Struct. Biol.*, 6(2):166–175.
- [Silva et al., 2001] Silva, J. L., Foguel, D., and Royer, C. A. (2001). Pressure provides new insights into protein folding, dynamics and structure. *Trends Biochem. Sci.*, 26(10):612–618.
- [Silva et al., 1986] Silva, J. L., Miles, E. W., and Weber, G. (1986). Pressure dissociation and conformational drift of the beta dimer of tryptophan synthase. *Biochemistry*, 25(19):5780–5786.
- [Silva et al., 2014] Silva, J. L., Oliveira, A. C., Vieira, T. C. R. G., de Oliveira, G. A. P., Suarez, M. C., and Foguel, D. (2014). High-Pressure Chemical Biology and Biotechnology. *Chem. Rev.*, 114(14):7239–7267.
- [Silva et al., 1992] Silva, J. L., Silveira, C. F., Correia, A., and Pontes, L. (1992). Dissociation Molten of a Native Dimer to a Globule Monomer. *J. Mol. Biol.*, 223:545–555.
- [Silva and Weber, 1993] Silva, J. L. and Weber, G. (1993). Pressure stability of proteins. *Annu. Rev. Phys. Chem.*, 44:89–113.
- [Silverstein and Boyer, 1964] Silverstein, E. and Boyer, P. D. (1964). Equilibrium Reaction Rates and the Mechanisms of Liver and Yeast Alcohol Dehydrogenase. *J. Biol. Chem.*, 239(11):3908–3914.
- [Simpson and Kauzmann, 1953] Simpson, B. and Kauzmann, W. (1953). The Kinetics of Protein Denaturation. I. The Behavior of the Optical Rotation of Ovalbumin in Urea Solutions. *J. Am. Chem. Soc.*, 75(21):5139–5152.
- [Smeller, 2002] Smeller, L. (2002). Pressure-temperature phase diagrams of biomolecules. *Biochim. Biophys. Acta*, 1595(1-2):11–29.
- [Smith et al., 2007] Smith, J. D., Saykally, R. J., and Geissler, P. L. (2007). The effects of dissolved halide anions on hydrogen bonding in liquid water. *J. Am. Chem. Soc.*, 129(45):13847–13856.
- [Sobry and Ciccariello, 2002] Sobry, R. and Ciccariello, S. (2002). Background subtraction and moments of the microscopic density fluctuation. *J. Appl. Cryst.*, 35(2):220–227.
- [Soper and Ricci, 2000] Soper, A. K. and Ricci, M. A. (2000). Structures of High-Density and Low-Density Water. *Phys. Rev. Lett.*, 84(13):2881–2884.
- [Sophianopoulos et al., 1962] Sophianopoulos, A., Rhodes, C., Holcomb, D., and Van Holde, K. (1962). Physical Studies of Lysozyme. *J. Biol. Chem.*, 237(4):1107–1112.
- [Soranno et al., 2014] Soranno, A., Koenig, I., Borgia, M. B., Hofmann, H., Zosel, F., Nettels, D., and Schuler, B. (2014). Single-molecule spectroscopy reveals polymer effects of disordered proteins in crowded environments. *Proc. Natl. Acad. Sci. USA*, 111(13):4874–4879.
- [Sörensson et al., 1998] Sörensson, J., Ohlson, M., Lindström, K., and Haraldsson, B. (1998). Glomerular charge selectivity for horseradish peroxidase and albumin at low and normal ionic strengths. *Acta Physiol. Scand.*, 163(1):83–91.

- [Sousa, 1995] Sousa, R. (1995). Use of glycerol, polyols and other protein structure stabilizing agents in protein crystallization. *Acta Cryst. D*, 51(3):271–277.
- [Spalla, 2002] Spalla, O. (2002). General Theorems in Small-Angle Scattering. In Lindner, P. and Zemb, T., editors, *Neutrons, X-rays and Light: Scattering Methods Applied to Soft Condensed Matter*, chapter 3, pages 49–71. Elsevier Science B.V., Amsterdam, 1st edition.
- [Spelzini et al., 2008] Spelzini, D., Peleteiro, J., Picó, G., and Farruggia, B. (2008). Polyethyleneglycol-pepsin interaction and its relationship with protein partitioning in aqueous two-phase systems. *Colloids Surf. B*, 67(2):151–156.
- [Stagg et al., 2007] Stagg, L., Zhang, S.-Q., Cheung, M. S., and Wittung-Stafshede, P. (2007). Molecular crowding enhances native structure and stability of alpha/beta protein flavodoxin. *Proc. Natl. Acad. Sci. USA*, 104(48):18976–18981.
- [Stanley and Strey, 2003] Stanley, C. B. and Strey, H. H. (2003). Measuring osmotic pressure of poly(ethylene glycol) solutions by sedimentation equilibrium ultracentrifugation. *Macromolecules*, 36(18):6888–6893.
- [Storey and Storey, 1988] Storey, B. and Storey, M. (1988). Freeze Tolerance in Animals. *Physiol. Rev.*, 68(1):27–84.
- [Street et al., 2006] Street, T. O., Bolen, D. W., and Rose, G. D. (2006). A molecular mechanism for osmolyte-induced protein stability. *Proc. Natl. Acad. Sci. USA*, 103(38):13997–14002.
- [Stumpe and Grubmüller, 2007] Stumpe, M. and Grubmüller, H. (2007). Interaction of Urea with Amino Acids: Implications for Urea-Induced Protein Denaturation. *J. Am. Chem. Soc.*, 129(51):16126–16131.
- [Sturgis et al., 2001] Sturgis, E., Dahlstrom, K., Guan, Y., Eicher, S., Strom, S., Spitz, M., and Wei, Q. (2001). Alcohol dehydrogenase 3 genotype is not associated with risk of squamous cell carcinoma of the oral cavity and pharynx. *Cancer Epidemiol. Biomark. Prev.*, 10(3):273–275.
- [Su et al., 2017] Su, Z., Mahmoudinobar, F., and Dias, C. L. (2017). Effects of Trimethylamine-N-oxide on the Conformation of Peptides and its Implications for Proteins. *Phys. Rev. Lett.*, 119(10):108102.
- [Sund and Theorell, 1963] Sund, H. and Theorell, H. (1963). Alcoholdehydrogenase. In Boyer, P. D., Lardy, H., and Myrback, K., editors, *The Enzymes Vol. 7*, page 25. Academic Press, New York, 2 edition.
- [Suzuki et al., 1994] Suzuki, Y., Mlyashita, S., Komatsu, H., Sato, K., and Yagi, T. (1994). Crystal growth of hen egg white lysozyme under high pressure. *J. Appl. Phys.*, 33(11A):L1568–L1570.
- [Svergun et al., 1988] Svergun, B. D. I., Semenvuk, A. V., and Feigin, L. A. (1988). Small-Angle Scattering-Data Treatment by the Regularization Method. *Acta Cryst. A*, 44(3):244–250.
- [Svergun et al., 1995] Svergun, D., Barberato, C., and Koch, M. H. J. (1995). CRY SOL - a Program to Evaluate X-ray Solution Scattering of Biological Macromolecules from Atomic Coordinates. *J. Appl. Cryst.*, 28(6):768–773.
- [Svergun and Koch, 2002] Svergun, D. and Koch, M. (2002). Advances in structure analysis using small-angle scattering in solution. *Curr. Opin. Struct. Biol.*, 12:654–660.
- [Svergun et al., 2013] Svergun, D., Koch, M., Timmins, P., and May, R. (2013). *Small Angle X-Ray and Neutron Scattering from Solutions of Biological Macromolecules*. Oxford University Press Inc., Oxford, 1st edition.
- [Svergun, 1992] Svergun, D. I. (1992). Determination of the Regularization Parameter in Indirect-Transform Methods Using Perceptual Criteria. *J. Appl. Cryst.*, 25(4):495–503.



- [Svergun and Koch, 2003] Svergun, D. I. and Koch, M. H. J. (2003). Small-angle scattering studies of biological macromolecules in solution. *Rep. Prog. Phys.*, 66(10):1735–1782.
- [Svergun et al., 1998] Svergun, D. I., Richard, S., Koch, M. H., Sayers, Z., Kuprin, S., and Zaccai, G. (1998). Protein hydration in solution: experimental observation by X-ray and neutron scattering. *Proc. Natl. Acad. Sci. USA*, 95(5):2267–2272.
- [Swinehart, 1962] Swinehart, F. (1962). The Beer-Lambert Law. *J. Chem. Educ.*, 39(7):333–335.
- [Takahashi and Sugimoto, 2013] Takahashi, S. and Sugimoto, N. (2013). Effect of pressure on the stability of G-quadruplex DNA: Thermodynamics under crowding conditions. *Angew. Chem. Int. Ed.*, 52(51):13774–13778.
- [Takahashi and Tadokoro, 1973] Takahashi, Y. and Tadokoro, H. (1973). Structural Studies of Polyethers,  $-(\text{CH}_2)_m\text{O}-$  $n$ . X. Crystal Structure of Poly(ethylene oxide). *Macromolecules*, 6(5):672–675.
- [Takano et al., 1997] Takano, K. J., Harigae, H., Kawamura, Y., and Ataka, M. (1997). Effect of hydrostatic pressure on the crystallization of lysozyme based on in situ observations. *J. Cryst. Growth*, 171(3-4):554–558.
- [Tanaka and Ataka, 2002] Tanaka, S. and Ataka, M. (2002). Protein crystallization induced by polyethylene glycol: A model study using apoferritin. *J. Chem. Phys.*, 117(7):3504–3510.
- [Tanford, 1964] Tanford, C. (1964). Isothermal Unfolding of Globular Proteins in Aqueous Urea Solutions. *J. Am. Chem. Soc.*, 86(10):2050–2059.
- [Tanford, 1970] Tanford, C. (1970). Protein Denaturation: Part C. Theoretical Models for the Mechanism of Denaturation. *Adv. Protein Chem.*, 1-95:2050–2059.
- [Tanford and Roxby, 1972] Tanford, C. and Roxby, R. (1972). Interpretation of protein titration curves. Application to lysozyme. *Biochemistry*, 11(11):2192–2198.
- [Tang and Ruan, 1996] Tang, G. Q. and Ruan, K. C. (1996). Pressure-induced dissociation of beef liver L-glutamate dehydrogenase. *Progress Biotechnol.*, 13:163–166.
- [Taratuta et al., 1990] Taratuta, V. G., Holschbach, A., Thurston, G. M., Blankschtein, D., and Benedek, G. B. (1990). Liquid-liquid phase separation of aqueous lysozyme solutions: effects of pH and salt identity. *J. Phys. Chem.*, 94(5):2140–2144.
- [Tardieu et al., 2002] Tardieu, A., Bonneté, F., Finet, S., and Vivarès, D. (2002). Understanding salt or PEG induced attractive interactions to crystallize biological macromolecules. *Acta Cryst. D*, 58(10 II):1549–1553.
- [Tardieu et al., 2001] Tardieu, A., Finet, S., and Bonneté, F. (2001). Structure of the macromolecular solutions that generate crystals. *J. Cryst. Growth*, 232(1-4):1–9.
- [Tardieu et al., 1999] Tardieu, A., Le Verge, A., Malfois, M., Bonneté, F., Finet, S., Riès-Kautt, M., and Belloni, L. (1999). Proteins in solution: from X-ray scattering intensities to interaction potentials. *J. Cryst. Growth*, 196(2-4):193–203.
- [Ten Wolde and Frenkel, 1997] Ten Wolde, P. R. and Frenkel, D. (1997). Enhancement of protein crystal nucleation by critical density fluctuations. *Science*, 277(5334):1975–1978.
- [Teraoka, 2002] Teraoka, I. (2002). *Polymer Solutions: An Introduction to Physical Properties*. John Wiley & Sons, Inc., New York.
- [Theorell, 1970] Theorell, H. (1970). Structural and Functional Relationships between Isoenzymes of Horse LADH. In Sund, H., editor, *Pyridine Nucleotide-Dependent Dehydrogenases*, pages 121–128. Springer, Berlin, 1 edition.

- [Thomson et al., 1987] Thomson, J. a., Schurtenberger, P., Thurston, G. M., and Benedek, G. B. (1987). Binary liquid phase separation and critical phenomena in a protein/water solution. *Proc. Natl. Acad. Sci. USA*, 84(20):7079–7083.
- [Tian et al., 2000] Tian, S. M., Ruan, K. C., Qian, J. F., Shao, G. Q., and Balny, C. (2000). Effects of hydrostatic pressure on the structure and biological activity of infectious bursal disease virus. *Eur. J. Biochem.*, 267(14):4486–4494.
- [Timasheff, 1998] Timasheff, S. (1998). Control of Protein Stability and Reactions by Weakly Interacting Cosolvents: The Simplicity of the Complicated. *Adv. Protein. Chem.*, 51:355–432.
- [Timasheff, 1993] Timasheff, S. N. (1993). The Control of Protein Stability and Association by Weak Interactions with Water: How Do Solvents Affect These Processes? *Annu. Rev. Biophys. Biomol. Struct.*, 22(1):67–97.
- [Timasheff, 2002] Timasheff, S. N. (2002). Protein-solvent preferential interactions, protein hydration, and the modulation of biochemical reactions by solvent components. *Proc. Natl. Acad. Sci. USA*, 99(15):9721–9726.
- [Timasheff and Xie, 2003] Timasheff, S. N. and Xie, G. (2003). Preferential interactions of urea with lysozyme and their linkage to protein denaturation. *Biophys. Chem.*, 105(2-3):421–448.
- [Tobias and Hemminger, 2008] Tobias, D. J. and Hemminger, J. C. (2008). Getting Specific About Specific Ion Effects. *Science*, 319:1197–1199.
- [Tokuriki et al., 2004] Tokuriki, N., Kinjo, M., Negi, S., Hoshino, M., Goto, Y., Urabe, I., and Yomo, T. (2004). Protein folding by the effects of macromolecular crowding. *Protein Sci.*, 13(1):125–33.
- [Tong et al., 1990] Tong, P., Witten, T. A., Huang, J. S., and Fetters, L. J. (1990). Interactions in mixtures of colloid and polymers. *J. Phys. France*, 51(24):2813–2827.
- [Torrent et al., 2015] Torrent, J., Lange, R., and Rezaei, H. (2015). The volumetric diversity of misfolded prion protein oligomers revealed by pressure dissociation. *J. Biol. Chem.*, 290(33):20417–20426.
- [Totani et al., 2008] Totani, K., Ihara, Y., Matsuo, I., and Ito, Y. (2008). Effects of macromolecular crowding on glycoprotein processing enzymes. *J. Am. Chem. Soc.*, 130(6):2101–2107.
- [Towey et al., 2013] Towey, J. J., Soper, A. K., and Dougan, L. (2013). What happens to the structure of water in cryoprotectant solutions? *Faraday Discuss.*, 167:159–176.
- [Trovasset et al., 2003] Trovasset, M., Dallet-choisy, S., Meersman, F., Heremans, K., Balny, C., and Legoy, M. D. (2003). Fluorescence and FTIR study of pressure-induced structural modifications of horse liver alcohol dehydrogenase (HLADH). *Eur. J. Biochem.*, 270(1):119–128.
- [Tubio et al., 2004] Tubio, G., Nerli, B., and Picó, G. (2004). Relationship between the protein surface hydrophobicity and its partitioning behaviour in aqueous two-phase systems of polyethyleneglycol-dextran. *J. Chromatogr. B*, 799(2):293–301.
- [Tuinier et al., 2003] Tuinier, R., Rieger, J., and De Kruif, C. G. (2003). Depletion-induced phase separation in colloid-polymer mixtures. *Adv. Colloid Interface Sci.*, 103(1):1–31.
- [Tyree et al., 2018] Tyree, T. J., Dan, R., and Thorne, R. E. (2018). Density and electron density of aqueous cryoprotectant solutions at cryogenic temperatures for optimized cryoprotection and diffraction contrast. *Acta Cryst. D*, 74(5):471–479.
- [Ueda et al., 2001] Ueda, T., Nagata, M., and Imoto, T. (2001). Aggregation and chemical reaction in hen lysozyme caused by heating at pH 6 are depressed by osmolytes, sucrose and trehalose. *J. Biochem.*, 130(4):491–496.

- [Uversky et al., 2002] Uversky, V., Cooper, E., Bower, K., Li, J., and Fink, A. (2002). Accelerated alpha-synuclein fibrillation in crowded milieu. *FEBS Lett.*, 515(1-3):99–103.
- [van den Berg et al., 1999] van den Berg, B., Ellis, R. J., and Dobson, C. M. (1999). Effects of macromolecular crowding on protein folding and aggregation. *EMBO J.*, 18(24):6927–6933.
- [van den Berg et al., 2000] van den Berg, B., Wain, R., Dobson, C. M., and Ellis, R. J. (2000). Macromolecular crowding perturbs protein refolding kinetics: implications for folding inside the cell. *EMBO J.*, 19(15):3870–3875.
- [Vanlint et al., 2011] Vanlint, D., Mitchell, R., Bailey, E., Meersman, F., McMillan, P., Michiels, C., and Aertsen, A. (2011). Rapid Acquisition of Gigapascal-High-Pressure Resistance by *Escherichia coli*. *mBio*, 2(1):e00130–10.
- [Vargas-Ortiz et al., 2013] Vargas-Ortiz, M. A., Quintana-Castro, R., Oliart-Ros, R. M., De la Cruz-Medina, J., Ramírez de León, J. A., and Garcia, H. S. (2013). High hydrostatic pressure induces synthesis of heat-shock proteins and trehalose-6-phosphate synthase in *Anastrepha ludens* larvae. *Arch. Insect Biochem. Physiol.*, 82(4):196–212.
- [Vekilov, 2004] Vekilov, P. G. (2004). Dense liquid precursor for the nucleation of ordered solid phases from solution. *Cryst. Growth and Des.*, 4(4):671–685.
- [Velev et al., 1998] Velev, O. D., Kaler, E. W., and Lenhoff, A. M. (1998). Protein interactions in solution characterized by light and neutron scattering: comparison of lysozyme and chymotrypsinogen. *Biophys. J.*, 75(6):2682–2697.
- [Venkataramani et al., 2013] Venkataramani, S., Truntzer, J., and Coleman, D. R. (2013). Thermal stability of high concentration lysozyme across varying pH: A Fourier Transform Infrared study. *J. Pharm. Bioallied Sci.*, 5(2):148–153.
- [Venturoli and Rippe, 2005] Venturoli, D. and Rippe, B. (2005). Ficoll and dextran vs. globular proteins as probes for testing glomerular permselectivity: effects of molecular size, shape, charge, and deformability. *Am. J. Physiol.-Renal Physiol.*, 288(4):F605–F613.
- [Vergara et al., 2006] Vergara, A., Capuano, F., Paduano, L., and Sartorio, R. (2006). Lysozyme mutual diffusion in solutions crowded by poly(ethylene glycol). *Macromolecules*, 39(13):4500–4506.
- [Verwey and Overbeek, 1948] Verwey, E. J. W. and Overbeek, J. T. G. (1948). *Theory of the stability of lyophobic colloids*. Elsevier Inc., New York.
- [Vivarès et al., 2002] Vivarès, D., Belloni, L., Tardieu, A., and Bonneté, F. (2002). Catching the PEG-induced attractive interaction between proteins. *Eur. Phys. J. E*, 9(1):15–25.
- [Vivarès and Bonneté, 2004] Vivarès, D. and Bonneté, F. (2004). Liquid-Liquid Phase Separations in Urate Oxidase/PEG Mixtures: Characterization and Implications for Protein Crystallization. *J. Phys. Chem. B*, 108(20):6498–6507.
- [Vliegenthart and Lekkerkerker, 2000] Vliegenthart, G. A. and Lekkerkerker, H. N. W. (2000). Predicting the gas-liquid critical point from the second virial coefficient. *J. Chem. Phys.*, 112(12):5364–5369.
- [Voet and Voet, 1990] Voet, D. and Voet, J. (1990). *Biochemistry*. Wiley, New York.
- [Vrij, 1976] Vrij, A. (1976). Polymers at Interfaces and the Interactions in Colloidal Dispersions. *Pure & Appl. Chem.*, 48(4):471–483.
- [Waghmare et al., 2000] Waghmare, R. Y., Webb, J. N., Randolph, T. W., Larson, M. A., and Glatz, C. E. (2000). Pressure dependence of subtilisin crystallization kinetics. *J. Cryst. Growth*, 208(1):678–686.

- [Wallqvist et al., 1998] Wallqvist, A., Covell, D. G., and Thirumalai, D. (1998). Hydrophobic Interactions in Aqueous Urea Solutions with Implications for the Mechanism of Protein Denaturation. *J. Am. Chem. Soc.*, 120(2):427–428.
- [Walter, 1999] Walter, H. (1999). Consequences of phase separation in cytoplasm. *Int. Rev. Cytol.*, 192:331–343.
- [Walter and Brooks, 1995] Walter, H. and Brooks, D. E. (1995). Phase separation in cytoplasm, due to macromolecular crowding, is the basis for microcompartmentation. *FEBS Lett.*, 361(2-3):135–139.
- [Wang and Bolen, 1997] Wang, A. and Bolen, D. W. (1997). A Naturally Occurring Protective System in Urea-Rich Cells: Mechanism of Osmolyte Protection of Proteins against Urea Denaturation. *Biochemistry*, 36(30):9101–9108.
- [Wang et al., 2000] Wang, B. N., Han, B. X., and Tan, F. (2000). Effect of Solution pH and Composition on Horse Liver Alcohol Dehydrogenase Thermostability. *J. Therm. Anal. Calorim.*, 62(1):317–324.
- [Wang and Sun, 2017] Wang, H.-l. and Sun, L. (2017). Comparative metagenomics reveals insights into the deep-sea adaptation mechanism of the microorganisms in Iheya hydrothermal fields. *World J. Microbiol. Biotechnol.*, 33(5):86.
- [Wang et al., 2017] Wang, P.-h., Yu, I., Feig, M., and Sugita, Y. (2017). Influence of protein crowder size on hydration structure and dynamics in macromolecular crowding. *Chem. Phys. Lett.*, 671:63–70.
- [Wang and Annunziata, 2007] Wang, Y. and Annunziata, O. (2007). Comparison between Protein-Polyethylene Glycol (PEG) interactions and the Effect of PEG on Protein-Protein Interactions using the Liquid-Liquid Phase Transition. *J. Phys. Chem. B*, 111(5):1222–1230.
- [Wang et al., 2012] Wang, Y., Benton, L. A., Singh, V., and Pielak, G. J. (2012). Disordered protein diffusion under crowded conditions. *J. Phys. Chem. Lett.*, 3(18):2703–2706.
- [Wanka and Peukert, 2011] Wanka, J. and Peukert, W. (2011). Optimized production of protein crystals: From 1D crystallization slot towards 2D supersaturation B22 diagram. *Chem. Eng. Technol.*, 34(4):510–516.
- [Webb et al., 1999] Webb, J. N., Waghmare, R. Y., Carpenter, J. F., Glatz, C. E., and Randolph, T. W. (1999). Pressure effect on subtilisin crystallization and solubility. *J. Cryst. Growth*, 205:563–574.
- [Webb et al., 2001] Webb, J. N., Webb, S. D., Cleland, J. L., Carpenter, J. F., and Randolph, T. W. (2001). Partial molar volume, surface area, and hydration changes for equilibrium unfolding and formation of aggregation transition state: High-pressure and cosolute studies on recombinant human IFN- $\gamma$ . *Proc. Natl. Acad. Sci. USA*, 98(13):7259–7264.
- [Weber, 1986] Weber, G. (1986). Phenomenological description of the association of protein subunits subjected to conformational drift. Effects of dilution and of hydrostatic pressure. *Biochemistry*, 25(12):3626–3631.
- [Weber, 1993] Weber, G. (1993). Thermodynamics of the association and the pressure dissociation of oligomeric proteins. *J. Phys. Chem.*, 97(27):7108–7115.
- [Weck et al., 2009] Weck, G., Eggert, J., Loubeyre, P., Desbiens, N., Bourasseau, E., Maillet, J.-B., Mezouar, M., and Hanfland, M. (2009). Phase diagrams and isotopic effects of normal and deuterated water studied via x-ray diffraction up to 4.5 GPa and 500 K. *Phys. Rev. B*, 80(18):180202.
- [Wei et al., 2010] Wei, H., Fan, Y., and Gao, Y. Q. (2010). Effects of Urea, Tetramethyl Urea, and Trimethylamine N-Oxide on Aqueous Solution Structure and Solvation of Protein Backbones: A Molecular Dynamics Simulation Study. *J. Phys. Chem. B*, 114(1):557–568.

- [Wenner and Bloomfield, 1999] Wenner, J. R. and Bloomfield, V. a. (1999). Crowding effects on EcoRV kinetics and binding. *Biophys. J.*, 77(6):3234–3241.
- [Wharton, 2002] Wharton, D. (2002). *Life at the Limits: Organisms in extreme environments*. Cambridge University Press, Cambridge.
- [Wilbur et al., 1976] Wilbur, D. J., DeFries, T., and Jonas, J. (1976). Self-diffusion in compressed liquid heavy water. *J. Chem. Phys.*, 65(5):1783–1786.
- [Wilf and Minton, 1981] Wilf, J. and Minton, A. P. (1981). Evidence for protein self-association induced by excluded volume. Myoglobin in the presence of globular proteins. *Biochim. Biophys. Acta*, 670(3):316–322.
- [Winter et al., 2007] Winter, R., Lopes, D., Grudzielanek, S., and Vogtt, K. (2007). Towards an Understanding of the Temperature / Pressure Configurational and Free-Energy Landscape of Biomolecules. *J. Non-Equilib. Thermodyn.*, 32(1):41–97.
- [Wirkert, 2015] Wirkert, F. J. (2015). *Die hydrophobe fest-flüssig-Grenzfläche unter hohem hydrostatischen Druck*. Phd thesis, TU Dortmund.
- [Wirkert et al., 2014] Wirkert, F. J., Paulus, M., Nase, J., Möller, J., Kujawski, S., Sternemann, C., and Tolan, M. (2014). X-ray reflectivity measurements of liquid/solid interfaces under high hydrostatic pressure conditions. *J. Synchrotron Radiat.*, 21(1):76–81.
- [Withers et al., 1994a] Withers, C., Morisson, G., and Guppy, M. (1994a). Buoyancy Role of Urea and TMAO in an Elasmobranch Fish, the Port Jackson Shark, *Heterodontus portusjacksoni*. *Physiol. Zool.*, 67(3):693–705.
- [Withers et al., 1994b] Withers, P. C., Morrison, G., Hefter, G. T., and Pang, T.-S. (1994b). Role of Urea and Methylamines in Buoyancy of Elasmobranchs. *J. Exp. Biol.*, 188:175–189.
- [Wong et al., 2016] Wong, K. H., Sandlin, R. D., Carey, T. R., Miller, K. L., Shank, A. T., Oklu, R., Maheswaran, S., Haber, D. A., Irimia, D., Stott, S. L., and Toner, M. (2016). The Role of Physical Stabilization in Whole Blood Preservation. *Sci. Rep.*, 6:1–9.
- [Wroblowski et al., 1996] Wroblowski, B., Diaz, J. F., Heremans, K., and Engelborghs, Y. (1996). Molecular mechanisms of pressure induced conformational changes in BPTI. *Proteins*, 25(4):446–455.
- [Wu et al., 2014a] Wu, J., Zhao, C., Hu, R., Lin, W., Wang, Q., Zhao, J., Bilinovich, S. M., Leeper, T. C., Li, L., Cheung, H. M., Chen, S., and Zheng, J. (2014a). Probing the weak interaction of proteins with neutral and zwitterionic antifouling polymers. *Acta Biomater.*, 10(2):751–760.
- [Wu et al., 2014b] Wu, J., Zhao, C., Lin, W., Hu, R., Wang, Q., Chen, H., Li, L., Chen, S., and Zheng, J. (2014b). Binding characteristics between polyethylene glycol (PEG) and proteins in aqueous solution. *J. Mater. Chem. B.*, 2(20):2983–2992.
- [Wyman, 1936] Wyman, J. (1936). The Dielectric Constant of Solutions of Dipolar Ions. *Chem. Rev.*, 19(3):213–239.
- [Wyman and McMeekin, 1933] Wyman, J. and McMeekin, T. L. (1933). The Dielectric Constant of Solutions of Amino Acids and Peptides. *J. Am. Chem. Soc.*, 55(3):908–914.
- [Xie and Timasheff, 1997] Xie, G. and Timasheff, S. N. (1997). The thermodynamic mechanism of protein stabilization by trehalose. *Biophys. Chem.*, 64(1-3):25–43.
- [Yancey, 2005] Yancey, P. H. (2005). Organic osmolytes as compatible, metabolic and counteracting cytoprotectants in high osmolarity and other stresses. *J. Exp. Biol.*, 208(Pt 15):2819–2830.
- [Yancey et al., 2002] Yancey, P. H., Blake, W. R., and Conley, J. (2002). Unusual organic osmolytes in deep-sea animals: Adaptations to hydrostatic pressure and other perturbants. *Comp. Biochem. Physiol. A*, 133(3):667–676.



- [Yancey et al., 1982] Yancey, P. H., Clark, M. E., Hand, S. C., Bowlus, R. D., and Somero, G. N. (1982). Living with Water Stress: Evolution of Osmolyte Systems. *Science*, 217:1214–1222.
- [Yancey et al., 2001] Yancey, P. H., Fyfe-Johnson, A. L., Kelly, R. H., Walker, V. P., and Aun, M. T. (2001). Trimethylamine oxide counteracts effects of hydrostatic pressure on proteins of deep-sea teleosts. *J. Exp. Zool.*, 289(3):172–176.
- [Yancey and Siebenaller, 1999] Yancey, P. H. and Siebenaller, J. F. (1999). Trimethylamine oxide stabilizes teleost and mammalian lactate dehydrogenases against inactivation by hydrostatic pressure and trypsinolysis. *J. Exp. Biol.*, 202(24):3597–3603.
- [Yancey and Siebenaller, 2015] Yancey, P. H. and Siebenaller, J. F. (2015). Co-evolution of proteins and solutions: protein adaptation versus cytoprotective micromolecules and their roles in marine organisms. *J. Exp. Biol.*, 218:1880–1896.
- [Yancey and Somero, 1979] Yancey, P. H. and Somero, G. N. (1979). Counteraction of urea destabilization of protein structure by methylamine osmoregulatory compounds of elasmobranch fishes. *Biochem. J.*, 183(2):317–323.
- [Yancey and Somero, 1980] Yancey, P. H. and Somero, G. N. (1980). Methylamine osmoregulatory solutes of elasmobranch fishes counteract urea inhibition of enzymes. *J. Exp. Zool.*, 212(2):205–213.
- [Ye et al., 1996] Ye, X., Narayanan, T., Tong, P., Huang, J., Lin, M., Carvalho, B., and Fetters, L. (1996). Depletion interactions in colloid-polymer mixtures. *Phys. Rev. E*, 54(6):6500–6510.
- [Yeomans, 1992] Yeomans, J. (1992). *Statistical Mechanics of Phase Transitions*. Oxford University Press Inc., New York.
- [Yu et al., 2015] Yu, G., Liu, J., and Zhou, J. (2015). Mesoscopic Coarse-Grained Simulations of Hydrophobic Charge Induction Chromatography (HCIC) for Protein Purification. *AIChE J.*, 61(6):2035–2047.
- [Zaslavsky et al., 1989] Zaslavsky, B. Y., Miheeva, L. M., Rodnikova, M. N., Spivak, G. V., Harkin, V. S., and Mahmudov, A. U. (1989). Dielectric properties of water in the coexisting phases of aqueous polymeric two-phase systems. *J. Chem. Soc. Faraday Trans.*, 85(9):2857–2865.
- [Zhang et al., 2006] Zhang, D., Carignano, M. A., and Szleifer, I. (2006). Cluster Structure and Corraling Effect Driven by Interaction Mismatch in Two Dimensional Mixtures. *Phys. Rev. Lett.*, 96(2):028701.
- [Zhang et al., 2012a] Zhang, D. L., Wu, L. J., Chen, J., and Liang, Y. (2012a). Effects of macromolecular crowding on the structural stability of human  $\alpha$ -lactalbumin. *Acta Biochimica Biophys. Sin.*, 44(8):703–711.
- [Zhang et al., 2012b] Zhang, F., Roosen-Runge, F., Skoda, M. W., Jacobs, R. M., Wolf, M., Callow, P., Frielinghaus, H., Pipich, V., Prévost, S., and Schreiber, F. (2012b). Hydration and interactions in protein solutions containing concentrated electrolytes studied by small-angle scattering. *Phys. Chem. Chem. Phys.*, 14(7):2483–2493.
- [Zhang et al., 2012c] Zhang, F., Roth, R., Wolf, M., Roosen-Runge, F., Skoda, M. W., Jacobs, R. M., Stzucki, M., and Schreiber, F. (2012c). Charge-controlled metastable liquid-liquid phase separation in protein solutions as a universal pathway towards crystallization. *Soft Matter*, 8(5):1313–1316.
- [Zhang et al., 2007] Zhang, F., Skoda, M. W. A., Jacobs, R. M. J., Martin, R. A., Martin, C. M., and Schreiber, F. (2007). Protein interactions studied by SAXS: Effect of ionic strength and protein concentration for BSA in aqueous solutions. *J. Phys. Chem. B*, 111(1):251–259.
- [Zhang and Cremer, 2009] Zhang, Y. and Cremer, P. (2009). The inverse and direct Hofmeister series for lysozyme. *Proc. Natl. Acad. Sci. USA*, 106(36):15249–15253.

- [Zhang and Cremer, 2010] Zhang, Y. and Cremer, P. S. (2010). Chemistry of Hofmeister Anions and Osmolytes. *Annu. Rev. Phys. Chem.*, 61(1):63–83.
- [Zhang et al., 2005] Zhang, Y., Furyk, S., Bergbreiter, D. E., and Cremer, P. S. (2005). Specific ion effects on the water solubility of macromolecules: PNIPAM and the Hofmeister series. *J. Am. Chem. Soc.*, 127(41):14505–14510.
- [Zhou et al., 2004] Zhou, B. R., Liang, Y., Du, F., Zhou, Z., and Chen, J. (2004). Mixed macromolecular crowding accelerates the oxidative refolding of reduced, denatured lysozyme: Implications for protein folding in intracellular environments. *J. Biol. Chem.*, 279(53):55109–55116.
- [Zhou, 2008] Zhou, H. X. (2008). Protein folding in confined and crowded environments. *Arch. Biochem. Biophys.*, 469(1):76–82.
- [Zhou et al., 2011] Zhou, Z., Yan, X., Pan, K., Chen, J., Xie, Z. S., Xiao, G. F., Yang, F. Q., and Liang, Y. (2011). Fibril formation of the rabbit/human/bovine prion proteins. *Biophys. J.*, 101(6):1483–1492.
- [Ziebacz et al., 2011] Ziebacz, N., Wiczorek, S. A., Kalwarczyk, T., Fiałkowski, M., and Hołyst, R. (2011). Crossover regime for the diffusion of nanoparticles in polyethylene glycol solutions: Influence of the depletion layer. *Soft Matter*, 7(16):7181–7186.
- [Zimmerman and Minton, 1993] Zimmerman, S. B. and Minton, A. P. (1993). Macromolecular Crowding: Biochemical, Biophysical, and Physiological Consequences. *Annu. Rev. Biophys. Biomol. Struct.*, 22:27–65.
- [Zimmerman and Trach, 1991] Zimmerman, S. B. and Trach, S. O. (1991). Estimation of macromolecule concentrations and excluded volume effects for the cytoplasm of *Escherichia coli*. *J. Mol. Biol.*, 222(3):599–620.
- [Zou et al., 2002] Zou, Q., Bennion, B. J., Daggett, V., and Murphy, K. P. (2002). The molecular mechanism of stabilization of proteins by TMAO and its ability to counteract the effects of urea. *J. Am. Chem. Soc.*, 124(7):1192–1202.
- [Zwicker et al., 2017] Zwicker, D., Seyboldt, R., Weber, C. A., Hyman, A. A., and Jülicher, F. (2017). Growth and division of active droplets provides a model for protocells. *Nature Physics*, 13(4):408–413.

# Acknowledgments

First, I would like to thank Prof. Roland Winter not only for co-supervising my thesis but also for the grand support and advice in publishing our research. I would like to thank Prof. Metin Tolan for the opportunity to write my thesis at the chair E IA and for giving me so much freedom in the design and performance of the research. I would like to thank Michael Paulus and Christian Sternemann for the supervision and the many lessons I learned throughout my time at the chair E IA. Further, I want to thank Michael Paulus for proof-reading this thesis. I thank Martin A. Schroer for his interest in my projects, his support and valuable professional input. I would like to thank Johannes Möller for making the 3-month internship abroad at ID02 (ESRF, Grenoble) possible for me and the great support as a beamline scientist on site. I want to thank Jonathan Weine for the nice company and his moral and experimental support in the lab and during numerous beam times. I thank Mirko Elbers for being the perfect colleague to me in good and hard times and for the wonderful atmosphere in our office. I want to thank Karin Esch for the numerous coffee breaks I enjoyed a lot. I would like to thank Thorsten Witt for the good company and helping me numerous times with everything in the broadest sense software- and hardware-related. I want to thank all persons who helped during the beam times, namely Jonathan Weine, Mirko Elbers, Melanie Berghaus, Mimi Gao, Jan Latarius, Nico König, Michael Paulus and all others who I may have forgotten. Further, I thank Miren Büyükasik, Anna Ott, Thomas Ato and Alina Sparenberg for experimental support during turbidity and density measurements. The synchrotrons ESRF, DLS, DELTA, PETRA III and SOLEIL as well as the FZ Jülich, GALAXI are kindly acknowledged for providing X-ray radiation and access to their facilities. The local contacts Javier Perez (SWING, Soleil), Wiebke Ohm (P03, PETRA III), Andy Smith (I22, DLS), Emmanuel Kentzinger and Margarita Krutyeva (GALAXI, FZ Jülich) and Ralph Wagner (BL8, DELTA) are kindly acknowledged for assistance during beam times. Furthermore, I thank all former and present members of the chair E IA for help and a nice atmosphere within office hours, beam times, and extra-curricular events. The Cluster of Excellence RESOLV (EXC 1069) funded by the DFG is gratefully acknowledged for financial support.

Last but not least, I would like to thank my family for their encouragement, love and support. Without them this work would not have been possible.

# Publications

## Publications related to this thesis:

Julius, K., Al-Ayoubi, S.R., Paulus, M., Tolan, M., and Winter, R., (2018). The effects of osmolytes and crowding on the pressure-induced dissociation and inactivation of dimeric LADH., *Phys. Chem. Chem. Phys.*, 20(10):7093-7104

Julius, K., Weine, J., Berghaus, M., König, N., Gao, M., Latarius, J., Paulus, M., Schroer, M.A., Tolan, M., and Winter, R., (2018). Water-Mediated Protein-Protein Interactions at High Pressures are Controlled by a Deep-Sea Osmolyte., *Phys. Rev. Lett.*, 121(3):038101

Julius, K., Weine, J., Gao, M., Latarius, J., Elbers, M., Paulus, M., Tolan, M., and Winter, R., (2019). Impact of Macromolecular Crowding and Compression on Protein-Protein Interactions and Liquid-Liquid Phase Separation Phenomena., *Macromolecules*, 52(4):1772-1784

## Conference Contributions:

Julius, K., Weine, J., Berghaus, M., König, N., Gao, M., Latarius, J., Paulus, M., Schroer, M.A., Tolan, M., and Winter, R., Modulation of Protein-Protein Interactions by Cosolvent Mixtures of Extremophiles - the Unique Role of TMAO. *RESOLV Klausurtagung 2018*, 19<sup>th</sup> - 21<sup>th</sup> of March 2018, Velen (Germany) - **Talk**

Julius, K., Paulus, M., Berghaus, M., König, N., Tolan, M., and Winter, R., Impact of Osmotic Stress and Excluded Volume on Protein-Protein Interactions at High Hydrostatic Pressure. *The 4th International Soft Matter Conference (ISMC2016)*, 12<sup>th</sup> -16<sup>th</sup> of September 2016, Grénoble (France) – **Poster**

## Further Publications

Lehmkühler, F., Forov, Y., Büning, T., Sahle, C. J., Steinke, I., Julius, K., Buslaps, T., Tolan, M., Hakala, M., and Sternemann, C., (2016) Intramolecular structure and energetics in supercooled water down to 255 K., *Phys. Chem. Chem. Phys.*, 18(9):6925-6930

Schulze, J., Möller, J., Weine, J., Julius, K., König, N., Nase, J., Paulus, M., Tolan, M., and Winter, R., (2016). Phase behavior of lysozyme solutions in the liquid-liquid phase coexistence region at high hydrostatic pressures., *Phys. Chem. Chem. Phys.*, 18(21):14252-14256

König, N., Paulus, M., Julius, K., Schulze, J., Voetz, M., and Tolan, M. (2017). Antibodies under pressure: A Small-Angle X-ray Scattering study of Immunoglobulin G under high hydrostatic pressure., *Biophys. Chem.*, 231:45-49

Gao, M., Berghaus, M., Möbitz, S., Schuabb, V., Erwin, N., Herzog, M., Julius, K., Sternemann, C., and Winter, R., (2018). On the Origin of Microtubules' High-Pressure Sensitivity., *Biophys. J.*, 114(5):1080-1090

# Eidesstattliche Erklärung

Ich erkläre hiermit an Eides statt, dass ich die vorliegende Dissertation mit dem Titel 'Impact of Organic Osmolytes and Crowding on the Protein-Protein Interaction at High Pressures - A Small-Angle X-ray Scattering Study' selbstständig und ohne unzulässige Hilfe angefertigt habe. Ich habe keine anderen als die angegebenen Quellen und Hilfsmittel verwendet sowie wörtliche und sinngemäße Zitate kenntlich gemacht. Die Arbeit wurde weder ganz noch in Teilen an anderer Stelle im Rahmen eines Prüfungsverfahrens vorgelegt.

---

Ort, Datum

---

Unterschrift





**Confirmation Number: 11808108**  
**Order Date: 04/17/2019**

### Customer Information

**Customer:** Karin Julius  
**Account Number:** 3001422432  
**Organization:** Karin Julius  
**Email:** karin.julius@tu-dortmund.de  
**Phone:** +49 22646575  
**Payment Method:** Invoice

**This is not an invoice**

### Order Details

**The biological bulletin**

Billing Status:  
**N/A**

**Order detail ID:** 71879006  
**ISSN:** 0006-3185  
**Publication Type:** Journal  
**Volume:**  
**Issue:**  
**Start page:**  
**Publisher:** LANCASTER PRESS, INC. [ETC.]  
**Author/Editor:** MARINE BIOLOGICAL LABORATORY (WOODS HOLE, MASS.) ; MARINE BIOLOGICAL LABORATORY (WOODS HOLE, MASS.)

**Permission Status:** **Granted**  
**Permission type:** Republish or display content  
**Type of use:** Thesis/Dissertation  
**Order License Id:** 4571211081461

<b>Requestor type</b>	Academic institution
<b>Format</b>	Print, Electronic
<b>Portion</b>	chart/graph/table/figure
<b>Number of charts/graphs/tables/figures</b>	1
<b>The requesting person/organization</b>	Karin Julius
<b>Title or numeric reference of the portion(s)</b>	Figure 2
<b>Title of the article or chapter the portion is from</b>	High contents of trimethylamine oxide correlating with depth in deep-sea teleost fishes, skates, and decapod crustaceans.
<b>Editor of portion(s)</b>	N/A
<b>Author of portion(s)</b>	Yancey, P H ; Kelly, R H
<b>Volume of serial or monograph</b>	196
<b>Issue, if republishing an article from a serial</b>	1
<b>Page range of portion</b>	22
<b>Publication date of portion</b>	Feb 1, 1999
<b>Rights for</b>	Main product
<b>Duration of use</b>	Life of current edition
<b>Creation of copies for the disabled</b>	no
<b>With minor editing privileges</b>	no
<b>For distribution to</b>	Worldwide
<b>In the following language(s)</b>	Original language of publication
<b>With incidental promotional use</b>	no
	Up to 499

**Lifetime unit quantity  
of new product**

**Title**

Impact of Organic  
Osmolytes and Crowding  
on the Protein-Protein  
Interaction at High  
Pressures - A Small-Angle  
X-ray Scattering Study

**Institution name**

TU Dortmund University

**Expected presentation  
date**

Apr 2019

**Note:** This item was invoiced separately through our **RightsLink service.** [More info](#)

**\$ 0.00**

---

**Total order items: 1**

**Order Total: \$0.00**

[About Us](#) | [Privacy Policy](#) | [Terms & Conditions](#) | [Pay an Invoice](#)

Copyright 2019 Copyright Clearance Center

**JOHN WILEY AND SONS LICENSE  
TERMS AND CONDITIONS**

Apr 17, 2019

---

This Agreement between Ms. Karin Julius ("You") and John Wiley and Sons ("John Wiley and Sons") consists of your license details and the terms and conditions provided by John Wiley and Sons and Copyright Clearance Center.

License Number	4571201234512
License date	Apr 17, 2019
Licensed Content Publisher	John Wiley and Sons
Licensed Content Publication	Angewandte Chemie
Licensed Content Title	Exploring the Piezophilic Behavior of Natural Cosolvent Mixtures
Licensed Content Author	Martin A. Schroer, Yong Zhai, D. C. Florian Wieland, et al
Licensed Content Date	Oct 6, 2011
Licensed Content Volume	123
Licensed Content Issue	48
Licensed Content Pages	4
Type of use	Dissertation/Thesis
Requestor type	University/Academic
Format	Print and electronic
Portion	Figure/table
Number of figures/tables	1
Original Wiley figure/table number(s)	Figure 3
Will you be translating?	No
Title of your thesis / dissertation	Impact of Organic Osmolytes and Crowding on the Protein-Protein Interaction at High Pressures - A Small-Angle X-ray Scattering Study
Expected completion date	Apr 2019
Expected size (number of pages)	209
Requestor Location	Ms. Karin Julius Zum Schlahn 22  Marienheide, NRW 51709 Germany Attn: Ms. Karin Julius
Publisher Tax ID	EU826007151
Total	0.00 EUR
Terms and Conditions	

**TERMS AND CONDITIONS**

This copyrighted material is owned by or exclusively licensed to John Wiley & Sons, Inc. or one of its group companies (each a "Wiley Company") or handled on behalf of a society with which a Wiley Company has exclusive publishing rights in relation to a particular work

(collectively "WILEY"). By clicking "accept" in connection with completing this licensing transaction, you agree that the following terms and conditions apply to this transaction (along with the billing and payment terms and conditions established by the Copyright Clearance Center Inc., ("CCC's Billing and Payment terms and conditions"), at the time that you opened your RightsLink account (these are available at any time at <http://myaccount.copyright.com>).

## Terms and Conditions

- The materials you have requested permission to reproduce or reuse (the "Wiley Materials") are protected by copyright.
- You are hereby granted a personal, non-exclusive, non-sub licensable (on a stand-alone basis), non-transferable, worldwide, limited license to reproduce the Wiley Materials for the purpose specified in the licensing process. This license, **and any CONTENT (PDF or image file) purchased as part of your order**, is for a one-time use only and limited to any maximum distribution number specified in the license. The first instance of republication or reuse granted by this license must be completed within two years of the date of the grant of this license (although copies prepared before the end date may be distributed thereafter). The Wiley Materials shall not be used in any other manner or for any other purpose, beyond what is granted in the license. Permission is granted subject to an appropriate acknowledgement given to the author, title of the material/book/journal and the publisher. You shall also duplicate the copyright notice that appears in the Wiley publication in your use of the Wiley Material. Permission is also granted on the understanding that nowhere in the text is a previously published source acknowledged for all or part of this Wiley Material. Any third party content is expressly excluded from this permission.
- With respect to the Wiley Materials, all rights are reserved. Except as expressly granted by the terms of the license, no part of the Wiley Materials may be copied, modified, adapted (except for minor reformatting required by the new Publication), translated, reproduced, transferred or distributed, in any form or by any means, and no derivative works may be made based on the Wiley Materials without the prior permission of the respective copyright owner. **For STM Signatory Publishers clearing permission under the terms of the [STM Permissions Guidelines](#) only, the terms of the license are extended to include subsequent editions and for editions in other languages, provided such editions are for the work as a whole in situ and does not involve the separate exploitation of the permitted figures or extracts**, You may not alter, remove or suppress in any manner any copyright, trademark or other notices displayed by the Wiley Materials. You may not license, rent, sell, loan, lease, pledge, offer as security, transfer or assign the Wiley Materials on a stand-alone basis, or any of the rights granted to you hereunder to any other person.
- The Wiley Materials and all of the intellectual property rights therein shall at all times remain the exclusive property of John Wiley & Sons Inc, the Wiley Companies, or their respective licensors, and your interest therein is only that of having possession of and the right to reproduce the Wiley Materials pursuant to Section 2 herein during the continuance of this Agreement. You agree that you own no right, title or interest in or to the Wiley Materials or any of the intellectual property rights therein. You shall have no rights hereunder other than the license as provided for above in Section 2. No right, license or interest to any trademark, trade name, service mark or other branding ("Marks") of WILEY or its licensors is granted hereunder, and you agree that you shall

not assert any such right, license or interest with respect thereto

- NEITHER WILEY NOR ITS LICENSORS MAKES ANY WARRANTY OR REPRESENTATION OF ANY KIND TO YOU OR ANY THIRD PARTY, EXPRESS, IMPLIED OR STATUTORY, WITH RESPECT TO THE MATERIALS OR THE ACCURACY OF ANY INFORMATION CONTAINED IN THE MATERIALS, INCLUDING, WITHOUT LIMITATION, ANY IMPLIED WARRANTY OF MERCHANTABILITY, ACCURACY, SATISFACTORY QUALITY, FITNESS FOR A PARTICULAR PURPOSE, USABILITY, INTEGRATION OR NON-INFRINGEMENT AND ALL SUCH WARRANTIES ARE HEREBY EXCLUDED BY WILEY AND ITS LICENSORS AND WAIVED BY YOU.
- WILEY shall have the right to terminate this Agreement immediately upon breach of this Agreement by you.
- You shall indemnify, defend and hold harmless WILEY, its Licensors and their respective directors, officers, agents and employees, from and against any actual or threatened claims, demands, causes of action or proceedings arising from any breach of this Agreement by you.
- IN NO EVENT SHALL WILEY OR ITS LICENSORS BE LIABLE TO YOU OR ANY OTHER PARTY OR ANY OTHER PERSON OR ENTITY FOR ANY SPECIAL, CONSEQUENTIAL, INCIDENTAL, INDIRECT, EXEMPLARY OR PUNITIVE DAMAGES, HOWEVER CAUSED, ARISING OUT OF OR IN CONNECTION WITH THE DOWNLOADING, PROVISIONING, VIEWING OR USE OF THE MATERIALS REGARDLESS OF THE FORM OF ACTION, WHETHER FOR BREACH OF CONTRACT, BREACH OF WARRANTY, TORT, NEGLIGENCE, INFRINGEMENT OR OTHERWISE (INCLUDING, WITHOUT LIMITATION, DAMAGES BASED ON LOSS OF PROFITS, DATA, FILES, USE, BUSINESS OPPORTUNITY OR CLAIMS OF THIRD PARTIES), AND WHETHER OR NOT THE PARTY HAS BEEN ADVISED OF THE POSSIBILITY OF SUCH DAMAGES. THIS LIMITATION SHALL APPLY NOTWITHSTANDING ANY FAILURE OF ESSENTIAL PURPOSE OF ANY LIMITED REMEDY PROVIDED HEREIN.
- Should any provision of this Agreement be held by a court of competent jurisdiction to be illegal, invalid, or unenforceable, that provision shall be deemed amended to achieve as nearly as possible the same economic effect as the original provision, and the legality, validity and enforceability of the remaining provisions of this Agreement shall not be affected or impaired thereby.
- The failure of either party to enforce any term or condition of this Agreement shall not constitute a waiver of either party's right to enforce each and every term and condition of this Agreement. No breach under this agreement shall be deemed waived or excused by either party unless such waiver or consent is in writing signed by the party granting such waiver or consent. The waiver by or consent of a party to a breach of any provision of this Agreement shall not operate or be construed as a waiver of or consent to any other or subsequent breach by such other party.
- This Agreement may not be assigned (including by operation of law or otherwise) by you without WILEY's prior written consent.



- Any fee required for this permission shall be non-refundable after thirty (30) days from receipt by the CCC.
- These terms and conditions together with CCC's Billing and Payment terms and conditions (which are incorporated herein) form the entire agreement between you and WILEY concerning this licensing transaction and (in the absence of fraud) supersedes all prior agreements and representations of the parties, oral or written. This Agreement may not be amended except in writing signed by both parties. This Agreement shall be binding upon and inure to the benefit of the parties' successors, legal representatives, and authorized assigns.
- In the event of any conflict between your obligations established by these terms and conditions and those established by CCC's Billing and Payment terms and conditions, these terms and conditions shall prevail.
- WILEY expressly reserves all rights not specifically granted in the combination of (i) the license details provided by you and accepted in the course of this licensing transaction, (ii) these terms and conditions and (iii) CCC's Billing and Payment terms and conditions.
- This Agreement will be void if the Type of Use, Format, Circulation, or Requestor Type was misrepresented during the licensing process.
- This Agreement shall be governed by and construed in accordance with the laws of the State of New York, USA, without regards to such state's conflict of law rules. Any legal action, suit or proceeding arising out of or relating to these Terms and Conditions or the breach thereof shall be instituted in a court of competent jurisdiction in New York County in the State of New York in the United States of America and each party hereby consents and submits to the personal jurisdiction of such court, waives any objection to venue in such court and consents to service of process by registered or certified mail, return receipt requested, at the last known address of such party.

## **WILEY OPEN ACCESS TERMS AND CONDITIONS**

Wiley Publishes Open Access Articles in fully Open Access Journals and in Subscription journals offering Online Open. Although most of the fully Open Access journals publish open access articles under the terms of the Creative Commons Attribution (CC BY) License only, the subscription journals and a few of the Open Access Journals offer a choice of Creative Commons Licenses. The license type is clearly identified on the article.

### **The Creative Commons Attribution License**

The [Creative Commons Attribution License \(CC-BY\)](#) allows users to copy, distribute and transmit an article, adapt the article and make commercial use of the article. The CC-BY license permits commercial and non-

### **Creative Commons Attribution Non-Commercial License**

The [Creative Commons Attribution Non-Commercial \(CC-BY-NC\) License](#) permits use, distribution and reproduction in any medium, provided the original work is properly cited and is not used for commercial purposes.(see below)

### **Creative Commons Attribution-Non-Commercial-NoDerivs License**

The [Creative Commons Attribution Non-Commercial-NoDerivs License](#) (CC-BY-NC-ND) permits use, distribution and reproduction in any medium, provided the original work is properly cited, is not used for commercial purposes and no modifications or adaptations are made. (see below)

**Use by commercial "for-profit" organizations**

Use of Wiley Open Access articles for commercial, promotional, or marketing purposes requires further explicit permission from Wiley and will be subject to a fee.

Further details can be found on Wiley Online Library

<http://olabout.wiley.com/WileyCDA/Section/id-410895.html>

**Other Terms and Conditions:**

**v1.10 Last updated September 2015**

**Questions? [customercare@copyright.com](mailto:customercare@copyright.com) or +1-855-239-3415 (toll free in the US) or +1-978-646-2777.**

---

---



**Title:** Impact of Macromolecular  
Crowding and Compression on  
Protein–Protein Interactions and  
Liquid–Liquid Phase Separation  
Phenomena

**Author:** Karin Julius, Jonathan Weine,  
Mimi Gao, et al

**Publication:** Macromolecules

**Publisher:** American Chemical Society

**Date:** Feb 1, 2019

Copyright © 2019, American Chemical Society

Logged in as:

Karin Julius

LOGOUT

### PERMISSION/LICENSE IS GRANTED FOR YOUR ORDER AT NO CHARGE

This type of permission/license, instead of the standard Terms & Conditions, is sent to you because no fee is being charged for your order. Please note the following:

- Permission is granted for your request in both print and electronic formats, and translations.
- If figures and/or tables were requested, they may be adapted or used in part.
- Please print this page for your records and send a copy of it to your publisher/graduate school.
- Appropriate credit for the requested material should be given as follows: "Reprinted (adapted) with permission from (COMPLETE REFERENCE CITATION). Copyright (YEAR) American Chemical Society." Insert appropriate information in place of the capitalized words.
- One-time permission is granted only for the use specified in your request. No additional uses are granted (such as derivative works or other editions). For any other uses, please submit a new request.

BACK

CLOSE WINDOW

**JOHN WILEY AND SONS LICENSE  
TERMS AND CONDITIONS**

Apr 17, 2019

This Agreement between Ms. Karin Julius ("You") and John Wiley and Sons ("John Wiley and Sons") consists of your license details and the terms and conditions provided by John Wiley and Sons and Copyright Clearance Center.

License Number	4571250231019
License date	Apr 17, 2019
Licensed Content Publisher	John Wiley and Sons
Licensed Content Publication	ChemPhysChem
Licensed Content Title	Effect of Osmolytes on Pressure-Induced Unfolding of Proteins: A High-Pressure SAXS Study
Licensed Content Author	Christina Krywka, Christian Sternemann, Michael Paulus, et al
Licensed Content Date	Dec 15, 2008
Licensed Content Volume	9
Licensed Content Issue	18
Licensed Content Pages	7
Type of use	Dissertation/Thesis
Requestor type	University/Academic
Format	Print and electronic
Portion	Figure/table
Number of figures/tables	1
Original Wiley figure/table number(s)	Figure 1
Will you be translating?	No
Title of your thesis / dissertation	Impact of Organic Osmolytes and Crowding on the Protein-Protein Interaction at High Pressures - A Small-Angle X-ray Scattering Study
Expected completion date	Apr 2019
Expected size (number of pages)	209
Requestor Location	Ms. Karin Julius Zum Schlahn 22  Marienheide, NRW 51709 Germany Attn: Ms. Karin Julius
Publisher Tax ID	EU826007151
Total	0.00 EUR
Terms and Conditions	

**TERMS AND CONDITIONS**

This copyrighted material is owned by or exclusively licensed to John Wiley & Sons, Inc. or one of its group companies (each a "Wiley Company") or handled on behalf of a society with which a Wiley Company has exclusive publishing rights in relation to a particular work

(collectively "WILEY"). By clicking "accept" in connection with completing this licensing transaction, you agree that the following terms and conditions apply to this transaction (along with the billing and payment terms and conditions established by the Copyright Clearance Center Inc., ("CCC's Billing and Payment terms and conditions"), at the time that you opened your RightsLink account (these are available at any time at <http://myaccount.copyright.com>).

## Terms and Conditions

- The materials you have requested permission to reproduce or reuse (the "Wiley Materials") are protected by copyright.
- You are hereby granted a personal, non-exclusive, non-sub licensable (on a stand-alone basis), non-transferable, worldwide, limited license to reproduce the Wiley Materials for the purpose specified in the licensing process. This license, **and any CONTENT (PDF or image file) purchased as part of your order**, is for a one-time use only and limited to any maximum distribution number specified in the license. The first instance of republication or reuse granted by this license must be completed within two years of the date of the grant of this license (although copies prepared before the end date may be distributed thereafter). The Wiley Materials shall not be used in any other manner or for any other purpose, beyond what is granted in the license. Permission is granted subject to an appropriate acknowledgement given to the author, title of the material/book/journal and the publisher. You shall also duplicate the copyright notice that appears in the Wiley publication in your use of the Wiley Material. Permission is also granted on the understanding that nowhere in the text is a previously published source acknowledged for all or part of this Wiley Material. Any third party content is expressly excluded from this permission.
- With respect to the Wiley Materials, all rights are reserved. Except as expressly granted by the terms of the license, no part of the Wiley Materials may be copied, modified, adapted (except for minor reformatting required by the new Publication), translated, reproduced, transferred or distributed, in any form or by any means, and no derivative works may be made based on the Wiley Materials without the prior permission of the respective copyright owner. **For STM Signatory Publishers clearing permission under the terms of the [STM Permissions Guidelines](#) only, the terms of the license are extended to include subsequent editions and for editions in other languages, provided such editions are for the work as a whole in situ and does not involve the separate exploitation of the permitted figures or extracts**, You may not alter, remove or suppress in any manner any copyright, trademark or other notices displayed by the Wiley Materials. You may not license, rent, sell, loan, lease, pledge, offer as security, transfer or assign the Wiley Materials on a stand-alone basis, or any of the rights granted to you hereunder to any other person.
- The Wiley Materials and all of the intellectual property rights therein shall at all times remain the exclusive property of John Wiley & Sons Inc, the Wiley Companies, or their respective licensors, and your interest therein is only that of having possession of and the right to reproduce the Wiley Materials pursuant to Section 2 herein during the continuance of this Agreement. You agree that you own no right, title or interest in or to the Wiley Materials or any of the intellectual property rights therein. You shall have no rights hereunder other than the license as provided for above in Section 2. No right, license or interest to any trademark, trade name, service mark or other branding ("Marks") of WILEY or its licensors is granted hereunder, and you agree that you shall



not assert any such right, license or interest with respect thereto

- NEITHER WILEY NOR ITS LICENSORS MAKES ANY WARRANTY OR REPRESENTATION OF ANY KIND TO YOU OR ANY THIRD PARTY, EXPRESS, IMPLIED OR STATUTORY, WITH RESPECT TO THE MATERIALS OR THE ACCURACY OF ANY INFORMATION CONTAINED IN THE MATERIALS, INCLUDING, WITHOUT LIMITATION, ANY IMPLIED WARRANTY OF MERCHANTABILITY, ACCURACY, SATISFACTORY QUALITY, FITNESS FOR A PARTICULAR PURPOSE, USABILITY, INTEGRATION OR NON-INFRINGEMENT AND ALL SUCH WARRANTIES ARE HEREBY EXCLUDED BY WILEY AND ITS LICENSORS AND WAIVED BY YOU.
- WILEY shall have the right to terminate this Agreement immediately upon breach of this Agreement by you.
- You shall indemnify, defend and hold harmless WILEY, its Licensors and their respective directors, officers, agents and employees, from and against any actual or threatened claims, demands, causes of action or proceedings arising from any breach of this Agreement by you.
- IN NO EVENT SHALL WILEY OR ITS LICENSORS BE LIABLE TO YOU OR ANY OTHER PARTY OR ANY OTHER PERSON OR ENTITY FOR ANY SPECIAL, CONSEQUENTIAL, INCIDENTAL, INDIRECT, EXEMPLARY OR PUNITIVE DAMAGES, HOWEVER CAUSED, ARISING OUT OF OR IN CONNECTION WITH THE DOWNLOADING, PROVISIONING, VIEWING OR USE OF THE MATERIALS REGARDLESS OF THE FORM OF ACTION, WHETHER FOR BREACH OF CONTRACT, BREACH OF WARRANTY, TORT, NEGLIGENCE, INFRINGEMENT OR OTHERWISE (INCLUDING, WITHOUT LIMITATION, DAMAGES BASED ON LOSS OF PROFITS, DATA, FILES, USE, BUSINESS OPPORTUNITY OR CLAIMS OF THIRD PARTIES), AND WHETHER OR NOT THE PARTY HAS BEEN ADVISED OF THE POSSIBILITY OF SUCH DAMAGES. THIS LIMITATION SHALL APPLY NOTWITHSTANDING ANY FAILURE OF ESSENTIAL PURPOSE OF ANY LIMITED REMEDY PROVIDED HEREIN.
- Should any provision of this Agreement be held by a court of competent jurisdiction to be illegal, invalid, or unenforceable, that provision shall be deemed amended to achieve as nearly as possible the same economic effect as the original provision, and the legality, validity and enforceability of the remaining provisions of this Agreement shall not be affected or impaired thereby.
- The failure of either party to enforce any term or condition of this Agreement shall not constitute a waiver of either party's right to enforce each and every term and condition of this Agreement. No breach under this agreement shall be deemed waived or excused by either party unless such waiver or consent is in writing signed by the party granting such waiver or consent. The waiver by or consent of a party to a breach of any provision of this Agreement shall not operate or be construed as a waiver of or consent to any other or subsequent breach by such other party.
- This Agreement may not be assigned (including by operation of law or otherwise) by you without WILEY's prior written consent.

- Any fee required for this permission shall be non-refundable after thirty (30) days from receipt by the CCC.
- These terms and conditions together with CCC's Billing and Payment terms and conditions (which are incorporated herein) form the entire agreement between you and WILEY concerning this licensing transaction and (in the absence of fraud) supersedes all prior agreements and representations of the parties, oral or written. This Agreement may not be amended except in writing signed by both parties. This Agreement shall be binding upon and inure to the benefit of the parties' successors, legal representatives, and authorized assigns.
- In the event of any conflict between your obligations established by these terms and conditions and those established by CCC's Billing and Payment terms and conditions, these terms and conditions shall prevail.
- WILEY expressly reserves all rights not specifically granted in the combination of (i) the license details provided by you and accepted in the course of this licensing transaction, (ii) these terms and conditions and (iii) CCC's Billing and Payment terms and conditions.
- This Agreement will be void if the Type of Use, Format, Circulation, or Requestor Type was misrepresented during the licensing process.
- This Agreement shall be governed by and construed in accordance with the laws of the State of New York, USA, without regards to such state's conflict of law rules. Any legal action, suit or proceeding arising out of or relating to these Terms and Conditions or the breach thereof shall be instituted in a court of competent jurisdiction in New York County in the State of New York in the United States of America and each party hereby consents and submits to the personal jurisdiction of such court, waives any objection to venue in such court and consents to service of process by registered or certified mail, return receipt requested, at the last known address of such party.

## **WILEY OPEN ACCESS TERMS AND CONDITIONS**

Wiley Publishes Open Access Articles in fully Open Access Journals and in Subscription journals offering Online Open. Although most of the fully Open Access journals publish open access articles under the terms of the Creative Commons Attribution (CC BY) License only, the subscription journals and a few of the Open Access Journals offer a choice of Creative Commons Licenses. The license type is clearly identified on the article.

### **The Creative Commons Attribution License**

The [Creative Commons Attribution License \(CC-BY\)](#) allows users to copy, distribute and transmit an article, adapt the article and make commercial use of the article. The CC-BY license permits commercial and non-

### **Creative Commons Attribution Non-Commercial License**

The [Creative Commons Attribution Non-Commercial \(CC-BY-NC\) License](#) permits use, distribution and reproduction in any medium, provided the original work is properly cited and is not used for commercial purposes.(see below)

### **Creative Commons Attribution-Non-Commercial-NoDerivs License**

The [Creative Commons Attribution Non-Commercial-NoDerivs License](#) (CC-BY-NC-ND) permits use, distribution and reproduction in any medium, provided the original work is properly cited, is not used for commercial purposes and no modifications or adaptations are made. (see below)

**Use by commercial "for-profit" organizations**

Use of Wiley Open Access articles for commercial, promotional, or marketing purposes requires further explicit permission from Wiley and will be subject to a fee.

Further details can be found on Wiley Online Library

<http://olabout.wiley.com/WileyCDA/Section/id-410895.html>

**Other Terms and Conditions:**

**v1.10 Last updated September 2015**

**Questions? [customercare@copyright.com](mailto:customercare@copyright.com) or +1-855-239-3415 (toll free in the US) or +1-978-646-2777.**

---

---